Inorganic geochemical characterisation of the Cretaceous source rocks of the Eastern Cordillera, Colombia

Carol Ann Mahoney

Supervised by Prof. Tom Wagner, Dr Christian März and Vladimir Blanco

Thesis submitted to Newcastle University in partial fulfilment of the requirements for the degree of Doctor of Philosophy in the Faculty of Science, Agriculture and Engineering

School of Natural and Environmental Sciences

June 2018

Abstract

The depositional environment of organic-rich mudstones in the Cretaceous greenhouse climate is a key area of Earth Systems and Energy research, as understanding the causes of carbon drawdown into these rocks has impacts for understanding the role of the carbon cycle in climate change and the formation of petroleum source rocks. The Eastern Cordillera basin in Colombia is a key region for investigating Cretaceous carbon burial in flooded continental areas and tropical regions. Both characteristics are essential to understanding the Cretaceous carbon cycle, a key question being: are the mechanisms which cause carbon burial in the open ocean similar those in more continental, tropical basins? To date, the EC is understudied, partly due to the basin's complex history, which includes deep burial (compromising organic geochemical analysis) and uplift (complicating geological reconstruction and exposing rocks to contemporary weathering, hence compromising inorganic geochemistry).

In this thesis, a combination of inorganic geochemical methods (bulk geochemistry, trace metal enrichment patterns, iron-sulphur speciation) with high-resolution electron microscopy and chemical micro-analysis is applied to a unique set of Cretaceous mudrock samples from the EC with the ultimate aim of a detailed paleoenvironmental reconstruction. In a first step, an artificial weathering experiment is presented and, following interrogation of the geochemical dataset, novel filters (carbonate content and passivated pyrite particles) are presented which identify samples from Eastern Cordillera mudstones less likely to have been geochemically altered by weathering. This allows, in a second step, the robust interpretation of redox conditions, productivity and climate in the Cretaceous Eastern Cordillera basin based on bulk geochemistry, trace elements and Fe-speciation for 208 new samples from 12 different outcrops across the basin. Also, it provides a methodology for future investigations using outcrop samples globally.

New evidence is presented that the Eastern Cordillera was anoxic in the Valanginian (different from open ocean sites), likely due to the sites more restricted nature. In the Mid-Late Cretaceous, extremely high and prolonged siliceous and calcareous productivity drove anoxia and carbon burial. Evidence is presented that sources of nutrients to drive this productivity resulted from upwelling (Albian and Santonian); intensive chemical weathering of land (especially in the Turonian); and possibly volcanogenic sources

(Cenomanian/Turonian boundary). In most cases, these mechanisms occur in other time equivalent facies, therefore this study suggests that global changes in climate and geochemistry of the oceans heavily influenced organic matter deposition in the Eastern Cordillera.

Declaration

This project was partly funded by Ecopetrol S.A. as part of a wider project aiming to model source rock variability in the study area. As such, much information, data and all of the sample material was provided by Ecopetrol and its subcontractors. This PhD is associated within another (Marin-Barba), working on the same samples, but concentrating on organic geochemistry. Where data have been provided by Ecopetrol, its subcontractors or from the associated PhD it is stated the text. Measurements of XRF were carried out at the ICBM laboratory in Oldenburg by Bernhard Schnetger and colleagues. The SEM work was carried out at Heriot Watt University under much guidance by Jim Buckman.

Acknowledgements

This PhD was carried out as part of a wider project to model organic facies distribution in the Eastern Cordillera of Colombia. I therefore am indebted to Vladimir Blanco and Ecopetrol for the inception and funding of this project as well as the School, who provided additional funding. I am especially grateful to the technical help, encouragement, support and patience of my supervisors, Dr Christian März and Tom Wagner. Also, I would like to thank another member of the team, PhD student Patricia Marin-Barba, for collaboration in preparation of the samples and useful discussions about this project.

Many thanks go to Bernhard Schnetger (University of Oldenburg) and his team who carried out the XRF analysis (often to tight deadlines) and provided assistance with interpretation. At Newcastle University, I would have achieved little without the help of Phil Green, Dave Earley and Bernie Bowler. I also would like to thank James Smith, who helped me grind the samples, and MSc student Taiwo Ishmail who prepared and analysed a subset of samples. Gerben de Jager was very generous with his time and knowledge explaining the process of organofacies modelling, in Newcastle and the lovely Trondheim. Jim Buckman assisted me greatly in using SEM EDX and put a lot of effort into generating large scale EDX maps.

This thesis involved a short period in Colombia. Here, I had great help getting to grips with the geology and living in Bucaramanga from Sebastian Luna Osorio, Claudia Juliana Orejuela Parra, Maria Alejandra Naranjo Calderon and Rolando Ramirez. Andres Mora and Hernan Dario Madero Pinzon were fantastic field guides in the wild and wonderful terrane of the Eastern Cordillera. I would like to especially thank Adriana Dueñes Garcés and her relatives

for being extremely hospitable and making me feel part of their family when I was far from mine.

I would like to acknowledge the community of PhD students in Drummond, who were always willing to lend an ear and share a tea whenever needed. My family, as always, have provided unwavering support during my PhD and all of my ventures. I would also like to especially thank Christian Tucker, who has been patient, supportive and encouraging throughout.

Contents

Table of Figures and Tables

Figures

Tables

Chapter 1 Introduction

1.1 Carbon Burial, Earth's Climate and Cretaceous Greenhouse oceans

During Earth's history, the global climate has been heavily regulated by the amount of greenhouse gases present in the atmosphere (Arrhenius, 1896; Barnola et al., 1987). In modern times, it is most likely that current trends of global warming are intrinsically linked to anthropogenic release of CO_2 and other greenhouse gases (IPCC, 2015). Over geological timescales, however, the amount of CO_2 in the atmosphere is regulated by the carbon cycle which comprises fluxes and long term sinks of carbon (Figure 1.1), with ocean sediments being major sinks (Mackenzie and Lerman, 2006). In marine sediments carbon is stored as inorganic carbon and organic carbon. The mechanisms leading to burial of organic carbon rich rocks in marine settings from the Cretaceous equatorial Atlantic Ocean is the subject of this thesis.

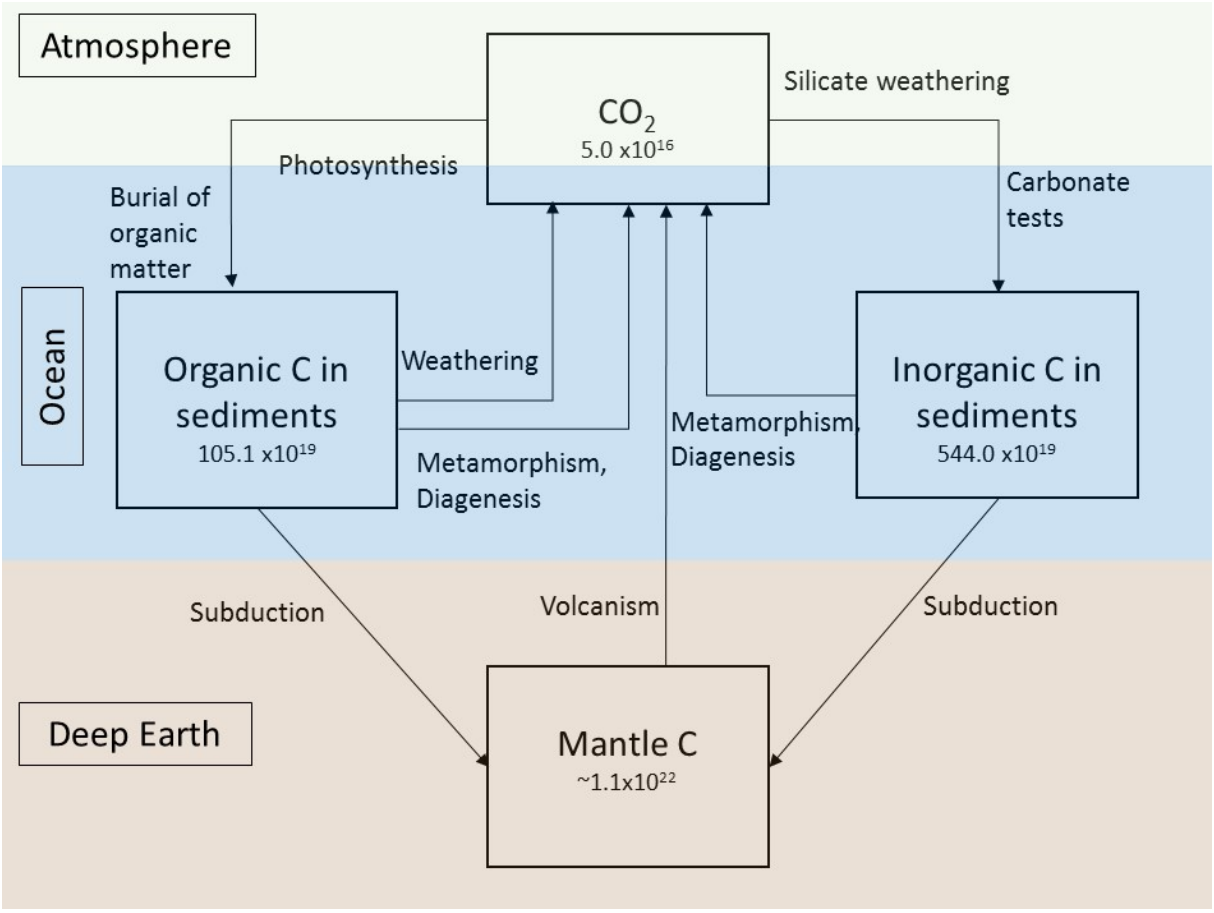

Figure 1.1.1. Carbon cycle from Berner, 2003. Values are estimates of carbon sink, as mol C from Mackenzie and Lerman, 2006 (Mantle C is an estimate for upper mantle).

The principle causes for organic rich sediment deposition are proposed to be: influxes of nutrients leading to increased primary productivity (and so increased flux of marine organic matter to the sediment); enhanced organic matter preservation (caused by bottom water

anoxia); and/or a decrease in dilution by inorganic material (carbonates or silicates). The relative importance of each factor has been the topic of intense and controversial debate (Demaison and Moore, 1980; Pedersen and Calvert, 1990; Trabucho Alexandre et al., 2010; Tyson, 2005; Negri et al., 2009). Understanding the driving forces behind organic matter production and accumulation is important for understanding the regulation of carbon dioxide in the atmosphere over geological and shorter timescales (Berner, 2003). It is also particularly important for the petroleum industry. With greater understanding of the interplay of these factors, modelling tools can be developed to predict the location and nature of potential source rocks and better constrain petroleum systems (e.g. Mann and Zweigel, 2008).

The Cretaceous period, from about 145 to 65 million years ago, is exceptional in the frequent occurrence and wide spatial coverage of organic rich marine sediments (Negri et al., 2006). In fact, the majority of known source rocks for conventional oil are Cretaceous in age (Tiratsoo, 1986). The extent of carbon burial had significant impacts on regulating the atmospheric concentration of CO_2 and thus global climate (e.g. Kuypers et al., 1999). The latter makes understanding the circumstances of organic rich sediment formation during past super-greenhouse conditions important for understanding the most extreme consequences and feedbacks caused by anthropogenic CO_2 release.

The Cretaceous was characterised by a “global greenhouse climate”, with sea surface temperatures (SST) higher than 35 °C and deep water temperatures of up to 20 °C (Jenkyns, 1994; Huber et al., 2002; Friedrich, 2012). It was also a time of globally high sea levels, up to 250 m higher than at present (Haq, 2014). The high SST and air temperatures were likely caused by CO_2 release from extensive volcanism and increased spreading rates at mid ocean ridges (Weissert and Erba, 2004; Barron et al., 1995; Larson, 1991; Leckie et al., 2002; Caldeira and Rampino, 1991).

Conditions in this Cretaceous greenhouse world favoured the accumulation of organic matter by increasing nutrient supply and primary productivity (with nutrients delivered directly from volcanism, increased upwelling of deep water masses, or chemical weathering driven by high temperatures/increased hydrological cycle) and/or by increasing preservation of organic matter in oxygen-depleted environments (due to sluggish thermohaline circulation, increased stratification via freshwater lids, widespread oxygen minimum zones due to expansion of flooded shelf, or the lower capacity of warm, saline oceans to hold

dissolved oxygen) (de Graciansky et al., 1984; Erbacher et al., 2001; Schlanger and Jenkyns, 1976; Brass et al., 1982; Föllmi, 2012; Arthur and Sageman, 1994; Beckmann et al., 2005; Hofmann and Wagner, 2011; Trabucho Alexandre et al., 2010). These processes were intensified during distinct periods in the Cretaceous when organic matter accumulation was more extreme and spatially extensive. These are termed oceanic anoxic events (OAE's, Schlanger and Jenkyns, 1976) and are the subject of much research because of the extremity of the extent carbon burial and the profundity of the climate change they represent. There are three major OAE's in the Cretaceous, the early Aptian OAE 1a, the early Albian OAE 1b, and the Cenomanian-Turonian boundary event (OAE 2), and the severity of carbon drawdown during these episodes had a profound effect on the carbon cycle and atmosphere.

1.2 Why study Colombian Cretaceous Shales? Global v local causes and consequences

Studies investigating the mechanisms behind organic matter burial in the Cretaceous have mostly focused on the open oceans as in these locations continuous and thick sequences of sediments can be found (i.e. sediments recovered by the deep sea drilling initiatives DSDP, ODP and IODP). In contrast, less work has been carried out on flooded continental areas (i.e. continental shelves and epicontinental seaways). However, such shallow areas are vital for understanding the Cretaceous carbon cycle, especially as shallow seas are sites of high organic matter burial rates in the modern ocean (Tyson and Pearson, 1991) and were likely of equal, or greater, importance in the Cretaceous (Hay et al., 2017). Most studies on flooded continental areas during the Cretaceous are concentrated at the mid-latitudes representing relatively temperate climate conditions (e.g. the Western Interior Seaway, English Chalk and Saxony Basin (e.g. Sageman et al., 2006; Jenkyns et al., 1994; Hetzel et al., 2011)). Low latitude sites representing tropical climates are less well studied. There is some evidence of a more equable climate during the Cretaceous with temperatures at high latitudes considerably higher, but at low latitudes, they may have been relatively comparable to today (Ruddiman, 2001; Wilson et al., 2002). Although the tropics seem to be resistant to increases in temperature, changes in the hydrological cycle have feedbacks which effect the tropics particularly. Being zones of intense precipitation and continental freshwater discharge, the tropics are sensitive to modest increases in runoff caused by an enhanced hydrological cycle. This can have variable effects, for example, switching sheltered basins into anoxic mode via the creation of freshwater lids (e.g off the Ivory Coast, Beckmann et al., 2005). Comparing tropical sites off Africa and South America suggests the

continent of South America may have been less sensitive to climatic changes, with less variable detrital input being recorded in marine sediments, however more sites in this location are required to understand the mechanism for these observations (Flögel et al., 2008). The Tropics are also loci for atmospheric heat and moisture transport via Hadley Cells. Although evidence is apparent that Hadley cells varied in size and stability over the Cretaceous with Milankovitch cycles, the consequences of these changes are not well constrained (Hoffman and Wagner, 2011; Wagner et al., 2013.

In this context, the following study investigates the paleodepositional environment of a Cretaceous, equatorial, epicontinental basin in Colombia – the Eastern Cordillera (EC). Here, thick organic rich sediment sequences were repeatedly deposited during the Cretaceous (e.g. the Macanal Formation with up to 5% TOC (this study) and up to 2.5 km thickness, Sarmiento-Rojas et al., 2006; Mora et al., 2015). These black shale sediments likely expelled significant quantities of oil, and have been suggested as a source of actively exploited oil reservoirs in Colombia's Llanos basin (Garcia, 2008; Dzou, 1999), where 73% of all oil produced in Colombia is located (EIA, 2014). Whilst there is a body of work reconstructing the depositional environment of the associated Venezuelan basins, with a focus on the La Luna shale as the main hydrocarbon source rocks in the Maracaibo basin (Erlich et al., 1999; Lo Monaco et al., 2002; Alberdi-Genolet and Tocco, 1999; Rey et al., 2004; Davis et al., 1999; Mongenot et al., 1996; Tribovillard et al., 1991; Perez Infante et al., 1996), the EC basin is understudied, especially from a geochemical point of view. The few published inorganic geochemical investigations are mostly centred on one or two locations (Villamil, 1996; Villamil and Arango, 1998; Villamil, 1999; Narvaez et al., 2013; Alvarez and Roser, 2007, Föllmi, 1992) leaving large uncertainties about the expression and sedimentological-geochemical properties of the source rocks along the EC. Therefore, the study presented here is pioneering research into the shallow tropical Cretaceous EC seaway by providing critical new data to reconstruct the paleoenvironmental conditions, as well as the causes and consequences of organic rich sediment deposition.

At a more generic level, the EC basin is well suited to investigate the potential impacts and interplay of productivity, preservation, and dilution on organic rich deposits. The basin had various and potentially changing sources for nutrients during different periods of the Cretaceous, providing an interesting example of a dynamic depositional setting. According to the conceptual model of Trabucho Alexandre et al. (2010), the proto north-Atlantic received

and effectively trapped nutrients from the Caribbean Large Igneous Province (CLIP) during the mid-Cretaceous Cenomanian-Turonian period. As will be evaluated in this study, these 'CLIP nutrients' may well have also influenced organic carbon production and deposition in the EC. The basin was relatively narrow and long (approximately 250 km long and 150 km wide during Early Cretaceous according to palinspastic reconstructions of Mora et al (2015)), and bordered by land masses in the east towards the Pacific and the cratonic Guyana Shield in the west. In such a geographically restricted marine setting it is likely that the effects of changing wind patterns as well as continental runoff, both key mechanisms to supply nutrients and enhance marine productivity (Wagner et al., 2013), should be well expressed in the sedimentary record. Previous studies in Venezuela emphasise the migration of northern South America across the equator as a critical component to increase in upwelling and widespread siliceous algal productivity in the EC (Villamil et al., 1999; Erlich et al., 1999). Connecting the northward migration of the EC to increases in upwelling may help constrain the influence of these long term geological processes on enhanced productivity and carbon burial. In addition, the rather restricted geometry of a sedimentary basin may have been conducive to support seafloor and bottom water anoxia which, in turn, would have affected nutrient mobilisation and organic matter preservation (e.g. Demaison and Moore, 1980). The EC developed from an Early Cretaceous basin bound by steep sided faults, likely disconnecting the deep waters from more open ocean (generating a silled EC basin similar to the modern Black Sea), to part of a wide marine basin during times of high sea level, which covered the whole of northern South America (generating an epicontinental sea similar to the Cretaceous Western Interior Seaway, Sarmiento-Rojas et al., 2006; Macellari et al., 1988). Both of these basin features would have supported seafloor and bottom water anoxia, modulated and potentially triggered by different climatic scenarios. These changing geometric and climatic boundary conditions may, at times, have isolated the basin from the open oceans. This may have resulted in the basin being shielded from shifts in ocean biogeochemistry which occurred during the OAE's or the influence of nutrients supplied from hydrothermal sources.

Three major episodes or organic matter burial are recorded in the Cretaceous EC and surrounding basins, which led to the formation of organic rich mudstone formations (and potential petroleum source rocks): i) the Berriasian and Valanginian Macanal Formation, (ii) the Hauterivian to Albian Fomeque Formation and (iii) the Cenomanian to Campanian

Chipaque Formation. With this rich archive of black shale deposits the EC offers a unique repository of information about organic matter deposition.

1.3 Approach for investigating the paleoenvironment

Geochemistry can provide much information about the varying factors which control the deposition of organic rich rocks. The type and amount of organic matter contained within the rocks can be determined via bulk geochemical techniques like Rock-Eval (Tissot and Welte, 1984). Fossil organic molecules are also preserved which can give specific information about the types of organisms living in the water column, and the associated paleoenvironment (e.g. isorenieratene and its derivatives for tracing photic zone euxinia, Sinninghe Damsté et al., 2001). Unfortunately, most of these biomarkers and bulk geochemical properties are altered or are expelled from the rock once it is buried and heated within the oil window (e.g. Farrimond et al., 1998). The majority of the rocks within the EC have been buried through the oil window (to a depth of up to 8.5 km) and so the application of organic geochemistry is very challenging and limited (Sanchez et al., 2015; Mora et al., 2015)

A partner PhD project to this study has concentrated on organic geochemistry and attempts to address these issues of maturity by searching for novel, thermally recalcitrant fossil organic molecules in EC mudrocks (Marin-Barba, 2018). To complement and further advance the paleoenvironmental interpretation of the EC, this project combines inorganic geochemistry and high resolution imaging coupled to element mapping. The strategic advantage of this approach is that it is less effected by thermal maturity (Mongenot et al., 1996), providing information which are no longer extractable from organic variables.

The element distribution within marine sediments informs about the nature and quantity of detrital material arriving at the basin and so dilution. This, in turn, is related to the provenance of the material, the climate in the hinterland, and sea level (e.g. Nesbitt and Young, 1982, Erlich et al., 1999; Campos Alvarez and Roser et al., 2007). Studies have shown that when the climate is humid, the hinterland becomes more extensively chemically weathered which supplies a greater amount of nutrients to the marine environment. This, in turn, actively increases productivity, linking the type of detrital mineral to the amount of organic material being deposited in the marine sediments (e.g. Schnieder et al., 1997; Zabel et al., 2001; Flögel et al., 2008; Beckmann et al., 2003; Hofmann and Wagner; 2013).

Inorganic geochemistry also provides critical information about variations in primary productivity, and hence the amount of organic material arriving at the sediment. For example, the shells/tests of organisms can make up the bulk of sediments deposited in high productivity settings (evident in the $CaCO_3$ or Si content). Other elements, including P, Cu, Ni and Zn, accumulate in sediments in high productivity settings due to their association with organic matter.

It is also well known that certain elements are enriched in anoxic sediments either because they change to insoluble species in a reducing environment (e.g. U, V), become more particle reactive (e.g. Cr and Mo), and/or form sulphides alongside sulphate reducing bacterial respiration in an oxygen limited environment (e.g. Fe) (Erickson and Helz, 1999; Elderfield, 1970; Wanty and Goldhaber, 1992; Klinkhammer and Palmer, 1990; Berner, 1970). Due to their response to redox conditions, these elements are powerful proxies for the identification of deposition under low oxygen (anoxic) or even euxinic ocean and pore water conditions (Poulton and Canfield, 2005; Calvert and Pedersen, 2007; Brumsack, 2006; Tribovillard et al., 2006).

This study goes one step further and applies a novel approach to investigating geochemistry on a much finer scale. Light microscopy is a standard approach to investigating coarser grained sedimentary rocks, but is of limited use when investigating fine grained lithologies, like mudstones. The higher magnification and resolution of scanning electron microscopy (SEM) is ideal for examining sedimentological features of mudstones, and its use is increasing alongside a rising interest in mudstones as unconventional source rocks/reservoirs (Camp et al., 2013). In back-scattered electron mode, SEM provides information about micrometre scale sedimentary structures, and therefore information about the depositional environment (e.g. presence or absence of bioturbation, location of pyrite framboids – dispersed versus concentrated within isolated sulphate reducing environments). When SEM is linked with energy-dispersive X-ray spectroscopy (SEM-EDX) and automated particle analysis, it develops into a powerful tool providing chemical and physical characteristics of 1000's of sediment particles on the millimetre to micron scale, which can be linked to the bulk geochemistry of the sediment horizon. For example, when those particles are pyrite framboids, the size information can be a proxy for water column euxinia (Wilkin et al., 1996).

Armed with this suite of inorganic and sedimentological proxies for anoxia, productivity and

detrital material volume and composition, this study sets out to enhance the interpretation of the paleodepositional environment in the Cretaceous EC. It is noteworthy, that these inorganic geochemical and imaging data are interpreted alongside field observations of sedimentary structures and lithology, provided by field geologists sub-contracted to the sponsor of this study, Ecopetrol in Colombia. These detailed field notes enable to ground truth the new geochemical data.

1.4 Fundamental Challenges

The basin in which the EC Cretaceous sediments were deposited has experienced deep burial, but this was followed by tectonic inversion and the establishment of the eastern of three Andean mountain ranges in Colombia. This poses fundamental challenges to this study, as the majority of the inorganic proxies selected to investigate anoxia and productivity are only reliable when taken from pristine samples which have not been exposed to air or water during contemporary weathering. The samples studied within this thesis have been exposed to weathering at outcrop in a tropical location and so may have lost Fe and TE through oxidative reactions and dissolution (e.g. Perkins and Mason, 2015; Pye and Miller, 1990; Tuttle and Breit, 2009; Zhu et al. 2008; Zhu and Wu, 2012). This process is often overlooked in studies using outcrop samples, turning this challenge into an opportunity to investigate how strongly paleo proxies are impacted by contemporary weathering and geochemical alteration. Artificial weathering experiments are conducted in this study to measure and quantify the effects of outcrop weathering on geochemical proxies. Using geochemical and visual data pre and post artificial weathering it is possible to identify proxies which may have been more affected by weathering and therefore rank proxies by weathering resilience. Also, the sample set is interrogated in order to identify particular lithologies which may be more resistant to contemporary weathering. Armed with this new knowledge a more reliable paleoenvironmental interpretation is offered as a key achievement of this study. Identifying proxies or lithologies more resistant to the influence of contemporary weathering is critical not only for this study, but also allows confident interpretation of proxies in other study areas, expanding temporal and spatial coverage of paleoenvironmental data.

1.5 Summary and thesis outline

This thesis explores the depositional environment of the EC basin throughout the Cretaceous. It is the first detailed and comprehensive study which uses newly collected

outcrop sediment material from multiple locations in the EC to link the paleo depositional environment of the EC to the wider Cretaceous world. The unique geography of the basin provides new insights into the mechanisms of organic matter burial during the Cretaceous period. The extreme level of outcrop weathering led to detailed investigations on the effects of contemporary weathering on inorganic proxies, and their impact on paleoenvironmental reconstructions. Building on an introduction to fundamental background information (chapters 1-3) the different chapters of this study aim to answer key questions:

Chapters 4 and 5

- Are some inorganic proxies more reliable than others in outcrops exposed to oxidative weathering?
- Are there mechanisms which limit contemporary weathering, and can they be used to decide if a sample is likely to have been affected by weathering?

Chapters 6-8

- Is the paleoenvironment inherently different in the EC compared to other time-equivalent basins due to the more restricted and equatorial position?

Chapter 2 Geological Context for Cretaceous Sedimentation in the Eastern Cordillera Basin of Colombia

This chapter provides a geological context for the samples that are discussed in this thesis. It will introduce the Eastern Cordillera basin in general, before summarising what is known about how the basin changed over time with rifting, sea level changes, and finally compression and uplift. The basin will also be discussed as part of the wider depositional system which covered northern South America during the Cretaceous. The location of the basin over time, as it moved from the Southern to the Northern Hemisphere will be tracked, and connections to the open oceans will be discussed.

2.1 Introduction

The Eastern Cordillera (EC) basin is a back-arc basin of the ancestral Central Cordillera, Figure 2.1 (Sarmiento-Rojas et al., 2006; Maze et al., 1984; Cortés et al., 2006; Cooper et al., 1995). The Eastern Cordillera was connected to the ocean via the now closed Colombia Marginal Sea and was variably separated from the Caribbean by the ancestral Central Cordillera (Figure 2.1). During periods of high sea level in the Cretaceous, the EC was also part of a wider depositional system covering the whole of northern South America, connecting the EC to the proto-Atlantic in the North and the Pacific in the South (Macellari, 1988; Erlich et al., 2003). The EC is bordered by the Middle Magdalena Basin (MMB) in the West, the Llanos Basin in the East, the Upper Magdalena Valley (UMV) in the South, and the Catatumbo Basin (and other Western Venezuelan Basins) in the North (Cooper et al., 1995). The EC itself is subdivided into three subbasins (Figure 2.1) two of which (Cocuy and Tablazo-Magdalena basin) were at times separated by the Santander-Floresta Massif paleo high (Sarmiento, 2001). Detrital material arrived at the basin variously from the emergent Central Cordillera in the West and the Santander-Floresta Massif in the centre of the basin, but predominantly from the Guyana Shield in the East (Sarmiento-Rojas et al., 2006; Villamil, 1996; Macellari, 1988). Areas of sediment deposition were bound by normal faults which were the loci of active rifting in the early Cretaceous, and of passive thermal subsidence in the late Cretaceous (Fabre, 1987; Mora et al., 2015). This rifting/subsidence, combined with generally high sea levels during the Mid-Cretaceous, provided accommodation space for up to six km of sediments (Cooper et al., 1995; Sarmiento-Rojas et al., 2006; Mora et al., 2015). During the Cretaceous, three depositional periods were dominated by shale. The Berriasian to Valanginian (identified as the Lutitas de Macanal in the EC), the Hauterivian to Albian (the Fomeque in the EC), and the Cenomanian to Campanian (the Chipaque in the EC) Figure 2.2.

The basin characteristics during these shale depositional periods will be discussed in this chapter.

Following deposition of the studied sedimentary formations in the Cretaceous, interactions between the South American continental plate and the Nazca and Caribbean oceanic plates in the early Cenozoic caused contraction, and normal faults previously associated with rifting were reactivated and inverted, exhuming the Eastern Cordillera mountain range from the Miocene/Oligocene (Cooper et al., 1995; Cortés et al., 2006; Mora et al., 2015 and 2006; Sarmiento-Rojas et al., 2006) Figure 2.3. The magnitude of crustal shortening associated with these orogenic processes is between 50 km (Mora et al., 2015) and > 70 km (Cortés et al, 2004). This shortening, combined with associated folding and faulting, makes it difficult to attribute present-day outcrops in the mountain range to specific locations in the EC paleo basin. Prior to orogenic uplifting, the tectonic compression buried the Cretaceous sediments to depths of up to 8.5 km (Mora et al., 2015), massively overprinting the sediments by thermal maturity. After uplift, the overlying sediments were eroded away, and Cretaceous sediments are now exposed across certain areas of the Eastern Cordillera in road cuttings and stream beds. Deep burial and associated thermal overprint is well known to affect the organic carbon content and composition and clay mineralogy of the original sediments and poses a challenge to paleoenvironmental reconstructions (discussed further in Chapter 3, 6-8). Furthermore, contemporary oxidative weathering of samples exposed at outcrop in the Eastern Cordillera mountain range in a tropical climate may also have affected the geochemistry (discussed further in Chapters 4 and 5).

In addition to structural deformation, the active tectonics that affected the EC basin also caused limited, localised igneous intrusions (Sarmiento-Rojas et al., 2006; Vásquez et al 2010), and hydrothermal fluids moving along faults in the Cenozoic produced mineral deposits (e.g. emeralds in the Macanal in the east and Fomeque equivalent formations in the west - Villamil, 1996; Beus, 1979; Cheilletz and Guiliani 1996). These igneous and hydrothermal processes have the potential to affect the inorganic geochemical composition of the Cretaceous sediments, at least at the local scale, and any related interpretation.

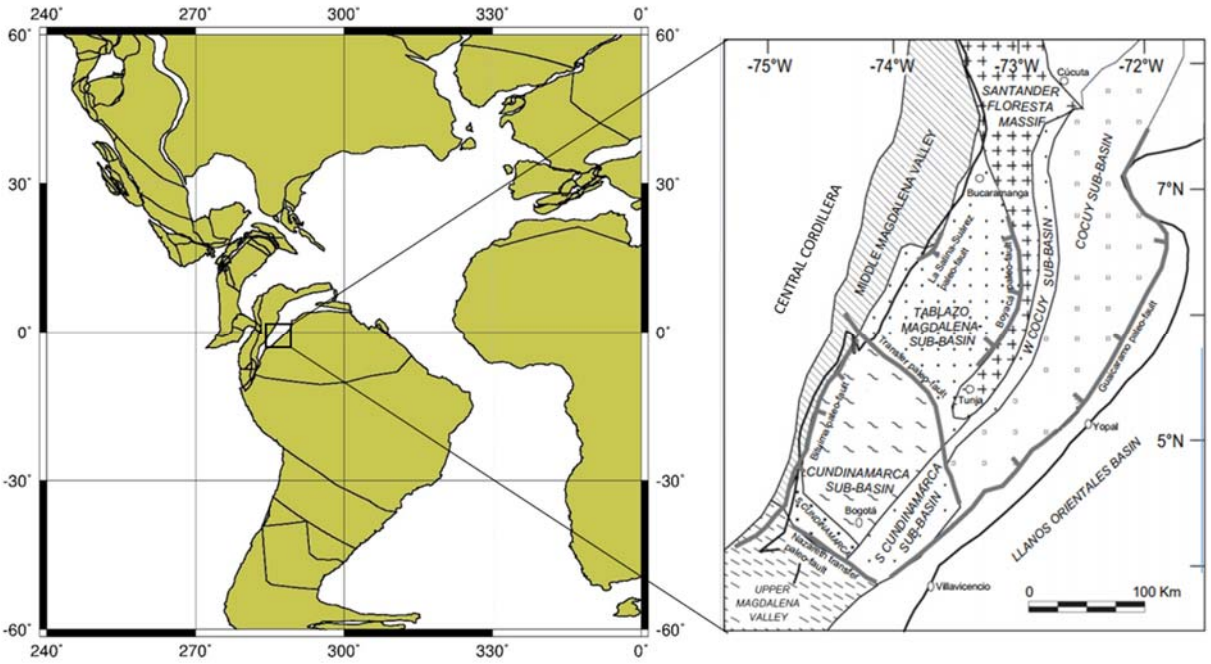

Figure 2.1 Approximate location of study area on a plate tectonic reconstruction from 72 Ma (from http://www.odsn.de/odsn/). Basin detail on right, modified from Vasquez et al., 2009, with modern day latitude and longitude.

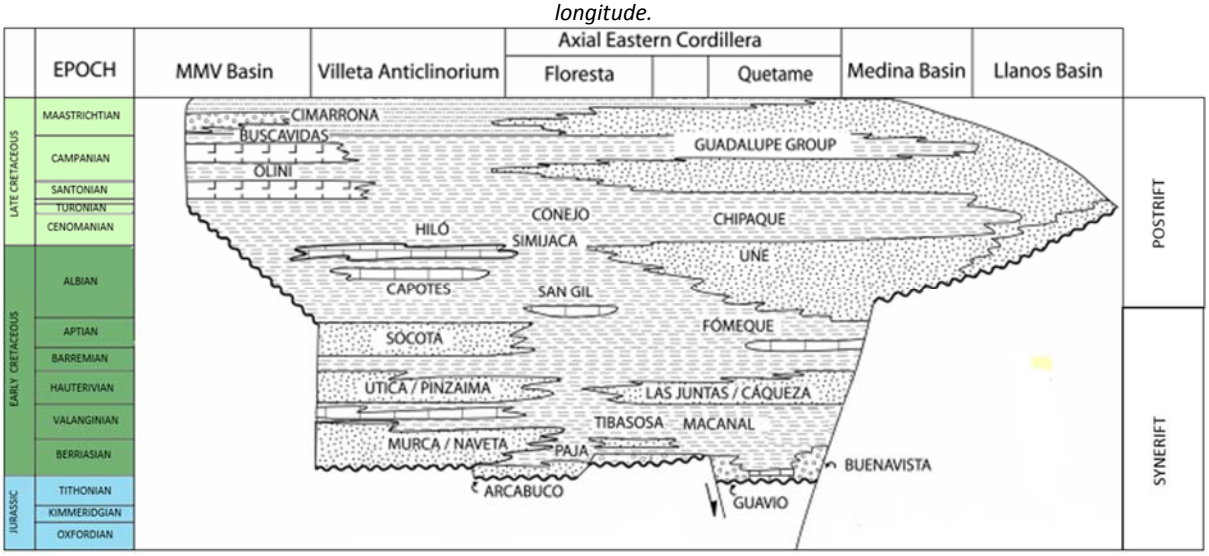

Figure 2.2 Generalised stratigraphy of formations deposited in the EC and adjacent basins. Shales are dashed lines, dots are sandstones, open circles are alluvial fan conglomerates and vertical lines are limestones. Colours of ages are used in Figure 3.1. From Parra et al., 2009.

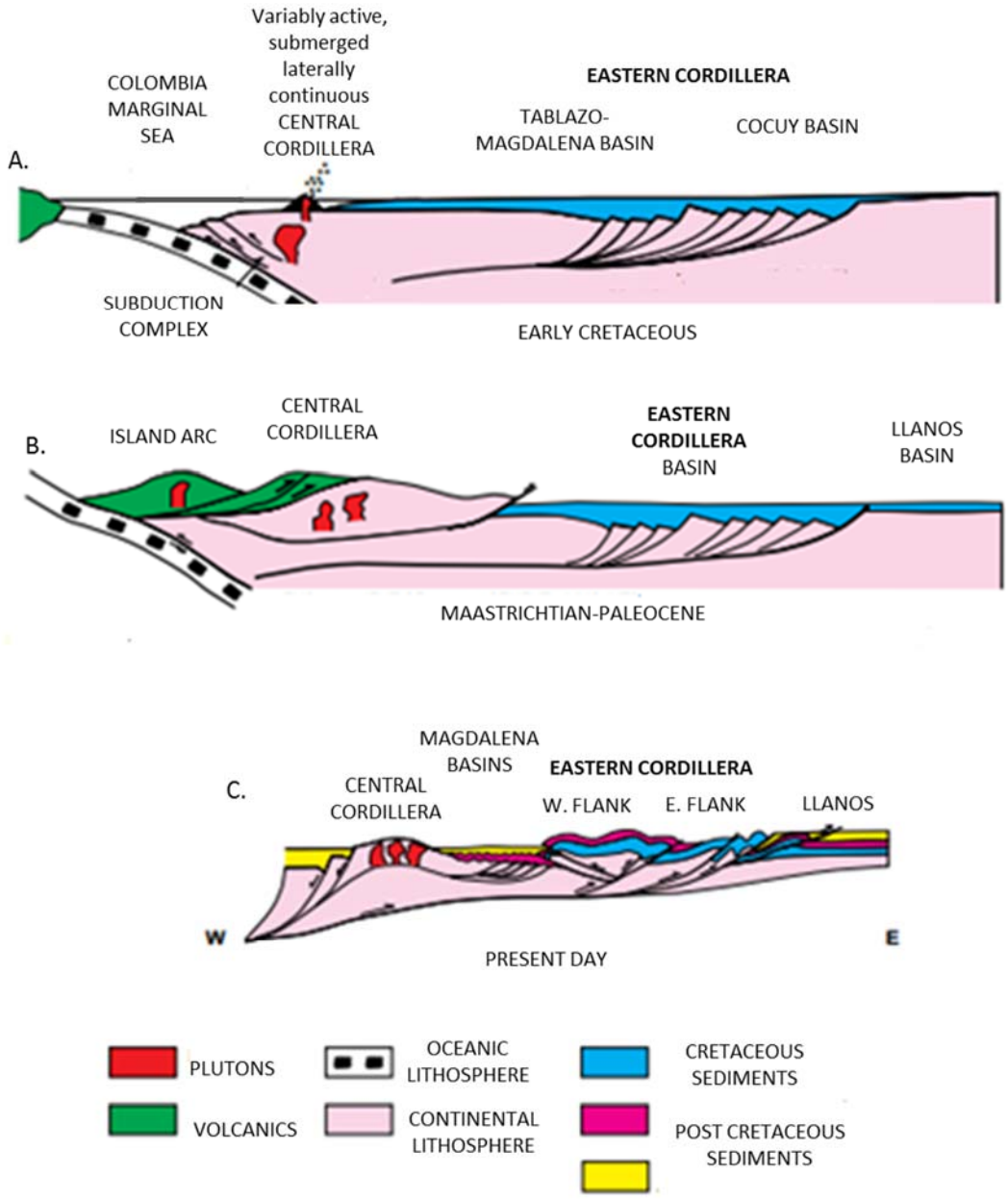

Figure 2.3 Conceptual model for the development of the Eastern Cordillera Basin and orogeny. Modified from Cooper et al., 1995. a. Early Cretaceous deposition in subsiding basin. B. onset of uplift Late Cretaceous, Paleogene. C. Modern day topography in Colombia.

2.2 Depositional Environments in the EC during the Three Shale Dominated Periods

2.2.1 Berriasian to Valanginian – Macanal

The EC basin during this period was actively rifting (Fabre, 1987), allowing deposition of thick sedimentary sequences (up to 2.5 km – Macellari, 1988; Sarmiento-Rojas et al., 2006). The Basin was bounded by steep faults, which limited marine deposition to the Cundinamarca Sub-basin and later the Cocuy and Tablazo Sub-basins (Cooper et al., 1995; Sarmiento-Rojas et al., 2006) Figure 2.1. The fine marine sediments of the Macanal formation were deposited on top of Jurassic/Lower Cretaceous coarse, fluvial material (Sarmiento-Rojas et al., 2006). Until the Valanginian, subsidence exceeded the supply of terrestrial material, leading to retrogradation. In the Valanginian, sediment supply increased, leading to progradation and eventually Hauterivian turbidite fans (Sarmiento-Rojas et al., 2006). A trigger for this change may have been eustatic sea-level fall in the Valanginian (Haq, 2014), although variable rifting rates may have also influenced deposition. During early marine deposition, the Santander-Floresta Massif was a topographic high which may have been a source of detrital material to the adjacent basins (Sarmiento-Rojas et al., 2006), in addition to material derived from the Guyana shield and emergent Central Cordillera (Villamil, 1996) Figure 2.4. Overall, Berriasian to Valanginian basin bathymetry and geometry are sedimentologically expressed by shales in the Cundinamarca basin and the Cocuy basin and shallow marine carbonate and alluvial and fluvial deposits in the Tablazo-Magdalena basin (Figure 2.4). Some evaporite deposits are observed close to Bogotá (Briceño, 1990; Branquet et al., 2002; Cortés et al., 2006). In the rest of Northern South America, deposition was mostly continental material (sandstones and conglomerates) Macellari (1988), therefore connections to the North Atlantic were minimal and Pacific unlikely, however, the site was connected to the Colombian Marginal Sea (Figure 2.3 and 2.4). Based on the plate tectonic reconstructions published by the Ocean Drilling Stratigraphic Network (http://www.odsn.de), the study was located at the western edge of the continent of Gondwana, and was south of the equator during this period (Figure 2.5).

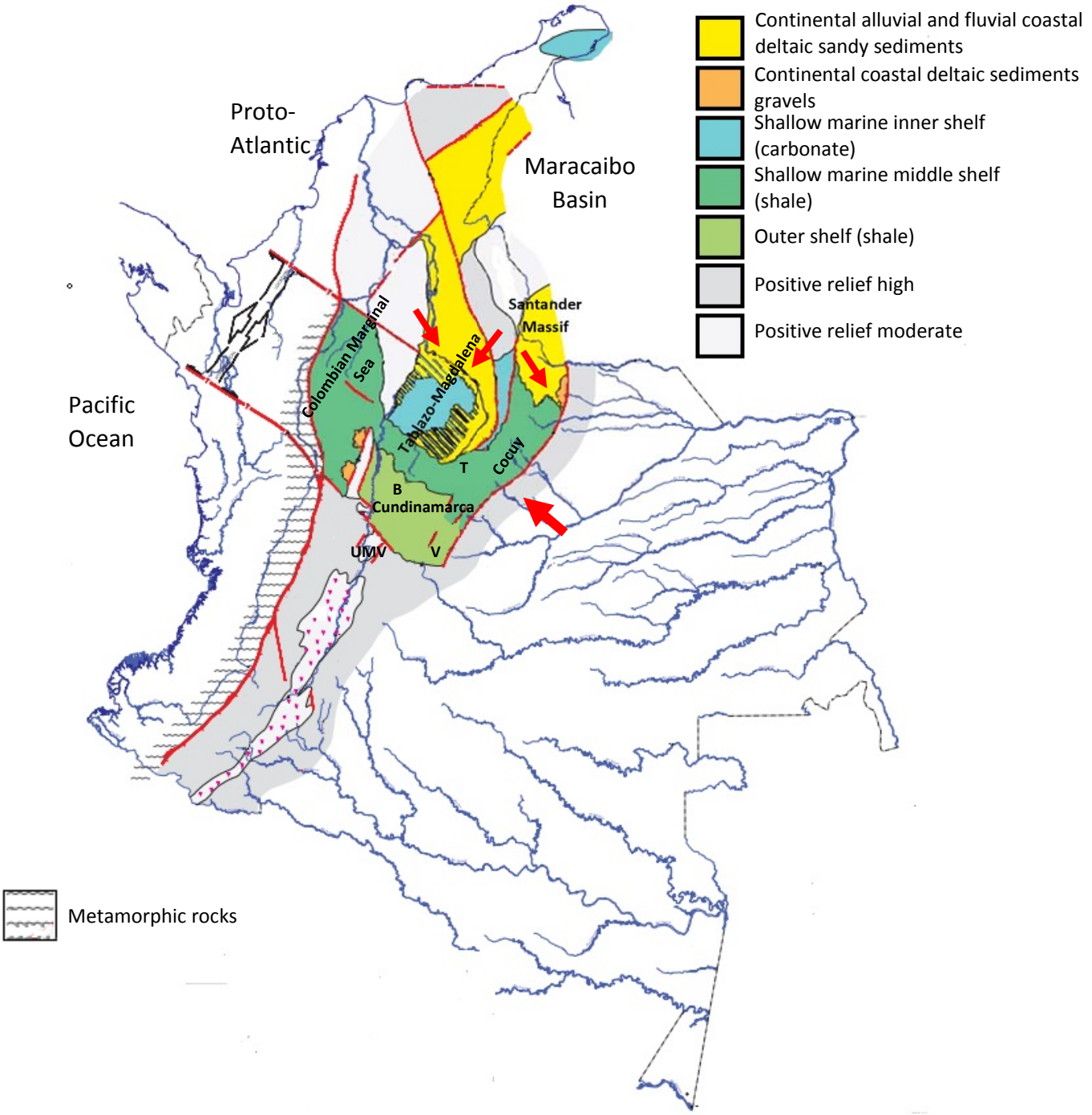

Figure 2.4 Berriasian-Valanginian facies distribution. Red arrows estimate direction of detrital material. Dashed line Colombian country boundary. B is Bogotá, V is Villavicencio and T is Tunja modified from Etayo et al., 1997. The small pink V in the south are extrusive volcanics.

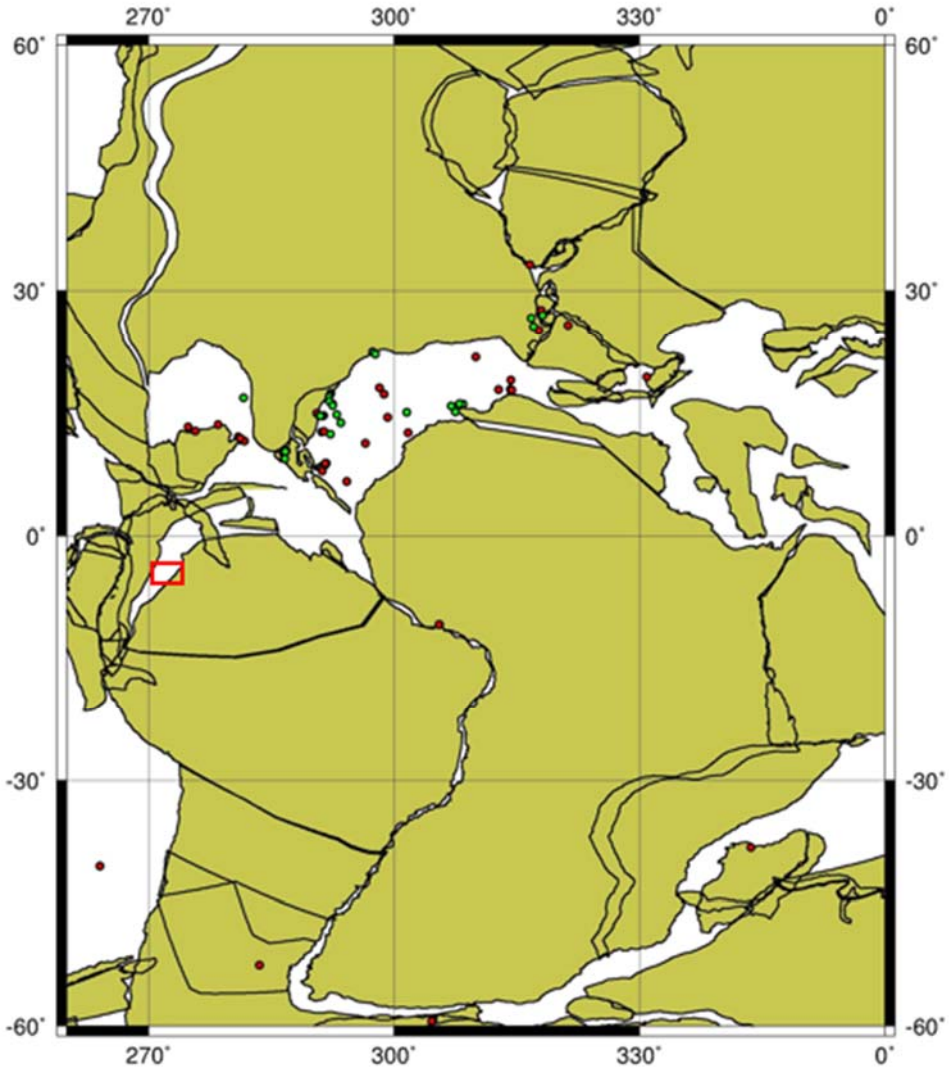

Figure 2.5. Plate tectonic reconstruction of northern S. America at 145 Ma , showing the seaway stretching from the Venezuelan coastline to the southern UMV, from. http://www.odsn.de (based on data from Hay et al., 1999). Site boundaries (red box) estimated from a length of 250 km, and northward boundary kink in North Andean plate which is the top of the EC mountain range (Bird, 2003; Mora et al, 2015). Red and green circles are IODP and ODP drilling locations.

2.2.2 Hautervarian to Albian – Fomeque

During the early Hauterivian, sandstones were prevalent in the EC and MMV before sea level began to rise, leading to the deposition of fine marine deposits (Figure 2.6) (Haq, 2014; Etayo et al., 1997; Macellari 1988). High sea level in the Aptian flooded the Santander-Floresta Massif, merging the EC sub-basins into one continuous basin and flooding the Upper Magdalena Valley in the south (Figure 2.7). Even after the flooding of the Santander-Floresta Massif, this paleo high affected deposition in the EC, with shale (intercalated with sandstone, siltstone and calcareous beds) dominating in the east (closer to primary detrital source i.e. the Guyana Shield), and more calcareous facies in the west (which was deprived of detrital sediment). The effect of sea level rise was likely accentuated by active rifting of the EC basin until the Early Albian, after which passive thermal subsidence dominated (Sarmiento-Rojas et al., 2006; Macellari, 1988, Mora et al., 2015). In the Late Albian, sea levels fell, as reflected in general shallowing upward of sedimentary successions across the EC (Sarmiento-Rojas et al., 2006).

Outside of the EC, deposition of marine deposits (characteristically interbedded with evaporites) extended over increasingly large areas of Venezuela and Colombia, connecting the EC to the tropical North Atlantic in the north and the Pacific in the south by the Albian, creating an epicontinental seaway which persisted until the Santonian (Macellari, 1988; Etayo et al., 1997; Erlich et al., 2003) Figure 2.6 and 2.7. The study area was south of the equator at the start of the Aptian, but by 120 Ma the northern portion had migrated to north of the equator (Figure 2.8).

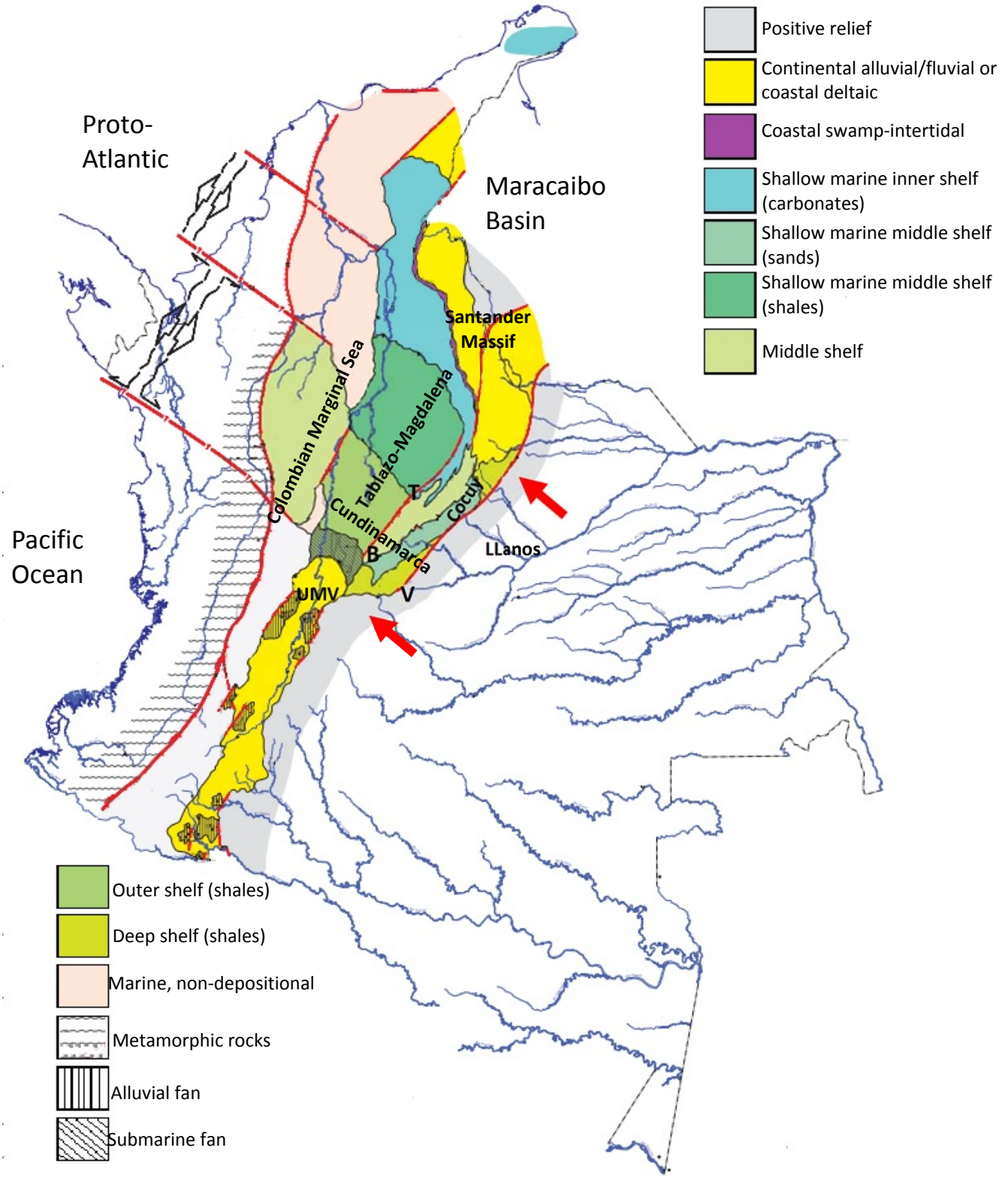

Figure 2.6 Hauterivian-Barremian facies distribution. Red arrows estimate direction of detrital material. Dashed line Colombian country boundary. B is Bogotá, V is Villavicencio and T is Tunja. Red lines are faults, red lines with a T are transform faults. Modified from Etayo et al., 1997

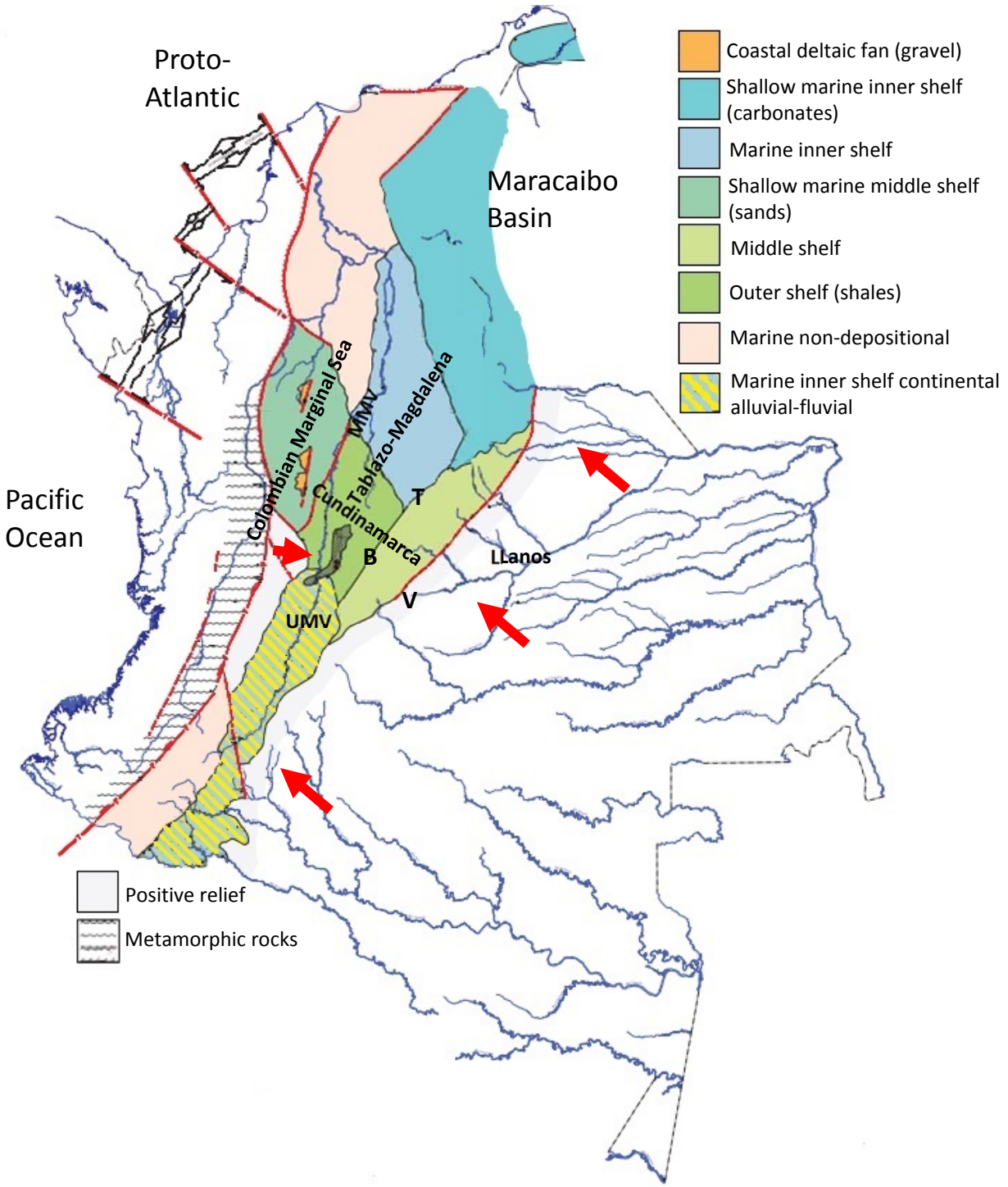

Figure 2.7 Aptian-Albian facies distribution. Red arrows estimate direction of detrital material. Dashed line Colombian country boundary. B is Bogotá, V is Villavicencio and T is Tunja. Red lines are faults, red lines with a T are transform faults. Modified from Etayo et al., 1997.

125 Ma

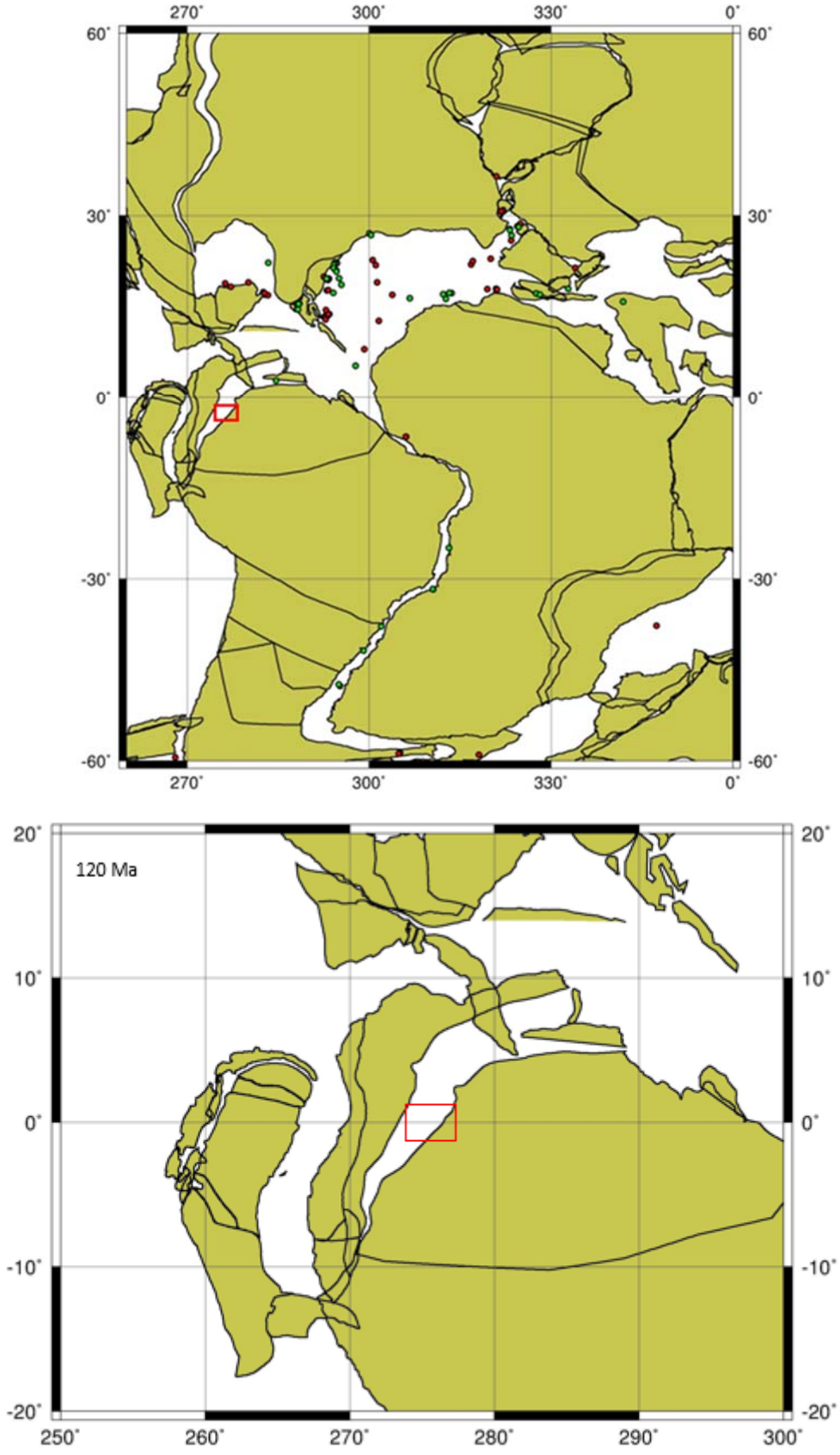

Figure 2.8 Plate tectonic reconstruction of northern S. America at 125-120 Ma, showing the seaway stretching from the Venezuelan coastline to the southern UMV, from http://www.odsn.de. Site boundaries (red box)

2.2.3 Cenomanian to Campanian

From the Cenomanian to the Turonian, global sea level rose to its maximum before generally falling for the remainder of the Cretaceous (Haq, 2014). This eustatic sea level rise is also expressed in the EC, with maximum transgression expressed as marine deposits across the majority of northern South America, including some parts of the Guyana Shield (the Llanos Basin) until the Coniacian/Santonian (Macellari, 1988: Sarmiento-Rojas et al., 2006; Etayo et al., 1997; Cooper et al., 1995) (Figure 2.9, Figure 2.10). Tectonics also played a role in relative sea level evolution in Colombia in the Late Cretaceous. Subduction of the Caribbean plate under the Central Cordillera caused subsidence in the EC basin and uplift in the Llanos basin during the Cenomanian (Sarmiento-Rojas et al., 2006). The effect of these tectonics can be seen in the lithology (Figures 2.9 and 2.10) with coastal/alluvial deposits in the Llanos during maximum eustatic sea level and marine deposits in the Coniacian as global sea levels are falling (Figures 2.9 and 2.10). From the Santonian/Campanian onwards, there was a more pronounced regression enhanced by uplift of the Central Cordillera in the west (Macellari, 1988; Villamil, 1998; Cooper et al, 1995), and marine facies were no longer deposited in the Llanos Basin (Figure 2.11). The uplift of the Central Cordillera provided increased detrital input and partly constrained the EC basin in the west by closing the Colombia Marginal Sea (Macellari, 1988).

There is evidence of upwelling across northern South America during the Cenomanian to Campanian by the deposition of chert, either interbedded with shales and siltstones up to 100 m thick (the lower Campanian Lidita Superior formation; Macellari, 1988; Villamil and Arango, 1998; Villamil et al,. 1999; Erlich et al., 1999; Cooper et al., 1995). Phosphatic lithologies are also prevalent (Föllmi et al., 1993; Cooper et al., 1995). Other geochemical characteristics are layers of iron-rich concretions in the EC and MMV, representing condensed sections during sea level high stands in these sediment-starved basins (Macellari 1988; Villamil, 1999).

Figure 2.12 shows that by the start of the Cenomanian, the South Atlantic has opened, and therefore the study area is no longer at the western edge of the super continent Gondwana. Half of the study area was south of the equator at the start of the Turonian, then gradually migrated across the equator towards the north reaching a maximum of 3 or 4°N in the at the start of the Santonian.

Some igneous intrusions were emplaced during the Cenomanian and Campanian in the Cundinamarca sub-basin (Vásquez et al., 2010). Also, sub-aerial volcanic activity led to the

deposition of single and bundled bentonite layers, which are laterally continuous at the Cenomanian/Turonian (C/T) boundary (Villamil, 1999; Villamil and Arango, 1998).

2.3 Conclusion

Cretaceous sediments deposited within the EC hold information about a variety of paleoenvironmental influences. The EC basin had a complex history regarding its connection to the open ocean, due to local tectonics and global sea level fluctuations. The EC was at first relatively isolated in the Early Cretaceous but later became part of an epicontinental seaway linking the Atlantic and Pacific for the majority of the Albanian till the Santonian. Uncertainties about connections to the open ocean relate to: the nature of the now extinct Colombial Marginal Sea in the west, which may have connected the EC to the proto-Carribean and; the exact timing, lateral extent and topography of the ancestral Central Cordillera, which may have confined the EC in the west. Geochemical results in this project, particularly relating to Mo (see Chapter 8) provide some additional information about ocean connections. The water depth of the basin likely varied through its history, also relating to tectonics (active rifting in Early Cretaceous, passive subsidence in Mid-Late Cretaceous, Late Cretaeous compression) and global sea levels. As mentioned in Chapter 3, water depth is difficult to constrain given the basin closure and uplift and the lack of preserved macro and micro fossils. The study area moved generally northward across the equator during the Cretaceous, and this may have resulted in changes in the dominant wind directions. These changes should have affected the supply of nutrients to the photic zone and ventilation of the water masses, and so ultimately the amount and quality of organic matter deposited on the sea floor.

After deposition, deep burial of the Cretaceous sediments likely caused alterations to this organic matter and the clay mineralogy. Finally, uplift and exposure of the sedimentary rocks at outcrop could have affected geochemical proxies. An understanding of how these post-depositional processes affect inorganic geochemical proxies is vital for robust paleoenvironmental interpretations.

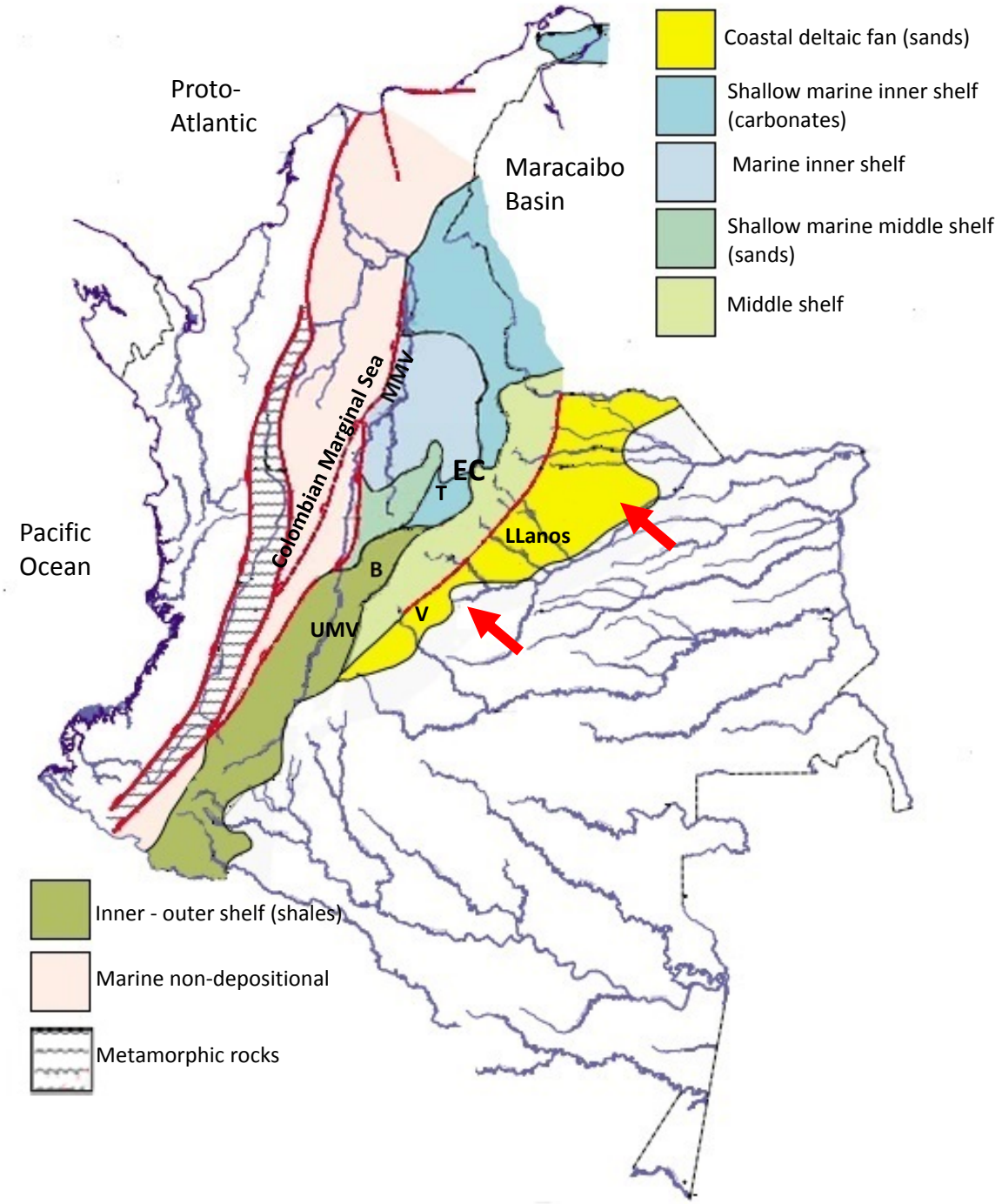

Figure 2.9 Cenomanian facies distribution. Red arrows estimate direction of detrital material. Dashed line Colombian country boundary. B is Bogotá, V is Villavicencio and T is Tunja. Red lines are faults. Modified from Etayo et al., 1997

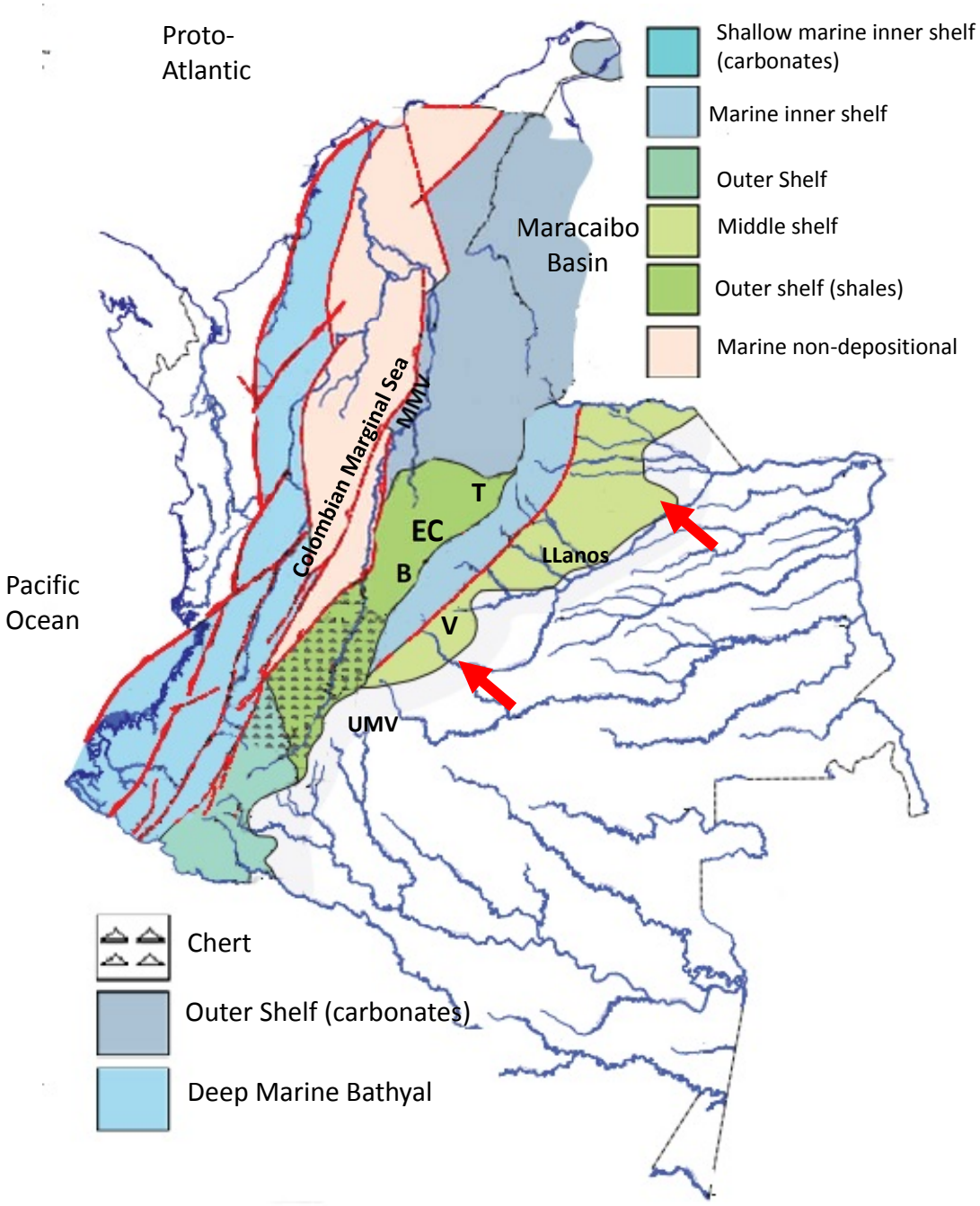

Figure 2.10 Coniacian facies distribution. Red arrows estimate direction of detrital material. Dashed line Colombian country boundary. B is Bogotá, V is Villavicencio and T is Tunja. Red lines are faults, red lines with a T are transform faults. Much of the Deep Marine Bathyal deposits contain composite crust and submarine mafic volcanics of the Western and Central Cordillera. Modified from Etayo et al., 1997

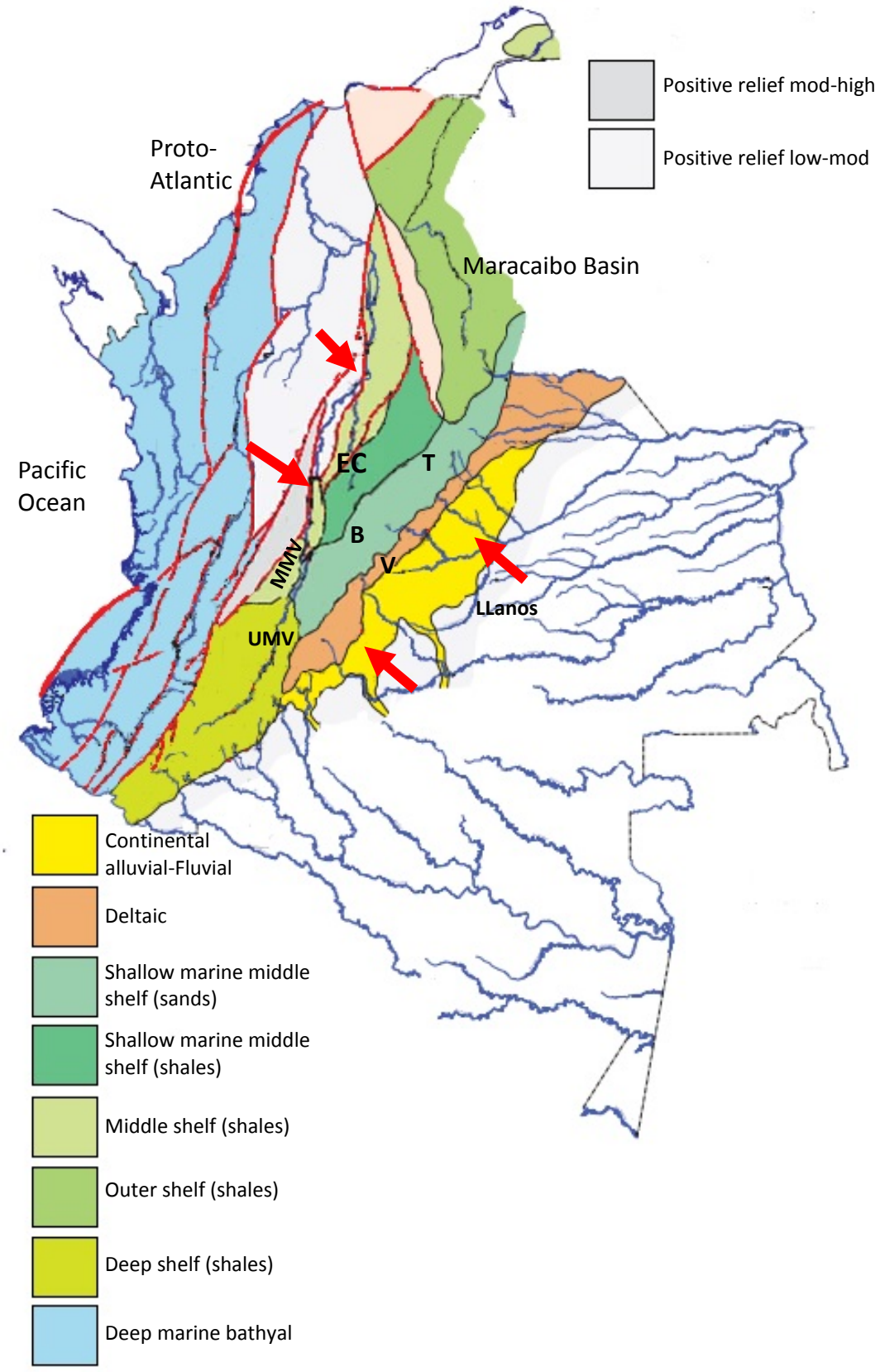

Figure 2.11 Santonian - Maastrichtian facies distribution. Red arrows estimate direction of detrital material. Dashed line Colombian country boundary. B is Bogotá, V is Villavicencio and T is Tunja. Red lines are faults, red lines with a T are transform faults. Much of the deep marine bathyal deposits contain composite crust and submarine mafic volcanics of the Western and Central Cordillera. Modified from Etayo et al., 1997.

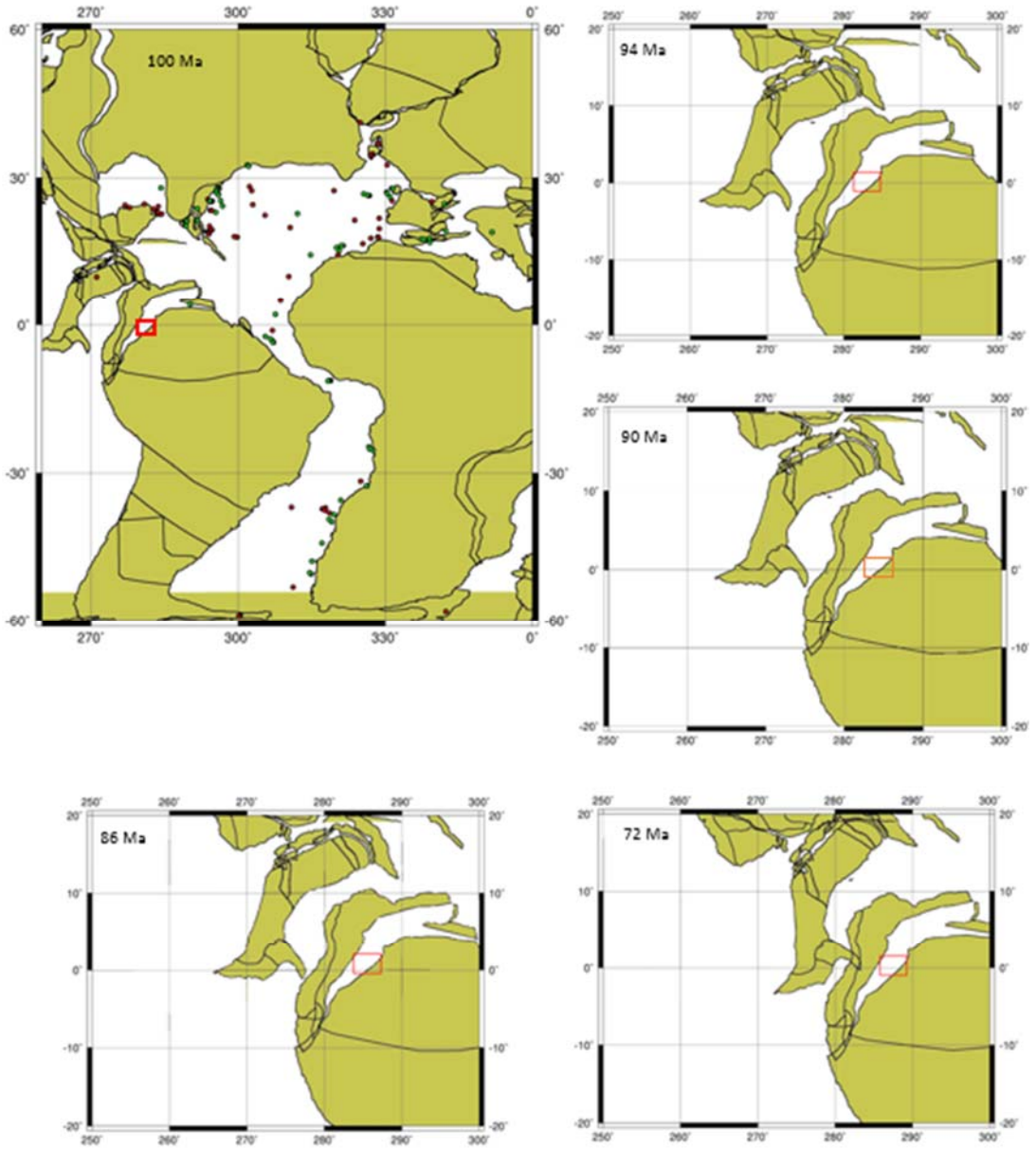

Figure 2.12 Plate tectonic reconstruction of northern S. America at 100-72 Ma, showing the seaway stretching from the Venezuelan coastline to the southern UMV, from http://www.odsn.de. Site boundaries (red box).

Chapter 3 Material, Analytical approach, and Methods

3.1 Introduction

This chapter introduces the material studied in this thesis, i.e., the location, the stratigraphic and geological context of the samples. This first part of the chapter is based on information provided by Ecopetrol. Subsequently, the analytical approach is explained, based on a short literature review of inorganic proxies for reconstructing the paleoenvironment. Finally, the analytical methods are presented.

3.2 Sample Material

3.2.1 Introduction to fieldwork

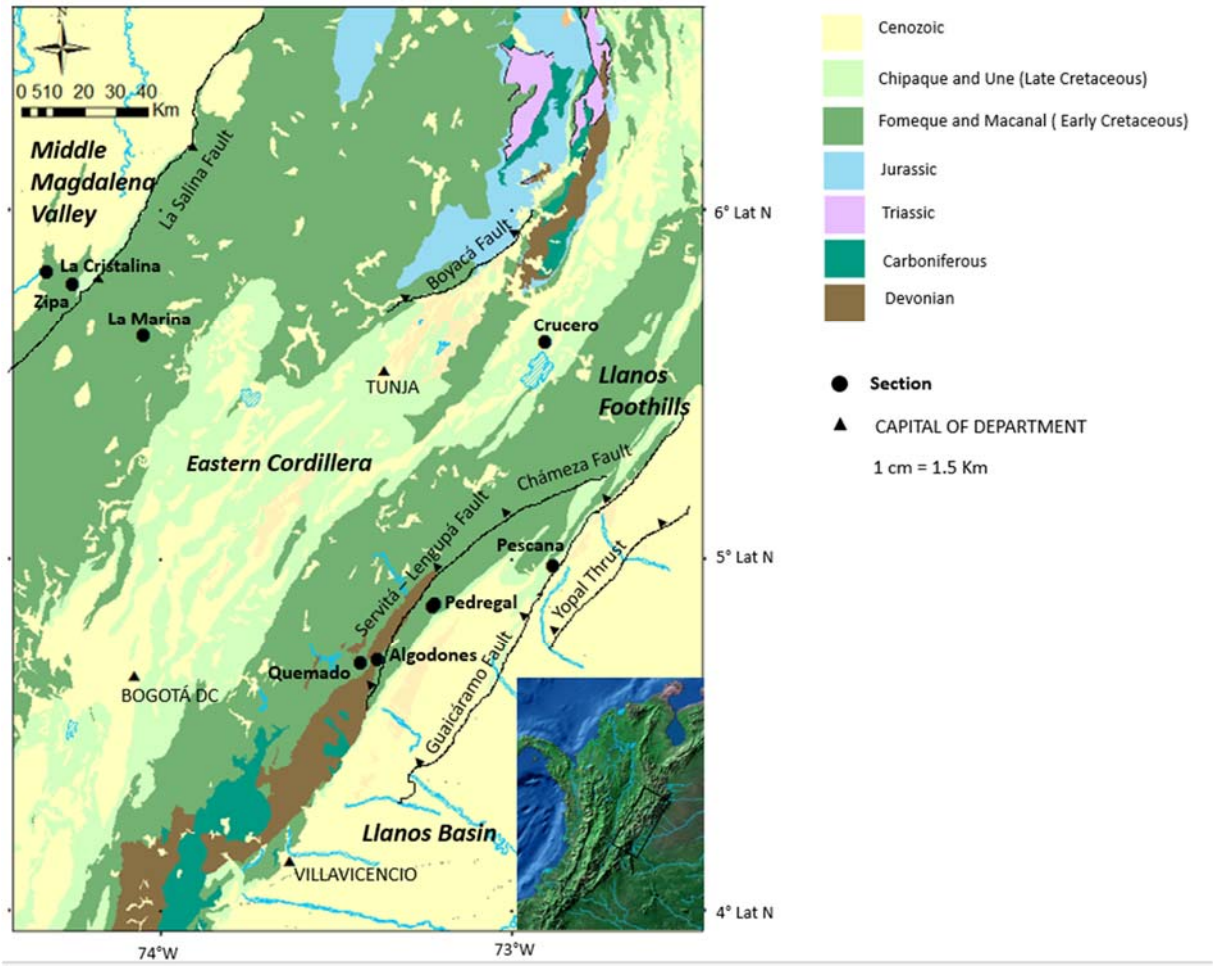

Figure 3.1 Location figure, showing location of samples, the basins and some major faults. Adapted from Map of Colombia, Gomez et al., 2015.

ICP-Ecopetrol S.A. contracted a geological consultancy agency (Georex S.A.S., hereafter called Georex) to collect new field samples for this project and to provide a detailed documentation of the geology of the outcrops. Nine outcrop sections were visited. Summaries of the outcrop locations and formations are included in Table 3.1. An estimate of palaeo-water depth is also included in Table 3.1. The figures of palaeo-water depth were provided by Ecopetrol, however no information has been provided as to how this figure was generated. They are included here only to allow comparison between the sections, as it is presumed that similar methods were used to estimate water depth at each location. Their

locations are shown in Figure 3.1. As discussed in Chapter 2, the basin has undergone considerable shortening since deposition and so the current locations of sections in Figure 3.1 are not the original depositional locations in the basin. A kinematic reconstruction was carried out by Mora et al. (2015) and the approximate locations of the sections within the basin before shortening are shown in Figure 3.2, and is based on the section position between faults.

Table 3.1 Summary of the location, type and formation of sampled outcrops from information provided by Georex. Palaeo-water depth was also provided by Ecopetrol and is included here in order to provide context.

Section	Noted formation	EC Equivalent Formation	Flank of basin	Palaeo-water depth (m)	Outcrop type	Thickness of section (m)
Algodones	Macanal	Macanal	Eastern	20	Stream	579
Quemado	Macanal	Macanal	Eastern	60	Road cutting	238
Pedegral	Fomeque	Fomeque	Eastern	15	Stream	300
Cantonera	Fomeque	Fomeque	Eastern	12	Stream	386
La Marina	Paja	Fomeque	Western	30	Road cutting	893
La Cristalina 1	Simiti/La Frontera	Chipaque	Western	100	Road cutting	372
La Cristalina 2	Paja/Hilo	Fomeque	Western	NA	Road cutting	151
La Cristalina 3	Simiti/Paja/Hilo	Fomeque	Western	NA	Road cutting	307
La Cristalina 4	Unidad intermedia de Shales/ Ruedas de Carretera	Chipaque	Western	120	Road cutting	1706
Zipa	Ruedas de Carretera	Chipaque	Western	110-120	Road cutting	80
El Crucero	Chipaque	Chipaque	Eastern	25-50	Road cutting	750
Pescana	Chipaque	Chipaque	Eastern	25-30	Road cutting	371

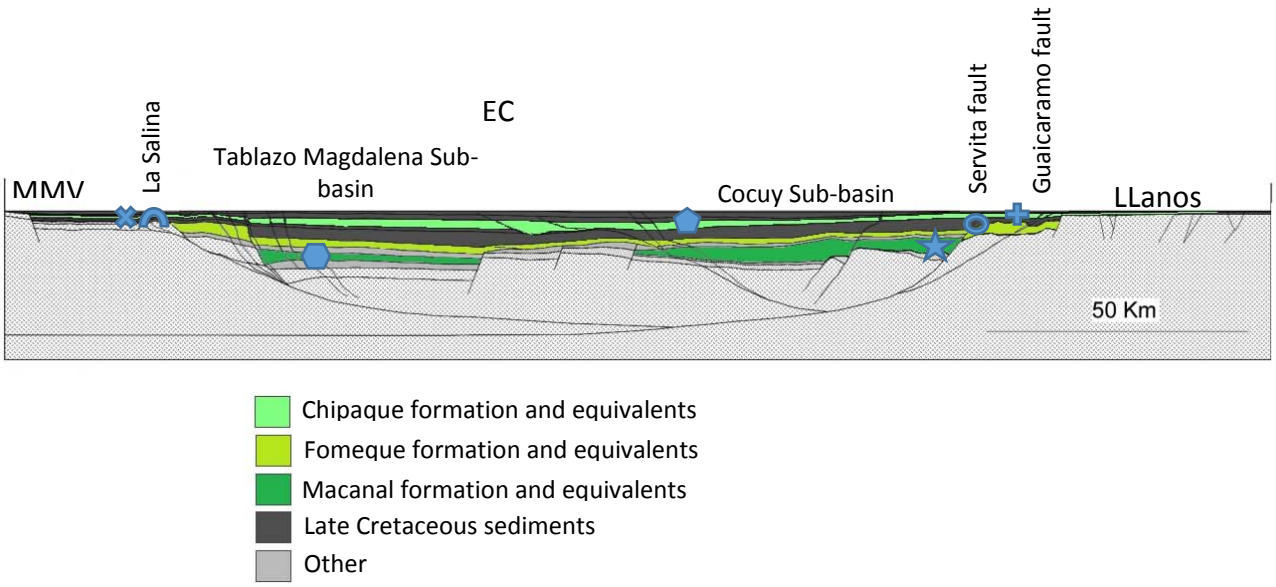

Figure 3.2 Kinematic reconstruction of the EC basin at 58 Ma, prior to shortening. Approximate location of Pescana is plus sign, pentagon is Crucero, x is La Cristalina and arch is Zipa. Hexagon is La Marina and open circle is Pedregal and Cantonera. Star is Algodones and Quemado. Modified from Mora et al. (2015).

These sections were logged in the field by Georex, and this information was compiled in nine reports. Fuller translations of the sedimentological descriptions and interpretations are included in Appendix A. The logs are summarised in Table 3.2.

Table 3.2. Table summarising the Georex S.A.S reports and logs

Section	Description	Minerals present	Bioturbation	Facies interpretation
Algodones	Mudstone and siltstone with occasional bands of sand, which increase in number and thickness towards the top of the column. Fossils of ammonites, bivalves and plant remains.	Mica	Ichnofossils and homogenised beds occasionally noted, often associated with sand beds. Planar, undulating or no lamination	Tidal plain, developing to pro-delta, submarine fan at the top of the column
Quemado	Mudstone and siltstone with thin beds of sandstone and siltstone, however one section 50m is monotonous. Ammonite and bivalve impressions and plant remains observed	Mica pyrite, phosphatic lens (with pellets)	No bioturbation noted. Mostly planar lamination.	Hemi pelagic submarine fan developing into distal prodelta
La Marina	Calcareous and siliceous mudstone with silt and sand beds of which generally increase in number and frequency towards the top of the column. Packstone/wackestone beds also present at the top of the column. Plant remains, ammonite and bivalve fossils (sometimes only fragments, sometimes concentrated in fossiliferous beds). Some depths completely fossil free.	Pyrite (disseminated and nodules), gypsum (veins and disseminated), mica, Fe oxides, veins of calcite	Ichnofossils noted in the base of the column, rare bioturbation during the rest of the depositional period	Protected internal platform, mudflats, tidal plain, sometimes hypersaline, sometimes influenced by open ocean (tides or swells) or with increased input from hinterland (tidal streams).
Pedregal	Periods alternating	Muscovite,	Lamination only	Internal to middle

Section	Description	Minerals present	Bioturbation	Facies interpretation
	mudstone and sandstone beds (up to 10 m thick), other periods alternating mudstone and wackestone beds. Thinner sandstone beds are located at the base of the column, alongside carbonate beds. Leaf fragments, fossils of mollusc, ammonite, bivalve (often in fragments) fish fragments, oil staining, interclasts and coal fragments noted.	glauconite, rare phosphatic lens	occasionally preserved. Occasional ichnofossils	platform shallowing to littoral zone at the top of the section.
Cantonera	Black mudstone (some beds calcareous at the base of the column) with mostly fine sand, siltstone and wackestone beds. Plant remains, interclasts, shell fragments noted and occasional fossil rich beds	Muscovite, glauconite	Ichnofossils present occasionally, lamination only occasionally preserved	Base of column internal to external platform, towards the top, mostly fluctuating between shoreface and intertidal plain
La Cristalina 2	Chert (dominating the top half of the section) and mudstones (calcareous and siliceous). Fossils of ammonites, bivalves and benthic and planktonic foraminifera noted	Mica	Limited bioturbation.	Outer shallowing to inner continental slope
La Cristalina 3	Relatively monotonous dark grey mudstone and siltstone (siltstone dominating towards the top), often calcareous sometimes siliceous (with chert present). Fossils of ammonites and bivalves noted.	Pyrite, calcareous nodules, veins of calcite, mica	Limited bioturbation, but occasional ichnofossils present	Mid-outer continental slope
La Cristalina 1	Relatively monotonous mudstone and siltstone (mostly calcareous but sometimes siliceous with chert. Ammonites, bivalves, and planktonic foraminifera occasionally beds are fossiliferous (with mechanical concentration suggested).	Muscovite, pyrite	Planar lamination occasionally undulating, bioturbation concentrated in the top of the column	Mid-outer continental slope
La Cristalina 4	Mudstone and siltstone calcareous and siliceous (thin beds of chert).). Mudstone dominates in the top portion of the column. Two layers of volcanic tuff noted. Ammonites, bivalves and fish scales (occasionally in fossiliferous layers),	Calcareous and pyrite nodules, muscovite, veins of calcite	Mostly planar lamination, bioturbation only noted in one instance	Distal delta deepening to mid-outer continental slope

Section	Description	Minerals present	Bioturbation	Facies interpretation
	occasional bed rich in foraminifera noted.			
Crucero	Mudstone, siltstone (often intercalated with planar parallel lamination), periodically dominated by thick, often bioturbated quartz sandstone beds (increasing in dominance towards the top of the column). Plant remains, fragments of shells and fish remains	Muscovite, phosphatic fragments and sandstone beds	Sandstone beds bioturbated, finer beds often planar parallel without bioturbation	Repeated successions shallowing from offshore, transition and shoreface, with the dominance of shoreface increasing up Storms concentrate phosphatic fragments
Pescana	Mudstone with siltstone laminations with medium to fine grain quartz sandstone beds and occasional limestone/calcareous bed. Fossils rare although there are occasional fossiliferous beds (bivalve, gastropods). There are three condensation levels (two are phosphatic)	Occasionally micaceous. Glauconite, thin phosphatic beds	Bioturbation and ichnofossils identified in most sections	Repeated successions representing shallowing upward sequences from offshore transition to lower shoreface or intertidal plain
Zipa	Mudstones and some siltstones at the base turning siliceous and calcareous (some chert) in the top portion. Fish, planktonic foraminifera, bivalve and ammonite noted. Benthic foraminifera noted at the top.	Phosphatic beds (pellets), pyrite concretions	Planar lamination preserved – no Occasional burrow and homogenised bed base towards the top.	Offshore transition to inner-middle continental shelf – under the influence of upwelling and post diagenetic silicification in the half portion of the section

3.2.2 Sample selection

A total of 1990 samples were collected during the field campaign. As there were set deadlines for the submission of geochemical interpretation to Ecopetrol, a smaller subset of samples was selected for more detailed geochemical analysis (summarised in Table 3.3). Ecopetrol provided TOC and Rock-Eval pyrolysis data, and a general description of the samples (shale or sandstone), forming the basis for the sample selection for this project (see Marin, 2017, for more details). A sample resolution of approximately 1 sample every 10 m was targeted and achieved in most sections. Samples for microscopy were chosen to have the most representative geochemistry (closest to average per section in terms of TOC, bulk, trace and Fe geochemistry).

Table 3.3. Summarises the number of samples available and analysed, and their approximate resolution.

Section	No. Samples collected	XRF	Fe speciation	CNS/LECO	SEM Microscopy	XRD	Sample resolution (m/sample)
Algodones	211	22	22	22	1	6	10
Quemado	117	12	12	12	1	5	10
Pedegral	109	16	16	16	2	6	7
Cantonera	195	24	24	24	-	7	8
La Marina	419	21	21	21	1	-	20
La Cristalina	471	50	50	50	1	-	9
El Crucero	234	26	26	26	1	6	9
Pescana	131	17	17	17	1	6	8
Zipa	103	20	20	20	1	6	5

A number of other samples were also analysed as part of a pilot study (summarised in Table 3.4). These samples do not have the same detailed background information (field report and logs, and higher resolution bulk organic geochemical data) and so are not included in the main body of the text. They are referred to when considering the whole of the EC. A set of immature, larger volume samples was taken from the Quebrada Vara Santa (QVS) and Paramo Guina (PG) section during a short field campaign (carried out in June 2014). A sample from QVS which appeared to not be affected by contemporary weathering was chosen for the weathering study (Chapter 4). Quebrada Vara Santa and PG were studied in detail by Blanco (2012). All additional samples were taken from the Chipaque formation or the MMV time equivalent of the Chipaque.

Table 3.4. Summarising details of additional samples, the data from which is not considered part of the main data set.

Section	Basin	Outcrop type	No. Samples	XRF	Fe speciation	CNS/LECO
Quebrada Vara Santa (QVS)	EC	Stream	8	8	8	8
Paramo Guina (PG)	EC	Road Cutting	7	7	7	7
La Luna-1	MMV	Borehole	14	14	14	14
Coyote-1	MMV	Borehole	4	4	4	4

3.2.3 Thermal Maturity

Full and thorough analysis of the maturity of the samples is discussed in the corresponding PhD (Marin, 2018). An estimation of thermal maturity and burial depth, based solely on vitrinite reflectance data (provided by Ecopetrol), T_{max} from Rock-Eval Pyrolysis data (provided by Ecopetrol) and literature information is included in Table 3.5, and published within Buckman et al. (2017). Samples with vitrinite reflectance over 0.5-0.7 have entered the oil window and lost at least some of the organic carbon originally buried within the rock (Tissot and Welte, 1984). Clay transformations also occur beyond 122°C (Hurst, 1985) and so any clay detected may not be an original signature beyond this burial temperature.

Table 3.5. Summary of information on thermal history from the selected sample set based on new data (T_{max} and Vitrinite reflectance) and reported maximum burial depth and temperature from Mora et al. (2015). The data from Mora et al. (2015) is estimated from vitrinite reflectance with a paleo thermal gradient of 20-25°C from Parra et al. (2009). The data are from specific locations in the basin and are applied here to sections of the same age. Mora et al. (2015) discuss heterogeneity in burial rates across the basin, however, information is included to provide a general idea of the extent of burial.

Section	**T_{max} (°C)**	**Average Vitrinite Reflectance (%Ro)**	**Estimated burial depth (m)**	**Max burial temperature (°C)**
Algodones	361 (118)	4.5 (3)	8500	249 ± 8
Quemado	359 (98)	4.0 (3)		
Pedegral	523 (87)	1.7 (2)	7000	237 ± 20
Cantonera	586 (154)	1.9 (3)		
La Marina	471 (68)	2.0 (2)	7000	237 ± 20
La Cristalina 2	459 (52)	1.3 (3)		
La Cristalina 3	512 (134)	1.6 (3)		
La Cristalina 1	454 (188)	1.0 (3)	4800	162 ± 25
La Cristalina 4	468 (96)	1.3 (3)	3500-4000	115 ± 17
El Crucero	481 (151)	1.0 (3)		
Pescana	434 (38)	0.6 (3)		
Zipa	463 (91)	1.1 (6)		

3.2.4 Age of samples

Ecopetrol provided information about the age of samples which are summarised in Figure 3.3. As there is a limited amount of biostratigraphy, ages are largely based on lithostratigraphy and correlation of the new sections to existing ones where biostratigraphy is better constrained. Where more detail was provided in Georex/Ecopetrol reports, it is included here. In the lower portion of Pedregal, fauna previously identified by Julviert (1968) as Barremanian were observed (the bivalve Trigonia). In Cantonera, the ammonite Chelonicera (Barremian-Aptian age according to Etayo and Caceres, 1969) was described. In La Cristalina 4, a bed of chert (which is a regionally correlative horizon) marks the top of the Turonian. In Crucero, the top of the Turonian is inferred by a switch to the dominance of sand beds, as this correlates to similar lithology changes in better-constrained sections (Vergara, 1997). Above the top of the Santonian in Crucero, the dinoflagellate Dynogymnium, given a Santonian to Campanian age, is identified. Given the lack of definitive biostratigraphy, stage boundaries are taken as tentative within this thesis.

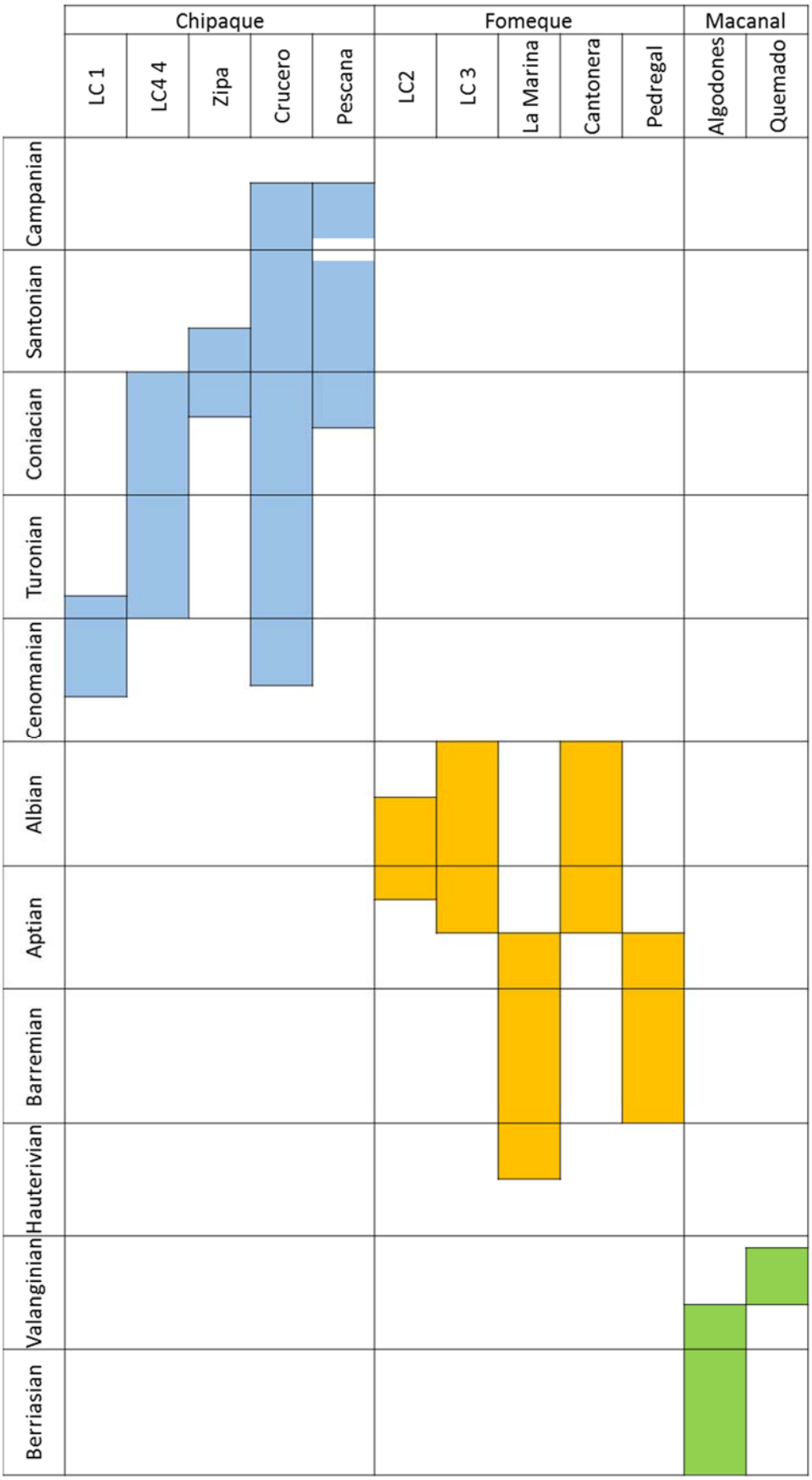

Figure 3.3 Age of the different sections from Ecopetrol lithostratigraphy.

3.3 Analytical Approach

A wealth of information exists on the inorganic geochemistry of shales. Here a literature review of methods to investigate the type and volume of detrital material, proxies for productivity and for redox which utilise inorganic and sedimentological data is presented. Armed with these data, a picture of the paleo depositional environment of the EC during the Cretaceous can be formed, providing information about how these organic rich mudstones could develop. An approach is presented to compare the EC to other Cretaceous deposits to see if the paleoenvironment of the EC is inherently different.

3.3.1 Detrital Material

Organic carbon contents (and the contents of TE used as proxies) in marine sediments can be significantly and variably diminished by dilution of organic-poor material, which is often siliciclastic sediment of terrestrial origin. It is therefore important to account for the fact that this dilution can variably affect different samples within a stratigraphic section. A standard approach is to normalise all data to a terrigenous reference element (Calvert and Pedersen, 2007; Martinez et al., 1996; Beckmann et al., 2005; Wagner et al., 2007; Hofmann et al., 2008; März et al., 2008; März et al., 2009; Poulton et al., 2015). Aluminium is commonly chosen because its concentration in igneous and metamorphic rocks is relatively similar (so should not be significantly influenced by variations in the lithology of the hinterland) and its content in average shale is similar to bulk upper crust, which emphasises its conservative behaviour during weathering (Taylor and McLennan, 1985). Also, Al is relatively abundant in marine sediments (average shale 16.7 %, Wederpohl, 1971), making it easy to quantify. In sediments, Al is dominantly contained in aluminosilicate phases (Calvert and Pederson, 1993), which is often the main diluting phase in marine sedimentary basins. Aluminium also does not significantly participate in any diagenetic or biological processes (Brumsack, 2006). Aluminium is also important for identifying authigenic enrichments. If within a number of samples, an element correlates well with Al, it is likely that this element entered the basin by the same transport mechanism and from the same source – i.e. with the fine-grained detrital siliciclastic phase. If it does not correlate, its content is likely controlled by some other mechanism (e.g. redox conditions, organic carbon export, winnowing) (e.g. März et al., 2009).

The relative proportion of fine versus coarse detrital material which arrives at the sea floor can provide useful information about the climate and depositional environment. The

delivery of coarser grains requires more energy, therefore grain size distribution can provide information about proximity to shore or the intensity of the hydrological cycle (Schmitz 1987, Martinez et al., 1996; Calvert and Fontugne, 2001; Hofmann et al., 2008; Hetzel et al., 2011). In an effort to directly measure grain size in the new Colombian samples, disaggregation (via the freeze-thaw method of Yang and Aplin, 1997) of pilot samples was attempted (full details available in Appendix B). This approach was unsuccessful, likely because of compaction and fusion of the grains due to their deep burial (see Table 3.5) or cementation (probably by siliceous cement). A chemical approach for estimating grain size distribution was investigated.

Since quartz (SiO_2) is often the dominant component of the coarser fraction of a sediment (as quartz silt and sand), Si contents can be used to estimate the silt and sand contents of a rock. Evidence that the majority of sand and silt in the EC is quartz comes from the low values of other minerals detected in XRD (e.g. maximum feldspar content noted 7%) and the field description identifying most sandstone beds as quartz sandstones. In order for a Si proxy for coarse grains to be useful, it is first important to discount the proportion of Si which is present within clays. Empirically, the maximum Si content within a sample which is pure clay is likely to be 25% (Illite, empirical formula $_{0.6}(H_3O)_{0.4}Al_{1.3}Mg_{0.3}Fe^{2+}_{0.1}Si_{3.5}O_{10}(OH)_2\cdot(H_2O)$).
A mudrock with less than 25% Si may, therefore, contain pure illite clay, or a mix of clay, quartz silt and sand. On the other hand, a sample with greater than 25% Si certainly contains another source of Si – most likely quartz sand and silt. Ecopetrol commissioned XRD analyses on a number of samples and therefore this approach can be tested by comparing the quartz results in XRD analysis on the >2µm fraction to Si contents measured by XRF. In Figure 3.3, it is shown that this method significantly underestimates the sand fraction. This is likely because there is a varying amount of quartz within the sub-25% Si proportion of the sediment. Hence, another approach is required.

The dominant source of Al to the sediments is within clay minerals, so Si/Al may offer a better grain size proxy than Si alone (Calvert and Pederson, 2007). Silica/Al ratios are different in different clay minerals. Kaolinite has a stoichiometric Si/Al ratio of 1, whilst smectite and illite have a stoichiometric Si/Al ratio of 2 (natural samples measured by Mermut and Cano, 2001; Nadeau and Bain, 1986 and Saika and Parthasarathy, 2010 yielding similar results). Small variations in Si/Al, even in pure clays, consequently need to be taken

into account when applying this approach. In this project, the Si/Al ratio was used to estimate sand fraction, with values greater than 2 (the highest likely in a pure clay sample) representing Si enrichments, likely in the form silt or sand sized quartz. These Si/Al ratios have been compared to an artificial sand-shale mix in order to validate the estimated sand content in our samples (Figure 3.4). Although the correlation between estimated sand fraction (by XRF) and measured sand fraction (by XRD) is not linear (Figure 3.5), the results are more promising than using Si content alone.

Silica can be delivered to marine sediments not only within siliciclastic material but also as biogenic opal, in the tests of radiolarians and diatoms. In order to discount these marine biogenic effects, Si can be corroborated with Zr (only significantly enriched by the presence of zircon, a heavy mineral) and Ti (in rutile crystals) both of which accumulate in the coarse fraction due to their high specific densities. These grain size proxies have been widely used to understand variations of run-off into basins due to hydrological variability (Schmitz 1987, Martinez et al., 1996; Schnieder et al., 1997; Calvert and Fontugne, 2001; Mutterlose et al., 2003; Hofmann et al., 2008; Hetzel et al., 2011). Ti/Al can be biased by differences in sediment provenance, as Ti is contained within numerous aluminosilicate fractions (including clay) as well as rutile and other titaniferous materials (Calvert and Pederson, 2007). Therefore, in order to ensure that estimated sand fractions are not overestimated by the presence of biogenic Si, the samples are first 'filtered' by correlation with Zr (Hofmann et al., 2008), the underlying assumption being that samples which do not correlate with Zr may have an additional input of Si not related to grain size, including biogenic opal.

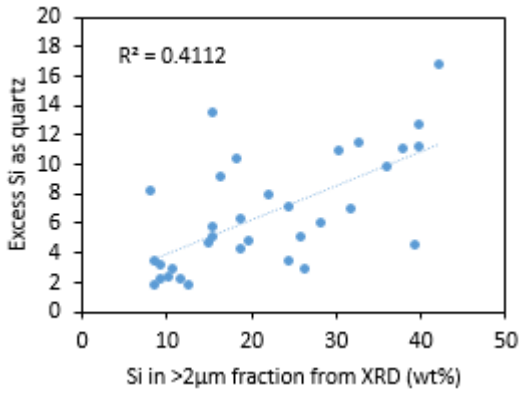

Figure 3.4 Quartz sand and silt content estimates by XRF (all Si greater than 25% - taken as the maximum in pure clay), compared to quartz identified in the > 2µm fraction by XRD (converted to wt% Si). Note that the excess quartz tends to underestimate Si measured in XRD and the poor r2 value. This is likely due to the presence of amorphous Si detected in XRF and not in XRD (eg biogenic Si) and the chosen value of 25% above which to count as excess. A sample with 25% Si is likely to contain a variable proportion of quartz and clay and so this method will always underestimate sand fraction. XRD data from Ecopetrol commissioned report – Gómez Caro and Carreño Parra, 2015.

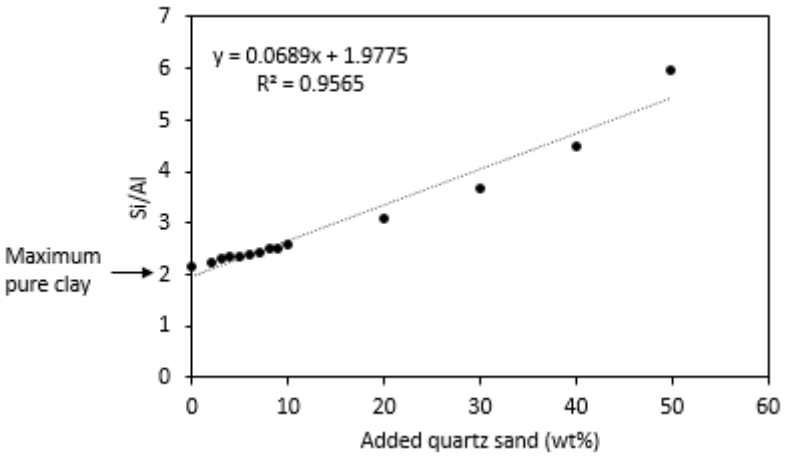

Figure 3.5 Results of sand spiking. A shale sample from the basin with no visible sand was spiked with varying amounts of pure quartz sand. Note that the unspiked clay has Si/Al value slightly greater than 2, suggesting either a smectite/illite clay with a small amount of sand or a kaolinite clay with quite a bit of sand. The straight line equation was used to calculate sand fraction based on Si/Al. Note that the fit of the line is not perfect. This is likely due to slight errors during weighing.

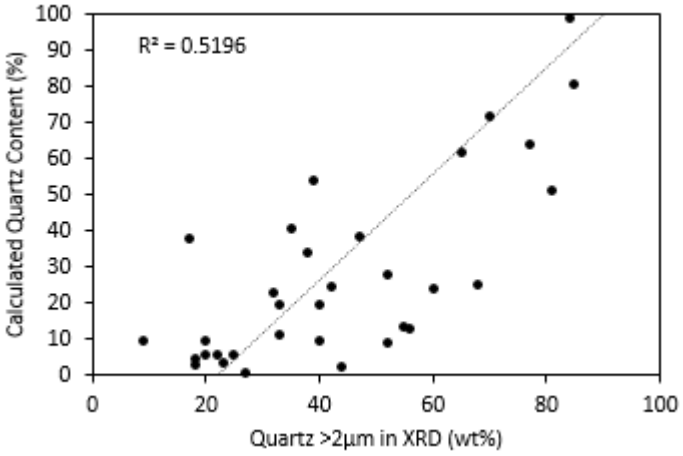

Figure 3.6 Calculated quartz fraction compared to XRD quartz fraction for a limited number of samples. Note that there are some very high quartz values unexpected in very fine grain dark mudrocks. There are also 2 values with over 100% quartz content. These discrepancies will be discussed in Chapter 8. XRD data from Ecopetrol commissioned report – Gómez Caro and Carreño Parra, 2015. Again there is considerable scatter, and this method still slightly under estimates quartz content compared to XRD, however this method was taken forward for use within the project.

Additional information which may be found within the detrital fraction includes variations in the extent of paleo chemical weathering in the hinterland. Potassium, Ca and Na are preferentially leached from feldspars during paleo chemical weathering (leading to the formation of clay minerals), controlling the chemical index of alteration (CIA, Nesbitt and Young, 1982; Fedo et al., 1997). Clay minerals derived from extensive paleo chemical weathering (warm and humid climates with high precipitation) or from the weathering of a very old, highly weathered hinterland are low in Ca, Na and K (and high in kaolinite) leading to a high CIA, whereas slow weathering under cold conditions and low precipitation or weathering of fresh crystalline material results in clay richer in Ca, Na and K (and so lower CIA values) or feldspar grains reaching the sediments. Consequently, variations in the CIA of

a sediment (or derivatives, e.g. K/Al, clay mineral contents) may reflect variations in hydrological regimes linked to regional or global climate (e.g. Nesbitt and Young, 1982; Schnieder et al., 1997; Zabel et al., 2001; Flögel et al., 2008; Beckman et al., 2003; Hofmann and Wagner; 2013), or variations in the source of detrital material (Campos Alvarez and Roser et al., 2007). In this project, a wide variety of mudstones are analysed, including carbonate rich and carbonate poor mudstones. Values for CIA are amended to discount the Ca contribution from $CaCO_3$ by using a calculation derived by Fedo et al. (1995). In carbonate rich samples from this project, this calculation often produced negative numbers for Ca, indicating that the lithology was not conducive to this amendment. It was decided that Ca would not be included in any of the CIA calculations (modified term CIA*) as per Flögel et al. (2008). Flögel et al. (2008) studied paleo chemical weathering using CIA* in two Cretaceous low latitude locations. One (from Demerara Rise) is associated with a watershed which should be geochemically similar to the watershed for the EC – the Guyana Shield - and is useful for comparison. Also, Kronberg et al. (1986) reported data from contemporary Amazon River suspended sediment, which provide a comparison as to the extent of modern day tropical weathering of the Guyana Shield (as well as other geological provenances in northern South America).

3.3.2 Productivity

In a general way, periods of enhanced primary productivity, for example in areas of upwelling, can be inferred from the amount of biogenic material within the sediment, including TOC, $CaCO_3$ or biogenic Si content (Schneider et al., 1997; Davis et al., 1999; März et al., 2008). Some trace metals offer additional proxies for productivity. It has been shown that Ba is incorporated into marine sediments with high TOC flux as barite ($BaSO_4$), and so barite is enriched in high productivity regions (Goldberg and Arrhenius, 1958). The reason for this apparent biogenic enrichment is not yet clear (see Calvert and Pedersen, 2007, for a review). Despite its regular use in paleo oceanographic research (Schnieder et al., 1997; Ganeshram, 1999; Villamil et al., 1996; Davis et al., 1999), there are a number of limitations and uncertainties to be considered when using Ba. Barite readily dissolves in the absence of sulphate and so can only be reliably used in sediments that were not affected by sulphate reducing conditions (Brumsack, 1986; Ganeshram, 1999; Henkel et al., 2012). Barite can also be supplied to the sediments via detrital material, and so variations may relate to detrital input, not productivity. Copper, Ni and Zn are all micro nutrients and are therefore

incorporated into organic matter (Whitfield, 2002), a portion of which enters the sediments (Calvert and Pedersen, 1993; Algeo and Maynard, 2004; Böning et al., 2004). They also have oxidised species which adsorb onto, or complex with, organic matter (Achterberg, 2003). Organic particles then shuttle these metals to the sediments, where they are released as OM is degraded, and can form metal sulphides or be incorporated into pyrite (Gregory et al., 2015; Huerta Diaz and Morse, 1992) which is well preserved in the sediments. These elements have been commonly used as paleo productivity proxies (e.g. Nameroff, 2002; Perkins et al., 2008), however, the redox state of the depositional environment must be taken into consideration before they are applied. As Ni, Cu and Zn are hosted within pyrite/form metal sulphides, they may becomeenriched in the presence of sulphide (anoxic/euxinic conditions) even in the absence of high productivity. It may, therefore, be difficult to detect changes in productivity in a depositional setting with varying redox.

Phosphate rich sediments have also been used as indicators of high productivity (e.g. Föllmi et al., 1992; Mort et al., 2007). Phosphorous is a major nutrient, and like Cu, Ni and Zn, it enters the sediments with organic biomass. It is efficiently recycled by microorganisms but can precipitate when high concentrations are reached, which can be the case in upwelling areas (Föllmi et al., 1992). In marine sediments, the dominant host for P is carbonate fluorapatite (Ruttenberg and Berner, 1992) although minor amounts are contained within fish debris, OM and adsorbed onto Fe-oxy(hydr)oxides. Redox conditions also affect sedimentary P concentrations, and P can more efficiently escape from sediments under anoxic conditions (Ingall et al., 1993; van Cappellen and Ingall, 1994).

3.3.3 Redox

In this section, a number of proxies commonly used to investigate bottom water redox conditions are presented. These proxies rely on the change in speciation of an element when exposed to oxygen, and when they are reduced.

Trace element based redox proxies

Manganese arrives in the ocean as (oxyhydr)oxide coatings on grains (clay or siliceous tests) (Burdige et al., 1993) or within submarine hydrothermal fluids (Aller, 1990), although diagenetic recycling plays an important role with marine sediments themselves also being an important source (Burdige et al., 1993). In an oxic water column, Mn exists as Mn^{3+} and Mn^{4+} Mn oxy(hydr)oxides which are insoluble, and so Mn is enriched beneath an oxic water column as Mn is hosted within oxy(hydr)oxides whichh accumulate in the sediments (Burdige et al., 1993). Under an anoxic water column, and when oxygen does not penetrate deeply into the sediments, Mn dissolves and is not preserved in the sediments (Calvert and Pederson, 1993; März et al., 2009). Due to these processes, enrichments or depletions in Mn can preserve information about bottom water redox conditions in the sedimentary record (e.g. Calvert and Pederson, 1993; März et al., 2009). Manganese depletions are less effectively preserved in coastal environments where high OM input and degradation makes the O_2 penetration depth shallower than in pelagic settings (Froelich et al., 1979).

In an oxic water column, U exists mainly as soluble U(VI) (Klinkhammer and Palmer, 1990), so little U accumulates in the sediments under oxic conditions. Uranium accumulates in anoxic sediments by diffusion across a concentration gradient, where it is reduced to U(IV) which is insoluble and is hosted in the sediment sorbed to particle surfaces (Klinkhammer and Palmer, 1991; Cochran et al., 1986). Enrichment in U is, therefore, a valuable proxy for anoxic sediments (Algeo and Maynard, 2004; Föllmi et al, 2012). However, as per Cu, Ni and Zn, U(VI) can be sorb to organic matter in its oxidised form and so U maybe enriched in high productivity, oxic conditions (Anderson, 1982; McManus et al., 2003, Calvert and Pederson 1993).

In oxic marine settings, V exists mainly as vanadate V(V) (soluble in oxic marine waters) (Breit and Wanty, 1990). In mildly reducing waters or sediments, V accumulates in sediments when V(V) is reduced to vanadyl (IV) which is less soluble. When H_2S is present in the water column or the sediments V can accumulate to a greater extent asinsoluble V(III) is form, which also competes with sulphide forming metals which complex to OM (Wanty and Goldhaber, 1992; Calvert and Pederson, 1993). High concentrations of V within a sediment have been used to deduce anoxic bottom waters (Wagner et al., 2007; März et al., 2008; Hofmann et al., 2008; März et al., 2009; Hetzel et al., 2011; Föllmi et al, 2012). Similarly to U, V can also be associated with organic matter in an oxic water column, however the process

is much more efficient in midly reducing waters, amplifying rather than complicating the use of V as a redox proxy (Brett and Wanty, 1990).

Chromium exists in oxic seawater as soluble Cr(VI) chromate (Elderfield, 1970). In anoxic settings, Cr(VI) is reduced to Cr(III) which forms hydroxyl cations (Elderfield, 1970) that are reactive and adsorb to Fe and Mn oxy(hydr)oxides as well as to organic acids in OM as they sink through the water column and is hosted within the sediments adsorbed to these sediment components (Calvert and Pederson, 1993). Cr does not become incorporated within pyrite (Huerta-Diaz and Morse, 1992), and so enrichments are not often preserved. Cr has been used to identify ferruginous conditions (Reinhard et al., 2012), where chromate is reduced and fixed as insoluble (Fe, Cr)$(OH)_3$ (Eary and Rai, 1989). Due to its numerous detrital sources, variations in sediments have been linked to detrital material (Hild and Brumsack, 1997). This may reduce its use in proximal sediments where detrital material dominates.

In an oxic water column, Mo exists as the dissolved molybdate ion, which is relatively conservative, but can accumulate in low concentrations in sediments adsorbed or co-precipited with Mn-oxyhydroxides (Scott and Lyons, 2012). Molybdate ions alter at certain concentrations of H_2S (a geochemical switch), changing to the more particle-reactive thiomolybdate, which is scavenged by detritus (including organic matter) as it sinks to the seafloor, enriching sediments in Mo within OM or directly precipitated as a sulphide mineral (Helz et al., 1996). Thiomolybdate forms in a stepwise manner, requiring persistent H_2S exposure to form the most stable tetrathiomolybdate, therefore Mo enrichments require long-term, non-seasonal euxinic conditions (Erikson and Helz, 1999). Mo enrichments have therefore been used to indicate long term euxinia. Scott and Lyons (2012) collated Mo data from numerous modern basins with varying redox states and suggest Mo values between 2 (average crust) and 25 mg/kg indicate free H_2S was present but limited to the pore waters, while at 25-100 mg/kg the redox conditions are ambiguous, and values greater than 100 mg/kg are a strong indicator of sulphide present in the water column throughout the year. Mo should also be examined normalised to Al, in order to discount a reduction of Mo by dilution.

The drawdown of Mo is so efficient in euxinic conditions that basins which are separated from the open ocean and sufficient resupply of Mo show decreased Mo/TOC ratios over time as Mo is removed quicker from the water mass than it is replaced (Algeo and Lyons,

2006). Values of Mo/TOC less than 14 reflect a strongly hydrographically restricted basin. This proxy is only reliable in the least mature rocks, where TOC has not been significantly lost by oil production.

Redox Proxies – Fe, S and C

In oxic, marine environments, Fe exists as Fe(III), which is generally a solid oxide or (oxyhydr)oxide (Stumm and Morgan, 1981). Under anoxic conditions (in the water column or sediment), Fe(III) is reduced to Fe(II), which is soluble (Burdige, 1993). In the presence of sulphide generated from sulphate reduction, Fe(II) forms insoluble Fe sulphides, the most stable of which is pyrite (Berner, 1970). Pyrite either sinks to the sediments (if formed in the water column) or is formed and retained within the sediments. As sulphide 'scavenges' extra Fe from the water column, an enrichment of pyrite and Fe within a sample can provide information about the extent of anoxia. As the main source of Fe to the oceans is detrital, ratio to the detrital elements Al is useful for normalisation of detrital input. An Fe/Al ratio greater than 0.5 (average shale value, Taylor and McClennan, 1986 and Wederpohl, 1970) has been suggested as an indicator of anoxia (Lyons and Severmann, 2006). Since the precipitation of pyrite depends on the availability of Fe and S, more comprehensive proxies have been developed based on the redox behaviour of Fe. The extent to which the sediment Fe pool which is reactive to sulphide (Fe_{HR}) has reacted with sulphide to form pyrite (Fe_{PY}) is an indicator of the availability of S in the water column, and so is an indicator of euxinia (Raiswell, 1988; Poulton and Canfield, 2005). A Fe_{PY}/Fe_{HR} ratio value over 0.8 is indicative of euxinic conditions (Poulton and Canfield, 2011). A greater amount of Fe_{HR} reaches the sediments in anoxic basins (Raiswell and Canfield, 1998). Additional Fe_{HR} enters the basin in anoxic waters via the Fe-shuttle (Canfield et al., 1996, Lyons and Severmann, 2006, Wijsman et al., 2000, Anderson and Raiswell, 2004). Figure 3.7 illustrates this mechanism. Where the chemocline intersects the shelf, the location of detrital Fe_{HR} accumulation, solid Fe(III) present as Fe oxyhydr(oxides) is reduced to soluble Fe^{2+} which can escape the sediments. This Fe^{2+} can advect to deeper in the basin in anoxic waters, be transported as particulate or colloidal Fe^{3+} upon contact with oxic waters, or drop out of the water column as pyrite when sulphidic waters are encountered. Oxic/suboxic basins have Fe_{HR}/Fe_T ratios <0.38, a value related to the average proportion of Fe in detrital material which is highly reactive, so a value greater than this is indicative of an active Fe-shuttle and ananoxic basin (Raiswell and Canfield, 1998). As this proxy is based on a source to sink relationship, the Fe_{HR}/Fe_T could

also be impacted by the size of the source compared to the size of the sink (i.e. the amount of flooded shelf in contact with the chemocline compared to the size of the basin) (Raiswell and Anderson, 2005). Also, if samples were taken from shelf sediments, they would likely have an Fe_{HR}/Fe_T complicated by very short term variations in the oxygen penetration depth, unrelated to the redox state of the basin.

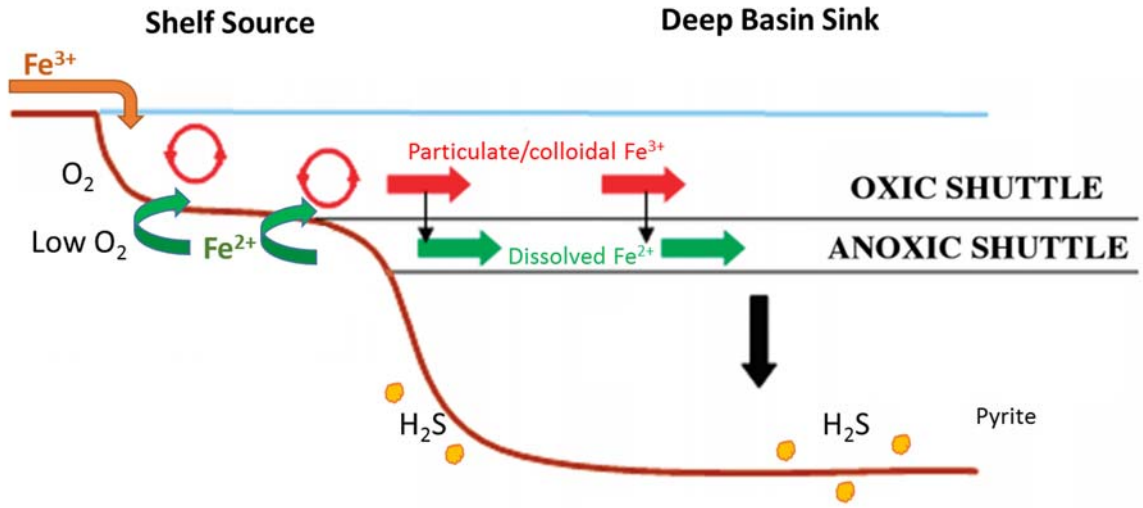

Figure 3.7. Illustration of the Fe-shuttle, providing an additional source of Fe_{HR} to deeper basins when anoxic water intersects shelf sediments. Modified from Algeo and Lyons (2006) and Raiswell and Canfield (2012).

Another pyrite based proxy is pyrite framboid diameter. Pyrite forms, as clusters of micro crystal called framboids, in any marine sediment or water column where Fe (oxyhydr)oxides are being dissolved and sulphate is being reduced. Pyrite framboids formed in the water column are typically smaller than pyrite framboids formed in the sediments, as they can only grow to a certain size, approximately 6µm diameter, before sinking (Wilkes et al., 1996, 1997). Measuring the diameter of a population of pyrite framboids can, therefore, identify sediments formed underneath a euxinic water column (Torres et al., 2015; Wignall and Newton, 1998). In these studies, pyrite framboid diameters were measured individually, limiting the number of framboids which can be used to calculate this average. In automated particle analysis (using SEM-EDX) the diameters of thousands of framboids can be measured. This new method is presented as an alternative to generating pyrite framboid diameter records manually.

As discussed in the introduction to this section, a lack of oxygen in the water column and the sediments allows the preservation of a greater amount of organic carbon as the degradation

of OM by microorganisms is less efficient in the absence of oxygen. Therefore, organic matter preferentially accumulates in anoxic periods compared to oxic periods (Arthur and Sageman, 1994). Also, when dissolved sulphide is present (oxygen free conditions when Fe_{HR} is in limited supply), it can react with labile OM, making it more recalcitrant by 'vulcanising' it into more stable macromolecules – sulphurised organic matter (e.g. carbohydrate – Damsté et al., 1998), and this further encourages the preservation of OM.

Relating to the precipitation of pyrite, S and TOC content together can also provide information about redox. Dissolved sulphate in seawater is reduced to sulphide by anaerobic microorganisms (as they respire reactive OM) in anoxic conditions in the water column or the sediment (Berner, 1974). Sulphide production is thus dependent on the supply of reactive OM. The sulphide produced is also soluble so can diffuse across concentration gradients out of the sediment or to the chemocline in the water column. Sulphide reduces certain metals and forms insoluble metal sulphides (mostly with Fe to form pyrite, but also with Zn, Cu, Ni) (Berner, 1984). These metal sulphides are preserved, so when there are metal sulphides forming in the water column the underlying sediments become enriched in S compared to TOC (Leventhal, 1983). An S/TOC of 0.4 is considered an indicator for anoxic conditions (Dean and Arthur, 1989; Leventhal, 1995). As discussed above, the precipitation of pyrite (and so the preservation of the majority of S) is also dependent on Fe_{HR} supply, so this needs to be taken into account when applying this proxy, as does the reactivity of the OM (Dean and Arthur, 1989). Also, thermal maturation causes a loss of TOC, making this proxy applicable only to immature samples (Raiswell and Berner, 1986). Enrichments of S compared to average shale have also provided supporting evidence for anoxia/euxinia (e.g. März et al., 2008; Hetzel et al., 2011).

3.4 Method of Application of proxies

In order to understand whether a given element content is particularly high or low, it is compared to published average shale values (Wedepohl, 1970, 1991), a method frequently used in sedimentary geochemistry (Brumsack, 2006; Hofmann et al., 2008; März, 2009; Hetzel et al., 2011). In order to understand the enrichment relative to a period of extreme organic carbon burial, i.e., the Cenomanian/Turonian boundary (OAE 2), the values are compared to a C/T mean generated by Brumsack (2006) as per other studies in the Cretaceous (e.g. März, 2009; Mütterlose et al., 2003). In order to identify differences between the EC basin and the well-studied Venezuelan source rocks of the same age, a

mean has been generated from the data reported by Lo Monaco et al. (2002), Alberdi-Genolet and Tocco (1999)), Rey et al. (2004), Davis et al. (1999) and Mongenot et al. (1996). The values used for this comparison are summarised within Tables 3.6 to 3.8.

Table 3.6 Redox proxies which are used for data comparison. Cretaceous Venezuela is from data from Lo Monaco et al. (2002), Alberdi-Genolet and Tocco (1999), Rey et al. (2004), Davis et al. (1999) and Mongenot et al. (1996). N is number of samples with data. Standard deviation in brackets. C/T mean from Brumsack, 2006. Average shale from Wedepohl (1970, 1991). Colours displayed here are used in further graphs.

	S (wt%)	Fe/Al	Mn/Al	Cr/Al	Mo/Al	V/Al	U/Al
Cretaceous Venezuela	1.07 (1.72) (n=88)	0.44 (0.74) (n=91)	0.004 (0.004) n=46	45.0 (±47.3) n=39	40.6 (±57.3) n=41	646.6 (±652.9) n=77	-
C/T mean	3.09	0.77	0.01	41.40	61.40	271.00	6.40
Average shale	0.20	0.55	0.001	10.20	0.15	15.00	0.42

Table 3.7. Detrital proxies which are used for data comparison. Cretaceous Venezuela is from data from Lo Monaco et al. (2002), Alberdi-Genolet and Tocco (1999), Rey et al. (2004), Davis et al. (1999) and Mongenot et al. (1996). Standard deviation in brackets, n is number of samples. C/T mean from Brumsack, 2006. Average shale from Wedepohl (1970, 1991). Colours displayed here are used in further graphs.

	Si/Al	Ti/Al	Ca/Al	Na/Al	K/Al	Zr/Al
Cretaceous Venezuela	5.31 (3.74) n=76	0.04 (0.01) n=36	27.2 (27.5) n=73	0.08 (0.05) n=36	0.26 (0.12) n=76	-
C/T mean	7.36	0.05	2.15	0.26	0.28	18.00
Average shale	3.11	0.05	0.18	0.13	0.34	18.00

Table 3.8. Productivity proxies which are used for data comparison. Cretaceous Venezuela is from data from Lo Monaco et al. (2002), Alberdi-Genolet and Tocco (1999), Rey et al. (2004), Davis et al. (1999) and Mongenot et al. (1996). Standard deviation in brackets, n is number of samples. C/T mean and Namibian Upwelling taken from Brumsack, 2006. Average shale from Wedepohl (1970, 1991). Colours displayed here are used in further graphs.

	P/Al	Ba/Al	Cu/Al	Ni/Al	Zn/Al
Cretaceous Venezuela	0.22 (0.58) n=76	152 (161) n=64	25.7 (23.6) n=74	123.9 (136.8) n=77	489 (±630) n=77
C/T mean	0.047	204	43.8	65.2	459
Average shale	0.008	66	5.10	7.7	11
Namibian Upwelling Mud	0.17	298	32	41.0	29

In the absence of quantitative oxygen concentration data, the definitions outlined by Tyson and Pearson (1991) are used. Euxinic conditions prevail when there is free H_2S in the water column, anoxic conditions are defined by very low oxygen in the bottom waters but no free H_2S. Additionally, ferruginous conditions exist when there is oxygen free water column but no free H_2S due to an excess of Fe_{HR} over $_S$ availability. Comparing TE behaviour can help

distinguish between anoxic and euxinic conditions. For example as U accumulates within the sediments enrichments will not further increase in euxinic conditions, whereas V forms additional complexes/ insoluble components. Given the number of factors which influence U and V (Section 3.3.3), Mo is used instead to distinguish between a euxinic and anoxic water column (Table 4). Ferruginous water column can be distinguished from euxinic water column by Fe_{HR}/Fe_T.. Table 3.9 summarises the multi-proxy approach which is used for assessing redox and is based on Algeo and Maynard, 2004, and Poulton and Canfield, 2005. In order to decipher the driving mechanism of enrichment of TE which are affected by redox and productivity (Cu, Ni, Zn and U), an independent measure of anoxia (Fe_{HR}/Fe_T), will be be incorporated into the interpretation.

Table 3.2.9. Summarising method which redox proxies are applied, based on Algeo and Maynard, 2004.

	Oxic	Anoxic	Euxinic
Enriched compared to average shale	Mn	Al normalised Fe, V, U, C 7 p8r, Mo > average shale (Mo <100 mg/kg) Fe_{HR}/Fe_T>0.38	Al normalised Fe, V, U, Cr, Mo > average shale (Mo> 100 mg/kg) Fe_{HR}/Fe_T>0.38 Fe_{PY}/Fe_{HR} > 0.8 Pyrite framboid diameter <6µm

3.5 Analytical Methods

The bulk and trace metal geochemical composition of our samples were determined using wavelength-dispersive X-ray fluorescence (XRF) (Axios Plus XRF, PANalytical). Around 0.7 g of finely ground sample (agate mortar and pestle) was mixed with 2 g of di-lithiumtetraborate ($Li_2B_4O_{10}$) and pre-oxidised overnight with 1 g ammonium nitrate (NH_4NO_3) for preoxidation of TOC and sulphides prior to fusion to produce a glass bead. Samples were measured alongside an in-house standard with a precision of RSD <5 % for all elements reported here except for U which was close to quantification limit (7 mg/kg, RSD 14 %). This analysis was carried out at the Institute of Chemistry and Biology of the Marine Environment, University of Oldenburg.

Iron speciation analysis was carried out using a sequential extraction method developed by Poulton and Canfield (2005). Four Fe pools were extracted, Fe_{carb} (carbonate associated Fe including siderite and ankerite), Fe_{OX1} (amorphous and poorly crystalline (oxyhydr)oxides, e.g., ferrihydrite and lepidocrocite), Fe_{OX2} (crystalline oxides, e.g., goethite, akaganéite and

hematite) and Fe_{mag} (magnetite). The resultant extraction solutions were analysed for Fe concentrations using atomic absorption spectroscopy (AAS). Pyrite was extracted using the stoichiometric technique prescribed by Canfield et al. (1986), whereby pyrite is reduced using a boiling $Cr(II)Cl_2$ solution. Repeated measurements indicate an average precision of 7 % RSD in the sequential extraction and 2 % RSD in the pyrite extraction.

Inorganic carbon (IC) was analysed by first measuring total carbon (TC) by Leco or Elementar analysis. The TOC value calculated by Ecopetrol was then deducted from this value of TC data in order to provide IC. Sulphur content was also determined by a combination of Leco and elemental analyser data. Freeze dried sample (100 mg) was weighted into a ceramic vessel for TC determination by a Leco CS230 Carbon-Sulphur analyser. Repeated measurements indicate average precision of just over 5 % RSD from LECO analysis. Fifty mg of powdered sample was accurately weighed into clean ceramic crucibles and analysed for C and S content using an Elementar Vario Max CNS Macro Elemental Analyzer, alongside sulfadiazine as a calibration standard. Repeated measurements show an average precision of <5 % RSD.

For the SEM analysis, thin sections were analysed. After vacuum impregnation with resin, rock fragments were polished into thin sections. They were then analysed, uncoated, using SEM (Quanta 650 field-emission SEM) operated in low-vacuum mode. Images were collected with a standard quad back-scattered electron (BSE) detector at 20kV, with a spot size of 4.5. In addition, an EDX detector (Oxford Instruments X-MaxN 150) was used to scan across the sample using the particle analysis software AZtecFeature to detect heavy mineral particles. A series of fields of view were scanned, with a dwell time of 35 microseconds, having a horizontal field of view of 259 microns and 1024 pixels. Each image was thresholded and all bright particles were automatically selected for analysis by EDX. The whole area of each feature was scanned, using a process time of 1 and an acquisition time of 0.50 live seconds. Particles smaller than 0.49 microns equivalent circular diameter (ECD), equating to 3 pixels, were automatically filtered out. Each particle was analysed in terms of its elemental composition and a range of physical parameters, which included X-Y location coordinates. Data was then interrogated using IncaFeature (Oxford Instruments).

Chapter 4 Contemporary Outcrop weathering of organic-rich mudrocks: carbonate enhances preservation of inorganic geochemical redox proxies

Authors

Carol Mahoney[1], Christian März[2], Jim Buckman[3], Tom Wagner[4], Vladimir- Orlando Blanco-Velandia[5]

1. School of Civil Engineering and Geosciences, Newcastle University, NE1 7RU, United Kingdom.
2. School of Earth and Environment, Leeds University, LS2 9JT, United Kingdom.
3. Institute of Petroleum Engineering, Heriot-Watt University, Edinburgh, EH14 4AS, United Kingdom
4. The Lyell Centre, Research Avenue South, Edinburgh, EH14 4AP, United Kingdom
5. Instituto Colombiano del Petróleo, Ecopetrol, Bucaramanga, Colombia

Submitted to Chemical Geology in June 2017.

4.1 Research Highlights

- Artificial weathering of organic-rich mudrocks results in pyrite oxidation and carbonate dissolution
- Pyrite is passivated at circum-neutral to high pH by Fe(oxyhydr)oxide rims
- Trace metals behave conservatively, perhaps due to co-precipitation with/sorption to Fe(oxyhydr)oxides
- Trace metals and the Fe_{HR}/Fe_T proxy appear reliable at quickly eroding outcrops
- Carbonate content is a useful indicator for reliability of geochemical proxies

Abstract

Organic-rich mudrocks are valuable sources of information about past environments when parts of the oceans experienced enhanced accumulation of organic material, frequently in association with oxygen-depleted bottom water conditions. Information about the state of oxygenation of such a depositional environment is often extracted from the sedimentary

record through the use of inorganic geochemical proxies, including Fe-speciation and trace metal enrichments. While fresh mudrock samples from wells offer ideal material for geochemical analyses, outcrops are equally important to increase temporal and spatial coverage for an integrated palaeo-environmental reconstruction. In outcrops, however, geochemical proxies may be altered by contemporary chemical weathering, creating a fundamental challenge that is not well addressed. Pyrite (FeS_2) plays a particularly important role in the geochemical interpretation of mudrocks, as it is a key component in the Fe-speciation redox proxy and is also host to various redox-sensitive or sulphide-forming trace metals. However, pyrite is prone to alteration at the Earth's surface, and pyrite oxidation is a key first stage of chemical weathering. Here the results from artificial weathering experiments of organic-rich mudstones with a high (35 %) and moderate carbonate content (3 %) are compared. The results provide evidence that pyrite in mudstone can be passivated in circum-neutral to high pH (up to pH 10) pore water environments by the build up of Fe(oxyhydr)oxide rims. The presence of carbonate may, therefore, limit the effects of chemical weathering, especially in high physical erosion situations, like coastal or river outcrops.

4.2 Introduction

Organic-rich mudrocks provide valuable sources of fossil energy and unique information on extreme palaeo-environmental conditions, often representing periods of global greenhouse climate (Negri et al., 2006). Understanding the lateral and temporal development of these rocks often requires a combination of well and outcrop material, the latter having experienced variable degrees of degradation due to outcrop weathering processes. The leaching of elements from organic-rich mudrock by weathering is well documented (e.g. Perkins and Mason, 2014; Pye and Miller, 1990; Tuttle and Breit, 2009; Zhu et al. 2008; Zhu and Wu, 2011), and known to be an important process mobilising nutrients and other critical elements from the bedrock to soils, rivers and eventually the ocean. However, the selective loss of elements from weathered organic-rich mudrocks and the related alteration of its geochemical inventory creates challenges for the interpretation of palaeo-environmental conditions from the chemical composition and can render weathered mudrock records unreliable unless the weathering effects are accounted for. This weathering bias is particularly pronounced for metal contents, which provide important information about palaeo-redox conditions of the ocean and pore waters at the time of deposition (Kraal et al., 2009). Well-established proxies for reconstructing anoxia, including

Mo, Re, V, U, Cd, Cu, Ni and Zn contents (see Brumsack, 2006; Calvert and Pederson, 2007 and Tribovillard et al., 2006 for reviews), the relationships between TOC, Fe and S (Lyons and Severmann, 2006), Fe-speciation (Poulton and Canfield, 2011), and pyrite framboid diameter (Wilkin et al., 1996) may be significantly affected by weathering.

Iron, while being an important proxy for palaeo-redox conditions, is also important to the process of weathering itself. The oxidation of pyrite (FeS_2), the dominant Fe sulphide in rocks, is key to the chemical weathering behaviour of organic-rich mudrocks. The net chemical reaction of pyrite in an aqueous solution is:

$$FeS_2 + 3.5O_2 + H_2O \rightarrow Fe^{2+} + 2H^+ + 2SO_4^{2-}$$ (Equation 4.1)

Ferrous iron produced in Equation 4.1 either remains in solution or produces a variety of Fe (oxyhydr)oxides), depending on the chemical environment. As evident from Eq. 1, pyrite oxidation provides protons, which are then available for the hydrolysis of aluminosilicate and dissolution of carbonates (Pye and Miller, 1990) and consumes oxygen thereby inhibiting organic matter oxidation (Petsch et al., 2000; Tuttle and Breit, 2009). Understanding the mechanism and balance of pyrite oxidation is, therefore, vital for understanding the mechanisms of mudrock weathering. Dissolution of carbonate minerals (mainly calcite) is considered a key reaction in response to proton release by pyrite weathering:

$$CaCO_3 + H^+ \rightarrow Ca^{2+} + 2HCO_3^-$$ (Equation 4.2)

Diagenetic carbonate dissolution increases porosity and allows oxygen and water to penetrate further into the mudrock fabric (Brantley and White, 2009; Jin et al., 2013; Pye and Miller, 1990). However, through the liberation of bicarbonate ions to solution, the dissolution of carbonate also acts as a pH buffer in the pore waters. It has been shown that high pH inhibits pyrite oxidation in laboratory experiments (Nicholson et al., 1988; Nordstrom, 1982), in soils (Lara et al., 2016), in acid mine drainage situations (Evangelou and Zhang, 1995; Huminicki and Rimstidt, 2009; Wiggering, 1993), and when storing shale samples (Kraal et al., 2009). In the field, carbonate and pyrite weathering fronts can coincide (e.g. Brantley et al., 2017), suggesting direct pyrite oxidation-carbonate dissolution relationships in mudrock. These processes are not well understood but can affect element composition in shale and thus their application as palaeo-environmental proxies.

Studies of Fe-speciation changes during weathering in organic-rich mudrocks to date are mostly limited to changes in pyrite contents (Jin et al., 2013; Liao et al., 2014; Littkle et al., 1991; Petsch et al., 2000; Wildman et al., 2004; Zhu et al., 2008). Iron mineral transformations due to weathering have been studied in naturally weathered rocks using X-ray diffraction (XRD) (Pye and Mason, 1990; Tuttle and Breit, 2009) and Mössbauer spectroscopy (Odin et al., 2014, 2015a, 2015b). To our knowledge, no experiment has examined changes in Fe mineralogy during organic-rich mudstone weathering using the wet chemical extraction method developed by Poulton and Canfield (2005). Taking advantage of this sequential extraction method, quantitative information on the different Fe species present in a sedimentary rock based on their reactivity with free hydrogen sulphide can be derived. In this scheme, all minerals that have already reacted with hydrogen sulphide (mainly pyrite, Fe_{PY} fraction) or can react with hydrogen sulphide over geologically short timescales (days to a few years; mainly Fe carbonates and (oxyhydr)oxides) are collectively summarised as the highly reactive Fe fraction (Fe_{HR}). In combination with the analysis of total Fe (Fe_T) in a sample, empirically tested ratios can be calculated that allow a differentiation of redox conditions in the water mass during the time of deposition. The Fe_{HR}/Fe_T ratio has consequently been proposed as palaeo-proxy to differentiate between anoxic (no free oxygen) and oxic conditions during deposition, while the Fe_{PY}/Fe_{HR} ratio allows to differentiate between anoxic, non-sulphidic (or ferruginous) and anoxic, sulphidic (or euxinic) conditions (e.g Poulton and Canfield, 2011; Poulton et al., 2015). Since the Fe_{HR} fraction includes both pyrite and the products of pyrite oxidation, Fe (oxyhydr)oxides), it is expected that the Fe_{HR}/Fe_T redox proxy will be less affected by outcrop weathering. The Fe_{PY}/Fe_{HR} is expected to be more strongly affected by outcrop weathering and therefore less reliable for palaeo-environmental reconstructions. Another commonly used pyrite-based redox proxy that could potentially be affected is the abundance and size population of pyrite grains preserved in a mudrock. Pyrite framboids formed within a euxinic water column reach a maximum size before they sink to the sediment, leading to the framboid diameter proxy proposed by Wilkin et al. (1996), as an indicator of water column euxinia. Populations of pyrite framboids with an average diameter <6µm and a small standard deviation are therefore considered to represent euxinic water column conditions. Although oxidation of pyrite would likely reduce the size of pyrite framboids and so alter the interpretation of this proxy, to our knowledge, no systematic study has yet been carried out.

Some redox-sensitive or sulphide-forming trace metals (e.g. Ni, Cu, Mo and Zn) are known to be associated with pyrite (Gregory et al. 2015; Huerta-Diaz and Morse, 1992), and their mobility during outcrop weathering should be determined by the degree of pyrite oxidation (Perkins and Mason, 2014; Zhu et al., 2008). Various studies have addressed the rates and mechanisms of loss of metals from organic-rich mudrocks during weathering, but often with inconclusive or contrasting outcomes. Cadmium, Co, Mn, Ni and Zn are lost from organic-rich mudrocks in the majority of studies (Perkins and Mason, 2014; Tuttle et al., 2009) while As, Cr, Mo, V and Se appear to be better preserved (Perkins and Mason, 2014; Tuttle et al., 2009). In contrast, Peng et al (2004) found little evidence for consistent loss or conservation of any elements apart from Co, Ni, Zn and Cd. These discrepancies highlight the need for further research.

There are two main types of weathering studies: One that compares outcrops at different locations with different degrees of weathering (Fischer at al., 2009a; Littke et al., 1991; Perkins and Mason, 2015; Tuttle and Breit, 2009), and another where weathering profiles at the same location but crossing bedding planes were studied (Clayton and Swetland, 1978; Leythaeuser, 1978; Wildman et al., 2004). Both types of studies incorporate a degree of inherent spatial and temporal variability that makes it difficult to unequivocally attribute a variation in composition to weathering alone. An alternative approach is to artificially weather an organic-rich mudrock in the laboratory. A limited number of artificial weathering experiments using organic-rich mudrocks (Jeng, 1991; Jin et al., 2013; Odin et al., 2014; Pye and Miller, 1990; Schillawaski, 2008; Senkayi et al., 1990;) focused on the behaviour of only a few selected elements rather than the wide suite of elements used as palaeo-proxies. Laboratory experiments can only aim to reproduce short term chemical weathering (weeks to months), but this timeframe may still be meaningful in investigating environments with high physical erosion rates. This includes river/stream beds (incision rates through high topography sedimentary rocks 10^{-3} – 10^{-2} m yr^{-1}, Cornwell et al., 2003; Hsieh and Knuepfer, 2001) or sea cliff faces (e.g. erosion rate 10^{-1} m yr^{-1}, Rosser et al., 2005), where physical erosion will likely remove rock material before its chemical weathering process is complete. These environments are often chosen for the collection of 'fresh' outcrop samples for geochemical analysis. Understanding and quantifying the short-term effects on chemistry and possible interim weathering products is therefore of central importance for the interpretation of geochemical proxies.

In this study, natural weathering was simulated over the course of four weeks to enhance our qualitative and quantitative understanding of organic-rich mudrocks. Major and trace elements, inorganic and organic carbon and Fe species are measured, and the original and residual organic-rich mudrock samples analysed using automated particle analysis data from scanning electron microscopy with energy-dispersive analysis and imaging (SEM-EDX) in samples with different amounts of carbonate (35 % versus 3 %). Our study focuses on changes to chemical properties of the mudrock that are commonly used as inorganic proxies to reconstruct palaeo-environmental conditions, and thus provides novel insights into their preservation or overprint at outcrop level.

4.3 Methods

4.3.1 Materials

Two types of organic-rich mudrock were selected for weathering experiments: The classical Blackstone band (BS) of the Jurassic Kimmeridge Clay Formation collected at Clavell's Hard, Kimmeridge, Dorset (e.g. Armstrong et al., 2016; Bolin et al., 2016; Washburn and Birdwell, 2013). The second sample is from a Late Cretaceous organic-rich mudrocks of the Chipaque Formation (QVS4), taken from Quebrada Vara Santa in the Eastern Cordillera of Colombia. Both samples differ markedly in their geochemistry. BS is a relatively carbonate-rich mudstone dominated by organic matter (OM) (~50 wt%; Raiswell et al., 2001; Tribovillard et al., 2004) and carbonate (35 %, this study). QVS4 is dominated by siliciclastic detrital material (Blanco, 2012) and has a low carbonate content (3.1 %, this study) and TOC contents (2.6 %, this study), representing a relatively carbonate-poor mudstone with a carbonate content close to average shale (average shale contains 3.9 % $CaCO_3$, assuming all Ca is from carbonate; Wedepohl, 1971 and 1991). Both samples, however, have similar amounts of pyrite (QVS4 2.2 %, BS 1.7 %). Comparison of these samples provides insights into the role of carbonate on pyrite oxidation reactions and the subsequent combined effect on weathering and palaeo-proxy preservation. Both samples were collected from surface outcrops, but are considered 'unweathered' for the purpose of this study as they show no macroscopic signs of weathering, and should be relatively freshly exposed due to the outcrop locations at a quickly eroding cliff face (BS) and in a mountainous river bed (QVS4).

4.3.2 Weathering Experiment

The weathering experiment follows the approach of Pedro et al. (1970), using a modified soxhlet extraction setup to continually drip distilled water over a sample contained within a cellulose thimble (Figure 4.1), mimicking continual rainfall. The condenser is left open,

allowing exchange with the atmosphere; no attempt was made to control/monitor O_2 and CO_2 concentrations.

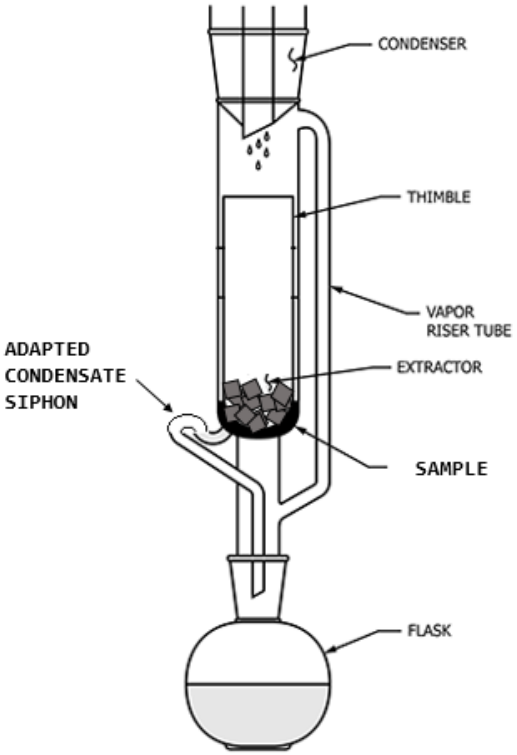

Figure 4.1. Modified soxhlet after Pedro (1970)

Around 35-40 g of freeze-dried rock chips, sieved to approximately 2 - 6 mm diameter, were added to a cellulose thimble in the sample container. Distilled water was added to the round bottom flask and heat was applied to generate water vapour which, when reaching the condenser, dripped onto the sample (3-6 drops/minute). The water (hereafter called effluent) was monitored regularly and the periods between changes and the volume of effluent was adjusted to attempt to minimise mineral precipitation within the effluent. Each time the effluent was changed, the temperature was recorded within the cellulose thimble, the pH of the effluent was measured using a pHenomenal pH1000L meter (Figure 4.2a), and samples of the effluent were taken. The temperature varied with ambient conditions from 33-58°C (Figure 4.2b). The effluent samples were treated with 20 % v/v nitric acid in order to adjust pH to <2 and stored at around 5 °C for further analysis. At the end of the four-week experiment, the rock chips were removed from the thimble, freeze-dried and ground in an agate ball mill for geochemical analysis. To test the reproducibility of the experiment, three subsamples of QVS4.1 were weathered concurrently in three identical setups.

4.2a

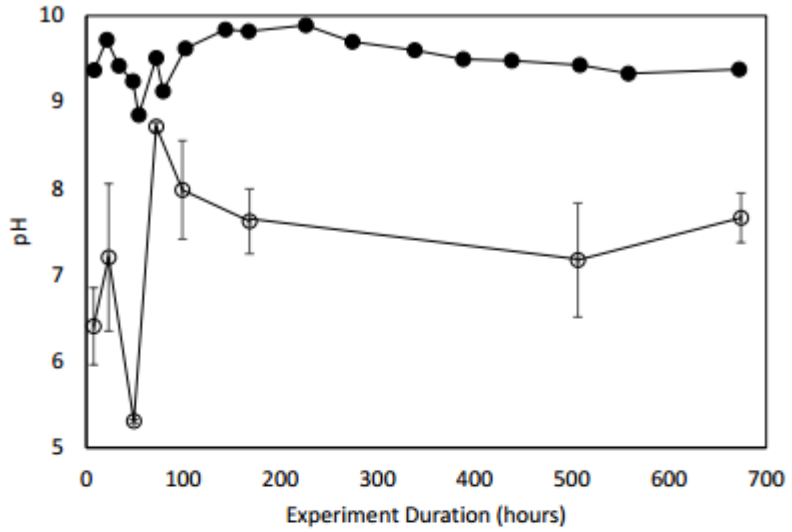

4.2b

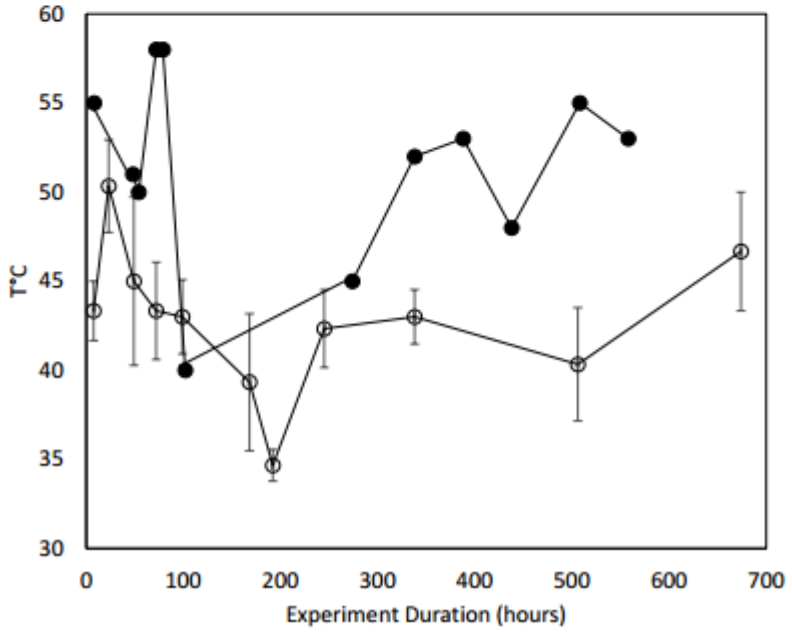

Figure 4.2a pH measured within effluent during sampling. 2b. Temperature measured within the sample thimble. Error bars are standard error measured in three replicate experiments. Open circles are QVS4, closed circles are BS.

4.3.3 Analysis of solid sample

The bulk and trace metal geochemistry were determined using wavelength-dispersive X-ray fluorescence (XRF) (Axios Plus XRF, PANalytical). Around 0.7 g of sample was mixed with 2 g of di-lithium tetraborate ($Li_2B_4O_{10}$) and pre-oxidised overnight with 1 g ammonium nitrate (NH_4NO_3) for preoxidation of TOC and sulphides prior to fusion to produce a glass bead. Samples were measured alongside an in-house standard with a precision of RSD <5 % for all elements reported here except for U which was close to quantitation limit (7 $mgkg^{-1}$, RSD 14 %).

Freeze dried samples (100mg) were weighted into a ceramic vessel for TC determination by

a Leco CS230 Carbon-Sulphur analyser. Total organic carbon was determined by the same method after the removal of carbonates by hot hydrochloric acid. Total inorganic C (TIC) was calculated as the difference between TC and TOC. Total inorganic carbon is likely to derive from calcium carbonate/calcite as well as small contributions by dolomite/magnesium calcite and Fe associated carbonates. Repeated measurements indicate average precision of 5.1 % RSD from LECO analysis. Fifty mg of powdered sample were accurately weighed into clean ceramic crucibles and analysed for S content using an Elementar Vario Max CNS Macro Elemental Analyzer, alongside sulfadiazine as a calibration standard. Repeated measurements show an average precision of <5 % RSD.

Iron-speciation was carried out using a sequential extraction method developed by Poulton and Canfield (2005). Four Fe pools were extracted, Fe_{carb} (carbonate associated Fe including siderite and ankerite), Fe_{OX1} (amorphous and poorly crystalline (oxyhydr)oxides, e.g.ferrihydrite and lepidocrocite), Fe_{OX2} (crystalline oxides, e.g. goethite, akaganéite and hematite) and Fe_{mag} (magnetite). The resultant extraction solutions were analysed for Fe concentrations using atomic absorption spectroscopy (AAS). Pyrite was extracted using the stoichiometric technique prescribed by Canfield et al. (1986), whereby pyrite is reduced using a boiling $Cr(II)Cl_2$ solution. Repeated measurements indicate an average precision of 7 % RSD in the sequential extraction and 2 % RSD in the pyrite extraction.

4.3.4 Effluent analysis

Acidified effluent samples were analysed using inductively coupled plasma optical emission spectroscopy (ICP-OES) (Varian Vista-MPX CCD simultaneous ICP-OES with argon torch gas). A multi-element standard was used for calibration every 10 samples and Sc was used as an internal recovery standard at 5ppm. Each sample was measured three times with an RSD of less than 5.5 % for major elements and 10 % for trace elements apart from one aliquot of effluent in BS (17 %), with all analyses below the limit of quantification (LOQ) are removed.

4.3.5 SEM analysis

After vacuum impregnation with resin, rock chips before and after weathering were made into polished thin sections. They were then analysed, uncoated, using SEM (Quanta 650 field-emission SEM) operated in low-vacuum mode. Images were collected with a standard quad back-scattered electron (BSE) detector at 20kV, with a spot size of 4.5. In addition, an EDX detector (Oxford Instruments X-Max^N 150) was used to scan across the sample using the particle analysis software AZtecFeature to detect heavy mineral particles. A series of fields of

view were scanned, with a dwell time of 35 microseconds, having a horizontal field of view of 259 microns and 1024 pixels. Each image was thresholded and all bright particles were automatically selected for analysis by EDX. The whole area of each feature was scanned, using a process time of 1 and an acquisition time of 0.50 live seconds. Particles smaller than 0.49 microns equivalent circular diameter (ECD), equating to 3 pixels, were automatically filtered out. Each particle was analysed in terms of its elemental composition and a range of physical parameters, which included X-Y location coordinates

4.3.6 Reproducibility

Three sub-samples of QVS4.1 were artificially weathered simultaneously, confirming that the experiment was overall reproducible. Within the solid samples (post-weathering), XRF analyses showed contents for most elements with an RSD below 5 %. Some elements with concentrations close to the LOQ (Na, Cu and Mo) or which have lower reported precision when analysing an in-house standard (e.g. U) have higher RSDs (up to 10 %). Ca has higher RSD (29 %) and this is not accountable for by analytical errors. The deviating results may be due to slight differences in the composition of the original material, or different solubility of host components caused by slight variation in temperature of the samples (see Figure 4.2b). The standard error is included in Figure 4.3 and 4.4 and is negligible in relation to the geochemical trends described below.

4.4 Results

4.4.1 Changes in bulk geochemistry of organic-rich mudrocks

The bulk geochemistry results highlight the differences between the BS and QVS4 samples before the weathering experiment (BS.1 and QVS4.1). Inorganic carbon content is an order of magnitude higher in BS.1 compared to QVS4 (34.8 wt% and 3.1 wt%, respectively; Table 4.1b). BS.1 is enriched in TOC, comparable with data previously published on the Kimmeridge Blackstone (on average 46.3 wt%, Raiswell et al., 2001), whilst it is depleted compared to QVS4.1 in elements associated with detrital material (Si, Ti, Al, Fe and K, Table 1a). BS.1 also contains elevated levels of selected major elements and trace metals (P, S, Cu, Mo, Ni and Zn, Table 4.1c). BS.1 has a lower Fe content, and corresponding slightly lower absolute contents of all Fe species (Table 4.2), with an excess of total S relative to pyrite S (Table 4.1b). This excess S is likely bound as sulphurised organic matter (SOM in Table 1b), confirming results by Raiswell et al. (2001). Within QVS4.1, the pyrite accounts for all of the S (Table 4.1b), indicating the absence or a very low sulphurised organic matter content.

Table 4.1a-c Concentrations of elements in solid sample before and after weathering. Determined by XRF (Table 1a and 1c), LECO analysis (Table 1b), CNS elementar analysis (Table 4.1b) combined with results of pyrite extraction (sulphurised organic matter – SOM). QVS4.1 is average of 3 with standard error in brackets.

a.

	SiO_2	TiO_2	Fe_2O_3	MnO	MgO	CaO	Na_2O	K_2O	P_2O_5
	(wt %)	(wt %)	(wt%)	(wt%)	(wt%)	(wt%)	(wt%)	(wt%)	(wt%)
BS	11.92	0.24	2.51	0.01	0.37	7.47	0.12	0.73	0.74
BS.1	11.83	0.24	2.52	0.01	0.34	6.48	0.09	0.73	0.79
QVS4	54.99	0.96	4.82	0.02	0.75	1.12	0.07	2.12	0.15
QVS4.1	55 (±0.2)	0.96 (±0.00)	4.81 (±0.03)	0.02 (±0.0)	0.71 (±0.01)	0.71 (±0.2)	0.06 (±0.01)	2.05 (±0.01)	0.15 (±0.00)

b.

	TOC	TIC	S	PyS	SOM
	(wt%)	(wt%)	(wt%)	(wt%)	(wt%)
BS	49.50	4.18	6.71	0.92	5.79
BS.1	51.15	2.16	6.60	0.59	6.01
QVS4	2.61	0.37	0.81	2.16	0
QVS4.1	2.77 (±0.06)	0.02 (±0.02)	0.62 (±0.02)	1.7 (±0.05)	0

c.

	Cr	Cu	Ni	U	V	Zn
	(mg/kg)	(mg/kg)	(mg/kg)	(mg/kg)	(mg/kg)	(mg/kg)
BS	49	51	96	3	69	125
BS.1	49	50	98	2	69	108
QVS4	79	8	31	8	88	73
QVS4.1	82 (±1.2)	7 (±0.3)	32 (±0.0)	8 (±0.9)	86 (±1.2)	84 (±1.9)

As element contents (reported in Table 4.1) are affected by changes in density and overall mass loss, we compare the changes of elements of concern to Ti, which is presumed to be resistant to weathering (Tuttle et al., 2009). Consistent with this behaviour, Ti is not lost from either sample during the experiments (Table 4.1a, Table 4.3a and 4.3b). This generates the mass transfer coefficient (τ, Equation 4.3) for monitoring loss or conservation in the absence of bulk density data, as developed by Brimhall et al. (1991) (Figure 4.3).

$$\tau = ((C_{j.w}/C_{j.p})/(C_{i.w}/C_{i.p}))-1 \qquad \text{Equation 4.3.}$$

Here the concentration of the element of concern (C_j) is ratioed between the weathered (w) and parent (p) sample, and this is then expressed as a proportion of the ratio of the index element (C_i) in the weathered and parent sample.

Figure 4.3a shows high negative τ values for inorganic carbon, with near 100 % loss (τ close to -1) in QVS4. This is matched with a loss of Ca, indicating most of the inorganic carbonate is

associated with Ca. The values of τ are also negative for Na, which may document slight weathering of feldspars (Nesbitt and Young, 1982), and for S, suggesting oxidation of pyrite. Other bulk elements (including Fe) show values no greater than -0.1 or slightly positive, indicating relative conservation of these elements during weathering. QVS4 shows a greater relative depletion of Ca, IC, S and Mn. Trace elements appear to be all relatively conservative during weathering (Figure 4.3b). Large error bars for Mo and U are due to their content close to quantification limits.

Some differences in Fe-speciation between BS.1 and QVS4.1 were found (Table 4.2). We observed slightly more Fe_{carb}, Fe_{OX2} and Fe_{Py} in QVS4.1 as compared to BS.1, and considerably more Fe_{OX1}. After weathering, both samples showed a decrease in Fe_{Carb} and Fe_{Py} (Table 4.2, Figure 4.3c), but an addition of Fe (oxyhydr)oxides. The latter is limited to the Fe_{OX2} fraction in QVS4.2, whereas in BS.2 there is an increase in both Fe_{OX1} and Fe_{OX2}. This increase is absolute, not due to a reduction in sample volume, as evident by the very positive τ values seen in Figure 4.3c. This phase transformation causes only minor changes in the Fe_{HR}/Fe_T ratios, as there is little net loss of Fe from the rock chips (Figure 4.3a), only a switch from reduced to oxidised Fe species, as reflected by the lower Fe_{PY}/Fe_{HR} ratios in both samples (Table 4.2).

Table 4.2 Results of Fe-speciation analysis on the two study samples before (.1) and after (.2) weathering experiment in wt%. QVS4.2 is average (n=3) with standard error in brackets.

	Fe (wt%)	**Fe_{Carb} (wt%)**	**Fe_{OX1} (wt%)**	**Fe_{OX2} (wt%)**	**Fe_{Mag} (wt%)**	**Fe_{Py} (wt%)**	**Fe_{PRS} (wt%)**	**Fe_{HR}/Fe_T**	**Fe_{PY}/Fe_{HR}**
BS.1	1.76	0.14	0.04	0.02	0.00	0.80	0.76	0.57	0.80
BS.2	1.76	0.11	0.18	0.26	0.01	0.51	0.69	0.61	0.54
QVS4.1	3.37	0.33	0.60	0.05	0.13	1.01	1.26	0.63	0.39
QVS4.2	3.36 (±0.01)	0.16 (±0.01)	0.54 (±0.02)	0.47 (±0.03)	0.08 (±0.01)	0.79 (±0.02)	1.32 (±0.02)	0.61	0.30

Figure 4.3.a

Figure 4.3.b

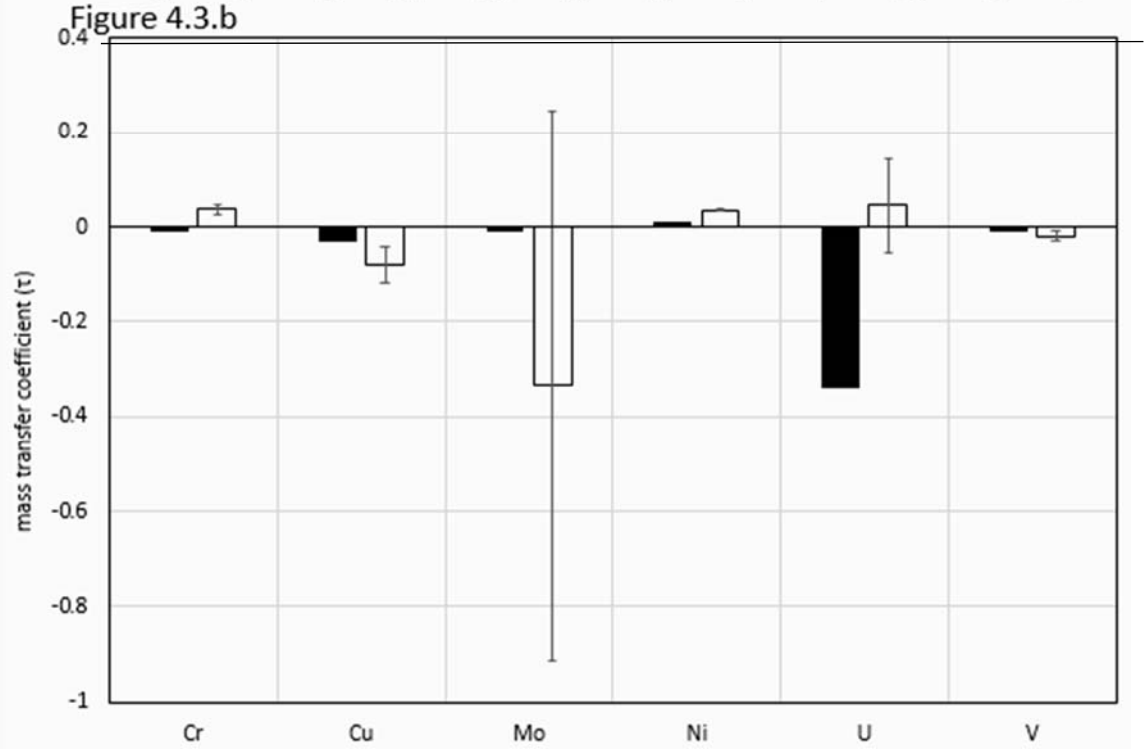

4.3c

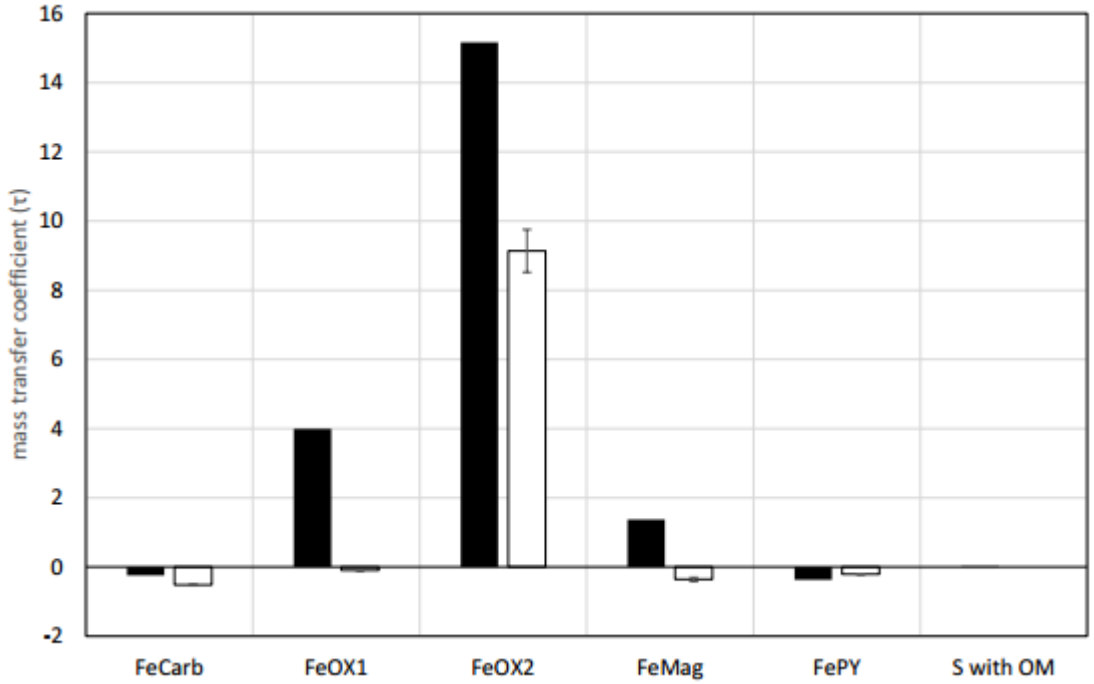

Figure 4.3 Mass transfer coefficient of elements and species calculated using Equation 4.3, with Ti as the index element. Black bars are BS samples, white are QVS4 samples. Positive values indicate conservation, negative values indicate loss. Complete loss is indicated by a mass transfer coefficient of -1. Error bars are standard error of three replicated experiments. Figure 4.3a shows the bulk elements determined by XRF (apart from TOC, IC and S, LECO analysis). Figure4.32b shows trace elements (determined by XRF). Figure 4.3c shows Fe speciation results determined by sequential extraction and S from CNS analysis.

4.4.2 Effluent chemistry for major and trace elements

Over the duration of the experiment, pH of the effluent increased from 8.9 to 9.9 in the BS experiment and, more pronounced, from 5.3 to 8.9 for QVS4 (Figure 4.2a). For the majority of the experiment the effluent was clear, however, in a few incidences (three in the BS experiment, two in the QVS4 experiment) a small amount of white precipitate was noted. Although not analysed separately, this weathering product was likely gypsum (discussed further below). To enable direct comparison of the loss of trace elements from the two samples into the effluent over time, we express them as relative percentages (rel%) of the original contents of these elements available in the original unweathered sample (actual concentrations available in Table 4.3, Appendix C). There are some noticeable differences in the development of effluent composition over time and between the BS and QVS4 samples.

Trace elements in effluents

Most effluent samples contained trace metals at levels below the limit of quantification (LOQ) in ICP-OES. Although these concentrations are not highly accurate it was useful to calculate the proportion of available trace metals leached into the effluent in order to

estimate their relative resistivity to weathering. Both samples leached less than 10 % of the available V, Cr, Ni, and Cu into the effluent during the experiment. Uranium has a higher LOQ in ICP-OES, (0.1 ppm as opposed to 0.01/ 0.02 ppm) and, due to the low amounts of U available in the BS.1 sample (0.1 mg), the cumulative % of U leached into effluent is calculated as 85 %, suggesting uranium is very labile in QVS4. However, given the relatively high LOQ, this number is likely unreliable. Further work using more sensitive instruments would be required in order to confirm U lability. A similar process prevents an accurate understanding of Mo leaching from QVS4 (Mo contents in original samples 0.03 mg, detection limit of ICP-OES 0.02 ppm). Both samples consistently lost measurable (above LOQ) fractions of Ni, with BS losing a smaller proportion (0.048 mg of 3.67 mg available in BS.1, which is 1.35 rel%) than QVS4 (0.054 mg of 1.1 mg available in QVS4.1, 4.96 rel%). Some elements were above the LOQ in a few of the effluent samples (BS: Mo; QVS4: Zn and Cu). In BS, a small but quantifiable fraction (0.2 rel%, 0.004 mg) of the initial content of Mo (2.18 mg) was leached within the first 8 hours of the experiment, thereafter the leached Mo concentrations were below LOQ. Zinc was only leached from QVS4 into the effluent in quantities above LOQ (0.30 mg of 2.49 mg available in QVS4.1, 11.54 rel%). As Zn was very high in the last two effluent samples of QVS4, and the Zn in the solid samples shows a measurable addition as well (Table 4.1c), we assume that the samples were contaminated with Zn in the later stages of the experiment. Zn is therefore not discussed in the remainder of this article. This significant increase towards the end of the experiment is only evident in Zn; contamination by other elements is therefore not indicated.

Major elements in effluents

In both samples, most Fe remained in the rock chips (loss of 0.15 rel% in BS, 0.004 rel% in QVS4). The elements K, Al, S, Na and Mg lost between 1.0 and 7.5 rel% of their original content into the effluent. Loss of Na (3.4 rel% in BS, 5.0 rel% in QVS4) and K (2.8 rel% in BS and 3.0 rel% in QVS4) is additional evidence of aluminosilicate weathering. The rate of loss of all elements was fastest in the first 100 hours of the weathering experiment (Figure 4.4). This initial high rate is consistent with other experimental weathering studies (e.g. Ritsema and Groenberg, 1993; Yao et al., 2010). After this initial period, the loss of effluent either gradually slowed down (e.g. Ca in BS, Figure 4.4a) or continued at a similar rate for the remainder of the experiment (e.g. Ca in QVS4, Figure 4.4a). It appears that Ca and S loss stalled in BS but continued in QVS4 (Figure 4.4a and b). The majority of inorganic carbon was

lost from the solid QVS4 (94 %, Table 4.1), however, Figure 4.4a shows that only approximately 70 % of the Ca was leached from the sample into the effluent. The Ca remaining in the sample may be in the form of newly precipitated gypsum or within aluminosilicate, or the carbonate loss may have been associated with the dissolution of minerals other than calcite (e.g. Fe or Mg carbonates). The same effect is apparent in BS, where 48 % of the carbonate was lost from the solid sample and only 30 rel% of the Ca was leached from the sample. Although possibly affected by differential gypsum precipitation, the greater relative proportion of Ca leached from QVS4 provides evidence for greater extent of carbonate dissolution.

Since sulphurised organic matter appears to be relatively stable under the experimental conditions (Table 4.1b), any S leached into the effluent is likely a product of pyrite oxidation (or secondary dissolution of the gypsum weathering product). Figure 4.4c (cumulative S released into effluent over time as a proportion of total pyrite S available in the unweathered sample) can, therefore, be used to estimate the rate of pyrite oxidation. In Figure 4.4c we see that pyrite oxidation appears to occur at similar rates in BS and QVS4. As for other elements, the rates begin to slow towards the end of the experiment in BS, a trend not seen in QVS4. At the rates measured in the last 100 hours of the experiment (0.014 mg/hour or 0.003 rel%/hour for QVS4 and 0.008 mg/hour or 0.002 rel% for BS), it would take approximately 2.5 years and 3.25 years, respectively, for all of the pyrite to be oxidised. We consider these time periods to under-estimate the weathering efficiency, as gypsum precipitates, found occasionally in effluent samples, were not analysed, and so the S with gypsum was not included in this S-budget. Nickel, the only trace metal which is above LOQ in most of the effluent samples, appears to behave similarly in both experiments.

Considering the amount (mg) of elements lost from the rock chips into solution over each time interval there does not appear to be a direct relationship between loss of S and Fe (r^2< 0.01, Figure 4.5). Sulphur, however, correlates well with Ca in the effluents from both samples (r^2 values of 0.93 in QVS4 and 0.89 in BS (Figure 4.5), and in QVS4 it also correlates well with Na (r^2 0.81) and Mg (r^2 0.95) (Figure 4.5).

Table 4.3. Concentrations of elements in the effluent during weathering of BS (a) and QVS4 (b) as measured by ICP-OES. QVS4 is an example based on one sample. Values in italic are below the LOQ.

a.

Experiment Duration (hours)	Volume Effluent (litres)	K	Ca	Cr	Cu	Fe	Mg	Mo	Na	Ni	S	Ti	Si	U	V	Zn
								(ppm)								
8	0.135	3.64	121.63	*0.0002*	*0.0027*	*0.032*	0.94	*0.0327*	0.89	*0.0127*	0.96	*0.0043*	57.81	*0.0227*	*0.0075*	*0.0034*
21.5	0.193	2.34	144.57	*0.0000*	*0.0003*	*0.044*	2.97	*0.0181*	0.70	*0.0109*	1.81	*0.0086*	36.14	*0.0294*	*0.0028*	*0.0023*
33.5	0.188	1.94	141.15	*0.0000*	*0.0000*	*0.021*	1.05	*0.0089*	0.53	*0.0063*	1.96	*0.0024*	29.63	*0.0170*	*0.0029*	*0.0037*
48	0.188	1.44	133.68	*0.0000*	*0.0000*	*0.016*	0.35	*0.0074*	0.38	*0.0043*	2.04	*0.0018*	31.47	*0.0157*	*0.0027*	*0.0000*
54	0.192	1.17	83.09	*0.0000*	*0.0006*	*0.026*	1.95	*0.0026*	0.27	*0.0052*	1.35	*0.0107*	18.48	*0.0164*	*0.0005*	*0.0024*
72	0.186	2.66	201.31	*0.0000*	*0.0000*	*0.011*	1.08	*0.0052*	0.48	*0.0056*	2.63	*0.0030*	36.51	*0.0232*	*0.0034*	*0.0000*
79	0.194	1.12	72.32	*0.0000*	*0.0029*	*0.023*	1.68	*0.0023*	0.15	*0.0039*	1.11	*0.0086*	17.48	*0.0270*	*0.0007*	*0.0075*
102	0.191	2.73	251.39	*0.0002*	*0.0015*	*0.006*	0.49	*0.0078*	0.49	*0.0058*	4.02	*0.0009*	46.41	*0.0389*	*0.0051*	*0.0001*
143	0.1775	2.65	389.26	*0.0000*	*0.0026*	*0.023*	2.36	*0.0086*	0.45	*0.0105*	5.94	*0.0070*	57.30	*0.0224*	*0.0071*	*0.0002*
167	0.2835	2.64	140.45	*0.0000*	*0.0005*	*0.016*	0.92	*0.0035*	0.14	*0.0048*	1.51	*0.0036*	29.64	*0.0174*	*0.0025*	*0.0004*
226	0.3745	*0.87*	193.92	*0.0000*	*0.0005*	*0.019*	1.53	*0.0045*	0.16	*0.0044*	2.12	*0.0070*	36.06	*0.0217*	*0.0037*	*0.0019*
274	0.386	1.44	140.86	*0.0000*	*0.0037*	*0.016*	1.02	*0.0039*	0.12	*0.0041*	1.56	*0.0064*	33.25	*0.0250*	*0.0023*	*0.0005*
338	0.272	1.13	229.73	*0.0000*	*0.0001*	*0.000*	0.10	*0.0061*	0.20	*0.0068*	3.15	*0.0003*	52.49	*0.0258*	*0.0047*	*0.0000*
388	0.273	*0.82*	169.97	*0.0005*	*0.0025*	*0.078*	6.83	*0.0055*	0.13	*0.0084*	1.99	*0.0245*	41.42	*0.0373*	*0.0034*	*0.0063*
438	0.27	*0.74*	173.33	*0.0000*	*0.0000*	*0.022*	0.16	*0.0042*	0.14	*0.0043*	2.14	*0.0000*	46.17	*0.0229*	*0.0036*	*0.0006*
508	0.271	*0.75*	177.59	*0.0000*	*0.0019*	*0.044*	1.82	*0.0056*	0.15	*0.0088*	2.05	*0.0110*	48.46	*0.0272*	*0.0040*	*0.0032*
558	0.269	*0.41*	105.59	*0.0000*	*0.0000*	*0.020*	1.03	*0.0030*	0.09	*0.0054*	1.19	*0.0066*	33.27	*0.0048*	*0.0012*	*0.0000*
672	0.269	1.09	239.32	*0.0000*	*0.0002*	*0.006*	0.29	*0.0066*	0.21	*0.0079*	3.36	*0.0006*	64.54	*0.0127*	*0.0038*	*0.0002*

b.

Experiment Duration	Volume Effluent	K	Ca	Cr	Cu	Fe	Mg	Mo	Na	Ni	S	Ti	Si	U	V	Zn
(hours)	(litres)	(ppm)														
7.5	0.354	4.80	16.05	0.0003	0.007	0.02	0.6275	0.01	0.0440	0.01	0.23	0.001	9.48	0.0000	0.0008	0.0052
23	0.356	5.20	26.43	0.0005	0.005	0.03	0.8554	0.01	0.0458	0.01	0.40	0.005	17.90	0.0092	0.0002	0.0105
49	0.369	2.44	28.94	0.0000	0.003	0.01	0.9498	0.00	0.0319	0.01	0.50	0.003	17.29	0.0000	0.0000	0.0066
72	0.359	2.32	25.64	0.0004	0.004	0.05	0.9784	0.00	0.0275	0.01	0.56	0.015	15.76	0.0084	0.0003	0.0072
99	0.356	8.11	14.92	0.0000	0.002	0.01	0.5507	0.00	0.0164	0.00	0.42	0.001	8.86	0.0000	0.0004	0.0125
168	0.358	3.65	46.98	0.0001	0.001	0.00	1.7323	0.00	0.0549	0.01	1.51	0.001	23.10	0.0000	0.0000	0.0027
192	0.156	1.69	49.09	0.0000	0.001	0.02	1.8797	0.00	0.0424	0.01	1.45	0.002	15.24	0.0066	0.0000	0.0023
245	0.156	3.65	90.63	0.0004	0.002	0.02	2.1812	0.00	0.1117	0.02	3.18	0.004	31.80	0.0076	0.0001	0.0024
338	0.156	2.44	100.71	0.0000	0.003	0.03	5.7001	0.00	0.0780	0.01	4.65	0.009	25.27	0.0110	0.0000	0.0038
506	0.156	17.30	228.26	0.0001	0.004	0.00	8.4521	0.01	2.1568	0.02	17.90	0.000	49.91	0.0270	0.0015	0.0617
674	0.192	10.85	203.86	0.0006	0.004	0.03	4.4004	0.01	1.2071	0.07	11.45	0.015	143.87	0.0177	0.0021	0.6740

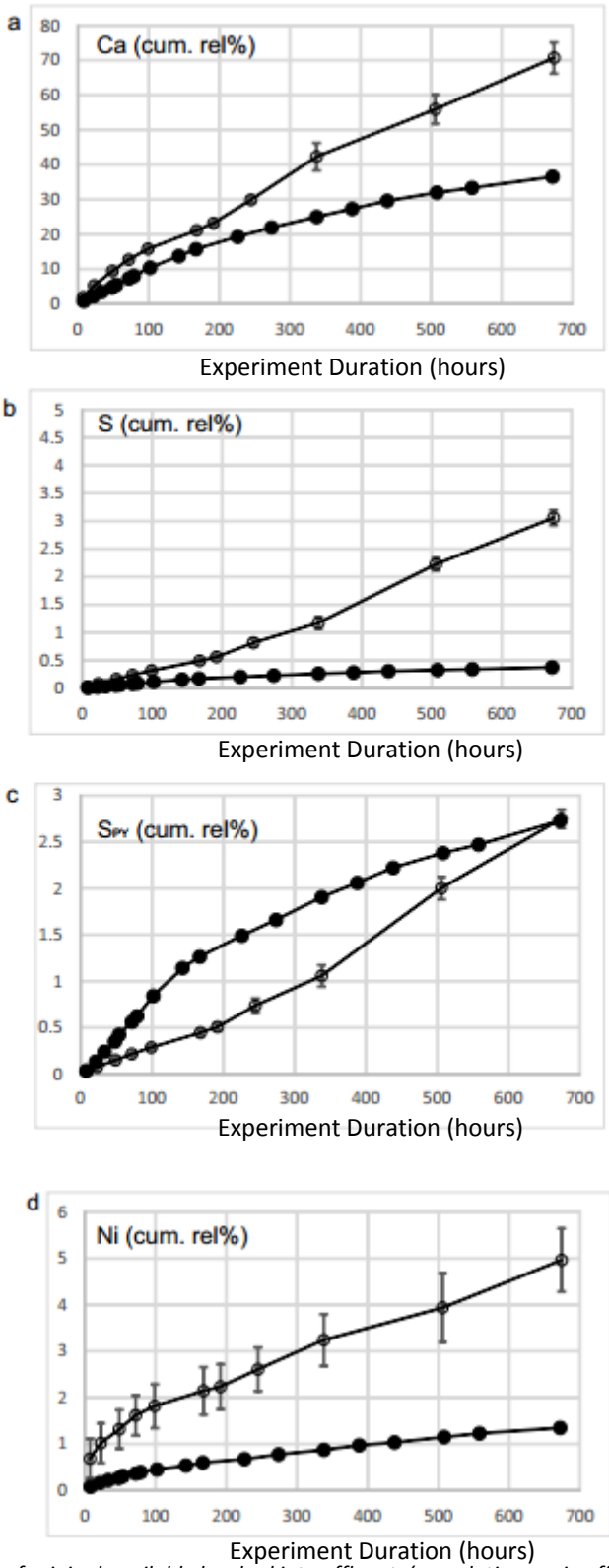

Figure 4.4 Relative percentage of original available leached into effluent (cumulative mg in effluent as a percentage of mg of element in original sample). Figure 4.4c is S in pyrite measured by pyrite reduction. Open circles QVS4 (error bars are standard error or three replicates), closed circles are BS.

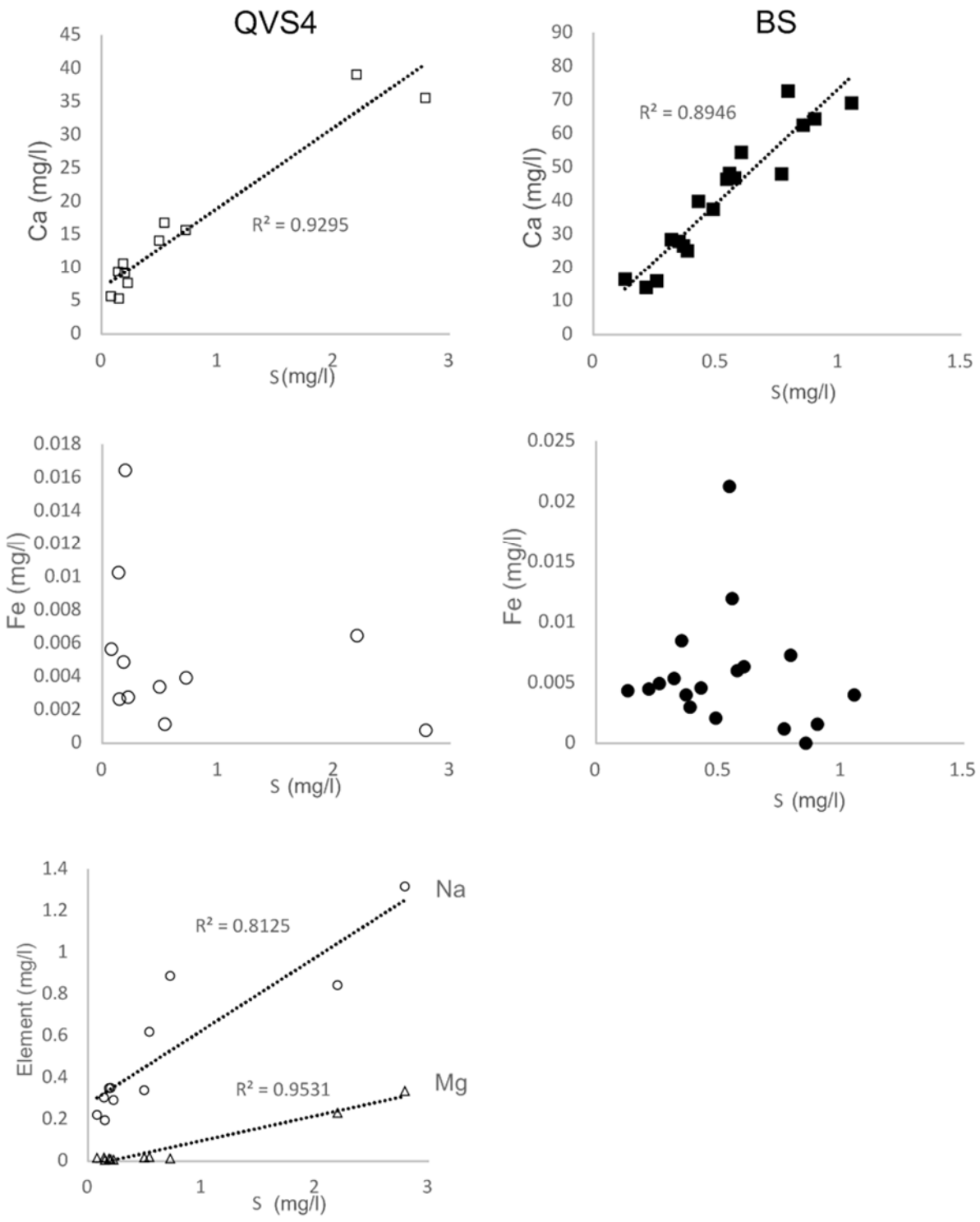

Figure 4.5 Correlations between concentrations of elements within the effluent samples. Open data points are effluent samples from QVS4 weathering (using values from one triplicate) and closed data points are BS.

4.4.3 SEM Results

When comparing randomly selected chips from the samples before and after weathering, there appears to be no gross change in either of the rock types. In BS.2 coccolith-shaped fragments remained in faecal clusters, whereas the organic matter remained concentrated in lenses (Figure 4.6b). In QVS4.2, a number of large pores were observed that were not present in QVS4.1 (Figures 4.7a and 4.7b). These could have been foraminifera plucked out in the sample preparation process, but more likely, given the evident loss of carbonate minerals during weathering, the tests were dissolved.

Automated heavy mineral particle analysis allows for the rapid assessment of geochemistry (EDX) and morphology of all dense particles in SEM (brighter in BSE mode), and for a quantitative analysis of Fe-containing minerals. Both samples contain populations of particles with Fe:S ratios indicative of pyrite or other Fe sulphides (Figures 4.8a and 4.9a, light grey and dark grey). As yet, no useful information about shape was retrievable from the automated partical analysis data which could distinguish framboidal morphology indicative of sedimentary pyrite from euhedral crystals which may have been formed during later diagenesis . However, upon inspection of 50 randomly selected pyrite particles (in QVS4.1), around 50 % of these Fe sulphides are framboidal, with the rest being present as individual or loose clusters of euhedral crystals. The pyrite particles have been subdivided into 'pristine' pyrite (Fe:S <1, using wt%; light grey in Figures 4.8 and 4.9) and 'sulphur-depleted' pyrite (Fe:S ratio >1, dark grey in Figures 4.8 and 4.9). 'Pristine' pyrite is recorded as smaller in BS.1, with automated particle analysis measuring an average ECD of 2.4 µm and an average area of 4.4 µm, compared to 2.82 µm ECD and area of 9.36 µm in QVS4.1. These statistical data imply a greater surface area: volume of pyrite particles in BS.1. The ECD suggests that both samples were deposited in an anoxic water column (mean ECD <6 µm, Wilkin and Barnes, 1998), although the standard deviations are quite high (0.9 µm in BS.1 and 2 µm in QVS4.1). Iron (oxyhydr)oxides (<5 % S, black circles in Figures 4.8 and 4.9) are often present as large (average ECD of 3.8 µm) euhedral crystals in QVS4.1, and small (average ECD of 1.3 µm) irregularly shaped particles, often associated with carbonate minerals in BS.1. The larger Fe (oxyhydr)oxide particles present in QVS4.1 but not in BS.1 may be the Fe_{OX1} fraction (lepidocrocite/ferrihydrite) identified by the sequential extraction (Table 4.4).

After weathering, both samples show a shift from 'pristine' (Fe:S <1) to 'sulphur-depleted'

(Fe:S >1) pyrite, and from Fe sulphides to Fe (oxyhydr)oxides or other Fe-containing materials (with <5 wt% Fe) (Table 4.4, Figures 4.8b and 4.9b). On visual inspection, the particles which switched from having a geochemistry defined as 'pristine' pyrite to 'sulphur-depleted' pyrite are framboids and euhedral crystals consisting of microcrystals with a pyrite core and Fe (oxyhydr)oxide rims (Figure 4.10a and 4.10b) and thus overall lower sulphur contents. BS shows a slightly more pronounced shift from 'pristine' to 'sulphur-depleted' particles (Table 4.4). Visual inspection of histograms show these new 'sulphur-depleted' particles have a very similar ECD distribution to 'pristine' particles in BS.2 (average 2.6 µm in both pyrite classes) Figure 4.11. In QVS4 however, 'sulphur-depleted' pyrite particles are generally smaller in QVS4.2 (average 2.13 µm, 'pristine' 4.06 µm) Figure 4.12. Comparing pre and post weathering in both samples, pristine particles are slightly smaller pre weathering in BS and whereas in QVS4 there is a notable increase in ECD (Figure 4.12).

Figure 4.13 shows that 'sulphur-depleted' particles are concentrated in the outer rim of chips, whereas 'pristine' particles are concentrated within the centre of chips in BS.2. The rim appears to be approximately 100 µm wide and roughly equal in each chip. This rim of 'sulphur-depleted' particles is not evident in the chips of BS.1.

As well as being greater in number (Table 4.4), the Fe (oxyhydr)oxides in BS.2 are larger (average 2.3 µm ECD) compared to BS.1 (average 1.3 µm ECD). Visual examination of 50 randomly selected Fe (oxyhydr)oxide particles in BS.2 shows ~50 % are framboidal in nature (Figure 4.10c), whereas before weathering BS.1 contained no framboidal Fe (oxyhydr)oxide particles. After weathering in QVS4.2, some of the Fe (oxyhydr)oxide particles had framboidal morphology (15 out of 50 randomly selected particles, Figure 4.10c), more than in QVS4.1 (2 out of 50 randomly selected particles). In QVS4.1, Fe (oxyhydr)oxides were also present as anhedral crystals (21 out of 50 randomly selected particles, Figure 4.10d). The anhedral crystals show some signs of alteration in QVS4.2 (Figure 4.10e).

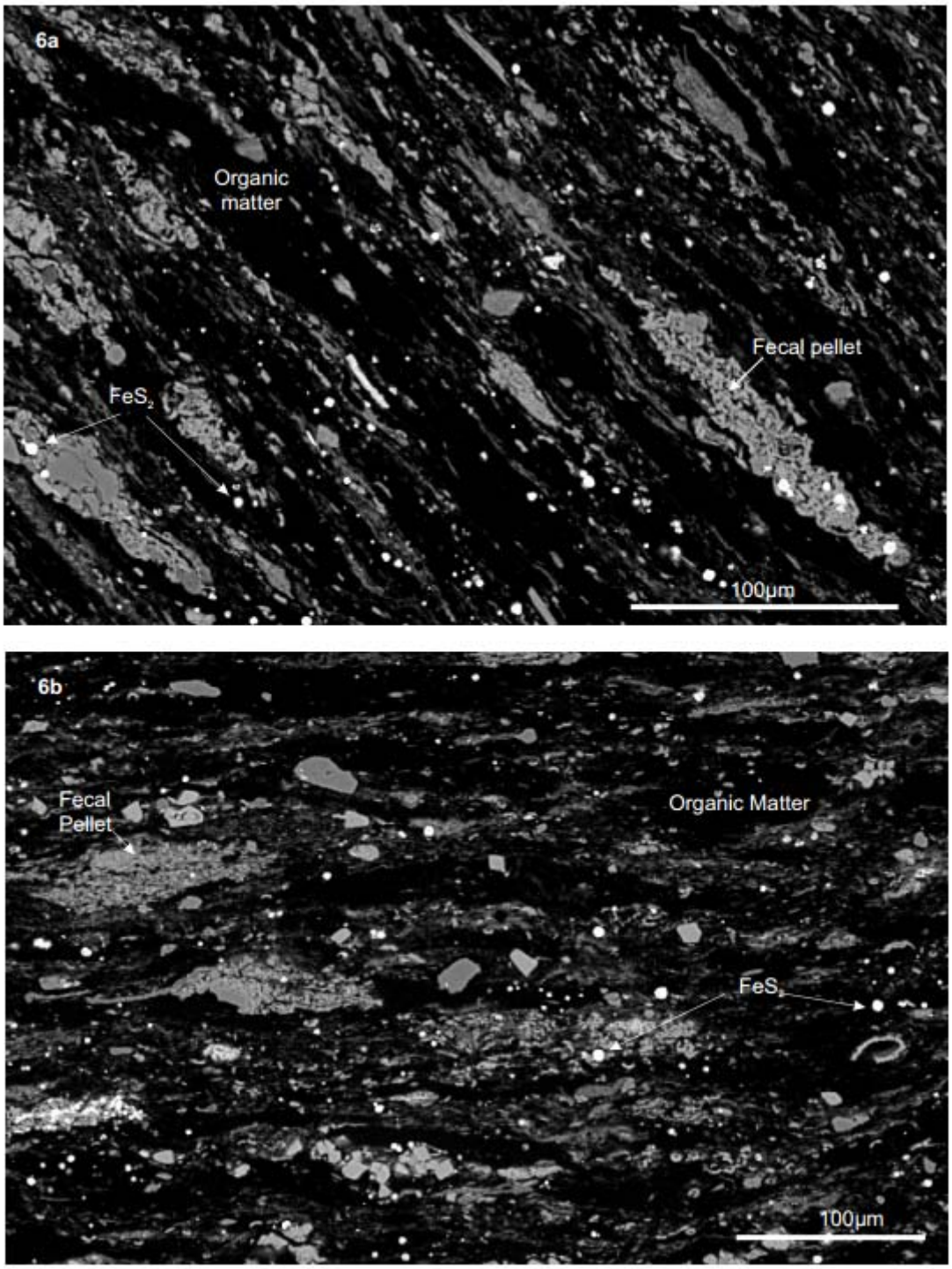

Figure 4.6 Comparing a randomly selected chip from BS.1 (6a) to BS.2 (6b) using BSE imagery .

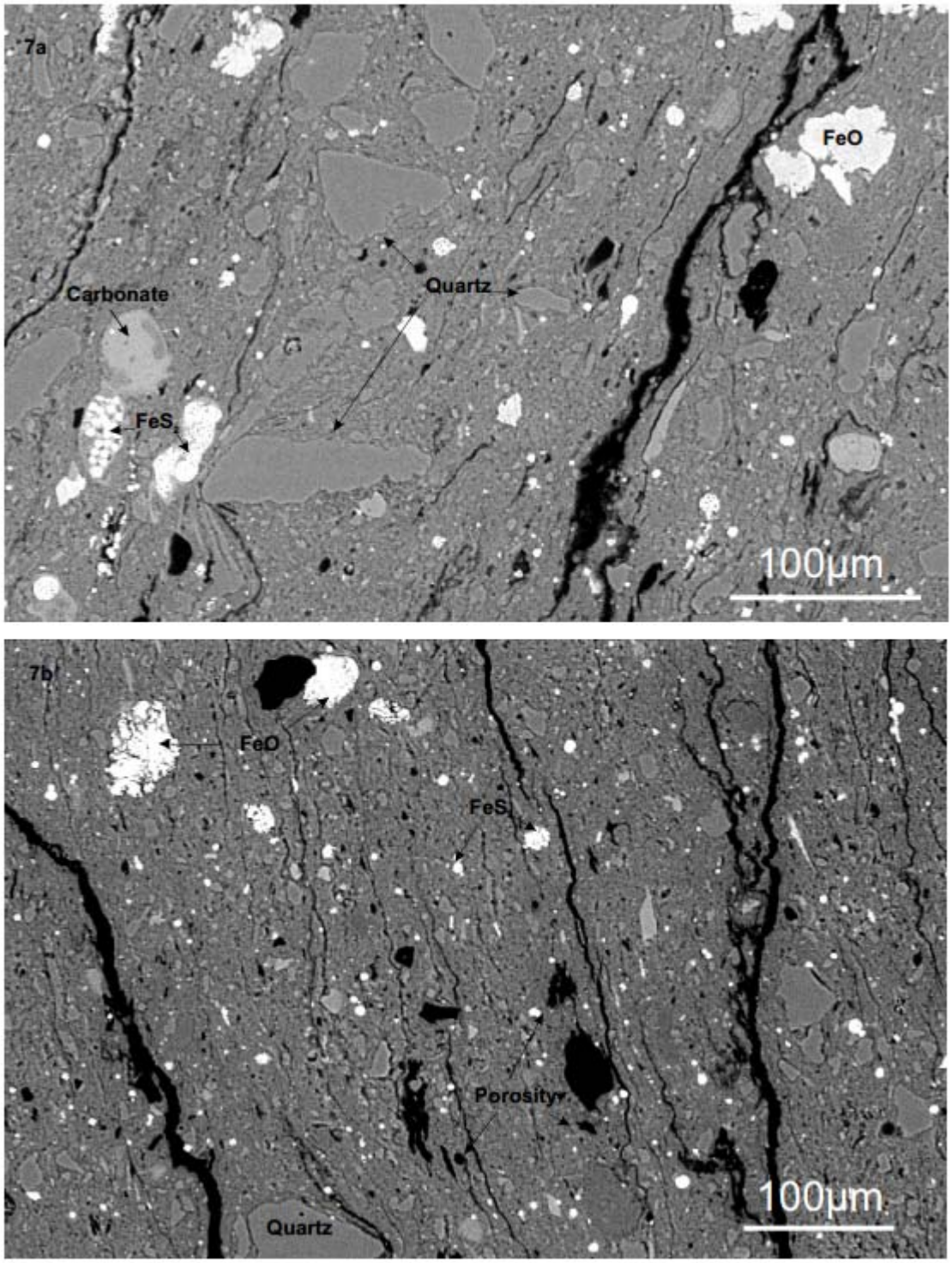

Figure 4.7 Comparing a randomly selected chip from QVS4.1 (7a) to QVS4.2 (7b) using SEM-BSE.

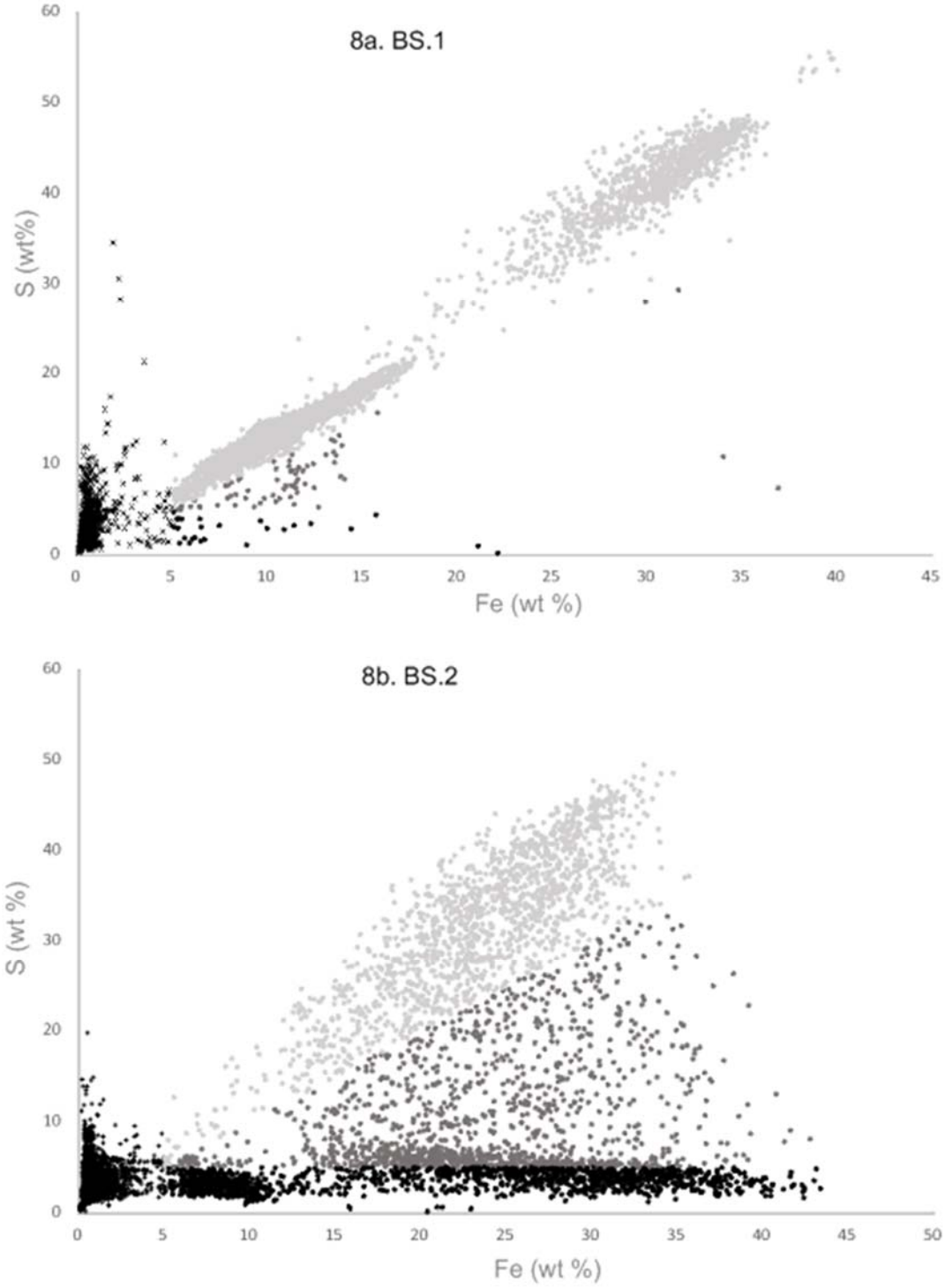

Figure 4.8 . Fe and S concentrations of Fe-containing particles measured in automated particle analysis by SEM EDX for chips of BS.1 (pre weathering) (top) and BS.2 (post (bottom) weathering), analysed in thin section. Each data point represents a dense Fe-containing particle analysed by automated particle analysis of a thin section of BS chips. Black crosses are <5% Fe and are considered to be other minerals containing minimal Fe, light grey are particles with a Fe content >5% and Fe:S ratio less than 1 and are considered 'pristine' pyrite. Dark grey data points have a Fe:S ratio greater than 1 and have more than 5% S. Black circles contain less than 5% S and are considered to be Fe oxides.

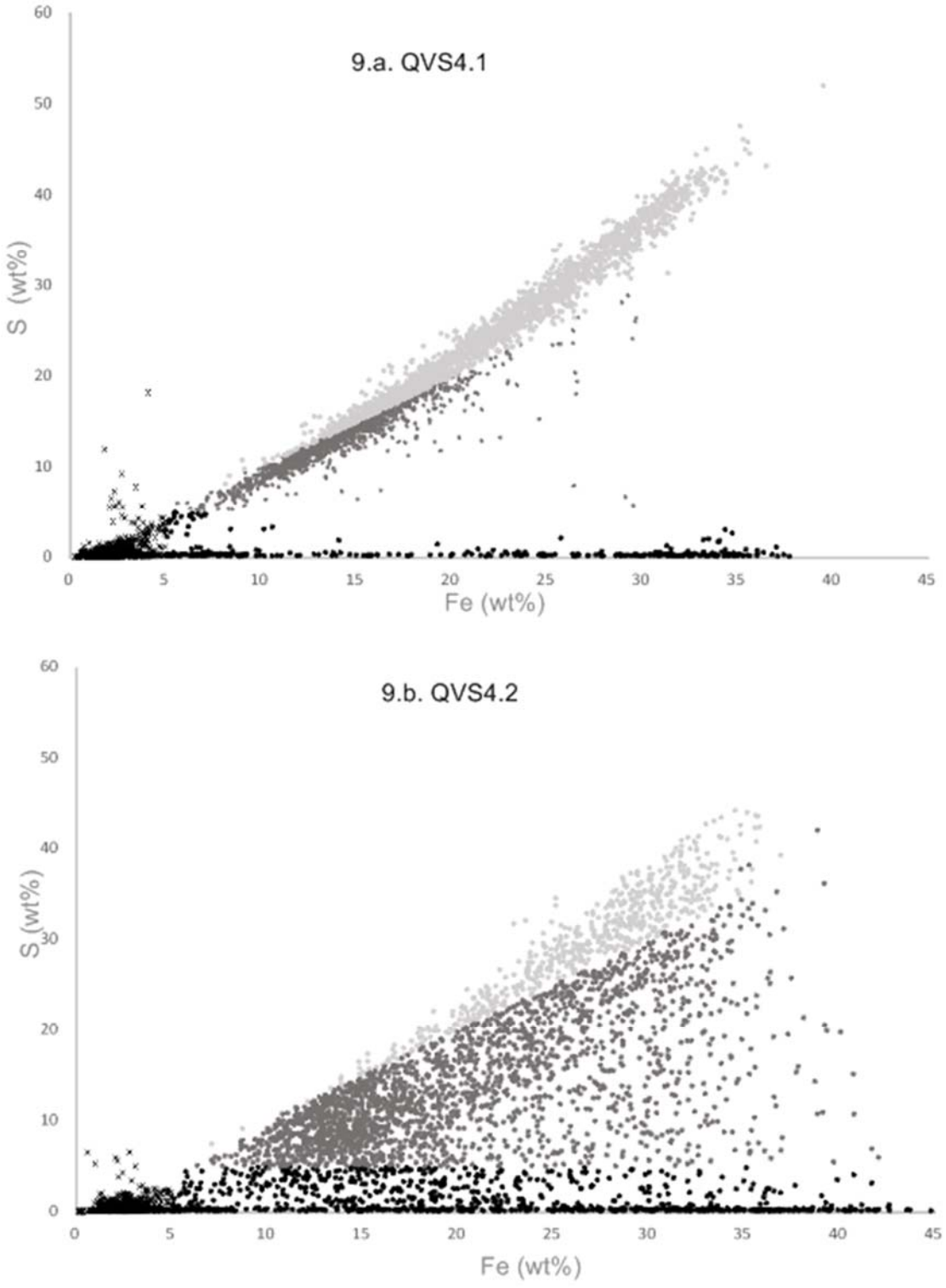

Figure 4.9. Fe and S concentrations of Fe-containing particles measured in automated particle analysis by SEM EDX for chips of QVS4.1 (pre weathering) (top) and QVS4.2 (post (bottom) weathering), analysed in thin section. Black crosses are <5% Fe and are considered to be other minerals containing minimal Fe, light grey are particles with a Fe content >5% and Fe:S ratio less than 1 and are considered 'pristine' pyrite. Dark grey data points have a Fe:S ratio greater than 1 and have more than % S. Black circles contain less than 5% S and are considered to be Fe oxides.

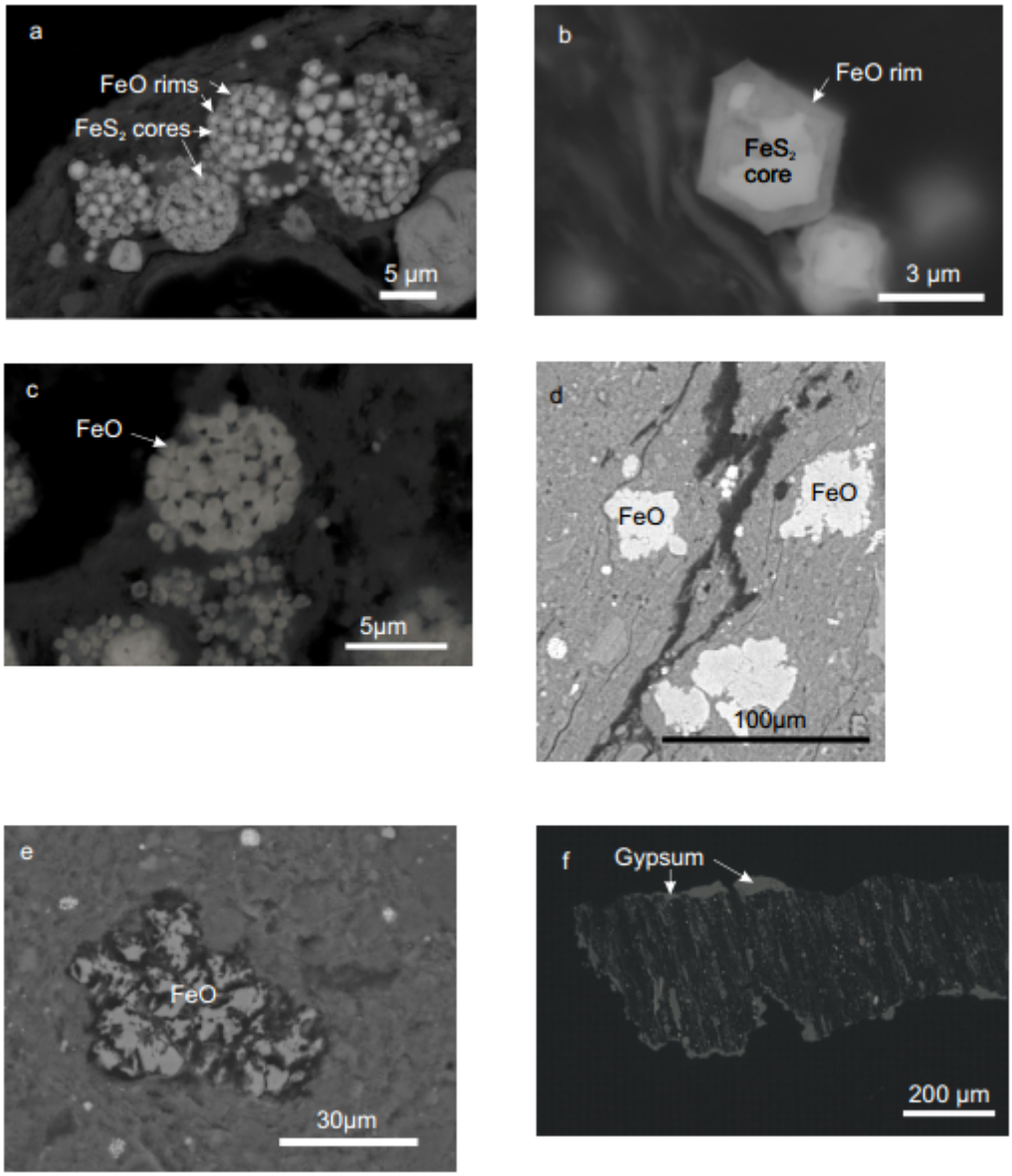

Figure 4.10 SEM Back scattered electron (BSE) images, examples of Fe particles and weathering products. 10a, b, c and e from QVS4.2, post weathering. 10d is from QVS4.1, pre weathering. 10f is from BS.2, post weathering.

Table 4.4 Table presenting information shown in Figure 4.8 and 4.9 in a numerical format. On the left proportions are calculated only from particles with chemical compositions indicating Fe sulphides (particles with a Fe and S>5 %), highlighting the shift to sulphur depleted pyrite after weathering (numbers of particles in brackets). On the right-hand side all of the Fe-containing particles are included, to show the increase in Fe (oxyhydr)oxides (particles with less than 5 % S). Particles identified in SEM-EDX with processing carried out by IncaFeature.

	Proportion of total pyrite particles		**Proportion of all Fe-containing minerals**			
	Pristine	**Sulphur depleted**	**<5 % Fe**	**Pristine**	**Sulphur depleted**	**Fe (oxyhydr)oxides**
BS.1	0.98(3763)	0.02 (70)	0.25 (1278)	0.73 (3763)	0.01 (70)	0.01 (26)
BS.2	0.5 (1460)	0.46 (1232)	0.61 (6205)	0.14 (1460)	0.12 (1232)	0.12 (1267)
QVS4.1	0.66 (2005)	0.37 (1156)	0.4 (2651)	0.3 (2009)	0.18 (1156)	0.11 (745)
QVS4.2	0.21 (567)	0.79 (2129)	0.46 (3212)	0.08 (567)	0.30 (2129)	0.16 (1090)

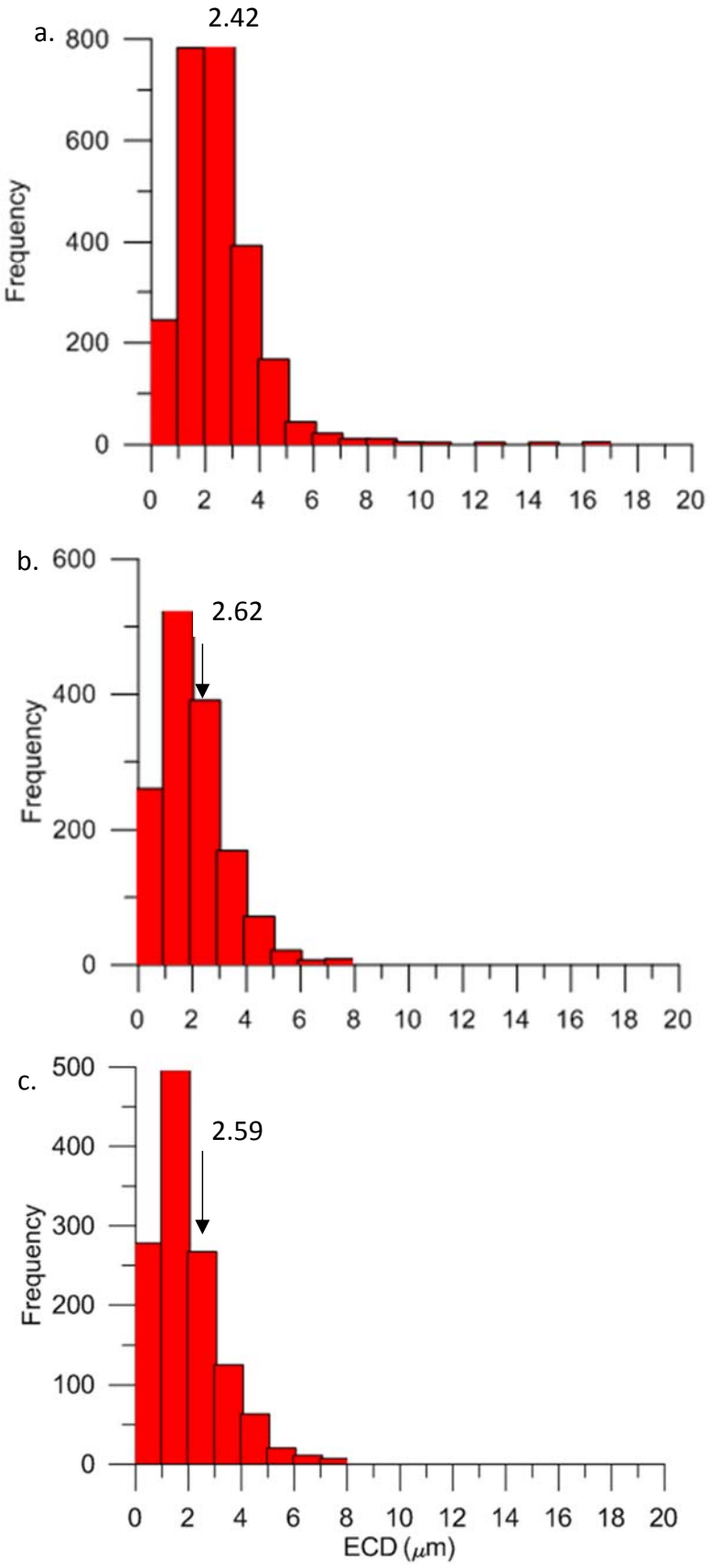

Figure 4.11 Histograms of Equivalent Circular diameter (ECD) for different pyrite populations with average (in µm) identified. a) BS.1 'pristine' pyrite particle population, b) BS.2 'pristine' pyrite particle population and c) BS.2 'sulphur-depleted' pyrite particle population.

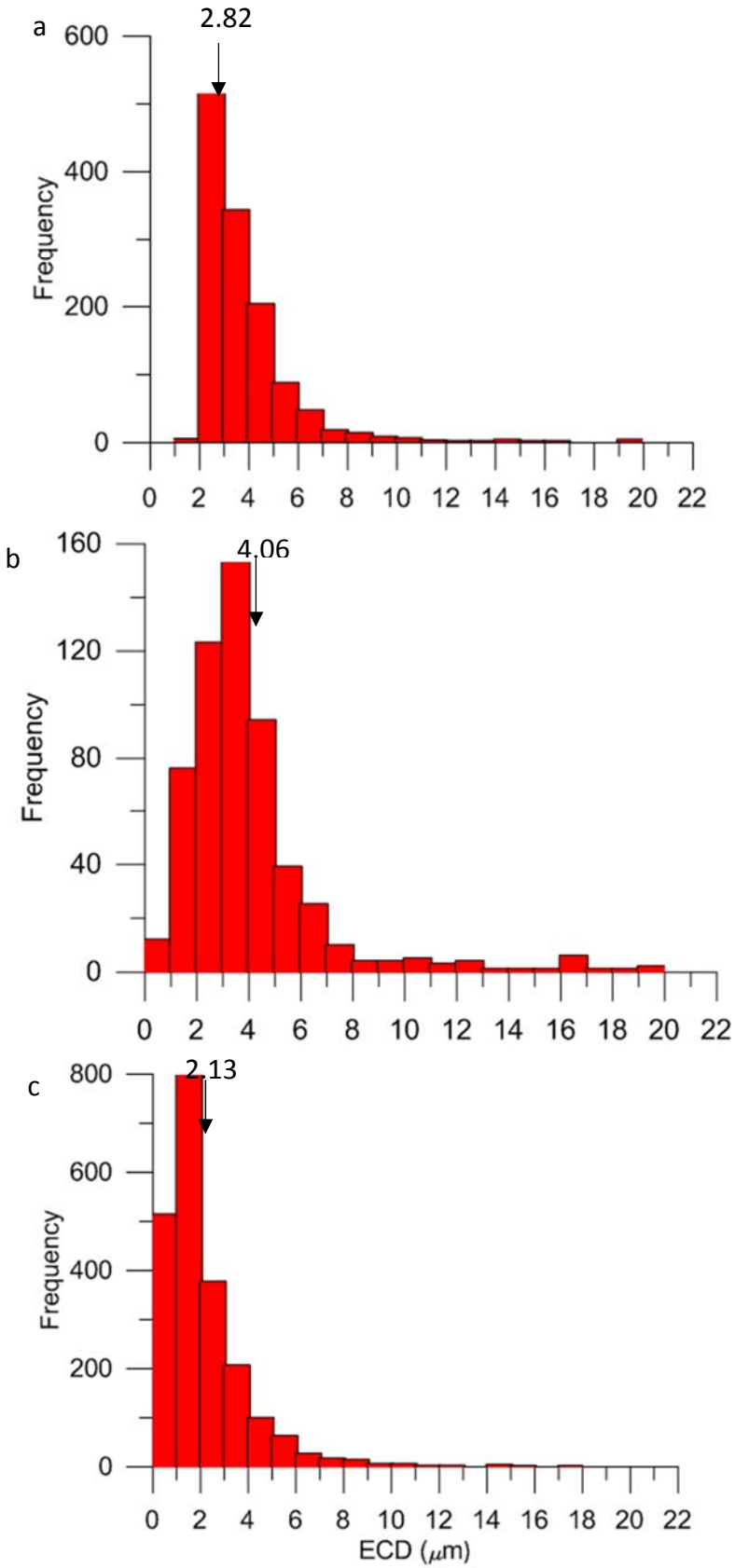

Figure 4.12 Histograms of Equivalent Circular diameter (ECD) for different pyrite populations with average (in µm) identified. a) QVS4.1 'pristine' pyrite particle population, b) QVS4.2 'pristine' pyrite particle population and c) QVS4.2 'sulphur-depleted' pyrite particle population

.

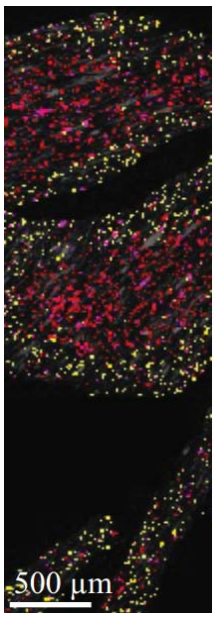

Figure 4.13. Aztec generated image of automated particle data of BS.2. Clearly visible are 'sulphur-depleted' pyrite particles in yellow concentrated around the outside of the chips and 'pristine' pyrite particles in red concentrated in the centre of each chip. Modified from Buckman et al., 2018.

4.5 Discussion

4.5.1 Evidence for organic-rich mudrock weathering

When visually comparing the rock chips before and after the experiment, there were no obvious signs of rock weathering (i.e. no colour changes, no efflorescent salts), which is consistent with observations by Liao et al. (2014). Using SEM in BSE mode, the BS.2 sample displayed gypsum rims around some rock chips that were not visible in BS.1 (Figure 4.10e), evidence of weathering products being generated during the experiment.

Geochemically, the slight loss of Na and K (negative τ Figure 4.3a) into the effluent provides evidence that weathering of aluminosilicate has been occurring during the experiments. The higher rates of removal of Na and K (and most other elements) into the effluent in the first 100 hours may suggest that both elements were additionally adsorbed to clay minerals (Pye and Miller, 1990). The subsequent leaching at a slower rate may suggest real acid hydrolysis of aluminosilicate. The leaching of carbonate minerals, presumably by dissolution of calcite, caused the most severe chemical change during weathering, identified by a decrease in inorganic carbon in the post-weathering samples and a high pH in the effluent (Figure 4.2a, Figure 4.3). The relative instability of carbonate/calcite in leaching experiments has been noted in previous experiments (e.g. Ritsemsa and Groenenberg 1993; White et al., 2005). The decrease in pyrite in both samples, identified by both wet chemistry (Table 4.2) and particle analysis (Table 4.4) and the increase in 'sulphur-depleted' pyrite particles (Table 4.4), implies that oxidative reactions were occurring as well. It is evident that the designed soxhlet experiment does artificially weather organic-rich mudrock components, even on relatively

short time scales of one month.

The fact that one of the measurable products of weathering, 'sulphur-depleted' pyrite particles, are restricted to a zone around the perimeter of the weathered rock chips (Figure 4.13) suggests a weathering front/redox front penetrating into the rock. The weathering reactants, dominantly water and oxygen (Equations 4.1, 4.2, 4.4 and 4.5), have been transported at least 100 μm into the rock chip over the four weeks, despite the relatively fine grained, impermeable nature of organic rich mudrocks in general. The thickness of the zone of weathering in BS.2 appears to be similar in every chip. Although the sample has lenses where coarser ($CaCO_3$) material appears to be more concentrated (Figure 4.6) there does not appear to be distinct areas where the reactants have penetrated at different rates. This may relate to the overall homogenous nature of the rest of the matrix in the BS samples.

The conditions of the weathering experiment in this study were different to previous organic-rich mudrock weathering experiments, mainly because the pH was much higher (e.g., Bhatti, 2015, pH 1.2-2.2; Liao et al., 2014, pH 4.2-6.0; Perkins and Mason, 2015, pH 3.6-6.2). These earlier experiments either removed carbonate prior to treatment or used organic-rich mudrocks that were initially very low in Ca (and so presumably low in carbonate). We suggest that in our study using mudrock samples with their original carbonate inventories, dissolution of carbonate acted as a pH buffer and consumed the majority of protons produced by pyrite oxidation, resulting in the comparatively high pH in the effluent. Assuming that pyrite oxidation was the dominant source of protons during the weathering experiments (with contribution of protons from CO_2 dissolution on these timescales being minimal), and S was released from pyrite oxidation as soluble SO_4^{2-}, Equations 4.4 and 4.5 may illustrate the strong correlation between Ca and S in the effluent (Figure 4.5) and the occasional precipitation of a white solid (presumed to be gypsum). Gypsum was also at least temporally retained within the rock, as confirmed by the gypsum rims in BS.2 (Figure 4.10e), and may also be the source of the new Ca-rich, low-Fe particles identified by SEM in BS.2 (Figure 4.8). Gypsum is a well-known weathering product of pyrite-rich rocks (Cockell et al., 2011; Joekel et al., 2005; Pye and Miller, 1990). The formation of gypsum prevented the use of S concentrations in the effluent as an accurate measure of the rate of pyrite oxidation (Nicholson et al., 1988 and 1989). An alternative measure of pyrite oxidation should be sought for further weathering studies on carbonate-containing organic-

rich mudrocks.

$$2FeS_2 + 7O_2\ (aq) + 2H_2O \rightarrow 2Fe^{2+} + 4SO_4^{2-} + 4H^+ \text{ (Equation 4.4)}$$

$$CaCO_3 + H_2O + SO_4^{2-} + 2H^+ \rightarrow CaSO_4.2H_2O + CO_2 \text{ (Equation 4.5)}$$

The good correlation between S and Na and Mg in the effluent of QVS4 (Figure 4.5) further suggests that in this sample, protons released during pyrite oxidation (Equation 4.1) may have also caused the hydrolysis of feldspar or pyroxene minerals and other carbonate minerals like dolomite.

The relatively high temperatures during the experiment (33-58°C, see Figure 4.2b) may have prevented the activity of any native microbial communities that might facilitate Fe oxidation in a natural weathering environment. Certain Fe oxidising microorganisms are, however, known to operate at temperatures as high as 45°C (Bhatti, 1990). Furthermore, the high pH of the effluent is more likely to have hampered the activity of microorganisms (e.g. *T. Ferroxidans*; Lundgren and Silver, 1980). We assume that this would also be the case in natural carbonate-containing rocks, at least until the carbonate is completely dissolved.

4.5.2 Weathering impact on iron-carbon-sulphur coupling

In both samples, Fe is behaving conservatively during weathering, consistent with similar findings by Liao et al. (2014), Perkins and Mason (2015) and Pye and Miller (1990), as well as some natural weathering studies (Jin et al., 2013; Littke et al., 1995; Odin et al., 2015). This, despite the clear penetration of pyrite oxidising reactants into the rock chips during the experiment (Figure 4.13). There is, however, the considerable change in Fe-speciation in our experiment, including the oxidation of pyrite, dissolution of Fe carbonates, and the production of Fe (oxyhydr)oxides (Table 4.1, Figures 4.8 and 4.9). These changes do not significantly affect the Fe_{HR}/Fe_T proxy as the Fe (oxyhydr)oxide products of pyrite oxidation are also within the Fe_{HR} pool. Different from that, the Fe_{PY}/Fe_{HR} ratio is significantly modified (Table 4.2). Our sequential extractions identify increased pools of Fe_{OX1} and Fe_{OX2}, indicating the formation of goethite/hematite in both samples, and formation of ferrihydrite/lepidocrocite during weathering of BS (Table 4.2). These Fe (oxyhydr)oxides have previously been noted on the surface of weathered organic-rich mudrocks (Cockell, 2011; Fischer et al., 2009; Tuttle et al., 2009).

Tuttle and Breit (2009) found Fe to be labile in naturally weathered organic-rich mudrocks,

suggesting that low pH and the lack of carbonate buffering were responsible for the instability of pyrite weathering products at low pH. This mechanism for higher rates of pyrite oxidation at lower pH relates to the generation of intermediatory product, Fe^{3+} which is in itself an effective oxidant (Equation 4.6), creating a positive feedback and speeding up pyrite oxidation (Williamson et al., 2006; Huminicki and Rimstidt, 2009).

$FeS_2 + 14Fe^{3+} + 8H_2O = 15Fe^{2+} + 2SO_4^{2-} + 16H^+$ Equation 4.6 (Williamson and Rimstidt (1994)

At higher pH, Fe^{3+} is readily hydrolysed to form an insoluble precipitate (Fe (oxyhydr)oxides), which slows the rate of reactions as it removes this additional oxidant from the aqueous phase (Nordstrom, 1982; Williamson et al., 2006; Chandra and Gerson, 2010). Also, in experiments where pyrite was weathered in the presence of carbonate (Nicholson et al., 1988; Huminicki and Rimstidt, 2009; Lara et al., 2016), the rate of the pyrite oxidation was shown to be limited by the build-up of solid Fe (oxyhydr)oxides at the mineral surface. These weathering products were identified as lepidocrocite (Nicholson et al., 1988) or lepidocrocite and goethite (Lara et al., 2016). It has been suggested that the decreasing reaction rates could be explained by the shrinking core model, where the rate of pyrite oxidation is limited by the rate of oxygen diffusion through the build-up of the oxidation product around the edge of a particle (Nicholson et al., 1998). The microscopic evidence for Fe (oxyhydr)oxide rims around pyrite cores on individual 'sulphur-depleted' microcrystals in this study (Figure 4.10 a and b) supports this model of rate limitation in carbonate-containing organic-rich mudrock (Figure 4.14). Since the Fe (oxyhydr)oxides are relatively stable compared to pyrite under prevailing weathering conditions (Schwertmann and Taylor, 1989) 'sulphur-depleted' pyrite particles are essentially 'passivated' by Fe (oxyhydr)oxide coatings. The retention of pyrite framboid morphology during this transformation may be due to the two stage process suggested by Huminicki and Rimstidt (2009). In this model, dissolved iron forms poorly crystalline Fe-oxyhydr(oxide) colloids which are attracted to the pyrite surface, forming a semi-permeable layer which encourages the precipitation of further Fe- oxyhydr(oxide)'s between the pyrite face and this colloidal layer.

There is evidence that the different carbonate contents in BS and QVS4 resulted in different levels of passivation. In BS, a higher original carbonate content maintained a higher pH throughout the experiment (Figure 4.2a). Compared to QVS4, during weathering of BS, there was a more pronounced increase in the Fe_{OX1} pool identified by sequential Fe extraction (Table 4.2). This may represent a greater surface area of pyrite rimmed with Fe

(oxyhydr)oxides. Also, a more pronounced shift from 'pristine' to 'sulphur-depleted' pyrite (Table 4.4) in BS is evident. Together with a slowing rate of S and Ca removal from the effluent (Figures 4.4a, 4.4b and 4.4c) in BS.1, this supports enhanced passivation and declining rates of pyrite oxidation. The conditions are different in QVS4, where the majority of the carbonate had been dissolved by the end of the 4-week experiment (Figure 4.3a), the pH was slightly lower (Figure 4.2a), and S and Ca continued to be leached from the rock during the latter experimental stages (Figure 4.4). There is the possibility that enhanced dissolution of carbonate in QVS4 was also influenced by the presence of dolomite or other Mg carbonate minerals. Magnesium carbonate minerals have a higher solubility, and this may explain the slightly steeper curve in Figure 4.4.

It remains unclear from this experiment how stable the Fe (oxyhydr)oxides rims are, and if any of the pyrite would be permanently passivated even at a lower pH. In QVS4, it is likely that all carbonate within the rock chips will dissolve before all pyrite grains are passivated, therefore allowing pyrite oxidation and other oxidative weathering reactions to continue. In BS, this is different; all pyrite particles may be passivated before all carbonate in the rock chips is dissolved. From this point onwards, further oxidative weathering of BS components would rely on the lower concentrations of protons generated by carbon dioxide dissolution. With further work, it would be possible to identify the threshold carbonate content of a given sample that would allow complete pyrite passivation by Fe (oxyhydr)oxides and therefore slower rates of weathering. However, this would be complicated by various factors, including surface area (Chandra and Gerson et al., 2010), and distance between pyrite and carbonate particles (sample heterogeneity) (Kraal et al., 2009), which may explain why there was a greater overall loss of pyrite from BS (τ -0.37) than from QVS4 (τ -0.21) (Figure 4.3c).

In both samples, the pyrite framboids indicate the same process of *in situ* Fe phase transformation from sulphides to (oxyhydr)oxides via diffusion at individual pyrite microcrystal surfaces, with little change in framboid morphology and negligible amounts of Fe being lost to the effluent. The preservation of framboid morphology has also been identified in various palaeo-redox studies which use outcrop samples (Luning et al., 2003; Wignall and Newton, 2004). Automated particle analysis allows for the identification of pyrite particles that have been affected by weathering, so that only 'pristine' pyrite particles are included in any diameter analysis. However, in QVS4 it appears that average 'pristine'

pyrite diameter is increasing, possibly as smaller particles are being preferentially converted to 'sulphur-depleted' pyrite (Figure 4.12). This, combined with the current inability to decipher euhedral from framboidal pyrite, limits the use of automated particle analysis in this study for the measurement of framboid diameter as an anoxia proxy.

In BS, the non-pyrite S fraction (Table 4.1b) increased during weathering. This was likely due to the conservative nature and oxidation resistance of sulphurised organic matter (Table 4.1b), supporting previous findings by Petsch (2000), and due to the formation of gypsum, some of which was retained within the rock chips. In both samples, TOC contents appeared to be stable over the course of the experiment (positive τ values, Figure 4.3a), supporting previous research that organic carbon compounds are relatively stable towards weathering when compared to pyrite (Clayton and Swetland, 1978; Petsch, 2000).

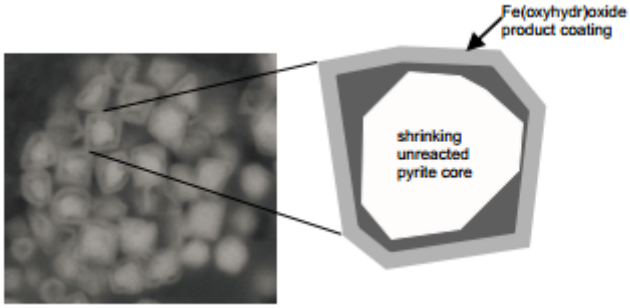

Figure 4.14 Conceptual model of shrinking core model as seen in SEM-BSE imagery of pyrite framboids in QVS4.2 (adapted from Nicholson et al.,1989).

4.5.3 Weathering impact on trace metal proxies

Overall, the trace metals in both samples appeared to be relatively resistant to experimental weathering, with most elements losing less than 10 % of the available trace metal content into the effluent. Mass transfer coefficient (Equation 4.3) also show either conservation (positive τ) or minor losses (<-0.1). This, again despite the clear penetration of weathering reactants into the rock chips (Figure 4.13). Nickel is the only trace metal consistently present in the effluent above limits of quantification. Nickel appears in lower concentrations in the BS effluent compared to QVS4 (Table 4.3, Appendix C), even though BS.1 contains higher original Ni contents before weathering than QVS4.1. One explanation could be that Ni is concentrated within a more resistant organic matter fraction in BS (Böning et al., 2015) explaining the lower Ni losses from BS compared to QVS4.

Interestingly, the studied trace metals (including Ni) are also known to be enriched in pyrite

(Gregory et al., 2015; Huerta-Diaz and Morse, 1992), so they should be released from the rock chips in an amount proportional to pyrite oxidation. This is evidently not the case, with as 21 rel% of the original pyrite has been oxidised in QVS4 during weathering (Table 4.2) whereas the trace elements lost no more than 10 rel% of their original quantities (Table 4.1c). AThere is no correlation between S and Ni, Zn or Mo concentrations in the leachate either. It, therefore, seems that most trace metals are retained in the rock chips despite significant pyrite weathering. In this context, there is evidence of enrichment of Mo, Ni, As, U, V, Ni, Cu and Zn in goethite weathering crusts (Fischer et al., 2009). These trace metals may, therefore, have been released during pyrite weathering within the oxidised zone/redox front in Figure 4.13, only to be instantaneously adsorbed onto, or co-precipitated with, Fe (oxyhydr)oxide rims around individual pyrite framboid microcrystals. Mn also appears to be conservative. As Mn oxides/hydroxides are also known to co-precipitate/sorb with trace elements (see Tebo et al., 2004 for a review) it would be interesting to investigate their role in weathering in future experiments.

In this experiment, little trace metals were lost from chips of shale which are approximately <6mm over the duration of the experiment (yr^{-1}). Therefore, it is unlikely that trace elements would be leached before physical erosion in high erosion environments like cliff faces (up to 10^{-1} m yr^{-1}, Rosser et al., 2005). If erosion continually erodes the weathering surface, then this study suggests that chemical weathering will not significantly affect trace metals in these environments and trace metal proxies would be reliable. In samples without carbonate (because of the original palaeo-environment) where pyrite may not be 'passivated' by the build-up of solid Fe(oxyhydr)oxides, leaching of trace metals may be more significant before physical erosion takes place.

4.5.4 Estimated chemical weathering rates versus physical weathering rates in high erosion environments

Pyrite oxidation accelerates chemical weathering of other rock components in pyrite-bearing organic-rich mudstones. Figure 4.13 shows that even in relatively impermeable mudrocks, oxygenated water had penetrated 100 µm into the mudrock in just four weeks, creating a redox front of oxidised pyrite. Our experiments suggest that, because of pyrite 'passivation', it would take years to oxidise all of the pyrite from the <6mm chips. Comparing this to rates calculated in high physical erosion areas where outcrop samples are usually taken from, i.e high topography stream beds (mm's to cm's/yr Cornwell et al., 2003; Hsieh and Knuepfer,

2001) or coastal cliffs (m's/yr, Rosser et al., 2005), it seems likely that physical erosion will occur before pyrite oxidation is complete. If carbonate is present to buffer the pyrite oxidation environment, the production of solid, seemingly relatively stable, Fe (oxyhydr)oxides rims should also prevent significant alteration of the Fe_{HR}/Fe_T ratio, and possibly the retention of the investigated trace metals before physical erosion takes place. The physical erosion of slightly chemically altered rock should, therefore, ensure that these proxies are reliable in samples taken in these high erosion environments. In samples without carbonate present to slow down pyrite oxidation and prompt precipitation of Fe (oxyhydr)oxides rims, chemical weathering may have a more significant effect before physical weathering removes the material. It would be useful to repeat this experiment with various proportions of carbonate removed prior to initiating artificial weathering (this would require a very careful approach and validation that no other phases were being removed) and to carry out a longer experiment, sacrificing portions of the sample, in order to explore changes in weathering rates beyond when all carbonate is lost and to test the stability of the newly formed Fe (oxyhydr)oxides.

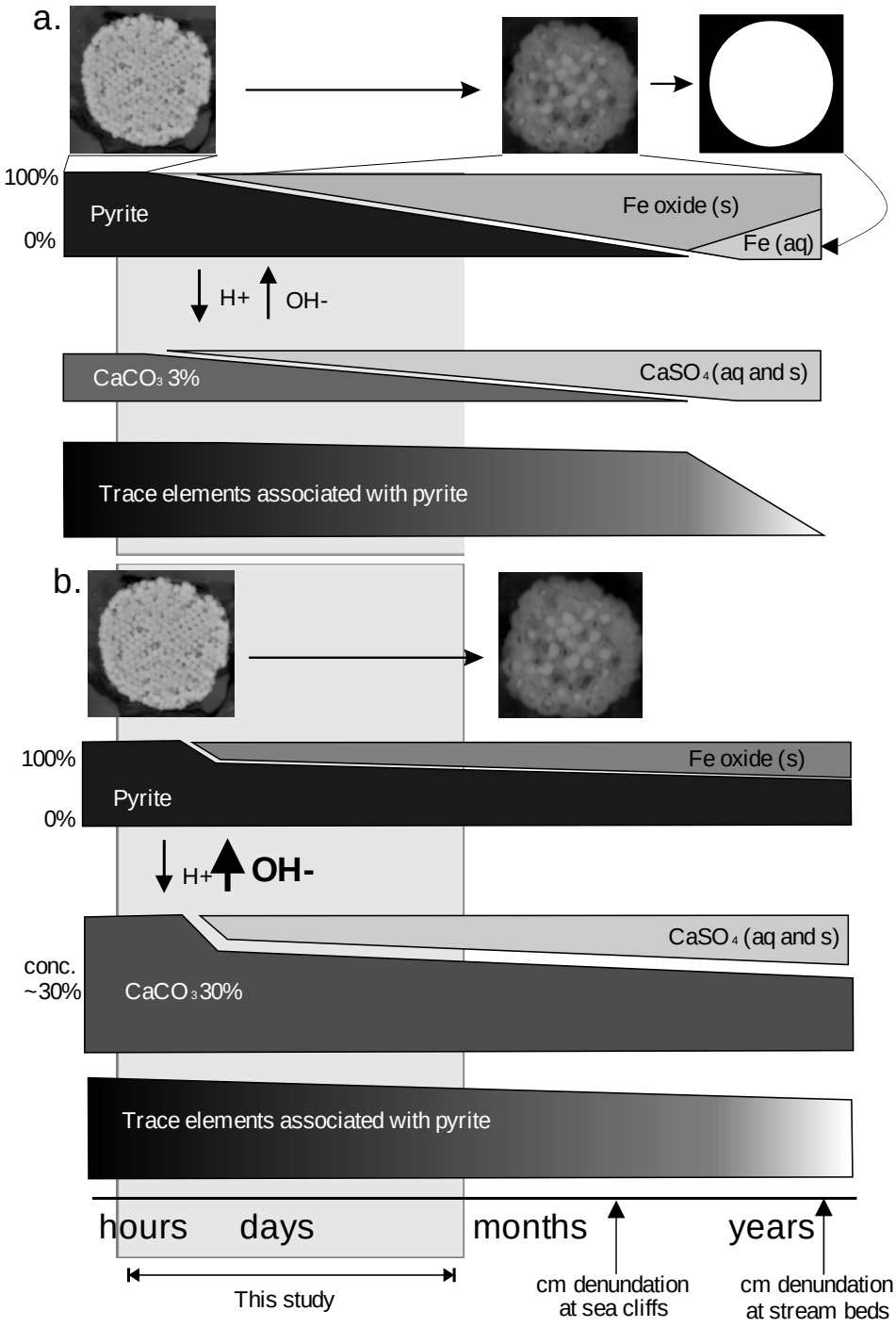

Figure 4.15 Conceptual model of pyrite oxidation in average carbonate content mudrock (a) and carbonate-rich mudrock (b). x axis is timescale and includes periods outside of this study therefore changes are presumed. Elements marked with (aq) can be lost from the system. Note greater OH- ions in b) due to greater initial CaCO content, buffering the pore environment and slowing pyrite oxidation, allowing physical erosion before oxidation is complete. This also leads to lower trace element losses

4.6 Conclusions

Evidence of pyrite oxidation, acid hydrolysis aluminosilicate minerals and carbonate dissolution suggests that the soxhlet weathering experiment by Pedro (1970) is effective at artificially weathering organic-rich mudrocks. Despite clear evidence for weathering, Fe is behaving conservatively and the Fe_{HR}/Fe_T ratio remains relatively unchanged. Also, trace metals are not leached from the sample in any significant quantities. This is contrary to natural observations of pyrite oxidation and trace metal leaching from organic-rich mudrocks into soils, groundwater and rivers (e.g. Peng et al., 2003; Yu et al., 2012).

Figure 4.15 summarises a conceptual model of our experiment. There is evidence that pyrite particles are passivated, and continuing oxidation is prevented by high pH values, as a result of carbonate dissolution. Iron (oxyhydr)oxides precipitate around pyrite particles, preventing further oxidation and encouraging co-precipitation or adsorption of trace metals. High pH was maintained throughout our experiment due to the presence of carbonate. In our samples, thus, it is realistic to assume that physical erosion of the outcrop would have occurred before any significant chemical alteration was able to modify the rock geochemistry. This, in turn, suggests that most geochemical proxies are still reliable in carbonate-rich samples, despite significant chemical alteration. In samples with lower carbonate content, it is likely that pH will be lower and less Fe (oxyhydr)oxides will precipitate, allowing Fe and trace metals to be lost from the rock. Results of this study suggests automated particle analysis is not a reliable method for ascertaining pyrite framboid diameter due to the difficulty in distinguishing euhedral from framboidal pyrite and the variable effects of weathering on pyrite particle diameter.

If carbonate dissolution does cause pyrite passivation and limit trace metal mobilisation, then carbonate contents of mudrocks could be used as a first filter to choose outcrop samples where geochemical proxies are more likely to be preserved and thus reliable. Also, the use of automated particle analysis on mudrock thin sections would allow to confidently identify passivated ‘sulphur-depleted’ pyrite. Further work is required to compare organic-rich mudrock samples with varying carbonate contents, type of carbonate minerals (calcite or dolomite) and to extend the weathering study beyond the carbonate dissolution period. Also, detailed microanalytical analyses could confirm the contents of trace metals retained within the Fe (oxy)hydroxide rims (Fischer et al., 2009) around pyrite particles and confirm the initial phase of trace metals (pyrite, clay, or organic matter). Increasing the suite of

analytes would be useful to aid understanding of weathering of contaminants into groundwater – e.g. As (Zhu et al., 2008) and elements used as tracers for weathering – e.g. Re for organic matter oxidation (Hilton et al., 2014).

Chapter 5 Testing the effects of contemporary weathering on the reliability of geochemical proxies in Colombian black shale

In this chapter, possible filters to identify weathered samples are investigated. This allows samples geochemically altered by contemporary weathering to be identified and removed from the sample set, leading to a more reliable data interpretation. With this scope, the study offers a new approach to be validated and further developed in future studies using outcrop samples.

5.1 Research Highlights

- Weathering reactions that have affected the bulk geochemistry (carbonate dissolution and pyrite oxidation) can be identified in SEM.
- Iron (oxyhydr)oxide rims seen in the artificial weathering experiment (Chapter 4) are evident in naturally weathered samples.
- Samples with lower $CaCO_3$ content have statistically lower TE, Fe_{Carb} and Fe_{PY} suggesting that these samples are geochemically more affected by weathering.
- Samples with less than 5 wt% $CaCO_3$ are considered more susceptible to weathering and their geochemical proxies interpreted with caution.
- Weathering does not appear to affect Fe_{HR}/Fe_T or TE content and so high contents can be taken as an original signature.
- The Fe_{PY}/Fe_{HR} and pyrite framboid diameter proxies are not deemed reliable in outcrop samples.
- With further development, high Fe_{OX2} and Fe_{Mag} contents could be used to identify weathering.

5.2 Introduction

During sample preparation, it was evident that the samples provided by Ecopetrol for this project had been affected by various degrees of weathering, either at outcrop or in storage. There was evidence of white, orange and brown weathering products (likely Fe oxy(hydr)oxides or gypsum – noted by Joekel et al., 2005; Cockell et al., 2011 and Pye and Miller, 1990) precipitating on the surfaces of samples (Figure 5.1a). These weathering products could often be physically removed during sample preparation, but frequently penetrated along laminae into the sample (Figure 5.1b), suggesting that geochemical changes would affect its geochemical inventory even if surface material was removed. Some

samples were also soft, others arrived as coarse sand/ fine gravel sized platy grains (Figure 5.1c), suggesting that physical sediment integrity had been affected. As it is known that weathering can affect geochemical proxies (see Chapter 4 for a thorough review), it is important that samples affected by weathering are reliably identified and 'filtered' out of the main sample set. This chapter aims to introduce a filter to exclude weathered samples from further paleoenvironmental interpretation.

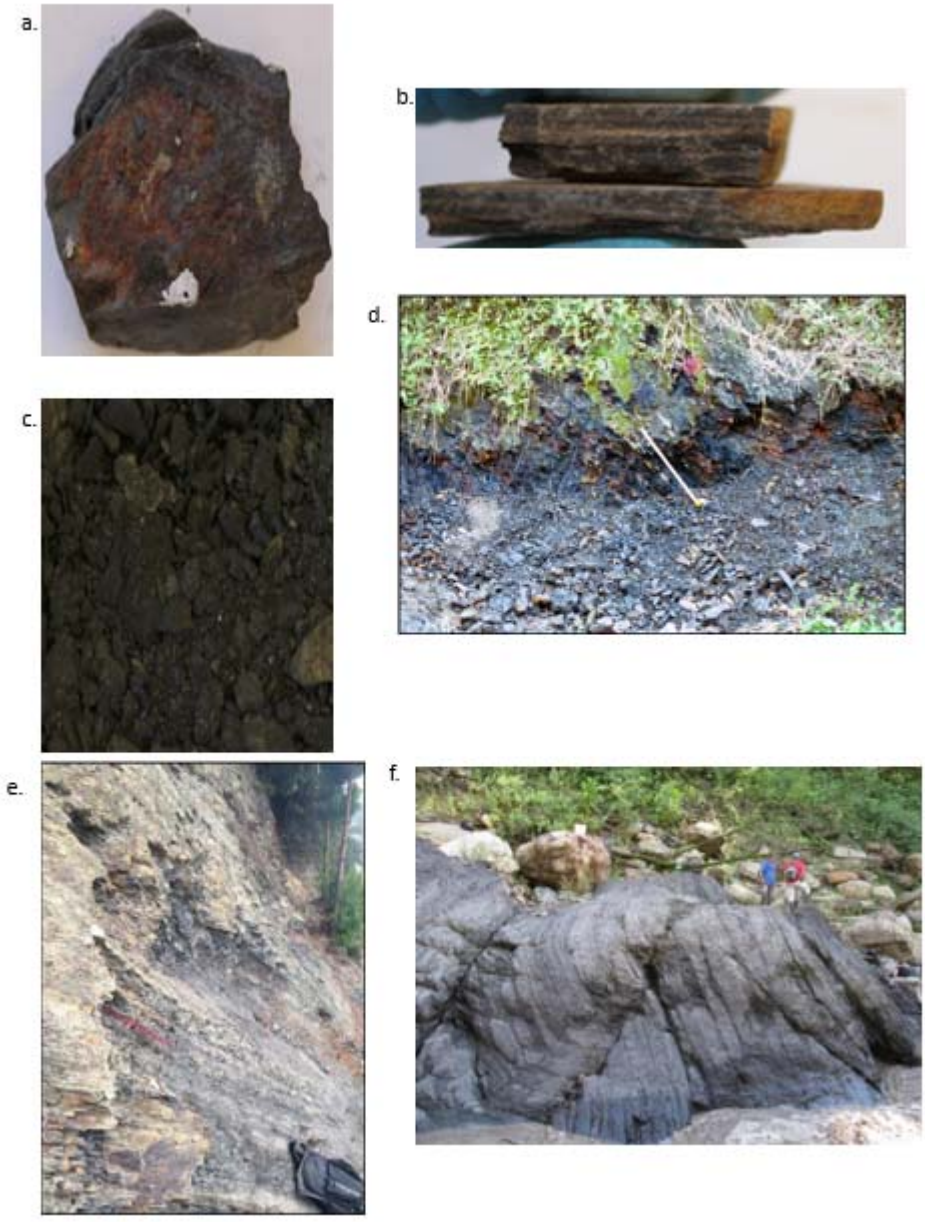

Figure 5.1 evidence for sample weathering. a. surface of a sample covered with a weathering product, likely Fe oxy(hydr)oxides. Here an unaffected internal part of a sample can be prepared. b. discolouration caused by weathering products along laminae, sample preparation cannot select unweathered portion for analysis. c. whole sample has disintegrated. d and e showing weathered road cuttings from which La Marina and Crucero samples were selected.

5.2.1 Three Possible Weathering Filters

Some samples were collected from outcrops in stream beds (Cantonera, Pedregal, Pescana and Quebrada Vara Santa) and from road cuttings (Algodones, Crucero, La Cristalina, La Marina, Paramo Guina, Quemado and Zipa). Although more often and more permanently exposed to water (key for weathering reactions), samples taken from streams should have been exposed to oxygen and water for a shorter period of time than road cuttings, as the surface material is constantly eroded away by the action of the water. Cornwell et al. (2003) and Hsieh and Knuepfer (2001) estimated erosion depth of sedimentary rocks by mountain streams (like those in the Eastern Cordillera) at between 10^{-3} and 10^{-2} m yr^{-1}. Although there are no dates available for the construction of the various road cuttings in Colombia, the surface material here was likely exposed to oxygen and water for much longer, at least a few decades. Also, photographs from the field reports show that some of the road cuttings support very extensive weathering (note pale colour, orange staining and disaggregation at road cuttings shown in Figure 5.1d and e). The photographs from the stream cuttings show less orange staining and disaggregation (Figure 5.1f), however, moss appeared to be prevalent in areas outside the main stream, which could have affected the geochemistry of the rock. The two groups of samples are compared in this study to find out if road cutting samples are indeed more strongly weathered than stream bed samples. If so, stream beds would be considered more suitable sampling locations, and the respective samples more reliable for geochemical proxy interpretation.

As previously mentioned, samples showed different visual signs of weathering (Figures 5.1). One of the products of pyrite oxidation can produce marked colouration of the rocks, e.g. Fe^{3+}(oxyhydr)oxides (red/orange, sometimes termed ochre), which also produces the distinctive orange staining of rivers in acid mine drainage areas (Equation 4.1). Gypsum (and other sulphate salts) and elemental sulphur have been identified as visual weathering products of organic-rich mudstones as well (e.g. Joekel et al., 2005; Odin et al., 2015 and Tuttle et al., 2009). Visual observation of colour changes and the presence of weathering products have been used to identify the intensity of weathering in previous studies (e.g., Fischer et al., 2009; Cockell et al., 2011; Peng et al., 2004; Odin et al., 2015). In this chapter, the hypothesis that visually less altered samples also have a more pristine geochemical composition is tested.

As discussed in Chapter 4, it is possible that the composition of samples that contain $CaCO_3$ is less affected by oxidative weathering than samples without $CaCO_3$. This is because pyrite oxidation is less extensive in a high pH environment (which occurs during $CaCO_3$ dissolution). Also, in a high pH environment, the products of pyrite oxidation, Fe oxy(hydr)oxides, can adsorb TE as they are being released from pyrite or other rock components, preventing their net loss from the sample. In this chapter, samples with low and high $CaCO_3$ are compared in order to see if pyrite and TE are present in greater quantities in higher $CaCO_3$ rocks. This filter is complicated by the possible co variation of $CaCO_3$ with TE related to productivity in the original depositional environment. As discussed in Section 3.3.2, in most basins $CaCO_3$ arrives at the sediments as the shells/tests of organisms, and so high values of $CaCO_3$ are likely linked to periods of higher productivity and higher productivity related TE contents. On the otherhand, $CaCO_3$ can also be a principal dilutor of TE, and its influence on TE and Fe contents can be major (e.g. Clarkson et al., 2014). It will be difficult to tease out the effects of accumulation alongside $CaCO_3$ and dilution by $CaCO_3$ given the susceptibility of of this component to weathering.

Figures 5.2 illustrates the complexity, with co-variation of some productivity indicators with $CaCO_3$ and the lack of, possibly negative correlation with other productivity TE. However, given the size of the data set, which encompasses a wide range of sedimentological environments and weathering regimes, the influence of $CaCO_3$, be it a weathering inhibitor or sediment component stimulating/diminishing TE content is interesting to investigate.

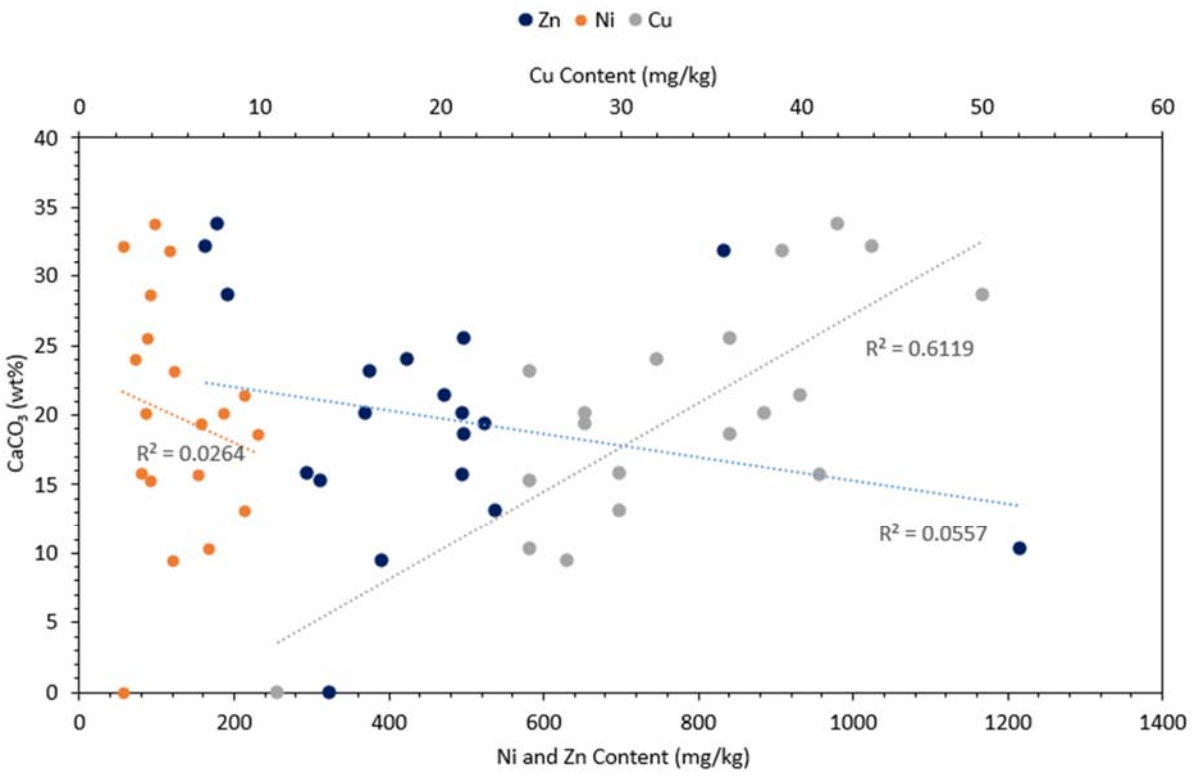

Figure 5.2. Example of correlations between CaCO3 and productivity proxies from La Cristalina 1.

5.2.2 Possible Characteristics of a Weathered Sample

It is important to determine the geochemical signatures that are expected in a sample which has been significantly altered by weathering. Studies have shown that a sample may have lost TE and so has lower TE contents than its equivalent unweathered sample (Perkins and Mason, 2014; Pye and Miller, 1990; Tuttle and Breit, 2009; Zhu et al. 2008; Zhu and Wu, 2011). Pyrite is readily oxidised and so its contents in the sediment may be lower (Jin et al., 2013; Liao et al., 2014; Littke et al., 1991; Petsch et al., 2000; Wildman et al., 2004; Zhu et al., 2008), whilst the products of pyrite oxidation may accumulate during weathering. This shift in Fe speciation should be noticeable in results of sequential Fe extractions (reduction in Fe_{Py}, increase in Fe_{OX1} and Fe_{OX2}). This transformation should also reduce the Fe_{Py}/ Fe_{HR} ratio used for distinguishing euxinic from ferruginous depositional paleoenvironments, but not the Fe_{HR}/Fe_T ratio that is indicative of anoxia (Poulton and Canfield, 2005). Iron (oxyhydr)oxides are relatively stable compared to pyrite during weathering (Schwertmann and Taylor, 1989). However, Fe weathering products are often seen on the surface of weathered outcrops (Cockell, 2011; Fischer et al., 2009; Tuttle et al., 2009), suggesting that Fe is leached from rocks, reducing not only their pyrite but also their total Fe content (Tuttle and Breit, 2009). The oxidation of pyrite should further lead to a reduction in S content, however, results of the artificial weathering experiment in Chapter 4 show that the

precipitation of gypsum can preserve the original S content of a sample. Calcium and Fe carbonates are readily soluble in acidic water (equation 4.2) and should, therefore, be lower in content in weathered rock samples. These changes should also be visible in thin section. Dissolution of calcium carbonate should be evident from pores within the rock that resemble in shape the morphology of carbonate tests (e.g. foraminifera tests). Chapter 4 has shown that pyrite oxidation products are also visible, and shifts can be semi-quantified using particle analysis (INCAFeature) coupled with SEM-EDX. Complete oxidation of pyrite framboids may leave spherical pores, likely smaller than carbonate tests with foraminifera typically a minimum size of 0.05mm and sedimentary pyrite framboids having a maximum diameter of around 10µm (Wilkes et al., 1996).

In this study, different from other weathering studies, there is not a definite weathered and unweathered sample set to directly compare geochemically. Instead, samples from the entire Colombian sample set are grouped according to the three potential weathering filters (outcrop type, visual alteration, $CaCO_3$ content), followed by a comparison of their geochemical composition. Statistically lower TE or pyrite contents would be indicative of increased weathering and unreliable samples for paleoenvironmental interpretation. The same statistical approach used by Pye and Miller (2015), i.e. comparison of medians is applied here. The sample set is very varied, with samples from different locations in the basin and different time periods (Berriasian to Campanian). Even samples from the same section show a great deal of variety in their geochemical signature (discussed further in Chapters 6-8). This statistical approach is therefore based on the premise that the sample groupings represent a similar distribution of sample types within them. Element contents are normalised to Al in an attempt to make samples diluted variably with detrital material more comparable (as discussed in Chapter 3). Alongside this statistical approach, the physical and chemical effects of weathering are investigated on a fine scale, via SEM EDX, on a subset of samples.

5.3 Results

5.3.1 Outcrop Type

Samples were assigned to either a road cutting or stream according to information provided by Georex (2015). Assignments and number of samples are shown in Tables 5.3 and 5.5.

Box plots in Figure 5.3 show that samples taken from stream beds overall have higher contents of Fe_{carb}, Fe_{OX1}, pyrite and Fe_{mag}. Samples from streams also appear to have higher Al normalised Fe content, and higher Fe_{PY}/Fe_{HR} ratios. Road cuttings appear to have higher contents of Al normalised TE related to productivity and redox (Figure 5.3) and higher P/Al than stream samples (5.2r).

Since data were not normally distributed (tested using Shapiro-Wilk), Mann-Whitney U tests were run to determine if there were differences in proxies between road and stream outcrop samples. Distributions of the proxy data were not similar for stream and road samples (as assessed visually from box plots in Figure 5.3), so only mean ranks can be compared. Samples taken from stream beds have statistically higher Al normalised Fe and Mn, and higher contents of some Fe-species. All the differences observed in box plots are shown to be statistically significant. The Mann-Whitney U statistic, the *p*-value and the mean ranks are shown in Table 5.1. using an exact sampling distribution for *U* (Dineen & Blakesley, 1973).

Table 5.5. Statistical results of Mann-Whitney U test comparing road and stream groups. Ranks in bold are the highest.

Proxy	p value	U-value	Mean rank road	Mean rank stream
Fe_{Carb}	<0.001	8080	88.03	**160.25**
Fe_{OX1}	<0.001	7342	92.82	**148.54**
Fe_{mag}	<0.001	7703	90.48	**154.28**
Pyrite	<0.001	6914	98.39	**139.38**
Fe_{PY}/Fe_{HR}	0.012	5901	102.18	**125.67**
Fe/Al	<0.001	6880	97.61	**140**
Ba/Al	<0.001	1802	**130.37**	60.66
Cr/Al	<0.001	2835	**123.71**	76.8
Cu/Al	<0.001	3295	**120.74**	83.98
Mo/Al	<0.001	1024	**135.39**	48.51
Ni/Al	0.003	3705	**118.09**	90.40
V/Al	<0.001	1454	**132.62**	55.22
U/Al	<0.001	3617	**118.66**	89.02
Mn/Al	<0.001	7466	93.96	**148.84**

Figure 5.3a-r

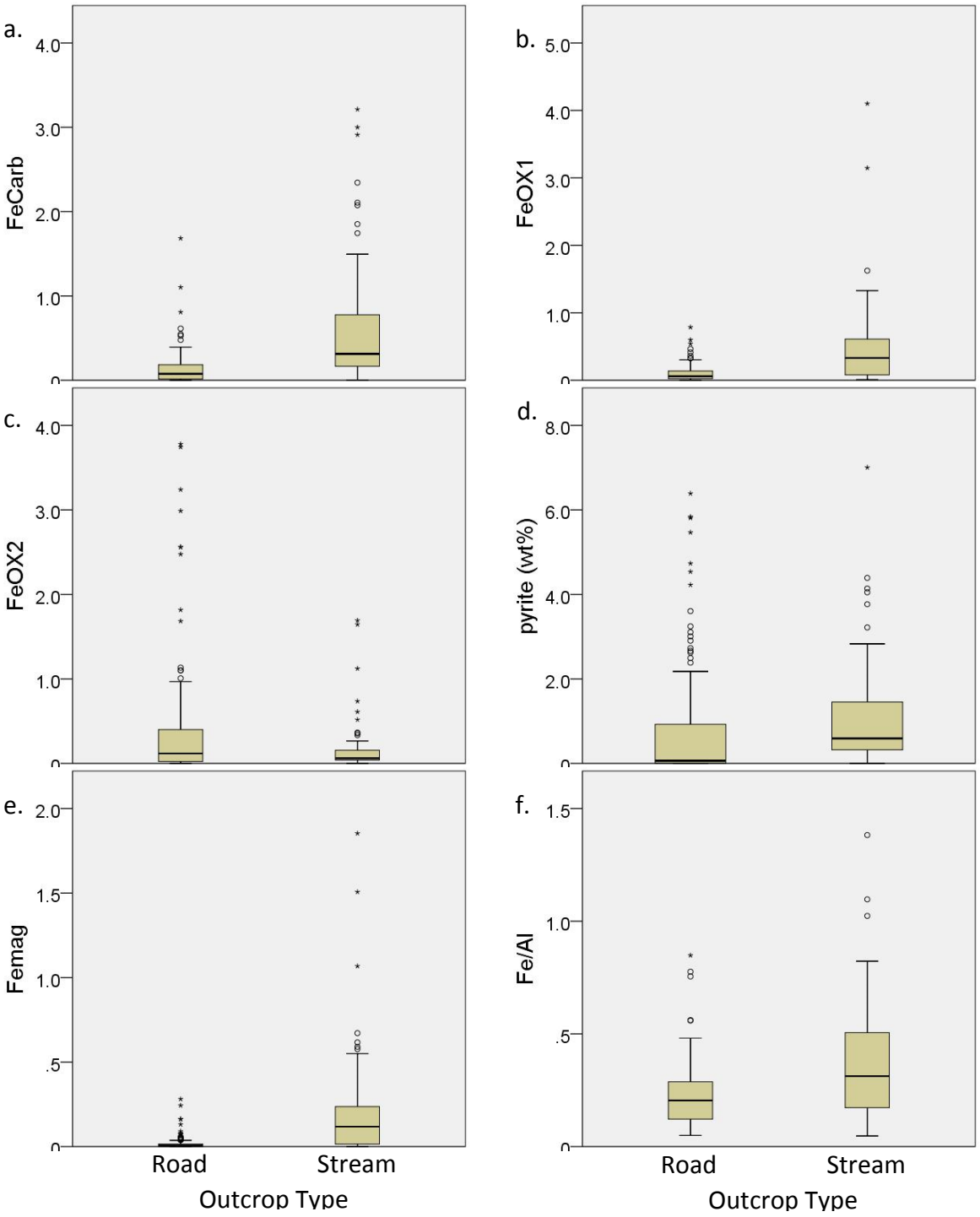
a.
FeCarb
4.0
3.0
2.0
1.0
0
b.
FeOX1
5.0
4.0
3.0
2.0
1.0
0
c.
FeOX2
4.0
3.0
2.0
1.0
0
d.
pyrite (wt%)
8.0
6.0
4.0
2.0
0
e.
Femag
2.0
1.5
1.0
.5
0
f.
Fe/Al
1.5
1.0
.5
0
Road
Stream
Outcrop Type
Road
Stream
Outcrop Type

Figure 5.3a-r

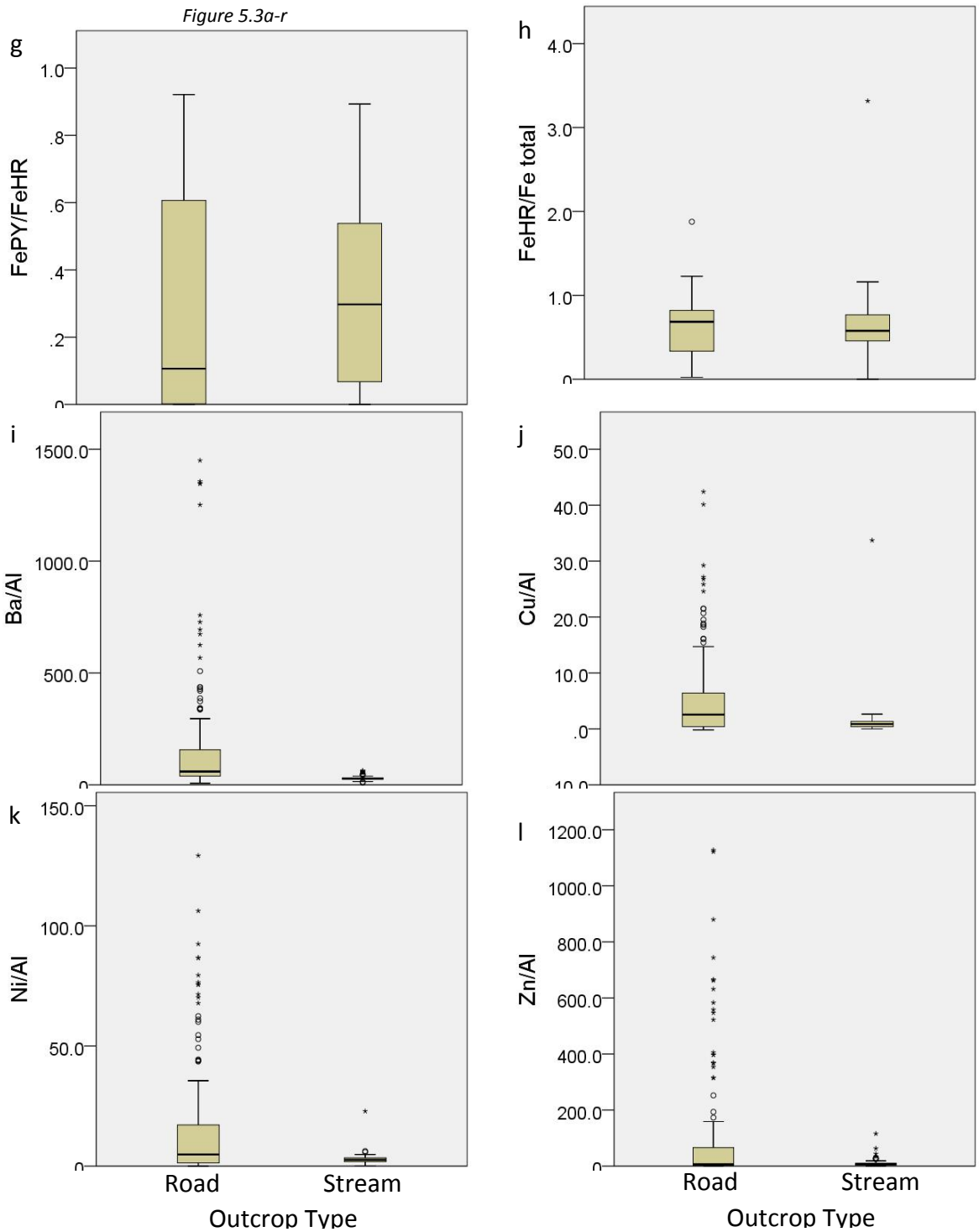
g
FePY/FeHR
1.0
.8
.6
.4
.2
0
h
FeHR/Fe total
4.0
3.0
2.0
1.0
0
i
Ba/Al
1500.0
1000.0
500.0
0
j
Cu/Al
50.0
40.0
30.0
20.0
10.0
.0
k
Ni/Al
150.0
100.0
50.0
0
l
Zn/Al
1200.0
1000.0
800.0
600.0
400.0
200.0
0
Road
Stream
Outcrop Type
Road
Stream
Outcrop Type

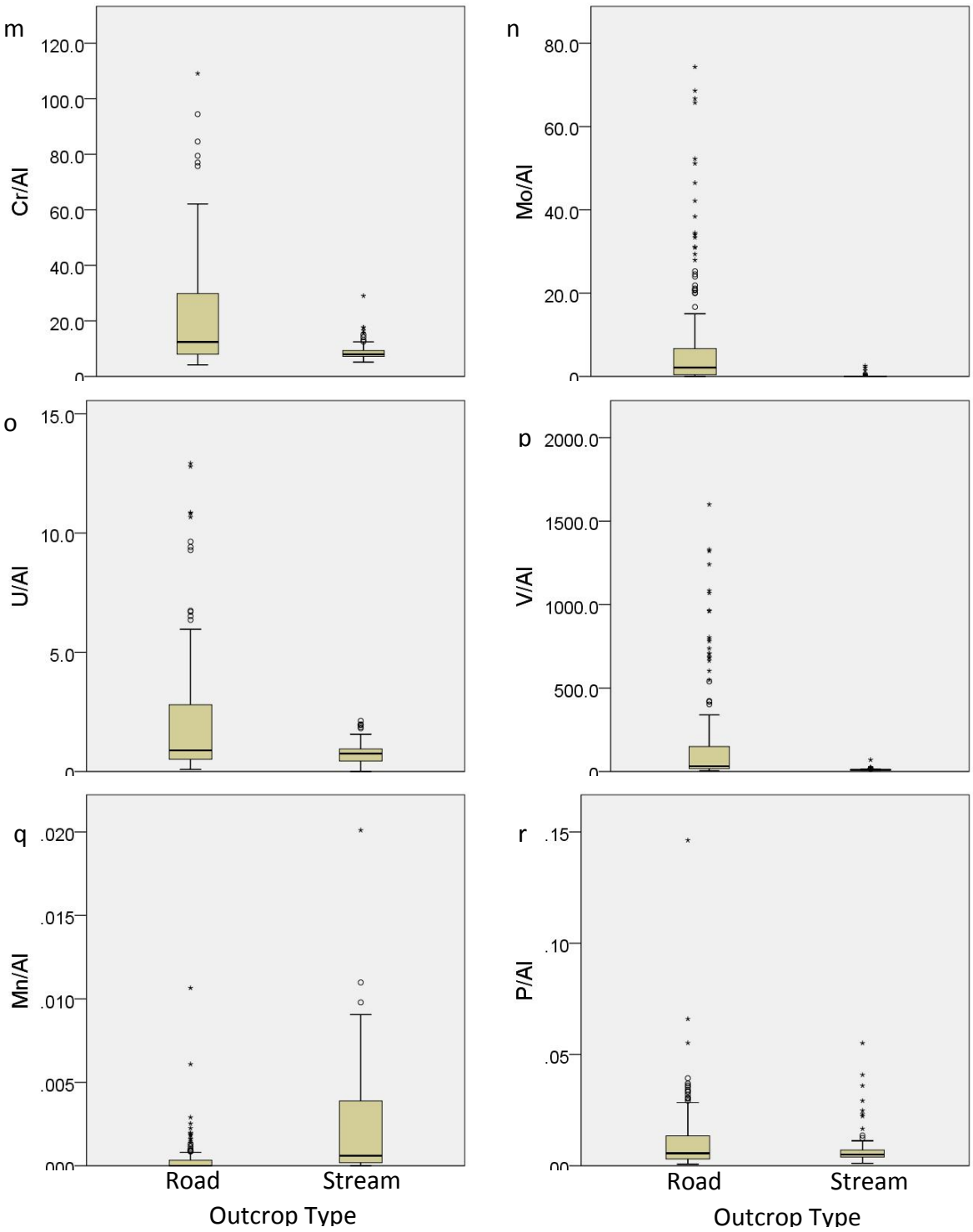

Figure 5.3 a-r. Box plots of sample data separated into outcrop type. Trace element, Fe, P and Mn data from XRF. Iron speciation data (in wt%) from sequential extraction. Dark line within the box is median, box shows interquartile range, outliers (circles and stars) are outside 1.5 x the interquartile range.

5.3.2 Visual Alteration

Table 5.2 summarises the approach used to assign visual states of alteration to each sample and was carried out on hand specimen before sample preparation. These assignments were

largely based on an approach by Peng et al. (2004), who described samples from parent rock to overlying soil based on their location within a section and their characteristics.

Table 5.6 Description of the method used to assign samples to different visual alteration groups.

Category	Colour Change	Integrity
1	None	Intact
2	Some yellow, orange, brown or white salts visible on the surface	Intact
3	Yellow, orange or brown colouring or a lightening of rock colour extends >1mm into the sample. Colouration extends along laminae into the sample	Intact
4	Yellow, orange or brown colouring or a lightening of rock colour extends >1mm into the sample. Colouration extends along laminae into the sample	Sample breaks into chips or is soft

Table 5.7. Numbers of samples assigned to each visual alteration group from each section.

	Location	1	2	3	4
Stream bed	Pedegral	1	6	1	1
	Cantonera	3	2		
	QVS	2	5		1
	Pescana	3	10	2	
Road Cutting	Algodones	1	11	3	4
	Quemado	1	7	1	
	La Marina	7	8	4	2
	La Cristalina 1	4	9	2	4
	La Cristalina 2	1	3	3	1
	La Cristalina 3	3	6	2	2
	La Cristalina 4		7		3
	Zipa	2	6	7	1
	El Crucero		11	5	1
	PG	2	3	1	1
Total		**30**	**94**	**31**	**21**

Table 5.3 shows that most sections only have a small proportion of samples which show signs of severe weathering (group 4). The majority of samples from all sections reveals some signs of surface colour alteration due to weathering (group 2). There does not appear to be a relevant difference in the visual weathering state of samples from streams or from road cuttings by visual inspection, with both types of outcrops samples mainly being assigned to group 2 (60 and 50 % of samples, respectively).

Figure 5.4

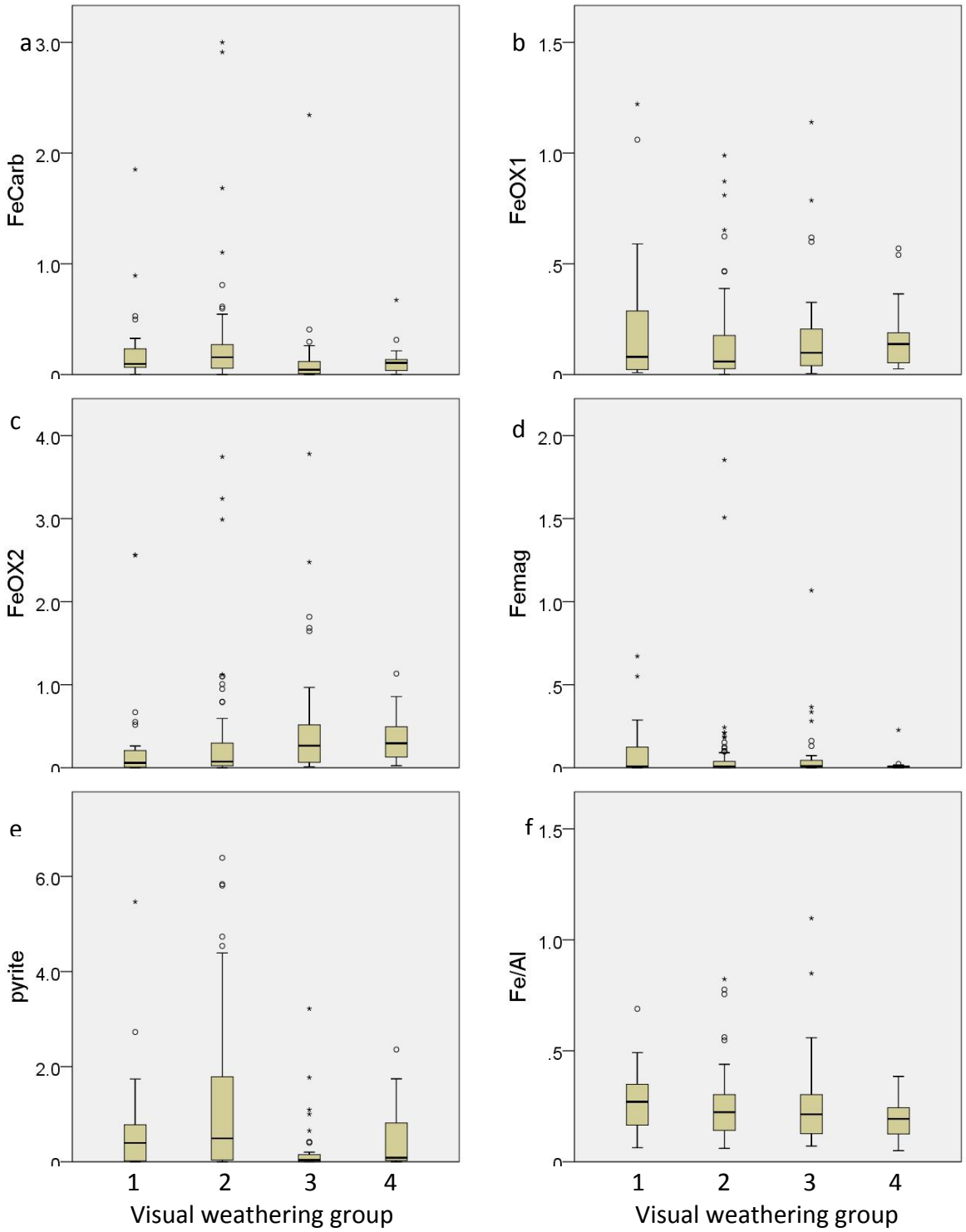
a
FeCarb
3.0
2.0
1.0
0
b
FeOX1
1.5
1.0
.5
0
c
FeOX2
4.0
3.0
2.0
1.0
0
d
Femag
2.0
1.5
1.0
.5
0
e
pyrite
6.0
4.0
2.0
0
f
Fe/Al
1.5
1.0
.5
0
1
2
3
4
Visual weathering group
1
2
3
4
Visual weathering group

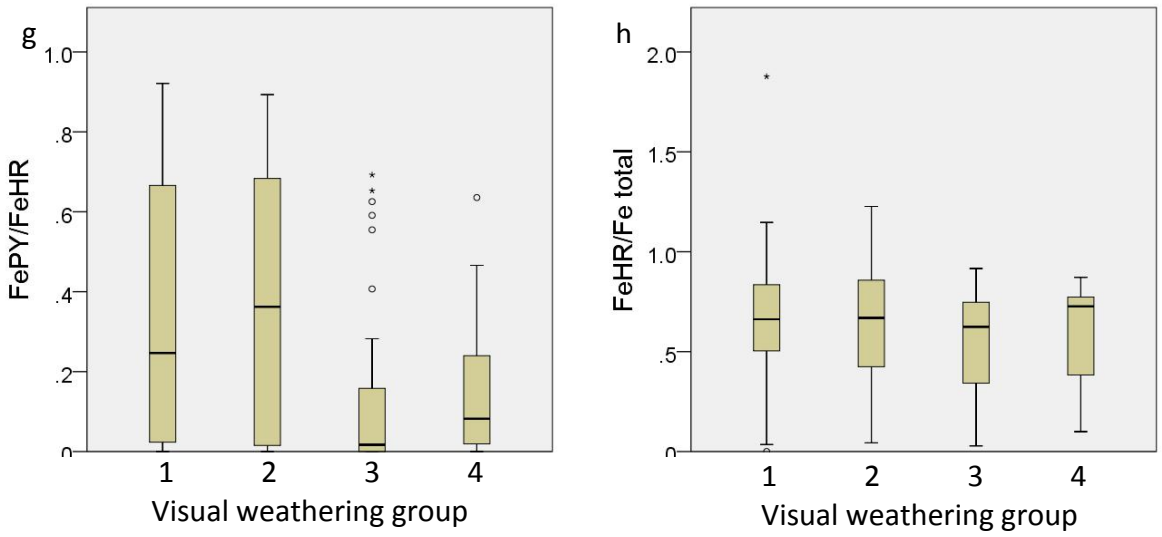
g
FePY/FeHR
1.0
.8
.6
.4
.2
0
1
2
3
4
Visual weathering group
h
FeHR/Fe total
2.0
1.5
1.0
.5
0
1
2
3
4
Visual weathering group

Figure 5.4

Figure 5.4

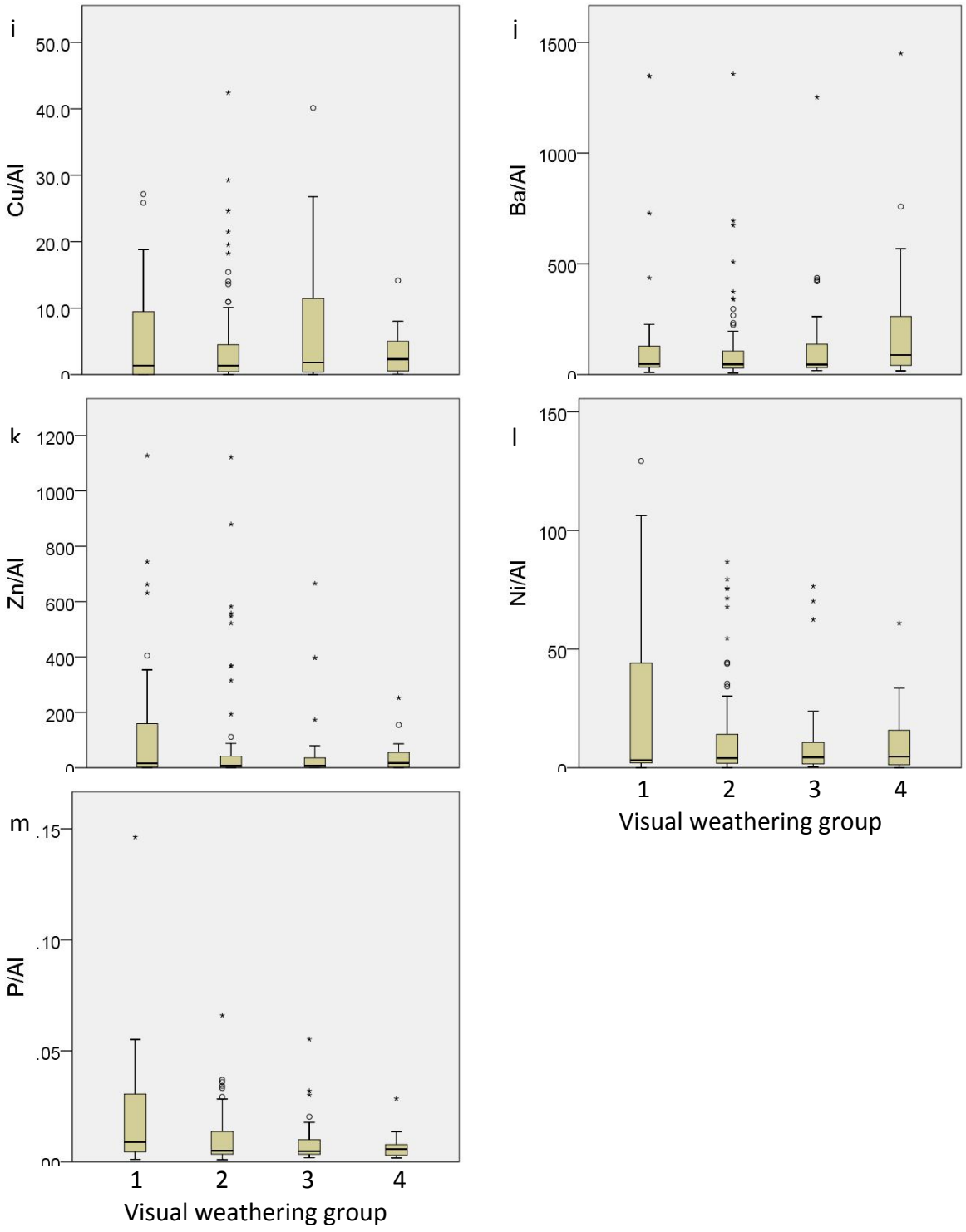
i
Cu/Al
50.0
40.0
30.0
20.0
10.0
0
i
Ba/Al
1500
1000
500
0
k
Zn/Al
1200
1000
800
600
400
200
0
l
Ni/Al
150
100
50
0
m
P/Al
.15
.10
.05
.00
1
2
3
4
Visual weathering group
1
2
3
4
Visual weathering group

Figure 5.4

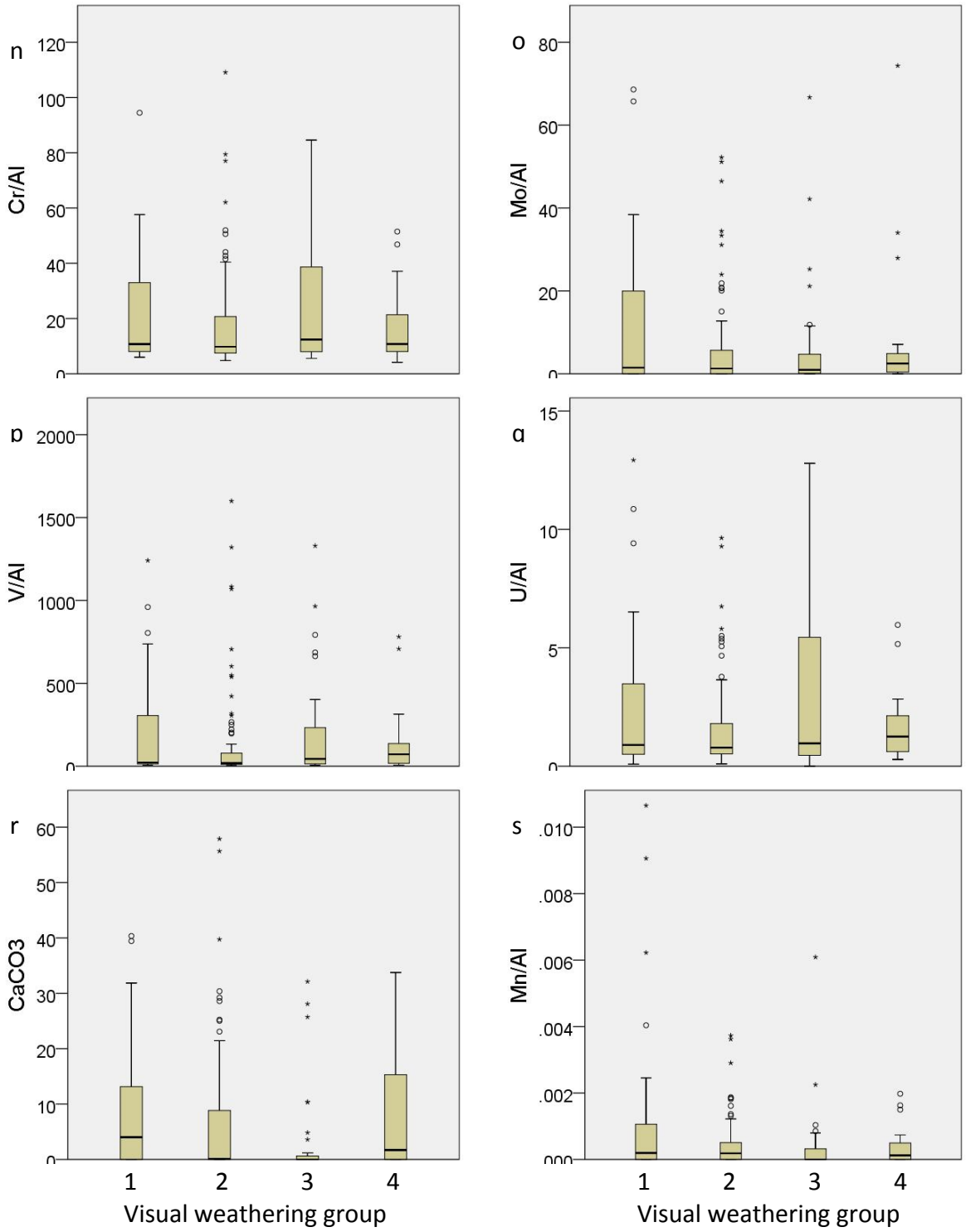

Figure 5.4 a-s Box plots of sample data separated into groups sorted by visual alteration as per Table 5.2. Trace element, Fe, P and Mn data from XRF. Iron speciation data from sequential extraction in (wt%). CaCO3 from LECO combined with CNS analysis (wt%). Dark line within the box is median, box shows interquartile range, outliers (circles and stars) are outside 1.5 x the interquartile range.

Figure 5.4 a-e shows outliers in every sample set for each of the Fe species analysed, which makes it difficult to identify any major differences between visual weathering groups. Visually unweathered or only surface-weathered samples (groups 1 and 2) appear to have slightly higher Fe_{carb} and pyrite contents, and slightly lower Fe_{OX2} compared to more extensively weathered samples in groups 3 and 4. Samples from group 3 also appear to have lower $CaCO_3$ content (Figure 5.4r)

A Kruskal-Wallis test (chosen as the majority of data was not normally distributed, tested by Shapiro- Wilk test) was conducted to determine if differences in Fe-species, Fe-species ratios, or Al normalised Fe were statistically significant between sample groups with different visual weathering extent. Statistically significant differences were found between sample groups in Fe_{carb}, Fe_{OX2}, pyrite and Fe_{Py}/Fe_{HR}. Test statistics are shown in Table 5.4. Subsequently, pairwise comparisons (a post hoc test) were performed using Dunn's (1964) procedure. A Bonferroni correction for multiple comparisons was made with statistical significance accepted at the $p < .0083$ level. Statistically significant differences in data between groups are recorded in Table 5.4. The most consistent differences are between groups 2 and 3 (statistically higher Fe_{carb} and pyrite contents, as well as Fe_{Py}/Fe_{HR} in group 2). Group 4 (visually most weathered samples) has significantly greater content of Fe_{OX2} than groups 1 and 2.

No clear differences are notable when examining box plots of productivity and redox TE proxies (Figures 5.4 I to r), and there is no statistical difference identified. Aluminium normalised P values are statistically different between each visual alteration category, with least visually weathered samples (group 1) having the highest content.

Table 5.8. Summarising results of Kruskal-Wallis statistical test comparing visually altered and unaltered samples, showing only data where there are statistical differences

Element	$X^2(5)$	p-value	Pairwise comparisons between groups
Fe_{Carb}	11.86	0.008	2 higher than 3
Fe_{OX2}	16.67	0.001	1 lower than 4, 2 lower than 4
Pyrite	13.10	0.004	2 higher than 3
Fe_{PY}/Fe_{HR}	15.83	0.001	2 higher than 3
P/Al	7.82	0.050	Each group statistically different, decreasing from group 1 to 4.

5.3.3 $CaCO_3$ content

The samples were grouped according to $CaCO_3$ content to investigate the effect of carbonate contents on TE contents and Fe species (categories shown in Table 5.5). The number of samples assigned to each category is shown in Table 5.5.

Table 5.5 shows that almost half of the samples do not contain any detectable $CaCO_3$ (n= 100). Most of the samples contain less than 1 wt% $CaCO_3$ in the sections representing land-proximal, shallow settings (La Marina, Pescana and Crucero), but also the more distal, deeper-water Algodones, Quemado and Zipa sections. The majority of samples from the La Cristalina sections have greater than 5 wt% $CaCO_3$. There is no clear difference in the distribution of $CaCO_3$ content in samples from streams or from road cuttings, with most samples in both groups (44 and 49 %, respectively) being assigned to group 0. There are, however, more samples from road cuttings assigned to groups 4 and 5 (mostly from the La Cristalina sections).

Figure 5.5f shows that samples with no $CaCO_3$ (group 0) have lower Fe/Al than samples with carbonate. Group 0 samples also have lower Fe_{HR}/Fe_T, lower Fe_{Py}/Fe_{HR} and lower pyrite content, and higher Fe_{Mag}. Easily reducible Fe oxides (Fe_{OX1}), Fe_{Carb} and Fe_{mag} show elevated contents in groups 1 and 2 (0.01-5 wt% $CaCO_3$), but diminishing contents in groups 4 and 5 (10 to >20 wt% $CaCO_3$), Figure 5.5a-f. A Kruskal-Wallis test, conducted to determine if differences in Fe-species, Fe-species ratios and Fe/Al seen in the box plots were statistically significant between groups with different $CaCO_3$ content, showed statistically significant differences between all tested parameters apart from Fe_{OX2}. Test statistics are shown in Table 5.6. Subsequently, pairwise comparisons (a post hoc test) were performed using Dunn's (1964) procedure and corrected as per the previous section. This analysis identified statistically significant differences in data between groups, as recorded in Table 5.6. Any combinations of parameters not mentioned are not statistically different. The statistical test confirms that samples with no detectable carbonate have significantly lower Fe/Al, pyrite, Fe_{Carb} Fe_{HR}/Fe_T and Fe_{Py}/Fe_{HR} than samples with over 10 wt% $CaCO_3$.

Figure 5.5 (i to q) shows that samples with less than 1 wt% $CaCO_3$ (group 0 and 1) have lower Al normalised TE (Ni, Cu, Mo, U and V) than samples with greater than 1 wt% $CaCO_3$.There are lower contents of Al normalised Zn and Ba in the less than 5 wt% carbonate groups (groups 0, 1 and 2). Also, Al normalised P appears to be present in decreasing quantities with decreasing carbonate content. Following the same procedure as for Fe/Al and Fe

species, a Kruskal-Wallis test was conducted to determine if differences in Al normalised redox and productivity TE (and P) seen in box plots were statistically significant between groups with different $CaCO_3$ content. Data were statistically significantly different between the different $CaCO_3$ content groups in all cases tested. The results of the pairwise statistical test are shown in Table 5.6. Statistical tests confirm that observations noted in boxplots are statistically different, but additionally, samples with less than 5 wt% $CaCO_3$ (group 2) have lower TE contents than samples with higher than 20 wt% carbonate (and in the case of Ba/Al and Zn/Al, lower than those samples with greater than 10 wt% $CaCO_3$).

Table 5.5. Number of samples from each section in each $CaCO_3$ category. N is number of samples. $CaCO_3$ estimated assuming all IC (measured by a combination of LECO and CNS) is from $CaCO_3$.

			Category					
			0	1	2	3	4	5
	Location	Total n	ND $CaCO_3$	0-1 wt% $CaCO_3$	1-5 wt% $CaCO_3$	5-10 wt% $CaCO_3$	10-20 wt% $CaCO_3$	>20 wt% $CaCO_3$
Stream bed	Pedegral	16	7	3	4		1	1
	Cantonera	14	6		5	1	2	1
	QVS	8		3	2	1		2
	Pescana	17	7	5	2	2	1	
Road Cutting	La Marina	21	13		3	4		1
	Algodones	22	14	2	3	1	1	
	Quemado	12	9	2	1			
	La Cristalina 1	19	1			1	7	10
	La Cristalina 2	8	2		1	1	1	3
	La Cristalina 3	13	3		1	2	2	5
	La Cristalina 4	10	1			4	3	2
	Zipa	20	15	1	1		2	1
	El Crucero	24	22	2				
	PG	7		1	6			
	Total	**211**	**100**	**19**	**29**	**17**	**20**	**26**

Figure 5.5

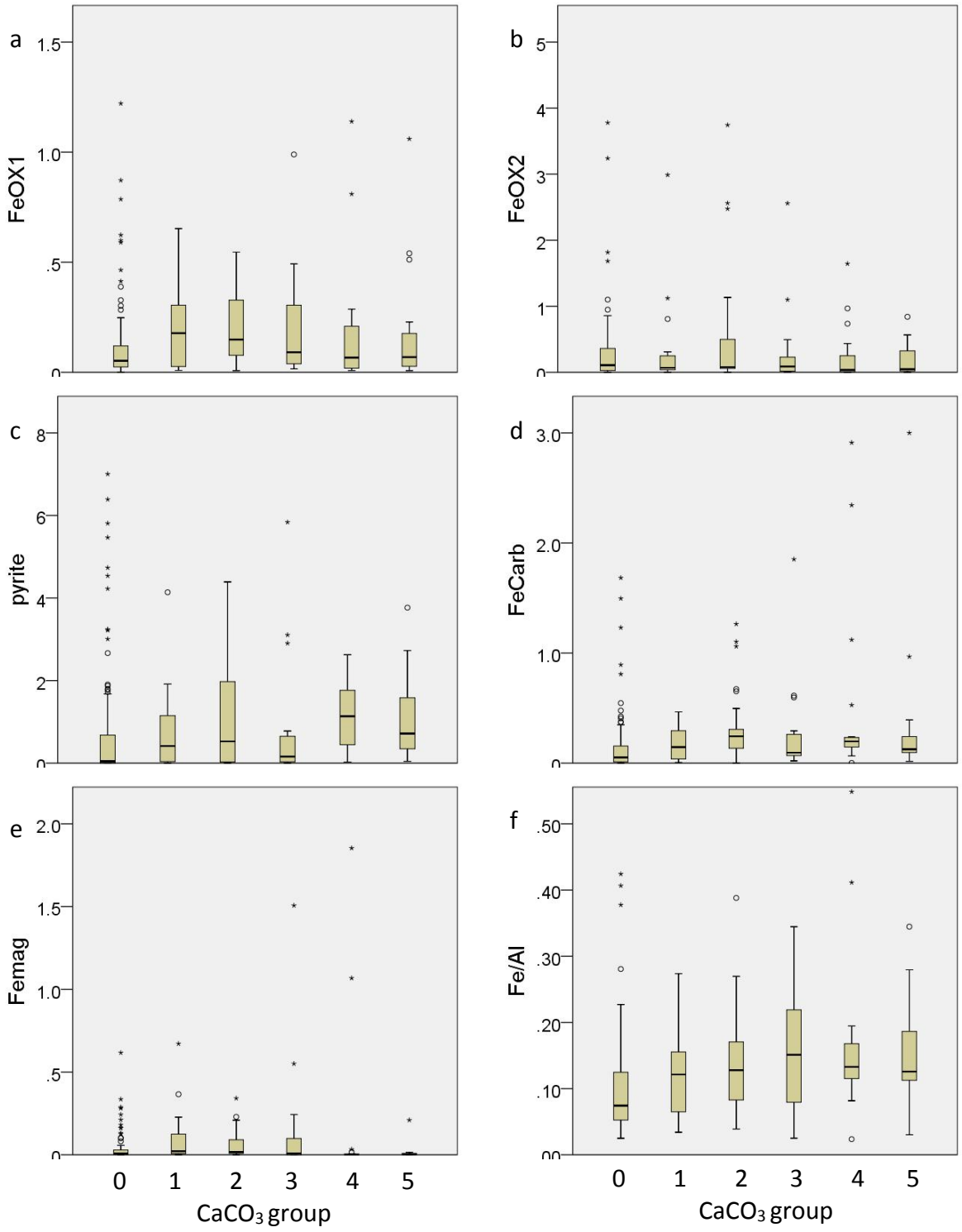
a
FeOX1
b
FeOX2
c
pyrite
d
FeCarb
e
Femag
f
Fe/Al
0
1
2
3
4
5
CaCO3 group

Figure 5.5

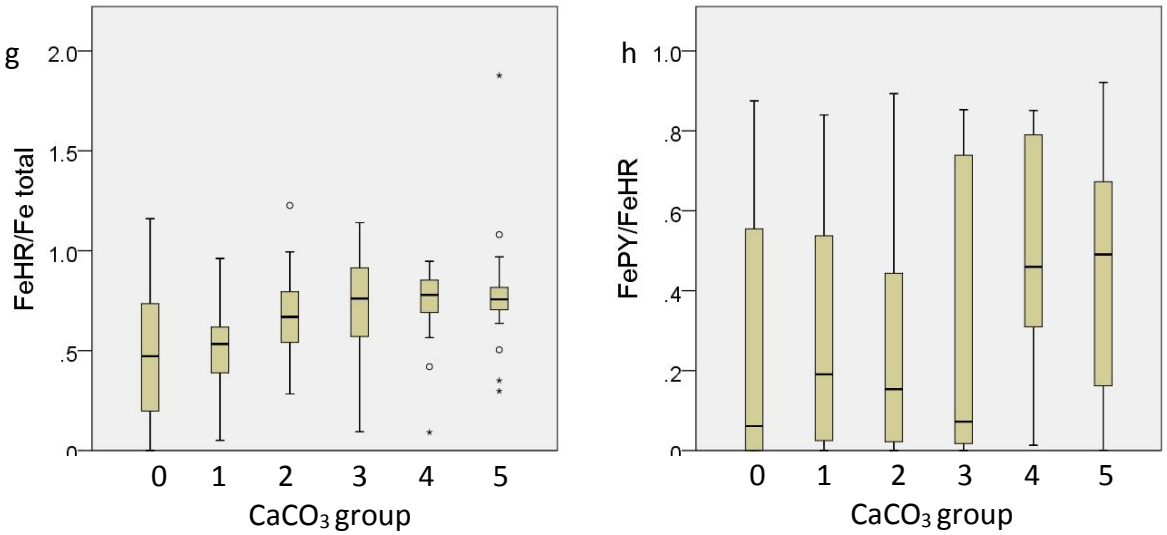
g
FeHR/Fe total
2.0
1.5
1.0
.5
0
0 1 2 3 4 5
CaCO3 group
h
FePY/FeHR
1.0
.8
.6
.4
.2
0
0 1 2 3 4 5
CaCO3 group

Figure 5.5

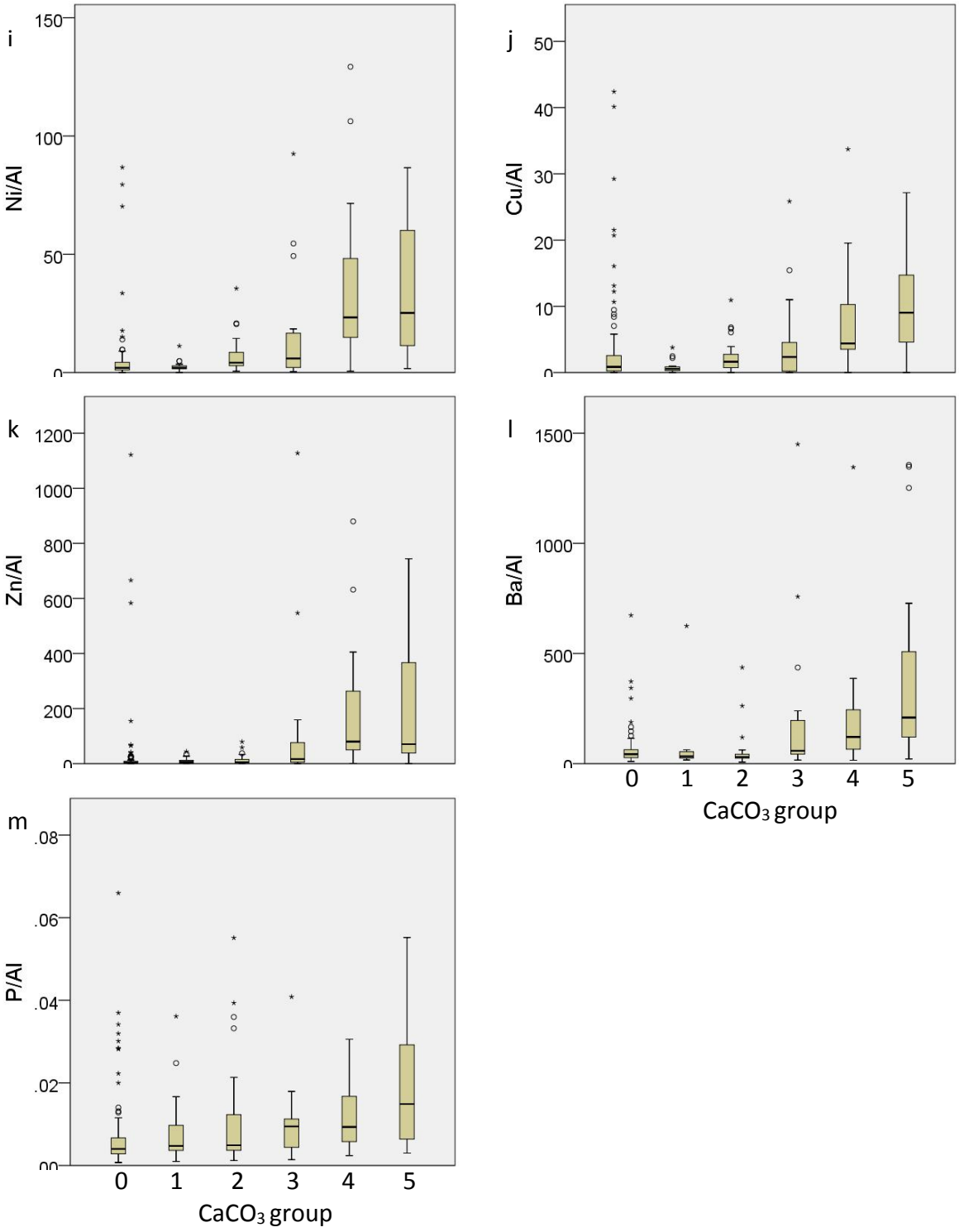
i
Ni/Al
150
100
50
0
j
Cu/Al
50
40
30
20
10
0
k
Zn/Al
1200
1000
800
600
400
200
0
l
Ba/Al
1500
1000
500
0
m
P/Al
.08
.06
.04
.02
.00
0
1
2
3
4
5
CaCO3 group

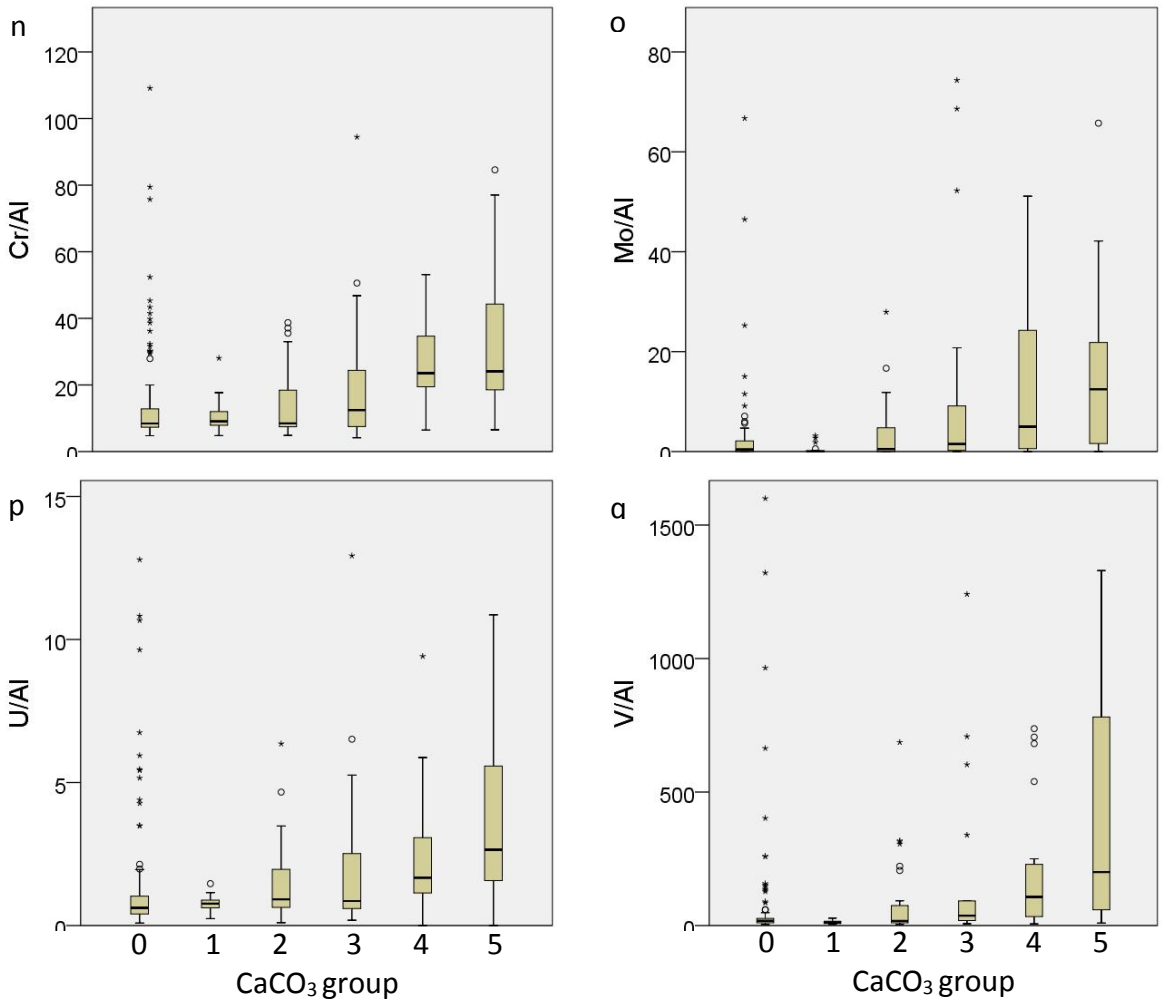

Figure 5.5 a-q Box plots of sample data separated by $CaCO_3$ group (Table 5.6). Trace element, Fe, P and Mn data from XRF. Iron speciation (wt%) data from sequential extraction. $CaCO_3$ (wt%) from LECO combined with CNS analysis. Dark line within each box is median, box shows interquartile range, outliers (circles and stars) are outside 1.5 x the interquartile range.

Table 9.6. Summary of results of Kruskal-Wallis tests between $CaCO_3$ groups, showing only data where a statistical difference was noted

Element	**$X^2(5)$**	**p-value**	**Result of pairwise comparison between groups**
Fe_{Carb}	31.8	<0.001	0 lower than 2,4,5
Fe_{OX1}	13.6	0.018	0 lower than 2
Fe_{Mag}	24.5	<0.001	1 higher than 4 and 5, 2 higher than 4,5
Pyrite	26.1	<0.001	0 lower than 4 and 5
Fe_{HR}/Fe_T	27.8	<0.001	0 lower than 4 and 5
Fe_{PY}/Fe_{HR}	21.4	0.001	0 lower than 4 and 5
Fe/Al	31.1	<0.001	0 lower than 2, 4 and 5
P/Al	38.9	<0.001	0 lower than 4 and 5, 1 lower than 5
Ba/Al	51.7	<0.001	0 lower than 4 and 5, 1 lower than 4 and 5, 2 lower than 3,4,5
Cr/Al	34.7	<0.001	0 lower than 4 and 5, 1 lower than 4 and 5, 2 lower than 5
Cu/Al	45.7	<0.001	0 lower than 4 and 5, 1 lower than 4 and 5, 5 higher than 2 and 3.
Mo/Al	40.2	<0.001	0 lower than 4 and 5, 1 lower than 3,4,5 2 lower than 5
Ni/Al	69.3	<0.001	0 lower than 2, 4 and 5 1 lower than 4 and 5 2 lower than 5
V/Al	49.0	<0.001	0 lower than 4 and 5 1 lower than 3, 4, 5 2 lower than 5
U/Al	32.8	<0.001	0 lower than 4 and 5 1 lower than 5
Zn/Al	60.8	<0.001	0 lower than 4 and 5 1 lower than 4 and 5 2 lower than 4 and 5
Mn/Al	13.5	0.019	0 diff 5

5.3.4 SEM-EDX

A limited number of samples has been analysed in thin section using SEM-BSE/EDX, in order to identify the extent of weathering and its physical and geochemical effects. These samples sit within different categories in the aforementioned groups. These sub-samples also have different bulk geochemistry, indicative of either anoxic or oxic depositional conditions (Table 5.7 and 5.8).

Table 5.7. Fe-speciation data for each sample analysed in thin section

Outcrop	Depth (m)	Visual alteration group	$CaCO_3$ group	S (wt %)	Fe_{Carb} (wt%)	Fe_{OX1} (wt%)	Fe_{OX2} (wt%)	Fe_{mag} (wt%)	Fe_{py} (wt%)	pyrite (wt%)	Fe_{HR}/Fe_T	Fe_{PY}/Fe_{HR}
Algodones	519.5	2	0	2.15	0.31	0.02	0.04	0.00	1.51	3.24	0.68	0.80
Crucero	79	2	0	0.23	0.02	0.02	0.11	0.01	0.00	0.00	0.14	0.00
La Cristalina 1	336	2	5	0.32	0.13	0.04	0.05	0.00	0.46	0.99	0.71	0.67
Zipa	74.5	3	0	0.34	0.04	0.16	0.41	0.01	0.00	0.00	0.77	0.00

Table 5.8. Aluminium normalised TE data for samples examined in thin section

Outcrop	Depth (m)	Fe/Al	P/Al	Ba/Al	Cu/Al	Ni/Al	Zn/Al	Cr/Al	Mo/Al	V/Al	U/Al
Algodones	519.5	0.26	0.00	52.8	1.58	3.07	4.18	7.15	1.30	17.9	0.74
Crucero	79	0.08	0.00	20.0	0.52	1.03	1.69	5.08	0.07	4.6	0.52
La Cristalina 1	336	0.17	0.02	232.6	4.49	22.27	67.53	21.55	12.75	266.0	3.05
Zipa	74.5	0.16	0.01	87.1	8.81	9.02	27.25	30.12	2.05	157.6	3.48

Algodones (519.5 m)

This sample was collected from an outcrop in a road cutting. The sample was assigned to visual alteration group 2 and carbonate group 0. The lithofacies interpretation provided by Georex suggests a marine shelf depositional environment, but with sand input from unstable sediment piles at the foot of a delta (Table 3.2). There is no carbonate detectable in the sample, nor are there any carbonate lithologies observed within 10 m of the sample. Geochemistry shows no enrichment in redox or paleo productivity related TE when compared to average shale (Table 5.8), apart from Mo. The Mo content of 14 mg/kg is greater than average shale and is indicative of sulphidic conditions limited to pore waters (Scott and Lyons, 2012). Iron speciation identified pyrite (3.2 wt %) which makes up the

majority of the Fe_{HR} pool (Fe_{Py}/Fe_{HR} is 0.8), and Fe_{HR}/Fe_T is 0.68, indicative of anoxic depositional conditions (Poulton and Canfield, 2005) (Table 5.7). Redox proxies, in this case, contradict, with Fe_{HR}/Fe_T indicating anoxic conditions and TE suggesting sulphate reduction is limited to the pore waters. Particles are relatively well aligned as evident from thin section (Figure 5.6a), and the sample comes from a part of the outcrop where planar parallel lamination has been noted, and evidence of bioturbation is absent. Sedimentological indicators would, therefore, suggest bottom water anoxia.

From particle analysis in INCAfeature and EDX, it is possible to analyse geochemical data for 1000 of heavy minerals identified in SEM (Figure 5.7), as discussed in Chapter 4. It is evident from this figure that 'pristine' pyrite (Fe:S<1) dominates, however, 'sulphur depleted' pyrite particles and Fe oxy(hydr)oxides exist. Visual analysis of the 'sulphur depleted' particles shows that 28 out of 50 particles are spherical in shape and are considered framboidal. It is therefore evident that the precipitation of Fe oxy(hydro)oxide rims around pyrite particles, which occurred in the artificial weathering experiment (outlined in Chapter 4), is also occurring in this natural outcrop sample.

In Figure 5.6a, carbonate shell/test shaped pores are visible in thin section by SEM-BSE. It is assumed that they are dissolved and not plucked out, as no $CaCO_3$ is measurable in the bulk material (Table 5.7). Framboid shapes which are not filled by pyrite, but are Fe oxy(hydr)oxides are visible in Figure 5.6b. The framboid shape is visible only as a rim, with the centre dissolved/plucked out. The framboids sit within a dark area, and not directly within the matrix. The dark area could be pore space, suggesting the framboids have diminished in size. An alternative is that the framboids were positioned within now dissolved carbonate tests, or within dark organic matter. Measurements of equivalent circular diameter suggest that pyrite with Fe oxy(hydr)oxide rims do have a smaller ECD (average 1.8 µm SD 0.6) than 'pristine' framboids (average 2.7 µm SD 1.9), providing evidence that the framboid size has been diminished by a dissolution process.

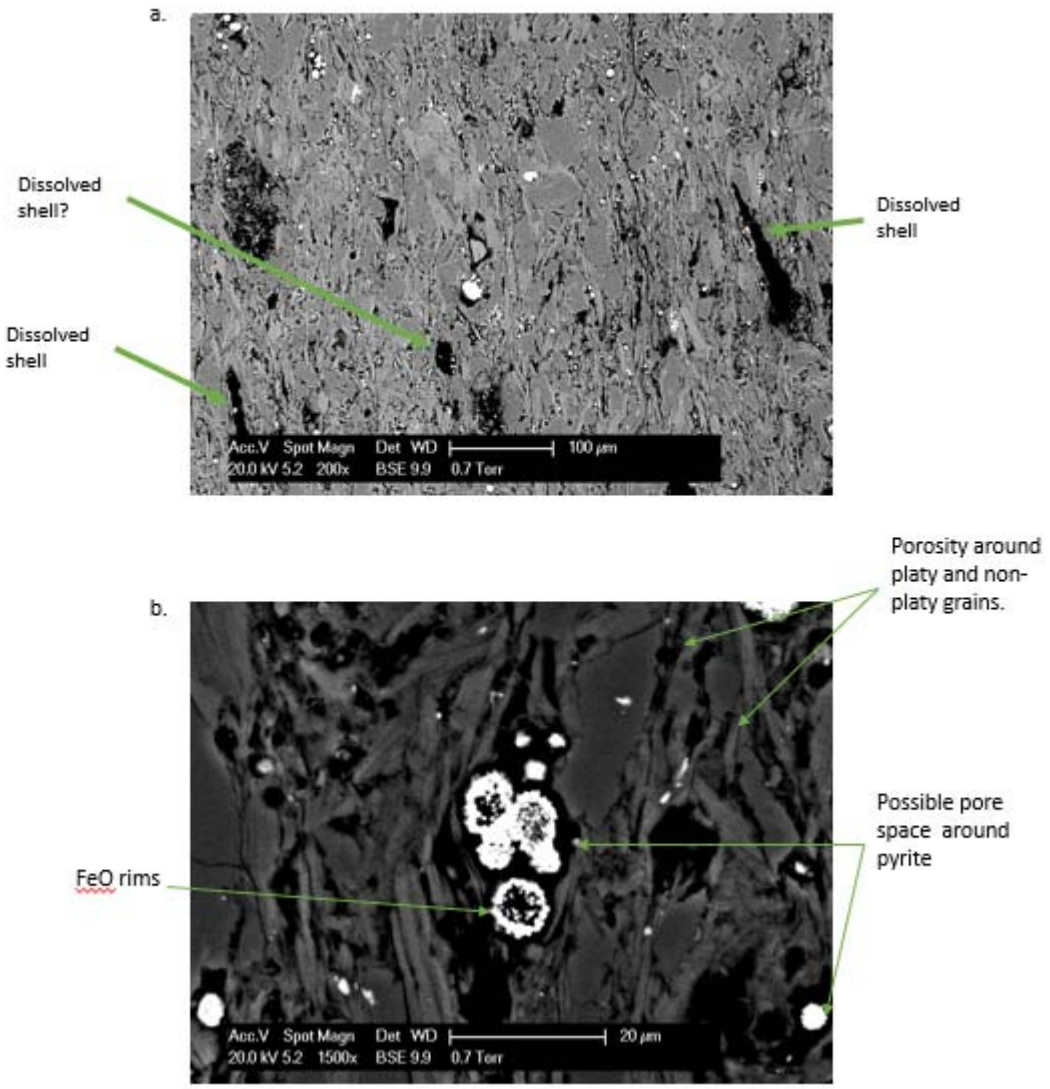

Figure 5.6 SEM BSE image of thin section from Algodones (519.5 m). In a. dissolved tests/shells are visible. These are assumed dissolved and not plucked out because the bulk sample has no IC detectable by bulk geochemistry. b. framboids composed of FeO with centres plucked out/ dissolved. The 'framboids' are present within a black area, which could be porosity caused by a diminished 'framboid' diameter, by the dissolution of a carbonate test/shell originally surrounding the pyrite, or it could be organic matter.

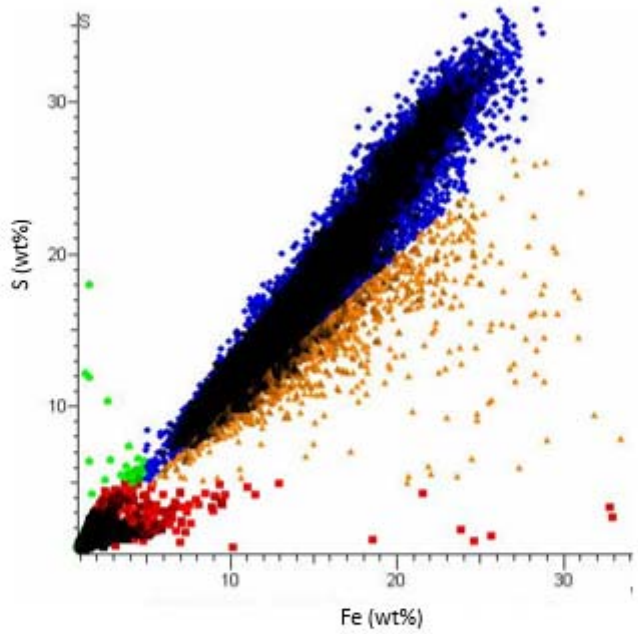

	'pristine' pyrite	sulphur depleted pyrite	Fe oxy(hydr)oxides
Number	16104	1338	1348
Proportion	0.86	0.07	0.07

Figure 5.7 Algodones (519.5 m) analysed by SEM- EDX particle analysis in INCAFeature. Fe and S contents of all Fe containing particles. Red particles are FeO (less than 5% S). Green particles not considered pyrite or FeO (greater than 5% Fe <5%S). Blue particles are considered 'pristine' particles (Fe:S<1). Orange particles are considered sulphur depleted pyrite (Fe:S>1). Table summarises particle numbers.

La Cristalina 1

The La Cristalina 1 (LC1) section was exposed along a roadside, is assigned to visual alteration group 2, and carbonate group 5. The lithofacies interpretation provided by Georex suggests an outer continental slope with carbonates (Table 3.2). Geochemistry of the bulk sample is enriched in paleo productivity proxies Ba, Cu, Ni and Zn and redox proxies Cr, Mo, V and U compared to average shale (Table 5.8). Euxinia cannot be confirmed, as Mo content is below 100 mg/kg (71 mg/kg), but when normalised to Al is higher than average shale, and so it is likely that the water column was anoxic (Scott and Lyons, 2012). Iron speciation analysis identifies anoxic waters (Fe_{HR}/Fe_T 0.70), the majority of Fe_{HR} is pyrite, Fe_{PY}/Fe_{HR} 0.67 (Table 5.7). In the thin section, it is difficult to identify if grains are well aligned (i.e. not affected by the action of bioturbation) due to the very fine clay matrix. Faecal pellets, the occasional detrital grain and shells did appear relatively well aligned. There was no bioturbation observed at outcrop and beds/laminae here are noted as planar. The sedimentary evidence therefore also supports anoxia.

Evidence for carbonate dissolution (in the form of large pores) is minimal within this sample. Also, given the high $CaCO_3$ content of the bulk sample, it is possible that some of this minor porosity is due to plucking out of tests/shells during sample preparation. In most cases, tests are intact and filled with calcite. There are some dark areas within shells, which may be dissolved calcite or organic matter. Pyrite is in the form of small and dispersed framboids, or larger and irregularly shaped within the tests (Figure 5.8).

Automated particle analysis identified pristine (31 % of Fe particles), sulphur depleted (18 % of Fe particles) and Fe oxy(hydr)oxide (50 % of Fe particles) particles (Figure 5.9). Many of the Fe oxy(hydr)oxides do not have a framboid morphology, they are amorphous and associated with carbonate rich areas of the sample. A greater proportion of the sulphur depleted particles has a framboid shape (32 out of 50 particles checked), and these particles are likely pyrite framboids with Fe oxy(hydr)oxide rims. Sulphur depleted framboids have an average ECD of 4.0 µm (SD 3.1), pristine framboids have a diameter of 4.4 (SD 3.8). Both of these values indicate an anoxic water column (<6µm) as defined by Wilkes et al. (1996), however, the standard deviations are large, casting some uncertainty on this assumption.

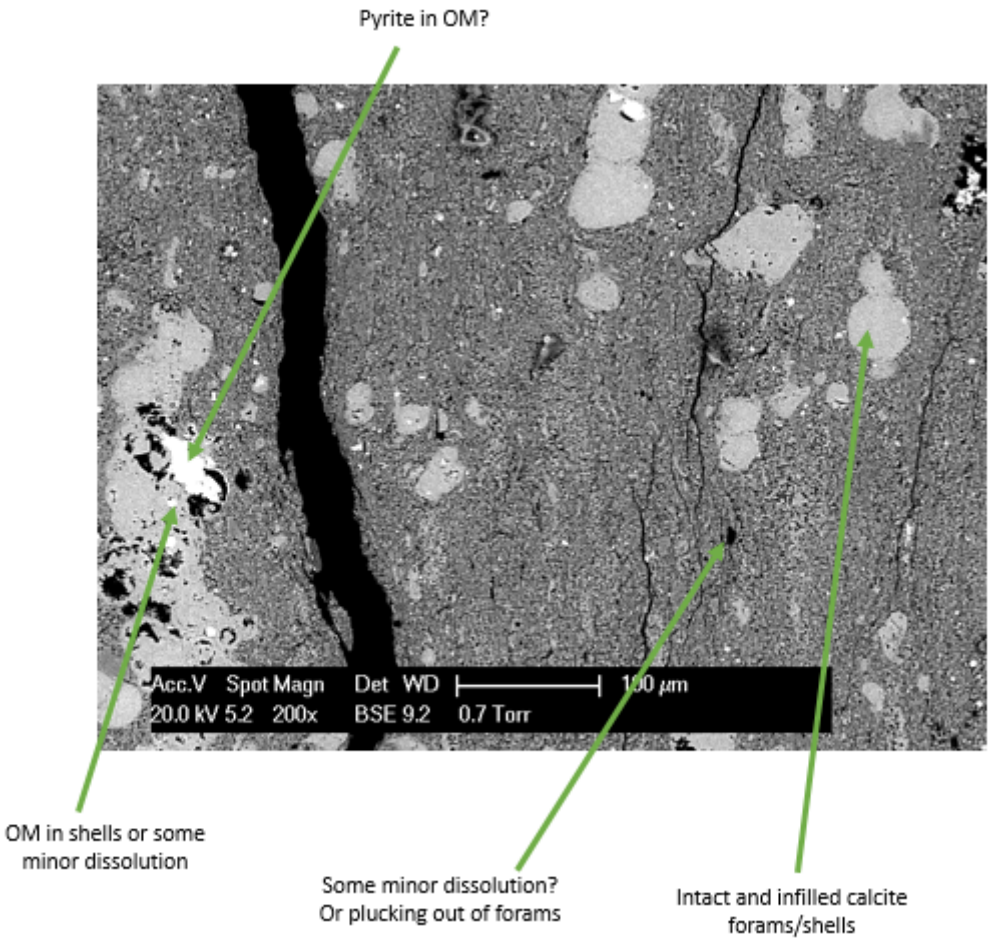

Figure 5.8 SEM BSE image of a thin section from La Cristalina (336 m). Sample with relatively high $CaCO_3$. Much less porosity in this sample compared to other the thin section from Algodones or Crucero, which could suggest less carbonate dissolution/pyrite oxidation. Pyrite is visible, both within shells and dispersed.

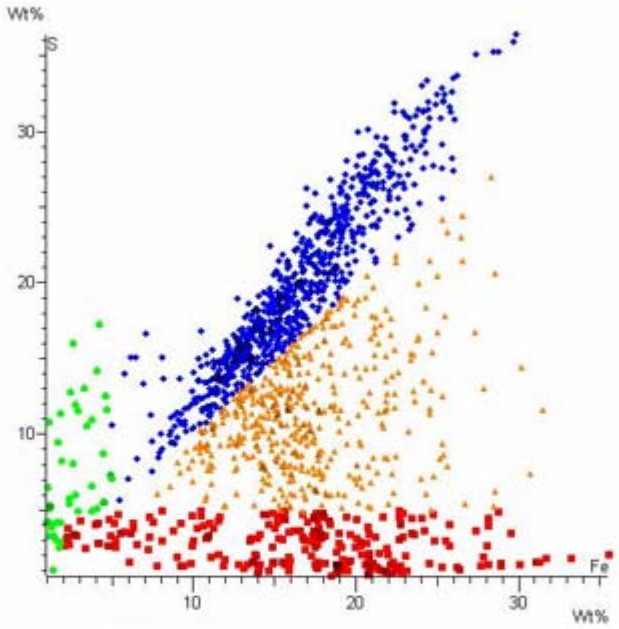

	'pristine' pyrite	sulphur depleted pyrite	Fe oxy(hydr)oxides
Number	746	436	1202
Proportion	0.31	0.18	0.50

Figure 5.9 La Cristalina (336 m) analysed by SEM EDX particle analysis in INCAFeature. Fe and S contents of all Fe containing particles. Red particles are FeO (less than 5% S). Green particles not considered pyrite or FeO (greater than 5% Fe <5%S). Blue particles are considered 'pristine' particles (Fe:S<1). Orange particles are considered sulphur depleted pyrite (Fe:S>1).

Crucero

The sample from Crucero (79 m) was taken from a road cutting, was assigned to visual alteration group 2 (light brown colour on the surface of the sample) and carbonate group 0. There is no $CaCO_3$ detected in the bulk sample, nor in other Crucero samples, and no carbonate lithologies were observed at outcrop in this section. No pyrite was detected in the bulk sample, and Fe exists mainly as poorly reactive or unreactive sheet silicates (Fe_{HR}/Fe_T is 0.14) (Table 5.7). No Al normalised redox-sensitive TE are present at contents above average shale (Table 5.8). Both redox proxies, therefore, indicate oxic depositional conditions. Sedimentology shows relatively well-aligned grains, which could be indicative of low oxygen conditions.

Figure 5.10a shows bimodal pore size distribution. There are a small number of large pores (10-30 µm) which could be a combination of dissolved shells/tests (Figure 5.10.c), or dark areas showing organic matter. There are many small (< 5 µm) spherical pores in this sample which, due to their small size, are unlikely to be shells/tests and may be the locations of

oxidised pyrite. In some locations, it appears that the clay matrix surrounding these small pores has been altered (Figure 5.10b), however, there is no notable difference in chemistry (this may be an effect of the EDX, which is not entirely quantitative and less effective at very small scales). Automated particle analysis (Figure 5.11) confirms low pyrite content in the bulk sample, with very few particles noted. There are more Fe oxy(hydr)oxides, however, none of these particles have framboidal morphology. The average ECD of the few pristine particles noted is 3.7 µm (SD 0.7). The sulphur depleted particle has a diameter of 4.1 µm.

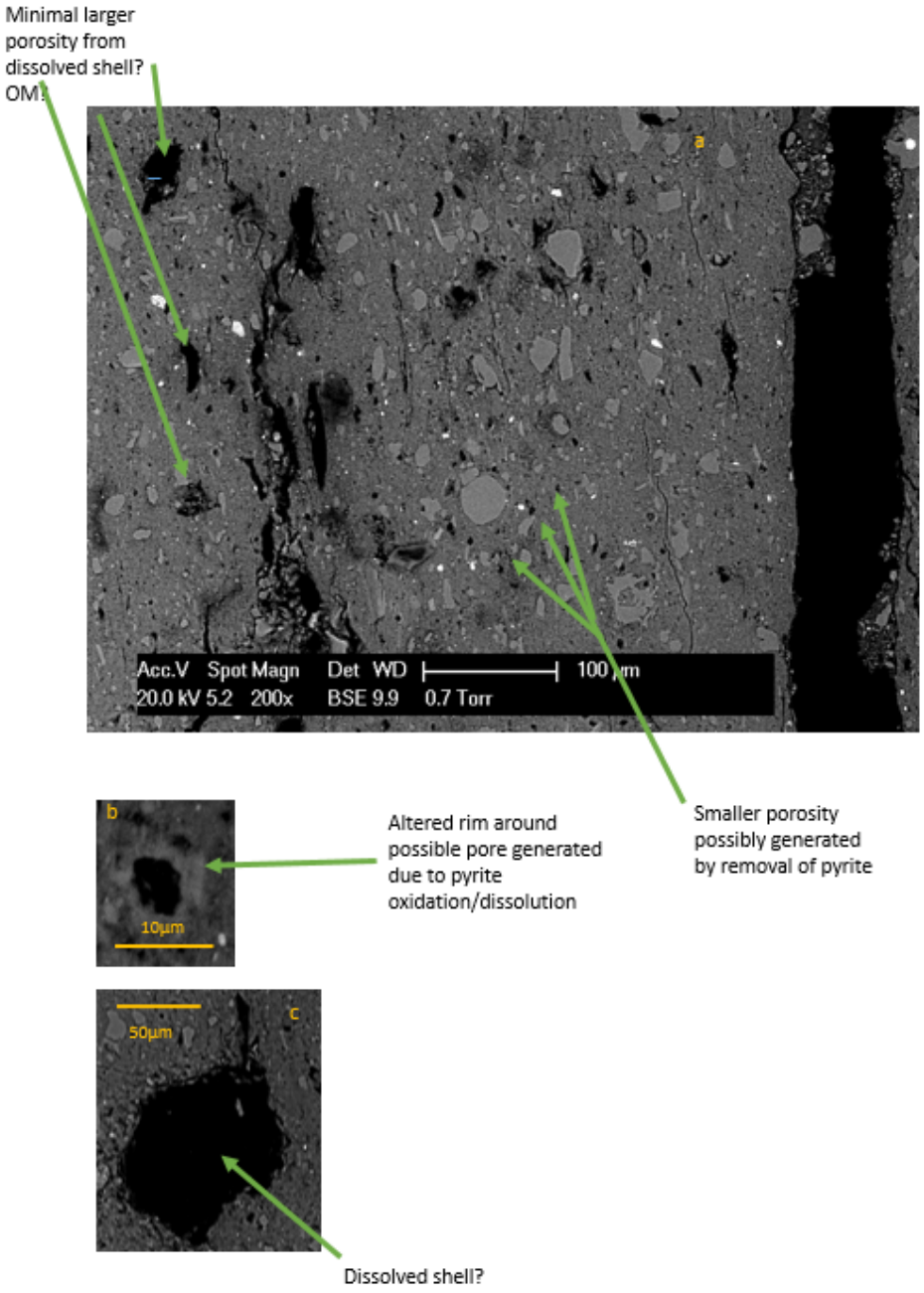

Figure 5.10 SEM BSE image from a Sample from Crucero, 79 m. A. Very little pyrite visible. Quite a bit of porosity which may have been carbonate (c). Some smaller spherical porosity may have been pyrite. B Some porosity has altered rims, although there is no detectable difference in the geochemistry. Grains are relatively well aligned, and in a larger view (not shown), planar lamination is visible

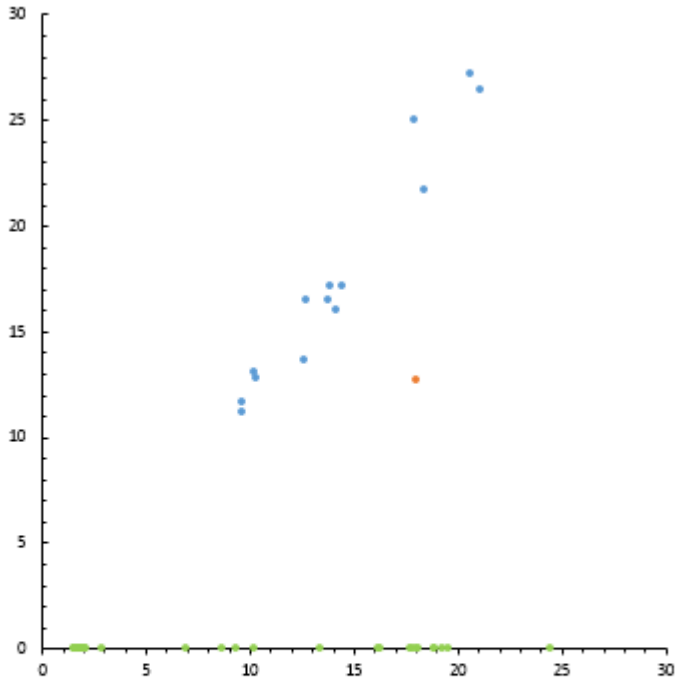

	'pristine' pyrite	sulphur depleted pyrite	Fe oxy(hydr)oxides
Number	15	1	31
Proportion	0.32	0.02	0.66

Figure 5.11 Crucero (79 m) analysed by SEM EDX particle analysis in INCAFeature. Fe and S contents of all Fe containing particles. Blue particles are considered 'pristine' particles (Fe:S <1). Orange particles are considered sulphur depleted pyrite (Fe:S>1).

Zipa

The Zipa sample is again taken from a road cutting. It has been assigned to the level 3 visual alteration group, as the light brown colour (presumed to be a pyrite oxidation product) on the outside of the sample also penetrates into the sample along planar parallel laminae (Figure 5.12a). The bulk sample contains no $CaCO_3$ and so was assigned to $CaCO_3$ group 0. It is enriched in redox and productivity TE compared to average shale (Table 5.8), suggesting deposition in an anoxic, high productivity setting. Iron speciation also suggests deposition in an anoxic environment (Fe_{HR}/Fe_T is 0.77), however, no pyrite is present. Mo contents (10 mg/kg) suggest any sulphide is limited to the pore waters. Continuous planar parallel features visible in thin section and in the unprepared sample and layers of higher porosity (light brown coloured layers, Figure 5.12b) imply a lack of bioturbation, supporting the view the sample was deposited in an anoxic environment.

There are many large (> 50 µm) irregular shaped pores in the Zipa sample, but also smaller

(<10 µm) pores (Figure 5.12d). Larger pores are likely dissolved carbonate tests and are concentrated in laminae which occur approximately every 0.5 mm. Element mapping indicates that Fe is concentrated in some of these layers (Figure 5.12c), and it is probable that they are the light brown layers seen in hand specimen with the Fe being present as brown Fe oxy(hydr)oxides (Fe_{OX1} or Fe_{OX2} as seen in Fe speciation). Smaller pores are potentially the remains of oxidised pyrite framboids. Very little pyrite is noted in automated particle analysis (Figure 5.13) as well as in the bulk geochemistry (Table 5.7), however, it is probable that pyrite was initially present, given the evidence for low oxygen depositional conditions.

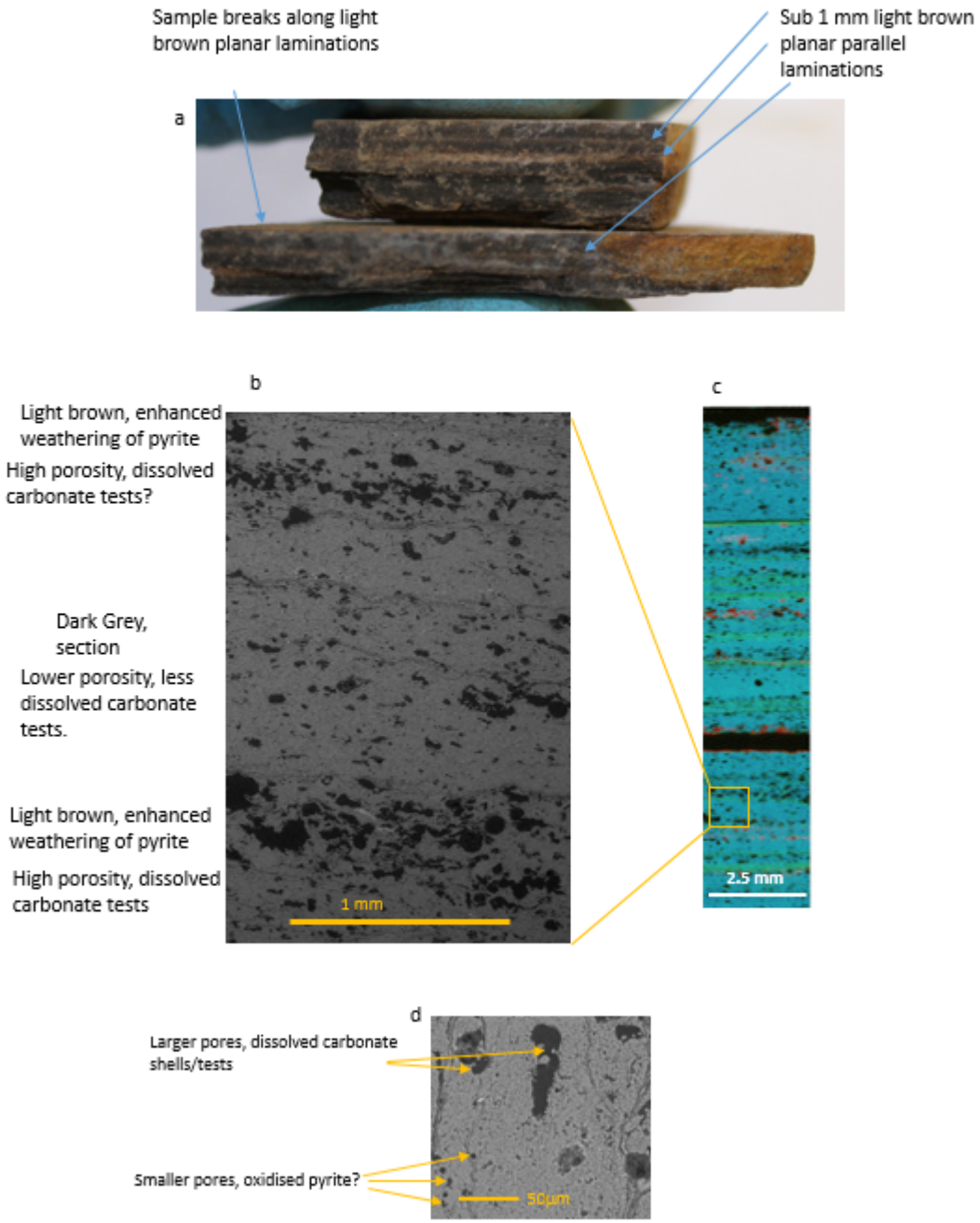

Figure 5.12 Zipa 74.5 m in hand specimen (a) and thin section (imaged using BSE SEM, b and d). Image c. SEM EDX elemental mapping (Blue is Si, green Al, red is Fe, S is yellow, Ti is white). Parallel sub-mm light brown laminations visible in hand specimen, on a smaller scale these laminations appear to be layers of higher porosity, likely to the dissolution carbonate tests/shells. Elemental mapping shows concentrations of Fe sometimes associated with more porous layers and S not associated Fe. This might be because pyrite previously deposited has been oxidised. As well as this large porosity, there are also many smaller pores, which could be oxidised pyrite (d)

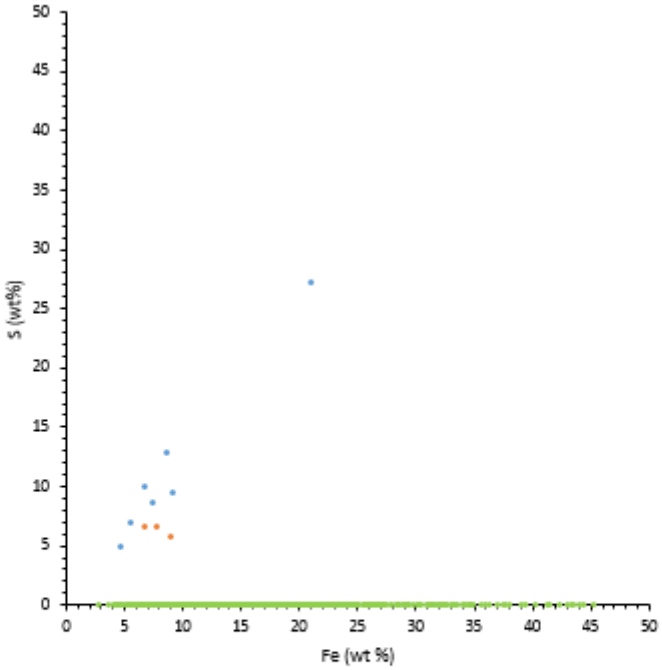

	'pristine' pyrite	sulphur depleted pyrite	Fe oxy(hydr)oxides
Number	6	3	1330
Proportion	0.004	0.002	0.993

Figure 5.13 Zipa 74.5 m analysed by SEM EDX particle analysis in INCAFeature. Fe and S contents of all Fe containing particles. Blue particles are considered 'pristine' particles (Fe:S<1). Orange particles are considered sulphur depleted pyrite (Fe:S>1). Green particles are Fe Containing but with less than 5% S.

5.4 Discussion

Grouping samples according to $CaCO_3$ content presented the most consistent differences between samples. After a statistical analysis, it is apparent that samples with no $CaCO_3$ have significantly lower Fe_{carb}, Fe_{mag}, Fe_{HR}/Fe_T, Fe_{Py}/Fe_{HR} and Fe/Al, P/Al and TE/Al than samples with greater than 10 wt% $CaCO_3$ (Table 5.6). Samples with low but detectable $CaCO_3$ content (<1 wt% and <5 wt%), also have statistically lower TE/Al than higher than 10 wt% $CaCO_3$ samples, but not statistically lower Fe species. The higher content of TE and Fe in samples with higher $CaCO_3$ is initially surprising, given that carbonate is considered to have a diluting effect on these elements (Poulton et al, 2015; Clarkson et al., 2015). As discussed in section 5.2.1, some TE (Ni, Cu and Zn) may be expected to increase with higher $CaCO_3$ in high productivity settings, and higher productivity settings can lead to anoxia, allowing the accumulation of redox sensitive TE and Fe. However, SEM data provide some evidence indepentdent from depositional environment that $CaCO_3$ influences the extent of weathering independent. A sample from the high $CaCO_3$ group (LC1 336 m) imaged with

SEM-BSE shows the lowest degree of carbonate dissolution out of the four samples displayed here (Figure 5.8), but a significant proportion of Fe-containing particles measured in automated particle analysis (18 %) are sulphur depleted pyrite, suggesting pyrite oxidation is occurring. Contents of Al normalised TE remain high (Table 5.8), suggesting there has been little TE leaching. Together, this information supports the conclusions presented in Chapter 4, whereby carbonate within a sample buffers pyrite oxidation, thereby minimising pyrite and TE loss. We, therefore, suggest that samples with > 5 wt% $CaCO_3$ have a greater capacity to buffer acid generated during pyrite oxidation and limit TE loss, and such samples are therefore more reliable for the interpretation of geochemical proxies. This value of 5% $CaCO_3$ is the same as independently suggested by Kraal et al. (2009) as the threshold carbonate content below which significant pyrite oxidation and apatite dissolution occurred in Cretaceous black shale samples.

In Chapter 4, it is suggested that the Fe oxy(hydr)oxides formed when pyrite oxidises in a high pH environment can quantitatively adsorb TE released by pyrite oxidation, either by adsorption or co-precipitation. In this scenario, pyrite should be diminished from a sample while TE contents should remain high. An example for this is shown by the Zipa sample (74.5 m), where it appears that it has experienced much carbonate dissolution, but TE contents remain high, whilst all pyrite has been oxidised (Table 5.7). The statistical approach described above suggests that TE loss occurs at a higher pore water pH (when $CaCO_3$ content is above 5 wt%) than the loss of pyrite and other Fe species (only statistically lower contents in the 0 wt% $CaCO_3$). This suggests that the TE are not dominantly hosted within the pyrite, but another rock component. Some TE also form sulphides separately (Cu, Ni, and Zn, Huerta-Diaz and Morse, 1992; Morse and Luther, 1999), and these may be more susceptible to oxidation at higher pH, however, none-sulphide forming TEs (U and V) behave similarly (Table 5.6). It is also possible that some TE (Mo, V, Ni) are associated with the OM component (Tribovillard et al., 2004; Brett and Wanty 1991; Lewen et al., 1984). Previous studies and the results presented in Chapter 4 suggest that pyrite successfully competes with OM for available oxidants during weathering (Clayton and Swetland, 1978; Petsch, 2000), and so this scenario is unlikely. In conclusion, the disparity between TE depletion and pyrite oxidation in most of the studied samples warrants further investigation.

Visual alteration of hand specimens was not a useful indicator of weathering type effects on TE contents within samples, with no statistical differences in TE contents between visually

very strongly visually altered samples and visually 'pristine' samples (Figure 5.4i-r). On the other hand, Fe_{carb} and pyrite are higher in samples with alteration limited to surface colour changes compared to samples with weathering penetrating into the sample (Figure 5.4a and e). This again indicates that pyrite oxidation (and Fe_{carb} dissolution) is more sensitive to weathering than TE. Also, P/Al was statistically higher in visually unaltered samples and became statistically lower with increasing visual extent of weathering, which could suggest that P was directly involved with the extent of colour change. Kraal et al. (2009) shows that as a result of pyrite oxidation, P can become bound to Fe, which may limit the expression of the colour of the newly formed Fe oxy(hydr(oxides). One sample investigated in thin section by SEM-BSE (Zipa, 74.5 m) is categorised in visual weathering group 3 because the light brown colour attributed to pyrite oxidation products extends into the sample along planar parallel laminae. It appears that these layers are characterised by concentrations of pores generated by dissolution of carbonate tests. Once dissolved, this added porosity/permeability likely allowed further penetration of oxygen and water, accelerating the removal of carbonate and oxidation of pyrite. It is possible that this mechanism is at work in all samples in group 3, supported by low pyrite, Fe_{Py}/Fe_{HR} and $CaCO_3$ contents seen in Figures 5.4 e, g and r.

Samples taken from road cuttings have lower Fe/Al and highly reactive iron species, but higher Al normalised TE contents (Figures 5.3a-h). This could indicate that pyrite oxidation (and eventually removal of pyrite oxidation products and Fe) was occurring to a greater degree in samples taken from road cuttings compared to stream beds, and that TE were less affected. It is possible that TE were leached from the stream bed at a higher rate than pyrite (present in a higher content in stream samples) before erosion could take place, however, it is more likely in this case that the samples taken from streams had inherently lower TE content even in an unweathered state. Evidence to support this comes from depositional environments assigned to the different sections and samples by Georex (Table 3.2). The samples taken from streams were deposited in very proximal paleoenvironments (shoreface to middle platform) where redox and productivity related TE may not have accumulated. Given this likely inherent challenge with the data set, the outcrop type is not used as a method of filtering samples.

Magnetite might be a weathering product, with higher contents in low $CaCO_3$ samples (Table 5.6). Also, Fe_{OX2} is present in statistically higher quantities in samples with the highest degree

of visual alteration (Table 5. 4). Further investigation of these potential products of pyrite oxidation may provide an alternative weathering filter. It is also useful to note that sample groups identified as more s trongly weathered (visual alteration or low $CaCO_3$) do not have elevated Fe_{HR}/Fe_T ratios, suggesting that Fe is not being converted from poorly reactive Fe in sheet silicates to Fe_{HR} during weathering. Therefore, a high value of this proxy is not a result of weathering, but rather an original paleo depositional signature. This helps when geochemical redox proxies contradict each other in the samples. In the Algodones (519.5 m) sample, for example, Fe_{HR}/Fe_T is high, indicative of bottom water anoxia, and this is supported by sedimentological features of a low oxygen environment. In contrast, TE contents are low, indicative of oxic depositional conditions. Here, it is likely that TE was leached from the sample to some extent, but Fe_{HR}/Fe_T was preserved due to quantitative conversion of pyrite to other Fe_{HR} phases (mainly Fe (oxyhydr)oxides). Samples with a greater visual extent of weathering and with a lower $CaCO_3$ content did have statistically lower Fe_{PY}/Fe_{HR} ratios (Figures 5.4g and 5.4h, respectively), suggesting that this ratio is not reliable as a redox proxy in weathered samples. Given pyrite oxidation occurs to some extent, even when $CaCO_3$ is present, this proxy is unlikely to be reliable if there is a possibility the sample has been affected by weathering. Another Fe based proxy which may be unreliable is framboid diameter, with a diameter reduction even in a sample where carbonate buffering appears to be generating Fe (oxyhydr)oxide rims (Figures 5.7 and 5.9).

Caution is recommended when interpreting differences between groups of samples. One problem with the statistical approach described above is that the “no carbonate” group contains samples which likely originally did not contain any carbonate (e.g. Crucero, Figure 5.10) as well as samples where carbonate was present but has since dissolved (e.g. Zipa, Figure 5.12 and Algodones, Figure 5.6). Different weathering processes are likely to have occurred in these samples. SEM analysis can identify samples that likely contained carbonate prior to weathering, by the presence of appropriately sized and shaped pores. In one sample where there is evidence that carbonate was once present (Algodones, 519.5 m), pyrite is present (3.2 wt%) and there is also evidence for Fe (oxyhydr)oxide rims preserving some of the pyrite framboid cores (Figure 5.6b and 5.7). Another sample which has clear signs of carbonate dissolution (Zipa, 74.5 m) has very few preserved pyrite framboids even though Fe (oxyhydr)oxides are prevalent (Table 5.7 and Figure 5.13). TE content in this latter sample is also high, perhaps preserved due to adsorption to Fe (oxyhydr)oxides. In the sample with

little evidence of carbonate dissolution (Crucero), there is a reasonably low Fe content (1 wt%, EC average is 3.5 wt%) and the Fe exists mainly as poorly reactive or unreactive sheet silicates (Fe_{HR}/Fe_T is 0.14). In this sample, it is possible that pyrite existed (as evidenced by <10µm spherical porosity, Figure 5.10), was oxidised without the buffering effect of carbonate, and so the products of pyrite oxidation and TE were leached out of the sample almost entirely.

Another challenge of using statistics to evaluate the effect of weathering of different sample types is that the grouping of samples biases the result. In the outcrop type test, for example, sediments representing the most proximal paleo depositional conditions, where the primary signature for may have been higher Fe_{HR} and lower TE contents, occurred in stream outcrops. Therefore as well as comparing road and stream outcrops, original depositional settings of proximal versus distal were also being onserved. In distal settings, the primary signature may have been lower Fe_{HR} and higher TE contents, possibly overiding any leaching in TE due to weathering. . Unlike grouping by outcrop type, each carbonate group contains samples from different sections and representing varying paleo depositional environments and so varied primary geochemical signatures (Table 5.5). However, the high carbonate samples dominantly occur in the La Cristalina sections. In Chapters 7 and 8, evidence is presented that these samples are deposited under enhanced primary productivity and anoxic redox conditions, and so are likely to have primary signatures with higher contents of TE related to high productivity and anoxia. Also, although in these sections, $CaCO_3$ does not directly correlate with TE content for productivity (Figures 7.7 and 8.9) higher $CaCO_3$ is in general likely to be indicative of higher biogenic carbonate productivity. Higher calcium carbonate productivity can also be associated with anoxia, as microorganisms consume oxygen within the water column and sediment, further highlighting the possible original signature differences of these sections. An ideal sample set to explore the effects of weathering would include samples from exactly the same depositional environment that were exposed to different weathering conditions. This situation does not occur often in the natural environment, and is an inherent problem of weathering studies, as discussed in Chapter 4. Also, carrying out multiple comparisons carried out by this statistical testing increases the chance of a Type 1 error. The *p*-values are much lower than the 0.05 required for significance in each test (Table 5.1, 5.4 and 5.6), suggesting low probability of incorrectly rejecting a null hypothesis. However, future work should involve the use of a different type

of statistical test, like principal component analysis, or use additional statistics like a Bonferroni method to correct for this multiple comparison problem.

Another reason to be cautious with the use of a $CaCO_3$ filter based on wt% is the spatial distribution of $CaCO_3$. Figure 5.12 is an example of how $CaCO_3$ can be concentrated in laminae, which likely causes high pH pore fluids to be concentrated in this region as they dissolve. If carbonate and pyrite are separated by relatively impermeable clay, even when $CaCO_3$ content in the bulk sample is high, the mechanism of carbonate buffering does not necessarily limit pyrite oxidation. However, examination of representative samples by SEM (especially if automated particle analysis is available to identify sulphur depleted pyrite) or light microscopy could recognise if this was the case.

5.5 Conclusion

After interrogation of geochemical data using statistical analysis it appears that a filter is available to identify samples which are more likely to have had their geochemical inventory affected by contemporary weathering. A weathering filter based on $CaCO_3$ content identifies the most consistent differences (lower pyrite, Fe_{Py}/Fe_{HR}, Fe_{carb} and $CaCO_3$ as well as lower TE contents). Samples with lower than 5 wt% $CaCO_3$ are considered as more susceptible to weathering, and therefore less reliable for geochemical interpretation. The results of this study may be biased original enrichments in TE in the more distal LC sections, where CaCO3 productivity was at its highest (further discussed in Chapter 7 and 8). Also, without SEM analysis of additional samples, there is no scope to distinguish samples which initially had very little $CaCO_3$, and samples where $CaCO_3$ was present and has been dissolved during weathering (thereby stalling pyrite oxidation and, to some extent, TE loss). This $CaCO_3$ filter should therefore, be applied with caution. The absence of increased Fe_{HR}/Fe_T or TE in sample sets assumed to be more weathered (low $CaCO_3$ or more visually weathered) confirms that elevated TE contents cannot be explained by weathering. Therefore, if an additional source (e.g. hydrothermal fluids) can be ruled out, elevated contents compared to average shale can be interpreted as a genuine depositional signature. The Fe_{PY}/Fe_{HR} proxy for distinguishing between euxinic and ferruginous redox conditions and the pyrite framboid diameter proxy are unlikely to be reliable in any sample where the effect of weathering cannot be completely discounted.

Chapter 6 Macanal Formation – First Marine Deposition in the Eastern Cordillera of Colombia.

6.1 Research Highlights

- The CIA* measure of paleo chemical weathering suggests a stable climate throughout the Berriasian and Valanginian which is arid compared to the samples from later in the Cretaceous.
- There is a slight increase in indicators for runoff, and an increase in terrestrial vegetation reaching the sediments, suggesting a slight increase in humidity from the Berriasian to the Valanginian seen in other locations.
- Unlike at other locations, both the Berriasian and Valanginian sea floor was dominantly anoxic for the majority of the depositional period, likely due to the relatively restricted nature of the basin.

In this chapter, inorganic and sedimentological data and interpretation of the two sections of the Macanal formation are presented and discussed. These sections represent Berriasian and Valanginian sediments deposited in the early basin filling phase of the EC. The sediments document tidal plain (Algodones) to submarine fan (Quemado) deposits as summarised in Table 6.1 (based on information provided by Georex, 2015). In order to understand the results, first, a summary of what is known about the global climate during the depositional period is presented. Results of proxies for detrital material, paleo productivity and redox conditions are presented. When discussing the results, any changes in climate/basin conditions through time which can be elucidated are considered within the basin, and also in a global context.

6.2 Introduction

The Macanal formation was deposited during the Berriasian and the Valanginian (Bürgl, 1961; Ulloa Rodriguez, 1979; Etayo-Serna, 1985), a greenhouse period with relatively stable average SST up to 32°C (Littler et al., 2011) and sea levels up to 125 m higher than today (Haq, 2014). There is evidence that the early Berriasian was dominated by arid conditions, with a shift to increasingly humid conditions from the start of the Valanginian. This shift is expressed in the sedimentary record as an increase in terrestrial flux (Föllmi, 1995; van de Schootbrugge et al., 2003, Westermann, 2013), changes in vegetation (Kujau et al., 2013) and more intense paleo chemical weathering (strontium isotopes, McArthur et al., 2007; CIA and clay mineralogy changes, Morales, 2013) linked to an enhanced hydrological cycle. The arid conditions in the Berriasian coincided with anoxia in many parts of oceans (Adatte et al.,

1996; Mutterlose et al., 2003; Richiano, 2014; Grabowski, 2016). Föllmi (2012) and Cotillon and Rio (1984) postulated that this was due to decreased runoff and increased evaporation reducing ocean circulation, eventually leading to water column stratification. The humid conditions in the Valanginian may have provided nutrients for enhanced marine productivity (Westermann, 2013; Lipinski 2002; Follmi 1995), whereas the consequences of more arid conditions in the earlier Berriasian were lower paleo chemical weathering rates and nutrient fluxes to the world's oceans. The aforementioned studies are dominantly concentrated in the Tethys (Westermann 2013; van de Schootbrugge et al 2003; Kujau et al., 2013; Grabowski, 2016; McArthur et al., 2007) or at high latitudes (Mutterlose et al., 2003; Richiano, 2014; Lipinski 2002). A limited number of studies has been carried out in the Caribbean area (Mexico and Cuba) which was connected to the Proto North Atlantic in the Cretaceous (Adatte et al., 1996; Pszczółkowski and Myczyński, 2010). No studies of more restricted, flooded continental areas at the tropics similar to the EC exist, making this a pioneering study to enhance our understanding of paleoenvironmental conditions across the complete spectrum of Cretaceous marine environments.

During the Berriasian-Valanginian the study area was located approximately 5° south of the equator (Figure 2.5) at the western edge of the supercontinent Gondwana (Hay et al., 1999). Its location therefore provides the opportunity to investigate the change from arid Berriasian to humid Valanginian conditions in a tropical climate, and to study the effect of these climate changes on organic matter burial in a restricted basin. Deposition of marine sediments in Colombia was initially limited by faults to the Cundinamarca sub-basin in the south of the EC, before reaching the Cocuy and Tablazo sub-basins by the Valanginian. Therefore, the basin was relatively isolated, connected only to the Colombian Marginal Sea (Figure 2.4). The basin was also relatively narrow, with deposition in the northern portion limited to an area approximately 80 km wide in the Cocuy Basin and 40 km wide Tablazo-Magdalena sub basin (Figure 3.2). This depositional environment in close proximity to terrestrial sediment sources should make the EC more sensitive to climatic shifts from arid to humid conditions, expressed as changes in the volume and type of terrestrial supply.

There are two sampled sections which have been ascribed to the Lutitas de Macanal formation, namely Algodones and Quemado. They are located in close proximity to each other so likely represent similar, relatively proximal depositional locations within the paleo basin (see location Figure 3.1 and 3.2). Algodones deposits have been assigned to the

Berriasian to Valanginian, and Quemado contains sediments of Valanginian age as determined by Georex (2015). As discussed in Chapter 2, the sections have been interpreted as representing slope to distal delta environments. Both contain mass deposits of terrestrial material, in Quemado from a submarine delta, in Algodones from unstable sediment piles and turbidites. The lithological columns show mudrock interspersed with sand beds (Appendix A). Bulk geochemical data show the fine grained sediments have average TOC contents of 1.0 % (SD 0.5) in Algodones (n= 210) and 2.3 % (SD 1.5) in Quemado (n=118), but some more extreme values are present (max 5.0 % in Algodones, 5.6 % in Quemado). The measured values of TOC are likely to be less than the initial contents, as the sections have been buried through the oil window, with T_{max} and vitrinite reflectance suggesting burial to around 300°C (See Chapter 3). For this reason, correlations with TOC is not discussed in this chapter.

Table 6.6.1. Summary of information about the Berriasian and Valanginian age sections covered in this chapter (provided by Georex, 2015).

Section	Age	Description	Paleo-water depth (m)	Facies interpretation
Algodones	Berriasian-Valanginian	Mudstone and siltstone with occasional bands of sand, which increase in number and thickness towards the top of the column. Fossils of ammonites, bivalves and plant remains.	20	Tidal plain, developing to pro-delta, submarine fan at the top of the column
Quemado	Valanginian	Mudstone and siltstone with thin beds of sandstone and siltstone, however, one section of 50 m is monotonous. Ammonite and bivalve impressions and plant remains observed.	60	Hemipelagic submarine fan developing into distal pro-delta

Table 6.2. Correlation coefficients calculated between elements in each of the Early Cretaceous sections. Correlations considered good if greater than 0.5 (marked as red) or less than -0.5 (marked as green)

		Quemado																								
		TOC	Si	Al	Fe	Ti	Mn	Mg	Ca	Na	K	P	Ba	Co	Cr	Cu	Mo	Ni	V	U	Zn	Zr	$CaCO_3$
Quemado	TOC		-0.46	0.32	0.11	-0.25	0.19	0.19	0.31	0.49	0.37	0.28	0.27	0.29	0.42	0.31	0.69	0.25	0.46	0.27	0.21	-0.28	-0.09
	Si	-0.46		-0.65	-0.76	0.66	-0.77	-0.50	-0.73	-0.68	-0.51	-0.84	-0.42	-0.74	-0.77	-0.83	-0.87	-0.87	-0.46	0.53	-0.80	0.61	-0.04
	Al	0.32	-0.65		0.23	-0.41	0.62	0.84	0.34	0.88	0.79	0.43	0.66	0.15	0.85	0.35	0.40	0.36	0.59	-0.45	0.28	-0.69	0.04
	Fe	0.11	-0.76	0.23		-0.47	0.34	0.06	0.32	-0.18	-0.51	0.17	-0.32	0.00	-0.29	-0.25	0.41	0.40	0.24	0.41	0.58	0.33	-0.05
	Ti	-0.25	0.66	-0.41	-0.47		-0.49	-0.62	0.24	-0.48	-0.57	-0.46	-0.59	-0.48	-0.62	-0.40	-0.46	-0.57	-0.53	0.51	-0.36	0.88	0.03
	Mn	0.19	-0.77	0.62	0.34	-0.49		0.84	0.32	0.88	0.79	0.43	0.66	0.15	0.85	0.35	0.40	0.36	0.59	-0.45	0.28	-0.69	0.04
	Mg	0.19	-0.50	0.84	0.06	-0.62	0.84		0.24	0.88	0.79	0.43	0.66	0.15	0.85	0.35	0.40	0.36	0.59	-0.45	0.28	-0.69	0.04
	Ca	0.31	-0.73	0.34	0.32	-0.18	0.24	0.24		0.88	0.79	0.43	0.66	0.15	0.85	0.35	0.40	0.36	0.59	-0.45	0.28	-0.69	0.04
	Na	0.49	-0.68	0.88	0.32	-0.18	0.24	0.24	0.24		0.79	0.43	0.66	0.15	0.85	0.35	0.40	0.36	0.59	-0.45	0.28	-0.69	0.04
	K	0.37	-0.51	0.79	0.32	-0.18	0.24	0.24	0.24	0.24		0.43	0.66	0.15	0.85	0.35	0.40	0.36	0.59	-0.45	0.28	-0.69	0.04
	P	0.28	-0.84	0.43	0.32	-0.18	0.24	0.24	0.24	0.24	0.24		0.66	0.15	0.85	0.35	0.40	0.36	0.59	-0.45	0.28	-0.69	0.04
	Ba	0.27	-0.42	0.66	0.32	-0.18	0.24	0.24	0.24	0.24	0.24	0.24		0.15	0.85	0.35	0.40	0.36	0.59	-0.45	0.28	-0.69	0.04
	Co	0.29	-0.74	0.15	0.32	-0.18	0.24	0.24	0.24	0.24	0.24	0.24	0.24		0.85	0.35	0.40	0.36	0.59	-0.45	0.28	-0.69	0.04
	Cr	0.42	-0.77	0.85	0.32	-0.18	0.24	0.24	0.24	0.24	0.24	0.24	0.24	0.24		0.35	0.40	0.36	0.59	-0.45	0.28	-0.69	0.04
	Cu	0.31	-0.83	0.35	0.32	-0.18	0.24	0.24	0.24	0.24	0.24	0.24	0.24	0.24	0.24		0.40	0.36	0.59	-0.45	0.28	-0.69	0.04
	Mo	0.69	-0.87	0.40	0.32	-0.18	0.24	0.24	0.24	0.24	0.24	0.24	0.24	0.24	0.24	0.24		0.36	0.59	-0.45	0.28	-0.69	0.04
	Ni	0.25	-0.87	0.36	0.32	-0.18	0.24	0.24	0.24	0.24	0.24	0.24	0.24	0.24	0.24	0.24	0.24		0.59	-0.45	0.28	-0.69	0.04
	V	0.46	-0.46	0.59	0.32	-0.18	0.24	0.24	0.24	0.24	0.24	0.24	0.24	0.24	0.24	0.24	0.24	0.24		0.41	0.58	0.33	-0.05
	U	0.27	0.53	-0.45	0.32	-0.18	0.24	0.24	0.24	0.24	0.24	0.24	0.24	0.24	0.24	0.24	0.24	0.24	0.24		0.58	0.33	-0.05
	Zn	0.21	-0.80	0.28	0.32	-0.18	0.24	0.24	0.24	0.24	0.24	0.24	0.24	0.24	0.24	0.24	0.24	0.24	0.24	0.24		0.33	-0.05
	Zr	-0.28	0.61	-0.69	0.32	-0.18	0.24	0.24	0.24	0.24	0.24	0.24	0.24	0.24	0.24	0.24	0.24	0.24	0.24	0.24	0.24		0.04
	$CaCO_3$	-0.09	-0.04	0.04	0.32	-0.18	0.24	0.24	0.24	0.24	0.24	0.24	0.24	0.24	0.24	0.24	0.24	0.24	0.24	0.24	0.24	0.24	
Algodones	Al		-0.59		-0.04	0.69	-0.23	0.44	-0.52	0.63	0.90	0.17	0.76	-0.01	0.91	0.14	0.12	-0.03	0.47	-0.35	-0.06	-0.79	-0.11
	Si	-0.59		-0.51	-0.63	-0.20	-0.49	-0.62	0.24	-0.48	-0.57	-0.46	-0.59	-0.48	-0.62	-0.40	-0.46	-0.57	-0.53	0.51	-0.36	0.88	0.03
	TOC	0.11	-0.51		0.35	-0.47	0.34	0.06	0.32	-0.18	-0.51	0.17	-0.32	0.00	-0.29	-0.25	0.41	0.40	0.24	0.41	0.58	0.33	-0.05

6.3 Results

Here, data are presented for the 34 samples from the Algodones and Quemado sections analysed by XRF, CNS/LECO and Fe-speciation and two samples analysed in thin sections by SEM. Firstly, correlations between elements are presented, in order to better understand which component of the sediment the elements are associated with and to allow for selection of appropriate paleoenvironmental proxies. Following this, trends in detrital input, intensity of paleo chemical weathering, productivity and redox conditions are explored. In order to test the hypothesis that the Berriasian climate was more arid compared to the Valanginian, samples from the two ages are compared.

6.3.1 Correlations between main components

As discussed in Chapter 3, a positive correlation between Al (mainly found within clay) suggests an association with detrital material, whereas a negative or no relation, could suggest an authigenic source or association with another sediment component which is diluted by fine detrital material source (correlation coefficients are recorded in Table 6.2, a good correlation is considered greater than 0.5 or less than -0.5). Both sections show a positive relationship of Al with Na and K which are major detrital elements (Figures 6.1a and 6.1b), but also with the proposed anoxia proxy Cr (which can be detrital if Chromite is present in the hinterland (Jones and Manning, 1994)) and the productivity proxy Ba (which can substitute for K in feldspars and micas (Puchelt, 1969)). In Quemado, there is also a positive correlation between Al and Mn, Mg and V, which suggests that these elements are also delivered to the basin within or adsorbed to the detrital component. Fe and P do not show a good positive relationship with Al (Figure 6.1c and 6.1d). Silica and Zr show a negative correlation with Al in both sections (Figure 6.1e and 6.1f)

Si and Zr correlate well with each other (correlation coefficient of 0.61 and 0.88 for Quemado and Algodones respectively, Figure 6.1g). As discussed in Chapter 3, this suggests that Si is dominantly within the coarse fraction, as quartz, and that Si/Al can be used to estimate the sand/silt fraction. As Si and Zr have negative relationships with Al, coarse material (containing quartz and zircon grains) is likely being diluted by fine, Al-rich clay. Uranium has a positive relationship with Si, which could suggest an association between U and the coarse fraction. Titanium has a positive relationship with Si in Quemado, suggesting the presence of detrital Ti (e.g. rutile or anatase), but has a positive relationship with Al in Algodones, indicating an association with the fine fraction. Apart from U and Zr (and Ti in Quemado), other elements in both sections negatively correlate with Si, suggesting a relatively pure quartz sand.

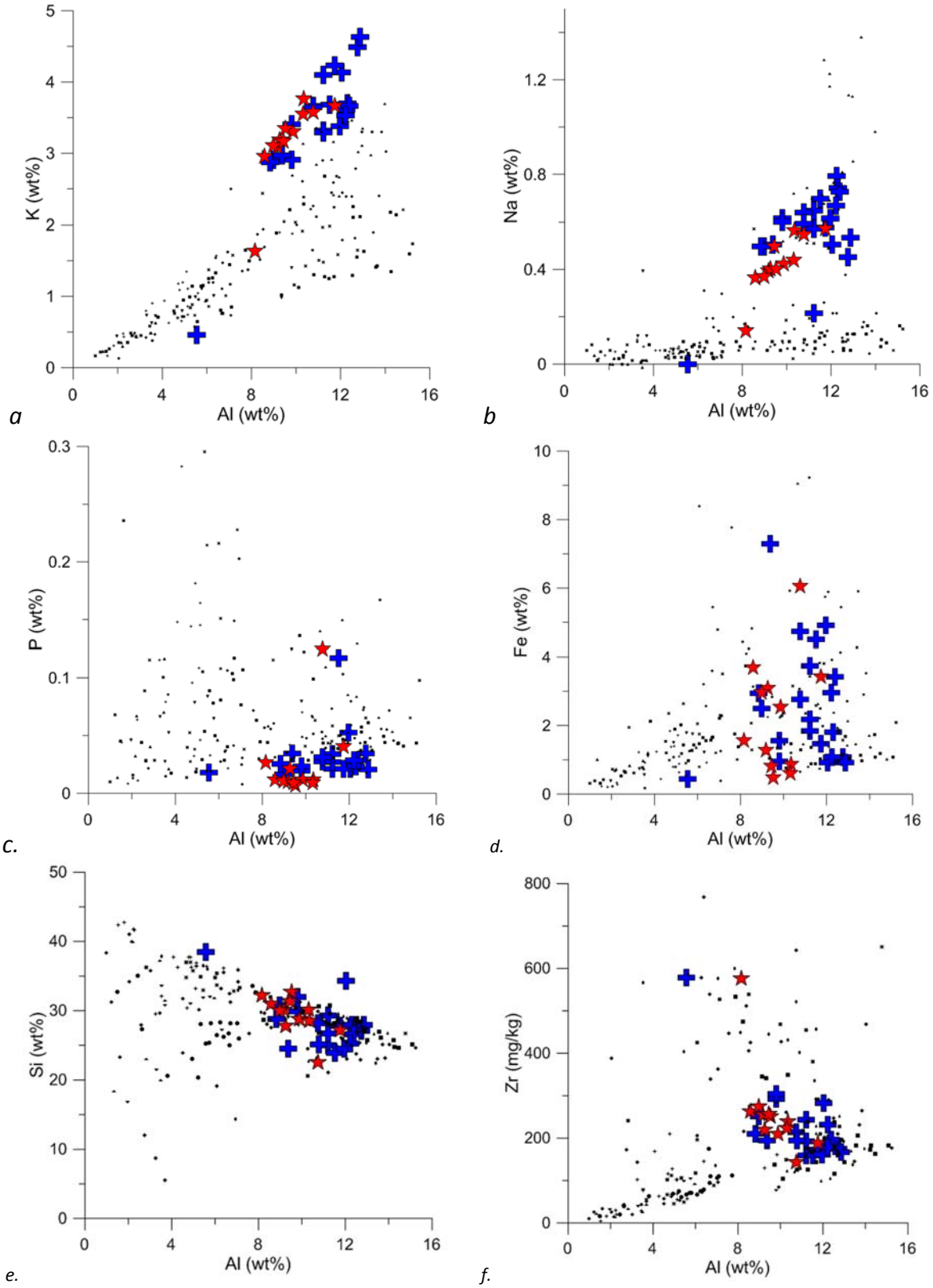

Figure 6.1a-g. Correlations of major and trace elements with Al. Macanal samples are Blue crosses (Algodones) and red stars (Quemado) with smaller data points are data from Chipaque and Fomeque sections.

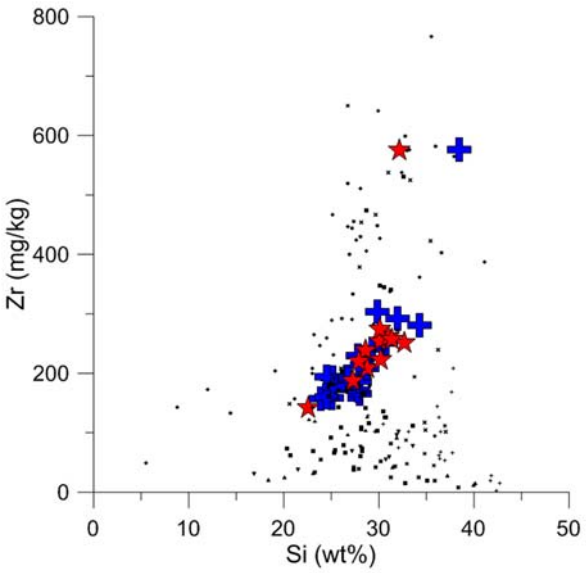

g. *Figure 6.1(continued)*

6.3.2 Main compositional components

Figure 6.2 shows that samples of Berriasian age have higher Al contents (average 11.3 wt% compared to 10.2 wt%), but similar Si contents (average 28.9 wt% compared to 28.4 wt%) to Valanginian sediments. This difference in Al was confirmed as statistically significant (p <0.5) using a Mann Whitney U test (p-0.06). The low Al and slightly higher Si content leads to higher calculated sand contents for the Valanginian (12.7 wt%) compared to the Berriasian sediments (average 11.9 wt%), however, this difference is not statistically significant. The Valanginian samples also have statistically higher levels of TOC (average 1.7 wt%) (p- <0.5) than Berriasian samples (average 0.9 wt%). Both sections have very low concentrations of $CaCO_3$. The Valanginian average (1.5 wt%) is higher than the Berriasian average (0.2 wt%), but the difference is not statistically significant, with the majority of samples of both ages less than 1 wt% $CaCO_3$.

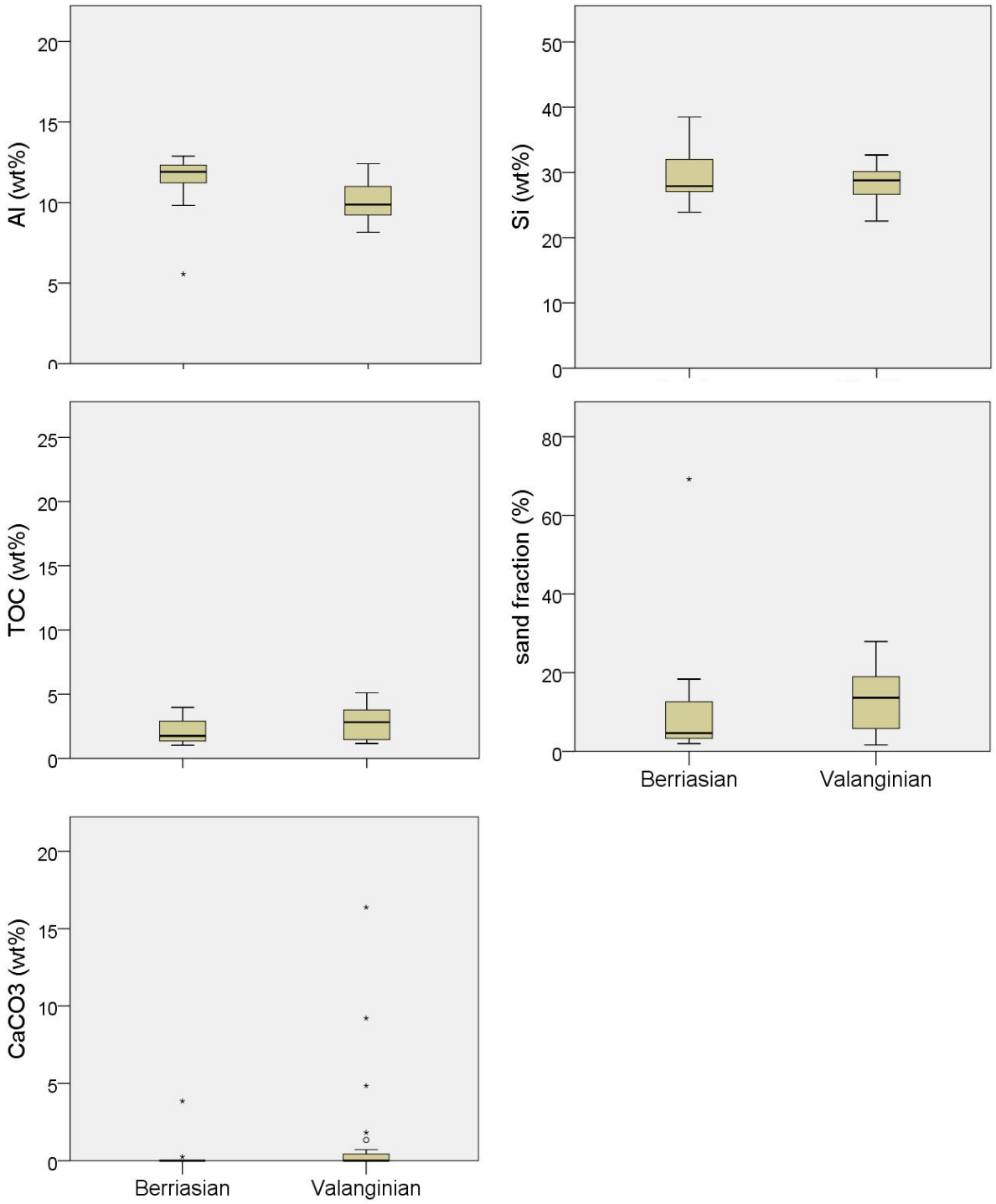

Figure 6.2 Box plots to display compositional differences between samples of Berriasian and Valanginian age. A statistically significant difference in Al and TOC between the Berriasian and Valanginian sediments was identified (p=0.06) using Mann-Whitney U test.

6.3.3 Detrital Proxies

Al contents remain relatively constant in both sections (average 11.0 wt%, SD 1.7 in Algodones, 9.7 wt% SD 1.0 in Quemado), as does Si (average 28.1 wt% SD 3.5 in Algodones, 29.4 wt% SD 2.7 in Quemado), Figure 6.3. Mean calculated sand content within the mudstone samples is 16% in Quemado (SD 7%) and 11% in Algodones (SD 14%). One sample has a lower Al at below 8 wt% (187m, Algodones), and this is matched with lower contents of elements presumably associated with the fine fraction (Ti, K, and Na). This sample also has higher contents of elements associated with the coarse fraction (Si and Zr) and the highest sand content within the Macanal samples (69%). The sample comes from an area of the section where there are repeated (approximately every metre) sandstone beds of around 20 cm thickness. Other samples with slightly higher Si and Zr (38 and 167 m) and lower Al in Algodones are also associated with sand beds. Samples towards the top of the section where beds are thicker (over one meter) do not have higher Si and calculated sand contents. Quemado, throughout most of the section, contains 0.5-1.0 m thick shale packages alternating with siltstone beds of similar thickness (with very fine sand laminae) and around 10 cm thick sand beds. In Quemado, there is a steady increase in calculated sand content (accompanied by a decrease in Al and increase in Si) from 30 .5 m (11.5 % sand) to 69 m (23 % sand) and again from 113.5 m (13.7 % sand) to 134.5 m (27.9 % sand). These are matched with decreases in elements associated with the fine fraction (K and Na). The sample at 134.5 m is particularly high in Ti/Al (0.10 compared to a section average of 0.07) and Zr/Al (70.6 compared to a section average of 27.6). In both instances, the changes in the amount of coarse material in the shales are not clearly coincident with an increase in coarse lithologies. Supporting the bulk geochemistry in Figure 6.2, Valanginian samples also have higher Zr/Al content than Berriasian samples (Figure 6.7).

Within the two thin sections analysed from these sampling sections (Quemado depth 14 m, Algodones 519.5 m), all the identified detrital grains were quartz, and all measured grains were silt sized (Figure 6.4 -6.6) corroborating field descriptions of silty mudstones.

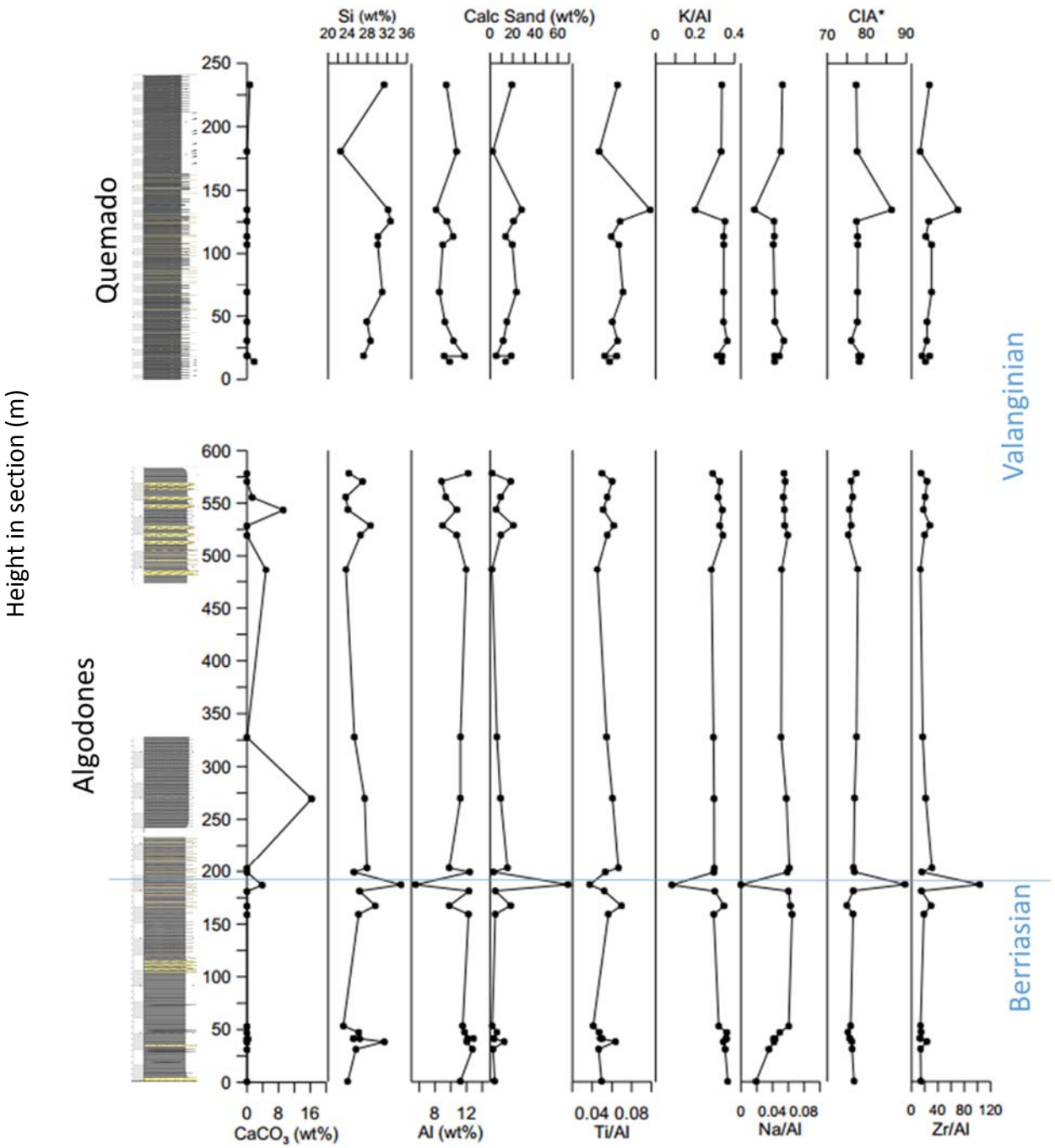

Figure 6.3 Detrital proxies and $CaCO_3$ with depth (m) for the Macanal Algodones and Quemado sections. Summary lithology and ages included from Georex reporting.

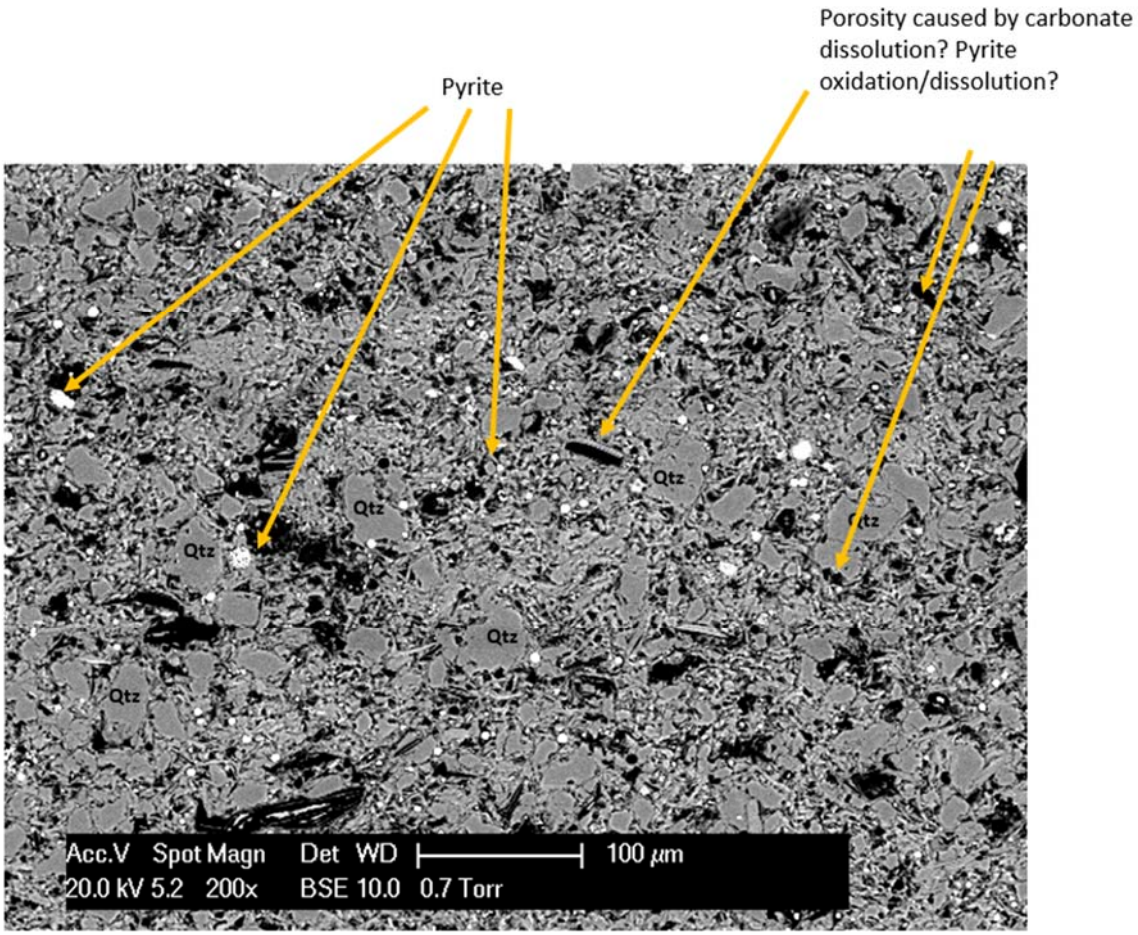

Figure 6.4 BSE-SEM image of Quemado sample (14 m) in thin section. Porosity and organic matter black. Chemical identification using EDX. Qtz, quartz. Note quartz grains appear to be detrital sub angular and some cracks present (note far right). Also note lack of grain alignment which may indicate bioturbation. Pyrite not associated with any particular lamination – distributed throughout, not consistently associated with any porosity (like shell outlines or organic matter lenses).

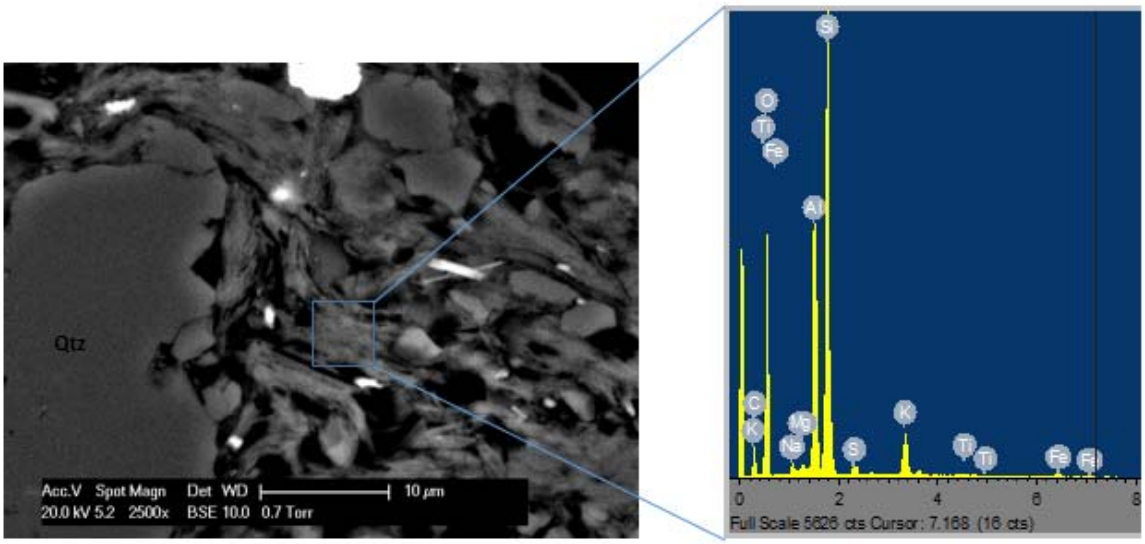

Figure 6.5 BSE-SEM image of Quemado sample (14 m) in thin section showing detail of detrital quartz grain and illite/mica (note K content). Illite/mica appears to be slumping around quartz grain, suggesting the clay is not diagenetic

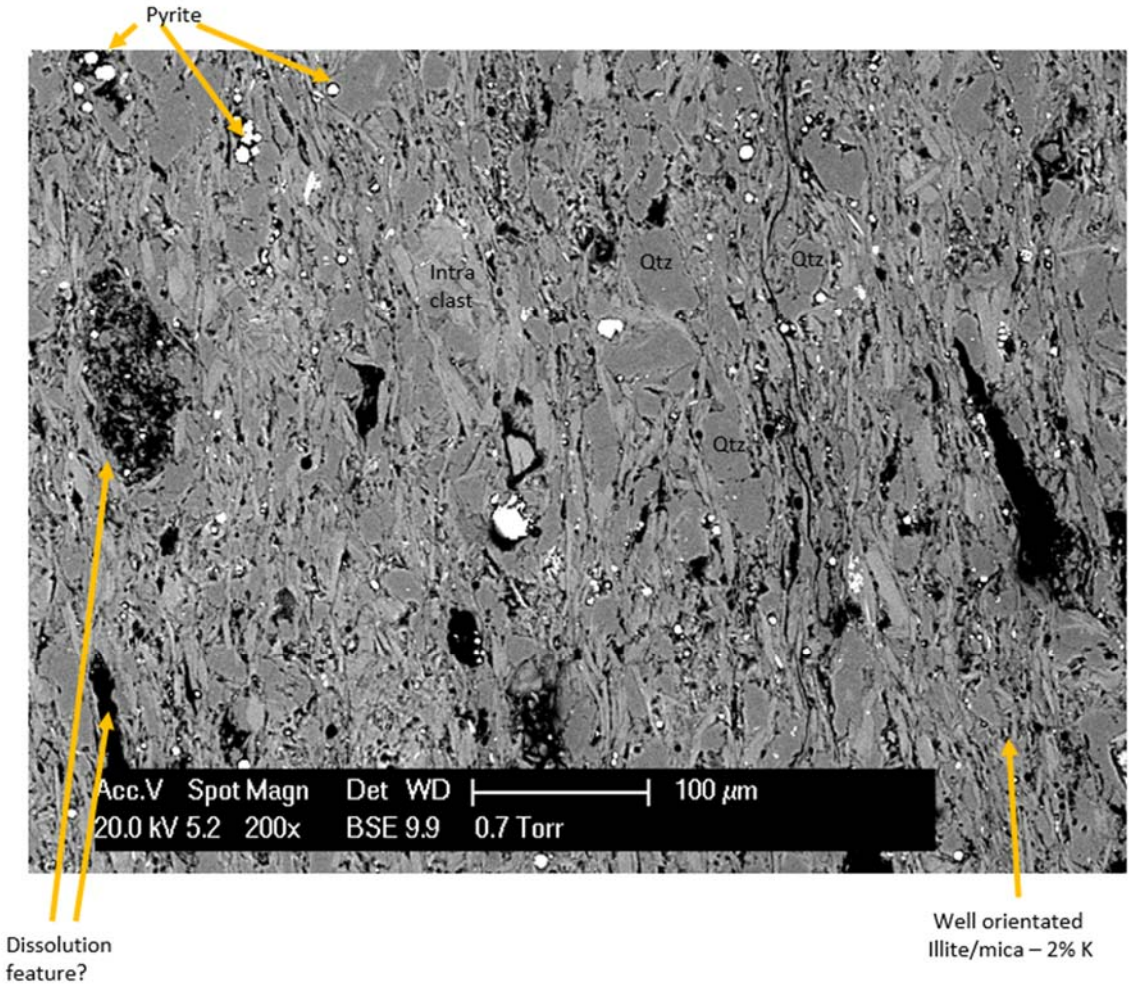

Figure 6.6 BSE-SEM image of Algodones sample from 519.5 m in thin section. Black is porosity or OM. Note dispersed pyrite and concentrated in distinct areas. Also note dissolution feature on the left, and the shell outline on the right, likely caused by dissolution due to contemporary weathering. Main component is relatively well aligned (laminated) illite/mica with silt sized quartz grains.

6.3.4 Paleo Chemical Weathering Intensity

As discussed in Chapter 3, when clays arriving at the basin are lower in K and Na, this is a signature of more intense paleo chemical weathering or a more weathered source of detrital material. In both sections, Na/Al and K/Al follow similar variations (Figure 6.3). There is a decrease at 187 m in Algodones (Na/Al zero compared to a section average of 0.05, and K/Al 0.08 compared to a section average of 0.37) linked to an increase in coarse, quartz material, whereas much of the rest of the sediment succession is relatively uniform. Similarly, a decrease in Quemado at 134.5 m (Na/Al 0.02 compared to a section average of 0.04, and K/Al 0.2 compared to a section average of 0.33) is linked to an increase in coarse material and a decrease in Al. However, in Algodones, there is a steady increase in Na/Al (from 0.02 to 0.06) in the first 53 m of the section which appears to be unrelated to other detrital proxies. The effect is that CIA* is relatively steady throughout the succession, with peaks in

Algodones (94.5 compared to a section average of 78.6) and Quemado (86.3 compared to section average of 78.3) linked to increases in the coarse fraction. From Figure 6.8 it appears that Berriasian age sediments have slightly lower Na/Al values and higher K/Al values, leading to slightly higher average CIA* values (mean value 79.0) compared to Valanginian samples (mean CIA* 78.2).

As can be seen from Figures 6.1a and 6.1b, the Macanal sections have higher Na and K contents than the rest of the studied Berriasian and Valanginian samples. High Na and K could suggest an ingression of hydrothermal fluids and related metasomatism. If this is the case, K and Na would not provide useful information about the intensity of paleo chemical weathering (Fedo et al., 1995), and another consequence is that some TE could have been leached from the shales (Beus, 1979). Sodium metasomatism has occurred in some regions of the EC, leading to emerald deposits (Beus, 1979; Cheilletz and Giuliani, 1996). Beus (1979) recommends using a low K/Na ratio to identify areas affected by this form of metamorphism. Values from Algodones and Quemado are above the 1.5 limit recommended by Beus for the identification of Na-metasomatised tectonic zones (Quemado average 7.5, Algodones 6.3), and so this measure does not identify significantly altered rocks. Also, on average, the studied samples do not have significantly higher K contents (average Quemado 3.2 wt%, Algodones 3.5 wt%) than unaltered shales in a database gathered by van de Kamp, 2016 (maximum 4 wt%) and average shale (3 wt%, Wedepohl, 1970, 1971). Five samples from the base of the Algodones section do have slightly higher K contents (4.1-4.6 wt%), which could suggest some minor alteration. The K/Rb ratio (an indicator for the circulation of hydrothermal fluids which are often Rb poor, van de Kamp, 2016) in the Macanal samples is very similar to other EC samples with lower K and Na contents (Figure 6.9), and the K/Rb is below the value of 200 which is common in unaltered mudstones (van de Kamp, 2016). The Macanal samples do have high quantities of illite (59-100 wt % of clay fraction, Table 6.3, Figures 6.4-6.6), which could suggest K-metasomatism or supply of material from a less weathered source/less intense paleo chemical weathering. In Figures 6.4-6.6, illite grains do look relatively well crystallised, which could be an indication that they are diagenetically formed (e.g. Bjølykke, 1998). Evidence that they may not be diagenetic comes from the fact that the crystals do not extend into pores as seen in Zhao et al. (2017) and Wurst et al. (2013) and also they appear to have slumped over detrital grains, suggesting they were in position early in the burial history (Figure 6.5).The identification of chlorite in three samples

using XRD is also an indicator of clay alteration (Hurst, 1984).

Fedo et al. (1995) offers a method of correcting for the addition of K during diagenesis using a ternary plot (Figure 6.10). Samples from the base of Algodones and seven samples from Quemado have a slightly higher corrected CIA (87) than the rest of the samples (corrected CIA, 85).

Table 6.3. XRD data for Quemado and Algodones sections, provided by Ecopetrol.

		> 2µm fraction (wt %)					**< 2µm fraction (wt%)**			
Outcrop	**Depth (m)**	**clay**	**sand**	**K feldspar**	**pyrite**	**other**	**illite**	**kaolinite**	**micro quartz**	**chlorite**
Quemado	18.5	60	25	< 5%	< 5%	< 5%	70	9	9	12
	107	52	33	< 5%	< 5%	< 5%	80	< 5%	10	< 5%
	134.5	38	52	< 5%	0	< 5%	100	0	0	8
	180.5	46	44	traces	5	< 5%	82	< 5%	< 5%	0
	233	50	40	< 5%	traces	< 5%	94	0	6	
Algodones	41	67	23	< 5%	0	< 5%	95	0	< 5%	0
	187	57	33	< 5%	0	< 5%	95	0	< 5%	0
	269.5	50	40	< 5%	traces	< 5%	95	0	< 5%	0
	519.5	65	20	< 5%	< 5%	< 5%	90	< 5%	< 5%	0
	555.5	86	9	traces	0	< 5%	59	25	0	16

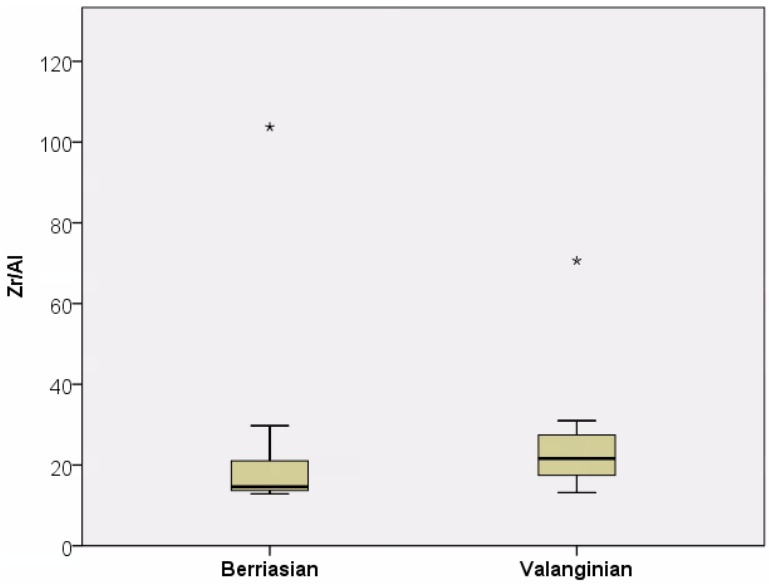

Figure 6.7 Box plot to display differences in coarse input from trace metal proxies between samples of Berriasian and Valanginian age.

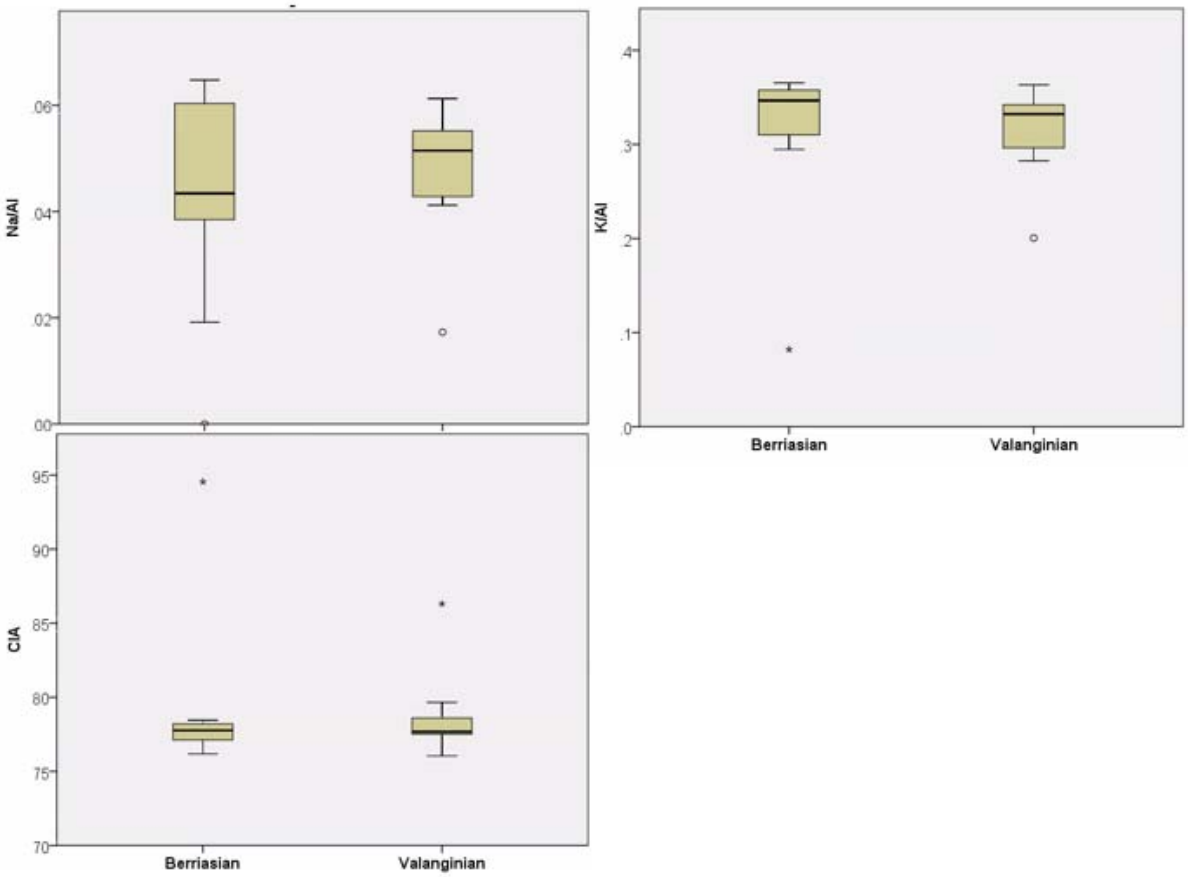

Figure 6.8 Box plots to display differences in paleo chemical weathering proxies between samples of Berriasian and Valanginian age.

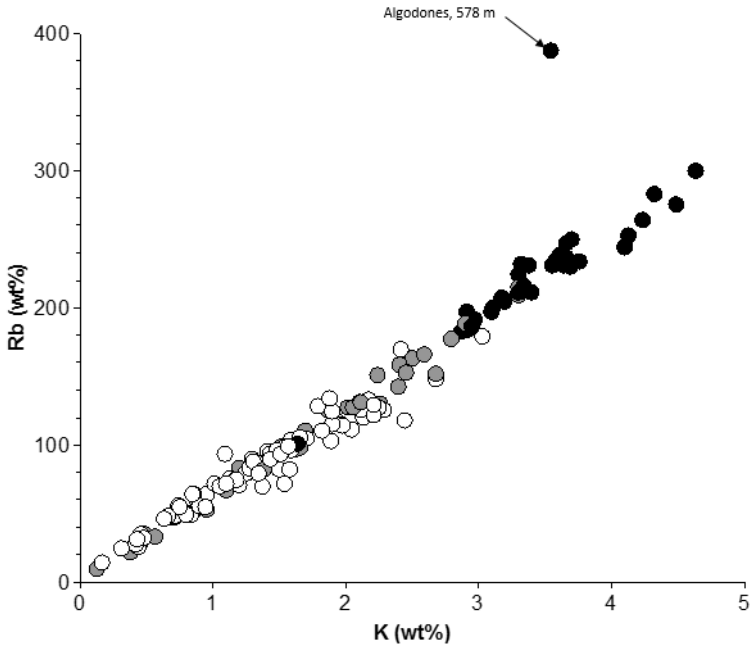

Figure 6.9 Correlation between K and Rb after van de Kamp (2016). Rubidium is normally depleted within hydrothermal fluids, so a higher ratio would be indicative of interaction with high K, low Rb hydrothermal solutions. One sample with higher ratios unlikely to be indicative of clay diagenesis, as this effect would have altered an entire area and in this case a sample from 8 m below is unaffected. No clear difference between Macanal samples (black) and Chipaque age (white) and Fomeque age samples (grey).

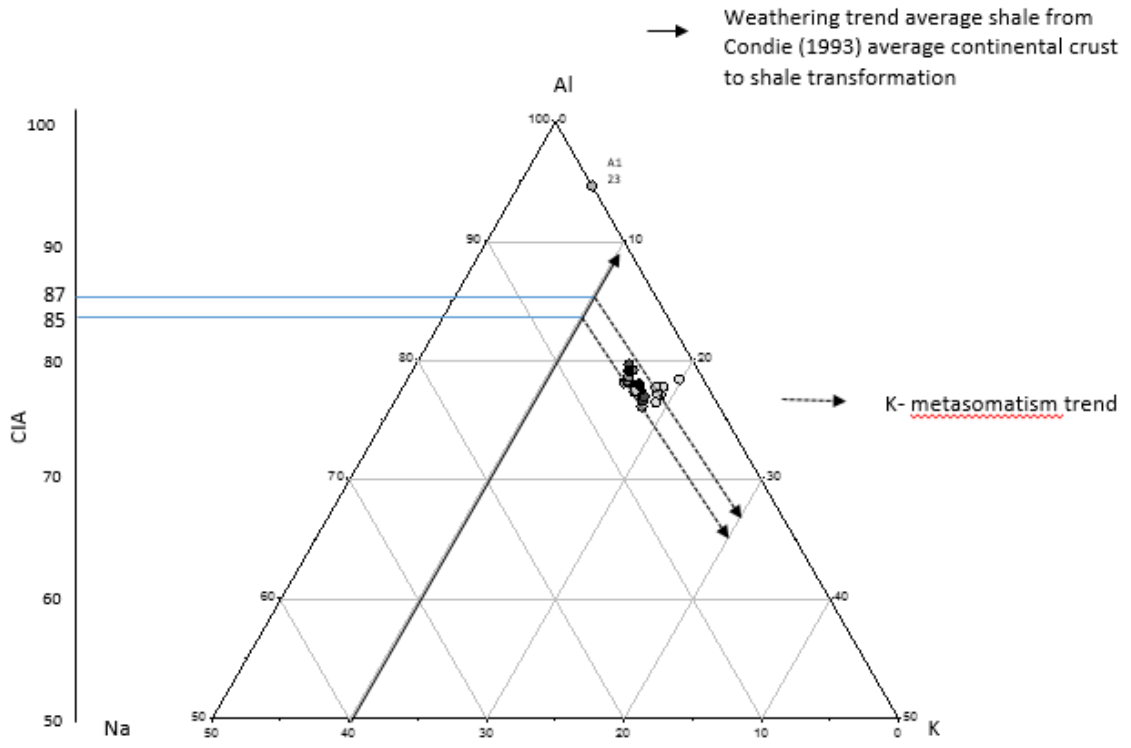

Figure 6.10 Ternary diagrams of Na, K and Al after Fedo (1995) to correct CIA for addition of K by metasomatism. Quemado has 7 samples around CIA 87 line, and some which sit closer to the CIA 85 line, rest of the samples appear to have slightly higher corrected CIA

6.3.5 Productivity

The Macanal samples are low in $CaCO_3$ which may indicate low calcareous productivity. There may have been higher $CaCO_3$ content before modern outcrop weathering, as there are pores visible in thin section likely derived from the dissolution of carbonate tests (Figure 6.4 and 6.6). As discussed, it appears that Si has a detrital source and so it is likely that any contribution by biogenic Si to the samples is also low. In both sections, there are intervals of elevated TOC. In Algodones, between 159-211 m, average TOC is 1.65 wt%, between 47.5-87.5 m average 1.31 wt% and between 483.5 m and the top of Algodones 1.72 wt%, compared to a section average of 0.97 wt%. In Quemado, between 170.5 m – 210 m average TOC is 3.50 wt%, between 86 m-120 m average is 2.67 wt%, between 0-16.5 m average is 2.61 wt% compared to section average 2.33 wt%).

As discussed in Chapters 4 and 5, contemporary weathering can affect TE proxies. As $CaCO_3$ appears to minimise the effects of weathering, Chapter 5 suggests using a 5% $CaCO_3$ as a filter for identifying samples less affected. Only two Macanal samples have higher than 5% $CaCO_3$, Algodones 269.5 m and 543.5 m. These samples have Al normalised TE contents of paleo productivity proxies below average shale (Figure 6.11). In fact, all samples have paleo productivity proxy contents below average shale apart from Algodones 486.5 m and 555.5 m and Quemado 180.5 m (Figure 6.11). These values are within areas of higher TOC mentioned in the previous paragraph.

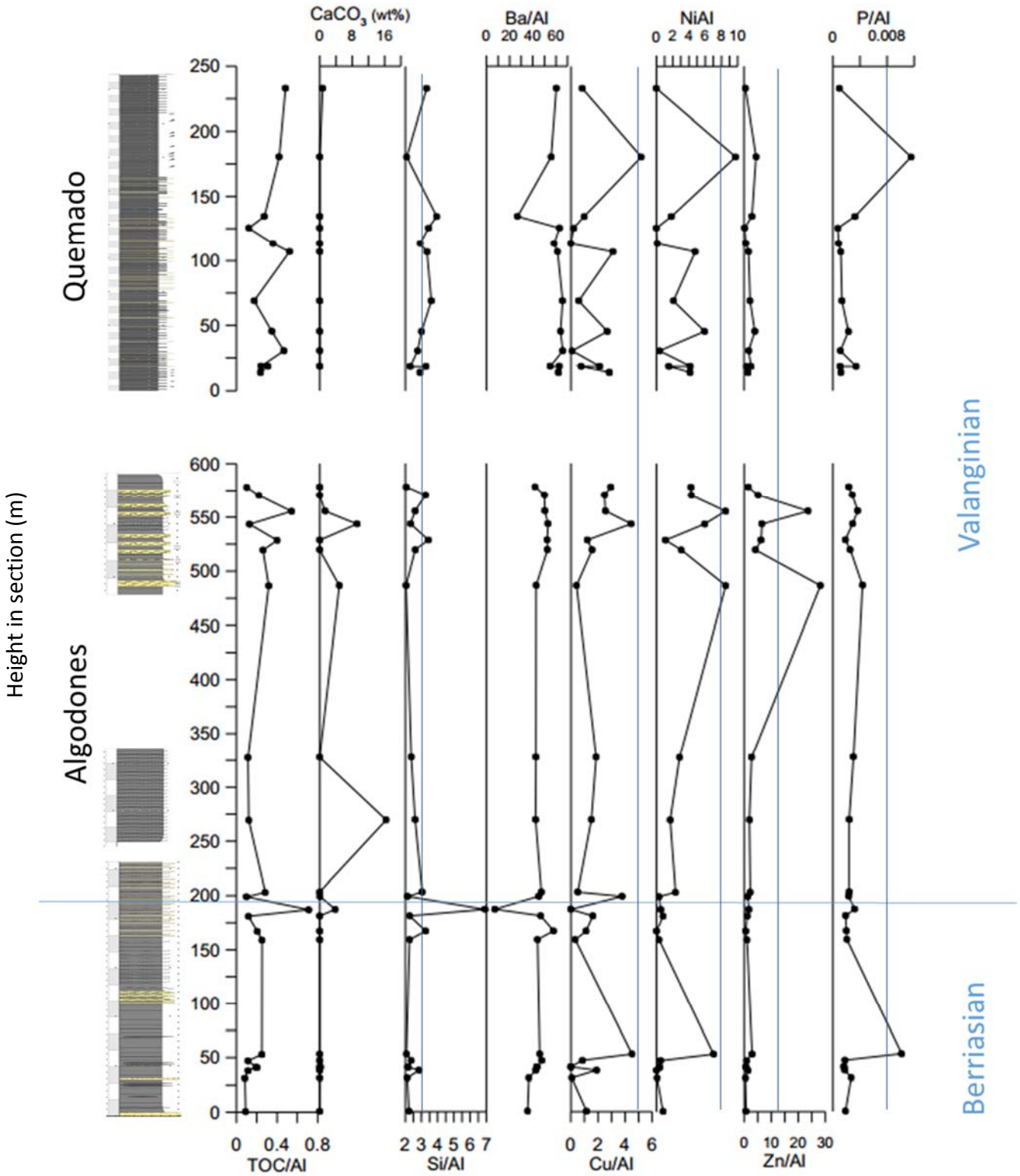

Figure 6.11. Paleoproductivity proxies with depth. Summary lithology and ages included from Georex reporting. Blue line is average shale (values and references in Chapter 3).

Figure 6.11 Paleo productivity proxies with depth (m) for two Macanal sections Algodones and Quemado. Summary lithology and ages included from Georex reporting. Blue line is average shale (values and references in Chapter 3).

6.3.6 Anoxia

Modern outcrop weathering can also affect redox proxies. Both of the Macanal samples deemed to be most resistant to the effects of weathering (Algodones 269.5 m and 543.5 m) contain Al normalised Mo, U and V contents close to, or slightly higher, than average shale (Figure 6.12). The majority of other samples (which may have had TE leached by contemporary weathering) also have redox sensitive TE levels higher than average shale. Molybdenum contents are elevated (Algodones average 15 mg/kg maximum 69 mg/kg, Quemado average 25 mg/kg, maximum 61 mg/kg), and Mo/Al is higher than average shale, but are below the values required to confidently identify euxinia (100 mg/kg, Scott and Lyons, 2012). Anoxia is indicated by Fe_{HR}/Fe_T greater than 0.38 in the majority of samples (Figure 6.13). Samples between 31 and 47 m in Algodones and 125.5 m and 134.5 m in Quemado have Fe_{HR}/Fe_T lower than 0.38. Each of these samples have lower than section average Fe contents (<2.4 wt%) but are not below the 0.5 wt% suggested as a filter by Clarkson et al. (2015). Sulphur is also present at concentrations greater than average shale, and at times exceeding the Venezuelan Cretaceous average and the C/T mean (values and references presented in Chapter 3 and Figure 6.13). Excess S (that is S not accounted for by pyrite) is present in most samples (up to 2.4 wt% in Algodones and 1.3 wt% in Quemado). Figures 6.12 and 6.13 show that Valanginian samples have higher values of all redox proxies compared to Berriasian samples (S, Fe_{HR}/Fe_T, Mo and V/Al, U/Al).

Sediments from both sections show dominantly planar parallel laminations and very few periods of bioturbation at outcrop scale (see Figure 6.13). In the two thin section samples analysed, one does not display good alignment of grains (Figure 6.4 and 6.5, Quemado depth 14 m), which could indicate a bioturbated sediment interval. This sample was taken from a section where no bioturbation was noted at the outcrop scale. The other sample from Algodones (519.5 m) does show good alignment of grains (Figure 6.6). Both thin sections show pyrite which appears to be relatively dispersed (Figure 6.4 and 6.6) suggesting that the bulk geochemistry is not 'averaging out' a concentration of pyrite concentrated in discrete lenses or precipitated in micro anoxic environments (like OM in shells).

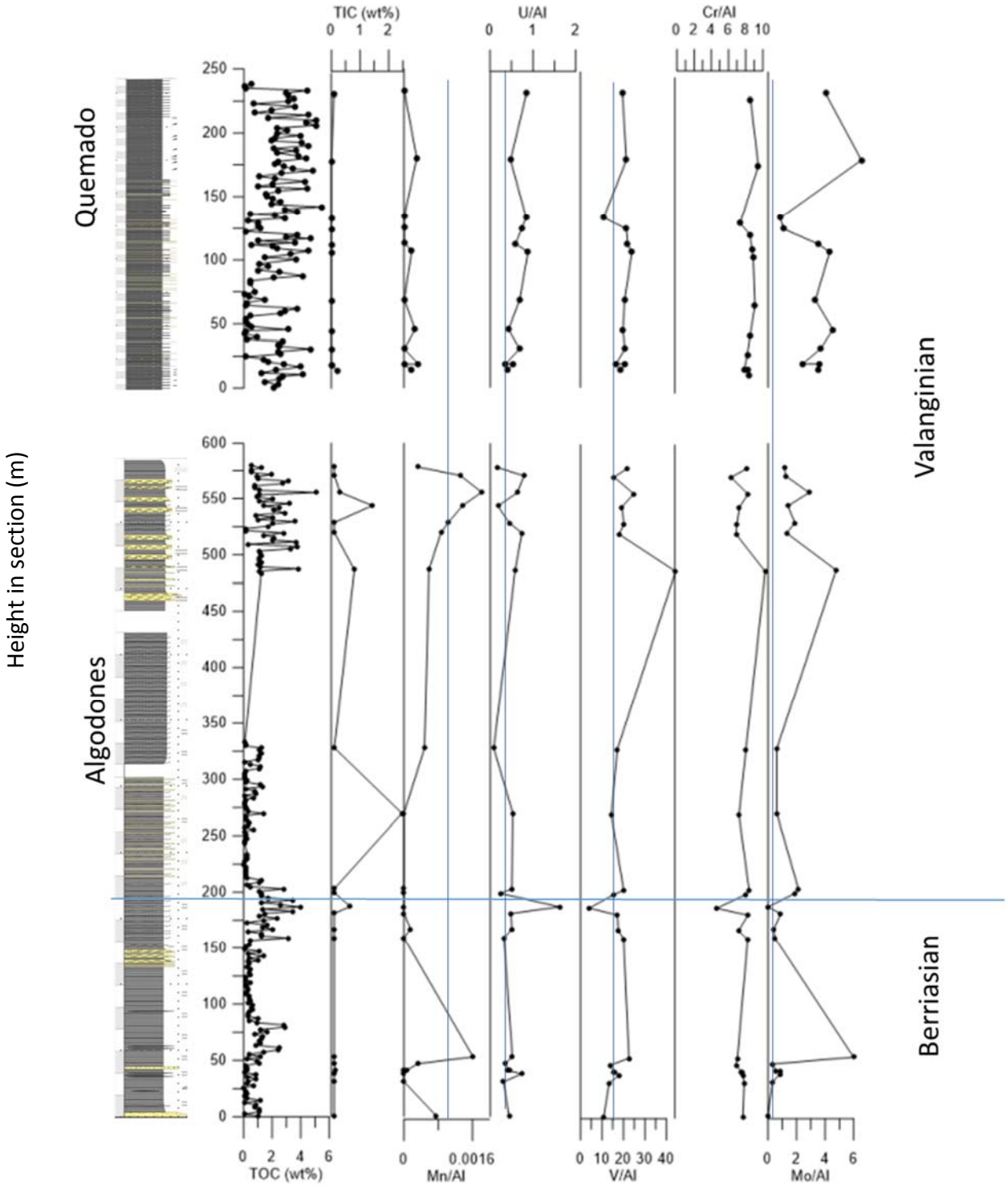

Figure 6.12 Redox proxies with depth in Quemado and Algodones. Blue line is Average shale, green line is C/T mean and red line is the Venezuela Cretaceous average. Note Cr is likely linked to detrital influx (good correlation with Al) and so content not likely due to redox conditions, as is V in Quemado. Ages and lithostrat column from Georex (2015)

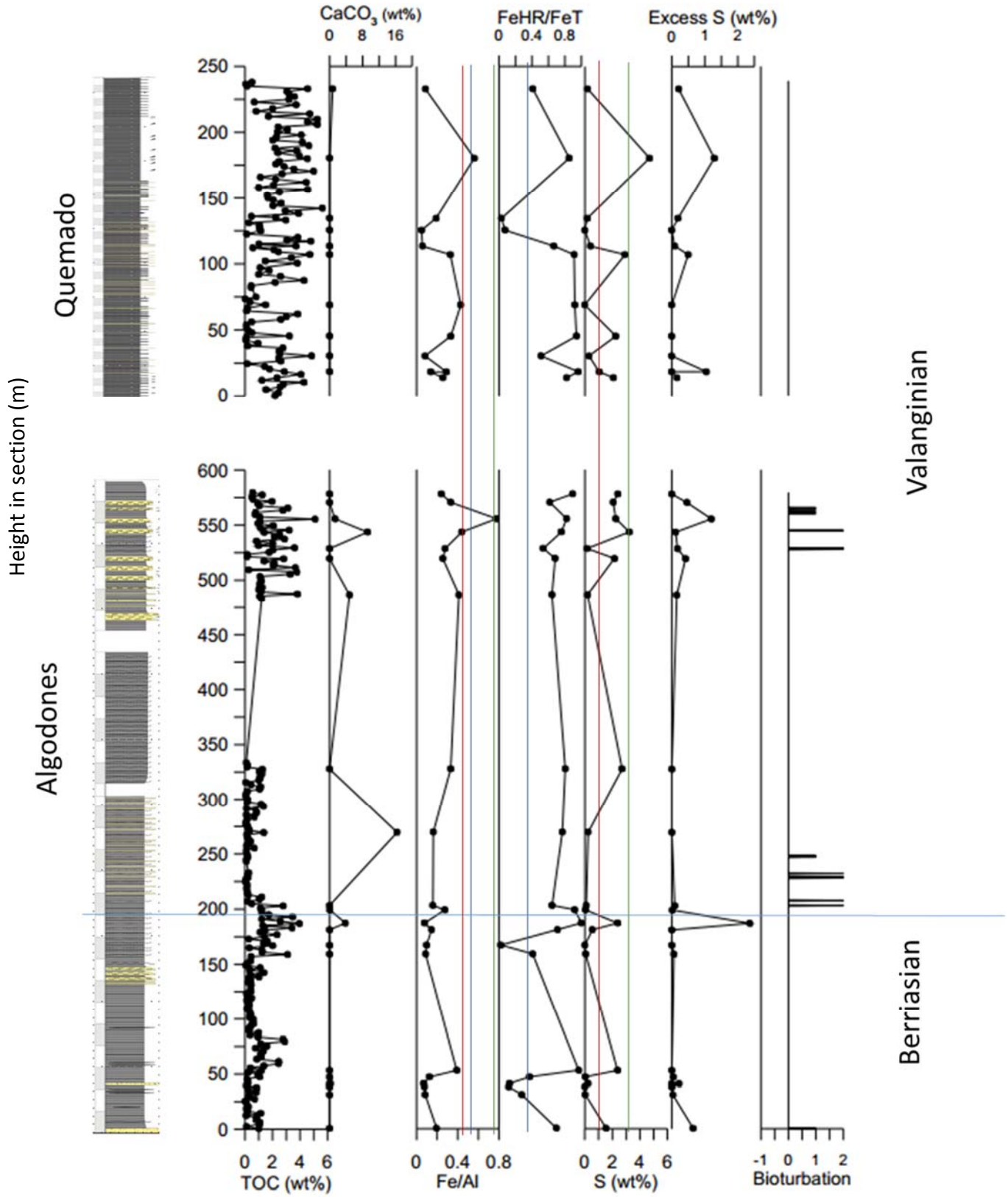

Figure 6.13 Redox proxies with depth (m) in Quemado and Algodones. Blue line is Average shale, green line is C/T mean and red line is the Venezuela Cretaceous averageAges and lithostrat column from Georex (2015).

6.4 Discussion

A more humid climate (with the consequence of increased runoff and upwelling due to enhanced hydrological cycle, Föllmi, 2012; Cotillon and Rio, 1984) in the Valanginian compared to the Berriasian is seen in locations in the Tethys, northern latitude boreal locations and to some extent in the proto-North Atlantic. The expression of this shift in climate, as seen in the sediments of the EC, are discussed in this section.

In the Macanal samples, there is good evidence from correlations between Si, Zr and Al that calculated sand content (as described in Chapter 3) is a reliable proxy for variations in coarse grain size. There is some evidence for higher amounts of detrital input in the Valanginian samples. They have a slightly higher calculated sand content (as well as higher Zr and Si) and statistically lower Al content (Figure 6.2 and 6.7) compared to Berriasian age sediments. This would indicate that the basin is receiving a greater quantity of coarse material compared to fine material in the Valanginian. This interpretation of the depositional system is complicated by tectonic activity around the EC during the depositional period. The increase in coarse material in the Valanginian compared to the Berriasian could suggest that subsidence caused by rifting was not fast enough to create accommodation space for the supply of material, and so progradation occurred. This could have been caused by an increase in the supply of detrital material due to changes in climate, a decrease in the rate of rifting, or a drop in sea level. The sedimentological interpretation by Georex (summarised in Appendix A) suggests a deepening of the depositional basin from the Berriasian sediments of Algodones (described as tidal plain to pro-delta), with the deepest period being represented by Valanginian sediments at the top of the Algodones and the base of Quemado (submarine fan). This interpretation matches well with lithological changes noted in the rest of the basin indicating deepening during the Berriasian (Etayo-Serna et al. 1976; Guerrero 2002). As the Berriasian-Valanginian was a syn-rift period, it has been suggested that changes in the rate of subsidence were a major driver of relative sea level fluctuations in the basin (Mora et al., 2009), with subsidence exceeding supply until some point in the Valanginian (Sarmiento-Rojas et al., 2006). Deepening during the Berriasian in the EC is opposed to eustatic sea level, which became shallower from the Berriasian to the Valanginian by approximately 50 m (Haq, 2014). In the EC, a deepening of the basin may even have led to an increased proportion of coarse material, due to physical erosion of the steep sides of the basin. In summary, there is some geochemical evidence that the mudstone beds received a greater volume of coarse material (Si and Zr) compared to the fine material (Al) in the Valanginian, even though sea

level rose due to local tectonics.

Many studies note more intense paleo chemical weathering in the Valanginian compared to the Berriasian using different chemical proxies. Phosphorus contents and the presence of phosphorite deposits were used to show enhanced paleo biogeochemical weathering rates from the Berriasian into the Valanginian in the Tethys, Atlantic and Tethyan sites (Follmi., 1995 and van de Schootbrugge et al., 2003). Also, higher kaolinite in the Valanginian is noted in the Tethys (Hallam et al., 1991 Duchamp-Alphonse et al., 2011), suggesting more intense paleo chemical weathering. Unfortunately, P cannot be used to trace paleo chemical weathering in the EC, as it does not correlate with Al or Si, and so its contents are likely controlled by other mechanisms (e.g. redox conditions, Ingall et al., 1993). There is very little kaolinite throughout the section, however, this could be due to the effect of burial.

The samples have been buried to a temperature (estimated 300°C, see Chapter 3) which exceeds that required for the transformation of smectite/kaolinite to illite (Elliott and Matisoff 1996; Thyberg et al. 2010). This diagenetic transformation may explain the higher K and Na values in these sections compared to the rest of the EC and relatively crystalline illite crystals (Figure 6.4 and 6.6). Contradictory evidence, suggesting instead a detrital source for the illite, are deformation of clay crystals around grains (Figure 6.5), a relatively constant K/Rb throughout the EC samples (Figure 6.9), and K contents which only occasionally exceed the 4 wt% threshold suggested as indicative of K metamorphosis (Figure 6.3) (van de Kamp (2016)). However, using clay type as a paleo chemical weathering proxy would be difficult in this context. Another theory for the dominance of illite and higher K or Na is that the hinterland was less weathered (more K-rich) in the Macanal samples (compared to later in the Cretaceous) or that physical weathering dominated over chemical weathering in the Macanal samples. A possible, less weathered K and Na rich hinterland for detrital material is the Floresta-Santander Massif, which is presumed submerged for the majority of the rest of the Cretaceous (Sarmiento-Rojas et al., 2006). The Floresta-Santander Massif comprises mafic and felsic metamorphic rocks as well as calc-alkaline plutonic rocks (Sarmiento-Rojas et al., 2006; Garcia et al., 2005) and was likely comparatively richer in Na and K than the reworked sediments which make up most of the Guyana Shield. Given the proximity of the samples to the Guyana Shield (Figure 3.1 and 3.2), it is presumed that the majority of the detrital material came from this direction. If this is the case, and the samples of the Macanal Formation have not been significantly affected by clay diagenesis, they represent a climate

with much lower intensities of paleo chemical weathering (much lower CIA*) and so a more arid climate than the rest of the Cretaceous.

Comparing the Berriasian samples to Valanginian samples there is very little difference in CIA* (average 79 and 78 respectively, Figure 6.8), supporting similar source rocks/climatic regimes. If it is accepted that the samples have been altered by K metasomatism, corrected values (Figure 6.10) also indicate only slightly more intense paleo chemical weathering in the Berriasian, but also later in the Valanginian (corrected CIA* 87) compared to the rest of the samples (corrected CIA*, 85). These differences are very small compared to fluctuations in CIA* noted in the Demerara Rise during the Coniacian-Santonian (50-65) by Flögel et al. (2008), where climate was fluctuating on orbital timescales. Another interesting trend in the EC samples is a steady increase in Na at the base of the Algodones section unrelated to other proxies. This could indicate a steady increase in the extent of paleo chemical weathering in the Berriasian. Unfortunately, due to an absence of chronological markers, it is not possible to match this to a global climatic change or a more local geological event (e.g. submersion of the Floresta-Santander Massif). Also, where the Berriasian/Valanginian boundary is located, and later in the Valanginian in the Quemado section, there is a decrease in Na and K and a resulting significant increase of CIA, matched with an increase in the coarse fraction. If climate is controlling these changes, they may relate to a temporary shift to a more humid climate. The high CIA* values are coupled with very low amounts of feldspars (Table 6.3) and descriptions of quartz sandstones, suggestive of a highly weathered source of detrital material. Uncorrected CIA* values are lower than modern day Amazon suspended sediment (84, Kronberg et al., 1987), but corrected values are similar. This may suggest a weathering of similar types of material or a similar weathering regime.

The slightly higher coarse grain input into the Basin in the Valanginian may have tentatively been supplied by increased runoff, supporting the hypothesis that the Valanginian was a more humid climate than the Berriasian. Further evidence for a more humid climate in the Valanginian are the plant remains which are frequently observed throughout the Valanginian age sediments but are absent from the Berriasian age sediments. An increase in terrestrial vegetation was used as evidence for higher humidity in the Valanginian in the Tethys and Proto-north Atlantic by Follmi (2012).

In previous studies, it has been possible to link more humid conditions in the Valanginian to higher marine productivity (due to more vigorous hydrological cycle causing greater run off

and upwelling), and more arid climates in the Berriasian to greater anoxia (caused by a diminished hydrological cycle and more stagnant water masses) (Föllmi, 2012; Cotillon and Rio, 1984; Follmi, 1995; Westermann et al., 2010). Unfortunately, in this case of our EC sections, the effect of variable contemporary weathering limits accurate interpretation based on TE, and the effect of thermal maturity limits the information provided by TOC. Tentatively, there may have been higher productivity in the Valanginian, given the statistically higher TOC (Figure 6.2), however, this may be a result of a greater contribution of more thermally recalcitrant terrestrial organic material. There is some evidence for anoxic conditions throughout the majority of deposition (Berriasian and Valanginian) from Fe_{HR}/Fe_T, high S and Mo contents. Anoxic conditions in the Valanginian would be contradictory to previous research in more open ocean locations, which suggest more oxic conditions in the Valanagian (Adatte et al., 1996; Mutterlose et al., 2003; Richiano, 2014; Grabowski, 2016). Anoxic conditions in the EC may relate to the restricted nature of the basin, with deep waters assumed to be more or less cut off from the open ocean by steep normal faults in the East and West, and continental facies in the North and South (Figure 2.4). Lower sea levels and active rifting may have isolated these deep waters further. The hydro-morphology of the basin during the deposition of the Macanal may have been similar to that of modern silled water bodies like the Black Sea, which becomes anoxic due to stratification between fresher water from runoff on the top of deep, more saline water (Demaison and Moore, 1980). Sections from more proximal locations, where this shallower fresher and oxic water intersects the slope, would be useful to confirm this hypothesis.

6.5 Conclusion

The Macanal samples of Berriasian-Valanginian age are affected by contemporary weathering and deep burial which has altered the organic matter and may have affected the clay mineralogy. This limits the use of many geochemical proxies. The slightly greater amounts of coarse material and the presence of terrestrial material in the Valanginian supports the compiled information in Föllmi, 2012 (from the Tethys, high latitudes and proto-North Atlantic) that there was a global shift from arid to humid climates from the Berriasian to the Valanginian, however the shift in climate here is very slight. Geochemical information relating to paleo productivity and redox conditions is scarce, due to contemporary weathering and high thermal maturity. There is, however, evidence that oxygen was limited in the EC throughout deposition, different to more open water locations where the Valanginian was a period of oxic conditions. This may be due to the restricted

nature of the basin, which may have resulted in the reduced mixing of deep waters, similarly to the Black or Baltic Sea.

Chapter 7 Fomeque Formation – Hauterivian to Aptian depositional environment in the Eastern Cordillera and beyond

7.1 Research Highlights

- Extremely high productivity was likely sustained through high runoff from a humid interior, coupled with upwelling driven by offshore winds and with P release from anoxic sediments.
- Anoxia was not limited to particular periods within the Fomeque (OAE's) but was sustained in the distal parts of the EC basin likely due to high productivity and/or by stratification caused by a freshwater lid.
- The particular combination of basin geography and climate led to organic matter accumulation exceeding most open ocean settings of similar age.

In this chapter, inorganic and sedimentological data and interpretation for the five sections of the Fomeque formation will be presented and discussed. These sections represent Hauterivian to Albian deposition in the EC and adjacent MMV. The sections document variable depositional settings, from internal platform and tidal plain (La Marina, Pedregal and Cantonera) to outer continental slope (La Cristalina 2 (LC2) and La Cristalina 3 (LC3)) and these different environments are compared

7.2 Introduction

The Early and Mid-Cretaceous is a period of extreme and fluctuating greenhouse conditions (e.g. Erbacher, 2001; Wagner et al 2008; Mutterlose et al., 2010), punctuated by significant climatic events which led to widespread deposition of organic-rich mudstones. Assumed *global* climatic events included the Faraoni Event (near end of Hauterivian), Taxy and Selli Events and the accompanying OAE 1a, (Late Barremanian-Early Aptian), and the Fallot, Paquier and associated Events (Late Aptian-Early Albian, OAE 1b). These have been linked to warming (possibly caused by increased volcanic activity) increasing the hydrological cycle, which either led to higher input of nutrients and high productivity (Tremolada et al., 2008; Company et al., 2005; Coccioni et al., 2006; Switzerland, Stein 2012; Italy, Stein et al., 2011; Heimhofer et al., 2008; Herrle et al., 2003), freshwater surface layers which caused stratification and increases in OM preservation (Erbacher, 2001), or increase in terrestrial organic matter input (during periods of falling sea level) (Erbacher et al., 1996). The majority of studies investigating these climatic changes in the Early to Mid-Cretaceous have paleo geographic locations around the Tethys Ocean, the Atlantic and Pacific. Since the majority of the extreme climatic events of this period are thought to be influenced by runoff and the

input of terrestrial nutrients (Föllmi et al., 2012), these should be well expressed in the spatially restricted, land-enclosed siliciclastic-dominated EC basin.

During the Hauterivian-Barremian the connection to the Atlantic and the Pacific (Figure 2.6) was restricted (mostly continental deposition occurring), but the Colombian Marginal Sea was present in the west, which in turn was variably connected to the Caribbean depending on the extent of the ancestral Central Cordillera. During the Aptian-Albian, marine deposition started in the Maracaibo Basin in the North, developing into carbonates of the Maraca formation by the mid-late Albian (Erlich et al., 2003). By the Albian, marine deposition was occurring in the north and south, and so the EC was part of an epicontinental seaway that connected the proto-North Atlantic and the Pacific (Macellari, 1988; Erlich et al., 2003, Figure 2.7). Until the end of the Hauterivian, the EC was still an active rift system (Mora et al., 2006, Parra et al., 2009). After the Hauterivian, accumulation of sediment was largely controlled by passive thermal subsidence and eustatic sea level fluctuations (Narvaez et al., 2013). The Santander-Floresta high (Figure 2.1), which separated the Tablazo and Cocuy sub-basins, became submerged creating one larger basin (Fabre, 1985) allowing deposition of marine sediments across a larger area than the Macanal (approximately 150 km, Figure 3.2). The submerged high still influenced the transport of sediment from the Guyana Shield in the East until the Aptian, when there was a basin-wide transgression. The location of this paleo high still appears to have a distinct influence on the basin, marking the transition from middle to outer shelf during the Aptian-Albian in Figure 2.7. The ancestral Central Cordillera in the west was variably emergent, at times restricted the EC and Colombian Marginal Sea and providing an additional source of detrital material (the extent and elevation of the ancestral Central Cordillera are poorly constrained). The general sea level falls during the late Albian led to a transition from fine grained marine deposits of the Fomeque and stratigraphic equivalents to the sand-dominated Une formation (Sarmiento-Rojas et al., 2006).

The Fomeque is dominated by dark grey and black mudstones interstratified with grey siltstones and marls, with lenses of limestone and beds of grey quartz sandstone from cm to m thick (Ulloa and Rodríguez, 1979). It is located between the sand dominated Caqueza and Une formations and was deposited during the Barremian and Albian (Parra et al., 2009). As discussed in Chapter 3, stratigraphic boundaries within the Fomeque are mostly based on lithostratigraphy, and therefore not well constrained. The Fomeque is exposed in the

Pedregal and Cantonera sections, in streams close to San Luis de Gaceno, Boyacá (see Figure 3.1). In the western flank of the Eastern Cordillera, the time equivalent formation is the Paja formation, which is also mudstone dominated, with lenses of sandstone and levels of evaporites (gypsum) and carbonates (Fuquen and Osorno, 2005; Narvaez et al., 2013). The Paja is followed by the Albian Hiló formation, which is dominated by silty shales, fine sandstones and cherts (Mojica and Scheidegger, 1984). The Paja and Hilo are represented in this study by the La Marina section (a road cutting close to San Pablo de Borbor, Figure 3.1) and La Cristalina 2 and 3 (also road cuttings on the road between Puerto Boyaca and Otanche, Figure 3.1). Their approximate paleo locations within the basin are shown in Figure 3.2, with Pedregal and Cantonera located in the far east, in the Cocuy Sub-Basin, the La Marina section located in the west, in the Tablazo Magdalena sub-basin, and the LC2 and LC3 sections located in the adjacent MMV.

Unlike the Macanal, there are a number of geochemical studies that have been carried out on the Fomeque or its lateral equivalents in the EC. Narvaez et al. (2013) studied a section just west of the Santander-Floresta Massif (See Figure 2.1), near Curiti, more northerly than any of the sections within this study. Here, limestones were deposited in the Barremian (the Rosablanca Formation), followed in the Aptian by the limestone-, marl- and shale-dominated Paja Formation. Villamil (1995) analysed a section from the very south of the EC basin, near Olini. Campos Alvarez and Roser (2006) studied Hauterivian to Aptian black shales, silty sandstones and sandy mudstones from the Bolivar region (close to the Santander-Floresta Massif). The results of these studies can be combined with our new data to give a more complete picture of the paleoenvironment during this depositional period.

Table 7.1 Summary of information about the Hauterivian to Albian sections covered in this chapter (provided by Georex, 2015). Formations introduced in Figure 2.2.

Section	Formation	Age	Flank of Basin	Palaeo-water depth (m)	Facies interpretation
La Marina	Paja	Hauterivian to Aptian	Western	30	Protected internal platform, mudflats, tidal plain, sometimes hypersaline, sometimes influenced by the open ocean (tides or swells) or with increased input from hinterland (tidal streams).
Pedregal	Fomeque	Barremian to Aptian	Eastern	15	Internal to middle platform shallowing to littoral zone at the top of the section.
Cantonera	Fomeque	Aptian to Albian	Eastern	12	Base of column internal to external platform, towards the top, mostly fluctuating between shoreface and intertidal plain
La Cristalina 2	Paja/Hilo	Aptian to Albian	Western	-	Outer shallowing to inner continental slope
La Cristalina 3	Simiti/Paja /Hilo	Aptian to Albian	Western	-	Mid-outer continental slope

7.3 Results

Here I will present data for the 82 samples from the Pedregal, Cantonera, La Marina, LC2 and LC3 sections analysed by XRF, CNS/LECO and Fe speciation, 13 samples analysed by XRD, and three samples analysed in thin sections by SEM. Firstly correlations between elements will be presented, in order to better understand which component of the sediment the elements are associated and to allow for selection of appropriate proxies. Following this, trends in detrital input, intensity of paleo chemical weathering, productivity and redox proxies will be explored.

7.3.1 Correlation between main components

As discussed in Chapter 3, identifying correlations with Al can help to distinguish between detrital and authigenic/diagenetic influence on the general sedimentation pattern. All correlation coefficients are recorded in Table 7.2 and correlations coefficients greater than 0.5 (or less than 0.5) will be considered good. Silica has a negative correlation with Al in all sections, however, this correlation is only considered good in the Pedregal section (Figure 7.1a). Zirconium also has a good negative correlation with Al in Pedregal, and a good positive correlation with Al in LC2 and LC3 (7.1b). In Pedregal and Cantonera, there are good positive correlations between Al and Ti (Figure 7.1c), Mg (Figure 7.1d) and K (Figure 7.1e). Na is strongly correlated to Al in Pedregal but not in Cantonera (Figure 7.1f), possibly due to some samples having Na contents close to limits of quantification in XRF (0.02 wt%). In La Marina,

there are no strong positive correlations between Al contents and Na, Mg and K, (Figure 7.1d, e and f). However, Ti content is well correlated with Al (Figure 7.1c). In Pedregal, Cantonera and La Marina, Fe does not correlate with Al (Figure 7.1f). In both LC2 and 3, Al strongly correlates with Ti, Fe and K (Figures 7.1c, 7.1e and 7.1f). Magnesium content correlates with Al in LC2 but not in LC3 (Figure 7.1d). Sodium strongly correlates with Al in LC3 but not LC2, where it is below the limits of detection in most samples (Figure 7.1f). There is not a good correlation between P and Al in any of the sections (Figure 7.1g), suggesting that its content is not controlled by detrital input. Therefore, in all the Fomeque samples, there are correlations with Al in Ti contents, correlations with K, Fe and Mg are more variable and no section has a correlation between P and Al.

There is also varying correlation between TE and Al in the different sections. In Pedregal and Cantonera, some redox and productivity proxies correlate well with Al, including Ba (Figure 7.1h) and Cr (Figure 7.1i). In Pedregal, V, Cu and Ni also correlate well with Al (Figure 7.1j, 7.1k and 7.1l). For Cu, this may be due to some samples having contents close to limits of quantification in XRF (12 mg/kg). This suggests that the TE are arriving with detrital material in Pedregal, and to some extent in Cantonera. In La Marina, there are no TE which positively correlate with Al, but U, Zn and Ni contents negatively correlate (Figure 7.1n, 7.1o and 7.2k). In LC2, Cr, Mo and V correlate well with Al (Figure 7.1i, 7.1m and 7.1l), whereas in LC3 there are no strong correlations between TE content and Al. These TE which correlate with Al should be used with caution as redox or productivity proxies, as variations are likely predominantly influenced by variations in detrital input.

As discussed in Chapter 3, Zr arrives at sediments as zircon grains with a high specific density, hence a correlation between Si and Zr is evidence that Si content is related to the coarse grain size fraction. When this is the case, the calculated sand fraction (described in Chapter 3 and based on Si/Al) is a reliable indication of the contribution of sand and silt to the sediments. In Pedregal and Cantonera, Si and Zr positively correlate (Figure 7.1p) and therefore calculated sand content should provide a relatively reliable estimation. In La Marina and LC2 and LC3, Si and Zr contents do not correlate, suggesting Si may be supplied by a different source (Figure 1q). In Pedregal, Mg, Na, K, Ba, Cr, Ni and V positively correlate with Al but negatively correlate with Si, suggesting that they are concentrated in the fine-grained detrital fraction (Table 7.2). In La Marina, Mg has a positive correlation with Si (0.5, Figure 7.1q), perhaps suggesting its concentration in the coarse fraction. In LC 2 and 3, there

are a number of elements which strongly negatively correlated with Si – Mn, Mg, and in LC2 – also Ni and Zn (Table 7.2).

As discussed in Chapter 3, samples from the Fomeque formation have been buried to temperatures within and past the oil window (Table 3.5, vitrinite reflectance between 1.3 (LC2) and 2.0 (La Marina)). Measured TOC is therefore unlikely to reflect pre-oil window values, and TOC-TE relationships are therefore unlikely to be pristine. However, good positive correlations between redox and anoxia TE proxies in LC2, LC3 and La Marina (Table 7.2, variable but including Mo, Ni, V, U and Zn) may hint at factors controlling the accumulation of TOC. There is also a good correlation between Al and TOC in LC2, which may hint that either both are being diluted by another major component, or they are delivered to the sediment together.

Figure 7.1

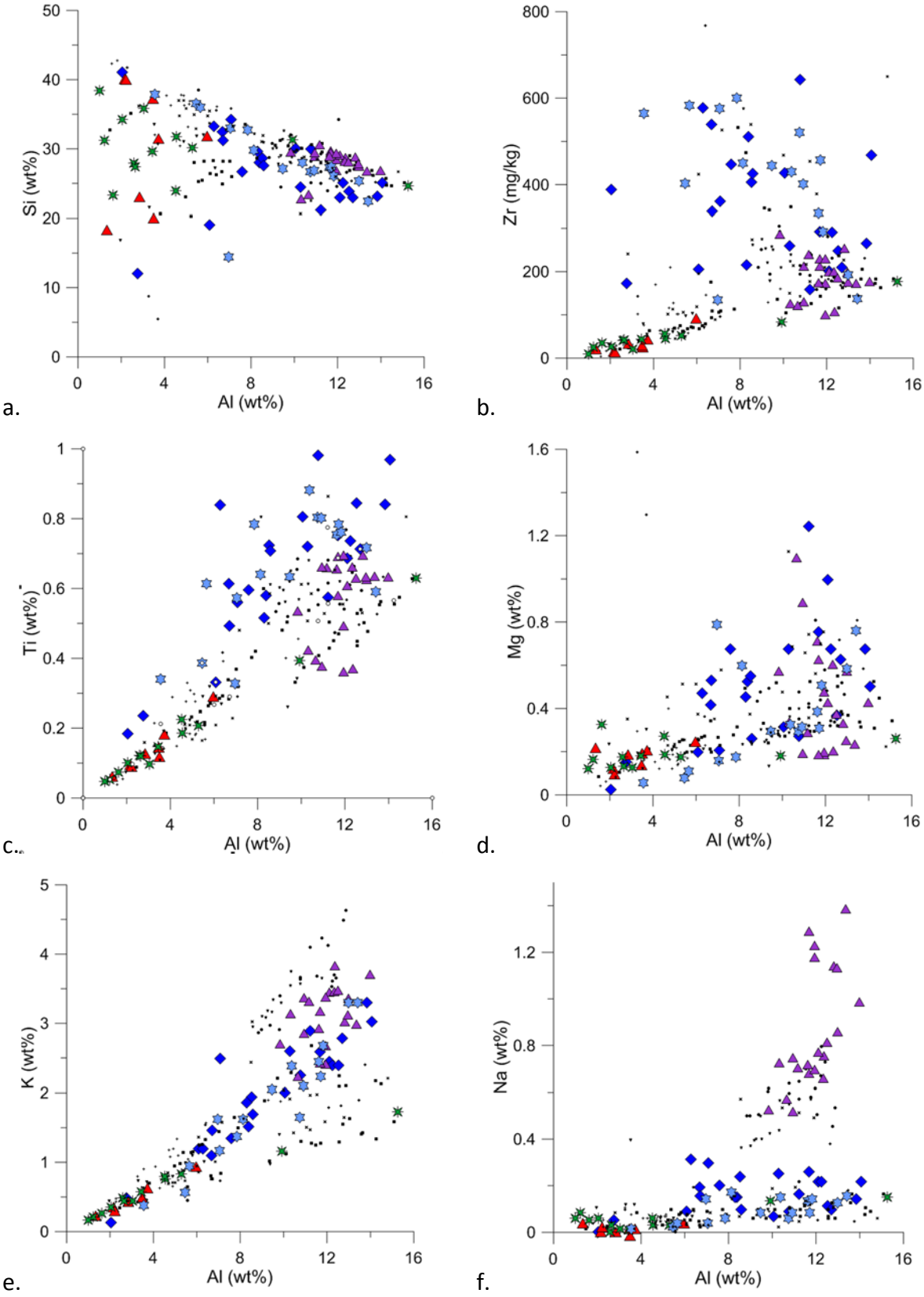
a.
Si (wt%)
Al (wt%)
b.
Zr (mg/kg)
Al (wt%)
c.
Ti (wt%)
Al (wt%)
d.
Mg (wt%)
Al (wt%)
e.
K (wt%)
Al (wt%)
f.
Na (wt%)
Al (wt%)

g.

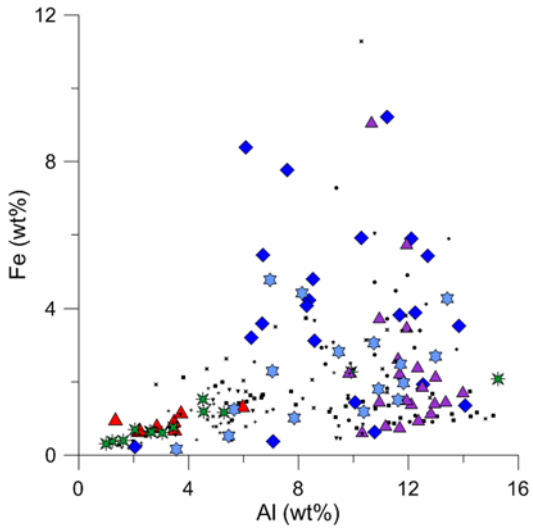
Fe (wt%)
Al (wt%)
0
4
8
12
16

h.

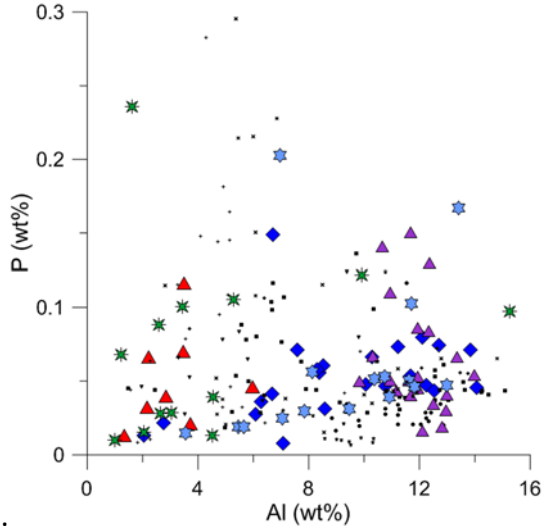
P (wt%)
Al (wt%)
0
0.1
0.2
0.3
4
8
12
16

i.

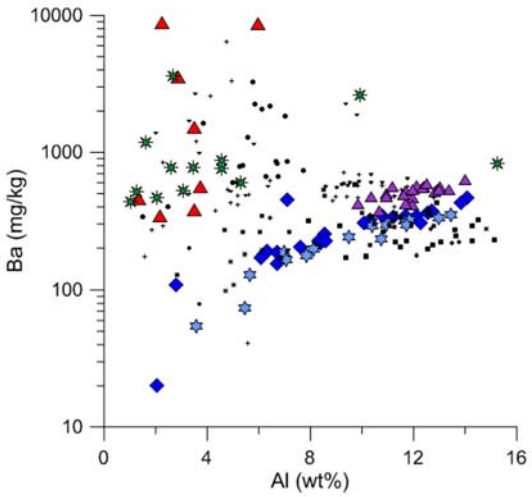
Ba (mg/kg)
Al (wt%)
10
100
1000
10000
0
4
8
12
16

j.

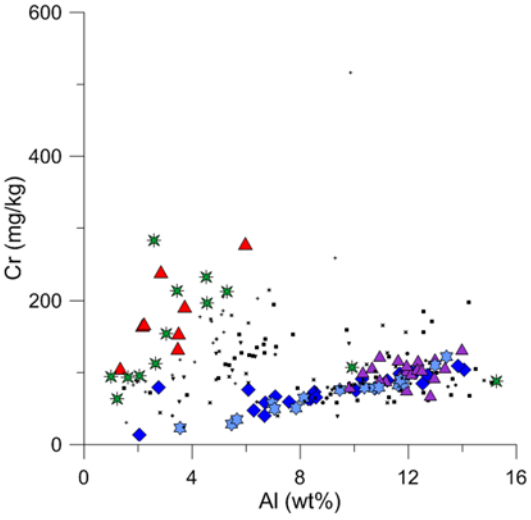
Cr (mg/kg)
Al (wt%)
0
200
400
600
4
8
12
16

Figure 7.1

k.

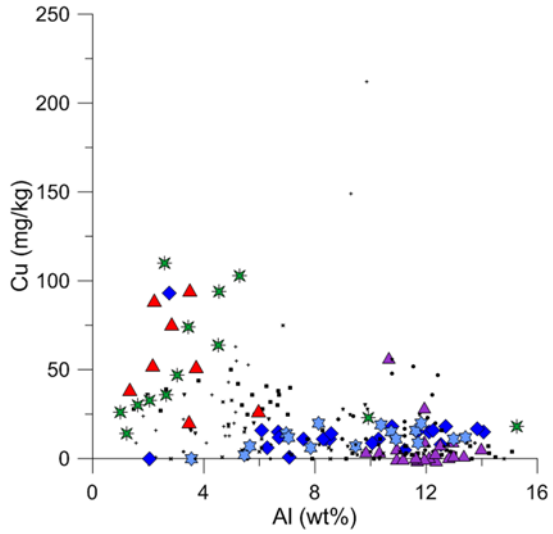

l.

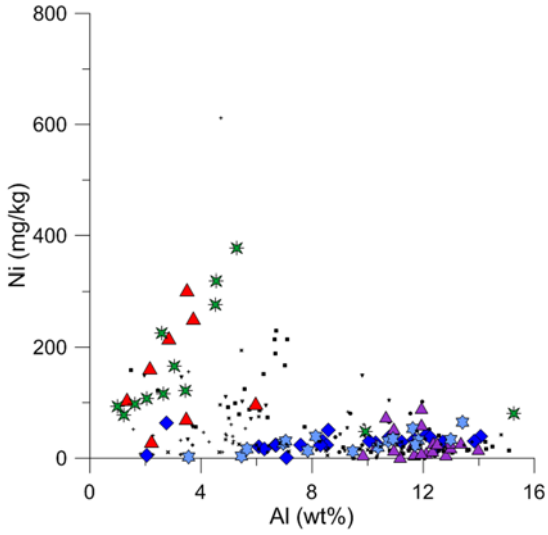

m.

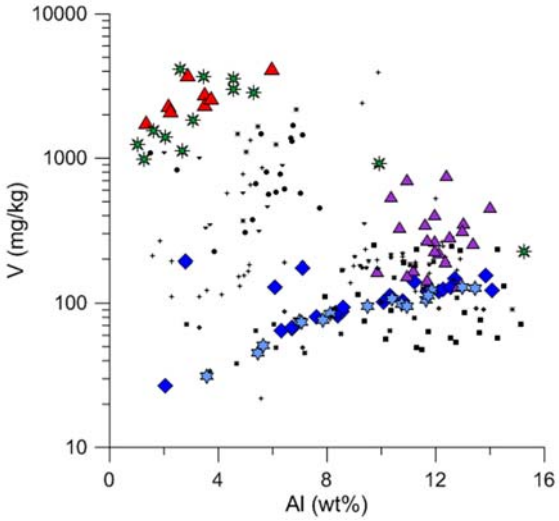

n.

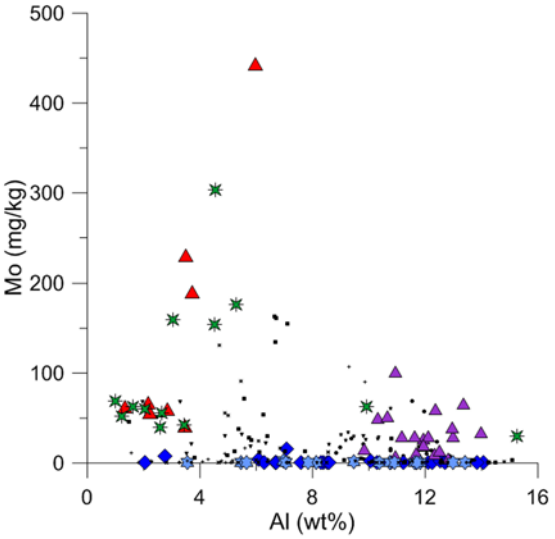

o.

p.

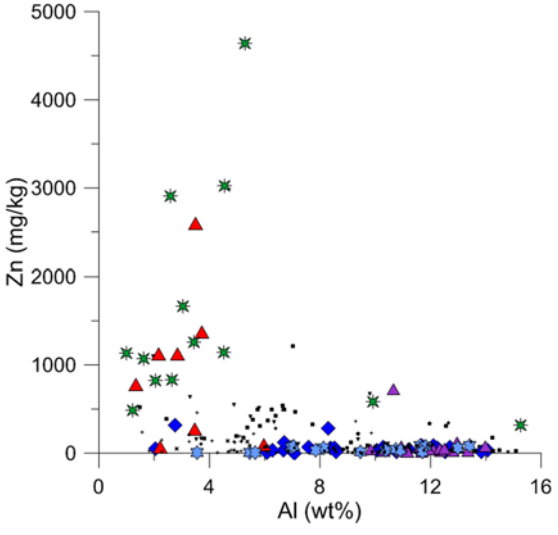

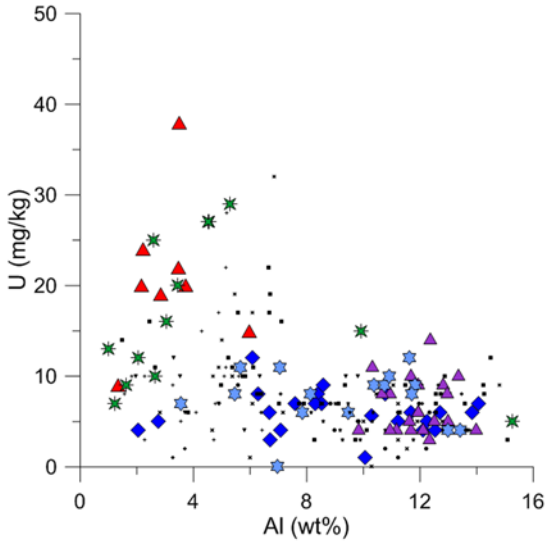

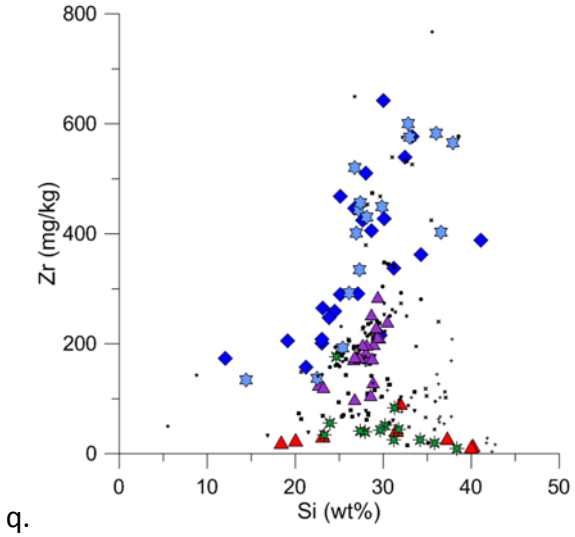

q.

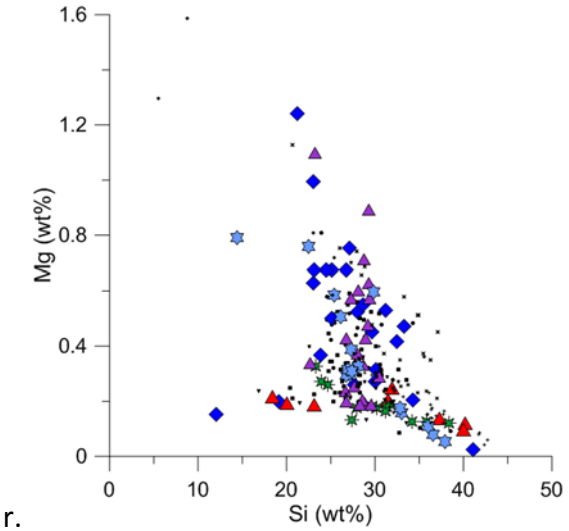

r.

Figure 7.1 a-r. Correlations of elements with Al and Si. Contents measured using XRF. Coloured points are from the Fomeque, small points are from the rest of the EC data set. Blue diamonds are Cantonera, red triangles are LC2 samples, green stars are LC3 samples, purple triangles are La Marina samples, light blue stars are Pedregal samples. Note that correlations between Al and Ba and V are shown with a logarithmic for the TE.

Table 7.2 Correlation coefficient for elements when correlated with Al, Si and TOC. IC and S from LECO and CNS analysis, other elements from XRF. Red data is good to very good positive correlations. Green data is good to very good negative correlations.

		Si (wt%)	Ti (wt%)	Al (wt%)	Fe (wt%)	Mn (wt%)	Mg (wt%)	Ca (wt%)	Na (wt%)	K (wt%)	P (wt%)	S (wt%)	IC (wt%)	Ba (mg/kg)	Cr (mg/kg)	Cu (mg/kg)	Mo (mg/kg)	Ni (mg/kg)	V (mg/kg)	U (mg/kg)	Zn (mg/kg)	Zr (mg/kg)
Cantonera	Al (wt%)	-0.28	0.80	1.00	-0.34	0.11	0.60	0.14	0.26	0.93	0.33	-0.49	0.17	0.86	0.82	-0.27	-0.32	0.24	0.34	-0.08	-0.35	-0.14
	Si (wt%)	1.00	0.03	-0.28	-0.76	-0.22	-0.31	-0.09	0.13	-0.25	-0.10	-0.62	-0.38	-0.20	-0.69	-0.67	-0.06	-0.68	-0.73	-0.19	-0.33	0.61
	TOC (wt%)	-0.36	-0.51	-0.47	0.41	-0.25	-0.55	-0.38	-0.43	-0.43	-0.45	0.65	-0.02	-0.37	-0.12	0.39	0.39	0.18	0.24	0.49	0.12	-0.26
Pedregal	Al (wt%)	-0.59	0.69	1.00	-0.77	-0.71	0.57	-0.19	0.64	0.95	0.31	0.21	-0.33	0.98	0.97	0.56	-0.18	0.70	0.98	-0.03	0.49	-0.54
	Si (wt%)	1.00	-0.10	-0.59	-0.10	-0.05	-0.87	-0.67	-0.72	-0.66	-0.83	-0.15	-0.53	-0.65	-0.66	-0.55	-0.63	-0.55	-0.64	0.58	-0.57	0.79
	TOC (wt%)	0.13	0.30	0.14	-0.10	-0.05	-0.36	-0.28	-0.34	-0.12	-0.11	0.13	-0.30	0.05	0.04	-0.10	-0.23	-0.10	0.06	0.39	-0.36	0.38
La Marina	Al (wt%)	-0.08	0.47	1.00	0.39	-0.38	-0.30	0.20	-0.31	0.01	0.26	-0.57	-0.39	-0.22	-0.45	-0.10	0.34	-0.57	0.00	-0.68	-0.54	-0.30
	Si (wt%)	1.00	-0.33	-0.08	-0.41	-0.02	0.54	0.24	0.68	-0.30	-0.08	-0.06	0.53	-0.17	-0.26	-0.13	-0.47	-0.03	-0.14	0.05	0.09	0.07
	TOC (wt%)	-0.11	-0.24	-0.63	-0.18	0.08	0.01	-0.11	0.08	0.01	-0.06	0.78	-0.01	0.40	0.19	0.28	-0.16	0.63	-0.31	0.63	0.69	0.34
LC2	Al (wt%)	0.10	0.97	1.00	0.68	-0.32	0.52	-0.42	0.13	0.98	0.23	0.39	-0.08	0.41	0.73	-0.31	0.87	0.11	0.79	0.12	-0.11	0.91
	Si (wt%)	1.00	0.15	0.10	-0.09	-0.89	-0.68	-0.94	0.09	0.09	-0.04	-0.11	0.00	0.35	0.09	-0.20	-0.13	-0.52	-0.13	0.00	-0.55	-0.04
	TOC (wt%)	-0.57	0.49	0.58	0.40	0.23	0.65	0.31	0.05	0.51	0.37	-0.09	-0.26	0.21	0.40	-0.10	0.50	0.17	0.66	0.10	0.08	0.58
LC3	Al (wt%)	-0.34	1.00	1.00	0.90	0.56	0.34	-0.64	0.72	0.98	0.18	0.69	-0.5	0.17	-0.10	-0.16	-0.06	-0.10	-0.32	-0.13	-0.15	0.96
	Si (wt%)	1.00	-0.39	-0.34	-0.32	-0.62	-0.83	-0.45	-0.16	-0.39	-0.53	-0.23	-0.37	-0.28	-0.19	-0.09	0.17	-0.10	-0.15	0.00	0.09	-0.51
	TOC (wt%)	-0.11	-0.25	-0.27	-0.15	0.27	-0.03	0.08	-0.76	-0.11	-0.19	0.11	-0.22	-0.20	0.91	0.92	0.54	0.79	0.88	0.82	0.72	-0.26

7.3.2 Main Compositional Differences

Figure 7.2 shows differences between the sections in the main components of the samples. Silica contents are similar in all sections. This is surprising given the greater number/thickness of sand beds noted within the sections in Pedregal and Cantonera and the much more proximal depositional environment. The La Cristalina sections 2 and 3 have statistically lower Al contents than the other sections ($p<0.005$). Aluminium contents in Pedregal, Cantonera and LC3 are very variable. La Marina has a much smaller range of Si and Al contents. Calcium carbonate content is lower in the more proximal La Marina, Pedregal and Cantonera sections. The LC sections have higher TOC contents, statistically higher when compared to Pedregal ($p= <0.005$).

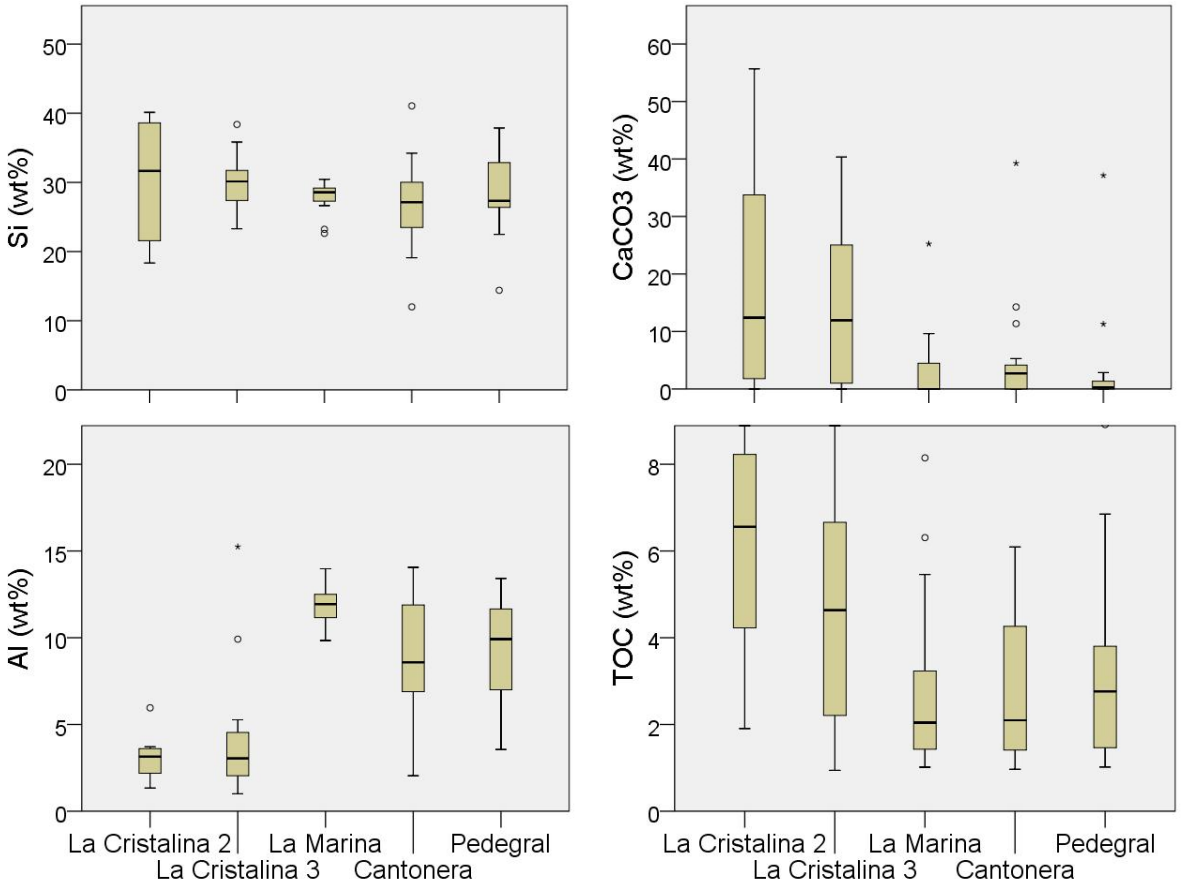

Figure 7.2 Compositional differences between the Fomeque age sections. There is a statistical difference (tested with Kruskal Wallis, with the same method as in Chapter 5) between Al contents ($p<0.005$), between LC2 and LC3 and Pedregal, Cantonera, La marina. There is a statistical difference between $CaCO_3$ content between La Marina and LC3 (p is <0.11). Cantonera, La Marina, Pedregal statistically different to LC3 and LC2 ($p<0.005$).

7.3.3 Detrital Proxies

Variations in proxies commonly ascribed to detrital input are displayed in Figure 7.3 to show changes over the length of the section, and to compare sections.

The calculated sand fraction is highly variable in Cantonera and Pedregal (average 26%, SD 52%; 25%, SD 33%, respectively), and maxima coincide with elevated Zr contents, confirming that the dominant Si origin is within the coarse fraction. Field descriptions of silty mudstone and muddy sandstone, together with this variable sand/silt content estimated in bulk chemistry, suggest variable mixing with overlying coarser beds and not distinct and sudden influxes of coarse material. Thin sections from Pedregal (at 2.5 m and 220 m) attest to this mixing, showing poorly graded quartz sand and silt within a clay matrix (Figure 7.4 and 7.5). Calculated sand fraction is very high in LC2 and LC3, reaching 100%, although these high values are not matched by Zr/Al (which is much lower in LC2 and LC3), confirming the Si is not associated with the coarse fraction. Field descriptions do not identify sand lamina, lenses or beds with these La Cristalina sections, however, siltstones are observed in LC3 and chert was noted. The switch to 100% calculated sand content is matched by a sharp decrease in Al, corresponding to the change from the Albian Paja to the more silt/chert dominated Aptian Hiló formation in LC3. No such dramatic change in Si and Al is noted at the same time boundary in LC2, however, calculated sand contents are very variable throughout. La Marina has a much higher Al content than LC2 and LC3, but with comparable Si and Zr/Al Silica and sand, contents remain relatively stable and low, even during periods with a greater number of sand lenses/beds, e.g. between 320 and 360 m (Figure 7.3). The La Marina section is described as proximal (internal platform, mudflats, tidal plain, Table 7.1) but the lack of coarse material supports the suggestion by Georex (2015) that the environment was protected from the open ocean.

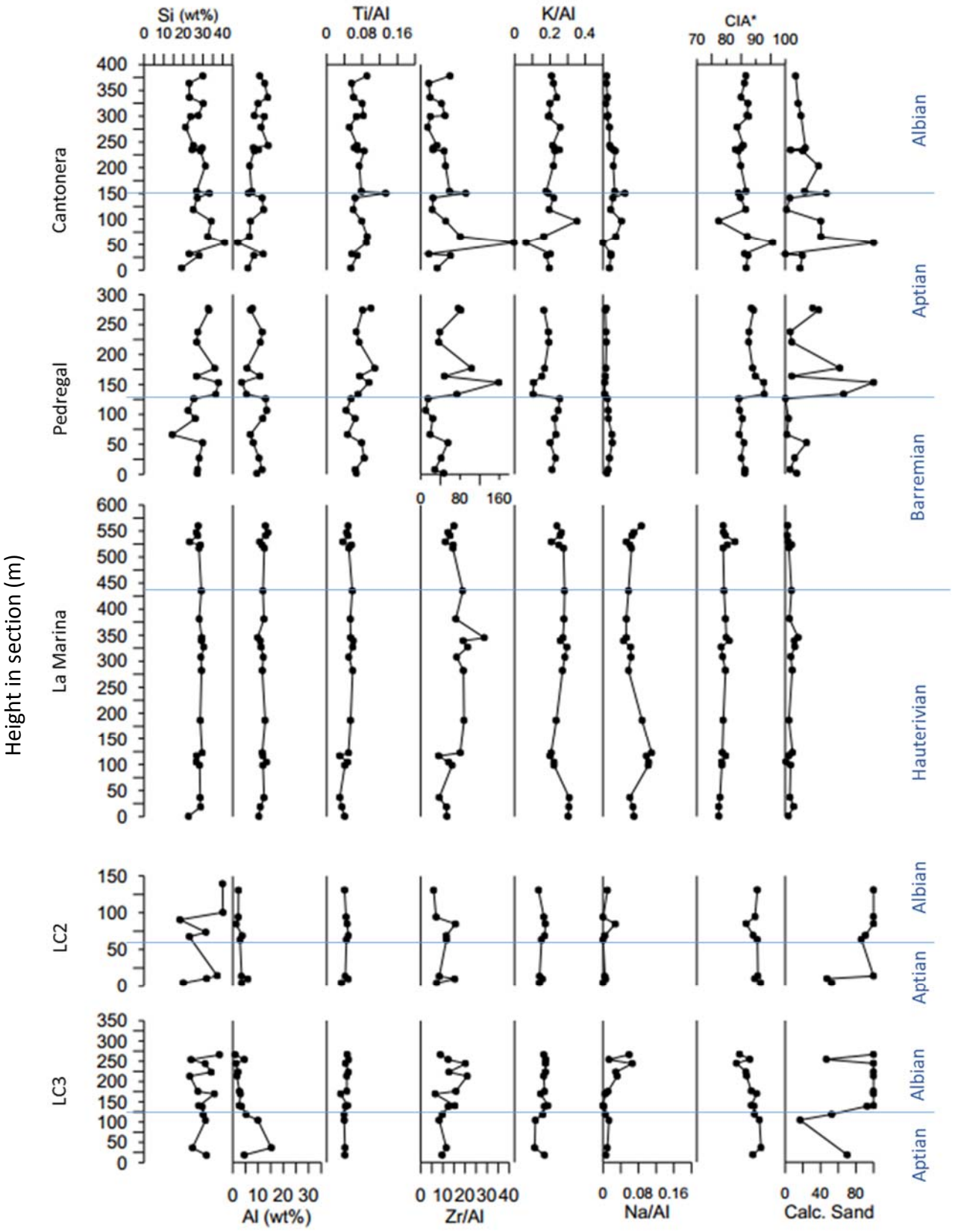

Figure 7.3 Variation in detrital proxies (measured using XRF) and sand fraction (based on Si/Al, see Chapter 3 for methodology) for the Fomeque age sediments. Plotted against height in section (m) and ages are from Georex (2015).

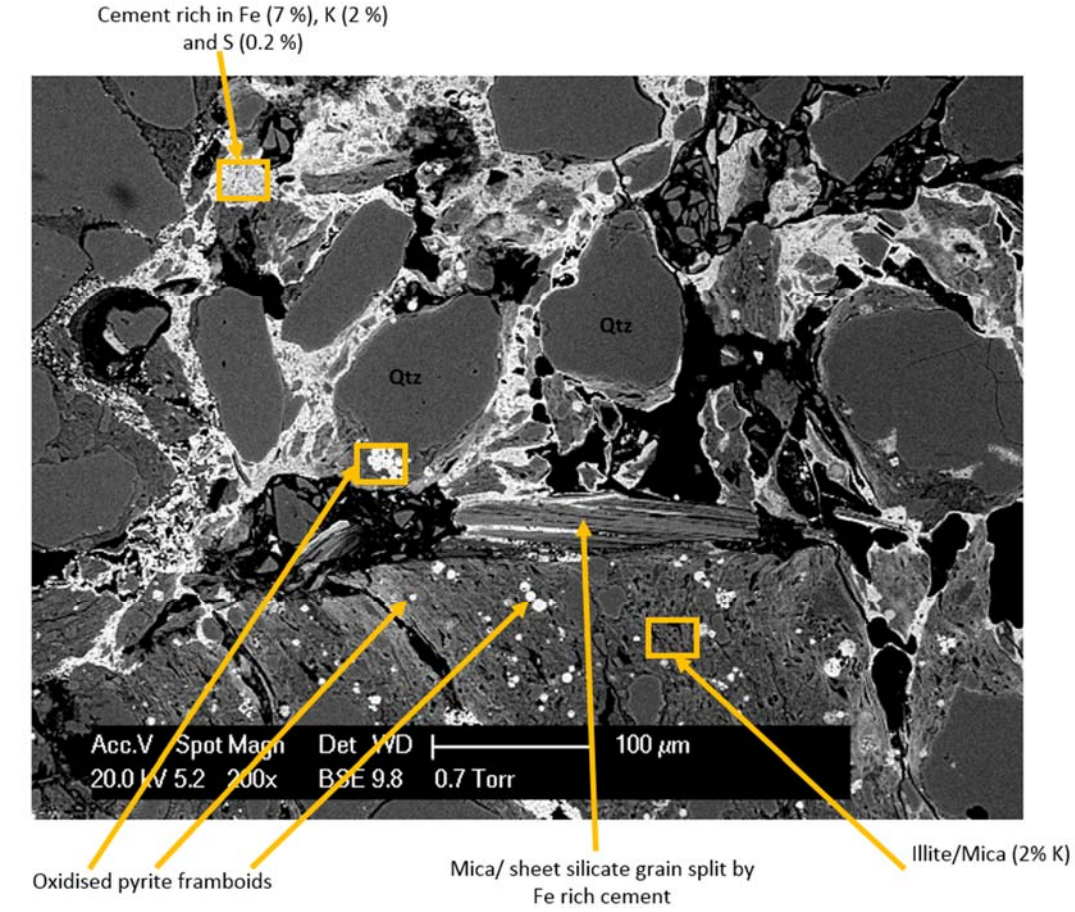

Figure 7.4 SEM BSE image of a thin section of sample from Pedregal -2.5 m , chemistry derived from EDX. Black is porosity or OM. Note sand size detrital quartz and Fe cement in this burrow through much finer sediment and oxidised pyrite

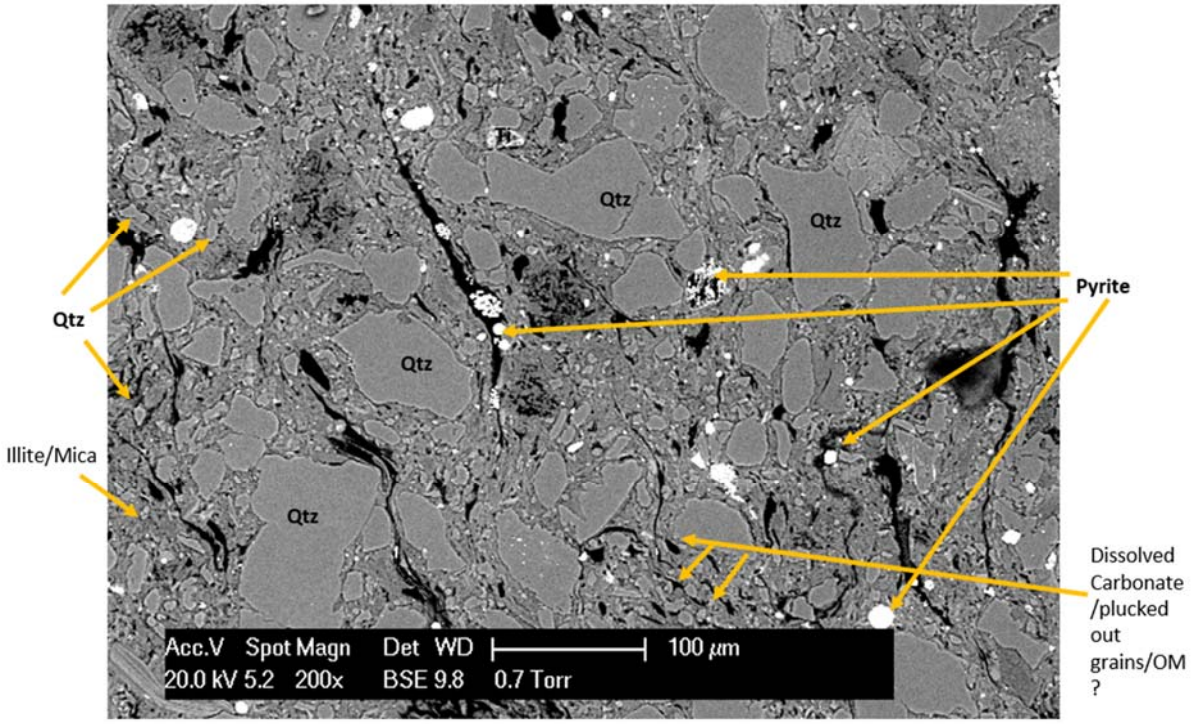

Figure 7.5 SEM BSE image of a thin section of sample from Pedregal –220 m, chemistry derived from EDX. Black is porosity or OM. Note heterogeneous grain size, lack of bedding, and dispersed pyrite. Most porosity/OM in lenses.

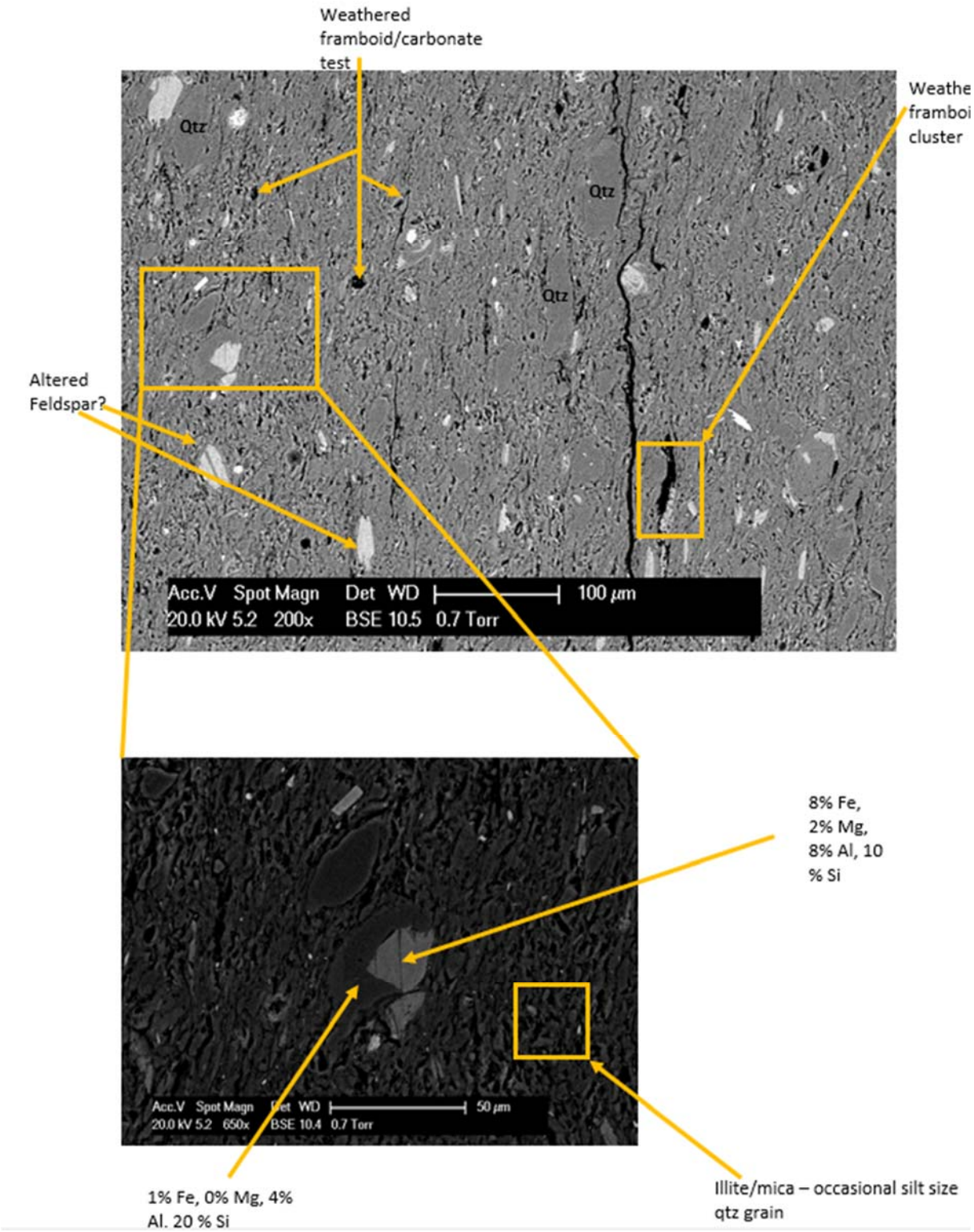

Figure 7.6 Sample from La Marina (547 m) in SEM-BSE mode, elemental contents derived from EDX. Black is porosity or OM. Note grain alignment suggesting a lack of bioturbation. Fractures could have been caused during thin section preparation. Some silt size grains are Mg and Fe rich (silt-sized) appear to be altered.

7.3.4 Paleo Chemical Weathering Intensity

Chemical index of alteration (CIA*) can provide information about the intensity of chemical weathering of feldspars to K and Na rich clay (Nesbitt and Young, 1982) which in turn provides information about climate and provenance. Values are quite different in each

section (Figure 7.3). CIA* values of La Cristalina 2 and 3 are relatively stable over the depositional period (average LC 2, 89.8, SD 1.5; LC 3 88.3, SD 2.4), and are the highest out of the five sections. There is, however, a slight decline in the Albian in LC3 (from 90 to 85 at the end of the depositional period) and in LC2 from 90 at 67.5 m to 87 at 90.5 m) caused by decreasing Al and increasing Na contents. CIA* values from La Marina samples are the lowest, but are also relatively stable (average 79.2, SD 1.2). The low values come from consistently higher Na/Al and K/Al compared to the other sections. The two elements seem to vary independently (Figure 7.3) which combine to cause the relatively steady CIA*. The La Marina samples not only contain detrital quartz grains but also weathered feldspars and other minerals (Figure 7.6). In Pedregal, average CIA* is 87.5 (SD 2.7) and in Cantonera it is 85.9 (SD 3.1). In Cantonera, the Aptian samples show a decrease before the Aptian/Albian boundary (from 95.7 at 54 m to 77.3 at 96.5 m). In Pedregal, there is an increase in CIA* at the Barremian/Aptian boundary (from 84.2 at 126 m to 92.8 at 133.5 m). In both cases, it appears the shift is largely controlled by variations in K/Al, although Na/Al shows corresponding lower magnitude changes. Also, shifts to higher CIA* are matched by higher Zr/Al and sand content in Cantonera and Pedregal. In the few samples analysed by XRD, clay mineralogy is mostly dominated by illite with some kaolinite. This is confirmed by SEM EDX, with most of the clay matrix containing K, and forming needle like structures (presumed illite) (Figure 7.4 and 7.5). A proportion of the <2µm proportion in XRD is identified as micro quartz, up to 20 % in Cantonera (96.5 m), Table 7.3.

Table 7.3 XRD data for the Fomeque age sediments. All values are wt %.

		>2µm portion								<2µm portion			
	Depth (m)	clay	sand	K feldspar	Na Feldspar	carbonate	pyrite	Anatase	Other	illite/smectite	Illite	kaolinite	micro quartz
Cantonera	96.5	50	35	traces	0	0	<5	<5	<5		47	33	20
	152.5	15	38	0	<5	0	32	<5	<5		48	42	10
	238.5	48	32	traces	<5	<5	traces	<5	<5		75	20	<5
	278.5	45	40	traces	<5	0	traces	<5	<5		69	31	0
	299	42	43	traces	0	0	<5	<5	<5		54	37	9
Pedregal	7.5	65	20	traces	traces	0	<5	<5	<5	0	63	37	0
	52.5	38	42	traces	5	0	5	<5	<5	5	65	25	<5
	177	25	65	0	0	0	0	<5	<5	0	50	40	10
	237.5	63	22	traces	traces	0	<5	<5	<5	0	65	35	0
	274	38	47	traces	traces	0	<5	<5	<5	0	66	34	0

7.3.5 Productivity

Calcium carbonate contents of samples from Cantonera (average 5.5 wt%), Pedregal (3.5 wt%) and La Marina (3.1 wt%) are considerably lower than those measured in LC2 (18.9 wt%) and LC3 (14.4 wt%), suggesting lower calcareous productivity (Figure 7.2, Figure 7.7). In Cantonera and Pedregal, carbonate is present in the sections as thick beds (up to 1.5 m) and in La Marina as thin beds (most about 0.1 m) of packstone and wackestone as well as nodules (Appendix A). In LC2 and LC3 such calcareous beds are largely absent, but the siltstones and mudstones are often described as calcareous (Appendix A), suggesting calcareous productivity was more constant than in the other, more proximal settings. As described in Chapters 4 and 5, $CaCO_3$ is readily dissolved during contemporary weathering. It is possible that samples from Cantonera, Pedregal and La Marina contained greater amounts of $CaCO_3$ just after deposition, and that the carbonate has since been dissolved. However, samples from Pedregal and La Marina, when investigated in thin section in SEM, showed little signs of large test/shell pores which would be evidence of $CaCO_3$ dissolution (Figure 7.4-7.6). Siliceous productivity may also have been higher in LC2 and LC3. As discussed in Section 7.21 and 7.23, Si content does not appear related to coarse grained detrital input in LC2 and LC3 and therefore could have a biological source. Silica and Zr relationships suggest that biogenic Si may also be present in La Marina, but Si/Al here is relatively low and no microcrystalline quartz was visible in SEM. The presence of minor microcrystalline quartz (up to 20% of the clay size fraction) from XRD suggests that authigenic/biogenic quartz may also be present in Pedregal and Cantonera. Average TOC is higher in LC2 (3.2 wt%) and LC3 (3.2 wt%) compared to the other sections (La Marina average 1.6 wt%, Pedregal 1.5 wt% and Cantonera 1.5 wt%). Samples from Cantonera have the highest maximum TOC contents in the Fomeque sections (and the highest in the whole of this study) with three samples containing 24.3 wt%, 15.5 wt% and 15.1 wt% TOC. There are some periods of elevated TOC in each section (Figure 7.8). In LC2 and LC3, TOC is high for a number of consecutive samples at the location assigned to the Aptian/Albian boundary. In La Marina, TOC is high in the first 35.5 m, 84.5-124.5 m, and 508-703 m. In Pedregal, TOC is higher above 125m, the approximate location of the Barremian to Aptian boundary, while in Cantonera, peaks in TOC are relatively isolated. In Pedregal and Cantonera, there is evidence that plant material may be contributing to the TOC content, with plant remains noted occasionally throughout the column and thin beds of coal present in Pedregal. However, as mentioned in Section 7.2.1, original TOC contents were likely diminished by thermal maturation depending on the OM

type. Oil stains were noted in the sandstone of Pedregal and Cantonera, indicating oil migration from the adjacent shale beds or from elsewhere in the basin, which could lead to elevated TOC contents.

Trace element based paleo productivity proxies have been developed for application in the open marine realm. Therefore, their application in more coastal environments with higher and more variable depositional energies like Cantonera, Pedregal and La Marina is not useful. In the more open marine LC sections, these TE proxies are useful, and here nearly every sample displays Al-normalised Ba, Cu, Ni and Zn contents above average shale values (Figure 7.7). In fact, accumulations of Ba, Cu, Ni and Zn in many samples exceed the respective values in the Venezuelan Cretaceous average, the C/T mean, and modern day upwelling sediments (Namibian mud)(references for these values are included in Chapter 3 section A). In LC3, a temporal trend can be observed (Figure 7.7). It appears that $CaCO_3$ and Si/Al, Cu/Al, Ni/Al and Zn/Al generally increase from 36 m to the top of the section. There is a jump at 140 m (which corresponds to higher contents of all paleo productivity proxies apart from Ba) which corresponds to a change to a more siltstone dominated lithology (Appendix A). At 175.5 m, Ba/Al also increases. There are two samples with elevated P/Al, and they correspond to samples with elevated $CaCO_3$ (213 m) and Si/Al (244 m).

In LC2, there is again a general increase in Cu/Al and Si/Al from the base of the section to the top, however, the other proxies are more variable. There are two periods of elevated contents of Zn/Al and Ni/Al, at the base of the section (4.5 m) and between 67.5 m and 100.5 m.

There is little sedimentological evidence of upwelling and high productivity (e.g. P beds or fish remains) observed in any of the columns (Appendix A), apart from isolated fish remains in La Marina, Cantonera and Pedregal. Chert beds (<0.5 m thick) are also noted in the lithological descriptions of LC2 and LC3.

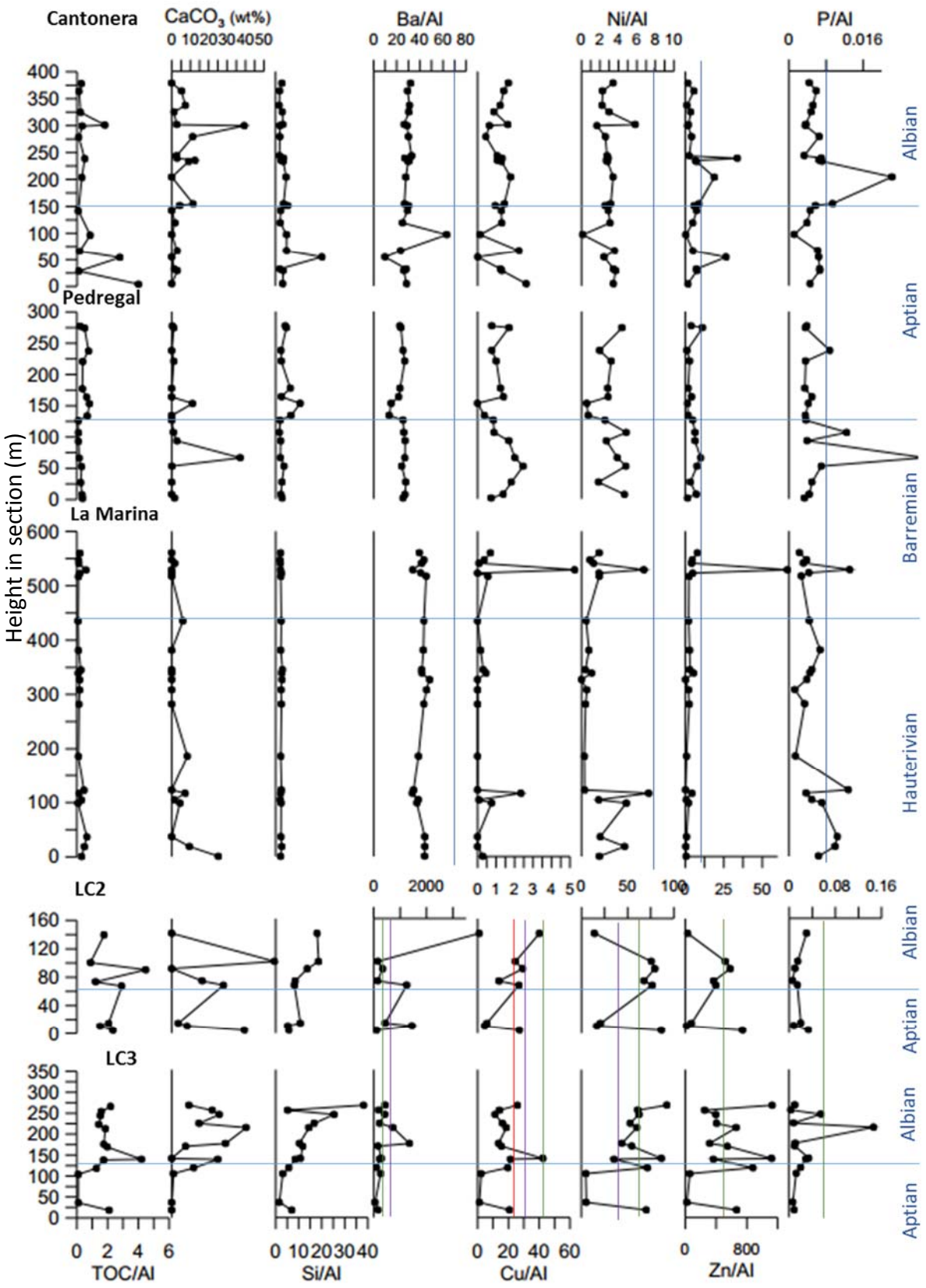

Figure 7.7 Variation in productivity proxies (measured using XRF) for the Fomeque age sediments plotted against height in section (m). Blue vertical line is average shale value, green is the C/T mean, red is a Cretaceous Venezuelan average (Lo Monaco et al.,2002 and Alberdi-Genolet and Tocco, 1999), and purple is Namibian modern day upwelling (Brumsack, 2006).

7.3.6 Anoxia

Due to the proximal nature of the Pedregal, Cantonera and La Marina sections (Table 7.1), redox proxies are less reliable, given the complexities of TE redox reactions in these environments. Proxies for anoxia in the more distal LC2 and LC3 will be more reliable. Also, samples have higher $CaCO_3$ contents; 5 out of 8 samples in La Cristalina 2, and 9 out of 13 in LC 3 contain greater than 5 wt%. In these samples, the original geochemical composition will have been better preserved from the effects of modern weathering.

There is sedimentological evidence of bioturbation in the Pedregal and Cantonera sections (discrete ichnofossils or lack of lamination, Figure 7.8). There are, however, intervals with less frequent bioturbation. In Cantonera, there is no bioturbation noted between 96 m and 187.5 m (across the interval assigned to the Aptian/Albian boundary). In Pedregal, there appears to be less bioturbation towards the top of the column (above 157 m). Bioturbation was noted in one of the thin sections from Pedregal (2.5 m) (Figure 7.4), filled with quartz sand and silt in an illite matrix. In turn, the Pedregal sample (220 m) without discrete burrows does not show signs of lamination (Figure 7.5), which may indicate that the sediment was affected by bioturbation. Pyrite (or oxidised pyrite framboids) within both thin sections analysed for Pedregal sections are quite dispersed, however, they are occasionally concentrated in lenses suggesting localised sulphate reduction within the sediments (perhaps associated with degrading OM). Within the burrow of the thin section from 2.5 m, Fe-rich cement suggests that Fe was remobilised from pyrite dissolution, perhaps during fluctuations in sea floor/sediment redox conditions (Figure 7.4). Samples within Pedregal and Cantonera do contain S at contents greater than the Venezuelan Cretaceous average, and approaching the C/T mean (Figure 7.8). At least some of this S is in excess of the pyrite fraction and may be present as sulphurised organic matter, supported by very high S coinciding with high TOC (for example, in Cantonera the sample with 15.0 wt% TOC at 152.5 m has 22.6 wt% S that is almost entirely non-pyritic). High S contents are often found within proximal sediments, likely due to intense sulphate reduction within the sediment caused by high OM input (Canfield et al., 1992). Another explanation is that the samples contain sulphur rich coal. One sample in particular (Cantonera 152.5 m) has a very particular geochemistry and so is not included in Figures 7.3, 7.7-7.9. It has an extremely high S content, 32% Fe (mostly as poorly or unreactive silicate-bound Fe, Fe_{HR}/Fe_T 0.09), 22% S (mostly excess S), and very high As (219 mg/kg), Cu (93 mg/kg) and Pb (827 mg/kg). In hand

specimen, it has a very low density and is black and lustrous, further evidence that the sample contains coal. Apart from this specific sample, the low TE contents, combined with more frequent observations of bioturbation, suggest that for the majority of the depositional period the bottom water was oxic. The high (>0.38) Fe_{HR}/Fe_T in most samples seems to contradict this and provides support for anoxic bottom waters (Figure 7.8). Fe and Fe_{HR} are concentrated in such proximal/coastal settings even in oxic bottom waters (Boyle, 1974; Wen et al., 1999; Aller et al., 2004; Lyons and Severmann, 2006), and so the Fe_{HR}/Fe_T is not a useful indicator of anoxia in these proximal settings.

Although likely complicated by the proximal nature of the sediments in the La Marina section, it is observed that Mo/Al contents are greater than average shale in all samples (Figure 7.9). Samples below 100 m, samples 308 m and 327 m, and samples above 523 m have Mo contents greater than the 25 mg/kg cut off where persistent euxinia may have occurred and water column conditions were at least oxygen limited (Scott and Lyons, 2015). Unlike Pedregal and Cantonera, however, there is little S or pyrite in the La Marina samples. Although likely complicated by the proximal nature of the sediments, V/Al values are elevated above average shale in the bottom 100 m of the samples and towards the top of the analysed section above 523 m), and this corresponds to higher Mo, TOC, Fe and FeHR/FeT (>0.38) (Figure 7.8 and 7.9). The low values of TOC and redox proxies in the mid portion of this section coincide with the presence of sand beds (which are interpreted to be the result of tidal streams and coastal sand bars by Georex). Tentatively (due to the concern of the reliability of proxies here), it is suggested that deeper waters in this protected interior platform were at least seasonally anoxic. In a thin section from 547 m, a lack of bioturbation is noted as grains are aligned (Figure 7.6), and there is a lack of bioturbation observed at the La Marina outcrop (Figure 7.8). This could suggest low oxygen bottom water conditions, however, hypersaline conditions noted within the column (veins, crystals of halite, gypsum, calcite - dispersed and in laminae) would also limit the prevalence of burrowing benthic life forms.

In LC2 and LC3, Fe_{HR}/Fe_T is consistently above 0.38, suggesting anoxic conditions (Figure 7.8). Apart from two samples at the base of LC3 (which contain little to no $CaCO_3$), Al-normalised redox sensitive TE are enriched compared to average shale, Venezuelan Cretaceous average (V), and CT mean (U, V, Cr) (Figure 7.9). Molybdenum is above the 100 mg/kg threshold for confident identification of euxinic conditions (Scott and Lyons, 2015) in three samples in LC2

(two in the Aptian and one in the Albian (4.5, 10.5 and 73.5 m)) and in LC3 in four samples (at 18 and 118 m (Aptian) and 169 and 254 m (Albian)). S contents remain relatively low in both sections (average 0.4 and 0.5 wt % in LC3 and LC3, respectively). In LC2, redox proxies are very variable, and the low sample resolution prevents any clear trend. In LC 3, there is a gradual increase in Al-normalised TE (U, V, Cr) towards a peak at 140 m, (which has been identified as the Aptian/Albian boundary), with Mo being more variable (Figure 7.9). There is very little bioturbation noted within LC2 and LC3, and no ichnofossils were observed.

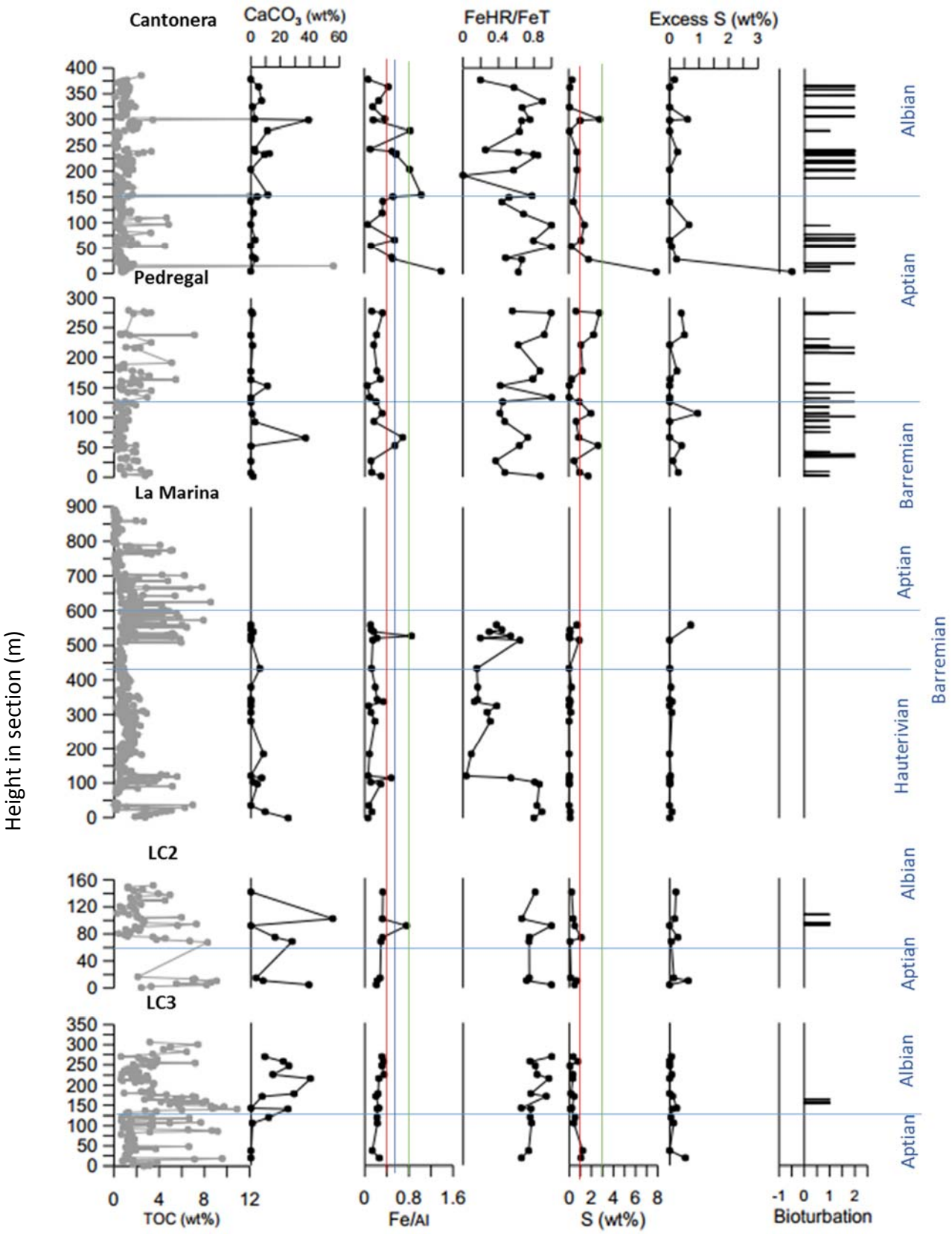

Figure 7.8 Anoxia proxies in S and Fe for the Fomeque age sediments plotted against height in the section (m). A Fe_{HR}/Fe_T greater than 0.38 is considered anoxic. The bioturbation is 1 if noted in the column as homogenised sediments and 2 if ichnofossils are present. Blue vertical line is average shale value, green is the C/T mean, and red is a Cretaceous Venezuelan average (Lo Monaco et al.,2002 and Alberdi-Genolet and Tocco, 1999).

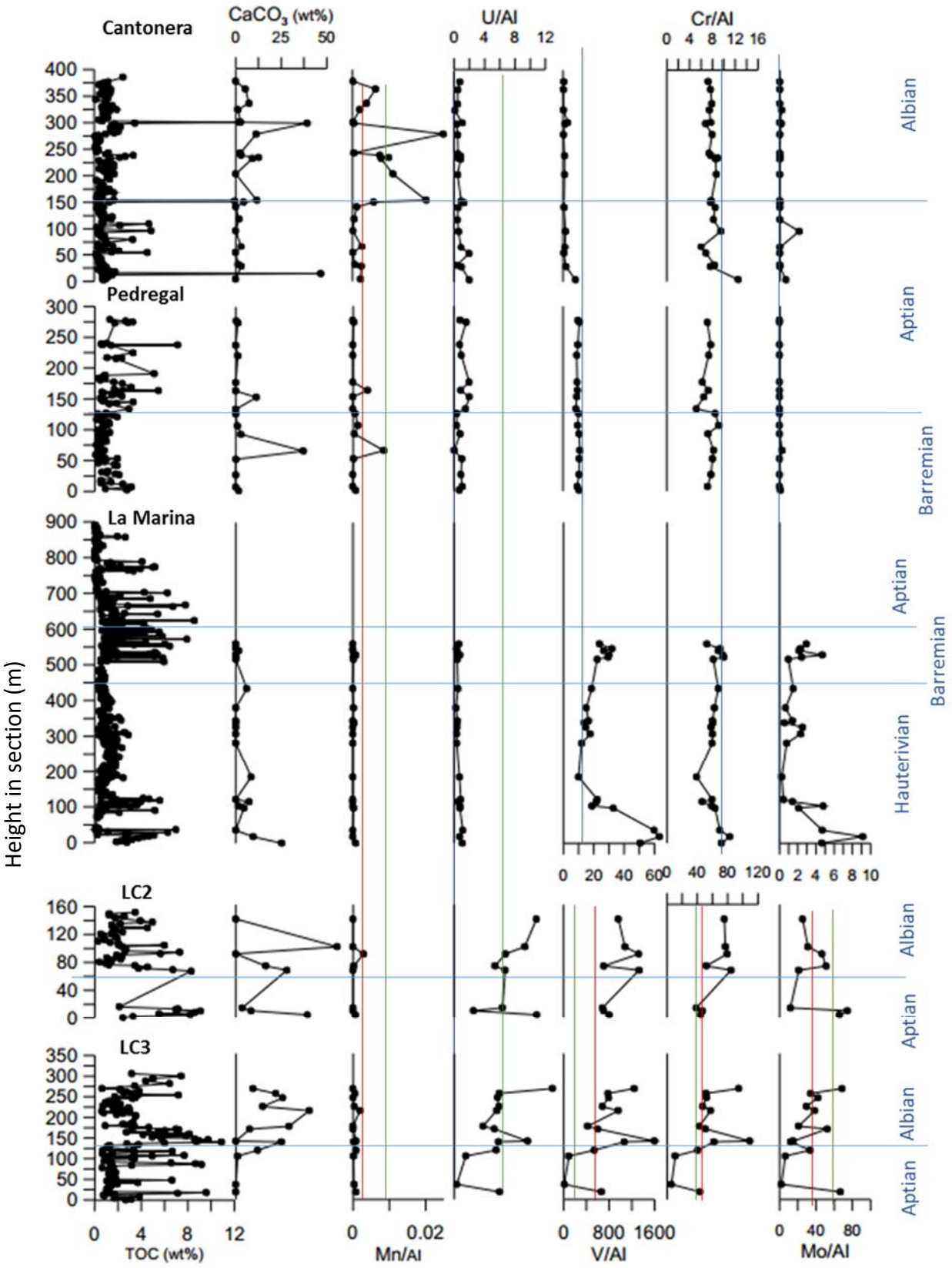

Figure 7.9 TE and Mn redox proxies (measured using XRF) for the Fomeque age sediments plotted against height (m). Blue vertical line is average shale value, green is the C/T mean, and red is a Cretaceous Venezuelan average (Lo Monaco et al.,2002 and Alberdi-Genolet and Tocco, 1999).

7.4 Discussion

The geochemistry, sedimentology and field descriptions suggest very diverse paleoenvironments represented in the studied Fomeque sections. The relatively proximal sections Pedregal and Cantonera, compared to the proximal but more protected La Marina environment and the more open marine LC2 and LC3 settings, show very different geochemistry. As anticipated, detrital proxies are higher (Al, Ti and Zr) in the more proximal Pedregal, Cantonera and La Marina sections, compared to LC2 and LC3, despite similar Si contents (Figure 7.2 and 7.3). In LC2 and LC3, the lack of correlation between Si and detrital Zr and Al, and covariation between Si/Al and TE productivity proxies suggests that the Si is derived from a biogenic source.

The proximal environments can be considered as an intermediate detrital source of TE. Thus comparisons can allow elucidation of detrital versus authigenic enrichments. The Cantonera and La Cristalina sections cover broadly the same time period and represent proximal (shoreface-intertidal plain) versus more distal (inner to outer continental slope) environments in the basin. As can be seen from Figure 7.9, redox sensitive TE (Cr, Mo, U, V) are present in much higher quantities in the distal LC sections (average 180 and 150, 144 and 162, 21 and 17, 2755 and 2038 mg/kg respectively Appendix C.2) compared to the proximal Cantonera (76, 1, 6 and 110 mg/kg respectively, Appendix C.2). This suggests an alternative detrital source of the material, or authigenic enrichments occurring due to basin processes. Figure 7.1 indicates that relationships between redox sensitive elements and Al are decoupled in the distal section, providing further evidence that enrichments within the distal section are not related to a particularly TE rich detrital source (which would also supply Al). Also, when normalised to Al, these differences still exist (Figure 7.9). This is also true of productivity related TE contents. The distal LC sections have much higher contents of Ba, Cu, Ni and Zn (average 3040 and 1070, 57 and 52, 155 and 162, 931 and 1531 mg/kg respectively, Appendix C.2) compared to the proximal Cantonera (average 276, 15, 29 and 70 mg/kg respectively), lower normalised contents (Figure 7.7) and TE contents decoupled from Al (Figure 7.1). Concentrations of Ba are extremely high in two samples from LC2 (8642 mg/kg at 10.5 m and 8872 mg/kg at 139.5 m) far exceeding Brumsack (2006) modern upwelling environments and the C/T at Gubbio and as discussed, a detrital source of this Ba can be discounted. Interestingly, P contents are similar in the proximal (average 0.05 mg/kg) and distal sections (average 0.05 and 0.07 mg/kg), however, again P is decoupled from Al (Figure 7.1g). These comparisons are limited, given the lack of $CaCO_3$ in the Cantonera

section, allowing weathering to leach TE from the outcrop, however, absence of a consistent enrichment of TE in the proximal sections lends evidence for an authigenic (or non-detrital) soure of TE.

It is not possible to confidentally investigate redox and paleo productivity proxies in all different Fomeque locations, as the proxies are not reliable in the very proximal settings and due to possible effects of contemporary weathering. It is tentatively suggested that the majority of deposition in Pedregal and Cantonera sections was under oxic conditions (regular observation of bioturbation at outcrop Figure 7.8), whereas in La Marina the lower 100 m (Hauterivian age) may have experienced lower oxygenation (V/Al greater than average shale and Mo content greater than 25 mg/kg). Redox proxies are likely more reliable in the more distal, carbonate containing LC2 and LC3, and here anoxic bottom waters may have been prevalent throughout Aptian and Albian (Fe_{HR}/Fe_T greater than 0.38, enrichment of redox sensitive TE above average shale). The samples collected from the central basin by Campos-Alvarez and Roser (2007) (Hauterivian to Aptian) also appear to indicate anoxic bottom water conditions, with a particular enrichment of V/Al (average 112 compared to average shale value of 15). There is also evidence of a euxinic water column in these distal sections, with high redox sensitive TE and high Fe_{HR}/Fe_T being matched with Mo contents greater than 100 mg/kg. Although higher Fe_{HR}/Fe_T in the LC2 and LC3 sections suggests an active Fe-shuttle, Fe/Al ratios do not increase from proximal to distal sections (average 0.79 to 0.34 and 0.26 in Cantonera, LC2 and LC3 repsectively), as would be expected in the presence of anoxic waters (Lyons and Severmann, 2006). However, there are some unusual enrichments in Cantonera increasing the average. In these samples, Fe may be enriched due to the very proximal location.

Similarly to the Macanal, the CIA* values in all Fomeque sections (ranging from 77-90) are considerably higher than those recorded on the Atlantic Demerara Rise during the Coniacian-Santonian, which was also receiving detrital material from the Guyana Shield (50 and 65, Flögel et al., 2008). Also, XRD data show that the coarse component of the Fomeque rock is dominated by quartz sand (Table 7.3), suggesting a highly weathered source. This suggests that either paleo chemical weathering intensity was reduced in the Coniacian/Santonian, or that the geological province on the Western flank of the Guyana Shield which supplied detrital material to the EC was significantly more weathered than the Eastern Flank supplying material to the Demerara Rise. Apart from the La Marina section,

average values for CIA* (86 in Cantonera to 90 in LC2) are also higher than modern day Amazon suspended sediment (84, Kronberg et al., 1987), suggesting either a more weathered source or more intensive chemical weathering in the Hautervarian–Albian times compared to modern times, or a slightly less weathered source (like the Andes).

La Marina has considerably higher Na/Al and K/Al contents compared to other sections (Figure 7.3). As discussed in Chapter 6, the EC sediments do not appear to have had significant K or Na added to the samples by hydrothermal fluids, and so the higher Na and K is a depositional signature, likely due to less intense chemical weathering, or a different source of detrital material. The fact that CIA* values in LC3 and LC2 in the far west of the basin are similar to Pedregal and Cantonera in the east (Figure 3.1) does not support a differing climate across the basin (for example, a rain shadow causing greater aridity on one side of the basin). Barremian samples from Pedregal have much higher CIA* than Barremian samples from La Marina (Figure 7.3) suggesting that the regional climate was not more arid during this depositional period. A source of less weathered, more Na and K rich rocks providing material to the EC is, therefore, a more likely scenario. The La Marina samples are located close to the Santander-Floresta high, which was submerged during this depositional period, but may have still affected deposition (Sarmiento-Rojas et al., 2006). A study carried out on Fomeque age samples by Campos-Alvarez and Roser (2007), whose samples were also collected close to the Santander-Floresta high, noted Na/Al (average value 0.03) higher than those recorded in this study for the Pedregal, Cantonera and LC2 and LC3, but still lower than those recorded in La Marina (0.07). Campos-Alvarez and Roser (2007) used rare earth element enrichments to suggest a dominant Guyana Shield source, but also Na-rich volcanic/granitic rocks contributing to the sediments. Other evidence for a less weathered sediment source comes from the investigation of the thin sections, where possible weathered feldspar grains were noted (Figure 7.6). As discussed in Chapter 6, the Santander Massif comprises mafic and felsic metamorphic rocks as well as calc-alkaline plutonic rocks (Sarmiento-Rojas et al., 2006; Garcia et al., 2005) and could have provided more Na and K than the reworked sediments which make up most of the Guyana Shield.

As discussed in Chapter 3, the ages of sediments within the EC are highly uncertain. Also, the $^{13}C_{org}$ is not analysed at sufficiently high resolution to identify potential CIEs relating to OAEs which may have provided a chemostratigraphic framework. However, it is useful to look at geochemical trends across the available timeframe, to see how they compare to global

trends.

There are changes in geochemistry in Pedregal at the Barremian-Aptian Boundary which may be representative of global environmental patterns seen elsewhere. The Late Barremian-Early Aptian period is punctuated by organic matter burial events, but in general this period is marked in the Atlantic and Tethys by a general increase in TOC and redox sensitive trace elements, culminating in the OAE 1a/Selli Event (e.g. Föllmi, 2012; Stein et al., 2011, 2012; Westermann et al, 2013; Bralower, 1994). Similarly to Narvaez et al. (2013), who analysed samples from the northwest of the EC, there is a marked increase in coarse terrestrial material entering the depositional basin (increase in Zr/Al, Si, and calculated sand), combined with an increase in CIA* (Figure 7.3), which suggests an increase in paleo chemical and physical weathering across the presumed Barremian-Aptian boundary. Redox proxies are difficult to interpret in this proximal section, however, there is also a marked decrease in the frequency of bioturbation and an increase in average TOC (from 1.1 wt% in Barremian to 2.3 wt% in Aptian). In the samples examined by Narvaez et al. (2013) this detrital input increase was matched with an increase in TOC and rare benthic fossils, suggesting low oxygen availability at the seafloor. Potentially this shift to more detrital input, increased paleo weathering and decreased oxygen availability may have been a basin-wide feature. The shift towards higher detrital input with an accompanied increase in organic matter burial (possibly due to higher marine productivity) may be an EC expression of the global OAE 1a, which shows similar changes in the Western Tethys (Switzerland, Stein, 2012; Italy, Stein et al., 2011). Volcanic activity is suggested to have increased nutrient input into oceans during this period either directly or via warming of the climate and enhanced hydrological cycle. Here increased paleo chemical weathering is matched with increased detrital input, suggesting that an enhanced hydrological cycle influenced sedimentation in the EC as well during this period.

Deposition in Cantonera and LC2 and LC3 should cover the Aptian-Albian boundary, the approximate period of the OAE 1b (Leckie et al, 2002). In Cantonera, there is an increasing contribution of Al in the sediments towards the tentative stratigraphic boundary, followed by a decrease. This is matched by an opposing trend in calculated sand and Zr, suggesting a decrease in coarse material compared to fine material in the Aptian, and an increase in the Albian. An increase of kaolinite of 10% over the same interval (Table 7.3, Figure 7.3), and a slight increase in CIA* (84-87) suggests that this shift to coarser material is also matched by

an increase in paleo chemical weathering. A sample with very high TOC (15 wt%) is present within the Aptian-Albian boundary area. In the more distal LC3, the opposite geochemical patterns are seen, i.e., a decrease in Al towards the boundary, and a decreasing CIA* matched with a slight increase in Zr/Al. The decrease in Al may be due to an increase in the relative proportions of biogenic material (Si, $CaCO_3$ and TOC/Al and a sustained period (36 m) of high but generally decreasing TOC (10.9-4.6 wt%)). An increase in detrital input at the Aptian-Albian boundary caused by an enhanced hydrological cycle in a warm climate has been noted by Herrle et al. (2003) and Wagner et al. (2007) in the Western Tethys and proto-North Atlantic, both of which are relatively open ocean locations. In the EC, at least in the proximal settings of Cantonera and Pedregal, increased paleo chemical weathering is coupled with increased coarse detrital input (Zr and Si) in a number of depth intervals, suggesting runoff from a humid interior instead of an aeolian source of coarse material. In the more distal LC3, there is a switch from high Al and CIA*, suggestive of humid conditions, to lower CIA* and higher aeolian coarse material, suggestive of drier climates and more intense offshore wind. Opposing trends in the LC3 and Cantonera may be a result of scale (different sample resolution) or it may be the case that coarse material was not being effectively moved across the basin. Conceptual models by Cooper et al. (1995) suggest the Floresta-Santander high limited movement of detrital material from the major source of sediment in the east to the west, starving the Tablazo Magdalena Basin and the MMV of clastic sediments.

Although all samples within the LC3 have geochemistry indicative of bottom water anoxia (Fe_{HR}/Fe_T >0.38), there appears to be an increase in the intensity of anoxia (increase in the enrichments of V, U and Cr) towards the Aptian-Albian boundary, followed by a decrease (in V, U and Cr) later in the Albian (Figure 7.9). Productivity trends in TE (Cu, P, Ni and Zn) and TOC appear to match this, suggesting that anoxia may have been driven by enhanced productivity (Figure 7.7). There is the possibility that Cu, Ni and Zn would have been enriched as sulphides because of decreasing oxygen contents even in the absence of high productivity settings. The concomitant enrichment in P and Si/Al, both of which do not become enriched in anoxic/euxinic setting, provide evidence that these elements became enriched due to higher productivity. Likewise, the enrichment of redox sensitive U and V alongside alternative measures of anoxia (Fe_{HR}/Fe_T) is evidence that these elements did not accumulate sorbed to the high amounts of organic matter. In LC2, the sample resolution is

too poor to see these temporal changes, however, TOC content is highest at the proposed Aptian-Albian boundary and steadily decreases afterwards, supporting an increase then decrease in anoxia/productivity (Figure 7.9). Although TOC is affected by thermal maturity, there are good correlations between TOC and TE redox and productivity indicators in LC2 and LC3 (Table 7.2). Barium contents in the LC2 and LC3 (value) far exceed those measured in the Mid-Late Albian at Olini section (around 200-800 mg/kg) in the south of the EC (Villamil, 1996), which suggests that the exceptionally high contents seen in the EC may be linked to localised high productivity cells, or high productivity only around the Aptian-Albian boundary. As discussed at the beginning of this section, Ba contents (and other TE) do not appear linked to some localised detrital source of high Ba from the hinterland. Hoffman et al. (2008) and Wagner et al. (2007) noted low oxygen but not anoxic conditions in the open proto North Atlantic. In the EC, there is clear support for anoxia and at least intermittent euxinia in the distal LC sections during the Aptian-Albian. In the proto North Atlantic and the Western Tethys, the enhanced monsoonal system which supplied nutrient to the ocean also is assumed to slow ocean circulation, reducing resupply of oxygen to bottom waters. Also, the presence of a freshwater lid reducing vertical mixing has been suggested to explain lower oxygen conditions at the Aptian-Albian boundary in the proto North Atlantic (Erbacher et al., 2001). Here, at least in the distal sections of the EC, there appears to be an increase in aridity suggestive of offshore winds and upwelling which may have caused the increased productivity.

The presence of biogenic/diagenetic Si appears to be endemic to Northern South America, with the Albian Hiló formation partly distinguished from the Aptian Paja formation by the presence of chert and siliceous mudstones (Mojica and Scheidegger, 1984). Enhanced biogenic Si productivity was identified during time equivalent facies in the Pacific (Robinson et al., 2004) and in the Atlantic (Hofmann et al., 2008). In the Pacific at Shatsky Rise, equatorial upwelling was supported by an influx of nutrients to the ocean (possibly due to weathering of volcanic basalts) resulting in distinct periods of enhanced chert deposition during the OAE 1a and b (Robinson et al, 2004). Offshore wind directions are considered the reason for persistent upwelling across the Aptian-Albian boundary off Northwest Africa (Hoffmann et al., 2008), and this similar mechanism may have been working in the EC.

The changes in the Atlantic and western Tethys are short lived, limited to the OAE 1b and lasting around 45 kyr (Wagner et al., 2007). In the EC (in LC2 and LC3) there is a shift to

higher productivity at the Aptian-Albian boundary which, in general, continues to increase for 10s of metres (the higher resolution TOC suggests 50 m). Although sedimentation rate is unknown for this period, a much more persistent increase in productivity is represented in the EC and this may represent a general shift to the more humid climate in the Late Aptian-Early Albian. Wagner et al. (2013) compiled Albian TOC contents from DSDP/ODP drill sites across the North and South Atlantic. The maximum TOC content in LC3 (10.9 wt%) exceeds all maxima noted apart from the Gambian Abyssal Plain, which has a maximum TOC of 25.1 wt% (Hofmann et al, 1999). It thus appears the particular combination of basin configuration/climatic features of the EC during the Aptian-Albian was ideal for organic matter preservation.

7.5 Conclusion

Five sections, three from proximal environments, two from more distal parts of the basin, record Hauterivian to Albian sedimentation in the EC basin. Geochemical proxies for anoxia and productivity are compromised in proximal sediments. Distal LC2 and LC3 sections are extremely enriched in TE related to productivity (calcareous and siliceous), anoxia and occasional euxinia, both of which contributed to relatively high and prolonged organic matter accumulations (average 3 wt% TOC over 300 m). These enrichments in TE and P appear to be unrelated to enrichments in the proximal settings discounting a purely detrital source of TE. A number of climatic and geographical factors may have combined to cause a further enhancement of OM burial around the Aptian-Albian boundary. The humid environment seen in the Tethys, Atlantic and Pacific may have occurred in the EC, increasing runoff and input of nutrients compared to the Early Cretaceous shales. Differently in the EC, potentially diluting clastic material was limited to coastal regions by the submerged Floresta-Santander Massif, allowing enhanced organic matter accumulation. There is evidence that high siliceous productivity in the Albian could have been caused by upwelling of nutrient rich waters as a result of offshore winds. This enhanced productivity may have prolonged anoxia so that it occurred beyond OAE events.

Chapter 8 Chipaque Formation – Cenomanian to Campanian depositional environment in the Eastern Cordillera and beyond

8.1 Research Highlights

- Sediments of Cenomanian to Campanian (incl. OAE 2 and OAE 3) age have geochemical and sedimentological markers of high productivity, especially in the more distal portions of the basin.
- The OAE 2, identified by a distinct positive CIE, occurred in an environment of long term high productivity and anoxia. Siliceous and calcareous productivity and anoxia increased during and after the CIE.
- The OAE 2 sediments corresponded to a period of enhanced paleo chemical weathering and influx of detrital material, suggesting that enhanced OC burial was linked to increased runoff from a more humid continental interior.
- The Caribbean Large Igneous Province (LIP) may have supplied additional nutrients, however not to the extents seen in parts of the Atlantic. However, high sedimentation rates inferred by the thickness of the CIE (11cm/kyr) suggest that the EC acted as a major sink of OC and TE.

In this chapter, inorganic geochemical data and interpretation for five sections located within the Eastern Cordillera (EC) Basin and Middle Magdalena Valley (MMV) are presented. The sections representing Cenomanian to Campanian age sediments document varied depositional environments, from the outer continental slope (La Cristalina 1, LC1) to shoreface (El Crucero and Pescana), as summarised in Table 8.1 based on information provided by Georex (2015). In order to place the results into the wider context of the Late Cretaceous, the global depositional and climatic conditions are summarised. Results of proxies for detrital material, palaeo-productivity and redox conditions are then presented. Finally, one section with a robust age model confirming preservation of OAE 2 is compared to other more open marine equivalents.

8.2 Introduction

The Cretaceous Cenomanian to Campanian period experienced the highest global sea level during the Mesozoic and Cenozoic, with a maximum at the Cenomanian/Turonian (C/T) boundary that possibly reached up to 250 m higher than present day (Haq, 2014). Sea surface and deep ocean temperature were also significantly higher than today, with a maximum in the Cenomanian (sea surface temperatures 35 °C, deep water 20 °C) (Jenkyns, 1994; Huber et al., 2002; Friedrich, 2012. The warmer climate in the Late Cretaceous caused,

amongst other effects, a globally enhanced hydrological cycle with more intense continental paleo weathering and greater runoff (Hallam, 1984; Wilson et al., 2002; Hofmann et al., 2008). Variations in sea level and continental run off should be particularly noticeable in the EC, which, at that time, was a relatively narrow, and shallow siliciclastic basin. The igneous activity, especially the Caribbean large igneous province (CLIP), is thought by some authors (Orth et al., 1993; Snow et al., 2005; Holmden et al., 2016; Turgeon and Creaser, 2008) to have provided the additional TE and nutrients required to sustain elevated productivity over the C/T boundary. Given the location of the EC, close to the CLIP and possibly connected to the Pacific via flooded basins in the south east (Figure 2.10), the effect of TE (especially Cr, Fe, Cu, Co, Zn) should be particularly pronounced.

As shown in Figures 2.9-2.10, high sea levels during the C/T period resulted in the EC being part of a wide epicontinental seaway which stretched from the open Equatorial Atlantic in the North (via the Maracaibo Basin in Venezuela), the Pacific the South (via the UMV), the Magdalena Valley in the West and the Llanos basin in the East (Villamil et al., 1999; Macellari, 1988; Erlich et al., 2003). . The basin was at its widest during the Cenomanian – Campanian period, with marine deposition across a 250 km wide basin (Figure 3.2). From the Santonian, the Colombian Marginal Sea was closed and the Central Cordillera started to uplift constraining the basin in the west (Macellari, 1988; Figure 2.11), however the Central Cordillera may have been a barrier in the West during other periods, as its paleo extent and altitude are poorly constrained. Lithologies vary temporally and spatially, but black mudstones are dominant. The main mudstone units of the Late Cretaceous are the (i) La Luna Formation, well developed in the Magdalena Valley, Maracaibo, and Western Flank of the EC, the (ii) Gacheta Formation in the Llanos Basin, and the (iii) Chipaque Formation in the Eastern Flank of the EC. As well as mudstones, widespread chert and phosphate beds are reported from this period across northern South America (Villamil et al., 1999; Martinez et al., 2003; Martinez and Vergara, 1999; Föllmi et al., 1993; Erlich et al., 1999; Davis et al., 1999). Deposition of mudstone dominated formations terminated in the Campanian, responding to a basin-wide regression. In the EC, this sea level regression is represented by the onset of massive sandstone beds of the Arenisca Dura (Vergara and Rodriguez, 1997).

Cenomanian to Campanian rocks have been intensely studied in northern South America, in Venezuela (e.g. Erlich et al., 1999; Davis et al., 1999; Villamil et al., 1999; Perez-Infante et al., 1996; Mongenot et al., 1996; Tribovillard, 1990; Macelarri and Vries, 1986; Terraza, 2003), in

the Upper Magdalena Basin in Colombia (Martinez et al., 2003; Mann and Stein., 1997; Villamil and Arango, 1998), and within the EC (Martinez and Vergara, 1999; Vergara et al., 1997; Villamil, 1996). These studies used sedimentological evidence, inorganic and organic geochemistry as well as micropaleontology to suggest upwelling and enhanced siliceous productivity from the Cenomanian throughout the majority of the Upper Cretaceous to the Campanian.

Previous studies in northern South America also provide evidence for anoxic bottom waters throughout most of the Cenomanian to Campanian interval (based on sedimentology and organic and inorganic geochemistry). As discussed in Chapter 1, it is possible that the more restricted, land-bound eastern EC sustained prolonged and more sustained anoxia. The new inorganic geochemical data from this study provides new insights into the cause and extent of enhanced productivity and anoxia during this critical time period of globally high carbon burial and greenhouse climate.

Assignment of stratigraphic stages is difficult in the EC, due to the scarcity of age indicative fossils and enhanced thermal maturity, challenging detailed biostratigraphy and palynological analysis (Vergara et al., 1997). However, uniquely in this project, a definitive age can be assigned to one section using chemostratigraphy. A distinct and well known positive carbon isotope excursion (CIE) is identified within LC1, confirming the coverage of ocean anoxic event (OAE) 2 at the C/T boundary (Figure 8.1) at this location. Ages estimated by Ecopetrol and Georex show the whole of LC1 is of Cenomanian age and so identification of the CIE substantially refines this interpretation. As critical new information, identification of the diagnostic OAE 2 CIE clearly defines the C/T boundary in the EC and thus provides an opportunity to compare geochemical characteristics in the EC to time equivalent records elsewhere on the globe. The environment of OAE 2 is well constrained in the open water conditions of Tethys Ocean and the proto North and South Atlantic (summarised in Wagner et al., 2013). Epicontinental basins were important sinks of OM during this period (Schlanger and Jenkyns, 1976) and many have been well studied (e.g. the WIS (Arthur and Sageman, 2005) and in Germany (Hetzel et al., 2011). Less is known about deposition in equatorial epicontinental basins, like the EC.

Within this chapter, temporal and spatial variations in the detrital component of the shales

are investigated, providing clues about multi-scale variations in the hydrological cycle over the Cenomanian-Campanian period. A focus is on observations that support variations in productivity, related to runoff and/or upwelling. Further, redox proxies test if the more restricted conditions in the EC were more susceptible to anoxia and euxinia than in the more northern open and oceanward Maracaibo Basin and other hemipelagic basins in the north. The EC is finally compared to other basins to see if there is a particular enrichment in TE or heightened productivity due to closer proximity to the supply of nutrients from the CLIP.

Table 8.1. Summary of information about the Cenomanian to Campanian sections covered in this chapter (provided by Georex, 2015). Formations introduced in Figure 2.2.

Section	**Noted formation**	**Age**	**Flank of basin**	**Palaeo-water depth (m)**	**Facies interpretation**
La Cristalina 1	Simiti/La Frontera	Cenomanian - Turonian	Western	100	Mid-outer continental slope
La Cristalina 4	Unidad intermedia de Shales/ Ruedas de Carretera	Turonian	Western	120	Distal delta deepening to mid-outer continental slope
Zipa	Ruedas de Carretera	Coniacian – Santonian	Western	110-120	Offshore transition to inner-middle continental shelf – under the influence of upwelling and post diagenetic silicification in the half portion of the section
El Crucero	Chipaque	Cenomanian -Campanian	Eastern	25-50	Repeated successions shallowing from offshore, transition and shoreface, with the dominance of shoreface increasing up Storms concentrate phosphatic fragments
Pescana	Chipaque	Coniacian - Campanian	Eastern	25-30	Repeated successions representing shallowing upward sequences from offshore transition to lower shoreface or intertidal plain

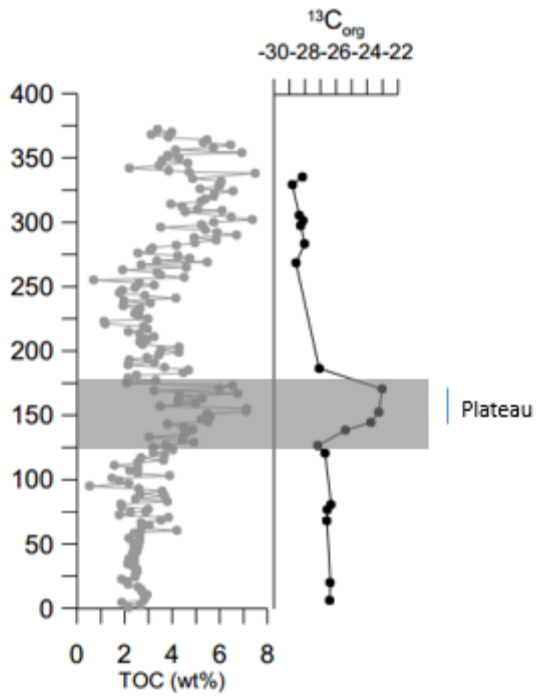

Figure 8.1 $^{13}C_{org}$ of LC1 samples with possible CIE identified as a decrease in $^{13}C_{org}$. OAE 2 in shaded grey box and the C/T boundary at the top of the OAE 2 (from Kolonic, 2005, based on signatures identified at Tarfaya).

8.3 Results

Here, data is presented for the 92 samples from the Pescana, Crucero, Zipa, LC1 and LC4 sections analysed by XRF, CNS/LECO and Fe-speciation, and five samples analysed in thin sections by SEM. Firstly, correlations between elements are presented, in order to better understand which component of the sediment the elements are associated and to allow for selection of appropriate proxies. Following this, spatiotemporal trends in detrital input, intensity of chemical paleo weathering, productivity and redox proxies are explored.

8.3.1 Correlations between main components

As discussed in the previous chapters, a positive correlation with Al (a purely detrital element, mainly found within clay in marine sediments) can help identify elements which likely arrive at the sediment associated with detrital material. All correlation coefficients are included in Table 8.2. In Pescana, the most proximal of locations according to sedimentological interpretation (Table 6.1), Al correlates positively with Ti, K, Cr and V (correlation coefficients 0.9, 0.6, 0.6 and 0.6, respectively, Figures 8.2b, e, j, and n). In Crucero, only Ti correlates with Al (correlation coefficient 0.5, Figure 8.2b). In Zipa, considered more distal than Crucero and Pescana, Al correlates with Ti, Fe, Mg, Na, K as well as Cr, Cu, Mo, V and Zr (with correlation coefficients of 0.9, 0.8, 0.7, 0.5, 0.9, 0.9, 0.8, 0.8., 0.8 and 0.6, respectively, Figures 8.2b, f, c, d, e, j, l, n and p). In the more distal LC1, Al correlates with Ti, Fe, Mg, K, P, Cr and Zr (correlation coefficients of 1.0, 0.7, 0.8, 0.8, 0.6, 0.8

and 0.8, respectively, Figures 8.2b, f, c, e, g, j and p). In LC4, also distal, Al correlates with Ti, Na, K, P and Zr (correlation coefficients of 0.8, 0.5, 0.9, 0.7 and 0.7, respectively, Figures 8.2a, d, e, g and P).

Correlations with Si help distinguish its source – within clay, the coarse fraction (as quartz sand and silt) or as biogenic Si. All of the aforementioned elements, which correlate positively with Al, correlate negatively with Si in Crucero, Pescana and Zipa (see Table 8.2). Si correlates negatively with Al in Crucero, Pescana and Zipa (correlation coefficients -0.9, -0.9 and -0.7, respectively, Figure 8.2a), supporting a dominant source of Si from the clay fraction. Si and Zr do not strongly correlate in any of the sections (Table 8.2, Figure 8.2q). As discussed in Chapter 3, Zr (usually within the coarse fraction) and Si should correlate if Si was to be used as a measure of sand content. If Zr and Si do not correlate, it is possible that there is a source of Si outside of the coarse fraction (e.g, biogenic opal). Going forward, calculated sand content is therefore not presented for the Chipaque Formation sediments. As can be seen in Figure 8.1q, in LC4, LC1 and Zipa, Si increases without a corresponding increase in Zr. In Pescana and Crucero, there is a general increase in Zr with an increasing Si, but it is not linear, with some samples having much higher Zr for the corresponding Si. One of the samples within LC4 (at depth 427.5 m) is enriched in Zr (178 mg/kg compared to a section average of 79 mg/kg) possibly due to volcanic ash (noted as taken from a tuff bed in the field observations, Georex, 2015).

If an element accumulates alongside TOC, it could provide information about the accumulation mechanism for organic matter. Only LC1 and Pescana have TOC contents which have been less altered due to thermal maturation, having not passed through the oil window (Table 3.5). Correlations with TOC may therefore not provide useful information. In Pescana, there is a positive correlation between TOC and Mo (correlation coefficient of 0.84). There are, however, very low concentrations of TOC (average 0.4 wt%, SD 0.3) and Mo (average 1.0 mg/kg, SD 2.9) in this section, so caution must be taken when interpreting this relationship. In LC1 there is a positive correlation between Mo, U and TOC (correlation coefficient 0.51 to 0.57, respectively) and the productivity proxies Cu and Ni (0.57 and 0.51, respectively). In LC1, there is a negative correlation between TOC and the productivity proxy Ba (correlation coefficient -0.55) as well as with the detrital elements Na and K (correlation coefficients -0.72 and -0.59, respectively). There are no strong positive correlations between TOC and detrital elements or the nutrients P and Fe in any of the sections.

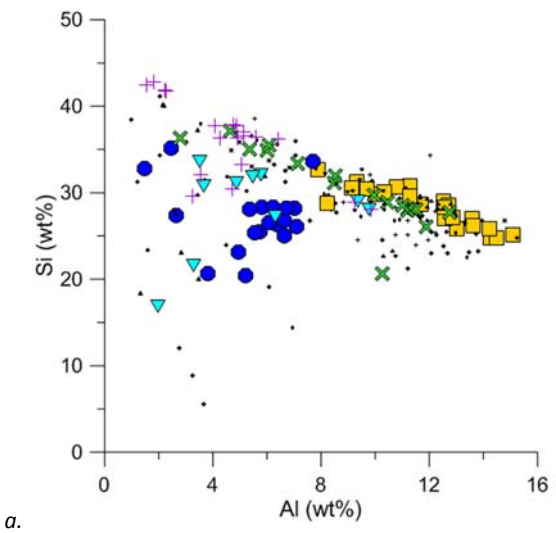
Si (wt%)
Al (wt%)
0
10
20
30
40
50
0
4
8
12
16

a.

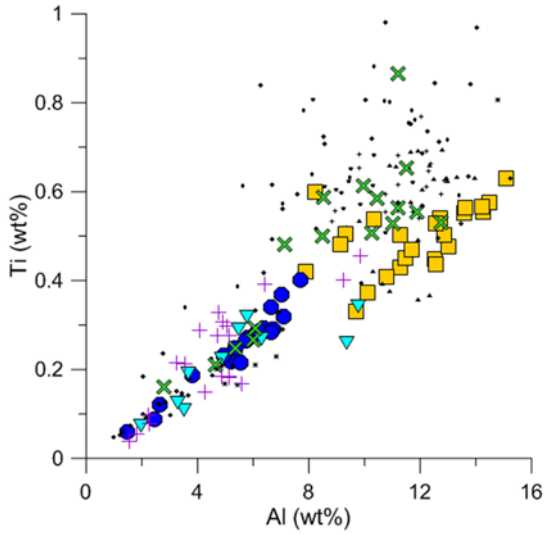
Ti (wt%)
Al (wt%)
0
0.2
0.4
0.6
0.8
1
0
4
8
12
16

b.

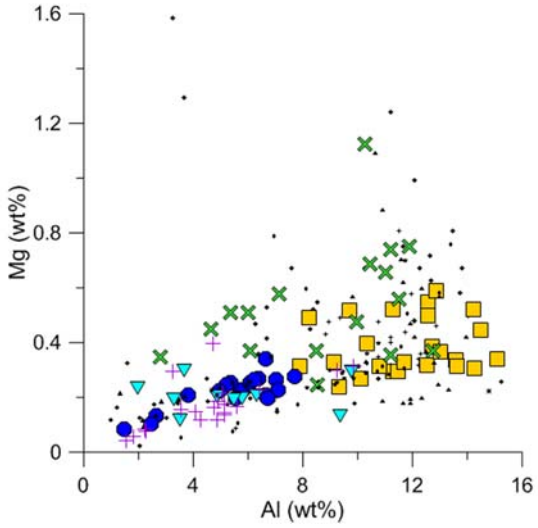
Mg (wt%)
Al (wt%)
0
0.4
0.8
1.2
1.6
0
4
8
12
16

c.

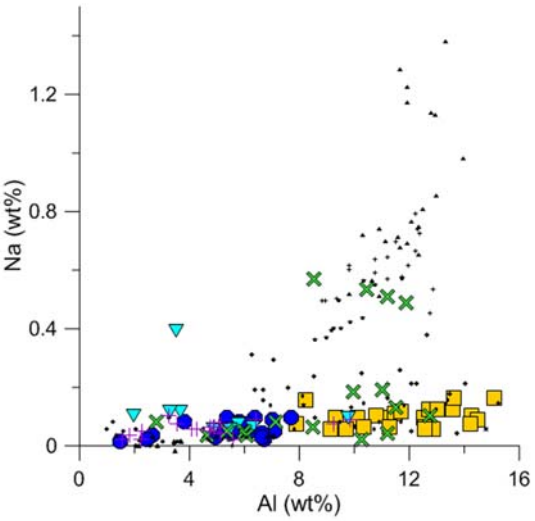
Na (wt%)
Al (wt%)
0
0.4
0.8
1.2
0
4
8
12
16

d.

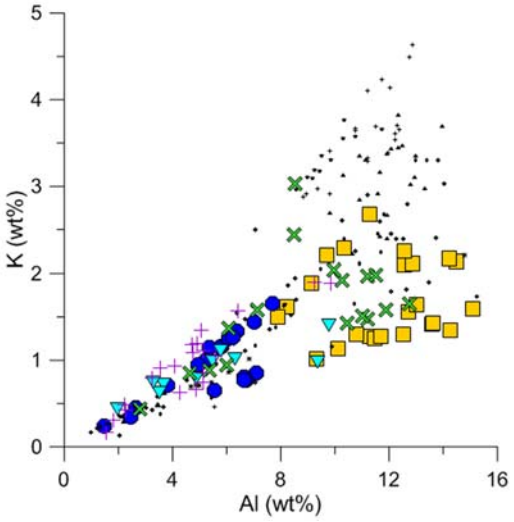
K (wt%)
Al (wt%)
0
1
2
3
4
5
0
4
8
12
16

e.

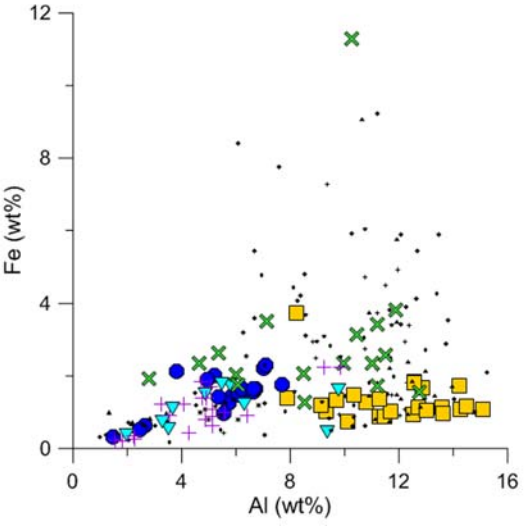
Fe (wt%)
Al (wt%)
0
4
8
12
0
4
8
12
16

f.

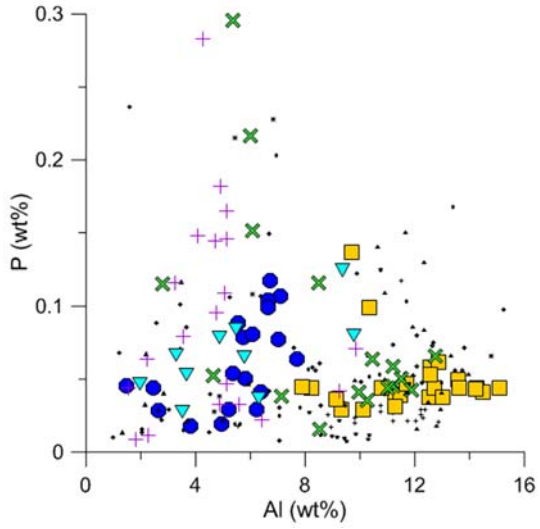
P (wt%)
Al (wt%)

g.

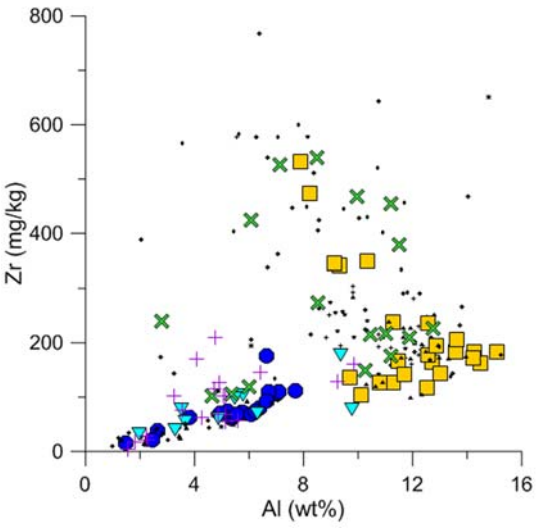
Zr (mg/kg)
Al (wt%)

h.

i.

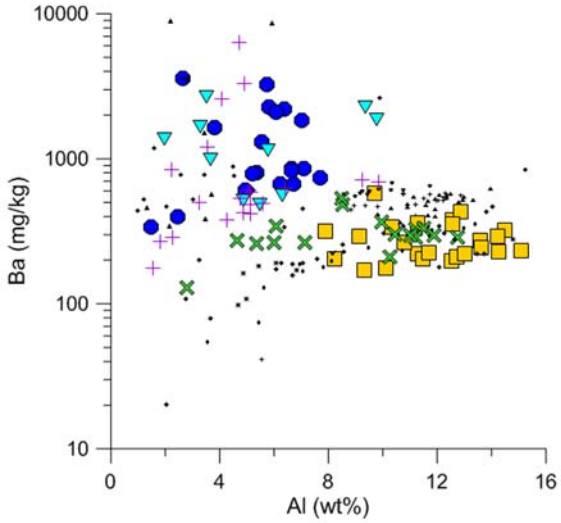
Ba (mg/kg)
Al (wt%)

j.

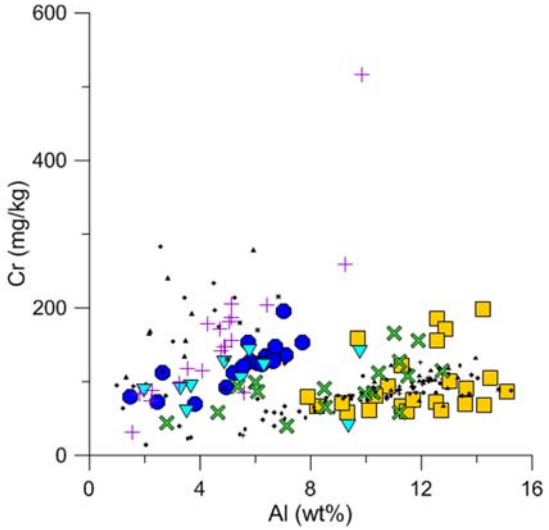
Cr (mg/kg)
Al (wt%)

k.

l.

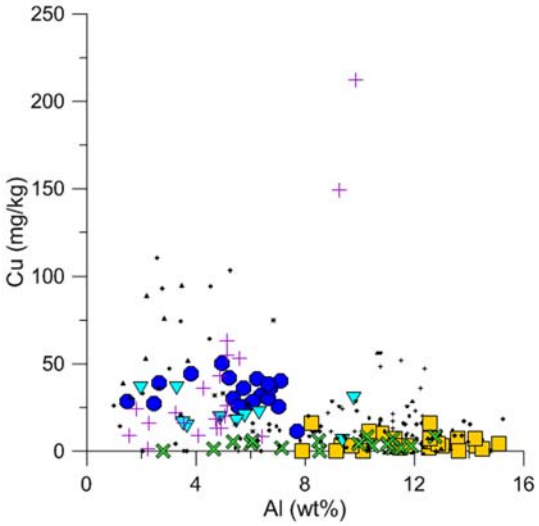
Cu (mg/kg)
Al (wt%)

m.

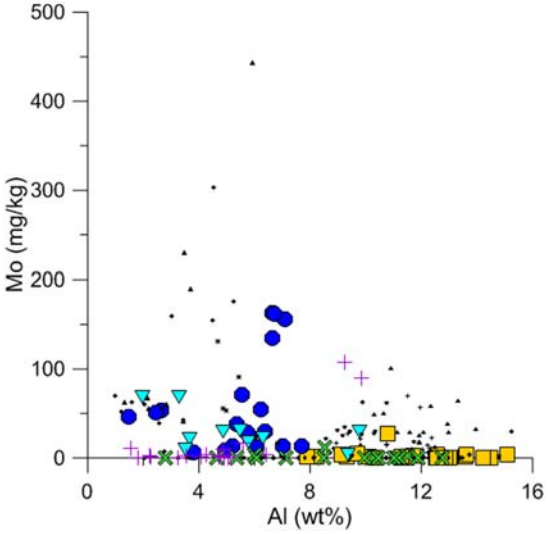
Mo (mg/kg)
Al (wt%)

n.

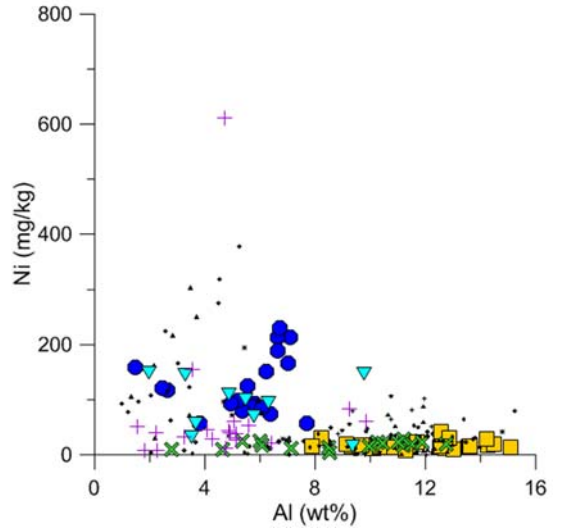

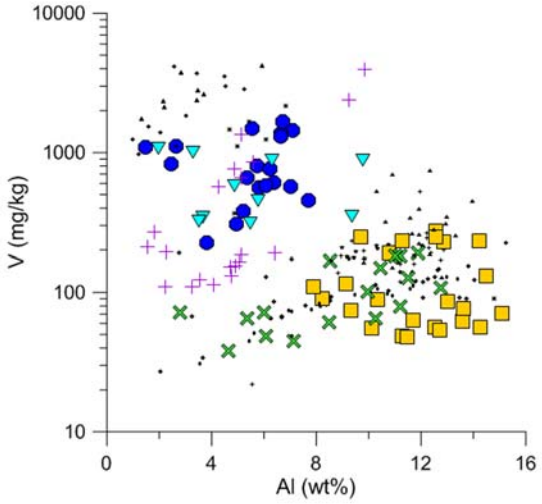

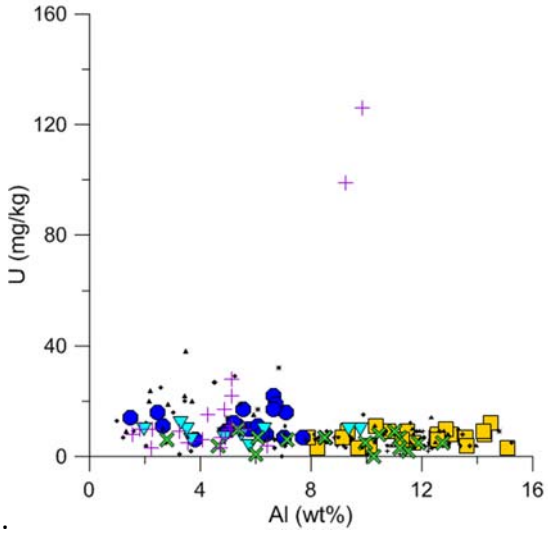

o.

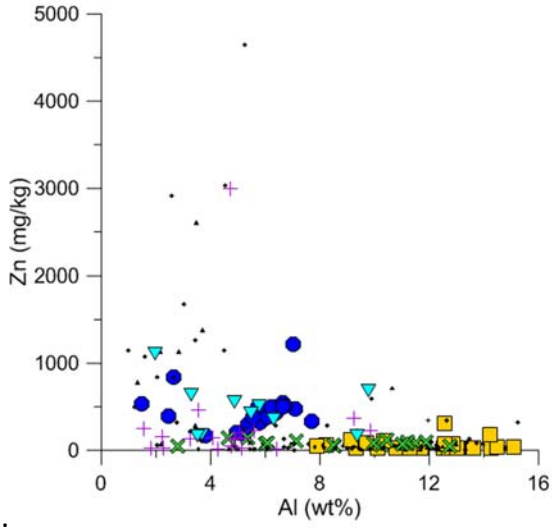

p.

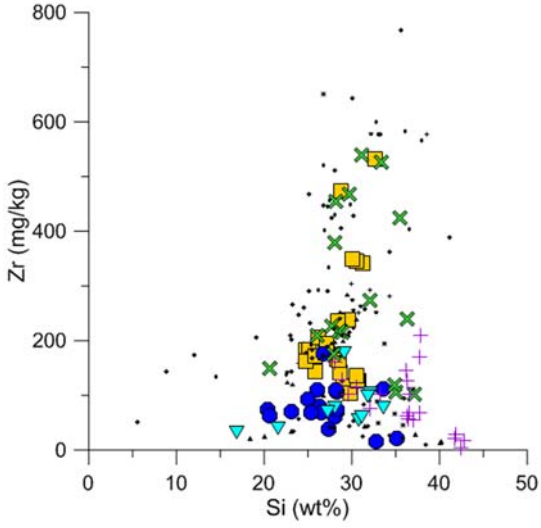

q.

Figure 8.2a-q. Correlations of elements with Al and Si. Contents measured using XRF. Coloured points are from the Chipaque, small black points are from the rest of the EC data set. Yellow squares Crucero, LC1 blue circle, LC4 light blue triange, green crosses Pescana, purple crosses are Zipa. Note that correlations between Al and Ba and V are shown with a logarithmic for the TE.

Table 8.2 Pearson's correlation coefficient for elements when correlated with Al, Si and TOC. IC and S from LECO and CNS analysis, other elements from XRF. Red data is good to very good positive correlations. Green data is good to very good negative correlations.

		Si	Al	Fe	Ti	Mn	Mg	Ca	Na	K	P	Ba	Co	Cr	Cu	Mo	Ni	V	U	Zn	Zr	$CaCO_3$
TOC	Pescana	**0.15**	**-0.23**	**-0.06**	**0.02**	**0.09**	**-0.32**	**0.10**	**0.33**	**0.40**	**-0.21**	**0.27**	**-0.23**	**-0.40**	**-0.41**	**0.84**	**-0.55**	**0.12**	**0.13**	**-0.38**	**-0.01**	**0.07**
	Crucero	-0.27	0.26	0.12	0.17	0.05	0.26	-0.01	-0.01	-0.02	-0.18	0.06	0.17	0.40	0.05	-0.05	0.53	0.23	0.13	0.30	-0.06	0.57
	Zipa	**-0.49**	**0.69**	**0.36**	**0.40**	**-0.13**	**0.31**	**-0.23**	**0.32**	**0.47**	**0.26**	**-0.16**	**-0.25**	**0.78**	**0.78**	**0.67**	**-0.02**	**0.76**	**0.74**	**-0.05**	**0.16**	**-0.22**
	LC1	-0.32	-0.21	0.09	-0.26	0.44	-0.22	0.22	-0.72	-0.59	0.09	-0.55	0.79	-0.44	0.57	0.51	0.51	0.33	0.57	-0.27	0.17	0.29
	LC4	**-0.56**	**-0.33**	**0.00**	**-0.32**	**-0.03**	**0.31**	**0.51**	**-0.55**	**-0.12**	**-0.22**	**-0.02**	**-0.38**	**0.30**	**0.87**	**0.83**	**0.84**	**0.71**	**0.47**	**0.61**	**-0.73**	**0.39**
Si	Pescana		-0.86	-0.63	-0.72	-0.57	-0.68	0.43	-0.28	-0.51	0.52	-0.08	-0.56	-0.46	-0.44	0.11	-0.41	-0.47	0.32	0.22	-0.02	0.02
	Crucero		**-0.88**	**-0.01**	**-0.62**	**0.00**	**-0.25**	**0.03**	**-0.37**	**-0.14**	**0.13**	**0.07**	**-0.20**	**-0.28**	**-0.03**	**0.24**	**-0.21**	**-0.01**	**-0.13**	**-0.10**	**0.41**	**-0.10**
	Zipa		-0.72	-0.84	-0.73	-0.29	-0.90	-0.51	-0.68	-0.77	-0.23	-0.30	-0.31	-0.65	-0.58	-0.54	-0.40	-0.52	-0.56	-0.37	-0.55	-0.53
	LC1		**-0.18**	**-0.56**	**-0.11**	**-0.64**	**-0.40**	**-0.75**	**-0.11**	**-0.07**	**0.11**	**-0.22**	**-0.51**	**0.04**	**-0.69**	**0.05**	**0.12**	**0.19**	**0.11**	**0.28**	**-0.20**	**-0.79**
	LC4		0.34	0.51	0.51	-0.01	-0.22	-0.89	0.08	0.40	0.12	-0.03	0.19	0.08	-0.77	-0.85	-0.66	-0.86	-0.55	-0.77	0.47	-0.88
Al	Pescana			**0.20**	**0.86**	**0.11**	**0.36**	**-0.63**	**0.41**	**0.60**	**-0.54**	**0.32**	**0.49**	**0.57**	**0.36**	**-0.04**	**0.36**	**0.62**	**-0.12**	**-0.15**	**0.16**	**-0.41**
	Crucero			-0.28	0.51	-0.34	0.14	-0.37	0.26	0.11	-0.13	-0.06	-0.13	0.29	-0.06	-0.16	0.04	0.02	0.20	0.01	-0.62	0.14
	Zipa			**0.80**	**0.85**	**-0.01**	**0.66**	**-0.21**	**0.50**	**0.92**	**0.02**	**0.04**	**-0.06**	**0.86**	**0.81**	**0.77**	**0.06**	**0.79**	**0.79**	**0.05**	**0.61**	**-0.18**
	LC1			0.71	0.97	-0.16	0.83	-0.48	0.46	0.77	0.56	-0.04	0.02	0.79	-0.19	0.27	0.20	0.08	0.00	0.08	0.81	-0.35
	LC4			**0.34**	**0.82**	**0.03**	**0.02**	**-0.72**	**0.51**	**0.87**	**0.66**	**0.15**	**0.93**	**0.14**	**-0.36**	**-0.54**	**-0.19**	**-0.16**	**0.03**	**-0.28**	**0.71**	**-0.68**

8.3.2 Compositional Difference

There are some differences in the proportions of the main components of the samples between the studied sections (Figure 8.3). Aluminium content is higher in proximal sections (Pescana average 8.6 wt%, SD 3.0; Crucero 11.8 wt%, SD 2.0) compared to distal sections (Zipa average 4.7 wt%, SD 2.1; LC1 5.5 wt%, SD 1.7; LC4 5.4 wt%, SD 8.6) (Figure 8.3). On the other hand, there is less notable difference in the Si content of the proximal compared to the distal sections (Pescana average 30.1 wt%, SD 4.3; Crucero 28.3 wt%, SD 2.2; Zipa 35.9 wt%, SD 4.4; LC1 27.1 wt%, SD 3.8; LC4 28.2 wt%, SD 5.2, Figure 8.3). Calcium carbonate is very low in the majority of samples from Pescana, Crucero and Zipa, but makes up a considerable proportion of the most distal LC samples (LC1 average 19.9 wt%, SD 8.6; LC4 average 16.4 wt %SD 16.9). The TOC content of samples appears to increase with distance from shore (Figure 8.3) from Pescana (average 0.4 wt%, SD 0.3), Crucero (0.8 wt%, SD 0.5), Zipa (average 1.6 wt%, SD 1.2), to the most distal LC4 (average 2.6 wt%, SD 1.0) and LC1 (average 3.6 wt%, SD 1.5).

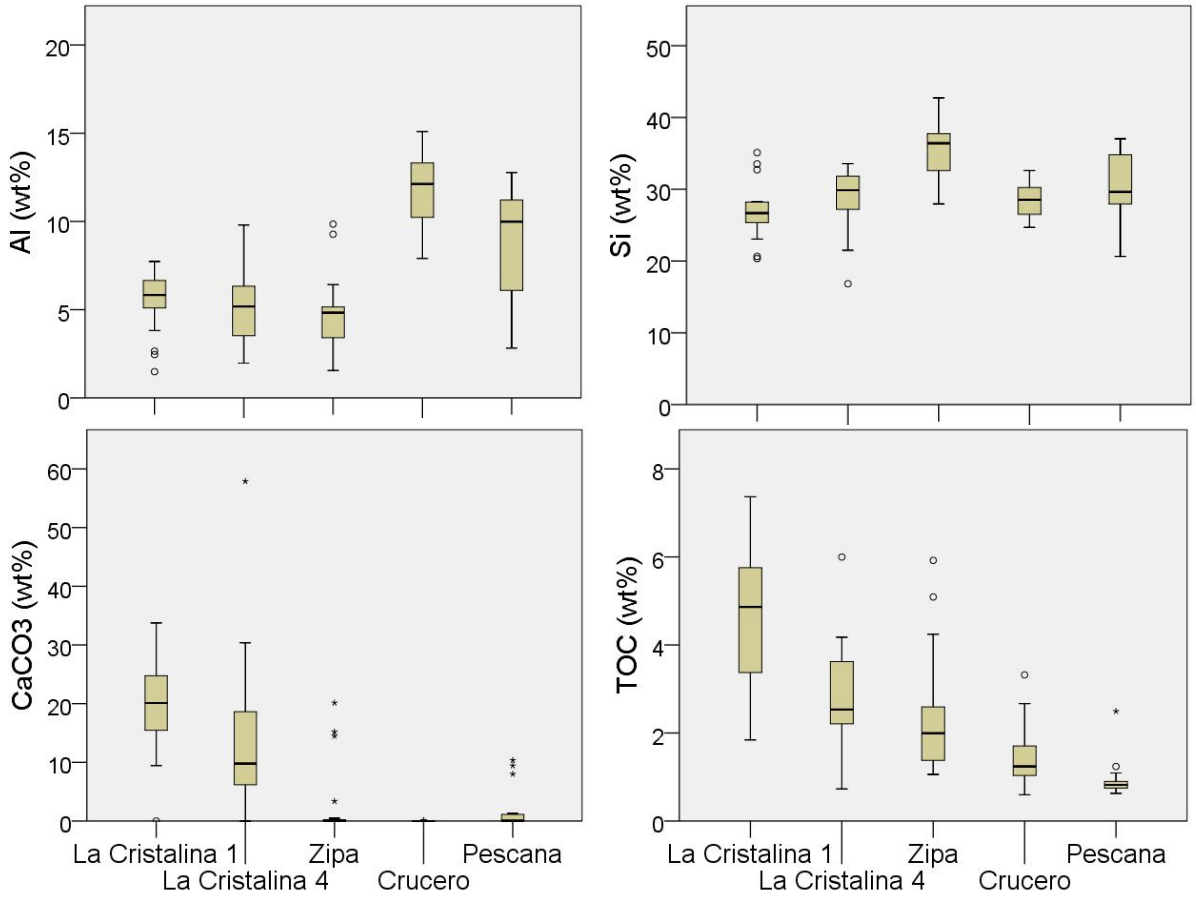

Figure 8.3. The composition differences between samples from different locations. A range of data for Si, Al, $CaCO_3$ and TOC (all wt%) for Chipaque age sediments from proximal on the right to distal on the left.
Bold line within the box is median, box edges and the 1st and 3rd percentiles.

8.3.3 Detrital proxies

Considering detrital proxies in Crucero (Figure 8.4), the first sample has higher Al normalised Ti and Zr, perhaps suggesting higher coarse detrital input. Between approximately 71 and 147 m, there is strong variability in Si and Al, although this may be due to the higher sampling resolution in this area. From 348-385.5 m, there is consistently higher Ti/Al, matched with higher Zr/Al and Si, suggesting a greater influence of coarse detrital material in this area. Aluminium normalised K and Na also show some increase during this period. SEM images were taken with BSE (Figure 8.5) from a sample at 79 m with representative Si (26.9 wt% compared to average 28.3 wt%). There is abundant fine to coarse quartz silt in a clay matrix. Volcanic sediments are also present, with a possible bentonite layer was observed at 530 m (Georex, 2015, orange rectangle in Figure 8.4).

In Pescana, the first sample has lower Si and Al normalised Ti, Zr, K and Na. After this, there is a steady increase in Si, Ti and Zr until 35 m. Si and Al remain relatively steady until there is a shift to higher Si, opposing in Al, at 148 m (Figure 8.4). The increase in Si is matched with an increase in Zr/Al and a modest increase in Ti/Al and is not within or near an area of the section assigned a shoreface facies. In general, these values then decrease (with opposing Al increase) towards the top of the Pescana section. Changes in K/Al mostly follow Ti, however, Na/Al does not follow any detrital element. In SEM, a sample from 255.5 m (within the high Si area) contains abundant silt and fine sand-sized quartz, as well as granular micro quartz (Figure 8.6). Silt-size zircon crystals are also present among the quartz crystals. At 133 and 211 m, thin (<0.5 m) phosphorite beds are present with associated faecal pellets, fish skeletal fragments and teeth as well as ichnofossils.

In Zipa, there is a gradual increase in Si with opposing decrease in Al from the base of the section to 116 m (Figure 8.4). A sample from 74.5 m shows pervasive granular micro quartz in SEM, which comprises the majority of the thin section, with only occasional detrital silt-size grains of Si (Figure 8.7). Above 116 m, Al increases, but the values remain lower than at the bottom of Zipa. Aluminium normalised Ti and K values increase in this uppermost section (from 150 m) and remain steadily high. Normalised values Zr also peak in the top half of the section. Aluminium normalised Na also increases at 150 m, but then behaves differently from other detrital elements, and steadily decreases after this.

In LC4, there is much variation in the detrital proxies through the section (Figure 8.4). The varying carbonate content throughout the section is mostly matched with opposing trends in

Al and Si (Figure 8.4). There are samples with high carbonate and Si, matched with high Aluminium normalised Ti (439.5 and 780.5 m). The samples with the highest Zr/Al are from within volcanic sediments (a tuffaceous bed 427.5 m and 433.5 m, marked with yellow bands in Figure 8.4).

In LC1, there is a steady decrease in Al and Si (which is matched with a decrease in Ti/Al and K/Al) to a low at 269 m, with an opposing general increase in calcium carbonate (Figure 8.4). Above 269 m, Al remains low until 330 m, but Si increases to a peak at 186 m, before decreasing at 330 m. Aluminium normalised Zr changes differently to Si. A sample taken from 336 m, when viewed in SEM-BSE (Figure 8.8) is dominated by microcrystalline quartz, however, Ca is also pervasive through this quartz matrix, and calcite is present as infilled shells/tests. Within the CIE (orange box in Figure 8.4), there is a steady decrease in Al. Calcium carbonate jumps from 15.8 – 33.8 wt% within the CIE and stays around 30 wt% for the rest of the CIE. Silica and Al normalised Zr are higher in this first portion of the CIE, before reducing at the same depth that $CaCO_3$ increases.

In Pescana and Crucero, there are massive sand beds which represent shoreface facies and the most regressive part of a sea-level cycle (grey boxes in Figure 8.4). The samples taken at these depths are from thin mudstone beds (1m to 0.1 m) in between larger sand beds. It could be predicted that these mudstones would have a consistently higher Si, but they do not. This suggests that their deposition represents repeated sharp decreases in the coarse input. In Pescana this fits with descriptions of mudstones without silt or sand, and an absence of fining upwards sequences (Georex, 2015). In Crucero, the Georex (2015) observations of fine laminations of silt and sand in mudstones throughout the column. Also in thin section under SEM-BSE, a coarser layer with randomly orientated grains is observed (Figure 8.5), perhaps representing a storm event. This sample was taken from a location not close to shoreface facies (79 m). Short influxes of coarser material may be common during shale deposition in these more proximal settings, causing a relatively steady bulk Si content when samples are homogenised (Figure 8.4).

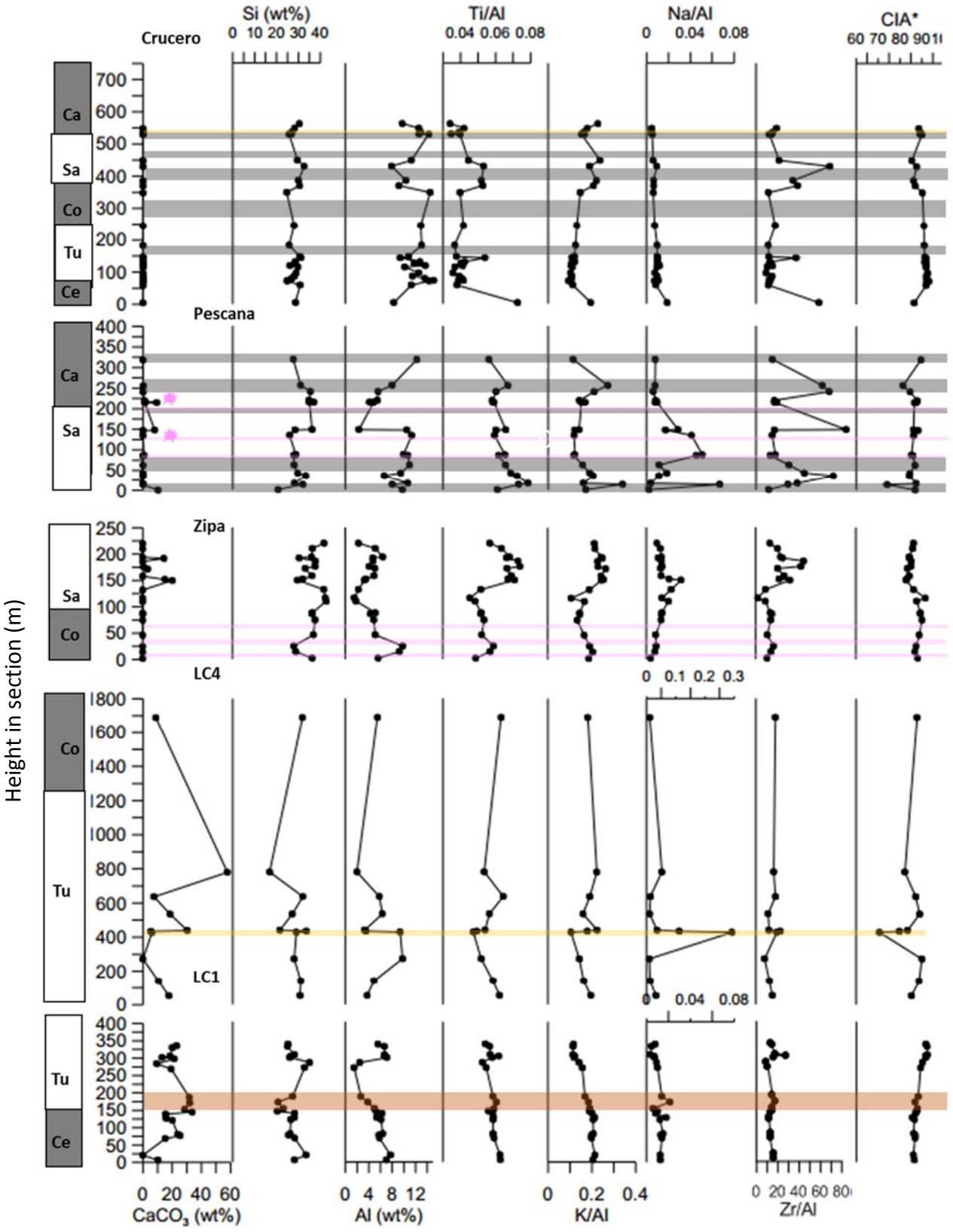

Figure 8.4 Variation in detrital proxies and major rock components (measured using XRF) and sand fraction (based on Si/Al, see Chapter 3 for methodology) for the Chipaque age sediments plotted against height in the section (m). Pink lines are p phosphatic lenses, grey boxes are sand beds, orange lines are tephra and the red box is the proposed C/T boundary.

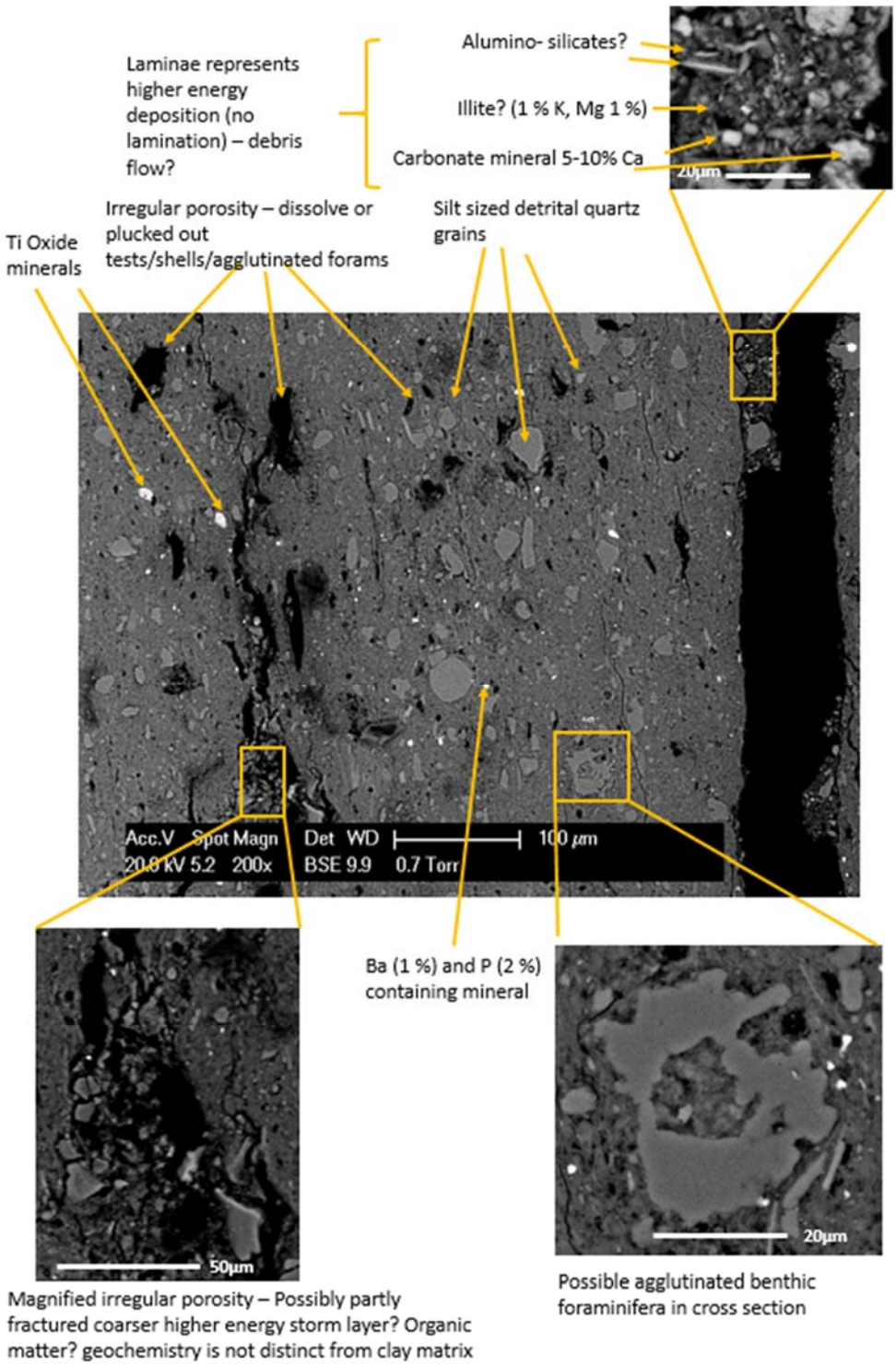

Figure 8.5 SEM BSE image of Crucero sample from 79 m in thin section. Features identified are irregular sized silt sized detrital quartz grains, silt sized Ti oxides, irregular porosity (possible dissolved/plucked out tests) and a possible agglutinated benthic foraminifera. Grains appear to sit within clay matrix in a relatively well laminated manner, and there are some planar features, however there are darker beds where grains are more irregular, which may represent a storm bed.

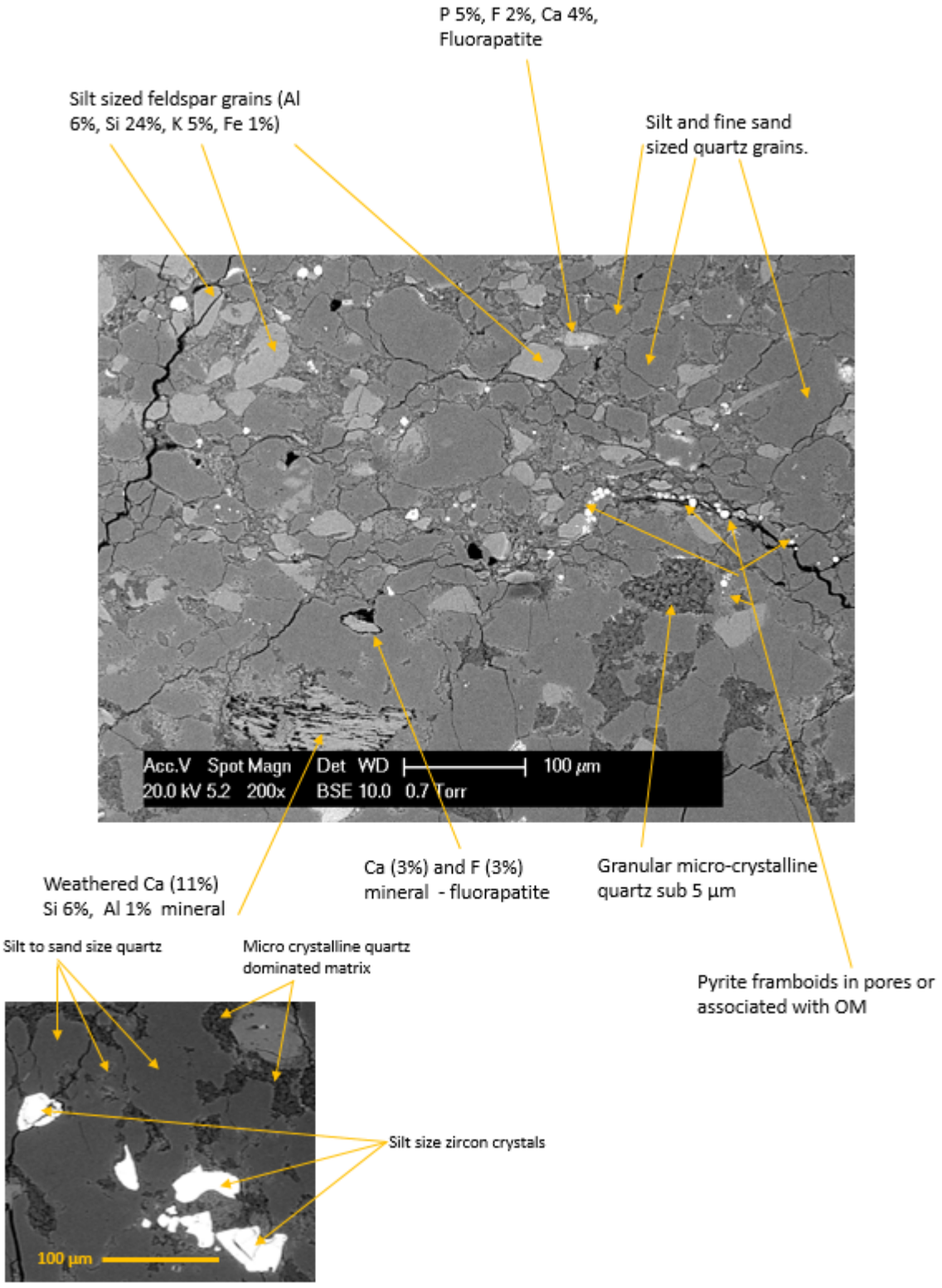

Figure 8.6 SEM BSE image of thin section from Pescana section from 255.5 m. A variety of silt and sand sized minerals present, including feldspars, fluoroapatite and zircon.

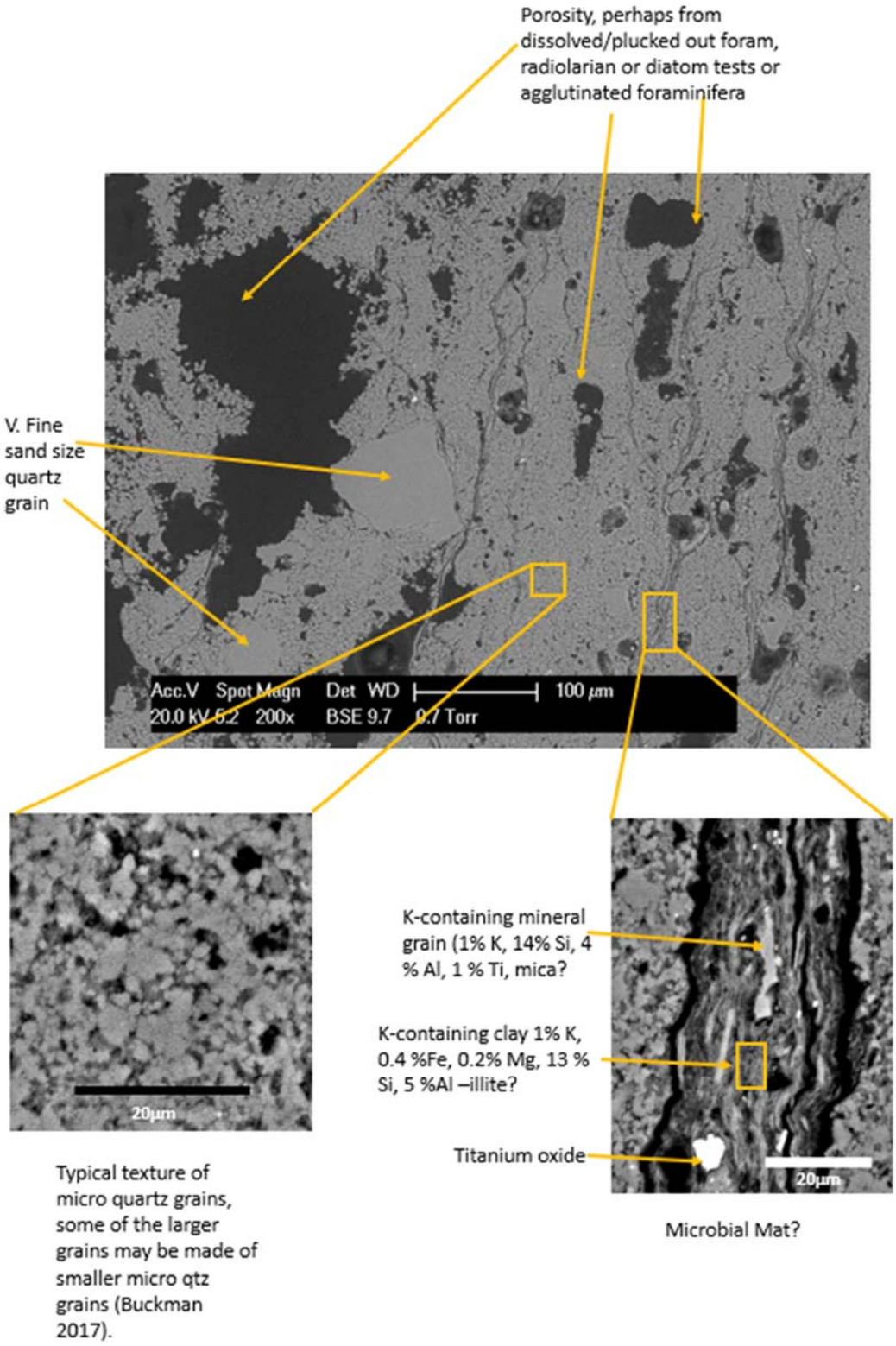

Figure 8.7 SEM BSE image of Zipa 74.5 m in thin section. Features identified are pervasive micro crystalline quartz, possible microbial mats/ clay layers and irregular porosity, likely caused by dissolution/plucking out of tests.

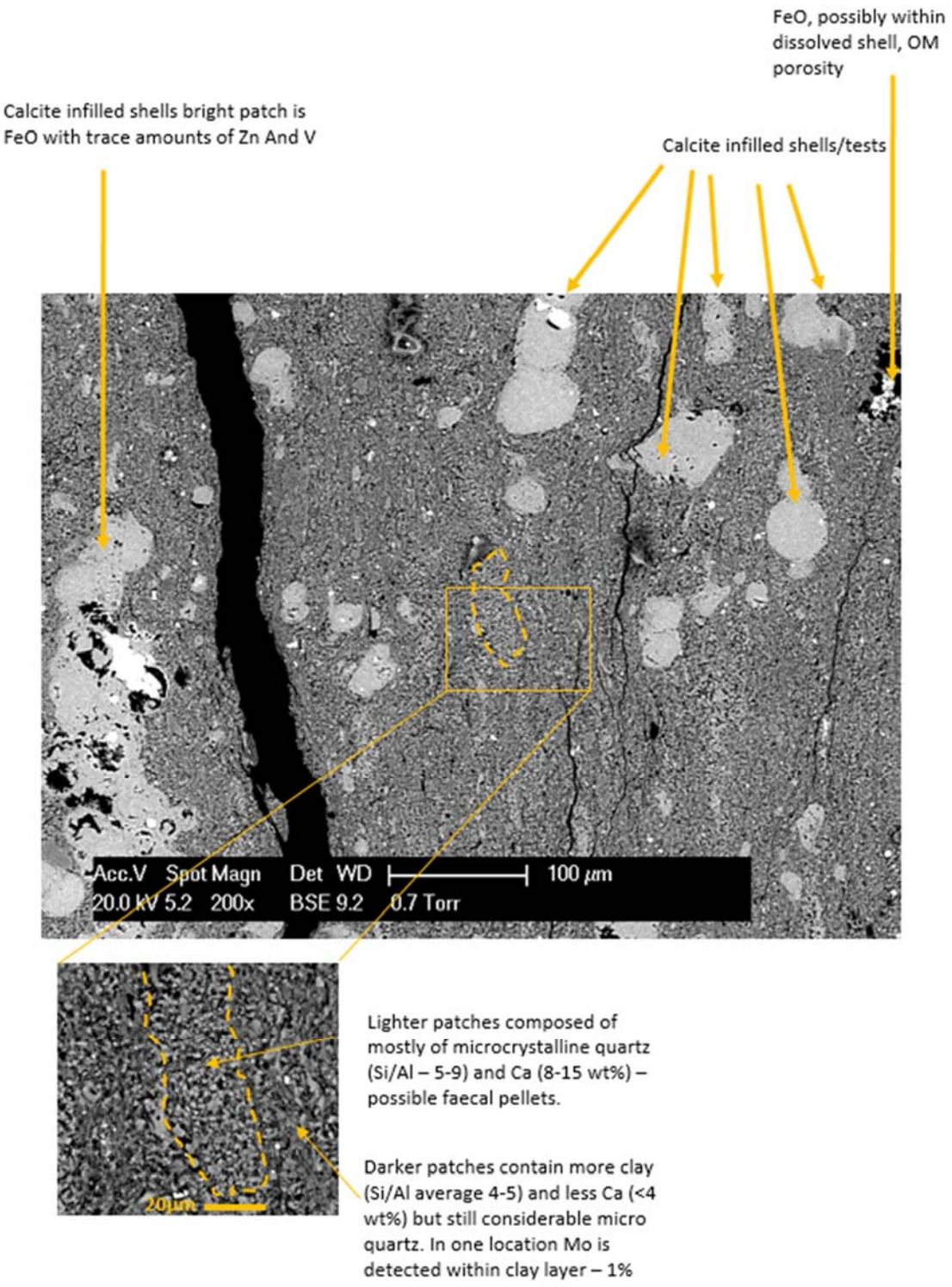

Figure 8.8 BSE SEM images of thin section from LC1 at 336 m. Key features identified are: many carbonate infilled tests/shells; irregular porosity which could be OM; possible faecal pellets; micro quartz abundant in the clay matrix but concentrated further in faecal pellets

8.3.4 Paleo chemical weathering Intensity

As discussed in Chapter 3, as well as being predominantly detrital, K and Na are generated by chemical weathering of feldspars, and together with CIA*, can provide information about the extent of chemical paleo weathering in the hinterland.

In Zipa, Al normalised K increases from 150 m and is matched with a decrease in CIA* from an average of 88.7 before 150 m to 84.6 after. Aluminium normalised Na behaves differently and peaks at 150 m at 0.03 before reducing again to average values (0.01). Kaolinite remains low throughout the Zipa section (only one sample has kaolinite above the LOQ, 88 m, 12 wt%). In LC4, Al normalised K peaks at 439.5 m and 780.5 m. Samples were taken from a tuff layer (at 427.5 and 433.5 m) have considerably higher Na/Al (0.29 and 0.11 respectively) than section average (0.06) and have the highest Na content in the EC sample set (2.74 and 0.39 mg/kg respectively). This high Na value distorts the CIA to much lower values at this point. Without these two values, CIA* is relatively constant (average 86.7, SD 2.8). In LC1, the CIA* gradually increases from 86.4 at the base of the section to 92.2 close to the top, and this is coupled with gradual decreases in Al normalised K and Na. Within the CIE, K/Al and Na/Al values fall, however, Na values increase again at 171 m. In Crucero, paleo chemical weathering indicators (kaolinite content, Na/Al, K/Al CIA*) are relatively constant until 370m, where there is an increase in K/Al (from average 0.12 to above 0.2) and a corresponding decrease in CIA* (from 91.5 to an average of 86.5). Within this area, there is also a kaolinite content is also lower (20 wt% compared to 50% lower in the section). In Pescana, there is a sharp increase in paleo chemical weathering proxies (CIA*, Na/Al and K/Al). Apart from this, Al normalised Na and K change differently, with K decreasing to a minimum of 0.13 at 85.5 m and then recovering, whilst Na increases to a maximum of 0.05 at 87 m before decreasing to the end of the column. The overall effect on the CIA is minimal, apart from a dip to 82.8 at 255.5 m in a sample with elevated K (to a value of 0.29). Kaolinite varies considerably (Table 8.3), and is apparently unrelated to K and Na, with samples with high contents (147, 240.5 and 255.5 m) corresponding to high K/Al and separately Na/Al. A sample from 255.5 m was examined in thin section by SEM-BSE and silt-sized K-containing mineral grains (assumed to be feldspar) were abundant. This sample also contains the highest amount of feldspar measured in the EC with XRD at 7%.

When comparing sections, Crucero has the highest CIA*(average 90.1), suggesting that this section received sediments from the most weathered source, or from a period/location of less intense chemical paleo weathering. However, the sections are not dramatically different, with averages ranging only from 90.1 to 86.6 (in Zipa) when tuff samples are not considered. Neither is there much variation in each section, with a maximum standard deviation of 3.4 (Pescana).

Table 8.3 XRD data for the Chipaque section. Depths in metres, values wt %. Taken from Ecopetrol report GTN-F-216 (2015).

		>2µm fraction								< 2µm fraction			
Section	**Depth**	**clay**	**sand**	**K-feldspar**	**Na-Feldspar**	**Carbonates**	**Pyrite**	**Anatase**	**Other**	**illite/smectite**	**Illite**	**kaolinite**	**micro quartz**
Crucero	58.5	62	33	trace			0	trace	<5%	15	20	45	20
	79	63	27	trace			trace	<5%	<5%	22	13	59	6
	130.5	77	18	trace			trace	trace	<5%	18	23	50	9
	385.5	35	55	0			trace	<5%	<5%	25	50	20	4.5
	530	77	18	trace			trace	trace	<5%	43	25	32	0
Pescana	13.5	27	68	0	0	0	0	trace	<5%	0	23	23	19
	35	68	17	<5%	trace	0	0	<5%	<5%	0	28	28	5
	147	38	52	<5%	trace	0	trace	trace	<5%	0	63	63	5
	148	10	85	trace	0	0	trace	trace	<5%	0	34	34	32
	214.5	8	77	<5%	0	trace	<5%	trace	<5%	0	18	18	64
	240.5	46	39	trace	trace	<5%	0.1	<5%	<5%	0	45	49	6
	255.5	23	60	7	0	0	<5%	trace	<5%	0	27	59	14
Zipa	2	11	84	0			trace	trace	<5%		73	<5%	22
	25	39	56	0			trace	trace	<5%		90	5	5
	46	14	81	trace			0	trace	<5%		60	<5%	35
	72	4.5	90	0			0	0	<5%		42	<5%	53
	74.5	10	85	0			0	trace	<5%		82	4.5	13
	88	25	70	0			trace	trace	<5%		68	12	20

8.3.5 Productivity

As discussed in Chapters 4 -7, when using productivity proxies, it is important to consider the sample location within the basin, the redox conditions, and the extent of contemporary weathering. Some of the samples from Crucero and Pescana were deposited in proximal conditions (note samples close to or within grey boxes in Figure 8.9, which are shoreface facies). Trace element productivity proxies are unlikely to be reliable in these very proximal conditions. Samples from Crucero and Pescana may also have been influenced to a greater extent by the effects of contemporary weathering at outcrop/in storage because of the lack of carbonate buffering capacity during pyrite oxidation. As discussed in Chapter 5, a sample Crucero (which has 0 wt% $CaCO_3$ content) contains large, irregular pores visible in SEM which could indicate shells/tests which have been dissolved by contemporary weathering – affecting the bulk geochemistry which may have originally had a signature of higher calcareous productivity (Figures 8.5). However, the sedimentological evidence does suggest a strong biological activity, with fish skeletal fragments and pellets observed throughout both columns and phosphate beds are noted in Pescana (Figure 8.9). There is also significant granular micro quartz visible in SEM in a Pescana sample, and abundant micro quartz identified here using XRD (maximum 63 wt%, average 21 wt% of the sub 2µm sample). This could be biological in origin. The more distal samples have higher TOC contents (Figure 8.3), however, when normalised to Al, background TOC levels are similar between sections (8.10), suggesting that dilution of organic matter may be a primary control on TOC content.

In Zipa, $CaCO_3$ is also low in the majority of samples (16 out of 21 samples), so here, low values of TE may have been caused by contemporary weathering. There are two samples displaying elevated Al normalised TOC compared to background (average 0.54), one at 86 m (1.2) and another at 116 m (1.4) (Figure 8.9). The sample at 86 m is not matched by enrichment of TE proxies for productivity, but this may be an effect of contemporary weathering in this $CaCO_3$ free sample. The sample at 116 m is matched with elevated Si/Al (27.3 compared to section average of 9.9), Ni/Al (33.5 compared to average 16.9) and Zn/Al (154.8 compared to average 66.7). At 150 m the first sample with $CaCO_3$ is present, above this, there is an enrichment of Ba/Al (average below 150 m 97.0, above 150 m 395.1), and another sample with elevated values for Ni/Al and Zn/Al (43.6 and 128.2 respectively). Aluminium normalised Ba, Ni and Zn reach a section high at a sample from 192 m (1345, 129.3 and 631.7 respectively). This sample is also marked by elevated $CaCO_3$ contents. In Zipa, there are a number of phosphate beds (at 13, 16.5, 26.5, 37 and 74 m) interpreted within Zipa as being indicative of upwelling by Georex (2015). Aluminium normalised phosphorous increases substantially (from an average of 0.007 below 75 m) above the final phosphate bed (average of 0.027), and is very variable. A more stable high between 150 and 192 m corresponds to a high in Ba/Al. Fish remains are also noted at 83.5, 155, 157.5 and 167 m. A number of samples from Zipa are grey mudstones, intercalated with sub-mm light brown planar parallel lamination, and the rock breaks into planar fragments along these edges (Figure 8.10). As discussed in Chapter 4, it appears that these regular, planar laminae did contain carbonate that has been dissolved by contemporary weathering (Figure 8.10). This suggests regular variation in dominant producers on a fine scale.

The average TOC in LC4 is higher than in Zipa, (average 2.6 wt%, SD 1.0). In LC4, TOC/Al is matched with elevated Si/Al, as well as Ba/Al at 433.5 and 780.5 m (Figure 8.9). The sample at 433.5 m is taken from a tuff layer, which may explain the high contents (Si/Al 9.5 compared to a section average of 6.1 and Ba/Al 758.3 compared to an average of 313.5). The next closest sample above this tuff layer (439.5 m) is enriched in $CaCO_3$ (30.4 wt%) and Cu/Al (10.9), Ni/Al (44.3), Zn/Al (193.5) and P/Al (0.02) compared to averages for the section (16.4, 5.5, 22.9, 125.1 and 0.013 respectively). The sample from 780.5 m is elevated in TOC/Al, $CaCO_3$, Si/Al, Ba/Al, Cu/Al, Ni/Al, Zn/Al and P/Al (1.83, 57.9 wt%, 8.5, 694.4, 18.2, 75.5, 558.2 and 0.023 respectively) and is not from a tuff, nor located close to an observed tuff layer. In LC4 there are no phosphatic beds noted, however, fish remains are noted at 5, 9.5, 14, 19

and 25 m.

In LC1, TOC is the highest within the studied Chipaque formation sections (Figure 8.3), however, this could be also because this section, alongside Pescana, is the only that has not passed completely through the oil window (T_{max} average 455 and 434°C, respectively). TOC/Al appears relatively constant until 145 m, then it increases from an average of 0.5 to a maximum of 3.7 at 269 m (Figure 8.9). The same pattern occurs when considering Cu/Al, which increases from an average of 4.7 to a maximum of 18.8 over the same range. Other proxies also increase in the top half of the section, but not until 171 m in the case of Ba/Al (average before this point 252.0, maximum after 1348.1) and 187 m for Si/Al (average before 4.5 maximum 22.0), Ni/Al (average before 16.2, maximum 106.2), Zn/Al (average before 66.5, maximum 353.7) and P/Al (average before 0.008, maximum 0.031). Calcium carbonate differs from other productivity proxies, as it is enriched compared to the section average (19.9 wt%) below 145 m (25 .5 wt% at 77 m) as well as towards the top of the section (maximum of 33.8 wt% at 145 m). In all cases, contents decrease at the top of the section from 298 m and in the case of calcium carbonate, from 302 m. A sample was taken from beyond this peak (336 m) shows abundant remains of organism infilled with calcite, what appear to be many faecal pellets, and pervasive granular microcrystalline quartz (Figure 8.8). Georex (2015) did not macroscopically observe phosphatic beds, pellets or fish remains in the whole section.

The CIE in LC1 (the orange shaded box in Figure 8.9) is the area where the majority of the increases in the productivity proxies are taking place (127-187 m), however, highest values of TOC/Al, Si/Al, Cu/Al Ni/Al and Zn/Al occur after the CIE, at 269 m.

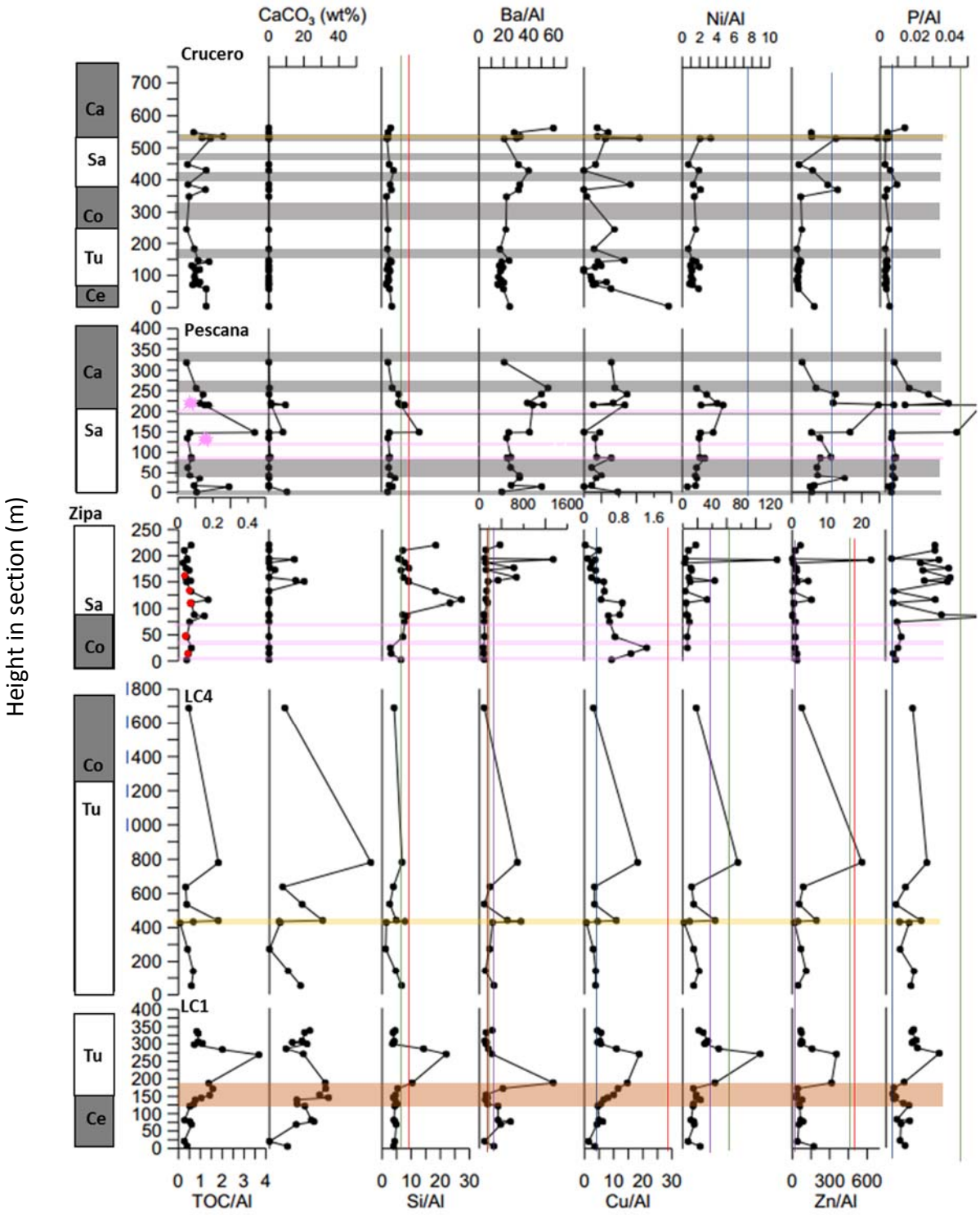

Figure 8.9 TE and productivity proxies (measured using XRF) for the Chipaque age sediments plotted against height in section (m). Blue vertical line is average shale value, green is the C/T mean, red is a Cretaceous Venezuelan average (Lo Monaco et al.,2002 and Alberdi-Genolet and Tocco, 1999), purple line is modern Namibian upwelling muds (Brumsack, 2006). Red spots in the Zipa section indicate samples with light brown coloured planar parallel lamination. Grey boxes are sand beds, horizontal pink lines are phosphate lenses, yellow lines are tephra and the red box is the proposed C/T boundary.

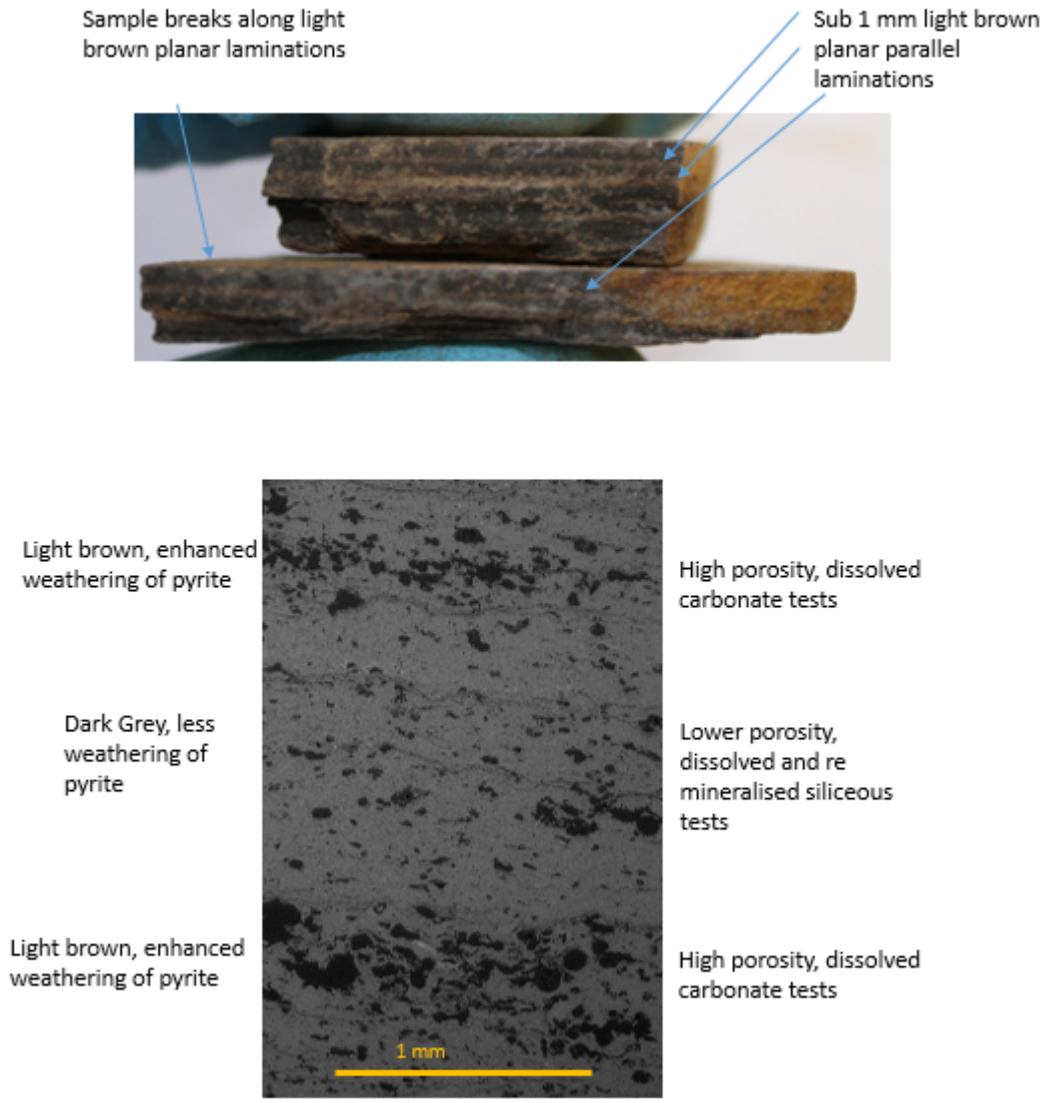

Figure 8.10 Zipa 74.5 m in hand specimen and thin section (seen using BSE SEM). Bottom figure Planar taken using SEM EDX mapping. Parallel sub-mm light brown laminations visible in hand specimen, on a smaller scale these laminations appear to be layers of higher porosity, likely to the dissolution of carbonate tests of foraminifera.

8.3.6 Anoxia

As discussed in Chapters 4 and 5, calcium carbonate can reduce the impact of modern oxidative weathering on TE and Fe-based proxies for anoxia. All of the Crucero samples contain no carbonate, thus TE and Fe-based proxies should be considered with caution. In Pescana and Zipa, most of the samples have no $CaCO_3$ present and again, caution should be taken when interpreting proxies. The majority of samples within LC4 and LC1 do contain carbonate, and here TE and Fe-based proxies ought to be reliable. Also, the majority of proxies were developed and applied for open marine conditions and therefore may not be reliable in the most proximal settings of Crucero and Pescana.

In Crucero, bioturbation was noted throughout the section, as both homogenised beds and

ichnofossils (Figure 8.11). In the absence of reliable geochemical data, this is good evidence that during the majority of the depositional period (Cenomanian – Campanian), oxic conditions prevailed. However, when a sample from 79 m was investigated in SEM (Figure 8.5), grains look relatively well aligned, suggesting a lack of bioturbation. Within the same part of the thin section agglutinated foraminifera, an infaunal organism has been observed. It is interesting that there is still S (average 0.1. SD 0.2) within the samples (S is easily leached from samples during contemporary weathering – see Chapter 3 and 4), however, this is mostly contained as non-pyritic, excess S (Figure 8.11). This could be present within the more weathering resistant organic matter, or as the contemporary weathering product gypsum.

In Pescana, again there are few $CaCO_3$ containing samples in this proximal section. Two samples contain >5% $CaCO_3$ (1.0 and 1.1 wt% $CaCO_3$) and were deposited during more distal, offshore transition periods (148 m and 214.5 m in the column). Here, the geochemical proxies are more likely to be reliable. These samples contain normalised Mn, U, V and Cr contents above average shale, and Fe_{HR}/Fe_T greater than 0.38 (Figure 8.11 and 8.12), and may represent anoxic/suboxic conditions. The sample at 148 m was taken from a location close to where ichnofossils were observed, and the sample from 214 m was taken from an area where no bioturbation was observed (Figure 8.11). A sample taken from 255.5 m was observed using SEM-BSE and shows quartz grains orientated in random directions. Here, pyrite framboids are seen associated with black laminae which could be OM (or porosity). Bioturbation is noted throughout the column (Figure 8.11).

Zipa is a more distal section which, according to Georex (2015), represents offshore transition to middle continental shelf. There are three samples (150 m, 152 m and 192 m) with $CaCO_3$ contents higher than 5 wt% (2.41, 1.82, 1.74 wt% respectively – Figure 8.11). These samples have Fe_{HR}/Fe_T greater than 0.38 (see Figure 8.11) and contain Cr, U and V higher than average shale (Figure 8.12). Molybdenum is present in only low concentrations (maximum 2 mg/kg) and normalised Fe contents are below average shale. Although likely affected by contemporary weathering, the fact that the majority of samples have Al normalised Mo, V and U greater than average shale suggests that there may have been suboxic/anoxic but not euxinic conditions, at least at these intervals. Ichnofossils are present at two depths (170 and 225 m), the only bioturbation observed, suggesting that the rest of the column may have been under anoxic/suboxic conditions during deposition. In Zipa, few

pyrite framboids are visible in a sample using SEM-BSE, however, there is some evidence that the number has been reduced due to contemporary weathering (Chapter 5). Relatively well-aligned grains within this sample (taken from 74.5 m) attest to the laminated beds and lack of biological homogenisation visible at outcrop. An agglutinated foraminifera was identified in a sample from the base of the section (74.5 m) by Buckman et al. (2017), which is considered anoxic by enrichment compared to average shale in Mo, V and U, evidencing at least temporary oxygenation. Phosphate beds may cause the enrichment of redox sensitive trace metals in samples at 25 m (Figure 8.12), however, samples adjacent to other phosphate beds in this section are not corresponding enriched.

La Cristalina 1 was deposited in a mid-outer continental slope environment and $CaCO_3$ is present in the majority of samples (apart from one at 20.5 m), so most of the geochemical proxies are deemed to be reliable. The Fe_{HR}/Fe_T anoxia proxy is above 0.38 in the majority of samples apart from at 171 and 298 m (0.35 and 0.30, respectively) (Figure 8.11). The sample at 171 m is the only sample where normalised Fe contents are slightly higher than average shale (0.56). There is also a sample where Fe_T is lower than 0.5 wt% (269 m, 0.3 wt%), and so here the proxy is unreliable (Clarkson et al., 2015). Sulphur content is mostly higher than average shale and is very variable (average 0.61 wt%, SD 0.51) (Figure 8.11). The majority of sulphur is within metal sulphides, with two samples containing excess S (171 and 298 m, containing 76% and 73% of excess S). Normalised contents of Cr, Mo, U and V are above average shale throughout the section (average 24.3, 11.3, 2.7 and 190.8 respectively). There is an interval between 187 and 298 m where the normalised content of U, V, Cr and Mo increase and approach, or exceed in the case of U, V and Cr, the normalised contents seen at the C/T mean (Brumsack, 2006). Normalised V and Cr also exceed the Venezuelan Cretaceous mean. Interestingly, this period (187-298 m) also contains the only observations of bioturbation (mostly as homogenised beds, but ichnofossils were observed at 280.5 m). Mo contents only exceed 100 mg/kg (euxinia threshold according to Scott and Lyons, 2012) after this 298 m. A sample taken from 336 m (where Mo is lower than 100 mg/kg) shows pyrite prevalent within calcite tests/shells and within black areas which could be OM (or porosity) (Figure 8.8). Zinc sulphide is also present, only observed within tests/shells Figure 8.13).

La Cristalina 4 was deposited in a distal delta to outer continental slope and $CaCO_3$ is present in all but one sample (271.5 m), so the majority of geochemical proxies are deemed to be

reliable. Here Fe_{HR}/Fe_T is above 0.38 in all samples, however, two samples have less than 0.5% Fe (427.5 and 780.5 m with 0.47 and 0.38 wt% Fe respectively) and so here the proxy is unreliable (Clarkson et al., 2015) (Figure 8.11). S content is very variable (average 0.54 wt%, SD 0.60), with very little S out with metal sulphides (max excess S is 0.03 wt% in the sample at 271.5 m, 79% of the S content within this low S sample). Similarly to LC1, the Al normalised content of Cr, Mo, V and U is above average shale (average normalised content 22.0, 8.5, 156.1 and 2.0 respectively) and approaches, or slightly exceeds, C/T mean (Brumsack, 2006) and Venezuelan Cretaceous average (Figure 8.12). Unfortunately, due to low sample resolution, it is difficult to decipher temporal changes over the depositional periods. There appear to be two peaks in TE accumulation, at 739.5 and 780.5 m. There appears to be no additional TE or Fe accumulation within the sample from the tuff layer (427.5). Bioturbation, in the form of homogenised beds, is only observed at one depth, 1633 m.

During the CIE in LC1, there is an increase in the Fe/Al which is not matched by an equal increase in Fe_{HR}, leading to the decrease in the Fe_{HR}/Fe_T proxy (minimum 0.35 compared to average 0.7). There are also two samples with higher S content (1.39 and 1.49 wt% compared to average 0.61 wt%). In the highest S content, Fe_{HR}/Fe_T is at a minimum and the S is mostly within OM (72%). Accumulation of TE significantly increases only towards the top of the CIE (reaching and surpassing the Brumsack (2006) C/T mean in V and Cr), and the enrichment continues beyond the CIE. Molybdenum content does not exceed 100 mg/kg in the CIE sediments and therefore the sediments are not likely euxinic, however Al normalised Cr, U and V do exceed average shale, and Fe_{HR}/Fe_T is above 0.38, therefore the sediments are likely at least suboxic-anoxic. Bioturbation, in the form of homogenised beds, follows the CIE, suggesting a switch to at least episodically oxic conditions.

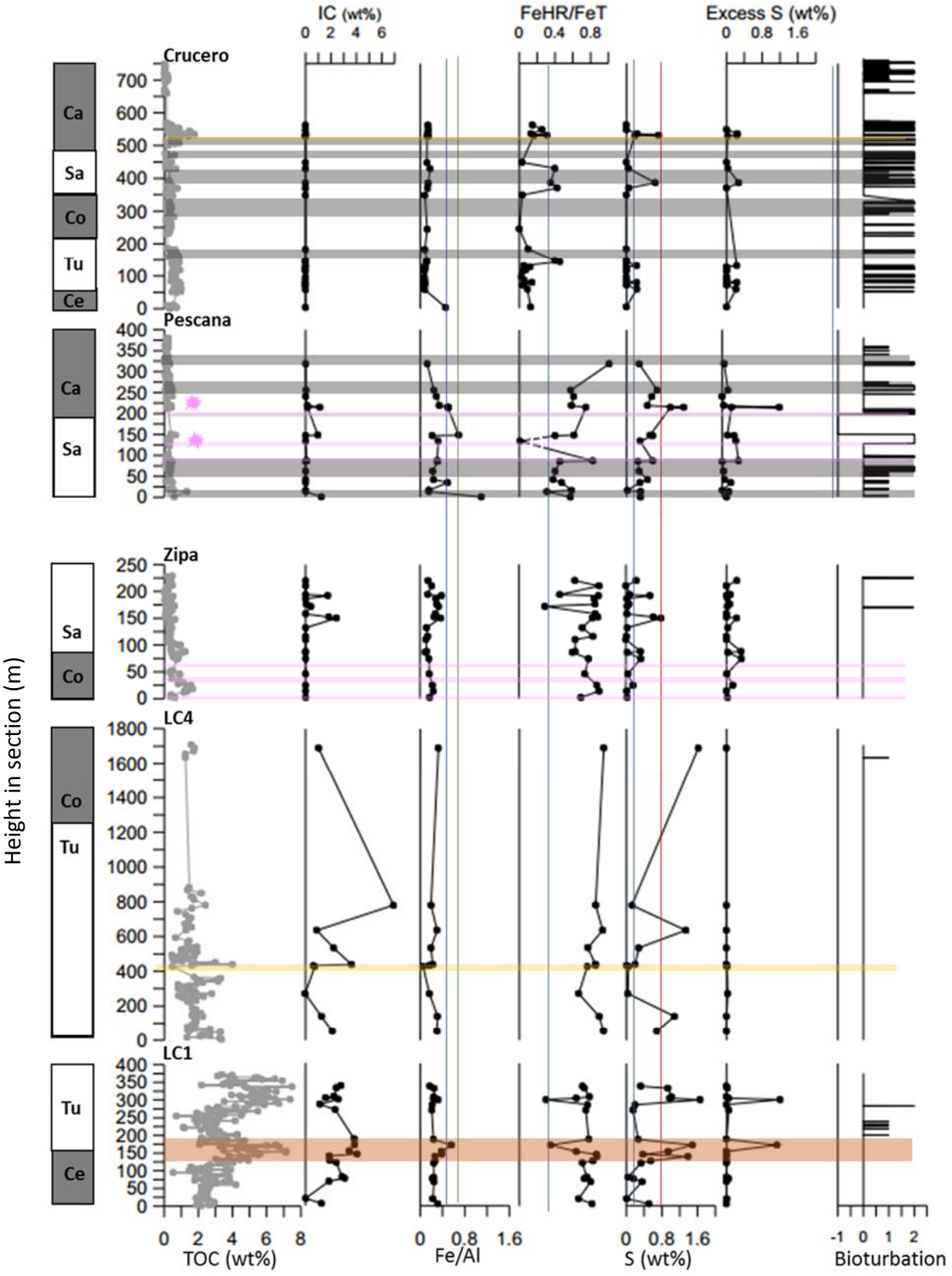

Figure 8.11. Fe, S and Fe speciation redox proxies, with CaCO3 and TOC for reference (measured using LECO or CNS, XRF and Fe-speciation with AAS), and bioturbation as observed by Georex (2015) (0 is no bioturbation, 1 is homogenised beds, 2 is ichnofossils observed) for the Chipaque age sediments. Blue vertical line is average shale value and red is a Cretaceous Venezuelan average. Grey shaded areas are the most proximal – shoreface sediments identified by Georex (2015). The CIE is shown as an orange box in LC1. Pink horizontal lines are phosphate beds, orange lines are tephra and grey boxes are sand beds.

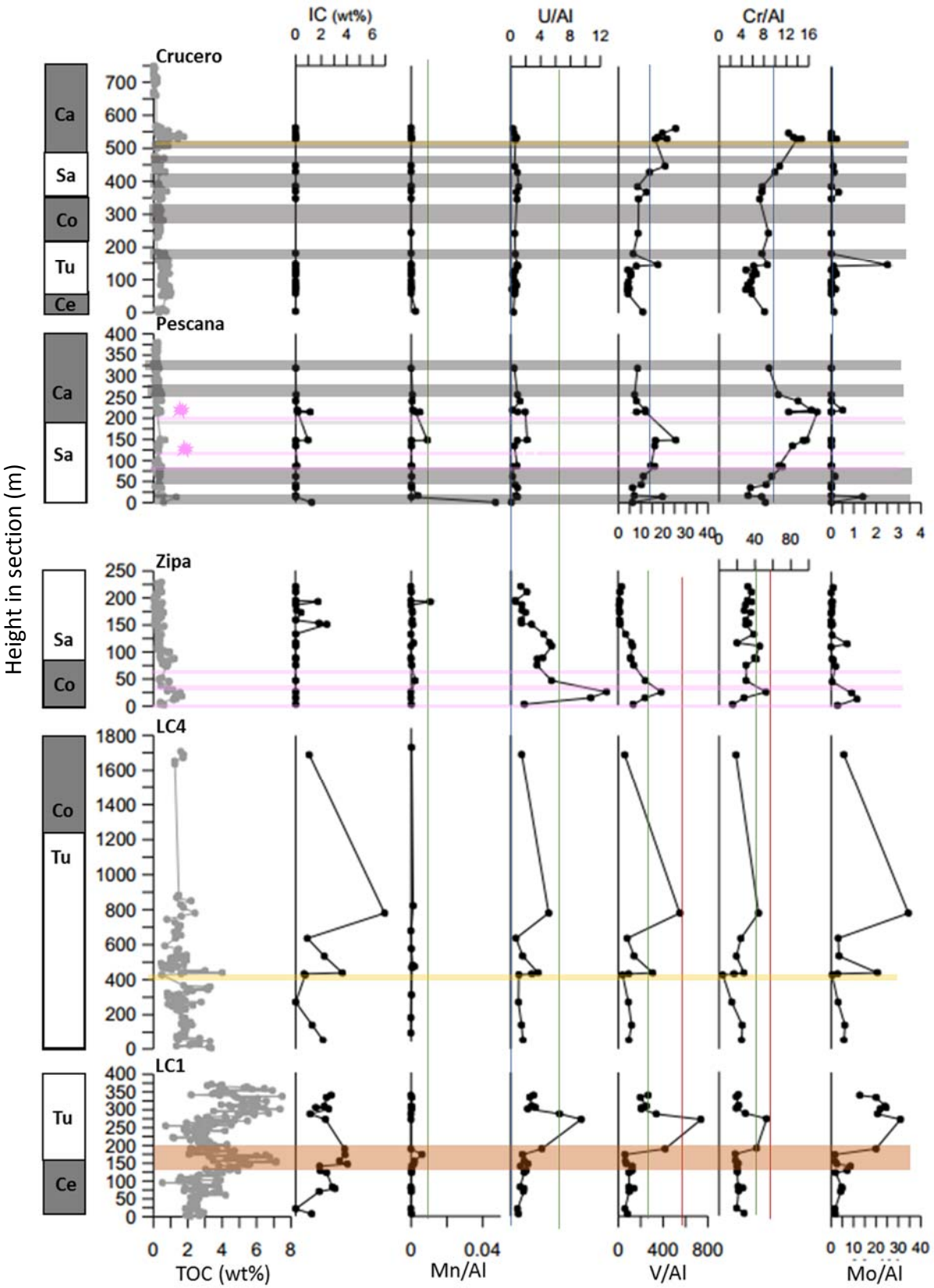

Figure 8.12 TE and Mn redox proxies (measured using XRF) for the Chipaque age sediments plotted against height in section (m). Blue vertical line is average shale value, green is the C/T mean, and red is a Cretaceous Venezuelan average (Lo Monaco et al.,2002 and Alberdi-Genolet and Tocco, 1999). Grey shaded areas are the most proximal – shoreface sediments identified by Georex (2015). The CIE is shown as an orange box in LC1. Pink rectangles are phosphorite. Phosphorite beds with star may be condestaiton beds as contains fish skeletal fragmenrs, teeth, icnofossils, pellets and heavily bioturbated, perhaps a condensation bed. Orange horizontal lines are tephra.

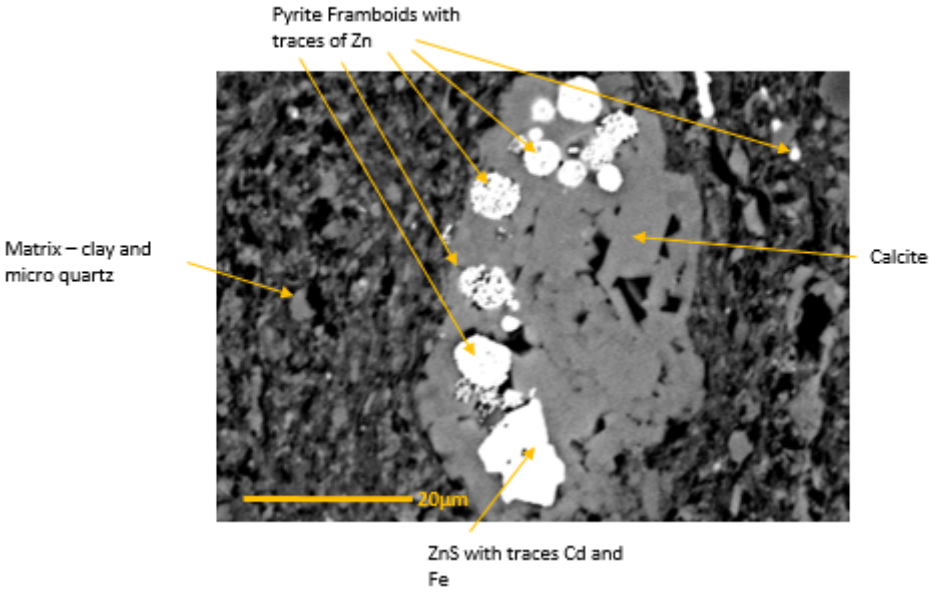

Figure 8.13 BSE-SEM images of LC1 336 m, observations of minerals. Sulphide minerals - Pyrite framboids and ZnS, which have grown within a carbonate/calcite test.

8.3.7 The C/T boundary (OAE 2) Carbon Isotopic Excursion

The bulk organic carbon isotope excursion (CIE) starts at approximately 127 m at a value of -27.16 ‰ and becomes more positive reaching a plateau at -23.74 ‰ at 145 m, with a slight increase to a peak at 171 m at -23.02 ‰ (Figure 8.1). The $^{13}C_{org}$ returns to background round levels of -27.08 ‰ at 187 m. Confidence that this excursion is related to the C/T boundary event comes from the magnitude, which is similar to that measured by Villamil and Arango (1998) in the UMV, Lenninger et al. (2014) in the WIS (Pueblo, USA), Eldrett et al. (2014) also in the WIS (Texas, USA) and by Mort et al. (2008) in the tropical North Atlantic (Tarfaya, Morocco), which all observe a range of ~4‰. In the La Luna, Western Venezuela, the CIE is measured as 3‰ (Perez-Infante et al., 1996). The sample resolution is not adequate for identifying the internal structure of the CIE (e.g. the Plenus Cold Event, Jenkyns, 2017), which would have provided further chemostratigraphy, however, the plateau is identified in the aforementioned studies (Figure 8.1). The CIE is matched with a variable, but increasing TOC, from an average of 2.8 wt% before, an average of 5.1 wt% during the CIE (with a maximum of 7.1 wt%) and an average 3.9 wt% after (Figure 8.1).

8.3.8 Comparing EC to other Cretaceous Basins

Here data from the more restricted EC is compared to the more proximal Llanos, deeper MMV and the more northern ocean-ward Maracaibo basins. Figure 8.14 shows that the Cenomanian – Campanian samples of the EC have a similar range of TOC values, and similar but slightly higher Si/Al and Ba/Al to samples taken from the MMV and Maracaibo basin. The more proximal Llanos basin sediments have much lower Si/Al and Ba/Al (no TOC data available). It appears that overall, the samples from the EC have similar, but slightly lower Al normalised Mo, U and V contents than MMV and Maracaibo basin (Figure 8.15), but higher contents than the Llanos Basin samples. Furthermore, the EC has lower Al normalised Fe than any other basin (Figure 8.15). All of the northern South American samples have U/Al and Fe/Al less than average shale.

The OAE 2 within LC1 offers the opportunity to compare time equivalent samples in the EC to other basins. Figure 8.16 shows that the EC has more TOC than samples from Mexico (Núñez-Useche et al., 2016), comparable but slightly higher TOC than Central Italy (Owens et al., 2017) and Galicia (Thurow et al., 1988) but less TOC than Tarfaya (Poulton et al., 2015) and Demerara Rise (Hetzel, 2009). The productivity proxy Ba/Al from EC is comparable to samples from Mexico, Demerara Rise and Galicia. Again, Al normalised Fe is low compared to other locations where data is available (8.17). Samples from the EC have comparable, or slightly lower in Al normalised contents of redox-sensitive metals (8.18).

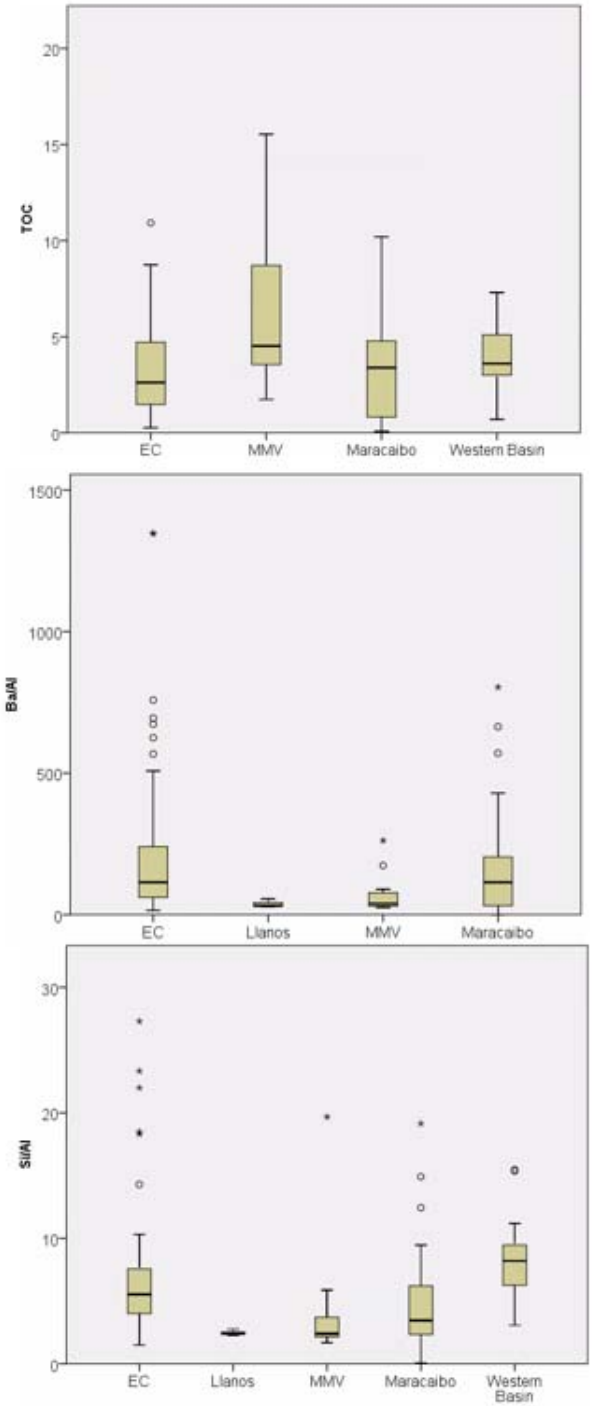

Figure 8.14 Comparing productivity proxies in samples of Cenomanian to Campanian age in basins of Northern South America. Llanos basin data from two wells reported by Jaramillo et al. (2004). Maracaibo Basin data from Davies et al. (1999), Rey et al. (2004), Erlich et al. (1999), Mongenot et al. (1996) and Genolet and Tocco (1999). Western Maracaibo Basin data from Lo Monaco (2002). Middle Magdalena Valley (MMV) from well samples provided to this project.

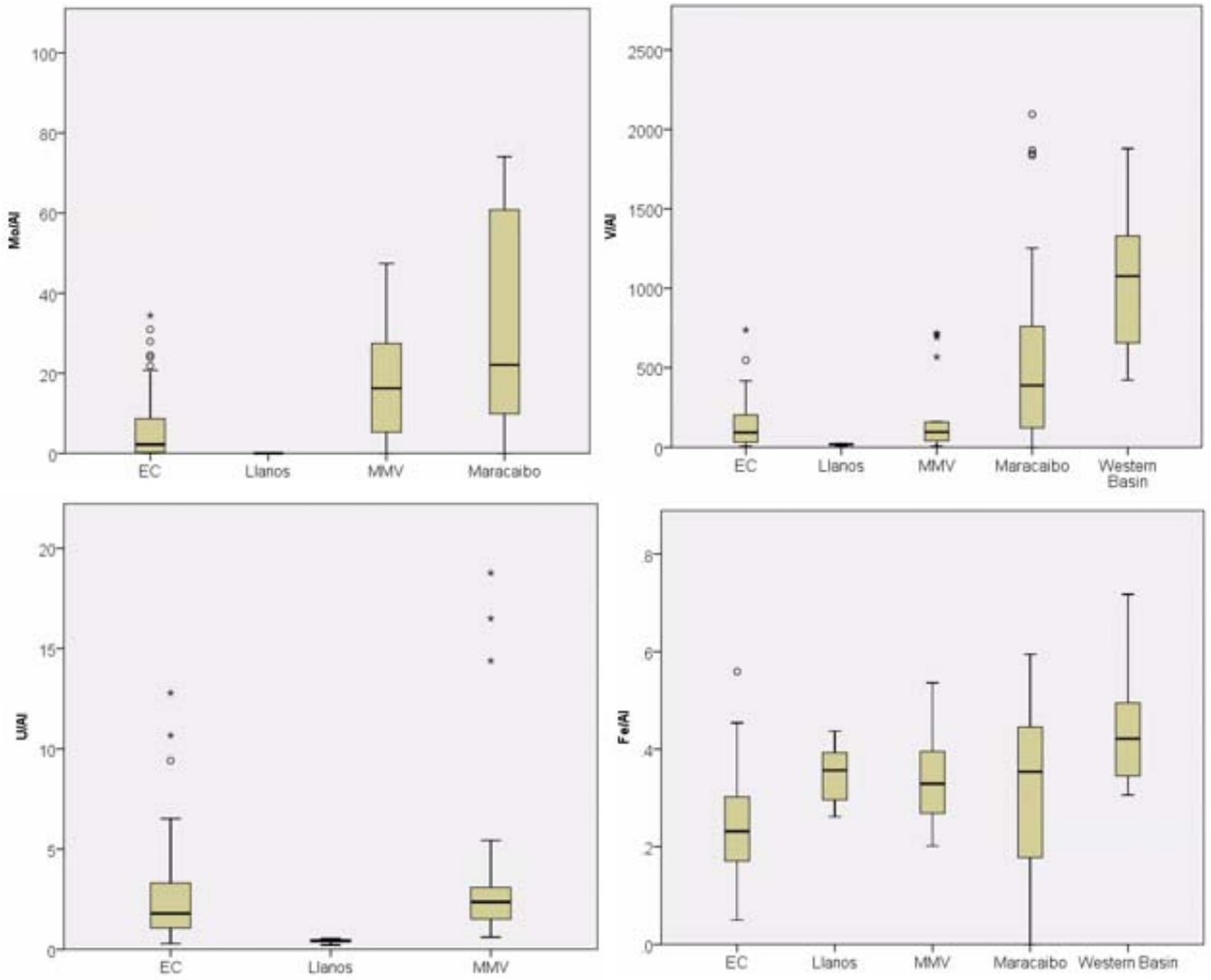

Figure 8.15 Comparing anoxia proxies in samples of Cenomanian to Campanian age in basins of Northern South America. Llanos basin data from two wells reported by Jaramillo et al. (2004). Maracaibo Basin data from Davies et al. (1999), Rey et al. (2004), Erlich et al. (1999), Mongenot et al. (1996) and Genolet and Tocco (1999). Western Maracaibo Basin data from Lo Monaco (2002). Middle Magdalena Valley (MMV) from well samples provided to this project.

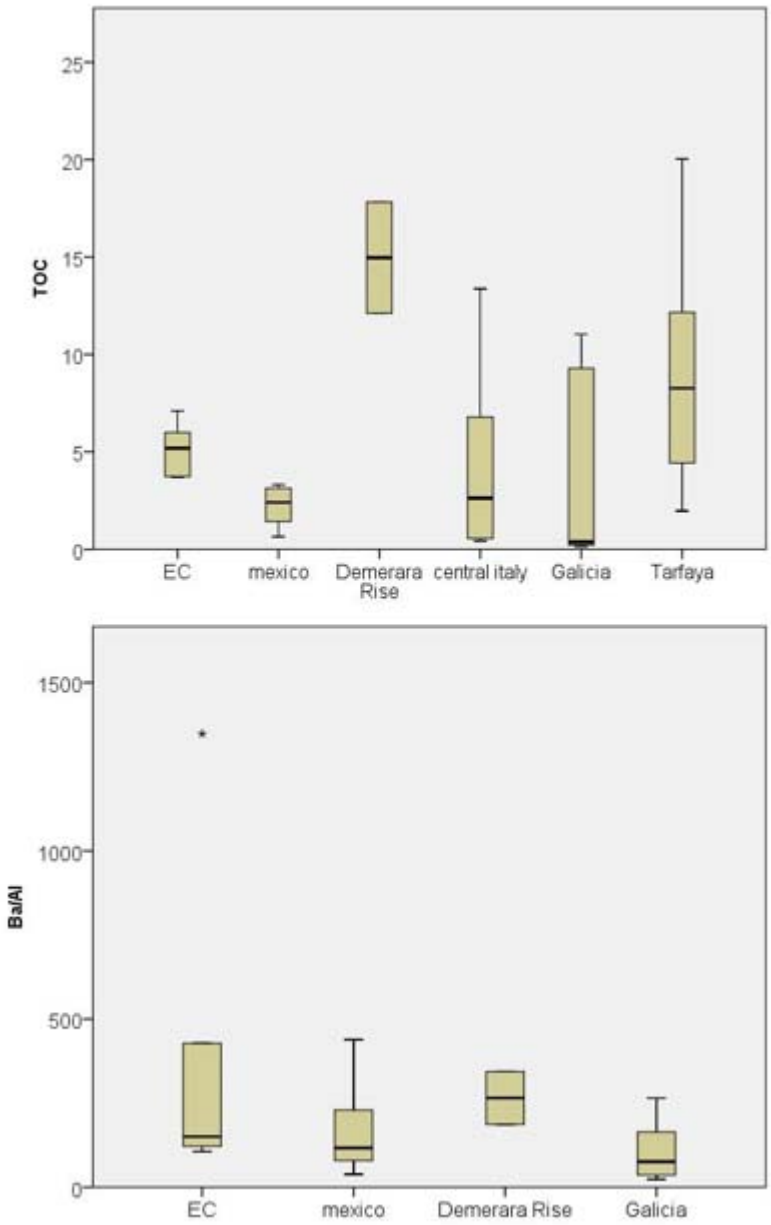

Figure 8.16 Comparing productivity proxy Ba/Al and TOC (wt%) for OAE 2 sediments from the EC to different locations. Data for Central Mexico from Núñez-Useche et al. (2016), Demerara Rise averages from Hetzel, 2009; Central Italy Owens et al. (2017), Galicia Thurow et al. (1988), Tarfaya Poulton et al. (2015). EC shows comparable levels of Ba/Al accumulation suggesting comparable productivity and also TOC accumulation.

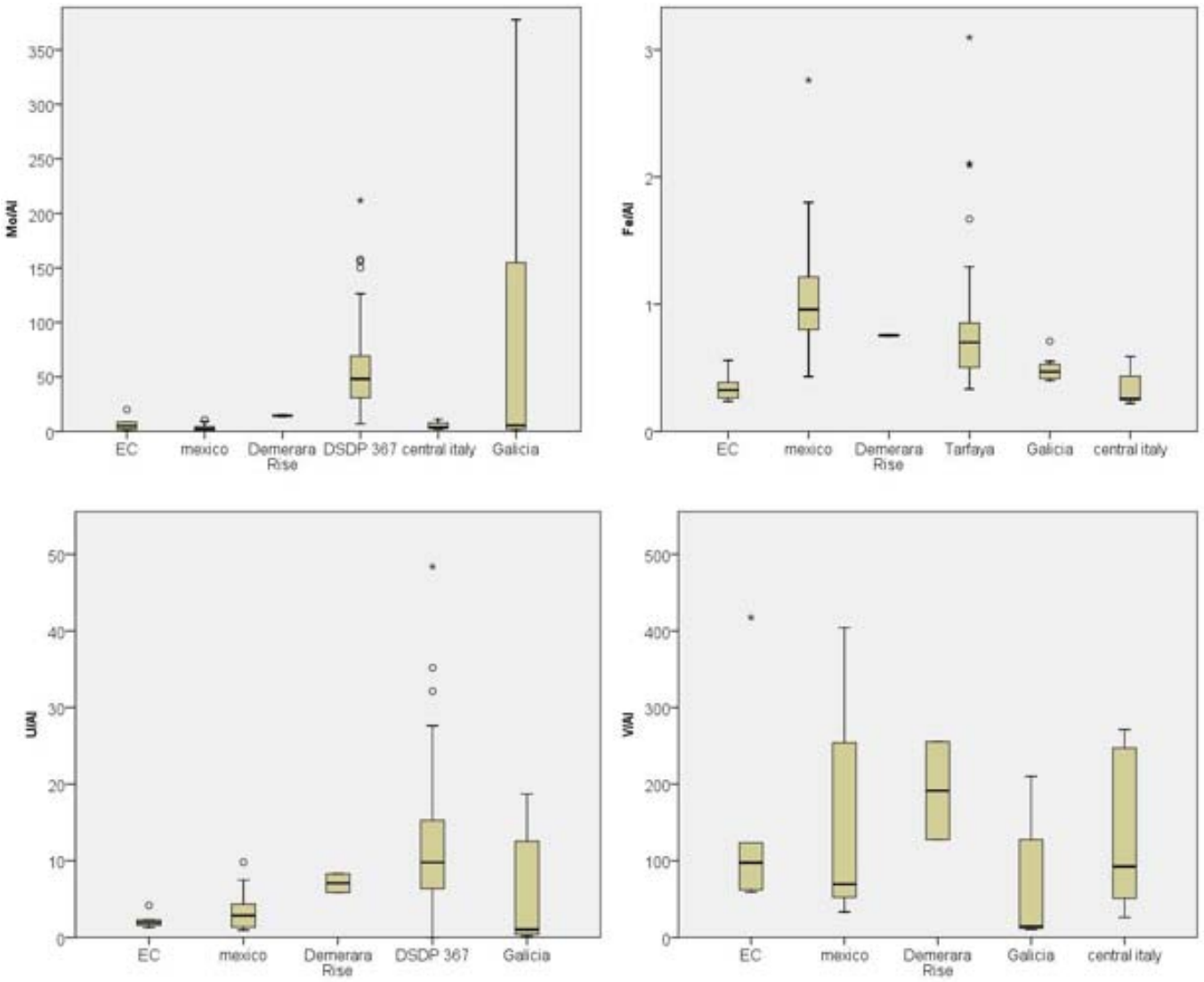

Figure 8.17 TE and Fe redox proxies in OAE 2 sediments. Data for Central Mexico from Núñez-Useche et al. (2016), Demerara Rise averages from Hetzel, 2009; Central Italy Owens et al. (2017), Galicia Thurow et al. (1988), Tarfaya Poulton et al. (2015), DSDP 367 data from Dickinson et al. (2016).

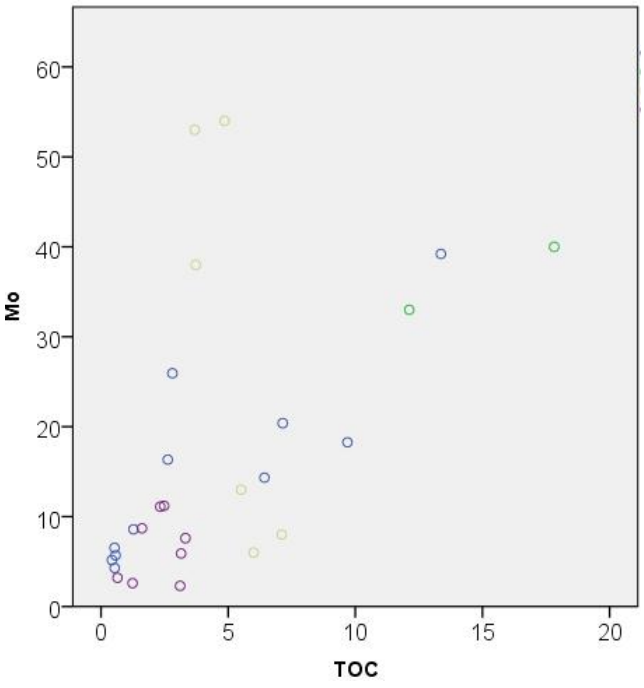

Figure 8.18 Comparing Mo (ppm) and TOC (wt%) relationships in OAE 2 samples from the EC (beige) to Mexico (purple) Núñez-Useche et al. (2016), Demerara Rise averages (green) from Hetzel, 2009 and Central Italy Owens et al. (2017) (dark blue). Three of the EC samples show higher Mo/TOC values, indicating plentiful supply and no restriction within the EC basin during the OAE 2.

8.4 Discussion

All results are compiled per section, in order to attempt to understand how the paleo depositional environment changes at each location over time. Although time constraints are not precise, information about paleo depositional environments within the EC for each stage are compared to those of similar age within tropical South America. As there is only one time constrained interval (OAE 2 CIE in LC1) this section is compared to other time equivalent sections across the globe.

8.4.1 La Cristalina 1 – Cenomanian –Turonian sedimentation on the mid-outer continental slope

In the LC1 section, there is evidence that the dominant Si supply to the sediment is biogenic (negative correlation between Zr and Si, and a positive relationship between Zr and Al (Table 8.2) and pervasive granular microcrystalline quartz (Figure 8.8 and Buckman et al., 2017). Si content co-varies with productivity proxies (Cu/Al, Ni/Al and Zn/Al, Figure 8.12), providing evidence that the primary control on these trace elements is productivity, rather than redox. Other studies of Late Cretaceous chert formations (Lidita Inferior and Superior) in in the UMV (Terraza, 2003) note chert replacing micrite and sparite and suggests an external source of Si (from clay diagenesis of quartz grain contact dissolution in adjacent sand beds). This replacement is not seen in SEM-BSE samples from LC1, with calcite infilled shells appearing pristine and unaffected by 'corrosion' by Si replacement (Figure 8.8). This observation appears relevant as it may suggest a different mechanism for chert formation in the EC compared to the UMV, or compositional differences in the rock (e.g. a greater proportion of carbonate in the UMV and so greater surface area for corrosion). The abundance of biogenic Si, as well as enrichments of TE productivity proxies above average shale, and consistently exceeding C/T and Venezuelan Cretaceous mean when considering Ba/Al, highlighting exceptional levels of productivity during deposition of LC1 sediments.

There is the possibility that these extreme enrichments in TE related productivity proxies are related to the erosion of particularly TE rich rocks in the hinterland. Proximal sediments are intermediate sources of detrital material for the more distal basin, and so comparison of these sediments with the more proximal (offshore to shoreface) Cenomanian and Turonian sediments of the Crucero section should provide source clarification. In Crucero, Ni, Cu and Zn content of samples is 15.8, 4.6 and 24.9 mg/kg respectively, compared to 126.6, 33.0 and 452.6 mg/kg respectively. These higher values, combined with an decoupling from detrital Al

(Figure 8.2), are evidence that these enrichments of TE are related to authigenic processes, not simply a TE rich source of detrital material.

In LC1 a gradual reduction in K/Al, which corresponds to an increase in CIA*, is observed, suggesting a gradual increase in the intensity of paleo chemical weathering or a change to a more strongly weathered hinterland from the Cenomanian to the Turonian. This trend is matched by a general decrease in Al manifesting a decrease in clay input and a slight increase in Zr/Al linked with a lithological change to coarse sediments (greater dominance of siltstone (Appendix A)). These gradual changes could be due to a decrease in sea level or increase in runoff. There is global evidence supporting a decreasing sea level following the C/T boundary (Haq, 2014), however, the uplift of the Llanos Basin in the Cenomanian (due to subduction of the Caribbean plate under Colombia) may have also increased supply (Sarmiento-Rojas et al., 2006). A decrease in global temperatures after the C/T hothouse should lead to a decrease in paleo chemical weathering in the hinterland that supplied run off to the EC (Jones et al., 1994; Huber et al., 2002; Friedrich, 2012). The increase seen at LC1 is therefore likely a more local climatic effect, perhaps related in part to local tectonics.

It appears that anoxia is prevalent throughout the depositional period in LC1, with redox sensitive metals above average shale and Fe_{HR}/Fe_T above 0.38 in the majority of samples. The absence of phosphate-rich beds visible at the outcrop (unlike Zipa, Crucero and Pescana) may also suggest more constant anoxia during this depositional period (Ingall et al., 2005). Similarly to productivity proxies, it is possible that these enrichments come from erosion of redox sensitive TE rich hinterland. In this case, the Cenomanian and Turonian samples of the proximal Crucero samples should have a higher content of these TE. These samples have average contents of U and V (6.4 and 74.0 mg/kg respectively) which are much lower than LC1 (12.2 and 855.7 respectively). This pattern is also evident in TE/Al ratios (Figure 8.12). This, along with the decoupling from detrital Al (Figure 8.2) suggests that these enrichments are not related to a switch to more TE rich detrital source and instead relate to authigenic enrichments related to processes in this deeper part of the basin. This comparison is complicated by the possible leaching of TE from the lower $CaCO_3$ Crucero samples.

The change in lithology in the Turonian to a siltstone dominated bed (in the uppermost portion of this section, directly after the CIE) corresponds to a marked change in geochemistry and so a change in climate. This bed contains peaks in TOC/Al, Si/Al, Ba/Al, Cu/Al, Ni/Al and Zn/Al, suggestive of an increase in siliceous productivity, but a matched

decrease in carbonate, which peaks at 33 % in the sample preceding the siltstone bed, suggesting a switch from calcareous to siliceous productivity. Within this siltstone dominated bed, samples exceed the C/T mean and Venezuelan Cretaceous average in both redox and productivity proxies (Figure 8.9, 8.11 and 8.12), and productivity proxies exceed values in the modern day upwelling sediments in Namibia, in combination testifying a highly productive setting. This period of high productivity also is combined with to the enhanced accumulation of redox-sensitive trace elements and S compared to the lower portion of the section, consistent with other high TOC black shale analogues. As mentioned in Chapter 3 and 4, U and V may become enriched in oxic, high productivity settings. However, this should not effect Mo, which is present in quantities indicative of euxinia (up to 163 mg/kg, above the 100 mg/kg required for euxinia by Scott and Lyons, 2012). The fact that there are two samples with high S (1.5 and 1.7 wt%), the majority of which is not contained within pyrite (76 and 73 %, respectively), argues that during at least some periods Fe_{HR} limited the amount of pyrite formation, and not the availability of sulphide (Figure 8.11). When sulphide is in excess of Fe_{HR}, sulphide becomes associated with organic matter, which leads to early geopolymerisation and an increased preservation potential (e.g. Damsté et al., 1998). This may explain the overall higher TOC in the LC1 section compared to other distal sections in the EC (Figure 8.3). Mongenot et al. (1995) also noted a scarcity of Fe compared to average shale, noted here to be a feature across the basins of northern South America in the Late Cretaceous (Figure 8.15). Iron limiting/increased S availability conditions have been noted during this period in other locations (Poulton et al., 2015; Hetzel et al., 2009) due to varying inputs of S and Fe from hydrothermal and detrital sources.

Due to the relative immaturity of this section (T_{max} 454°C, Vitrinite reflectance 1 %Ro, Table 3.5), TOC relationships provide meaningful information. TOC decreases with an increase in coarse material in the siltstone bed, however TOC/Al increases, suggesting that the organic matter has been diluted by continental mineral matter. There is also a strong positive correlation between TOC and redox proxies Mo and U, supporting that organic matter was effectively preserved during periods of greater anoxia, especially in the siltstone beds (Table 8.2).

8.4.2 Cenomanian-Turonian Boundary CIE within La Cristalina 1

A distinct positive CIE associated with the OAE 2 C/T boundary is identified within LC1 (Figure 8.1). The C/T boundary itself has been identified in other parts of the EC as a condensed

section with phosphatic lags, repeated layers of bentonite and pyrite nodules (Vergara et al., 1997; Villamil and Arango, 1998; Villamil et al., 1999). These sedimentological markers are, however, not seen in LC1 (nor in the Crucero section), suggesting that they are not laterally continuous, or have been eroded. Villamil and Arango (1998) blame condensation and whinnowing on the lack of ash beds in one of the sections they have studied in the UMV. In the distal LC1, this could also be the case, however there is no geochemical evidence (e.g enrichment in Zr). Similarly to the Demerara Rise (Erbacher et al., 2005), the CIE in LC1 exists in mudstone, although three beds of wackestone (<1m thick) within the CIE were observed at outcrop. In the WIS-USA and Dover-UK, there is also an increase in $CaCO_3$ content during the CIE, with a switch from marls to more pure carbonates (Jenkyns, 2017).

Voigt et al. (2006) estimated the length of the CIE, from a minor decrease in ^{13}C at the onset to the end of the plateau (last high ^{13}C value before the decrease to background levels) as a period of 400 kyr. Although the end of the CIE in LC1 is not well recorded (due to low sample resolution), if the end of the plateau is considered the end of the CIE (*sensu* Voigt et al, 2006), this gives a thickness of 44 m and a sedimentation rate of 11cm/kyr, which is very high. For comparison, the CIE covers a thickness of sediment greater than the 9 m on the Demerara Rise (Erbacher et al., 2005); 15 m in Tarfaya (Tsikos et al., 2004); 17 m in the WIS (Eldrett et al., 2014); 15 m measured in Eastbourne, UK (Tsikos et al., 2004) but closer to the 37 m measured by Perez-Infante et al. (1996) in Venezuela. This testifies to much higher accumulation rates in this relatively narrow, proximal basin and in Western Venezuela, and provides outstanding opportunities for future high-resolution research of OAE 2. The thickness of the CIE in the more proximal, more southern section investigated by Villamil and Arango (1998) in the UMV is only 8 m, suggesting wide heterogeneity in rates of deposition in Colombia. There is a large gap between the end of the CIE and the next post-CIE sample. It is, therefore, possible that the observed decrease in $^{13}C_{org}$ after the plateau which is currently considered to be the end of the CIE plateau is actually an internal fluctuation seen in many highly resolved sections (e.g. the Plenus Cold Event seen in the Vocontian Trough, Du Vivier et al., 2014, or Tarfaya, Tsikos et al., 2004). This would mean that the CIE at LC1 could potentially cover an even greater thickness.

Different to most reported OAE 2 sections from the open ocean, at the onset in of the CIE, there is no dramatic change in any of the proxies at LC1. Rather, the beginning of a steady increase in Cu/Al and TOC (normalised to Al and total) and a modest increase in Mo/Al and

Fe_{HR}/Fe_T (suggesting a decrease in overall oxygen availability) is observed. The clay fraction (in Al) also begins to steadily reduce to a minimum (lowest measured in all Chipaque formation samples, possibly diluted by biogenic Si and $CaCO_3$) with the onset of a steady increase in the coarse fraction relative to the fine (Zr/Al). More changes occur at the start of the CIE plateau, i.e. the period of maximum global carbon-climate perturbation. Iron, S and TOC increase, but Mo/Al and Fe_{HR}/Fe_T drop (Figure 8.11). This is a similar response to the OAE 2 previously investigated in the adjacent basin UMV, with enrichments in TE not occurring until the centre of the CIE (Villamil and Arango, 1998). At the sample which represents the onset of recovery to background $^{13}C_{org}$ values (end of CIE plateau) a dramatic increase in productivity and redox-sensitive trace elements is recorded, signalling the onset of extreme productivity and anoxia (but not euxinia, Mo remains below 100 mg/kg, Scott and Lyons, 2012). This is matched with a decrease in the coarse fraction (Zr/Al) and a switch from shale dominated to a siltstone (likely biogenic Si) dominated lithology. The increases in productivity and anoxia proxies all continue beyond the CIE (in the previously discussed siltstone bed) and markers for euxinia are detected towards the top of the column. This feature is not observed in the samples taken from the UMV by Villamil and Arango (1998), again suggesting inter basin heterogeneity in the wider seaway. The CIE is contained within a period of prolonged low oxygen conditions in LC1, other sections in Colombia, and the wider northern South America (Perez-Infante, 1993; Martinez et al., 2003; Erlich et al., 1999; Villamil and Arango, 1998). It appears that in LC1, the factors involved in OAE 2 may have primed the EC for euxinia. An alternative is that the CIE does extend beyond the last low $^{13}C_{org}$ value into the siltstone bed, as mentioned above, and euxinia and enhanced siliceous productivity is indeed a feature of the peak CIE and not the post-CIE.

There is also an increase in CIA* in the CIE, caused by a sharp decrease in Na/Al and a general decrease in K/Al which continues into the Turonian (Figure 8.4). This increase in the intensity of paleo chemical weathering may have provided nutrients for increased productivity, as evidenced by a strong negative correlation between Na and K and TOC (Table 8.2). Increased paleo chemical weathering is a common global signature during the OAE 2 and is thought to be caused by a hotter, more humid climate and a greater volume of basalts exposed due to increased volcanism and is identified using isotope systems (Li, Pogge von Strandmann et al., 2013; Ca, Blättler et al., 2011) and modelling (Handoh and Lenton, 2003). In the EC, increasing chemical paleo weathering is linked to increasing Zr/Al

suggesting a humid environment with increased runoff of coarse grain material from the coast. An increase in the detrital material at the C/T boundary is also noted in some parts of the Maracaibo Basin (Davis et al., 1999) but a decrease is noted elsewhere (Erlich et al., 1999), negating a uniform response to a global eustatic sea level change and emphasizing the importance of local response on the architecture and composition of OAE 2 sediments in the wider EC. Here the uplift of the Llanos Basin may have had a variable influence on the type and volume of material arriving at each location in northern South America. In other locations, orbital shifts in climate identified with CIA* and proxies for coarse grain input, track wind direction and the intensity of runoff during the C/T and other OAE's (seen in Atlantic settings by Kolonic et al., 2005; Beckmann et al., 2005; Hofmann and Wagner, 2011; Wagner et al., 2013; Poulton et al., 2015). These studies suggest that a shifting position of the ITCZ causes these orbitally forced changes in climate. The broader, more long term increase in chemical paleo weathering seen in the LC1 section across the CIE (400 kyr, Voigt et al., 2006) may be indicative of a longer term shift in the position of the ITCZ. The orbital timescale shifts evident in other locations are not resolvable in this study, and this warrants further investigation in order to identify the extent of the ITCZ influence.

Throughout the CIE there is a general increase in Cu (Figure 8.9) and Co (not shown) which are considered mafic elements (Eldrett et al., 2014; Snow et al., 2005; Orth et al., 1993), and a mid CIE increase in Fe (which can also be a result of volcanic activity - Duggen et al., 2010; Olgun et al., 2011). This could suggest an accumulation of igneous derived TE and Fe throughout the CIE, alongside increased continental paleo weathering input. Volcanoclastic sediments indicative of aerial volcanism are noted at the C/T boundary in other parts of the EC and northern South America (Vergara et al., 1997; Villamil et al., 1999). Snow et al. (2005) investigated the effect of the subaerial Caribbean Large Igneous Province (CLIP) on mafic TE accumulation during the CIE in Colorado. The CLIP is also relatively close to the EC basin and could be affected by the same mafic TE enrichment mechanism. Molybdenum and TOC relationships are similar to or higher than non-restricted basins of the same age (Figure 8.18), suggesting that the basin is not particularly restricted from the open ocean during the CIE, possibly as a direct result of the high sea level during the C/T event (Haq, 2014). A taxonomic study of agglutinated foraminifera in the EC also suggests a good connection to the Caribbean and the Atlantic Oceans during this period (Vergara et al., 1997). In Colorado, TE accumulation is at its maximum in the middle of the CIE (Snow et al., 2005). This may

explain the more gradual input of possibly igneous source of elements, and the later input of Fe (Figure 8.11). The low content of Fe within sediments throughout the deposition of the Chipaque formation points to a low Fe source of detrital material. The Guyana Shield is the likely source of detrital material (Cooper et al, 1995) and CIA* suggest that it is consistently heavily weathered (this study, Campos Alvarez and Roser, 2007). In the absence of a more local source of Fe rich detrital material, an additional source of Fe from the CLIP is particularly attractive to explain the increase in Fe seen within the later CIE. Comparing CIE sediments in LC1 to those from other basins of the world provide further insights into the effect of the CLIP (Figures 8.16 and 8.17). The EC sediments show similar accumulations of TOC, as well as productivity and redox-related trace elements to other basins in the C/T boundary. Aluminium normalised Fe is low in the EC compared to other basins, but apart from that, there appear to be similar amounts of TE available for enhanced productivity. If the CLIP is providing TE to a water mass travelling through the Caribbean into the Atlantic during the OAE 2, as suggested by Trabucho Alexandre et al. (2010), it would be expected that the EC, much closer to the source, would have higher TE content. This is not apparent (Figures 8.16 and 8.17), suggesting the deep, CLIP influenced waters are not reaching the EC basin. Nevertheless, the thickness of the CIE in the EC compared to other locations implies that the basins of northern South America although small in area, were a significant sink of TE and OC during this critical period in the Cretaceous.

8.4.3 La Cristalina 4 – distal delta to outer continental slope. Turonian

The samples from La Cristalina have a relatively low resolution (1 sample every 170 m) and so it is difficult to ascertain any distinct trends over time. However, a similar relationship between Si, Al and Zr is observed as at LC1, so Si content can tentatively be assumed to be primarily controlled by siliceous productivity. The samples from LC4 are much more strongly dominated by $CaCO_3$ (up to 57.9 %), compared to LC1, which dilutes Al and Si (Figure 8.4, Table 8.2). In two samples, $CaCO_3$ and Si increase in tandem, suggesting enhanced siliceous and calcareous productivity. In one of these samples from the Turonian (780.5), this is matched with increased detrital material (Ti/Al), increased continental paleo weathering/switch to less weathered source (K/Al) as well as a section peak in productivity (Ba/Al, Cu/Al, Ni/Al and Zn/Al) and anoxia proxies (Cr/Al, U/Al, V/Al, Mo/Al). Together, this indicates enhanced productivity causing anoxia, driven by increased runoff, similar to the mechanisms seen in LC1. Similary to LC1, these enrichments in TE are not replicated in

Turonian samples from the proximal (offshore to shoreface) Crucero, where TE contents and TE/Al are much lower (as illustrated in Figure 8.9 amd 8.12). Also, co-enrichment of redox sensitive U and V, alongside Mo and high Fe_{HR}/Fe_T again provides evidence that these elements are not being enriched purely as a result of high productivity. Again, this comparison is complicated by the effect of weathering, which may have preferentially leached TE from the proximal Crucero samples (low $CaCO_3$)Anoxic and high productivity conditions prevail throughout the section (Figures 8.9, 8.11 and 8.12), with accumulation of redox-sensitive V and U and productivity proxies (particularly Ba) exceeding average shale and approaching the C/T mean and the Venezuelan Cretaceous average (and exceeding them at the 780.5 m samples). Prolonged euxinia cannot be confirmed here, with Mo remaining below 100 mg/kg (Scott and Lyons, 2012) in every sample studied. Two samples taken from a tuff layer are high in Na, $CaCO_3$, Cr, V, U, Mo, Ba, Cu, Ni, Zn, Mg and Zr. Unfortunately, due to a lack of biostratigraphy and low sample resolution for carbon isotope chemostratigraphy, it is not possible to associate the tuff layers to a particular time period, for example, the C/T boundary as in other studies (Vergara et al., 1997; Villamil et al., 1999).

8.4.4 Zipa – offshore transition to middle continental slope. Coniacian – Santonian

In Zipa, there also appears to be a predominance of biogenic Si (no relationship with Zr, co-variation of Si/Al and productivity TE/Al, XRD data and SEM evidence Table 8.3 and Figure 8.7 and 8.9) and so Si content. Siliceous productivity is lower in the bottom 110 m of Zipa (Figure 8.9). This portion of the La Zipa section also has the highest TOC and greater enrichment of redox sensitive TE suggesting more intense/sustained anoxia, although Mo indicates that euxinia is unlikely (Figure 8.12). As in LC1 and LC4, in order to discount the possible switch to a more TE rich hinterland causing TE enrichment, a comparison was made to the Santonian samples of the more proximal (offshore to shoreface) Pescana section. These Pescana samples have much lower contents of Cu, Ni, Zn, Cr, V and U (average 2.7, 17.4, 79.6, 96.0, 130.3 and 5.8 mg/kg respectively) compared to Santonian Zipa (average 15.0, 86.5, 356.4, 125.7, 162.7 and 7.2 mg/kg respectively). Similar differences are apparent when normalised to Al (Figure 8.9 and 8.12) and when plotted against Al on a cross plot (Figure 8.2). Again, these comparisons are complicated by the variable affect of TE leaching by weathering, which in this case, may affect both the proximal Pescana and Zipa sections.

Between 110-150 m, there appears to be an increase in siliceous productivity linked to very high (but variable) TE based productivity proxies at levels close to or exceeding the C/T

mean, Venezuelan Cretaceous average and modern day Namibian upwelling sediments (Figure 8.9). This is not linked to an increase in overall TOC and is tentatively associated with a decrease in the intensity of anoxia (Figure 8.2). The increase in productivity may have been driven by greater input of terrestrial material caused by increased runoff or decreasing sea level, as evidenced by increased Al, Ti/Al, Zr/Al (Figure 8.4). Differently, decreasing in paleo chemical weathering is suggested by a sharp increase in K/Al and a decrease in CIA* (Figure 8.4). This, along with an increase in Zr and Ti, could suggest an increase in the aeolian component due to offshore winds from more arid climate. Above 150 m, because $CaCO_3$ is above 5 wt% in some samples redox proxies should be more reliable. Here, although TE redox proxies are low, they are still greater than average shale, and Fe_{HR}/Fe_T is indicative of anoxic conditions (Figure 8.11). It is likely that other carbonate free samples are also anoxic as redox-sensitive TE contents are greater than average shale throughout the column (Figure 8.12). These changes occur at or around the assumed Coniacian/Santonian boundary, the time interval associated with OAE 3. This is a more regional anoxic event affecting continental margin and shelf/epicontinental sea setting assumed to be largely driven by upwelling and nutrients supplied by runoff (Wagreich et al., 2012; Beckmann et al., 2005; März et al., 2008; Hofmann and Wagner, 2011).

There is evidence for fluctuations in siliceous and carbonate productivity on a mm scale in Zipa, alongside variations in Al (and so clay) content (Figure 8.10). A switch from siliceous to calcareous productivity over short (orbital and lower) time scales may be caused by variations in the influx of sedimentary material, with high detrital influx preventing $CaCO_3$ saturation and causing turbidity (Davis et al., 1999; Carmo and Pratt, 1999; Vergara et al., 1997). These sub mm scale variations may therefore relate to climate, with carbonate rich layers representing drier periods, and siliceous layers representing more humid periods with greater runoff. As reliable sedimentation rates are not available within this section, these may represent seasonal to annual variations. Samples with similar bedding are noted throughout the Zipa section (Figure 8.9) and so this may be a persistent feature of deposition at Zipa. Changes in sediment $CaCO_3$ content have been used to investigate climatic changes and feedbacks during Coniacian and Santonian on orbital time scales (Flögel et al., 2008; Beckmann et al., 2005), with variations in content the sub metre scale. Frequency analysis on the fine scale variations of $CaCO_3$ content apparent in the Zipa section could provide unprecedented detail for tuning these models.

Interestingly, the samples from Zipa have considerably higher CIA* (average 86 SD 2.5) than those recorded on the Atlantic Demerara Rise during the Coniacian-Santonian, which is also receiving detrital material from the Guyana Shield (50 and 65, Flögel et al., 2008). This may highlight a significant variation in lithology of the Guyana Shield between the western catchments (providing detrital material to the EC) and the eastern catchments (providing material to the Demerara Rise), or a variation in climate (being much more humid in the eastern catchments). An alternative is that the more distal Demerara Rise sediments received clays which had been density segregated, providing a greater proportion of less dense smectite, which would lower the CIA*.

8.4.5 Pescana – offshore transition to lower shoreface. Coniacian – Campanian

The Pescana section was deposited in a proximal environment and has low carbonate, so geochemical proxies here provide little information available about redox conditions. Two samples in the more distal portions of the section which also have carbonate have redox-sensitive TE and Fe_{HR}/Fe_T indicative of anoxic/suboxic conditions (Figure 8.11, 8.12). Bioturbation observed throughout the column and the proximal nature of the sediments is suggestive of dominantly oxic conditions (Figure 8.11).

Productivity proxies are also unlikely to be reliable but are below (Ba, Cu and Ni) or close to (Zn) average shale (Figure 8.9). Biogenic Si is unlikely to be affected by contemporary weathering and could be a proxy for productivity. In Pescana, however there is evidence Si is not predominately biogenic in origin (Si and Zr crudely co-vary across the section), however, there is some evidence for micro-crystalline quartz within this sample (Figure 8.6) and some other Pescana samples (Table 8.3). However, in this sediment with a greater proportion of detrital grains, the role of grain to grain contact dissolution as a source of this microcrystalline quartz cannot be ruled out. Given the proximal and slightly coarse nature of the sediments, in Pescana Si and microcrystalline quartz is unlikely to be dominantly biogenic Si and thus offer no information on palaeo-productivity. There is some different sedimentological evidence for high productivity. Fish skeletal fragments and pellets observed throughout the column, and also associated with phosphate beds are noted in Pescana coupled with P/Al values higher than C/T mean in one sample (Figure 8.9), evidence for at least moderate biological activity.

The lower 150 m of the section has a higher clay content (as indicated by Al and XRD, Table 8.3 Figure 8.4) and a decreasing coarse fraction (Ti/Al and Zr/Al representing rutile and

zircon grains). Above 150 m there is a sharp increase in the coarse component (Si Zr/Al and sand), which then generally reduces until the top of the section. The decreasing coarse content between 50-150 m followed by a switch to increased coarse component at 150 m may represent a period of sea level regression, followed by a gradual transgression. These sea level fluctuations are also recorded in the column as varying thicknesses of sand beds

In Pescana, the Al normalised Na content is higher than in other sections (apart from tuff influenced samples in LC4). This may be because there are feldspar grains reaching these proximal sediments (Table 8.3, Figure 8.6), however, the feldspars in this sample are mostly K-rich. It is quite surprising that the hinterland provided many feldspars grains, considering the high CIA of the sediments throughout the Cretaceous, indicative of extremely chemically weathered sediments. The CIA* appears unaffected by this and is similar to other sections (Figure 8.4). This may be because Na and K appear to be opposing in the Pescana section, so even with changes in the individual proxies, there is little effect on CIA*. In conclusion, it is likely that the Pescana sediments received material from a less weathered source, possibly due to changes in the paleo river system during this time of active tectonics.

8.4.6 Crucero – offshore to shoreface. Cenomanian to Campanian

As Pescana, anoxia proxies are not reliable in the Crucero section because it is relatively proximal, and has low carbonate so proxies could have been readily affected by contemporary weathering. Bioturbation (homogenised sediments and ichnofossils) are observed throughout the column in sand and shale beds. A sample analysed by SEM-BSE (Figure 8.5) shows relatively well-aligned grains, which suggests deposition without being reworked by infaunal organisms. However, within this same thin section, an agglutinated foraminifera has been tentatively identified. Phosphatic sandstones noted at the outcrop (Appendix A) provide support for oxic/fluctuating redox conditions. Given the absence of geochemical information, predominantly oxic conditions but fluctuating with some periods of anoxia/suboxia are cautiously ascribed. Vergara et al. (1997) studied a section the same area (and same age) and noted many agglutinated foraminifera in shale beds, but also some shale beds with clear planar parallel lamination, suggesting a lack of bioturbation. This study therefore also supports fluctuating redox during deposition.

Productivity proxies are also unlikely to be reliable in Crucero, however, biogenic Si is unlikely to be affected by contemporary weathering and could cautiously be used as a proxy for productivity. No micro quartz was identified, and little was noted via XRD in the clay-

sized fraction (Table 8.3, max 20%). It is likely here that Si is dominantly from quartz, suggesting low biogenic Si productivity. Dissolution of a large quantity of $CaCO_3$ due to contemporary weathering is unlikely given the relatively low (compared to Zipa) amounts of porosity seen in thin section in Crucero (Figure 8.5). It is possible that high calcium carbonate productivity was prevented by under saturation of calcium carbonate in this proximal, high detrital influx setting (Vergara et al., 1997). Within the Crucero section, therefore, low Si and $CaCO_3$ productivity is suggested. Evidence of agglutinated foraminifera (noted here and by Vergara et al., 1997) and pellets and fish fragments within the column does suggest at least moderate biological activity.

In Crucero, the first sample of the section has high Zr, as well as Ti, K and Na, indicative of relatively high coarse and fine detrital input. In samples between 49.5 to 147 m, which roughly corresponds to the Turonian, detrital proxies are very variable and chemical paleo weathering proxies are relatively constant (Figure 8.4). At outcrop, many thin sandstone beds intercalate the shale. Together, this is suggestive of highly variable sea level. Between 370 m and 450 m, an area of the section which should represent the Santonian, there is an increase in coarse material (Si and Zr) relative to Al. This is matched with an increase in chemical paleo weathering (increase in K/Al, decrease in kaolinite and CIA*). Also, the 370-450 m contains higher FeHR/FeT, TOC/Al, and Ba/Al. This could tentatively indicate a period of greater chemical paleo weathering, runoff leading to increased productivity and lower oxygen conditions (although bioturbation is still prevalent in the sand beds).

8.4.7 Comparison to time equivalent sections in the rest of Northern South American

Here data from the more landlocked EC (especially if the Central Cordillera in the west is emergent) is compared to the more distal MMV and the more ocean-ward Maracaibo Basin. Figure 8.14 shows that the Cenomanian – Campanian samples of the EC have a similar range of TOC values to samples taken from the MMV and Maracaibo basin, even given the variation in the maturity of samples within each sample set. It appears that the EC was as highly productive, if not occasionally more productive than the MMV and Maracaibo basin (Ba/Al and Si/Al values). The high productivity signature is not seen in the more proximal Llanos basin sediments. It appears that overall, the samples from the EC were not deposited during more sustained or more extensive anoxia, compared to the deeper MMV or more ocean-ward Maracaibo Basin (Figure 8.14), with lower contents of redox sensitive trace metals and Fe. It could be expected that this shallower, more hydrographically restricted

basin would be more prone to anoxia than the Maracaibo, likely directly connected to the equatorial Atlantic throughout the period. This is further evidence that waters were free to move unrestricted around this epicontinental seaway during the Late Cretaceous, and that low oxygen content was a characteristic of most of this water column. An interesting feature is that the whole of the northern South America appears to have low Fe, and also U, content compared to average shale, and other temporal equivalents (Figure 8.17).

8.5 Conclusions

The Cenomanian to Campanian is a period of sustained and enhanced siliceous and calcareous productivity in the distal portions of the EC and the wider northern South America, exceeding at times modern day upwelling settings, such as the upwelling system off Namibia and leading to significant carbon burial. In this way, the EC is similar to sustained carbon burial evident from off the coast of Ghana and the Demerara Rise, where black shale was deposited more or less continuously from the Cenomanian to the Santonian (Wagreich, 2009). In the EC, it is likely that high productivity was sustained for an extended period via the supply of nutrients from various sources. During the Cenomanian and Turonian, highest periods of productivity are linked to greater runoff and paleo weathering, especially at the C/T boundary, linking depositional conditions in the EC to more global climatic changes. Late Coniacian/Early Santonian sediments show an increase in productivity unrelated to paleo weathering proxies where upwelling may be the main supplier of nutrients to the system.

Tentatively, the CLIP could have provided an additional supply of nutrients to the EC basins (especially during the OAE 2). Conceptual models about the distribution of nutrients from the CLIP (Orth et al., 1993; Trabuco Alexandre et al., 2010) show supply of CLIP enriched waters close to the EC. Comparing the TE inventories of samples sets from OAE 2 does not show a preferential enrichment, highlighting the importance of the ocean circulation in the Atlantic for accumulating the CLIP sourced TE. In fact samples across northern South America during this period appear to be depleted in Fe (which can be supplied by igneous and volcanic sources) when compared to average shale (Figure 8.15). More comprehensive and high-resolution sampling may identify brief intervals with more significant enrichments in the EC. Furthermore, analysis of isotopes systems like S (Adams et al., 2010), Os (Jenkyns et al., 2017) or Cr (Holmden et al., 2017) could help distinguish varying influence of the CLIP on productivity and associated anoxia and organic matter burial.

This period of long term high productivity was coupled with and may have caused persistent

and widespread anoxia and occasional euxinia in the EC. Evidence from Mo TOC relationships indicates that the EC was well connected to the open ocean to be replenished with TE, at least during the OAE 2 (8.21), perhaps due to the extremely high sea level during this period. If this is the case, these open ocean waters may have been prone to anoxia by being already low in oxygen before they entered the basin area. The correlation between TOC and TE redox proxies, even in sediments deposited during extremely high levels of productivity, emphasises the importance of low oxygen content on the carbon cycle is (Table 8.2, Figures 8.12).

Chapter 9 Research Synthesis and Outlook

This study is composed of two complementary parts. The first part aims to improve the understanding of inorganic geochemical proxies when applied to deeply weathered samples from outcrops to achieve a robust interpretation. The second part uses this new information to reconstruct the paleo depositional environment of Cretaceous petroleum source rocks in the EC and adjacent basins. The EC basin is understudied (only Villamil, Erlich, Narvaez, Föllmi and co-authors have published on its geochemistry to reconstruct the paleoenvironment in the EC) and so this thesis provides important new information about how this basin accumulated organic matter in the Cretaceous, compared to other sedimentary basins across the globe. This new information is used to identify key areas for future work, to further constrain paleo depositional settings as well as to develop improved methodologies to assess and validate the impact of contemporary weathering on proxy reliability.

9.1 Reliability of inorganic geochemical proxies

The first two chapters of this thesis discuss a key challenge faced by most projects that rely on rock samples from outcrops in tropical environments. It was clear from field and laboratory observations that mudstone samples taken from outcrop in the EC for this project were variably affected by contemporary weathering (Figure 5.1). Initial geochemical data further identified generally low Fe contents in these samples (Figure 8.15 and Figure 8.17), compared to the values of the reference material average shale, as well as some inconsistencies between commonly used inorganic proxies (Figure 6.12 and 6.13), likely caused by leaching of TE and Fe by contemporary weathering. Given the variety of paleoenvironments represented by the samples (Table 3.2), from shoreface to outer slope, it was not possible to use geochemistry data to unequivocally identify samples which were affected by contemporary weathering. Challenges circled around two questions: (1) Were samples with low levels of redox sensitive TE content deposited during oxic conditions, or (2) was the sample originally deposited under anoxic conditions and the TE were later leached due to contemporary weathering? Given the difficulty in answering these fundamental questions, Chapters 4 and 5 aim to identify novel filters that can be applied to identify samples whose geochemical composition was likely altered by outcrop weathering. Chapter 4 further attempts to identify proxies which may be more resistant to contemporary

weathering by means of an artificial weathering experiment.

The artificial weathering experiment summarized in Chapter 4 succeeded in inducing pyrite oxidation and carbonate dissolution, which are essential first steps in the chemical weathering of shales in the natural environment. Different from other weathering experiments reported in the literature, little net loss of Fe and TE from the samples was observed. Also, although there were changes in the Fe species, no overall change in the anoxia proxy, Fe_{HR}/Fe_T, was observed. Automated particle analysis of the samples using SEM EDX before and after artificial weathering established a novel method of identifying and quantifying pyrite oxidation. In this approach, individual pyrite framboids that had been affected by pyrite oxidation are clearly identifiable by their lower Fe:S ratios (Figures 4.8 and 4.9). Closer examination of the pyrite framboids using SEM showed that these 'sulphur depleted' framboids contained microcrystals of pyrite with Fe (oxyhydr)oxide rims. Previous work in the laboratory and in soils (Lara et al., 2015; Nicholson et al., 1988; Huminicki and Rimstidt, 2009) hypothesised that the buildup of these rims occurred at high pH and limited the rate of pyrite oxidation. Since redox sensitive TE are often hosted in pyrite (Gregory et al., 2015; Huerta-Diaz and Morse, 1992), this rate limiting mechanism for pyrite oxidation should also be critical to the loss of TE during outcrop weathering. Due to carbonate dissolution in some of the samples, the artificial weathering environment remained neutral to alkaline throughout the experiment. It was concluded that the limited loss of Fe and TE during the artificial weathering experiment occurred because pyrite oxidation was stalled by the generation of Fe (oxyhydr)oxide rims which, in turn, could only be precipitated under relatively elevated pH values caused by carbonate dissolution. It was further proposed that if the weathering experiment had been continued until all $CaCO_3$ in the sample had dissolved, the pH would drop and the environment within the sample would again be conducive to pyrite oxidation. In such an instance, any pyrite that had not been stabilised by Fe (oxyhydr)oxide rims would get oxidised. This led to the working hypothesis that natural samples containing an appropriate amount of carbonate may be more resistant to the effects of contemporary weathering. This conclusion is a major outcome as it suggests that the degree of outcrop weathering, and the suitability of samples for paleoenvironmental studies using inorganic geochemical methods, can be assessed and estimated by determining the carbonate content.

In Chapter 5, this novel hypothesis was applied to the main sample set from the EC. Detailed

statistical analysis showed that samples with a carbonate content greater than 5 wt% had higher TE and pyrite contents, suggesting that they had been less affected by contemporary weathering. Comparison of samples which appeared pristine or visually altered by weathering showed fewer geochemical differences than those categorised based on their $CaCO_3$ content. Also, samples traditionally considered to be unweathered – e.g. from quickly eroding stream beds - were not consistently geochemically different to road outcrop samples. This gave further support to the concept that carbonate content could be used as a filter to identify samples which are more susceptible to geochemical alteration by contemporary weathering. An unrelated study of samples which had been weathered in storage also considered 5 wt% carbonate as an appropriate filter for samples reliable for geochemical analysis (Kraal et al., 2009). Combined, these studies suggest that future work with outcrop/ stored samples should consider filtering samples by carbonate content to ensure a more robust geochemical interpretation.

For the second part of the thesis, samples with less than 5 wt% $CaCO_3$ would not necessarily carry an original signature of the paleoenvironment. This means a significant reduction in the number of samples, from 196 to 60, where TE proxies are reliable (Figure 9.1). For some sections, no samples exist where TE proxies for productivity and anoxia will be reliable (Crucero and Quemado). However, knowledge of these limitations allowed the confident interpretation of geochemical proxies in the 60 unweathered samples in order to make implications about the paleoenvironment in Chapters 6-8. Also, when considering only these filtered (higher than 5 wt% $CaCO_3$) samples, it is clear that the EC (and adjacent basins in Mexico) still retain a signature of lower TE and Fe contents than other Cretaceous organic-rich shales worldwide (Figure 8.17), indicating a depositional mechanism for this difference.

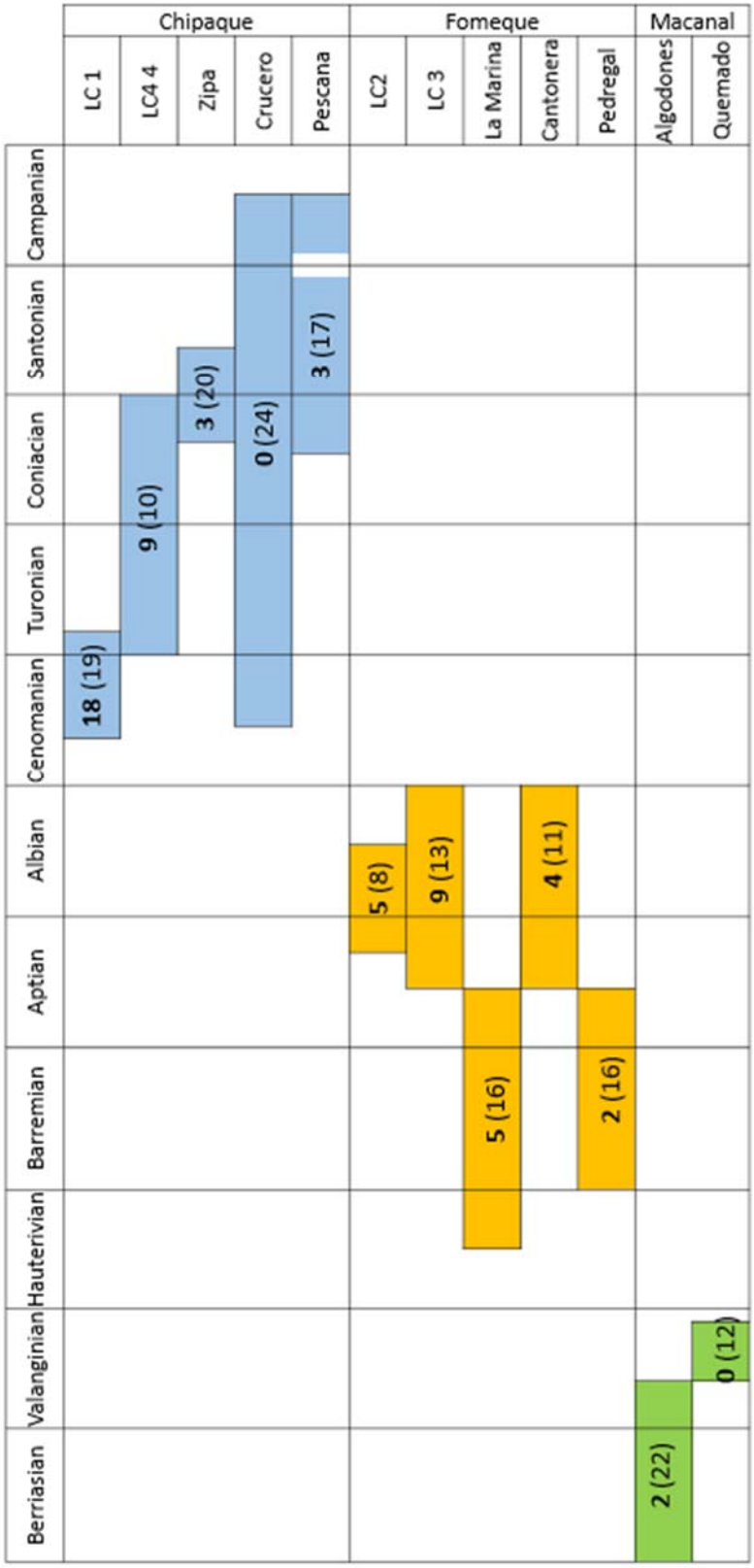

Figure 9.1 Adaptation of Figure 3.3, with the age of the different sections (from Ecopetrol lithostratigraphy) displayed. The numbers of samples whose geochemistry is presumed to be less affected by contemporary weathering (>5 wt% CaCO3) are included in bold, the total samples analysed are in brackets. Samples in bold are assumed to have reliable TE proxies for redox and productivity reconstructions, other samples are to be interpreted with caution (e.g. low TE values do not necessarily mean low original values)

9.2 Paleoenvironmental Synthesis – why shales were deposited and OM was preserved

In this section, information from all 12 sections described in Chapters 6-8 are combined in order to understand how the depositional environment of the study area changed through the Cretaceous. Figure 9.1 shows a compilation of data sets from the most distal sections from each time period discussed in this thesis to evaluate changes over time. These most distal sections were chosen as traditional TE proxies for redox conditions and productivity have been developed for these environments, and because these sections tend to contain more carbonate and hence the original TE inventory. The Hauterivian, Barremian and Campanian are only represented in much more proximal environments in the EC, so these periods are not discussed here.

In order to elucidate gross changes in climate and the hinterland as a source of nutrients over the Cretaceous, proxies related to terrigenous input are presented. The CIA* is chosen to track humidity in the continental interior, although (as discussed in Chapters 6-8) it can be affected by changes in the provenance of the terrigenous material. This should alter with gross changes in climate and rock weathering rates seen over the Cretaceous (e.g. Hofmann and Wagner, 2011). To trace coarse grained detrital material, either through aeolian input when the climate is arid (Hofmann et al., 2008) or via river systems when it is humid, Zr/Al has been used (as it correlates well with detrital Al or Si throughout deposition of these sections, Table 6.2, 7.2 and 8.2). In terms of redox conditions, there may have been periods when the basin was more prone to anoxia as the basin geography changed throughout the Cretaceous due to progressive rifting, sea level variations and uplift in adjacent areas. To trace how anoxia (which increases preservation of organic matter) changes with basin geography, Fe_{HR}/Fe_T has been used, as it has been shown to be less affected by contemporary weathering than TE contents or enrichment patterns (Chapters 4 and 5). To identify periods of sustained euxinia, Mo is presented as an enrichment factor (normalised to Al then to average shale values, Brumsack, 2006) although, as discussed, this proxy is considered with caution due to its potential loss from the samples by contemporary weathering.

There are numerous sources of nutrients which may have driven high productivity during the Cretaceous. Studies have identified the Caribbean Large Igneous Province (CLIP) as a possible source for additional TE which accumulated preferentially in some parts of the Atlantic

during the Cenomanian and Turonian (Orth et al., 1993; Alexandre Trabucho et al., 2010). Deep CLIP influenced waters travelled through the Caribbean Seaway into the Atlantic and during the Cenomanian and Turonian, and these provide nutrients to surface waters when upwelled on to the shelf (e.g off the coast of northern South America and Africa). The CLIP may also have provided TE rich waters to the EC, enhancing productivity, however this relies on efficient transport of upwelled water from the proto-North Atlantic. Previous studies have suggested a northward movement of northern South America as driving enhanced productivity in the study area (Erlich et al., 1999; Villamil et al., 1999). This mechanism is based on the fact that with easterly trade winds, Eckman transport will drive winds south in the EC and adjacent basins when they are located south of the equator (and so onshore in these NE-SW trending basins, causing downwelling), but when the basin moves north of the equator, Ekman transport drives waters north and offshore, causing upwelling. This mechanism was implicated in a productivity maximum across northern South America (represented by widespread chert formation) occurring during the Santonian to Maastrichtian stages when the coast of northern South America was between 5 and 10° north. This should be identified in the EC as increasing productivity throughout the Late Cretaceous until the site has migrated completely over the equator (Santonian, Figure 2.12). In this synthesis, productivity is traced using Ba and P, although these proxies must also be treated with caution due to potential primary and secondary effects affecting their contents in samples, including contemporary weathering.

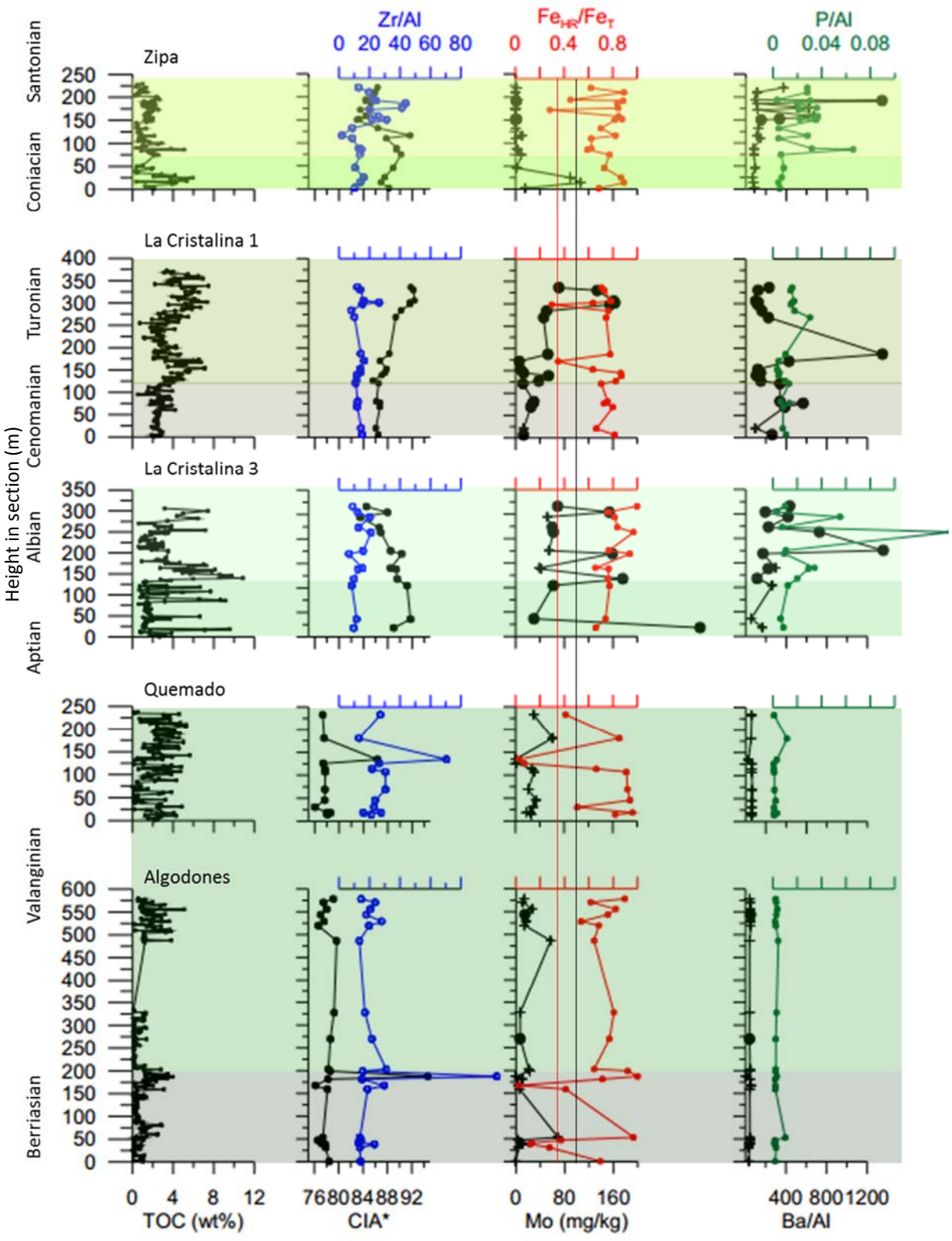

Figure 9.2 Compilation of proxies for distal sections. For graphs of Mo and Ba, samples with less than 5 wt% $CaCO_3$ are shown with crosses, and here the measured values may be lower than original due to contemporary weathering. The red line marks a value of 0.38 for the Fe_{HR}/Fe_T ratio, beyond which a sample is considered to be deposited under anoxic bottom water conditions (Poulton and Canfield, 2005). The black line marks the 100 mg/kg Mo suggested to be evidence for euxina (Scott and Lyons (2006).

9.2.1 Berriasian

During the Berriasian, CIA* is significantly lower than at other ages (Figure 9.2), and Figure 6.1 identifies both the Macanal sections as containing significantly more K and Na. This could suggest that this period (and the Valanginian) was one of relatively low paleo chemical weathering compared to later in the Cretaceous. In Chapter 6, the possibility that these elements were added during late diagenesis by K and Na metasomatism was dismissed. The CIA could be reduced by segregation of different clay particles based on density, leading to a greater amount of the less dense smectite (higher K and Na content than kaolinite) accumulating in more distal sources. The Algodones and Quemado samples are the most proximal of all of the locations used in this summary (tidal plain to prodelta) and therefore this mechanism for reducing CIA can be discounted. The most likely scenario then is that the Guyana Shield, the proposed dominant source of detrital material to the EC (Villamil, 1996), was not being as extensively chemically weathered in the Berriasian compared to the later Cretaceous, and therefore that the climate was relatively arid. This corresponds to other climate records (strontium isotope and P burial records of global paleo weathering) which show low geochemical weathering and therefore relative aridity in the Berriasian, corroborating an overall arid global climate (Jones et al, 1994; Föllmi, 2012; McArthur et al., 2007). Also, during the Early Cretaceous, evidence from plant and animal fossils and climate sensitive sediments (e.g. laterite and coal) indicate a tropical-equatorial hot arid belt, possibly related to the super continent Gondwana (Hay and Floegel, 2012; Chumakov, 1995). Evidence from CIA can be affected by provenance of detrital material and this study has not provided clear indications for variations (apart from at the La Marina section, Chapter 7), and further work is suggested in order to constrain this variable. The Berriasian (and Valangingian) have higher Zr/Al (Figure 9.2) than the later sections, evidencing a greater proportion of detrital material. This may a result of the more proximal nature of the sections, however it may also be a response to the basin basin geometry, with steep fault shoulders possibly reducing the size of the shelf (a trap for coarse sediment) in the early rifting history of the basin.

The EC sediments appear to be deposited under periodically anoxic conditions (Fe_{HR}/Fe_T, Figure 9.2 and S and Mo contents, Figure 6.12 and 6.13). In the absence of evidence for high productivity (low Si/Al (less affected by contemporary weathering), $CaCO_3$ and TE for productivity, Figure 9.2 and 6.13) anoxia, in this case, may have been driven by basin

geography. The location of the basin between major fault shoulders may have acted to prevent the exchange of deep and intermediate waters with the Colombian Marginal Sea (Figure 9.3). Although no detailed information about water depth is available (e.g. macro fossils) Georex estimated a water depth of 20-60 m for Algodones and Quemado (Table 3.1), although the complete depth of the basin and the depth of the sill has not been investigated. If the basin was relatively shallow, it may have become a stratified, silled basin, similar to the Baltic Sea (Arthur and Sageman, 1994), or if deeper, like the Black Sea (Demaison and Moore, 1980). Stratification in these silled basins requires a positive water balance (runoff greater than evaporation, causing a general outflow of low-density fresh water and preventing inward movement of denser deeper oxygenated open ocean water) (e.g. Demaison and Moore, 1980, Erbacher et al., 2001; Arthur and Sageman, 1994). Therefore, although this period may have been more arid than later in the Cretaceous, there is still likely runoff significant to cause this freshwater lid. This is supported by the fact that, although the CIA* is relatively low for the Cretaceous, it is still high (average 79), and comparable to modern day tropical weathering in the Amazon (CIA* 84, Kronberg et al., 1985).

The nature of the basin, bound by steep fault shoulders, should also have reduced the shelf:basin ratio compared to later periods, when limited thermal subsidence instead of active rifting dominated and higher sea levels flooded a wider area). This lower shelf:basin ratio could reduce the area of chemocline intersect with the shelf and the capacity of the Fe-shuttles capacity to enrich the basin in Fe_{HR} (Lyons and Severmann, 2006). While the Fe_{HR}/Fe_T ratio is similar in later periods, the earlier Berriasian and Valanginian samples do have lower Fe/Al (average 0.23 in Berriasian and Valanginian) compared to later samples (average 0.34 in LC3, 0.27 in LC1). This could evidence a less effective Fe-shuttle due to basin geography in the early basin history.

9.2.2 Valanginian

The intensity of paleo chemical weathering did not significantly increase between the Berriasian and the Valanginian (Figure 9.2 and 6.10), suggesting little change in climate from the Berriasian. This is different to studies recording climate in other parts of the world, where a change to a more humid climate is observed (Föllmi, 1995; van de Schootbrugge et al., 2003, Westermann, 2013; McArthur et al., 2007; Morales, 2015). A possible reason why the EC may not have experienced a significant increase in humidity, as represented by an

elevated CIA*, is its position at the western margin of Gondwana during the Early Cretaceous. If the dominant wind direction was easterly during this period, as suggested by Hay et al. (2008) and Flögel (2008), the wind across this large land mass may have prolonged an arid environment in the hinterland. This mechanism to generate aridity may have been less prominent later in the Cretaceous as Gondwana broke up and the South Atlantic was formed, as in the climate maps generated by Chumakov et al. (1995), which show an equatorial humid belt from the Albian onwards.

Also, in the EC anoxia proxies suggest more persistent anoxia in the Valanginian than during the Berriasian, contradictory to other studies across the globe (summarised by Föllmi, 2012). In the absence of indicators for higher productivity, this anoxic state was most likely caused by basin geography. The lower global (and local) sea levels in the Valanginian compared to the Berriasian (Sarmiento-Rojas et al., 2006; Haq et al., 2014) could have enhanced the effects of sills and may have led to more sustained periods of anoxia (Figure 9.3), leading to greater accumulation of organic matter (Figure 6.2).

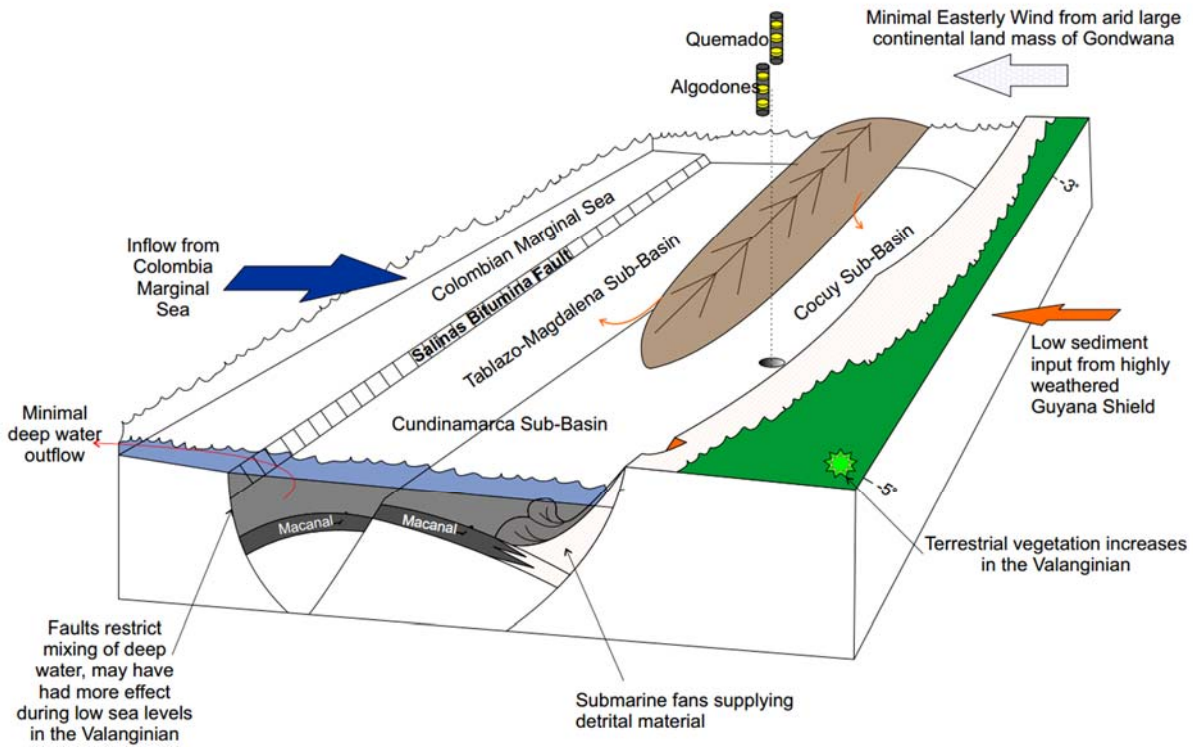

Figure 9.3. Generalised schematic for the paleo depositional environment during the Early Cretaceous (Berriasian and Valanginian). Adapted from Cooper et al. (1995) with information from Etayo et al. (1997) (Figure 2.4), and paleo latitude from http://www.odsn.de.

9.2.3 Aptian

The conditions in the EC during the Aptian were more humid and relatively stable compared to the Berriasian and Valanginian (relatively high and mostly uniform CIA* in all sections), supporting some geochemical studies which suggest higher humidity than the Valanginian and Hauterivian (Western Tethys, Stein et al., 2012; Föllmi, 2012), and higher equatorial humidity seen in the climate maps of Chumakov et al. (1995) but opposing a shift to greater global aridity seen in other studies (Jones and Jenkyns 2001; Föllmi et al., 1995). The hinterland was relatively highly weathered, leading to an average CIA* of 89 (note a CIA* of 100 represents most intense paleo chemical weathering, i.e. kaolinite). The amount of coarse material arriving at the study sites was highly variable near the coast (Pedregal and Cantonera), and co-varies with CIA* (Figure 7.3). Further offshore in the distal LC sections, these variables are more stable, consistent with the distal nature of the sediments and detrital material being concentrated in the east of the basin (Figure 9.4). There is a disparity in redox conditions, too, with anoxia evident throughout the distal sections, but at least regular oxic periods (confirmed by bioturbation) nearer the coast (Figure 7.8). High values of redox sensitive TE in other samples of Aptian age, collected from close to the centre of the EC, also support anoxia (Campos Alvarez and Roser, 2006). Given that marine deposition extended beyond the fault bounded EC during the Aptian (due to rifting ceasing and higher sea levels, Sarmiento Rojas et al., 2006; Cooper et al., 1995; Haq, 2014), one would have assumed that the bottom waters of the EC would have been better ventilated and more oxic in the Aptian than the Early Cretaceous (Figure 9.4). An alternative mechanism to generate anoxia may have been higher regional productivity, as indicated by TE and P proxies higher than average shale and well above values seen in the Berriasian and Valanginian (Figure 9.2 and 7.8). Nutrients for these higher levels of productivity could have come from the increased chemical weathering of the hinterland in comparison to earlier sediments, but also the open Ocean, with limited connections to the proto-Atlantic being initiated in the Aptian.

9.2.4 Albian

In all sections, there is indication of increasing aridity in the hinterland (decreasing CIA*) after the Aptian-Albian boundary, suggesting a gradual change to a more arid climate in the Albian. This suggests that climate in the EC may have been modulated by global (or at least Atlantic) climate, which some records indicate is becoming cooler and more arid in the Albian compared to the Aptian (McAnena et al., 2013; Follmi, 1995). In the distal sections,

this is matched with a general increase in Zr, which may indicate an increasing aeolian component and offshore winds from an arid interior. The distal Albian sections are anoxic, similarly to the Aptian samples, and a number of samples have geochemical signatures of euxinia (Figure 9.2, elevated Mo EEF and Mo contents greater than 100 mg/kg indicative of euxinia (Scott and Lyons, 2012). There is a dramatic increase in TOC at the proposed Aptian-Albian boundary (e.g. 2.8 wt% to 10.9 wt% in LC3), which is linked to an increase in Mo and a possible euxinic period. Differently to the Aptian, there are Albian samples where productivity proxies exceed those seen in modern day upwelling sediments (Brumsack, 2006), suggesting extremely high productivity. This increase in productivity could be connected to enhanced connectivity of the basin to nutrient rich waters of the open ocean, with the basins connecting from the Pacific to the Atlantic to form an epicontinental seaway which persisted until the Santonian (Erlich et al., 2003). High productivity in samples of Albian age has also been identified in the very south of the EC (Villamil et al., 1996), supporting the idea of basin wide higher productivity. Similar to the Aptian, it is suggested that it is this high productivity that drove bottom water anoxia/euxinia. In the EC, decreasing humidity in the Albian was linked to increased productivity which is suggestive of an offshore wind pattern causing upwelling of nutrient-rich waters. Differently, in the western Tethys and the proto-North Atlantic, anoxia (during OAE 1b) were driven by increased freshwater runoff from land, supplying nutrients and creating a freshwater lid (Herrle et al., 2003; Wagner et al., 2007; Erbacher et al., 2001).

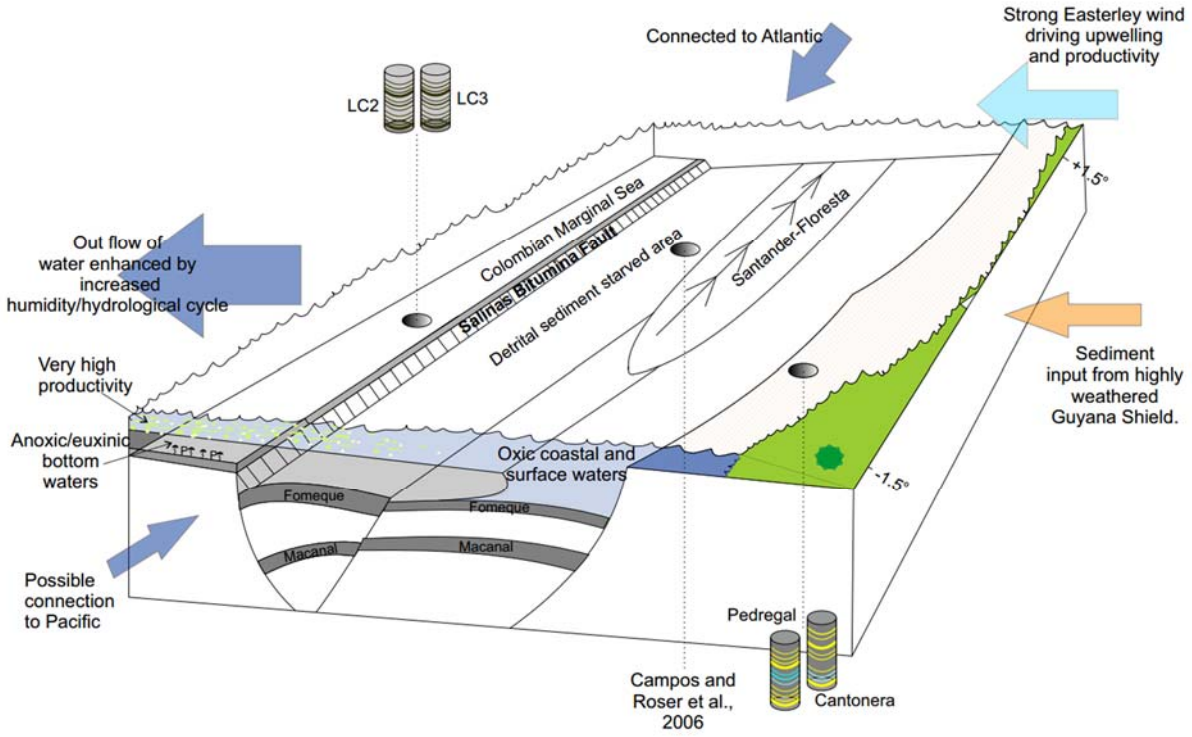

Figure 9.4 Generalised schematic for the paleo depositional environment during the mid- Cretaceous (Aptian and Albian). Adapted from Cooper et al. (1995) with information from Etayo et al. (1997) (Figure 2.7), and paleo latitude from http://www.odsn.de.

9.2.5 Cenomanian

The Cenomanian was a time of high and rising global sea level (Haq, 2014). This high sea level linked decreased the effect of local bathymetric highs located within the epicontinental seaway (eg the Santander Massif between the EC and the Maracaibo Basin) and likely was the period of most unhindered flow through the seaway. Despite the opportunity for water mass mixing with the open Atlantic and Pacific during this time of high sea level, the distal samples of the LC1 are consistently anoxic. Cenomanian samples are deposited under high siliceous productivity, with TE and bulk proxies suggesting similar levels of productivity to the Aptian, and productivity may have driven the low oxygen concentrations. It appears that the climate was relatively stable, with CIA* values comparable to the Albian but lower than the Aptian in all sections (Figure 7.3, 8.4, 9.2). This suggests that the climate in the hinterland was not getting significantly more humid, even with the increase in sea surface temperatures seen globally (Jenkyns, 1994; Huber et al., 2002; Friedrich, 2012), perhaps suggesting relative aridity in this part of the tropics. As discussed in the Berriasian section, it is possible that the rise in sea level could have reduced the CIA*, cancelling out any signal of increasing paleo chemical weathering with increased humidity (Westermann, 2013) and so an alternative measure of paleo chemical weathering should be sought to confirm this observation. The global sea level maximum during the Cenomanian (up to 250 m higher than

today (Haq, 2014)) did not result in significantly less detrital material arriving at the LC1 location when compared to the Early Albian (when global sea level was 150 m higher than today) in LC3 (Figure 9.1). In fact, in the more proximal settings (like Crucero), there is a higher proportion of coarse detrital material reaching the sediments than during later periods in the Cretaceous with lower sea levels (Figure 8.4). This is likely due to local tectonics, including the subduction of the Caribbean plate under the Central Cordillera causing uplift in the Llanos basin (Sarmiento-Rojas et al., 2006).

9.2.6 Turonian

The OAE 2 CIE in LC1 offers the opportunity to directly compare the EC/MMV records to temporal equivalents in other parts of the world. During the CIE itself, an increase in CIA* corresponds to increased paleo chemical weathering rates seen in global proxies for weathering (e.g. Sr isotopes, Jenkyns, 2010). This increased weathering may have supplied nutrients for increased productivity. An alternative source of nutrients according to conceptual models of Trabucho Alexandre et al. (2010) and Orth et al. (1993) is the CLIP. There is an increase in elements which may have been derived from the CLIP (Cu, Fe, Cr) during OAE 2 (Figure 8.9 and Figure 8.12). However, Figures 8.16 and Figure 8.17 show that the EC has lower TE contents and productivity proxies compared to sites within the Atlantic. This could be evidence supporting the nutrient trap concept, i.e. that the CLIP sourced TE and nutrients only accumulated to extreme extents due to the particular geography of the Proto-North Atlantic (Trabucho Alexandre et al., 2010). The CIE does not correspond to exceptionally high productivity or TOC compared to other time periods in the EC. In fact, samples directly following the CIE show signs of being deposited in conditions of even higher productivity. This suggests that factors globally associated with the CIE are not the dominant controls on carbon accumulation in the MMV. An alternative mechanism is that the TE inventory of the sea water was drawn down during the large scale euxinic conditions of the OAE 2, preventing their circulation and subsequent accumulation in the sediments under in euxinic conditions. This mechanism appeared to occur off the coast of northern South America (Hetzel et al., 2009) and in the southern Tethys (Dickinson et al., 2017).

In the Turonian, the intensity of paleo chemical weathering increased, especially towards the top of the LC1 section. The Turonian is still a greenhouse world, likely with high global humidity, however a decrease in humidity should be expected in a cooling world (Jenkyns, 1994; Huber et al., 2002; Friedrich, 2012), suggesting a more local climatic feature may be

controlling extents of paleo chemical weathering around the EC. Perhaps the continuation in humidity relates to the breaking up of Gondwana and the opening of the South Atlantic. Westerly winds blowing across the equator would have been drier until the South Atlantic was wide enough to accommodate greater water vapour transfer to the continent (Hay and Floegel, 2012). Samples from LC1 have TE proxies indicating that productivity (calcareous or siliceous) was generally high but variable (Figure 9.2). Geochemistry indicates bottom water anoxia throughout the majority of the Turonian. The Turonian has the only samples with Mo/Al significantly higher than average shale and Mo contents indicative of euxinia (according to the definition by Scott and Lyons, 2012) in the Late Cretaceous. Samples from this period also show more intense paleo chemical weathering (and more coarse material) suggesting increased runoff, possibly driving anoxia by causing stratification and supplying nutrients for increased productivity (Figure 9.4). Euxinia were also identified in Turonian sediments in the Maracaibo basin (Davis et al., 1999; Perez Infante et al., 1996), suggesting extreme redox conditions was a wider basin feature in the Turonian. This may have reinforced enhanced productivity by releasing the essential nutrient P from anoxic-euxinic sediments (Poulton et al., 2015). The TOC content in the LC1 section should be similar to the original depositional content as the samples have not been buried through the oil window. There are correlations between TOC and proxies for anoxia/euxinia (Table 8.2), suggesting that preservation under anoxic conditions was important for the accumulation of TOC, even in this high productivity setting.

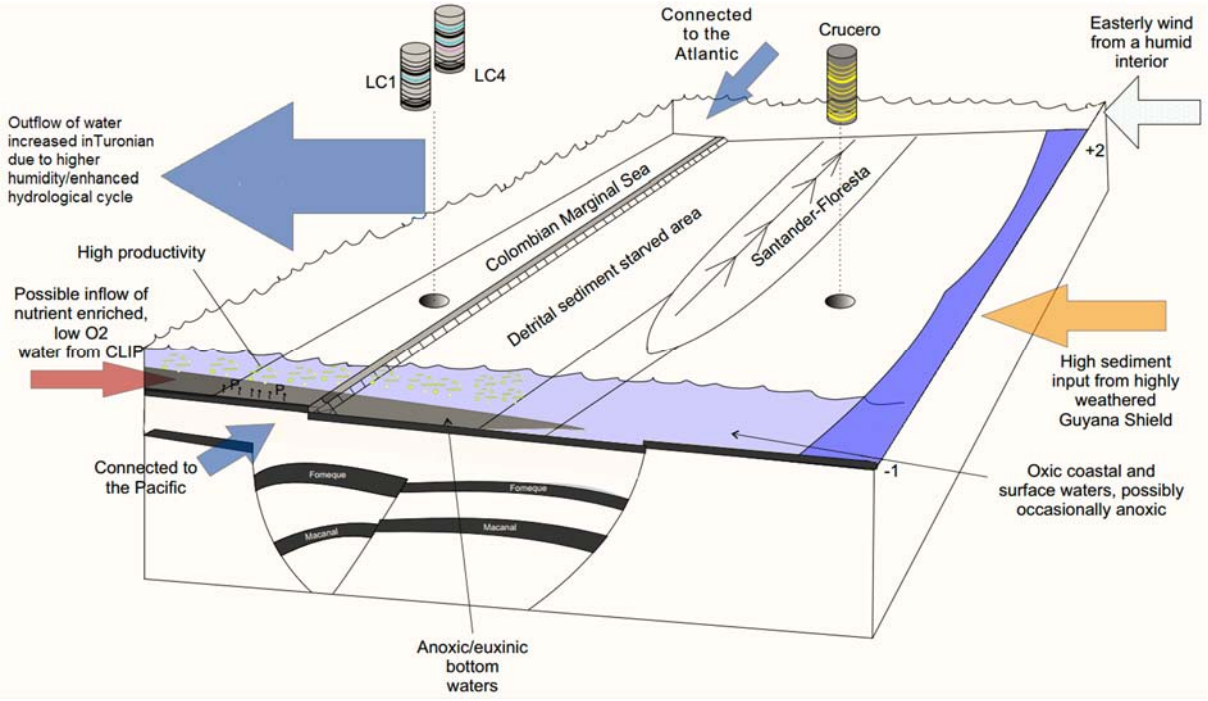

Figure 9.5. Generalised schematic for the paleo depositional environment during the Turonian. Adapted from Cooper et al. (1995) with information from Etayo et al. (1997) (Figure 2.9), and paleo latitude from http://www.odsn.de.

9.2.7 Coniacian

During the Coniacian, CIA* is relatively low, similar in level to the Albian and Cenomanian sediments, but increases towards the boundary with the Santonian, suggestive of a gradual increase in the humidity of the continent, again opposing a generally cooling trend seen globally, as in the Turonian. Coarse detrital input is relatively steady in Zipa, although Al content (and so likely clay content) varies (Figure 8.4), likely influenced by dilution by the biogenic material.

Coniacian samples within Zipa and LC4 contain productivity proxies at levels higher than average shale, but lower than samples taken from the Turonian and the Aptian when the site was located south of the equator, providing further evidence that the northward migration of the EC is not the dominant cause of upwelling. However, TE enrichments may have been reduced via leaching from these low $CaCO_3$ samples, and they may well have been higher in the past (Figure 9.1). Beds rich in phosphorous are also present within the Zipa section (Figure 8.9). The phosphate beds in Zipa are were deposited during periods with the highest redox sensitive TE contents, so they may be associated with high productivity and mostly anoxic but fluctuating redox conditions (Ingall et al., 2005). It is interesting to note that phosphate beds are limited to the Coniacian at Zipa, whereas in other locations in Colombia,

and the Maracaibo basin phosphate beds (linked to rapid algal growth and resultant mass fish mortality by Erlich et al., 1999) are limited to the Santonian (Erlich et al., 2000). The assumed spatial variation in P beds in chert dominated Coniacian and Santonian sediments across northern South America may be due to a variation in the loci of upwelling. Some of the samples from Zipa show characteristic planar lamination (Figure 8.10). On closer examination, it appears that this lamination is due to a switch from siliceous to calcareous productivity on a sub mm scale. This suggests that the dominant planktonic community during the Coniacian (and Santonian) was particularly sensitive to changes in the environment. Samples from the Coniacian in Zipa and LC4 document anoxic or euxinic bottom waters (Figure 9.1). The Coniacian section of Crucero is devoid of sedimentological indicators of bioturbation, which may indicate generally low levels of oxygen even in this proximal location. These anoxia/euxinia may have been driven by the high productivity.

9.2.8 Santonian

There is a shift to higher siliceous productivity at the assumed Coniacian-Santonian boundary in Zipa. This is linked to a shift to a more arid interior, with CIA* decreasing over the Santonian to levels comparable to those in the Berriasian and Valanginian. This change to greater aridity may be caused by the globally cooling temperatures (Friedrich et al., 2012). This period is one of major turnovers in the Upper Magdalena Valley Basin coupled with an increase in radiolarian productivity (Martinez et al., 2003). An increase in the dominance of chert going into the Santonian is assumed to be widespread across northern South America (Villamil et al., 1999). Trace element and P proxies for productivity are high, with TE contents exceeding modern day upwelling settings, but are variable throughout the rest of the Zipa section. In Pescana, TE proxies are not useful due to the proximal nature of the sediments, but sedimentological evidence (faecal pellets, skeletal remains, P beds) indicates relatively high productivity even in proximal settings. Although the Coniacian-Santonian boundary is not categorically defined within the Zipa section (using bio- or chemostratigraphy), there are some geochemical changes in these samples which are comparable to other sections. The shift to higher siliceous productivity linked to greater runoff and higher paleo chemical weathering at the supposed stage boundary in Zipa are similar to changes seen at Demerara Rise (Flögel et al., 2008) and off the coast of Northwest Africa (Beckmann et al., 2005).

In Zipa, the Santonian sediments contain redox sensitive TE and Fe_{HR}/Fe_T proxies which indicate bottom water anoxia, but TE are less enriched compared to Coniacian sediments

(Figure 9.2 and 8.12). This is surprising as the Colombian Marginal Sea closed during the Santonian, restricting the basin in the west (Figure 9.6). Again, these differences might be caused by contemporary weathering, however, $CaCO_3$ containing samples also have low redox sensitive TE (Figure 9.2).

The enrichments in productivity proxies in Zipa are similar in magnitude those seen in samples from the Turonian, but they are related to lower, not higher extents of paleo chemical weathering (Figure 9.2). In this more arid environment, high productivity (and related anoxia) is not likely to be fuelled by increased nutrients from land, like during periods in the Turonian. There is a corresponding increase in coarse material which, when linked to a more arid interior and increased ventilation, provides evidence for an increase in the intensity of offshore winds, which would result in upwelling as main source of nutrients.

High siliceous productivity and upwelling in the Santonian, when the site had migrated to north of the equator (Figure 2.12), may support models of Villamil et al. (1999) and Erlich et al. (1999) that this geographic migration is an important factor driving stronger offshore winds and upwelling. However, there are samples of Turonian and Albian age (when the site straddled the equator) which have TE contents suggestive of similar levels of productivity (Figure 9.2). This could indicate that upwelling of nutrient rich proto-North Atlantic waters was occurring in northern hemisphere locations in Venezuela, and they were being efficiently transported to southern hemisphere locations, as shown in climate models (Donnadieu et al., 2016), or it could indicating that the location relative to the equator was not the only dominant mechanism for driving high productivity.

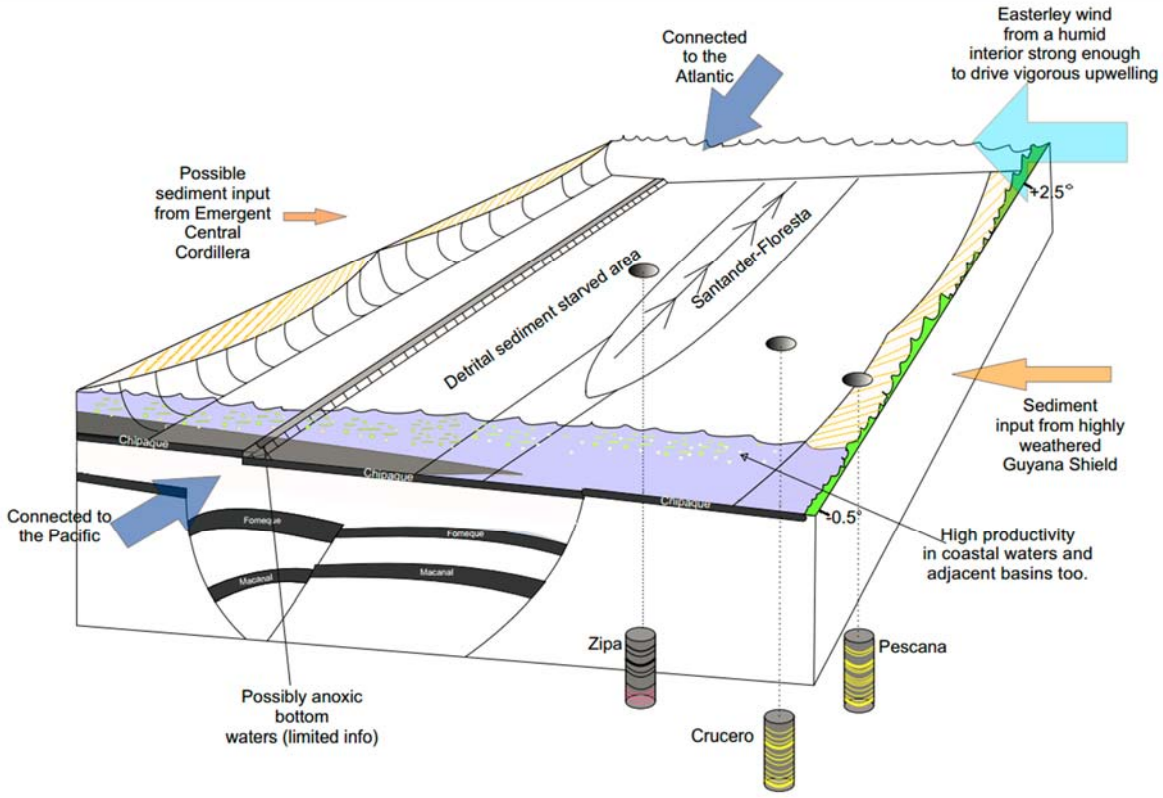

Figure 9.6 Generalised schematic for the paleo depositional environment during the Turonian. Adapted from Cooper et al. (1995) with information from Etayo et al. (1997) (Figure 2.11), and paleo latitude from http://www.odsn.de

9.2.9 Conclusions about paleoenvironmental evolution in the EC during the Cretaceous

It is evident from first bulk organic geochemistry provided by Ecopetrol (Appendix A) that depositional conditions in the EC and surrounding basins allowed significant accumulations of organic matter during the Cretaceous. Chapters 6-8 and the summary provided here show that the factors which caused the accumulation of organic matter varied over the Cretaceous. In the Early Cretaceous, the active rifting of this isolated basin caused the bottom waters to become anoxic allowing the preservation of organic matter and the formation of the TOC rich Macanal Formation. In the Aptian and Albian, sea levels were higher and sedimentation was no longer limited by the fault bound EC basin. Very high productivity (Ba contents higher than those in modern day upwelling sites), likely caused by wind driven upwelling, generated organic matter and reduced oxygen availability, allowing this organic matter to be preserved. This, coupled with low dilution by detrital material (in the west of the basin) allowed the formation of the organic rich Fomeque Fm. (and time equivalents). During the C/T boundary and the Lower Turonian, periods of enhanced organic matter burial are linked to high productivity (and consequent anoxia/euxinia) with nutrient input from land generated by paleo chemical weathering, but also a possible influx of

nutrient rich waters from the CLIP. Later in the Cretaceous, it appears that organic matter burial was also linked to productivity with a dominance of siliceous plankton. In the Santonian, enhanced productivity was linked to wind driven upwelling across large parts of northern South America. This is tentatively linked to a northward migration of the continent across the equator, as suggested by Erlich et al. (1999) and Villamil et al. (1999), but TE proxies indicate similar levels of upwelling related productivity in the Albian, when the site was further south, straddling the equator. These different mechanisms to enhance productivity allowed the accumulation of organic matter for the Chipaque Formation (and time equivalents). Even in samples where there is evidence for extremely high productivity, where TOC correlations are available (LC1 section), they are most strongly positively correlated with TE for anoxia, suggesting a redox control on organic matter preservation even in very high productivity settings. Information about the climate derived from CIA* agrees with global climate proxies trends in most cases, but there appears to be some evidence for the maintenance of aridity for much longer in the Early Cretaceous, and increases in humidity in a globally cooling world from the Turonian and Coniacian, both of which may relate to the sites position on the most Westerly part of the supercontinent Gondwana as it breaks up. This is would affect models of Cretaceous ocean circulation which rely on precipitation over South America to produce a deep water creation in the high latitude South Atlantic (e.g. Donnadieu et al., 2015)

9.3 Future work

9.3.1 Benefits of increasing sample resolution

In this pioneering study, a relatively coarse sampling resolution was used in order to gain a broad understanding of the paleoenvironment over most of the Cretaceous at several locations within the EC. Therefore, an increased resolution of the geochemical records could be especially helpful to better understand various aspects of basin evolution. One major benefit of increased sample resolution would be an improved age model using chemostratigraphic correlations. There is a problem assigning ages to samples of the EC, due to sparse and poorly preserved microfossils (Vergara et al., 1997). Most geological studies carried out in the EC have required lithostratigraphy to correlate sections to ones where biostratigraphy was possible (Georex, 2015; Villamil, 1998), which arguably introduced a large uncertainty. High resolution geochemical analysis would allow different sections to be better correlated across the basin. Also, with a high resolution data set, time series analysis

can be applied, constraining changes in the environment to orbital forcing providing further information about durations of environmental change (Weedon et al., 2003; Schwarzacher,1993). Although the age models produced in this way are not absolute and need to be ground-truthed with biostratigraphy/chemostratigraphy, they could be used to better estimate sedimentation rates (vital for varying fluxes of elements to the sediments) in between these known absolute dates (Villamil, 1996; Wagner et al., 2007). Analysis of bulk $\delta^{13}C_{org}$ or Sr isotopes could be used to correlate sections between basins (e.g. Voigt et al., 2000; Meyers et al., 2012, Jenkyns et al., 2002), further improving dating. This high resolution could be achieved with hand-held XRF, although it is possible that variable permeability of the mudstones and so variable water content could affect the data (Lemiere et al., 2014). Also, ensuring samples are unweathered will increase the number of samples which are reliable for geochemical analysis. This could be done by using excavating tools, or hand-held corers and after sample collection, freeze drying the samples as soon as possible.

Orbital scale variations in paleo chemical weathering and upwelling have been noted in the prot-Atlantic during OAE's in the Cretaceous (e.g. Hoffman and Wagner, 2011; Beckmann et al., 2005), linking provision of nutrients to fuel productivity to orbitally induced variations in the ITCZ and Hadley Cells. In this thesis, the low sampling resolution has only allowed interpretation about the long term effect of runoff versus upwelling on organic matter accumulation. Increased resolution of samples in the EC could, due to its equatorial location, provide additional information about the effects of these tropical phenomena, and determine cause and effect. Refining the effects of short scale changes in the climate at the tropics (related to the ITCZ) on the global climate during greenhouse periods like the Cretaceous is vital, given the current observations of an expanded tropical belt due to anthropogenic global warming at the equator (Seidel et al., 2008).

This thesis has identified specific locations where increased resolution could provide potentially novel information about Cretaceous paleoclimate. In the La Zipa section, there is evidence for sub mm scale variation in the dominant plankton type (siliceous or calcareous) close to the OAE 1b (Figure 5.11). Further, elemental mapping by SEM could constrain the geochemistry of these different layers and so provide some depositional context for the fluctuations – likely changes in the amount or type of nutrient influx on a possibly seasonal/annual resolution. Since the fluctuations are visible at outcrop scale due to variable effects of contemporary weathering, these sub mm variations could be tracked over the

scale metres, provide vital information about longer term (millennial) trends of these seasonal/annual changes. Such a study may combine fine scale geochemistry (SEM-EDX or laser ablation ICP-MS) with large scale visualisation and quantification (using photos and visualisation software). Also, analysis of further samples from the OAE 2 CIE in the LC1 section could provide an unprecedented level of detail about this global climatic event due high sedimentation rate (11 cm/kyr compared to 4 cm/kyr in the WIS at another relatively thick section).

A sub set of the larger sample set collected by Georex (see Chapter 3 for details) was selected for analysis for this thesis. Although chosen to cover the full length of the section, samples with higher TOC were preferentially selected to allow for concurrent organic geochemical analysis. This, combined with a selection of samples from only the fine lithologies, may have biased the sample set towards more anoxic or higher productivity samples. Analysing a greater number of the larger sample set (which was taken on a more systematic basis, mostly every 2 m) would remove any bias.

9.3.2 Additional analysis for further clarification/insights

In this study, CIA* has been used to assess the extent of paleo chemical weathering, with its inferences towards the climate in the hinterland. Interpretation has, however, been complicated by the possibility of a variable source of detrital material, especially when considering the evolution of the Central Cordillera, and by the effect of sea level change. Analysis of rare earth elements, or heavy mineral analysis of adjacent sandstone beds (possibly automated in SEM), would be useful to assess provenance, and thus decipher changes in provenance material versus changes in paleo chemical weathering (e.g. Campos Alvarez and Roser, 2006; Nie and Peng, 2014).

During OAE 2 in the EC, an increase in paleo chemical weathering intensity is evident, which may have provided nutrients to stimulate the high productivity seen in the samples. A similar mechanism during the OAE 2 is seen elsewhere (Baroni et al., 2014; van Helmond et al., 2014). According to the conceptual model of Trabucho Alexandre et al. (2010), the EC could also be affected by hydrothermally nutrient enriched waters from the CLIP during OAE 2. Further work with Sr, Cr and Os isotope systems could help to distinguish the relative dominance of supply from land by increased paleo chemical weathering and supply of nutrients from hydrothermal sources (Holmden et al., 2016; Jenkyns et al., 2010). It may also help to pick out more subtle changes in the extents of weathering, like those that may have

been missed in the Valanginian.

This study has highlighted the low Fe contents of Cretaceous shales in the EC, along with other basins across northern South America, when compared to studied sections in other parts of the world (Figure 8.17). As discussed in Chapter 3, in anoxic/euxinic conditions, basins with low availability of Fe (more precisely low Fe_{HR}) have more sulphide available to react with OM than basins where there is an excess of Fe_{HR} to react with all of the sulphide, forming pyrite (as summarised in Meyers et al., 2007). The most commonly used proxy to investigate this balance between availability of Fe_{HR} and S is Fe_{PY}/Fe_{HR} (Poulton and Canfield, 2011; Anderson and Raiswell, 2004; März et al., 2008). However, as discussed in Chapters 4 and 5, this proxy is susceptible to contemporary weathering and so this interesting aspect of deposition in the EC during the Cretaceous was not investigated. However, from the dataset presented here, there are hints that there were times when Fe_{HR} limited the amount of pyrite formed and that S was available to react with OM. Samples from Cantonera, Algodones, Quemado and LC1 in particular have varying amounts of sulphur not related to pyrite (up to 4 wt%), and this S is likely associated with OM (Figures 6.13, 7.8 and 8.11). Sulphurised organic matter has also been reported in other Cretaceous shales in northern South America (Mongenot et al., 1996) and oils of Venezuela (Lo Monaco, 2003). An alternative reason that some samples may contain S in excess of Fe_{HR} is variation in the supply of sulphate. There is mounting evidence that the availability of sulphate in the world's oceans has varied during the Phanerozoic, and was significantly lower than the modern day concentrations in some periods of the Cretaceous (Poulton and Canfield., 2011; März et al., 2008, Owens et al., 2013, Adams et al., 2010, Poulton et al., 2015). Periods with higher sulphate may be the result of increase input from volcanic/hydrothermal influences (Adams et al., 2010) but also from continental weathering of pyrite containing shales (Poulton et al., 2015). Using S isotopes of pyrite and carbonate from the EC samples would help to identify variations in changes the amount of S available and thus help distinguish if locally low Fe, or varying S content of the world's oceans contributed to sulphurised organic matter in the EC and Venezuela (Poulton et al., Owens et al., 2013, Adams et al., 2010).

9.3.3 Further exploration into the effects of contemporary weathering

The identification of methods to quantify the effects of pyrite oxidation in a neutral to high pH environment described in Chapter 4 has a lot of potential and should be further explored as a method of identifying samples affected by contemporary weathering. Also, it is assumed

that TE which are liberated from the pyrite are adsorbed onto the newly precipitated Fe (oxyhydr)oxide rims. Further work with laser ablation ICP-MS could identify the presence of TE within the pyrite, which was not apparent when using SEM-EDX (Gregory et al., 2015). Time-of-flight Secondary Ion Mass Spectrometry could also identify the location of TE, either within the pyrite core of within the Fe (oxyhydr)oxide rim. If TE could be seen to be trapped within the rim, this could have inferences for the release of TM from shales, which is an environmental problem in some regions (e.g. Hunan in China, Peng et al., 2004). With further work, controlling the pH of shale outcrops/soils could encourage the precipitation of Fe (oxyhydr)oxides, offering a potential remediation solution for these natural sources of heavy metals to ground and surface waters.

Since pyrite oxidation is a key proton donor for accelerating silicate weathering, the stalling of pyrite oxidation by the presence of carbonate could affect models of oxygen, carbon and sulphur cycles on geological timescales (e.g. Petsch and Berner, 1998; Wildman et al., 2004). Further research should take into account the exposure of carbonate rich lithologies during orogenesis when calculating fluxes of elements from mountain belts. New research indicates that contemporary weathering of mountain ranges can actually be a source, not a sink of carbon dioxide via the oxidation of organic matter (Hilton et al., 2014). Since pyrite oxidation also provides protons for organic matter oxidation, the presence of carbonate could also significantly impact this source versus sink balance. Further research could compare the rates of organic matter weathering (perhaps using rhenium as in Hilton et al., 2015) between catchments draining hillsides where carbonate rich, or non-carbonate rich mudstones were exposed.

9.4 Final words

This study has revealed long term anoxia and high productivity in Colombia, making the basin a significant carbon sink during the Cretaceous. These under investigated mudstones, therefore, have the potential to provide answers to key questions about the Cretaceous climate and carbon cycling – the relative importance of nutrients sourced from igneous provinces or the weathering of the land; the fine detail of the causes and effects of OAE 2 and the causes of short term variation in the dominant producers in an extremely high productivity (and so high carbon burial) setting. Armed with a new understanding of how geochemical proxies can be affected by contemporary weathering at outcrop, geochemists would greatly benefit from probing further into the mudstones exposed in this beautiful part

of the world.

Appendix A – Summary of field observations and lithological columns provided by Georex

Algodones

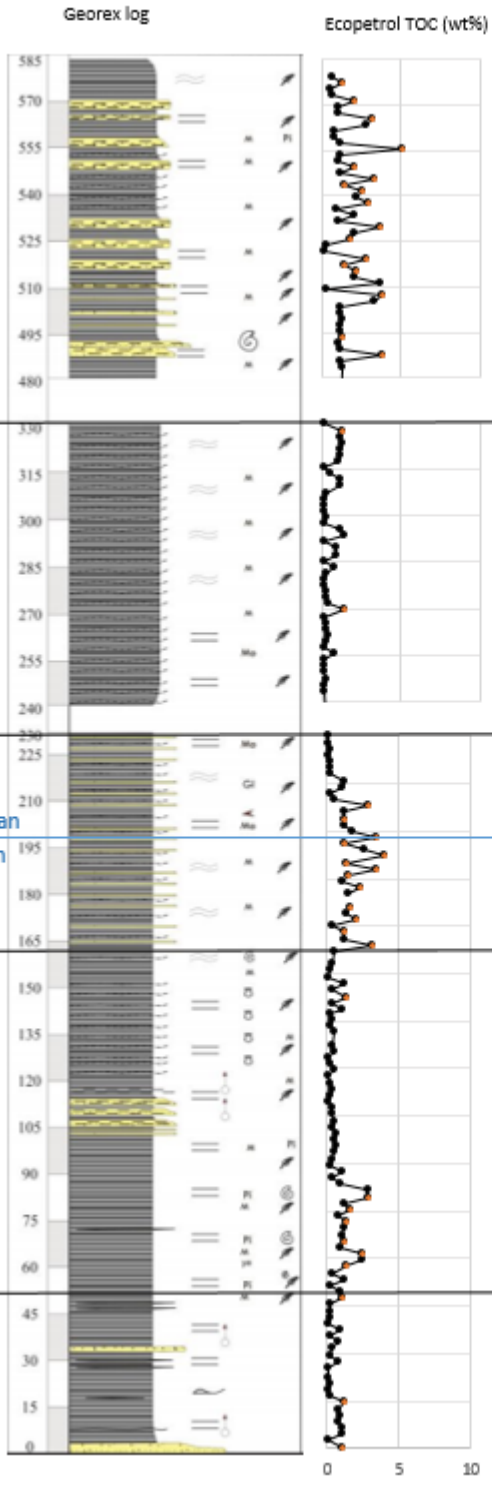

Valanginian

Berriasian

Georex field descriptions and interpretation

This section has the coarsest sediments. It mainly comprises siltstones, mudstones with planar parallel siltstone laminations. Muddy sandstone (quartz arenite) beds with normal gradation and have planar parallel and undulating lamination. Ammonite fossils are present in the base and fossil plant remains are present throughout. The environment of low energy deposition with mixed coarse and fine sediment arriving through fluid flows, is a **hemipelagic submarine fan close to a delta**.

Silty mudstones and mudstones with fine laminations of silt with mica. Preservation of parallel and undulating lamination suggests a lack of bioturbation. Again sedimentation in a low energy environment, but many plant remains indicate steady influx of terrestrial material. Here there are no sand beds so this **pro-delta** section is more distal than the previous.

Mudstones intercalating with siltstones with planar parallel or undulating lamination. There are beds of muddy sandstones (quartz arenite). At the top of this section there is sandstone with grey interclasts followed by monotonous grey mudstone with parallel lamination. The environment again is interpreted as **pro-delta**, with sand arriving as gravitational flows. As sand beds are less frequent, this section is more distal than the previous.

Top and bottom grey and to black mudstone with planar lamination and no evidence bioturbation. Fine muddy sandstone and mudstone in thin beds with lenticular and flasser lamination are also present alongside dark grey shales with thin light grey silt layers where with bivalve fossils are present. Well preserved ammonites confirm marine but close to shore due to plant remains. The environment is interpreted as low energy with sedimentation by decantation and gradation in sandstone beds suggests gravitational flows in a **pro-delta** with large sediment loads. The thicker sand beds in the middle suggest the peak of progradation.

Grey to black mudstone which is occasionally laminated (parallel to slightly undulating) with siltstone. There are thin, sandier (quartz arenite) beds with lenticular or wavy bedding. At the top of this section there is no lamination or alternation of beds due to bioturbation. The environment is interpreted as from the bottom, **pro-delta** with suspension settling sediments, **tidal plain** alternating periods of decantation of sediments and more active sedimentation

Quemado

Georex log

Ecopetrol TOC (wt%)

Georex field descriptions and interpretation

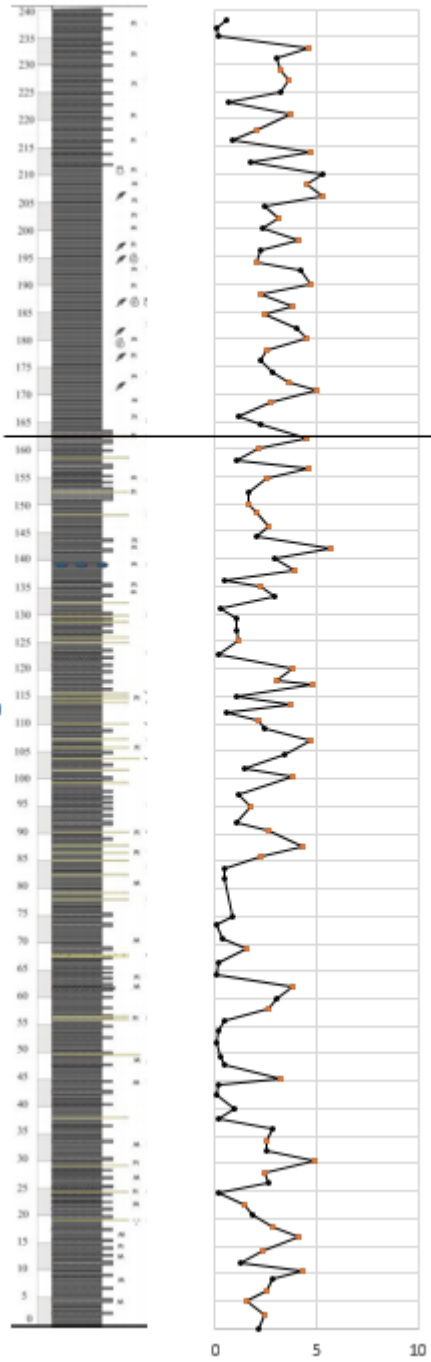

Monotonous beds of black and dark grey mudstone with planar parallel lamination with very little evidence of bioturbation. There are some layers with abundant disseminated pyrite. Imprints of plant remains are common. Fossiliferous layers contain ammonite and bivalve impressions. Towards the top of the column there are dark grey mudstones (occasionally with layers of disseminated pyrite) with laminations of siltstone. The environment is interpreted as low energy, marine but with supply of continental material. Pyrite indicates low oxygen conditions. **Distal pro-delta** offshore coastal plain.

Black and grey mudstones and siltstones with planar parallel lamination. Often micaceous. Very little evidence of bioturbation. Occasional thin beds of sandstone which show gradation from coarse and mixed sands to finer beds with either planar parallel or undulating lamination followed by siltstone with undulating or planar parallel lamination. Disseminated pyrite is visible in most lithologies. At the base there is a bed of phosphatic sandstone with pellets. The environment is interpreted as being low energy (due to fine nature of the sediments). The phosphatic layer is a condensation level and represents hemipelagic environment. The presence of pyrite suggests low oxygen conditions. The coarser layers are indicative of turbidite flows. So the environment is interpreted as **submarine fan** with turbidite flows.

Pedregal

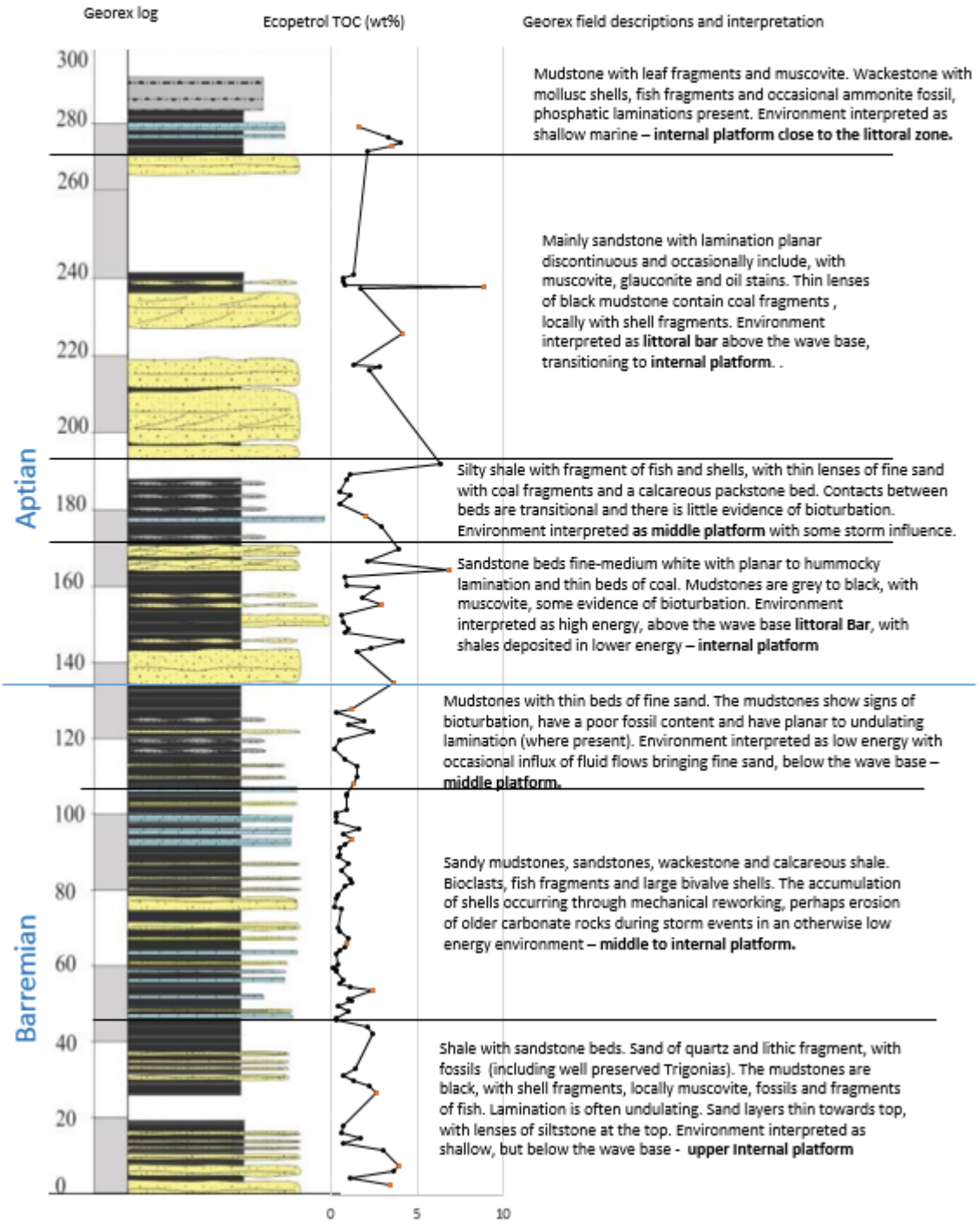
Georex log
Ecopetrol TOC (wt%)
Georex field descriptions and interpretation
300
280
260
240
220
200
180
160
140
120
100
80
60
40
20
0
0
5
10
Aptian
Barremian
Mudstone with leaf fragments and muscovite. Wackestone with mollusc shells, fish fragments and occasional ammonite fossil, phosphatic laminations present. Environment interpreted as shallow marine – internal platform close to the littoral zone.
Mainly sandstone with lamination planar discontinuous and occasionally include, with muscovite, glauconite and oil stains. Thin lenses of black mudstone contain coal fragments , locally with shell fragments. Environment interpreted as littoral bar above the wave base, transitioning to internal platform. .
Silty shale with fragment of fish and shells, with thin lenses of fine sand with coal fragments and a calcareous packstone bed. Contacts between beds are transitional and there is little evidence of bioturbation. Environment interpreted as middle platform with some storm influence.
Sandstone beds fine-medium white with planar to hummocky lamination and thin beds of coal. Mudstones are grey to black, with muscovite, some evidence of bioturbation. Environment interpreted as high energy, above the wave base littoral Bar, with shales deposited in lower energy – internal platform
Mudstones with thin beds of fine sand. The mudstones show signs of bioturbation, have a poor fossil content and have planar to undulating lamination (where present). Environment interpreted as low energy with occasional influx of fluid flows bringing fine sand, below the wave base – middle platform.
Sandy mudstones, sandstones, wackestone and calcareous shale. Bioclasts, fish fragments and large bivalve shells. The accumulation of shells occurring through mechanical reworking, perhaps erosion of older carbonate rocks during storm events in an otherwise low energy environment – middle to internal platform.
Shale with sandstone beds. Sand of quartz and lithic fragment, with fossils (including well preserved Trigonias). The mudstones are black, with shell fragments, locally muscovite, fossils and fragments of fish. Lamination is often undulating. Sand layers thin towards top, with lenses of siltstone at the top. Environment interpreted as shallow, but below the wave base - upper Internal platform

Cantonera

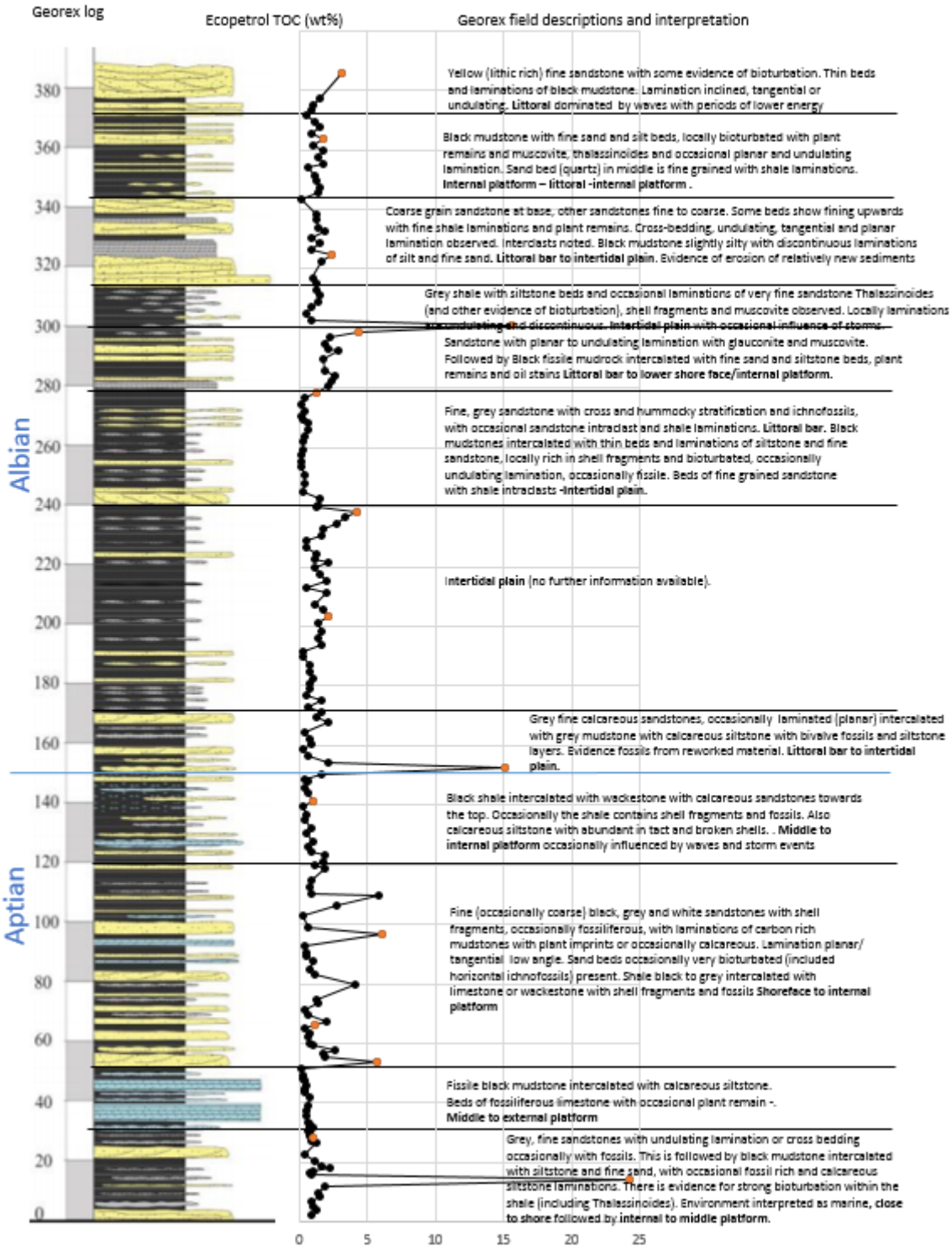
Georex log
Ecopetrol TOC (wt%)
Georex field descriptions and interpretation
Albian
Aptian
380
360
340
320
300
280
260
240
220
200
180
160
140
120
100
80
60
40
20
0
0
5
10
15
20
25
Yellow (lithic rich) fine sandstone with some evidence of bioturbation. Thin beds and laminations of black mudstone. Lamination inclined, tangential or undulating. Littoral dominated by waves with periods of lower energy
Black mudstone with fine sand and silt beds, locally bioturbated with plant remains and muscovite, thalassinoides and occasional planar and undulating lamination. Sand bed (quartz) in middle is fine grained with shale laminations. Internal platform – littoral -internal platform .
Coarse grain sandstone at base, other sandstones fine to coarse. Some beds show fining upwards with fine shale laminations and plant remains. Cross-bedding, undulating, tangential and planar lamination observed. Interclasts noted. Black mudstone slightly silty with discontinuous laminations of silt and fine sand. Littoral bar to intertidal plain. Evidence of erosion of relatively new sediments
Grey shale with siltstone beds and occasional laminations of very fine sandstone Thalassinoides (and other evidence of bioturbation), shell fragments and muscovite observed. Locally laminations undulating and discontinuous. Intertidal plain with occasional influence of storms.
Sandstone with planar to undulating lamination with glauconite and muscovite. Followed by Black fissile mudrock intercalated with fine sand and siltstone beds, plant remains and oil stains Littoral bar to lower shore face/internal platform.
Fine, grey sandstone with cross and hummocky stratification and ichnofossils, with occasional sandstone intraclast and shale laminations. Littoral bar. Black mudstones intercalated with thin beds and laminations of siltstone and fine sandstone, locally rich in shell fragments and bioturbated, occasionally undulating lamination, occasionally fissile. Beds of fine grained sandstone with shale intraclasts -Intertidal plain.
Intertidal plain (no further information available).
Grey fine calcareous sandstones, occasionally laminated (planar) intercalated with grey mudstone with calcareous siltstone with bivalve fossils and siltstone layers. Evidence fossils from reworked material. Littoral bar to intertidal plain.
Black shale intercalated with wackestone with calcareous sandstones towards the top. Occasionally the shale contains shell fragments and fossils. Also calcareous siltstone with abundant in tact and broken shells. . Middle to internal platform occasionally influenced by waves and storm events
Fine (occasionally coarse) black, grey and white sandstones with shell fragments, occasionally fossiliferous, with laminations of carbon rich mudstones with plant imprints or occasionally calcareous. Lamination planar/ tangential low angle. Sand beds occasionally very bioturbated (included horizontal ichnofossils) present. Shale black to grey intercalated with limestone or wackestone with shell fragments and fossils Shoreface to internal platform
Fissile black mudstone intercalated with calcareous siltstone. Beds of fossiliferous limestone with occasional plant remain -. Middle to external platform
Grey, fine sandstones with undulating lamination or cross bedding occasionally with fossils. This is followed by black mudstone intercalated with siltstone and fine sand, with occasional fossil rich and calcareous siltstone laminations. There is evidence for strong bioturbation within the shale (including Thalassinoides). Environment interpreted as marine, close to shore followed by internal to middle platform.

La Marina

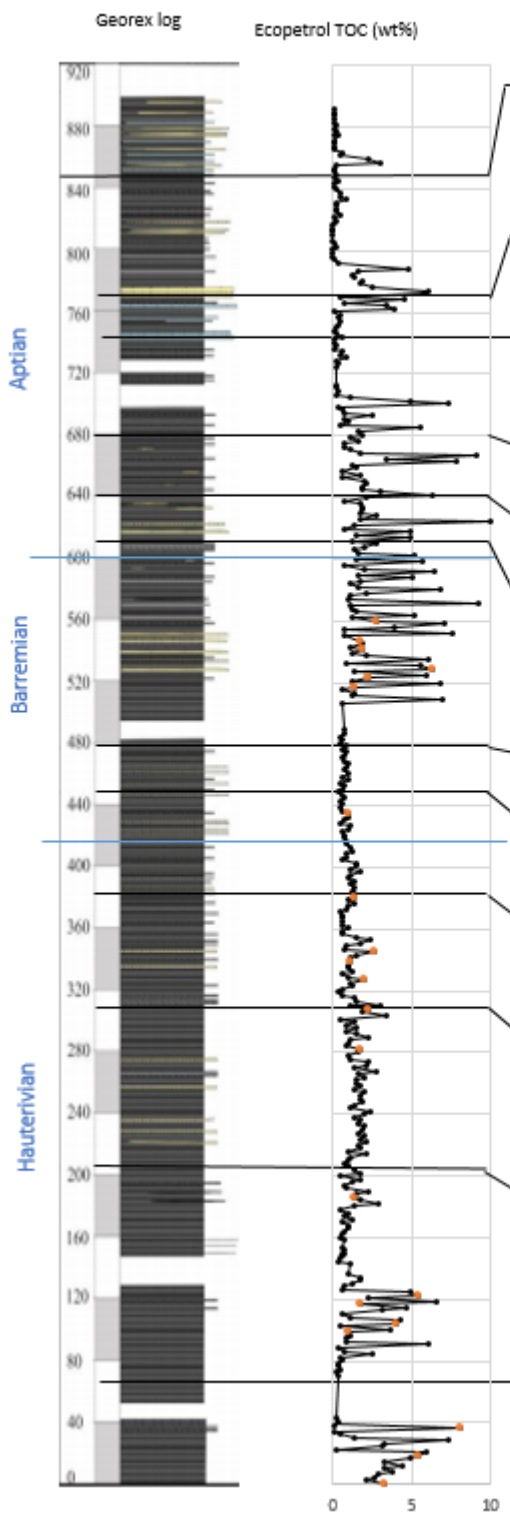

Georex field descriptions and interpretation

Intercalations of mudstone with lenses of silt, fine, muddy, calcareous sandstone and beds of wackestone and packstone. Lamination undulating and parallel. Fossils of ammonites observed. **Internal platform** but also **sublittoral, increasing sea level.**

Mudstone and siltstone with occasional lenses of siliceous siltstone laminations of gypsum and nodules of pyrite in lenticular beds and laminations undulating and planar parallel. Later, muddy fine sandstones with abundant mica and veins of quartz. Followed by thin lenticular beds of silt intercalated with silty mudstone, calcareous mudstone and silty sandstone. Here veins of fibrous calcite, and gypsum. Occasional lens/lamination of wackestone, packstone and quartz fine grained sandstone. Some layers containing fossil fragments (ammonites). **Platform internal – restricted but some link to the open sea**

Base dominantly packstone and calcareous mudstones with terrigenous and calcite intercalations, gypsum (laminations). Rest of section siltstones and shale lenses, with thin beds of calcareous mudstones, pyrite nodules and concretions, mica, sporadic lenses of wackestone, veins of gypsum and calcite lamination undulating and sometimes parallel. Beds lenticular. **Interior platform, shallow marine, very low energy, possibly mud flats**

Black mudstones with lamination discontinuous at the base, to planar and undulating in the rest of the column. Contacts between beds clear. With some lenses of greywackes and siltstones with fining upward sequences and disseminated pyrite, iron oxides, mica and veins of gypsum (from 725 m). Locally ammonite and bivalve fossils. **Interior platform in quiet water, varying sea level (or storm inundation).**

Mudstones with disseminated mica, undulating and not erosive contacts, undulating lamination to mixed beds. Abundant mica and lenses of siltstone and silty sandstone and concretions. From 660m increase in silt. Pyrite, mica and haematite observed. At 647 m ammonite shell fragments. **Protected platform with poor circulation, varying sea level**

Mudstones with disseminated mica, undulating and not erosive contacts, sporadic lamination of pyrite, and nodules of pyrite. Lenses of foliated sandstone, greywackes that are slightly calcareous and siltstone. Gypsum and pyrite in fractures. Principally parallel and undulating lamination until 631m, from then only undulating with lenses of siltstone and fining upward sequence. **Interior platform, tidal flats** but influence of **tidal currents, tidal streams**

Monotonous succession of mostly siliceous mudstones with heterogeneous, undulating to planar lamination, disseminated pyrite and crystals of gypsum. Ammonite fossils and nodules and concretions of pyrite are observed. Close to 534 m there are slightly calcareous sandstones. Evidence for moderate activity of organisms. **Interior platform, influence of tidal currents, swells and storms.**

Mudstones with thin lenses and beds of sandy siltstone, siltstone and greywacke (calcareous at the top of this section), pyrite, mica and beds of sandstone with fining upward sequence. Lamination is undulating and planar towards top. **Protected interior platform, below influence of tidal currents and waves**

Siliceous mudstones, undulating lamination (occasionally planar), occasionally fissile, intercalations of sandy siltstone and greywacke locally as lenses, laminations and beds. Pyrite (disseminated, in laminations and nodules), occasional gypsum (420-428) and mica are observed. One thick band <3m dominated by greywacke observed. Absence of fossils. **Protected interior platform, mud flats, network of tidal streams** (or storms) – occasionally supplies sediments of larger grains

Grey siliceous mudstone undulating lamination, with pyrite, fossils present 310 and 319 (ammonites and bivalves). From 354 m mudstone becomes dark grey, and lamination planar, with levels pyrite, gypsum and intercalation of fine sand and silt. Towards top, mudrock alternates between siliceous and carbonate with bivalve, ammonite, fish fragments and plant remains with nodules of pyrite. **Protected interior platform, mud flats, network of tidal streams** – occasionally supplies sediments of larger grains

Dark grey and black siliceous mudstones with occasional fine sand and silt layers/lenses. Pyrite and mica present. From 247-261 only mudstone, lamination planar or undulating, without fossils, with nodules of pyrite. Deformed ammonite fragments (223 m), but most section fossil free. Pyrite (disseminated and nodules) observed locally. **Platform interior platform, mudflats**, network of **tidal streams** occasionally supplies sediments of larger grain size.

Grey and dark grey/brown mudstones, siliceous occasionally carbonaceous, lamination undulating until top of section, where it is occasionally planar and the mudstone is fissile, with fossils (ammonites) concentrated in fossiliferous beds at the base of this section. Pyrite (disseminated in concretions) and gypsum (crystals), veins of sulphur and plant remains observed throughout. **Mudflats in protected interior platform** with periods of higher sea level

Calcareous (bottom 14 metre) and siliceous black and grey mudstone, with undulating and planar lamination, pyrite (often oxidised), laminations of gypsum and fine crystals of calcite observed throughout. Plant remains present.. Sandy beds42, 70-76 m) rich in organic matter, top band fractured with pyrite and gypsum, ammonites fragments present and vertical burrows. **Protected interior platform, mud flats** occasionally **hypersaline** (gypsum, little bioturbation, dehydration crack)

La Cristalina Section 3

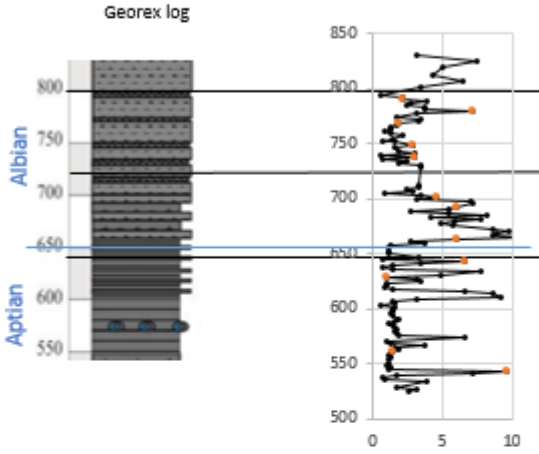

Georex field descriptions and interpretation

Monotonous succession of dark grey mudstone with calcareous siltstone, planar parallel lamination. Impressions of ammonites noted locally as is beds with disseminated pyrite. **Outer continental slope**.

Monotonous succession of calcareous siltstones, partially silicified, intercalated with calcareous mudstones with planar parallel lamination and bivalve and ammonites observed. Grey chert present towards the top, with planar parallel lamination. **Mid- outer continental slope**.

Black to dark grey fossiliferous mudstone with ammonites, calcareous mudstone and laminated siltstone. Planar parallel lamination. Within more calcareous packages are micritic nodules. Veins of calcite and disseminated pyrite noted in the siltstones. There are some ichnofossils. **Middle continental slope.**

Monotonous succession of black and dark grey siliceous (commonly micaceous) mudstones with planar parallel lamination. Little bioturbation noted. Towards the base are very thin beds of chert, with siltstone, veins of calcite and bivalves. Bivalves and ammonites noted throughout and disseminated pyrite noted. Concretions with FeO present in the middle and siltstone again present at the top. **Outer continental slope**

La Cristalina Section 2

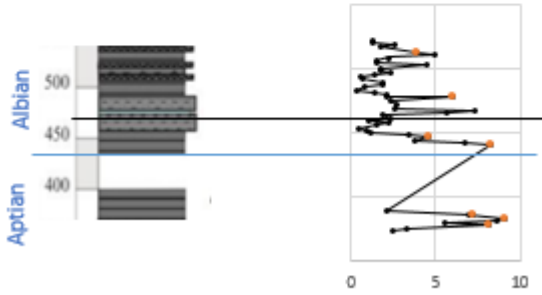

Light and dark grey chert with planar parallel lamination, in thick packets intercalated with mudstones. Frequent fossils of foraminifera planktonic and benthic. In between these thick packets of chert and mudstone are monotonous black and grey mudstone. At the base of this section is a bed of micritic limestone and grey wackestone with shell fragments (bivalves). Contact between beds is clear and planar. **Middle continental slope**

Monotonous succession of dark grey mostly siliceous (occasionally calcareous) mudstones with planar parallel lamination. Impressions of ammonites, bivalves (in the upmost section) and mica (restricted to base) observed. Towards the top there is some dark grey chert intercalations. **Outer continental slope**

La Cristalina 4

Georex log

Ecopetrol TOC (wt%)

Georex field descriptions and interpretation

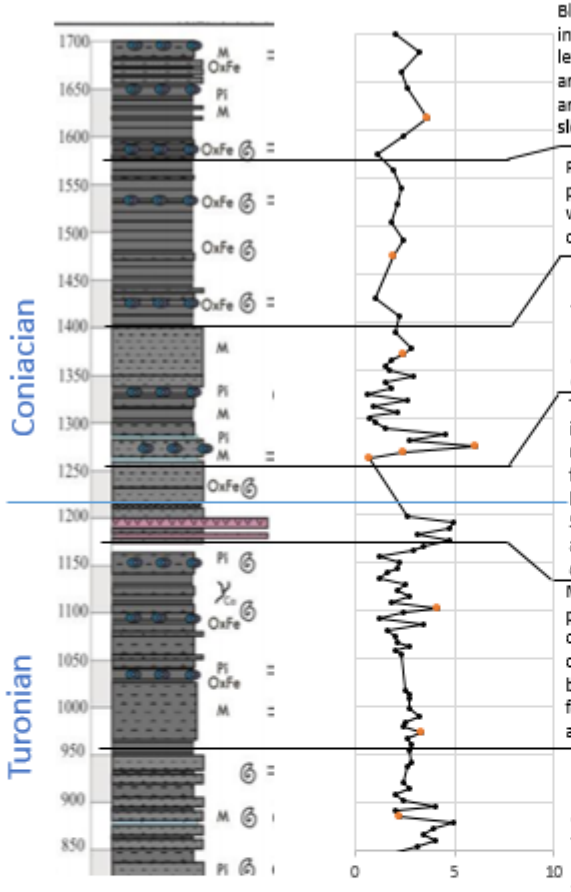

Black to grey mudstone and siltstone with planar parallel lamination, intercalated with calcareous mudstone. Towards the base there are lenses of micrite. Within calcareous mudstone layers, impressions of ammonites and bivalves and pyrite concretions noted. Two beds (1649 and 1679 m) contain concretions up to 1 m across. **Mid Continental slope**

Predominantly beds of black to dark grey mudstone with planar parallel lamination, intercalated with calcareous mudstones within which impressions of ammonites and bivalves and concretions are noted. **Outer continental slope**

Dark grey to black (locally calcareous) mudrocks with planar parallel lamination, with carbonate rich laminations with foraminifera. Towards the centre there are thin beds of siltstone, muscovite and pyrite concretions. Locally bivalve impressions noted, as well as concretions (mostly restricted to siltstone beds). **Mid-outer continental slope**

This interval starts with thick beds of dark grey volcanic tuff intercalated with silt and mudstones. Above this, calcareous mudstones with planar parallel lamination were noted, with shell fragments, bivalves and concretions with pyrite and Fe oxides. A limestone mud was noted, after which siltstone intercalations began. Some beds are fossiliferous with impressions of bivalves and ammonites. Locally the mudstones are siliceous, with thin beds of chert. **Mid-continental slope**

Monotonous succession of dark grey mudstones with planar parallel lamination. At the base, there are some siliceous beds with occasional carbonate levels. Towards the top it is completely calcareous, and is intercalated with calcareous siltstones. There are beds with nodules with iron oxides, pyrite concretions and bivalve fossils and muscovite is observed. 308-318 m there are many ammonite fossils. **Distal delta-outer continental slope.**

Dark grey to black, locally bituminous mudstone with planar parallel lamination. At the base there are minor interpositions of limestone mudstones and calcareous nodules. Towards the top there are minor interpositions of black calcareous siltstone. Beds were observed with fossils (ammonites, bivalves and fish scales. **Outer Ramp**

La Cristalina 1

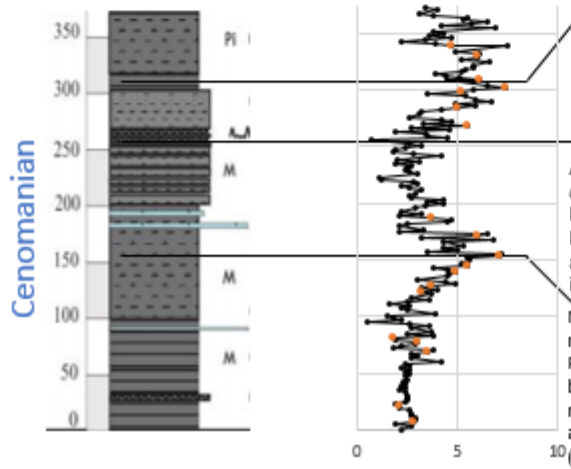

Fault at 310 m. Succession of monotonous dark grey, calcareous mudstones with planar parallel lamination. Fine, disseminated pyrite concentrated in recurrent beds. Fossils of ammonites noted, increasing in frequency towards the top of the section. **Outer continental slope.**

Dark grey to black., mostly calcareous siltstone with planar parallel lamination. Intercalated with thin to medium beds of siliceous siltstone and chert. Occasional laminations with disseminated pyrite. Bioturbation is very low. Fossils (ammonite) only encountered in one bed. **Outer continental slope**.

A succession of black and grey mudstones and siltstones, mostly calcareous and without bioturbation, with planar parallel lamination. This is intercalated with micritic limestones (mostly laminated) and grey wackestone. Muscovite, shells of bivalves and planktonic foraminifera observed. In some siltstone beds incipient silicification is observed. Muddy **Mid-continental slope.**

Monotonous thick packets of mostly calcareous, dark grey and black mudstone, with lamination planar parallel and slightly undulating. Regular beds with very little bioturbation. Close to the base thee are beds of chert. In the middle there is micritic limestone. Some mudstone beds have ammonite fossils. Toward the top, some beds are fossiliferous (bivalves) . **Outer continental slope with carbonate** (either via mechanical accumulation/reworking of shells or precipitation)

La Zipa

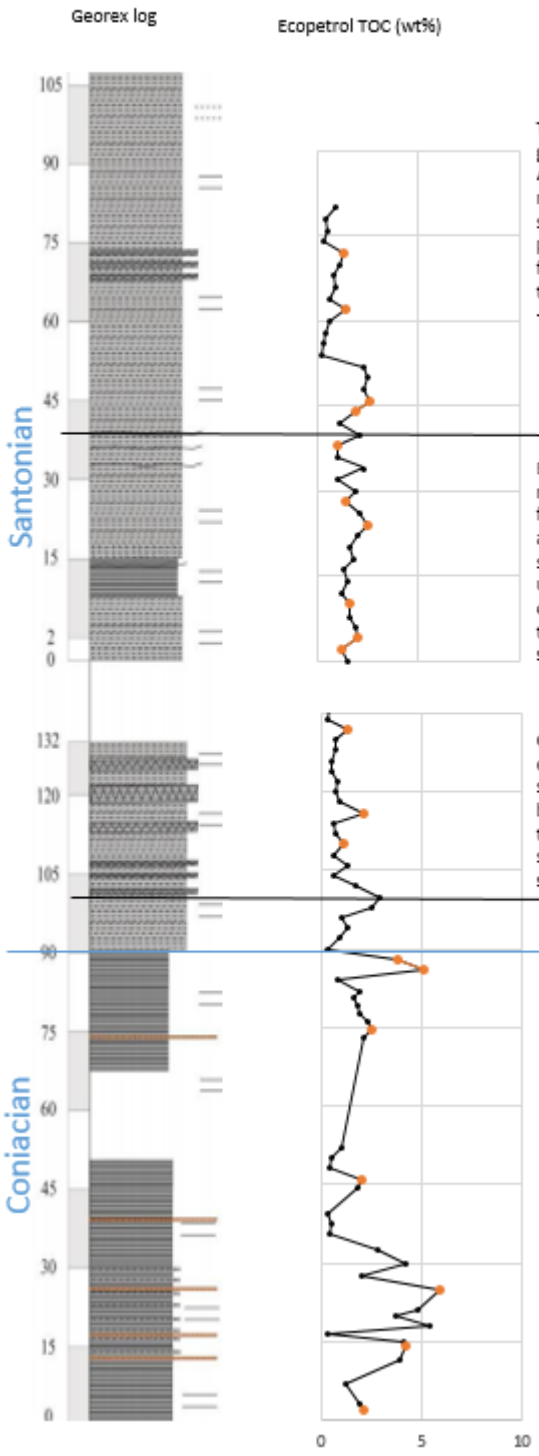

Georex field descriptions and interpretation

The bottom half comprises black mudstones beds intercalated with grey siliceous siltstone beds with planar parallel lamination. Abundant benthic foraminifera and occasional sea urchin remains noted. The top half comprises brown to black siltstone, dark grey siliceous siltstone, dark grey mudstones and chert, with planar parallel (often discontinuous) to undulating lamination. Planktonic foraminifera and nodules of pyrite are noted. . Towards the top, there are also benthic foraminifera and horizontal burrows. **Offshore - inner shelf**

Black calcareous and siliceous siltstone with occasional black siliceous mudstone, with benthic (siltstone)and planktonic (mudstone) foraminifera, mica, occasional plant remains and fish pieces noted, and planar parallel lamination observed. Close to the top, the siltstones have laminations of very fine sandstone, and occasional undulating lamination. Bioturbation is noted as low, however occasional vertical burrows and benthic foraminifera noted throughout the column suggest some bottom water oxygen. **Inner shelf to offshore transition.**

Chert and silicified micrite with lamination planar parallel discontinuous, intercalated with siliceous siltstone. In the top of this section black to grey mudstone is noted. Varied bioturbation (some bed contacts are irregular). Planktonic foraminifera are common throughout this section. Nodules of pyrite and occasional bivalve shell are noted. **Offshore inner shelf** with post-diagenetic chert **silicification**

Grey, brownish grey or black mudstones with planar parallel lamination and ammonites. Towards the base and the top are thin beds pf light grey and brown siliceous siltstone. Fragments of fish and bivalve fossils are noted. Brown, phosphatic levels, with pellets visible are noted (very altered). Planktonic foraminifera, iron oxides, pyrite concretions and bivalve shells also observed. **Offshore internal to middle continental shelf** possibly under influence of **upwelling currents**

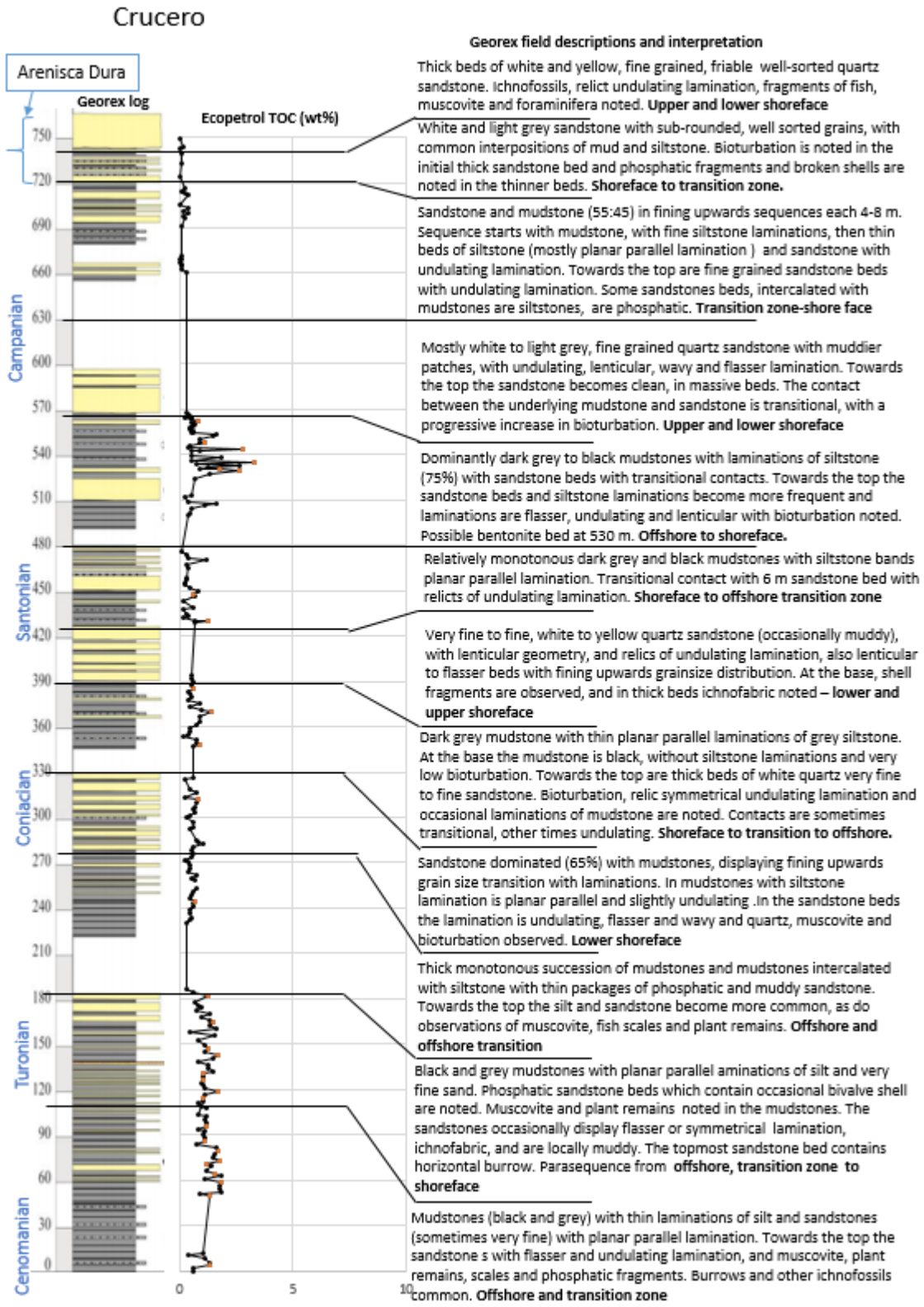
Crucero
Arenisca Dura
Georex log
Ecopetrol TOC (wt%)
Georex field descriptions and interpretation
Thick beds of white and yellow, fine grained, friable well-sorted quartz sandstone. Ichnofossils, relict undulating lamination, fragments of fish, muscovite and foraminifera noted. Upper and lower shoreface
White and light grey sandstone with sub-rounded, well sorted grains, with common interpositions of mud and siltstone. Bioturbation is noted in the initial thick sandstone bed and phosphatic fragments and broken shells are noted in the thinner beds. Shoreface to transition zone.
Sandstone and mudstone (55:45) in fining upwards sequences each 4-8 m. Sequence starts with mudstone, with fine siltstone laminations, then thin beds of siltstone (mostly planar parallel lamination) and sandstone with undulating lamination. Towards the top are fine grained sandstone beds with undulating lamination. Some sandstones beds, intercalated with mudstones are siltstones, are phosphatic. Transition zone-shore face
Mostly white to light grey, fine grained quartz sandstone with muddier patches, with undulating, lenticular, wavy and flasser lamination. Towards the top the sandstone becomes clean, in massive beds. The contact between the underlying mudstone and sandstone is transitional, with a progressive increase in bioturbation. Upper and lower shoreface
Dominantly dark grey to black mudstones with laminations of siltstone (75%) with sandstone beds with transitional contacts. Towards the top the sandstone beds and siltstone laminations become more frequent and laminations are flasser, undulating and lenticular with bioturbation noted. Possible bentonite bed at 530 m. Offshore to shoreface.
Relatively monotonous dark grey and black mudstones with siltstone bands planar parallel lamination. Transitional contact with 6 m sandstone bed with relicts of undulating lamination. Shoreface to offshore transition zone
Very fine to fine, white to yellow quartz sandstone (occasionally muddy), with lenticular geometry, and relics of undulating lamination, also lenticular to flasser beds with fining upwards grainsize distribution. At the base, shell fragments are observed, and in thick beds ichnofabric noted – lower and upper shoreface
Dark grey mudstone with thin planar parallel laminations of grey siltstone. At the base the mudstone is black, without siltstone laminations and very low bioturbation. Towards the top are thick beds of white quartz very fine to fine sandstone. Bioturbation, relic symmetrical undulating lamination and occasional laminations of mudstone are noted. Contacts are sometimes transitional, other times undulating. Shoreface to transition to offshore.
Sandstone dominated (65%) with mudstones, displaying fining upwards grain size transition with laminations. In mudstones with siltstone lamination is planar parallel and slightly undulating .In the sandstone beds the lamination is undulating, flasser and wavy and quartz, muscovite and bioturbation observed. Lower shoreface
Thick monotonous succession of mudstones and mudstones intercalated with siltstone with thin packages of phosphatic and muddy sandstone. Towards the top the silt and sandstone become more common, as do observations of muscovite, fish scales and plant remains. Offshore and offshore transition
Black and grey mudstones with planar parallel aminations of silt and very fine sand. Phosphatic sandstone beds which contain occasional bivalve shell are noted. Muscovite and plant remains noted in the mudstones. The sandstones occasionally display flasser or symmetrical lamination, ichnofabric, and are locally muddy. The topmost sandstone bed contains horizontal burrow. Parasequence from offshore, transition zone to shoreface
Mudstones (black and grey) with thin laminations of silt and sandstones (sometimes very fine) with planar parallel lamination. Towards the top the sandstone s with flasser and undulating lamination, and muscovite, plant remains, scales and phosphatic fragments. Burrows and other ichnofossils common. Offshore and transition zone
Campanian
Santonian
Coniacian
Turonian
Cenomanian
750
720
690
660
630
600
570
540
510
480
450
420
390
360
330
300
270
240
210
180
150
120
90
60
30
0
0
5
10

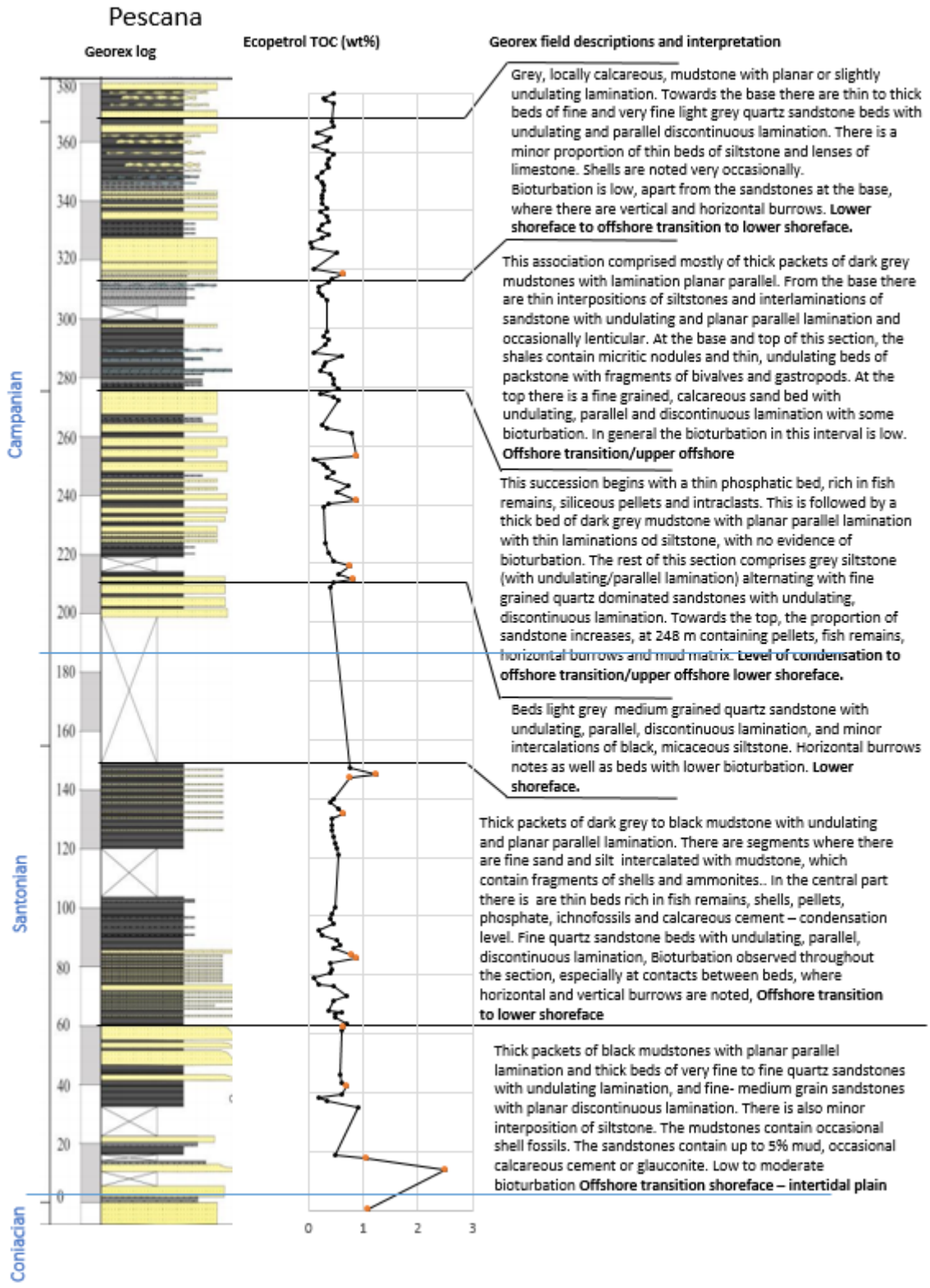
Pescana
Georex log
Ecopetrol TOC (wt%)
Georex field descriptions and interpretation
Campanian
Santonian
Coniacian
380
360
340
320
300
280
260
240
220
200
180
160
140
120
100
80
60
40
20
0
0
1
2
3
Grey, locally calcareous, mudstone with planar or slightly undulating lamination. Towards the base there are thin to thick beds of fine and very fine light grey quartz sandstone beds with undulating and parallel discontinuous lamination. There is a minor proportion of thin beds of siltstone and lenses of limestone. Shells are noted very occasionally. Bioturbation is low, apart from the sandstones at the base, where there are vertical and horizontal burrows. Lower shoreface to offshore transition to lower shoreface.
This association comprised mostly of thick packets of dark grey mudstones with lamination planar parallel. From the base there are thin interpositions of siltstones and interlaminations of sandstone with undulating and planar parallel lamination and occasionally lenticular. At the base and top of this section, the shales contain micritic nodules and thin, undulating beds of packstone with fragments of bivalves and gastropods. At the top there is a fine grained, calcareous sand bed with undulating, parallel and discontinuous lamination with some bioturbation. In general the bioturbation in this interval is low. Offshore transition/upper offshore
This succession begins with a thin phosphatic bed, rich in fish remains, siliceous pellets and intraclasts. This is followed by a thick bed of dark grey mudstone with planar parallel lamination with thin laminations od siltstone, with no evidence of bioturbation. The rest of this section comprises grey siltstone (with undulating/parallel lamination) alternating with fine grained quartz dominated sandstones with undulating, discontinuous lamination. Towards the top, the proportion of sandstone increases, at 248 m containing pellets, fish remains, horizontal burrows and mud matrix. Level of condensation to offshore transition/upper offshore lower shoreface.
Beds light grey medium grained quartz sandstone with undulating, parallel, discontinuous lamination, and minor intercalations of black, micaceous siltstone. Horizontal burrows notes as well as beds with lower bioturbation. Lower shoreface.
Thick packets of dark grey to black mudstone with undulating and planar parallel lamination. There are segments where there are fine sand and silt intercalated with mudstone, which contain fragments of shells and ammonites.. In the central part there is are thin beds rich in fish remains, shells, pellets, phosphate, ichnofossils and calcareous cement – condensation level. Fine quartz sandstone beds with undulating, parallel, discontinuous lamination, Bioturbation observed throughout the section, especially at contacts between beds, where horizontal and vertical burrows are noted, Offshore transition to lower shoreface
Thick packets of black mudstones with planar parallel lamination and thick beds of very fine to fine quartz sandstones with undulating lamination, and fine- medium grain sandstones with planar discontinuous lamination. There is also minor interposition of siltstone. The mudstones contain occasional shell fossils. The sandstones contain up to 5% mud, occasional calcareous cement or glauconite. Low to moderate bioturbation Offshore transition shoreface – intertidal plain

Appendix B - Freeze-Thaw disaggregation for direct measurement of grain size

Yang and Aplin (1997) developed a technique to disaggregate mudstones so that that grain size may be measured directly using sieves. The main premise is that chips of shale are soaked in water under vacuum, so that the water enters the pore space. Then the sample is frozen so that the water expands, and then thawed. This process is repeated many times, this replicating the freeze thaw cycles which disaggregate rocks in nature. The disaggregated rocks are then mixed with sodium hexametaphosphate for clay dispersal before the sand is separated by wet sieving using a 0.062 mm sieve. The results of a trial carried out on selected samples of different maturity and composition, are shown in Table 8. The majority of the pilot samples could not be completely disaggregated and remained as chips of gravel, very thin coarse sand size platelets or fine sand size material which appeared to include clay (perhaps silt covered with a thin layer of clay – increasing its size. Five samples were *almost* completely disaggregated and their sand fraction values are recorded in Table B.1.

Table B.1. Calculated and measured sand fraction. ND are samples which were not successfully disaggregated.

Sample	Measured sand fraction (wt%)
QVS1	ND
QVS2	ND
QVS3	1.0
QVS4	ND
QVS5	3.7
QVS6	ND
QVS7	ND
QVS8	ND
PG9	31.4
PG10	ND
PG11	ND
PG12	4.7
PG13	2.3
PG14	ND
PG15	ND

0

Appendix C – Raw Data

Appendix C.1. C and S data and Fe Speciation

		LECO and Elementar			Fe speciation (wt%)						
	Depth (m)	TOC (wt%)	S (wt%)	$CaCO_3$ (wt%)*	Fe_{Carb}	Fe_{OX1}	Fe_{OX2}	Fe_{mag}	Fe_{py}	Fe_{HR}/Fe_T	Fe_{PY}/Fe_{HR}
Algodones	0.5	1.02	1.54	0.00	0.48	0.11	0.15	0.00	0.78	0.70	0.51
	31	1.07	0.03	0.00	0.01	0.03	0.25	0.00	0.00	0.28	0.00
	38	1.39	0.00	0.00	0.02	0.03	0.05	0.01	0.00	0.12	0.00
	41	2.47	0.24	0.25	0.04	0.03	0.02	0.00	0.02	0.13	0.19
	47	1.35	0.05	0.00	0.04	0.05	0.45	0.01	0.00	0.37	0.00
	53	2.89	2.38	0.00	0.81	0.46	0.34	0.04	2.70	0.97	0.62
	159	3.10	0.06	0.00	0.04	0.10	0.29	0.01	0.00	0.41	0.00
	167	2.03	0.00	0.00	0.01	0.01	0.01	0.00	0.00	0.02	0.00
	181	1.46	0.55	0.00	0.09	0.10	0.59	0.02	0.48	0.71	0.37
	187	3.96	2.38	3.85	0.00	0.01	0.50	0.01	0.01	1.23	0.03
	199	1.24	0.05	0.06	0.01	0.05	2.99	0.05	0.03	0.92	0.01
	203	2.79	0.10	0.00	0.00	0.11	0.86	0.02	0.01	0.64	0.01
	269.5	1.37	0.25	16.37	0.22	0.02	0.01	0.00	1.16	0.77	0.82
	327.5	1.28	2.71	0.00	0.33	0.10	0.03	0.01	2.54	0.81	0.85
	486.5	3.82	0.20	4.84	0.24	0.33	2.48	0.07	0.05	0.64	0.01
	519.5	2.82	2.15	0.00	0.31	0.02	0.04	0.00	1.51	0.68	0.80
	528.5	3.61	0.17	0.00	0.00	0.60	0.71	0.03		0.54	0.00
	543.5	1.40	3.24	9.21	0.61	0.09	0.15	0.01	2.72	0.76	0.76
	555.5	5.10	2.25	1.34	1.10	0.13	3.74	0.09	0.92	0.82	0.15
	570.4	1.97	2.06	0.00	0.33	0.04	0.02	0.02	1.40	0.62	0.77
	578	1.26	2.39	0.00	0.27	0.08	0.07	0.01	2.20	0.90	0.83

		LECO and Elementar			Fe speciation (wt%)						
	Depth (m)	TOC (wt%)	S (wt%)	$CaCO_3$ (wt%)*	Fe_{Carb}	Fe_{OX1}	Fe_{OX2}	Fe_{mag}	Fe_{py}	Fe_{HR}/Fe_T	Fe_{PY}/Fe_{HR}
Cantonera	4	24.31	7.89	0.00	1.50	0.14	0.33	0.01	3.26	0.62	0.62
	28.5	1.02	1.75	3.02	0.65	0.55	0.07	0.23	1.32	0.67	0.47
	31.5	0.97	1.38		0.64	1.33	0.11	0.59	0.17	0.48	0.06
	54	5.69	0.21	0.00	0.13	0.01	0.00	0.01	0.12	1.15	0.46
	66	1.15	1.07	2.99	1.06	0.52	0.05	0.11	1.12	0.79	0.39
	96.5	6.09	1.39	0.00	0.35	0.09	0.21	0.00	0.63	3.32	0.49
	118.5	1.83	0.61		0.12	0.36	1.69	0.35	0.15	0.68	0.05
	141.5	1.02	0.39	0.00	0.30	0.59	0.09	0.29	0.42	0.44	0.25
	150.5	1.60	0.85		0.57	0.72	0.04	0.19	0.16	0.52	0.09
	152.5	15.07	22.63	14.26	1.12	0.10	0.74	0.03	0.03	0.09	0.01
	154	2.10	0.74		2.08	3.15	0.10	0.58	0.15	0.78	0.02
	193.5	1.66	1.05	0.00	0.88	0.60	0.04	0.06	0.15		0.09
	203.5	2.14	0.72		1.23	0.09	0.37	0.62	0.80	0.57	0.26
	232.5	1.71	0.34		2.11	1.63	0.04	0.14	0.15	0.84	0.04
	234.5	2.74	0.71	2.85	3.21	1.16	0.07	0.12	0.15	0.80	0.03
	238.5	4.18	0.73		1.26	0.47	0.08	0.34	0.40	0.62	0.16
	243	1.54	0.55	11.36	0.08	0.05	0.04	0.02	0.15	0.25	0.44
	278.5	1.22	0.03	39.26	2.91	0.81	0.21	1.85	0.09	0.64	0.02
	299	4.34	1.00	2.70	0.22	0.07	0.04	0.01	0.93	0.66	0.73
	301	15.55	2.77	1.24	0.31	0.07	0.10	0.01	1.89	0.76	0.80
	324.5	2.38	0.04		0.40	0.33	0.06	0.02	0.16	0.67	0.17
	336.5	1.28	0.68	5.29	1.74	1.19	0.04	0.04	0.16	0.90	0.05
	363.5	1.74	0.07	0.00	1.85	0.49	0.17	0.55	0.07	0.58	0.02
	378	3.08	0.27	0.00	0.02	0.02	0.00	0.00	0.09	0.20	0.74

		LECO and Elementar			Fe speciation (wt%)						
	Depth (m)	TOC (wt%)	S (wt%)	$CaCO_3$ (wt%)*	Fe_{Carb}	Fe_{OX1}	Fe_{OX2}	Fe_{mag}	Fe_{py}	Fe_{HR}/Fe_T	Fe_{PY}/Fe_{HR}
Crucero	4	1.34	0.00	0.00	0.01	0.02	0.42	0.01	0.00	0.13	0.00
	58.5	1.83	0.24	0.00	0.02	0.02	0.02	0.00	0.02	0.09	0.24
	71	1.21	0.00	0.00	0.01	0.00	0.03	0.00	0.00	0.03	0.00
	73	1.77	0.00	0.00	0.00	0.01	0.03	0.00	0.02	0.06	0.35
	79	1.71	0.23	0.00	0.02	0.02	0.11	0.01	0.00	0.14	0.00
	86	1.13	0.00	0.00	0.01	0.01	0.01	0.01	0.01	0.06	0.27
	96	1.19	0.00	0.00	0.01	0.01	0.00	0.00	0.00	0.02	0.00
	114.5	1.03	0.00	0.00	0.00	0.00	0.00	0.00	0.03	0.04	0.87
	118.5	1.70	0.00	0.00	0.01	0.01	0.01	0.00	0.04	0.07	0.55
	126.5	1.04	0.00	0.06	0.00	0.01	0.06	0.02	0.03	0.12	0.25
	130.5	1.01	0.23	0.00	0.02	0.02	0.02	0.01	0.00	0.05	0.00
	143	1.67	0.00	0.00	0.03	0.03	0.40	0.01	0.00	0.45	0.00
	147	1.25	0.00	0.00	0.01	0.03	0.46	0.01	0.00	0.40	0.00
	182.5	1.23	0.00	0.00	0.01	0.03	0.06	0.00	0.00	0.10	0.00
	348	0.93	0.00	0.00	0.01	0.01	0.01	0.00	0.00	0.03	0.00
	369.5	1.44	0.06	0.00	0.01	0.01	0.44	0.00	0.05	0.42	0.10
	385.5	0.60	0.65	0.00	0.13	0.02	0.03	0.00	0.33	0.35	0.64
	429.5	1.28	0.04	0.00	0.13	0.12	0.21	0.08	0.01	0.40	0.02
	448	0.63	0.00	0.00	0.01	0.01	0.02	0.00	0.00	0.03	0.00
	529	2.67	0.19	0.00	0.06	0.03	0.04	0.01	0.14	0.16	0.51
	530	1.74	0.73	0.13	0.10	0.02	0.02	0.00	0.43	0.31	0.75
	535	3.32	0.24	0.00	0.04	0.04	0.12	0.01	0.00	0.13	0.00
	547.5	1.13	0.00	0.00	0.01	0.03	0.41	0.01	0.00	0.25	0.00
	562	0.84	0.00	10.35	0.09	0.06	0.05	0.00	0.00	0.15	0.00

		LECO and Elementar			Fe speciation (wt%)						
	Depth (m)	TOC (wt%)	S (wt%)	$CaCO_3$ (wt%)*	Fe_{Carb}	Fe_{OX1}	Fe_{OX2}	Fe_{mag}	Fe_{py}	Fe_{HR}/Fe_T	Fe_{PY}/Fe_{HR}
La Cristalina 1	6.5	2.81	0.51	0.00	0.12	0.19	0.97	0.02	0.51	0.81	0.28
	20.5	2.11	0.01	15.31	0.01	0.03	1.10	0.02	0.00	0.66	0.00
	68.5	3.53	0.35	25.54	0.13	0.18	0.44	0.01	0.39	0.80	0.34
	77	3.00	0.16	23.95	0.11	0.14	0.57	0.01	0.10	0.73	0.11
	81	1.84	0.04	20.15	0.13	0.16	0.84	0.01	0.03	0.76	0.03
	121	3.22	0.33	15.85	0.11	0.18	0.36	0.01	0.38	0.70	0.37
	127	3.73	0.55	15.64	0.23	0.22	0.08	0.00	0.65	0.82	0.55
	139	4.86	1.39	33.75	0.20	0.02	0.00	0.00	1.22	0.87	0.85
	145	5.51	0.37	28.60	0.12	0.54	0.27	0.00	0.81	0.86	0.47
	153	7.11	0.94	32.12	0.24	0.06	0.05	0.00	0.86	0.64	0.71
	171	6.00	1.48	31.85	0.26	0.07	0.11	0.01	0.30	0.35	0.41
	187	3.69	0.27	19.39	0.11	0.03	0.00	0.00	0.36	0.78	0.73
	269	5.48	0.15	9.44	0.07	0.06	0.02	0.00	0.08	0.74	0.36
	284	4.95	0.20	21.44	0.07	0.03	0.00	0.00	0.30	0.76	0.75
	298	5.23	1.66	13.15	0.24	0.03	0.02	0.00	0.39	0.30	0.58
	302	7.37	0.98	18.67	0.16	0.02	0.01	0.00	0.81	0.64	0.81
	306	6.11	1.02	20.12	0.24	0.04	0.01	0.00	1.01	0.78	0.78
	330	6.04	0.94	23.09	0.37	0.03	0.01	0.00	0.80	0.73	0.66
	336	4.71	0.32	39.44	0.13	0.04	0.05	0.00	0.46	0.71	0.67
La Cristalina 2	4.5	8.18	0.49	8.35	0.10	0.01	0.00	0.00	1.27	1.88	0.92
	10.5	9.06	0.68	3.60	0.07	0.36	0.49	0.00	0.04	0.72	0.04
	14.5	7.14	0.16	28.09	0.01	0.15	0.55	0.00	0.01	0.75	0.02
	67.5	8.27	0.08	16.44	0.02	0.10	0.48	0.00	0.02	0.75	0.03
	73.5	4.53	1.10	0.00	0.18	0.01	0.00	0.00	0.71	0.75	0.79
	90.5	5.97	0.50	55.67	0.24	0.01	0.00	0.01	0.89	1.14	0.77
	100.5	1.91	0.36	0.00	0.10	0.07	0.14	0.00	0.16	0.66	0.35
	139.5	3.92	0.23	0.00	0.04	0.22	0.32	0.01	0.01	0.82	0.02

		LECO and Elementar			Fe speciation (wt%)						
	Depth (m)	TOC (wt%)	S (wt%)	$CaCO_3$ (wt%)*	Fe_{Carb}	Fe_{OX1}	Fe_{OX2}	Fe_{mag}	Fe_{py}	Fe_{HR}/Fe_T	Fe_{PY}/Fe_{HR}
La Cristalina 3	18	9.57	1.06	0.00	0.18	0.08	0.05	0.00	0.47	0.66	0.59
	36	1.47	1.22	1.01	0.20	0.05	0.03	0.03	1.24	0.74	0.80
	104	0.94	0.42	11.94	0.14	0.24	1.13	0.01	0.24	0.77	0.14
	118	6.66	0.52	25.03	0.20	0.25	0.03	0.00	0.42	0.76	0.47
	138	5.99	0.11	0.00	0.02	0.23	0.32	0.00	0.02	0.77	0.04
	140	10.89	0.25	7.58	0.00	0.14	0.28	0.01	0.00	0.66	0.00
	169	6.03	0.44	29.21	0.14	0.14	0.01	0.00	0.29	0.94	0.50
	175.5	4.64	0.16	40.35	0.09	0.13	0.03	0.00	0.23	0.76	0.48
	213	2.98	0.31	14.78	0.08	0.01	0.00	0.00	0.31	0.97	0.77
	223	2.92	0.34	25.73	0.07	0.09	0.21	0.00	0.23	0.84	0.39
	244	1.88	0.07	21.98	0.07	0.02	0.02	0.00	0.20	0.82	0.63
	254	7.18	0.77	9.43	0.21	0.18	0.03	0.01	0.74	0.76	0.64
	266	2.21	0.36	17.84	0.08	0.02	0.01	0.00	0.26	1.14	0.72
La Cristalina 4	53	2.21	0.68	10.75	0.20	0.02	0.00	0.00	0.83	0.95	0.79
	140.5	3.35	1.08	0.00	0.18	0.04	0.03	0.00	1.11	0.90	0.82
	271.5	4.18	0.04	6.18	0.01	0.10	0.95	0.02	0.01	0.67	0.01
	427.5	0.73	0.05	5.47	0.08	0.12	0.13	0.00	0.03	0.77	0.08
	433.5	2.42	0.01	30.38	0.11	0.05	0.29	0.00	0.03	0.86	0.06
	439.5	6.00	0.20	18.64	0.11	0.02	0.18	0.00	0.31	0.86	0.49
	535	2.41	0.28	7.64	0.20	0.08	0.24	0.00	0.43	0.77	0.45
	636.5	1.93	1.33	57.89	0.23	0.04	0.02	0.00	1.35	0.94	0.82
	780.5	3.62	0.12	8.84	0.08	0.01	0.02	0.00	0.23	0.86	0.68
	1689	2.65	1.62	25.24	0.23	0.02	0.00	0.00	1.45	0.95	0.85

		LECO and Elementar			Fe speciation (wt%)						
	Depth (m)	TOC (wt%)	S (wt%)	$CaCO_3$ (wt%)*	Fe_{Carb}	Fe_{OX1}	Fe_{OX2}	Fe_{mag}	Fe_{py}	Fe_{HR}/Fe_T	Fe_{PY}/Fe_{HR}
La Marina	0.5	3.23	0.10	9.62	0.25	0.05	0.11	0.00	0.08	0.80	0.16
	18.5	5.43	0.10	0.00	0.07	0.09	1.10	0.02	0.02	0.89	0.01
	36.5	8.15	0.00	4.47	0.01	0.07	0.67	0.01	0.02	0.83	0.03
	98.5	1.02	0.02	1.51	0.08	0.28	2.56	0.07	0.01	0.86	0.00
	104.5	4.09	0.01	7.37	0.06	0.06	1.01	0.05	0.00	0.81	0.00
	116.5	1.73	0.00	0.00	0.05	0.26	2.56	0.24	0.00	0.54	0.00
	122.5	5.46	0.04	8.52	0.00	0.01	0.01	0.01	0.00	0.04	0.00
	186	1.37	0.01	0.00	0.02	0.04	0.03	0.02	0.00	0.09	0.00
	282	1.77	0.00	0.00	0.12	0.22	0.06	0.28	0.00	0.31	0.00
	308	2.20	0.15	0.00	0.03	0.04	0.21	0.04	0.06	0.27	0.16
	327	2.04	0.01	0.00	0.09	0.07	0.07	0.03	0.03	0.38	0.11
	339	1.09	0.10	0.00	0.11	0.16	0.03	0.16	0.01	0.13	0.02
	345	2.66	0.00	0.00	0.08	0.08	0.07	0.13	0.01	0.16	0.03
	381	1.39	0.22	6.12	0.10	0.09	0.01	0.04	0.15	0.17	0.38
	435	1.03	0.01	0.00	0.06	0.07	0.03	0.07	0.00	0.16	0.00
	517	1.43	0.93	0.00	0.12	0.05	0.17	0.02	0.82	0.64	0.69
	523	2.23	0.06	0.00	0.07	0.12	0.22	0.04	0.08	0.20	0.15
	529	6.31	0.00	1.70	0.10	0.79	3.78	0.16	0.03	0.54	0.01
	541	1.82	0.11	0.00	0.09	0.19	0.24	0.02	0.09	0.30	0.14
	547	1.76	0.07	0.00	0.07	0.25	0.36	0.02	0.05	0.44	0.07
	560	2.79	0.72	1.55	0.18	0.03	0.32	0.01	0.00	0.38	0.00

		LECO and Elementar			Fe speciation (wt%)						
	Depth (m)	TOC (wt%)	S (wt%)	$CaCO_3$ (wt%)*	Fe_{Carb}	Fe_{OX1}	Fe_{OX2}	Fe_{mag}	Fe_{py}	Fe_{HR}/Fe_T	Fe_{PY}/Fe_{HR}
Pedegral	1.5	3.43	1.72	0.00	0.67	0.08	0.61	0.01	1.10	0.87	0.44
	7.5	3.92	0.95	0.00	0.10	0.03	0.01	0.00	0.57	0.47	0.80
	27	2.62	0.45	0.13	0.09	0.03	0.02	0.00	0.30	0.37	0.68
	52.5	2.43	2.62	37.13	0.38	0.29	0.07	0.15	1.93	0.64	0.68
	66	1.02	0.87	2.85	0.97	0.51	0.05	0.21	1.75	0.73	0.50
	93	1.24	0.63	0.92	0.25	0.09	0.02	0.02	0.55	0.47	0.59
	106.5	1.29	1.97	0.00	0.47	0.37	0.06	0.00	0.89	0.42	0.50
	126	1.25	0.92	0.00	0.16	0.12	0.03	0.04	0.87	0.45	0.72
	133.5	3.68	0.00	11.29	0.02	0.03	0.35	0.13	0.00	1.01	0.00
	153	2.91	0.02	0.00	0.00	0.01	0.05	0.00	0.01	0.42	0.18
	163.5	6.85	0.23	0.00	0.89	1.22	0.11	0.00	0.19	0.79	0.08
	177	2.06	1.21	1.14	0.12	0.01	0.02	0.10	0.84	0.87	0.76
	220.5	4.11	1.07	0.00	0.14	0.03	0.00	0.00	0.96	0.62	0.85
	237.5	8.92	2.22	1.17	0.41	0.03	0.02	0.34	1.50	0.92	0.65
	274	3.54	2.74	0.37	0.23	0.01	0.01	0.00	2.04	0.99	0.89
	277	1.64	0.62	10.35	0.07	0.02	0.00	0.00	0.47	0.56	0.84
Pescana	0.5	1.09	0.31	0.00	2.34	1.14	1.64	1.07	0.19	0.57	0.03
	13.5	2.49	0.32	0.00	0.06	0.01	0.18	0.00	0.14	0.30	0.36
	16.5	1.04	0.02	0.08	0.42	0.39	0.15	0.02	0.01	0.58	0.01
	35	0.90	0.30	0.00	0.30	0.62	0.27	0.37	0.09	0.47	0.06
	42	0.69	0.47	0.00	0.17	0.19	0.05	0.10	0.36	0.37	0.41
	62	0.65	0.29	0.00	0.21	0.33	0.08	0.18	0.22	0.39	0.21
	85.5	0.88	0.26	0.80	0.34	0.62	0.09	0.24	0.25	0.45	0.16
	87	0.80	0.59	0.00	0.43	0.65	1.12	0.18	0.19	0.82	0.07
	134	0.65	0.31	0.05							
	147	0.75	0.59	8.02	0.26	0.27	0.04	0.08	0.28	0.39	0.30
	148	1.24	0.53	1.29	0.29	0.35	0.05	0.12	0.36	0.61	0.31
	214.5	0.82	0.99	9.45	0.50	0.54	0.06	0.17	0.68	0.74	0.35
	214.5	0.82	1.28	1.13							
	219	0.75	0.47	0.06	0.27	0.37	0.05	0.12	0.38	0.58	0.32
	240.5	0.88	0.57	0.28	0.18	0.18	0.03	0.06	0.60	0.60	0.57
	255.5	0.89	0.69	0.00	0.28	0.26	0.05	0.10	0.49	0.57	0.42
	318.5	0.63	0.28	1.18	0.37	0.87	0.16	0.21	0.21	1.16	0.11

		LECO and Elementar			Fe speciation (wt%)						
	Depth (m)	TOC (wt%)	S (wt%)	$CaCO_3$ (wt%)*	Fe_{Carb}	Fe_{OX1}	Fe_{OX2}	Fe_{mag}	Fe_{py}	Fe_{HR}/Fe_T	Fe_{PY}/Fe_{HR}
PG		5.43		2.43	0.10	0.06	0.08	0.01	0.02	0.33	0.07
		3.33		3.55	0.30	0.21	0.08	0.01	0.02	0.51	0.03
		10.92		1.09	0.23	0.08	0.15	0.01	0.01	0.54	0.02
		2.62		3.26	0.28	0.15	0.30	0.01	0.02	0.70	0.03
		8.74		1.59	0.21	0.14	0.30	0.01	0.01	0.68	0.02
		7.30		0.21	0.23	0.08	0.14	0.01	0.01	0.60	0.02
		0.61		1.82	0.00	0.01	0.23	0.01	0.01	0.26	0.04
Quemado	14	2.35	2.08	0.00	0.30	0.06	0.02	0.00	1.68	0.82	0.81
	18.5	2.86	1.05	0.14							
	18.5	2.86		0.00	0.29	0.07	0.11	0.01	0.75	0.96	0.61
	30.5	4.85	0.30	0.00	0.02	0.02	0.10	0.01	0.29	0.51	0.67
	45.5	3.25	2.26	0.00	0.37	0.09	0.47	0.01	1.97	0.94	0.68
	69	1.51	0.00	0.00	0.02	0.05	3.24	0.06	0.02	0.92	0.01
	107	4.71	2.92	0.00	0.55	0.03	0.01	0.00	2.11	0.91	0.78
	113.5	3.72	0.42	0.00	0.03	0.04	0.04	0.01	0.29	0.66	0.72
	125.5	1.16	0.00	0.00	0.02	0.01	0.00	0.00	0.00	0.07	0.00
	134.5	2.25	0.19	0.00	0.01	0.02	0.01	0.00	0.00	0.03	0.00
	180.5	4.54	4.71	0.72	1.68	0.09	0.36	0.04	2.97	0.85	0.58
	233	4.57	0.21	1.01	0.01	0.02	0.31	0.00	0.00	0.41	0.00
QVS		0.66		39.74	0.16	0.27	0.05	0.21	0.25	0.32	0.26
		0.26		5.58	3.00	4.10	15.43	19.80	0.04	1.08	0.00
		0.52		0.13	0.60	0.99	0.14	1.51	0.11	0.57	0.03
		0.50		2.97	0.31	0.57	0.09	0.23	0.38	0.38	0.24
		2.94		0.23	0.27	0.47	0.06	0.19	0.85	0.54	0.46
		0.40		26.16	0.15	0.32	0.05	0.67	0.18	0.53	0.13
		0.26		0.14	0.23	1.06	0.52	10.04	0.41	0.50	0.03
		0.50		0.00	0.08	0.02	0.04	0.01	0.58	0.58	0.79

		LECO and Elementar			Fe speciation (wt%)						
	Depth (m)	TOC (wt%)	S (wt%)	$CaCO_3$ (wt%)*	Fe_{Carb}	Fe_{OX1}	Fe_{OX2}	Fe_{mag}	Fe_{py}	Fe_{HR}/Fe_T	Fe_{PY}/Fe_{HR}
Zipa	2	2.13	0.03	20.14	0.02	0.10	0.55	0.00	0.00	0.69	0.00
	2	1.22	0.79	15.19	0.39	0.09	0.01	0.01	0.49	0.82	0.49
	4	2.01	0.61	0.00	0.16	0.01	0.01	0.00	0.62	0.88	0.77
	10	1.67	0.02	0.00	0.06	0.30	0.79	0.01	0.02	0.85	0.02
	14	4.24	0.02	3.38	0.00	0.12	1.82	0.05	0.02	0.89	0.01
	24	2.55	0.03	0.00	0.06	0.33	0.07	0.02	0.01	0.28	0.01
	25	5.92	0.16	0.49	0.01	0.18	1.68	0.04	0.01	0.87	0.01
	28	1.47	0.07	0.00	0.04	0.18	0.81	0.02	0.00	0.85	0.00
	36	1.98	0.04	0.00	0.05	0.28	0.28	0.00	0.03	0.73	0.05
	38	1.06	0.02	14.48	0.08	0.41	0.66	0.01	0.00	0.84	0.00
	44	1.92	0.54	0.00	0.53	0.29	0.26	0.00	0.55	0.89	0.34
	46	2.63	0.09	0.00	0.01	0.02	0.38	0.00	0.00	0.45	0.00
	62	1.43	0.00	0.00	0.01	0.14	0.79	0.01	0.01	0.89	0.01
	72	1.32	0.23	0.00	0.00	0.05	0.16	0.00	0.00	0.62	0.00
	74.5	2.54	0.34	0.00	0.04	0.16	0.41	0.01	0.00	0.77	0.00
	86	5.09	0.03	0.00	0.05	0.13	0.08	0.00	0.00	0.59	0.00
	88	3.78	0.33	0.00	0.07	0.17	0.15	0.01	0.00	0.63	0.00
	110	1.08	0.00	0.00	0.00	0.05	0.08	0.00	0.00	0.62	0.00
	116	2.12	0.01	0.00	0.00	0.03	0.13	0.00	0.02	0.82	0.11
	131.5	1.30	0.03		0.01	0.05	0.14	0.00	0.00	0.70	0.00

Appendix C.2. XRF Data

		wt%										mg/kg											wt %
	Depth (m)	Si	Ti	Al	Fe	Mn	Mg	Ca	Na	K	P	As	Ba	Co	Cr	Cu	Mo	Ni	V	U	Zn	Zr	Total
Algodones	0.5	25.0	0.56	11.2	2.18	0.01	0.42	0.04	0.22	4.10	0.02	20	400	10	89	13	0	9	120	5	8	159	88.6
	31	27.1	0.59	12.8	1.07	0.00	0.52	0.03	0.45	4.49	0.03	5	468	6	103	1	4	1	170	4	6	174	91.7
	38	34.3	0.77	12.1	0.92	0.00	0.48	0.04	0.50	4.13	0.02	9	516	5	96	23	10	0	215	9	17	281	105.5
	41	28.0	0.63	12.9	0.91	0.00	0.46	0.03	0.53	4.63	0.02	11	560	5	100	0	7	5	201	6	9	166	94
	47	27.8	0.55	11.8	1.48	0.00	0.44	0.04	0.58	4.23	0.02	11	563	6	84	10	4	6	161	4	11	172	91.9
	53	23.9	0.47	11.5	4.50	0.02	0.81	0.04	0.70	3.69	0.12	52	531	17	84	52	69	81	259	6	34	158	93.7
	159	27.7	0.69	12.3	1.08	0.00	0.34	0.03	0.79	3.61	0.03	8	541	6	104	4	6	4	246	4	13	230	91.8
	167	32.0	0.68	9.8	0.95	0.00	0.28	0.04	0.62	3.40	0.02	3	570	6	73	11	4	0	174	5	6	292	95.2
	181	28.0	0.65	12.3	1.80	0.00	0.36	0.03	0.74	3.70	0.02	16	578	7	105	20	11	10	209	6	14	187	94.7
	187	38.5	0.21	5.6	0.43	0.00	0.09	0.04	0.00	0.46	0.02	0	41	6	27	0	0	3	22	9	10	577	94.8
	199	26.6	0.66	12.4	3.41	0.00	0.34	0.03	0.73	3.66	0.03	30	562	3	102	47	23	4	192	3	16	195	92.9
	203	29.9	0.65	9.8	1.55	0.00	0.28	0.07	0.60	2.91	0.02	11	466	6	85	5	21	23	197	5	22	304	91.1
	269.5	29.3	0.68	11.2	1.83	0.00	0.32	0.03	0.65	3.32	0.03	13	478	10	84	17	7	19	161	6	22	242	94.4
	327.5	26.7	0.61	11.2	3.73	0.01	0.40	0.04	0.57	3.30	0.03	16	481	27	93	21	7	32	192	1	31	191	97.7
	486.5	24.5	0.54	12.0	4.92	0.01	0.58	0.04	0.62	3.38	0.05	28	515	13	126	5	57	102	529	7	337	160	89.9
	519.5	28.2	0.60	10.8	2.76	0.01	0.35	0.04	0.64	3.67	0.03	17	568	10	77	17	14	33	193	8	45	214	93.6
	528.5	30.8	0.56	9.0	2.50	0.01	0.48	0.04	0.50	2.91	0.02	8	471	5	65	11	17	10	182	4	56	251	92.9
	543.5	25.1	0.55	10.8	4.73	0.01	0.48	0.04	0.59	3.64	0.03	18	573	16	81	48	15	64	206	2	71	193	96.6
	555.5	24.5	0.52	9.4	7.29	0.02	0.49	0.04	0.50	2.97	0.03	21	474	15	80	24	27	80	232	6	222	194	90.9
	570.4	28.8	0.53	8.8	2.94	0.01	0.43	0.04	0.50	2.87	0.03	10	444	11	58	22	11	38	138	7	46	209	93.6
	578	25.3	0.61	12.2	2.95	0.00	0.32	0.03	0.67	3.54	0.03	23	515	14	102	36	14	52	265	2	19	178	94.5

		wt%										mg/kg											wt%
	Depth (m)	Si	Ti	Al	Fe	Mn	Mg	Ca	Na	K	P	As	Ba	Co	Cr	Cu	Mo	Ni	V	U	Zn	Zr	Total
Cantonera	4	19.1	0.33	6.1	8.40	0.01	0.20	0.05	0.09	1.20	0.03	17	173	17	76	16	4	21	130	12	10	205	75
	28.5	28.0	0.58	8.4	4.23	0.02	0.52	1.19	0.15	1.52	0.06	9	219	21	64	11	0	31	82	8	63	511	92
	31.5	23.0	0.69	12.1	5.90	0.01	0.99	0.69	0.22	2.45	0.08	13	343	22	101	15	0	42	120	4	88	201	91
	54	41.1	0.18	2.0	0.23	0.00	0.02	0.04	0.00	0.13	0.01	0	20	7	14	0	0	5	27	4	54	388	93
	66	32.4	0.61	6.7	3.60	0.02	0.42	0.17	0.19	1.10	0.04	4	156	20	40	15	0	24	67	6	33	539	94
	96.5	34.2	0.56	7.1	0.38	0.00	0.21	0.03	0.30	2.50	0.01	4	448	5	67	1	15	1	175	4	2	362	92
	118.5	25.1	0.74	12.3	3.91	0.00	0.68	0.24	0.22	2.40	0.05	9	306	15	100	16	0	38	125	5	59	290	89
	141.5	27.1	0.75	11.7	3.83	0.01	0.75	0.21	0.26	2.59	0.05	11	342	18	99	15	0	34	121	6	86	291	93
	150.5	33.2	0.84	6.3	3.21	0.04	0.47	0.14	0.31	1.20	0.04	6	190	17	48	6	0	16	65	8	36	577	93
	152.5	12.0	0.24	2.8	22.2	0.02	0.15	0.07	0.05	0.49	0.02	219	108	85	80	93	7	63	193	5	319	173	72
	154	26.7	0.60	7.6	7.77	0.15	0.68	0.40	0.20	1.35	0.07	5	202	13	59	11	0	24	81	7	67	447	88
	203.5	31.2	0.49	6.7	5.45	0.07	0.53	0.44	0.16	1.47	0.15	9	187	20	58	12	0	23	68	3	126	338	95
	232.5	28.7	0.72	8.5	4.82	0.07	0.55	0.24	0.24	1.94	0.06	4	255	14	73	11	0	24	88	7	61	406	90
	234.5	24.5	0.72	10.3	5.92	0.10	0.68	0.53	0.25	2.61	0.07	4	320	18	92	11	0	28	113	6	68	260	88
	238.5	29.7	0.52	8.3	4.09	0.06	0.45	0.19	0.15	1.87	0.06	11	224	24	64	11	0	24	86	7	280	215	91
	243	25.1	0.97	14.1	1.36	0.00	0.50	0.08	0.22	3.03	0.05	4	463	27	104	15	0	39	123	7	35	468	89
	278.5	21.2	0.58	11.2	9.23	0.28	1.24	0.34	0.16	2.90	0.07	8	338	10	89	5	0	29	141	5	46	158	88
	299	23.8	0.84	12.5	1.94	0.00	0.37	0.09	0.11	2.40	0.04	9	364	25	85	8	2	21	130	4	18	247	83
	301	27.6	0.71	8.6	3.13	0.00	0.26	0.04	0.10	1.69	0.03	17	227	38	66	14	0	50	93	9	17	425	85
	324.5	30.1	0.81	10.0	1.45	0.02	0.31	0.08	0.07	2.01	0.05	5	306	24	75	9	2	30	102	1	35	427	90
	336.5	23.1	0.84	13.8	3.53	0.05	0.68	0.17	0.14	3.30	0.07	9	431	16	109	17	0	31	155	6	15	265	88
	363.5	23.0	0.71	12.7	5.44	0.08	0.63	0.30	0.10	2.79	0.07	9	373	15	97	18	0	29	148	6	70	209	88
	378	30.0	0.98	10.8	0.64	0.00	0.27	0.05	0.09	2.26	0.05	15	344	34	78	18	0	37	104	8	18	642	91

		wt%										mg/kg											wt%
	Depth (m)	Si	Ti	Al	Fe	Mn	Mg	Ca	Na	K	P	As	Ba	Co	Cr	Cu	Mo	Ni	V	U	Zn	Zr	Total
Crucero	4	28.7	0.60	8.3	3.75	0.02	0.49	2.49	0.16	1.61	0.04	10	204	17	67	16	1	31	90	3	53	474	94.8
	58.5	30.7	0.43	11.3	0.89	0.00	0.30	0.04	0.10	1.28	0.04	1	222	6	66	7	0	21	49	6	22	126	91.6
	71	24.7	0.55	14.3	1.07	0.00	0.31	0.04	0.10	1.34	0.04	2	227	8	68	3	0	17	57	8	25	182	84.9
	73	25.1	0.63	15.1	1.08	0.00	0.34	0.04	0.16	1.59	0.04	3	230	6	86	4	3	13	71	3	27	182	87.9
	79	26.9	0.55	13.6	1.13	0.00	0.34	0.05	0.13	1.41	0.05	3	272	7	69	7	1	14	62	7	23	182	88.7
	86	28.2	0.45	11.5	0.88	0.00	0.30	0.04	0.11	1.25	0.04	0	202	8	59	2	0	14	48	9	17	166	86.5
	96	29.0	0.45	12.5	0.94	0.00	0.32	0.04	0.10	1.29	0.04	1	197	8	72	2	0	13	57	7	23	116	90.3
	114.5	29.8	0.37	10.1	0.76	0.00	0.27	0.04	0.10	1.13	0.03	0	175	6	61	0	1	11	56	4	20	104	86.8
	118.5	26.1	0.56	13.6	0.97	0.00	0.31	0.04	0.16	1.43	0.04	2	244	6	91	0	3	15	77	4	21	205	86.8
	126.5	28.6	0.47	11.7	1.02	0.00	0.33	0.04	0.12	1.28	0.05	2	226	7	75	3	2	23	63	5	22	142	88.1
	130.5	28.5	0.54	12.7	1.14	0.00	0.39	0.04	0.13	1.55	0.04	1	211	6	61	5	0	12	54	8	25	163	90.6
	143	31.2	0.50	9.3	1.04	0.00	0.24	0.04	0.10	1.02	0.03	2	171	6	58	3	1	15	75	9	25	341	88.8
	147	30.6	0.41	10.8	1.29	0.00	0.31	0.04	0.10	1.30	0.04	4	262	6	93	10	27	13	191	9	25	126	91.1
	182.5	25.7	0.48	13.0	1.06	0.00	0.37	0.04	0.13	1.64	0.04	1	221	7	100	3	0	9	86	8	20	143	85.1
	348	24.7	0.58	14.5	1.18	0.00	0.45	0.07	0.09	2.13	0.04	3	321	8	105	1	0	20	131	12	37	162	86.7
	369.5	30.5	0.48	9.1	1.20	0.00	0.33	0.04	0.06	1.89	0.04	3	290	9	70	0	3	19	115	7	120	345	88.6
	385.5	30.1	0.54	10.3	1.47	0.00	0.40	0.04	0.07	2.29	0.10	4	339	8	80	11	0	13	89	11	106	348	91.4
	429.5	32.6	0.42	7.9	1.38	0.00	0.31	0.04	0.07	1.50	0.04	3	315	6	79	0	1	15	110	7	47	532	90.4
	448	29.6	0.50	11.3	1.36	0.00	0.52	0.04	0.07	2.68	0.03	1	358	5	122	3	1	8	235	6	23	238	91.9
	529	25.7	0.57	14.2	1.74	0.00	0.52	0.04	0.07	2.17	0.04	4	289	12	198	7	0	29	235	9	179	172	89.8
	530	26.9	0.44	12.6	1.86	0.00	0.55	0.04	0.07	2.10	0.06	4	380	14	185	16	3	41	274	8	307	178	89
	535	27.1	0.50	12.9	1.68	0.00	0.59	0.06	0.06	2.11	0.06	3	428	7	171	4	0	31	228	10	73	195	89.8
	547.5	28.3	0.53	12.6	1.80	0.00	0.50	0.04	0.06	2.25	0.05	6	356	7	156	7	0	16	247	6	70	236	91.8
	562	30.4	0.33	9.7	1.34	0.00	0.52	0.05	0.06	2.21	0.14	4	580	8	159	3	5	17	249	3	83	136	90.1

		wt%										mg/kg											wt%
	Depth (m)	Si	Ti	Al	Fe	Mn	Mg	Ca	Na	K	P	As	Ba	Co	Cr	Cu	Mo	Ni	V	U	Zn	Zr	Total
La Cristalina 1	6.5	28.2	0.37	7.0	2.22	0.00	0.27	5.32	0.09	1.44	0.08	18	1840	6	195	25	13	167	572	7	1216	106	89.6
	20.5	33.5	0.40	7.7	1.75	0.00	0.28	0.30	0.10	1.65	0.06	9	741	6	153	11	13	56	453	7	324	112	92.9
	68.5	28.2	0.27	5.8	1.43	0.00	0.23	6.67	0.08	1.15	0.05	18	2255	6	127	25	25	92	561	10	312	70	87.3
	77	25.4	0.26	5.7	1.27	0.00	0.23	9.22	0.07	1.15	0.08	22	3261	5	153	36	28	88	797	10	497	71	83.9
	81	26.2	0.29	6.4	1.56	0.00	0.27	8.20	0.10	1.33	0.04	19	2180	5	135	32	30	73	613	8	426	79	85.5
	121	26.5	0.28	6.1	1.47	0.00	0.25	8.17	0.07	1.25	0.08	18	2069	8	124	28	12	86	581	11	371	67	86.6
	127	28.0	0.25	5.4	1.43	0.00	0.25	7.28	0.10	1.15	0.05	10	803	6	111	30	38	79	663	11	294	61	87.7
	139	28.3	0.28	6.3	1.65	0.00	0.27	5.28	0.05	1.26	0.03	16	663	9	123	41	54	152	770	8	495	74	89.2
	145	20.3	0.22	5.2	2.01	0.01	0.25	13.1	0.05	0.99	0.03	14	789	8	112	42	13	99	377	12	177	74	80.1
	153	23.1	0.23	5.0	1.90	0.01	0.22	10.2	0.03	0.95	0.02	11	605	11	92	50	8	92	308	9	192	69	83.1
	171	20.6	0.19	3.8	2.13	0.02	0.21	14.1	0.08	0.71	0.02	13	1633	11	69	44	6	56	225	6	164	63	82
	187	27.4	0.12	2.7	0.63	0.00	0.13	11.4	0.04	0.45	0.03	23	3575	6	111	39	53	117	1107	11	833	38	84.1
	269	32.7	0.06	1.5	0.31	0.00	0.08	7.90	0.01	0.23	0.05	2	337	6	79	28	46	158	1097	14	526	15	85.8
	284	35.1	0.09	2.5	0.52	0.00	0.10	4.91	0.02	0.35	0.04	4	398	7	72	27	51	121	833	16	391	20	89.6
	298	26.0	0.32	7.1	2.29	0.00	0.23	5.32	0.05	0.85	0.11	20	856	8	136	40	155	214	1441	16	473	109	87.7
	302	26.7	0.34	6.6	1.57	0.00	0.21	5.30	0.04	0.81	0.10	13	852	9	139	30	163	214	1384	22	539	175	85.4
	306	28.2	0.29	6.7	1.66	0.00	0.20	4.10	0.02	0.76	0.12	15	667	8	147	36	161	230	1680	19	499	109	87.3
	330	25.0	0.28	6.7	1.65	0.00	0.34	7.32	0.03	0.76	0.10	13	823	9	127	38	134	188	1316	17	495	93	84.4
	336	25.3	0.22	5.6	0.97	0.00	0.20	9.45	0.04	0.65	0.09	10	1295	7	120	25	71	124	1481	17	376	67	83.1
La Cristalina 2	4.5	20.0	0.12	3.5	0.73	0.00	0.19	14.9	-0.01	0.49	0.12	12	383	7	155	95	230	303	2813	38	2603	25	76.1
	10.5	31.9	0.29	6.0	1.36	0.00	0.25	0.04	0.04	0.94	0.05	62	8642	3	279	27	443	99	4221	15	95	92	86.8
	14.5	37.2	0.15	3.5	0.97	0.00	0.14	0.16	0.01	0.49	0.07	17	1512	5	134	21	41	72	2376	22	275	29	90
	67.5	23.1	0.13	2.8	0.83	0.00	0.19	12.7	0.00	0.43	0.04	47	3551	4	240	76	60	217	3772	19	1127	33	77.2
	73.5	31.5	0.18	3.7	1.20	0.00	0.21	5.38	0.01	0.63	0.02	32	563	8	193	52	190	252	2623	20	1372	43	89.3
	90.5	18.4	0.06	1.3	1.01	0.00	0.22	21.3	0.04	0.23	0.01	50	458	5	106	39	62	106	1762	9	778	21	77.3
	100.5	40.1	0.09	2.2	0.69	0.00	0.12	0.21	0.00	0.36	0.03	34	344	5	166	53	67	163	2334	20	1125	15	93.8
	139.5	40.0	0.09	2.2	0.73	0.00	0.10	0.04	0.02	0.30	0.07	63	8872	6	168	89	56	31	2140	24	71	13	93.9

		wt%										mg/kg											wt%
	Depth (m)	Si	Ti	Al	Fe	Mn	Mg	Ca	Na	K	P	As	Ba	Co	Cr	Cu	Mo	Ni	V	U	Zn	Zr	Total
La Cristalina 3	18	31.7	0.19	4.5	1.20	0.00	0.19	2.82	0.03	0.76	0.04	49	756	9	197	94	303	319	3015	27	3024	44	87.9
	36	24.7	0.63	15.2	2.10	0.00	0.26	0.19	0.15	1.73	0.10	19	832	20	88	18	30	80	227	5	320	177	92.4
	104	31.3	0.39	9.9	2.28	0.00	0.18	0.17	0.13	1.16	0.12	34	2600	6	107	23	62	47	920	15	583	83	93.3
	118	30.1	0.21	5.3	1.18	0.00	0.17	4.04	0.03	0.84	0.11	33	602	9	213	103	176	377	2843	29	4638	52	86.5
	138	29.6	0.15	3.4	0.78	0.00	0.18	6.78	0.01	0.58	0.10	47	773	5	214	74	42	122	3683	20	1263	43	83.4
	140	27.9	0.12	2.6	0.66	0.00	0.17	9.15	0.00	0.49	0.09	63	768	5	283	110	39	225	4149	25	2909	40	81.2
	169	35.8	0.10	3.0	0.62	0.00	0.13	2.62	0.01	0.45	0.03	29	523	6	154	47	159	166	1835	16	1665	20	90
	175.5	27.4	0.12	2.6	0.64	0.00	0.13	11.5	0.03	0.45	0.03	22	3589	6	113	36	55	116	1118	10	835	42	84.3
	213	23.3	0.07	1.6	0.41	0.00	0.33	16.7	0.05	0.27	0.24	13	1175	6	93	30	62	97	1550	9	1069	34	80.4
	223	34.2	0.10	2.0	0.71	0.00	0.13	6.60	0.06	0.36	0.02	18	463	5	96	33	60	108	1392	12	828	26	89.6
	244	31.2	0.05	1.2	0.38	0.00	0.16	11.0	0.08	0.22	0.07	12	519	5	64	14	52	77	977	7	490	25	87.1
	254	23.9	0.22	4.5	1.53	0.00	0.27	9.91	0.06	0.80	0.01	49	879	7	233	64	154	276	3534	27	1141	56	82.4
	266	38.4	0.05	1.0	0.31	0.00	0.12	4.61	0.06	0.17	0.01	19	439	6	95	26	69	93	1248	13	1134	9	92.6
La Cristalina 4	53	30.7	0.19	3.7	1.11	0.00	0.30	8.03	0.12	0.72	0.05	9	986	5	93	14	21	56	342	6	171	55	90.6
	140.5	31.1	0.22	4.9	1.51	0.00	0.21	5.66	0.06	0.80	0.08	9	516	5	126	19	30	110	577	7	545	60	91.8
	271.5	28.0	0.34	9.8	1.63	0.00	0.30	2.74	0.10	1.40	0.08	27	1851	8	140	30	30	148	880	10	675	77	88.4
	427.5	29.0	0.26	9.4	0.47	0.00	0.13	3.92	2.74	0.98	0.12	10	2247	8	39	6	4	15	348	10	159	178	92.3
	433.5	33.6	0.11	3.5	0.56	0.01	0.12	6.35	0.39	0.63	0.03	13	2673	5	59	16	10	33	325	10	157	78	90.6
	439.5	21.5	0.13	3.3	0.74	0.00	0.19	15.3	0.12	0.74	0.07	15	1673	5	91	36	68	146	1007	12	637	39	78.4
	535	27.2	0.27	6.3	1.22	0.00	0.21	7.73	0.07	1.01	0.04	13	560	7	122	22	22	95	891	10	351	70	86.6
	636.5	32.0	0.32	5.8	1.75	0.00	0.20	3.89	0.07	1.10	0.07	16	1135	7	141	20	18	70	457	4	509	103	94.5
	780.5	16.8	0.07	2.0	0.38	0.00	0.24	21.6	0.10	0.44	0.05	10	1371	5	87	36	68	149	1083	10	1102	32	73.6
	1689	31.8	0.29	5.5	1.78	0.00	0.19	3.92	0.06	1.00	0.08	8	480	6	103	17	31	101	310	8	418	97	93.6

		wt%										mg/kg											wt%
	Depth (m)	Si	Ti	Al	Fe	Mn	Mg	Ca	Na	K	P	As	Ba	Co	Cr	Cu	Mo	Ni	V	U	Zn	Zr	Total
La Marina	0.5	22.6	0.42	10.3	0.62	0.01	0.33	7.44	0.72	3.13	0.07	7	455	7	99	3	48	20	523	11	6	122	86
	18.5	28.8	0.37	10.9	1.45	0.00	0.19	0.23	0.74	3.35	0.11	20	485	8	121	-1	100	51	691	8	3	127	91
	36.5	28.6	0.37	12.4	0.94	0.00	0.20	0.14	0.75	3.82	0.13	36	547	9	115	-2	58	25	739	14	10	104	93
	98.5	28.3	0.49	11.9	3.48	0.00	0.18	0.16	1.22	2.66	0.09	10	447	12	101	9	25	58	392	9	25	170	95
	104.5	26.6	0.63	13.3	1.45	0.00	0.23	0.19	1.38	2.97	0.07	7	515	14	105	1	64	25	251	10	7	169	92
	116.5	26.7	0.36	11.9	5.74	0.00	0.19	0.12	1.17	2.40	0.04	3	399	15	74	28	17	87	259	6	51	97	94
	122.5	29.5	0.58	11.7	0.74	0.00	0.18	0.32	1.28	2.42	0.15	3	404	7	93	0	5	4	261	10	2	209	93
	186	28.6	0.69	12.8	1.13	0.00	0.33	0.06	1.14	3.01	0.02	3	496	5	67	0	3	4	127	9	10	251	94
	282	29.3	0.69	11.7	2.22	0.00	0.62	0.06	0.68	3.16	0.04	7	507	3	93	0	9	5	140	4	30	226	95
	308	28.9	0.60	12.1	1.38	0.00	0.42	0.06	0.76	3.44	0.02	12	554	6	97	0	28	7	214	4	25	197	94
	327	30.4	0.66	11.2	0.79	0.00	0.28	0.05	0.70	3.30	0.04	26	540	5	87	0	28	0	163	4	2	237	94
	339	29.3	0.66	10.9	3.73	0.00	0.89	0.04	0.51	2.84	0.05	6	457	2	88	5	6	12	150	4	58	210	96
	345	29.4	0.53	9.8	2.25	0.00	0.57	0.05	0.52	2.69	0.05	6	410	4	79	3	14	4	162	4	29	283	91
	381	28.1	0.66	12.3	2.38	0.00	0.60	0.06	0.65	3.44	0.08	11	531	11	103	2	8	10	186	3	34	196	95
	435	29.2	0.69	11.9	1.49	0.00	0.47	0.04	0.69	3.37	0.05	8	519	4	108	0	18	6	221	6	25	227	94
	517	28.0	0.63	12.5	1.85	0.00	0.37	0.15	0.81	3.46	0.03	15	568	10	102	7	12	24	278	5	30	182	96
	523	28.7	0.65	11.6	2.62	0.00	0.71	0.08	0.71	2.91	0.05	8	474	4	116	0	28	22	341	5	56	171	95
	529	23.2	0.39	10.7	9.05	0.01	1.09	0.22	0.56	2.22	0.14	3	361	8	105	56	50	72	320	8	707	119	90
	541	27.3	0.62	13.0	2.13	0.00	0.57	0.09	0.85	3.34	0.04	8	539	4	117	1	28	17	344	5	53	172	94
	547	26.7	0.63	14.0	1.70	0.00	0.42	0.12	0.98	3.69	0.05	11	611	7	131	5	32	13	447	4	63	174	94
	560	27.6	0.63	13.0	1.41	0.00	0.25	0.10	1.13	3.10	0.03	13	515	9	91	9	38	25	308	8	102	195	94

		wt%										mg/kg											wt%
	Depth (m)	Si	Ti	Al	Fe	Mn	Mg	Ca	Na	K	P	As	Ba	Co	Cr	Cu	Mo	Ni	V	U	Zn	Zr	Total
Pedegral	1.5	27.2	0.63	9.5	2.84	0.01	0.30	0.05	0.08	2.05	0.03	10	242	8	76	7	1	12	96	6	14	444	88.5
	7.5	27.3	0.75	11.6	1.50	0.00	0.39	0.06	0.13	2.45	0.05	6	316	23	83	16	0	54	106	12	83	334	88.3
	27	28.1	0.88	10.4	1.20	0.00	0.33	0.05	0.15	2.39	0.05	7	289	13	80	19	0	19	107	9	33	430	87.7
	52.5	29.8	0.64	8.1	4.44	0.00	0.60	0.19	0.17	1.63	0.06	9	197	23	65	20	0	39	84	8	61	449	91.9
	66	14.4	0.33	6.9	4.79	0.06	0.79	15.8	0.14	1.63	0.20	7	188	16	57	14	2	27	75	0	69	134	83.2
	93	26.1	0.76	11.8	1.98	0.00	0.51	0.15	0.14	2.68	0.05	10	323	18	85	20	0	32	122	9	74	292	88.6
	106.5	22.5	0.59	13.4	4.28	0.02	0.76	0.65	0.16	3.30	0.17	16	351	29	122	12	0	65	126	4	85	137	92.7
	126	25.3	0.72	13.0	2.71	0.01	0.58	0.16	0.13	3.30	0.05	10	330	24	110	11	0	33	129	4	62	192	92.2
	133.5	36.5	0.39	5.5	0.52	0.00	0.08	0.07	0.02	0.57	0.02	0	74	6	28	2	0	4	45	8	10	403	91
	153	37.9	0.34	3.6	0.17	0.00	0.05	0.04	0.01	0.38	0.01	0	54	7	23	0	0	2	31	7	5	565	89.4
	163.5	26.7	0.80	10.7	3.06	0.04	0.30	0.18	0.06	1.65	0.05	3	233	24	78	15	0	31	99	9	44	520	87
	177	36.0	0.61	5.6	1.26	0.00	0.11	0.03	0.04	0.95	0.02	1	129	10	35	7	0	16	51	11	10	583	92.4
	220.5	26.9	0.80	10.9	1.80	0.00	0.31	0.15	0.08	2.11	0.04	6	294	22	80	11	0	35	95	10	30	401	88.3
	237.5	27.4	0.78	11.7	2.50	0.00	0.31	0.06	0.08	2.24	0.10	17	298	16	90	9	0	23	112	8	13	456	90.8
	274	33.0	0.57	7.1	2.30	0.00	0.16	0.03	0.04	1.17	0.02	3	166	22	50	12	0	31	74	11	79	576	90.8
	277	32.8	0.78	7.8	1.01	0.00	0.17	0.04	0.06	1.38	0.03	3	178	16	51	6	0	13	76	6	30	600	91.6
Pescana	0.5	20.6	0.51	10.3	11.3	0.48	1.13	0.40	0.02	1.92	0.04	2	211	13	85	8	0	23	65	0	59	149	86.9
	13.5	32.0	0.59	8.5	1.29	0.00	0.25	0.04	0.57	3.03	0.02	4	486	6	65	0	12	5	168	7	45	273	92.6
	16.5	28.1	0.86	11.2	1.72	0.04	0.36	0.14	0.04	1.97	0.04	4	324	18	58	2	0	17	79	7	72	454	88.9
	35	33.3	0.48	7.2	3.51	0.00	0.58	0.13	0.08	1.58	0.04	1	262	5	40	2	0	12	45	6	108	526	94.3
	42	29.6	0.61	10.0	2.36	0.00	0.48	0.25	0.19	2.04	0.04	7	364	11	84	4	0	15	102	5	74	468	91.9
	62	28.0	0.65	11.5	2.58	0.00	0.56	0.22	0.13	1.98	0.05	6	330	10	108	2	2	19	128	2	83	379	91.1
	85.5	27.9	0.56	11.2	3.43	0.00	0.74	0.21	0.51	1.48	0.06	4	284	12	127	7	0	29	182	3	92	176	91.9
	87	28.8	0.59	10.4	3.16	0.00	0.69	0.19	0.53	1.43	0.06	3	300	9	112	3	0	21	151	8	117	214	91.6
	134	26.0	0.56	11.9	3.82	0.00	0.75	0.21	0.49	1.59	0.04	3	296	10	156	3	0	23	193	5	96	209	89.5
	147	28.5	0.53	11.0	2.36	0.00	0.66	0.39	0.19	1.51	0.04	2	295	9	166	4	0	23	183	9	62	217	90.5
	148	36.2	0.16	2.8	1.94	0.03	0.35	3.81	0.08	0.44	0.12	0	129	5	44	0	0	10	72	6	47	240	93.2
	214.5	34.9	0.25	5.4	2.64	0.01	0.51	0.99	0.05	0.89	0.30	1	261	11	94	5	0	25	65	10	133	105	94.1
	214.5	37.0	0.21	4.7	2.36	0.02	0.45	0.32	0.04	0.85	0.05	0	272	6	58	1	0	10	38	4	136	102	94.9
	219	34.8	0.27	6.0	2.05	0.01	0.51	0.74	0.05	0.95	0.22	1	263	9	99	4	3	24	72	1	71	118	94.1
	240.5	35.5	0.29	6.1	1.76	0.00	0.37	0.62	0.04	1.37	0.15	1	345	9	86	6	0	17	49	7	76	424	96
	255.5	31.0	0.50	8.5	2.06	0.01	0.37	0.36	0.07	2.44	0.12	6	532	9	90	6	0	14	61	7	59	539	92.8
	318.5	27.7	0.53	12.8	1.57	0.00	0.37	0.06	0.10	1.65	0.07	3	288	7	114	8	0	19	109	5	38	227	89.6

		wt%										mg/kg											wt%
	Depth (m)	Si	Ti	Al	Fe	Mn	Mg	Ca	Na	K	P	As	Ba	Co	Cr	Cu	Mo	Ni	V	U	Zn	Zr	Total
PG		33.7	0.21	6.1	0.80	0.00	0.26	0.06	0.03	0.86	0.11	9	192	4	169	11	24	75	1255	17	18	195	
		32.8	0.23	6.9	1.20	0.00	0.35	0.10	0.03	1.01	0.23	19	169	6	215	75	16	28	2179	32	18	88	
		32.9	0.16	5.5	0.90	0.00	0.25	0.16	0.02	0.74	0.21	27	182	4	180	15	91	194	1667	19	83	49	
		37.0	0.21	4.9	1.08	0.00	0.21	0.04	0.04	0.71	0.04	24	162	6	90	18	55	34	366	11	32	112	
		34.8	0.20	4.7	0.99	0.00	0.23	0.04	0.02	0.70	0.03	39	98	6	174	32	131	96	1474	10	13	66	
		35.8	0.17	5.0	0.79	0.00	0.24	0.03	0.03	0.71	0.02	22	108	5	130	33	53	72	1109	14	14	45	
		26.7	0.81	14.8	1.01	0.00	0.22	0.04	0.06	2.21	0.07	13	278	6	89	0	1	42	90	9	16	650	
Quemado	14	28.8	0.57	9.9	2.52	0.00	0.27	0.04	0.42	3.30	0.01	20	613	10	83	28	26	41	173	3	14	209	96
	18.5	27.2	0.62	11.8	3.41	0.00	0.70	0.03	0.57	3.66	0.04	24	648	10	92	25	18	49	183	3	30	188	95
	18.5	30.1	0.60	9.2	1.28	0.00	0.25	0.03	0.39	3.09	0.01	10	577	8	76	7	25	14	181	4	9	254	92
	30.5	28.6	0.68	10.4	0.86	0.00	0.36	0.03	0.56	3.76	0.01	10	682	6	85	1	29	4	204	6	18	239	90
	45.5	27.9	0.56	9.3	3.09	0.00	0.25	0.03	0.40	3.19	0.02	36	593	15	79	25	34	55	175	3	37	220	94
	69	31.0	0.61	8.6	3.68	0.00	0.24	0.03	0.36	2.95	0.01	30	564	5	78	5	21	18	168	5	19	262	94
	107	30.1	0.60	9.0	2.96	0.00	0.30	0.03	0.37	3.10	0.01	22	552	13	80	28	31	43	207	7	15	274	95
	113.5	30.1	0.61	10.3	0.60	0.00	0.29	0.03	0.44	3.55	0.01	8	603	6	90	0	27	1	216	5	7	223	92
	125.5	32.7	0.65	9.5	0.48	0.00	0.27	0.04	0.40	3.34	0.01	6	600	6	81	2	2	0	195	6	2	251	95
	134.5	32.2	0.81	8.2	1.55	0.00	0.24	0.03	0.14	1.64	0.03	11	219	12	60	8	0	15	80	6	24	576	92
	180.5	22.5	0.51	10.8	6.04	0.00	0.40	0.06	0.55	3.58	0.12	57	601	22	102	56	61	105	220	4	48	142	92
	233	31.4	0.62	9.4	0.82	0.00	0.29	0.04	0.50	3.17	0.01	3	570	5	81	8	30	0	176	7	5	257	93
QVS		25.2	0.63	13.7	2.90	0.01	0.58	0.26	0.04	2.41	0.06	9	220	16	83	9	3	29	91	4	74	231	
		5.5	0.14	3.7	39.2	0.66	1.30	1.04	0.01	0.46	0.09	5	79	6	24	0	0	23	34	2	103	50	
		23.0	0.53	13.5	5.90	0.05	0.81	0.34	0.18	1.90	0.06	7	219	10	81	9	0	23	92	8	132	144	
		25.4	0.50	12.7	4.13	0.01	0.72	0.34	0.38	1.82	0.07	6	278	10	117	7	0	25	145	9	343	168	
		25.4	0.57	12.1	3.42	0.01	0.48	0.54	0.05	1.79	0.06	10	179	8	85	7	1	35	92	7	92	182	
		35.5	0.42	6.4	2.57	0.00	0.36	0.31	0.19	1.54	0.11	6	335	6	59	0	1	11	87	6	281	767	
		8.8	0.15	3.3	24.3	0.43	1.59	6.94	0.10	0.42	2.35	10	200	0	40	4	0	7	68	1	207	143	
		35.9	0.29	7.1	1.26	0.00	0.15	0.08	0.03	0.74	0.03	5	189	7	125	3	0	25	49	8	62	95	

		wt%										mg/kg											wt%
	Depth (m)	Si	Ti	Al	Fe	Mn	Mg	Ca	Na	K	P	As	Ba	Co	Cr	Cu	Mo	Ni	V	U	Zn	Zr	Total
Zipa	2	36.4	0.17	5.6	0.99	0.00	0.17	0.08	0.02	1.05	0.03	13	490	5	85	53	16	54	852	10	221	57	92
	2	29.6	0.21	3.3	1.22	0.00	0.30	7.21	0.10	0.80	0.12	3	502	8	97	22	0	32	111	9	127	102	87
	4	32.1	0.21	3.6	0.92	0.00	0.16	6.93	0.07	0.90	0.08	7	1197	6	118	16	2	155	123	5	456	76	87
	10	36.3	0.31	4.9	1.40	0.00	0.19	0.71	0.07	1.20	0.18	17	3307	8	147	13	0	40	155	7	125	127	92
	14	28.8	0.40	9.3	2.25	0.00	0.30	0.03	0.07	1.90	0.04	34	713	5	259	149	107	83	2397	99	366	129	93
	24	33.2	0.30	5.1	1.71	0.00	0.22	3.19	0.07	1.34	0.11	8	609	7	181	20	0	61	166	10	192	102	89
	25	28.0	0.46	9.9	2.23	0.00	0.31	0.04	0.09	1.88	0.07	50	690	5	516	212	90	61	3963	126	225	160	91
	28	37.7	0.29	4.1	1.24	0.00	0.15	1.49	0.06	0.94	0.15	14	2560	7	115	9	1	46	114	6	142	169	96
	36	36.9	0.18	5.2	0.88	0.01	0.14	0.03	0.04	0.85	0.05	10	483	9	156	55	2	31	1342	28	136	54	96
	38	37.8	0.33	4.8	1.38	0.00	0.16	0.05	0.07	1.09	0.10	7	534	5	141	13	2	11	132	7	38	209	95
	44	30.4	0.28	4.7	1.84	0.05	0.40	5.41	0.05	1.18	0.14	32	6361	13	171	18	1	611	153	3	2986	115	85
	46	36.1	0.39	6.4	0.91	0.00	0.23	0.04	0.09	1.57	0.02	6	625	5	203	8	4	22	191	4	10	145	91
	62	36.4	0.28	5.1	1.09	0.00	0.17	0.25	0.07	1.10	0.15	5	589	7	186	26	0	39	185	11	130	102	93
	72	41.8	0.10	2.3	0.34	0.00	0.08	0.23	0.02	0.48	0.06	0	844	3	73	1	2	40	110	3	148	29	91
	74.5	37.7	0.18	4.9	0.80	0.00	0.12	0.03	0.07	0.66	0.03	7	425	6	147	43	10	44	769	17	133	67	95
	86	36.3	0.15	4.3	0.43	0.00	0.12	0.36	0.06	0.63	0.28	0	375	5	178	36	4	29	571	15	9	63	95
	88	36.5	0.18	5.2	0.63	0.00	0.14	0.11	0.07	0.75	0.16	2	415	6	205	63	2	26	656	22	23	68	91
	110	42.7	0.05	1.8	0.20	0.00	0.06	0.03	0.04	0.31	0.01	-2	269	6	83	24	0	8	269	10	22	16	94
	116	42.3	0.04	1.6	0.22	0.00	0.04	0.75	0.02	0.17	0.04	-3	176	6	31	9	11	52	212	8	240	3	92
	131.5	41.7	0.08	2.3	0.27	0.00	0.08	0.03	0.05	0.43	0.01	-3	288	6	88	16	1	7	194	10	17	20	96

References

Achterberg, E.P., van den Berg, C.M. and Colombo, C., 2003. High resolution monitoring of dissolved Cu and Co in coastal surface waters of the Western North Sea. *Continental shelf research*, *23*(6), pp.611-623.

Adams, D.D., Hurtgen, M.T. and Sageman, B.B., 2010. Volcanic triggering of a biogeochemical cascade during Oceanic Anoxic Event 2. *Nature geoscience*, *3*(3), p.201.

Adatte, T., Stinnesbeck, W., Remane, J. and Hubberten, H., 1996. Paleoceanographic changes at the Jurassic–Cretaceous boundary in the Western Tethys, northeastern Mexico. *Cretaceous Research*, *17*(6), pp.671-689.

Alberdi-Genolet, M. and Tocco, R., 1999. Trace metals and organic geochemistry of the Machiques Member (Aptian–Albian) and La Luna Formation (Cenomanian–Campanian), Venezuela. *Chemical Geology*, *160*(1), pp.19-38.

Algeo, T.J. and Lyons, T.W., 2006. Mo–total organic carbon covariation in modern anoxic marine environments: Implications for analysis of paleoredox and paleohydrographic conditions. *Paleoceanography*, *21*(1).

Algeo, T.J. and Maynard, J.B., 2004. Trace-element behavior and redox facies in core shales of Upper Pennsylvanian Kansas-type cyclothems. *Chemical geology*, *206*(3), pp.289-318.

Alvarez, N.C. and Roser, B.P., 2007. Geochemistry of black shales from the Lower Cretaceous Paja Formation, Eastern Cordillera, Colombia: Source weathering, provenance, and tectonic setting. *Journal of South American Earth Sciences*, *23*(4), pp.271-289.

Anderson, R.F., 1982. Concentration, vertical flux, and remineralization of particulate uranium in seawater. *Geochimica et Cosmochimica Acta*, *46*(7), pp.1293-1299.

Anderson, T.F. and Raiswell, R., 2004. Sources and mechanisms for the enrichment of highly reactive iron in euxinic Black Sea sediments. *American Journal of Science*, *304*(3), pp.203-233.

Armstrong, H. A., Wagner, T., Herringshaw, L. G., Farnsworth, A. J., Lunt, D. J., Harland, M. & Atar, E. F. (2016). Hadley circulation and precipitation changes controlling black organic-rich mudrock deposition in the Late Jurassic Boreal Seaway. *Paleoceanography*, *31*(8), 1041-1053.

Arrhenius, S., 1896. XXXI. On the influence of carbonic acid in the air upon the temperature of the ground. *The London, Edinburgh, and Dublin Philosophical Magazine and Journal of*

Science, *41*(251), pp.237-276.

Arthur, M.A. and Sageman, B.B., 1994. Marine black shales: depositional mechanisms and environments of ancient deposits. *Annual Review of Earth and Planetary Sciences*, *22*(1), pp.499-551.

Bahlburg, H., & Dobrzinski, N. (2011). A review of the Chemical Index of Alteration (CIA) and its application to the study of Neoproterozoic glacial deposits and climate transitions. *Geological Society, London, Memoirs*, *36*(1), 81-92.

Barron, E.J., Fawcett, P.J., Peterson, W.H., Pollard, D. and Thompson, S.L., 1995. A "simulation" of Mid-Cretaceous climate. *Paleoceanography*, *10*(5), pp.953-962.

Barnola, J.M., Raynaud, D.Y.S.N., Korotkevich, Y.S. and Lorius, C., 1987. Vostok ice core provides 160,000-year record of atmospheric CO2. *Nature*, *329*(6138), pp.408-414.

Beckmann, B., Flögel, S., Hofmann, P., Schulz, M. and Wagner, T., 2005. Orbital forcing of Cretaceous river discharge in tropical Africa and ocean response. *Nature*, *437*(7056), p.241.

Bergamaschi, B.A., Tsamakis, E., Keil, R.G., Eglinton, T.I., Montluçon, D.B. and Hedges, J.I., 1997. The effect of grain size and surface area on organic matter, lignin and carbohydrate concentration, and molecular compositions in Peru Margin sediments. *Geochimica et Cosmochimica Acta*, *61*(6), pp.1247-1260.

Berner, R.A., 1970. Sedimentary pyrite formation. *American journal of science*, *268*(1), pp.1-23.

Berner, R.A., 1984. Sedimentary pyrite formation: an update. *Geochimica et cosmochimica Acta*, *48*(4), pp.605-615.

Berner, R.A., 2003. The long-term carbon cycle, fossil fuels and atmospheric composition. *Nature*, *426*(6964), p.323.

Beus, A.A., 1979. Sodium-a geochemical indicator of emerald mineralization in the Cordillera Oriental, Colombia. *Journal of Geochemical Exploration*, *11*(2), pp.195-208.

Bhatti, T. M. (2015). Bioleaching of organic carbon rich polymetallic black organic-rich mudrock. Hydrometallurgy, 157, 246-255

Bird, P., 2003. An updated digital model of plate boundaries. *Geochemistry, Geophysics,*

Geosystems, *4*(3).

Bjørlykke, K., 1998. Clay mineral diagenesis in sedimentary basins—a key to the prediction of rock properties. Examples from the North Sea Basin. *Clay minerals*, *33*(1), pp.15-34.

Blanco, V. (2012). Modelling and Geochemical Characterization of Organic Facies in the Upper Cretaceous Chipaque Formation, Eastern Cordillera and Llanos Foothills, Colombia. (Unpublished MSc thesis). Newcastle University, UK.

Blättler, C.L., Jenkyns, H.C., Reynard, L.M. and Henderson, G.M., 2011. Significant increases in global weathering during Oceanic Anoxic Events 1a and 2 indicated by calcium isotopes. *Earth and Planetary Science Letters*, *309*(1), pp.77-88.

Bolin, T. B., Birdwell, J. E., Lewan, M. D., Hill, R. J., Grayson, M. B., Mitra-Kirtley, S., ... & Pomerantz, A. E. (2016). Sulfur Species in Source Rock Bitumen before and after Hydrous Pyrolysis Determined by X-ray Absorption Near-Edge Structure. *Energy & Fuels*, *30*(8), 6264-6270.

Böning, P., Brumsack, H.J., Böttcher, M.E., Schnetger, B., Kriete, C., Kallmeyer, J. and Borchers, S.L., 2004. Geochemistry of Peruvian near-surface sediments. *Geochimica et Cosmochimica Acta*, *68*(21), pp.4429-4451.

Böning, P., Shaw, T., Pahnke, K., & Brumsack, H. J. (2015). Nickel as indicator of fresh organic matter in upwelling sediments. *Geochimica et Cosmochimica Acta*, *162*, 99-108.

Bralower, T.J., Arthur, M.A., Leckie, R.M., Sliter, W.V., Allard, D.J. and Schlanger, S.O., 1994. Timing and paleoceanography of oceanic dysoxia/anoxia in the Late Barremian to Early Aptian (Early Cretaceous). *Palaios*, pp.335-369.

Branquet, Y., Cheilletz, A., Cobbold, P.R., Baby, P., Laumonier, B. and Giuliani, G., 2002. Andean deformation and rift inversion, eastern edge of Cordillera Oriental (Guateque–Medina area), Colombia. *Journal of South American Earth Sciences*, *15*(4), pp.391-407.

Brantley S.L., and White A.F., (2009). Chapter 10. Approaches to modeling weathered regolith. *Thermodynamics and kinetics of water-rock interaction*. 435-484

Brantley, S. L., Lebedeva, M. I., Balashov, V. N., Singha, K., Sullivan, P. L., & Stinchcomb, G. (2017). Toward a conceptual model relating chemical reaction fronts to water flow paths in

hills. *Geomorphology*, *277*, 100-117.

Brass, G.W., Southam, J.R. and Peterson, W.H., 1982. Warm saline bottom water in the ancient ocean. *Nature*, *296*(5858), pp.620-623.

Breit, G.N. and Wanty, R.B., 1991. Vanadium accumulation in carbonaceous rocks: a review of geochemical controls during deposition and diagenesis. *Chemical Geology*, *91*(2), pp.83-97.

Briceño, A., Buitrago, J., Lopez, C., 1990. Edad y origen de los depósitos de sal de la Sabana de Bogotá. Bc.S Thesis, Universidad Nacional de Colombia, Bogotá, 83pp.

Brumsack, H.J., 1986. The inorganic geochemistry of Cretaceous black shales (DSDP Leg 41) in comparison to modern upwelling sediments from the Gulf of California. *Geological Society, London, Special Publications*, *21*(1), pp.447-462.

Brumsack, H. J. (2006). The trace metal content of recent organic carbon-rich sediments: implications for Cretaceous black shale formation. *Palaeogeography, Palaeoclimatology, Palaeoecology*, *232*(2), 344-361.

Buckman, J., Mahoney, C., März, C., Wagner, T. and Blanco, V., 2017. Identifying biogenic silica: Mudrock micro-fabric explored through charge contrast imaging. *American Mineralogist*, *102*(4), pp.833-844.

Burdige, D.J., 1993. The biogeochemistry of manganese and iron reduction in marine sediments. *Earth-Science Reviews*, *35*(3), pp.249-284.

Bürgl, H., 1961. El Jurásico e Infracretáceo del río Batá, Boyacá. *Boletín Geológico, Servicio Geológico Nacional, VI* (1958), No. 1-3: 169-211. Bogotá.

CÁCERES, C. and ETAYO, F., 1969. Bosquejo geológico de la región del Tequendama. 1 Congr. *Col. Geol., guía de excursión precongreso*.

Caldeira, K. and Rampino, M.R., 1991. The Mid-Cretaceous Super Plume, carbon dioxide, and global warming. *Geophysical Research Letters*, *18*(6), pp.987-990.

Calvert, S.E. and Fontugne, M.R., 2001. On the late Pleistocene-Holocene sapropel record of climatic and oceanographic variability in the eastern Mediterranean. *Paleoceanography*, *16*(1), pp.78-94

Calvert, S.E. and Pedersen, T.F., 1993. Geochemistry of recent oxic and anoxic marine sediments: implications for the geological record. *Marine geology*, *113*(1-2), pp.67-88.

Calvert, S.E. and Pedersen, T.F., 2007. Chapter fourteen elemental proxies for palaeoclimatic and palaeoceanographic variability in marine sediments: interpretation and application. *Developments in Marine Geology*, *1*, pp.567-644.

Canfield, D. E., Raiswell, R., Westrich, J. T., Reaves, C. M., & Berner, R. A. (1986). The use of chromium reduction in the analysis of reduced inorganic sulfur in sediments and shales. *Chemical geology*, *54*(1-2), 149-155.

Carmo, A.M. and Pratt, L.M., 1999. Deciphering Late Cretaceous subequatorial ocean-climate interactions in the Sergipe Basin, Brazil. *SPECIAL PAPERS-GEOLOGICAL SOCIETY OF AMERICA*, pp.231-244.

Chandra, A. P., & Gerson, A. R. (2010). The mechanisms of pyrite oxidation and leaching: a fundamental perspective. *Surface Science Reports*, *65*(9), 293-315.

Cheilletz, A. and Giuliani, G., 1996. The genesis of Colombian emeralds: A restatement. *Mineralium Deposita*, *31*(5), pp.359-364.

Chumakov, N.M., 1995. The problem of the warm biosphere. *Stratigraphy and Geological Correlation*, *3*(3), pp.205-215.

Clayton, J. L., & Swetland, P. J. (1978). Subaerial weathering of sedimentary organic matter. *Geochimica et Cosmochimica Acta*, *42*(3), 305-312.

Coccioni, R., Luciani, V. and Marsili, A., 2006. Cretaceous oceanic anoxic events and radially elongated chambered planktonic foraminifera: paleoecological and paleoceanographic implications. *Palaeogeography, Palaeoclimatology, Palaeoecology*, *235*(1), pp.66-92.

Cochran, J.K., 1984. Fates of Uranium and Thorium Decay Series, Nuclides in the Estuarine Environment. *The Estuary as a Filter, Academic Press, Orlando FL. 1984. p 179-220, 10 fig, 1 tab, 66 ref. OCE 76-02-39.*

Cockell, C. S., Pybus, D., Olsson-Francis, K., Kelly, L., Petley, D., Rosser, N., ... & Mosselmans, F. (2011). Molecular characterization and geological microenvironment of a microbial community inhabiting weathered receding shale cliffs. *Microbial ecology*, *61*(1), 166-181.

Company, M., Aguado, R., Sandoval, J., Tavera, J.M., de Cisneros, C.J. and Vera, J.A., 2005. Biotic changes linked to a minor anoxic event (Faraoni Level, latest Hauterivian, Early Cretaceous). *Palaeogeography, Palaeoclimatology, Palaeoecology*, *224*(1), pp.186-199.

Cooper, M.A., Addison, F.T., Alvarez, R., Coral, M., Graham, R., Hayward, A.B., Howe, S., Martinez, J., Naar, J., Peñas, R. and Pulham, A.J., 1995. Basin development and tectonic history of the Llanos Basin, Eastern Cordillera, and middle Magdalena Valley, Colombia. *AAPG bulletin*, *79*(10), pp.1421-1442.

Cornwell, K., Norsby, D., & Marston, R. (2003). Drainage, sediment transport, and denudation rates on the Nanga Parbat Himalaya, Pakistan. *Geomorphology*, *55*(1), 25-43.

Cortés, M., Colletta, B. and Angelier, J., 2006. Structure and tectonics of the central segment of the Eastern Cordillera of Colombia. *Journal of South American Earth Sciences*, *21*(4), pp.437-465.

Cotillon, P. and Rio, M., 1984. Cyclic sedimentation in the Cretaceous of Deep-Sea-Drilling-Project Site-535 and Site-540 (Gulf of Mexico), Site-534 (Central Atlantic), and in the Vocontian Basin (France). *Initial Reports of the Deep Sea Drilling Project*, *77*(SEP), pp.339-376.

Damsté, J.S.S., Kok, M.D., Köster, J. and Schouten, S., 1998. Sulfurized carbohydrates: an important sedimentary sink for organic carbon?. *Earth and Planetary Science Letters*, *164*(1), pp.7-13.

Damsté, J.S.S., Schouten, S. and van Duin, A.C., 2001. Isorenieratene derivatives in sediments: possible controls on their distribution. *Geochimica et Cosmochimica Acta*, *65*(10), pp.1557-1571.

Davis, C., Pratt, L., Sliter, W., Mompart, L. and Mural, B., 1999. Factors influencing organic carbon and trace metal accumulation in the Upper Cretaceous La Luna Formation of the western Maracaibo Basin, Venezuela. *Evolution of the Cretaceous ocean-climate system*, p.203

de Graciansky, P.D., Deroo, G., Herbin, J.P., Montadert, L., Müller, C., Schaaf, A. and Sigal, J.,

1984. Ocean-wide stagnation episode in the late Cretaceous. *Nature*, *308*(5957), pp.346-349.

Dean, W.E. and Arthur, M.A., 1989. Iron-sulfur-carbon relationships in organic-carbon-rich sequences I: Cretaceous Western Interior Seaway. *American Journal of Science*, *289*(6), pp.708-743.

Demaison, G.J. and Moore, G.T., 1980. Anoxic environments and oil source bed genesis. *Organic Geochemistry*, *2*(1), pp.9-31.

Dickson, A.J., Saker-Clark, M., Jenkyns, H.C., Bottini, C., Erba, E., Russo, F., Gorbanenko, O., Naafs, B.D., Pancost, R.D., Robinson, S.A. and Boorn, S.H., 2017. A Southern Hemisphere record of global trace-metal drawdown and orbital modulation of organic-matter burial across the Cenomanian–Turonian boundary (Ocean Drilling Program Site 1138, Kerguelen Plateau). *Sedimentology*, *64*(1), pp.186-203.

Donnadieu, Y., Pucéat, E., Moiroud, M., Guillocheau, F. and Deconinck, J.F., 2016. A better-ventilated ocean triggered by Late Cretaceous changes in continental configuration. *Nature communications*, *7*.

Du Vivier, A.D., Selby, D., Sageman, B.B., Jarvis, I., Gröcke, D.R. and Voigt, S., 2014. Marine 187 Os/188 Os isotope stratigraphy reveals the interaction of volcanism and ocean circulation during Oceanic Anoxic Event 2. *Earth and Planetary Science Letters*, *389*, pp.23-33.

Duggen, S., Olgun, N., Croot, P., Hoffmann, L.J., Dietze, H., Delmelle, P. and Teschner, C., 2010. The role of airborne volcanic ash for the surface ocean biogeochemical iron-cycle: a review. *Biogeosciences (BG)*, *7*(3), pp.827-844.

Dzou, L.I., Holba, A.G., Ramón, J.C., Moldowan, J.M. and Zinniker, D., 1999. Application of new diterpane biomarkers to source, biodegradation and mixing effects on Central Llanos Basin oils, Colombia. *Organic Geochemistry*, *30*(7), pp.515-534.

Eary, L.E. and Rai, D., 1989. Kinetics of chromate reduction by ferrous ions derived from hematite and biotite at 25 degrees C. *American Journal of Science*, *289*(2), pp.180-213.

Elderfield, H., 1970. Chromium speciation in sea water. *Earth and Planetary Science Letters*, *9*(1), pp.10-16.

Eldrett, J.S., Minisini, D. and Bergman, S.C., 2014. Decoupling of the carbon cycle during Ocean Anoxic Event 2. *Geology*, *42*(7), pp.567-570.

Elliott, W.C. and Matisoff, G., 1996. Evaluation of kinetic models for the smectite to illite transformation. *Clays and Clay Minerals*, *44*(1), pp.77-87.

Erbacher, J., Friedrich, O., Wilson, P.A., Birch, H. and Mutterlose, J., 2005. Stable organic carbon isotope stratigraphy across Oceanic Anoxic Event 2 of Demerara Rise, western tropical Atlantic. *Geochemistry, Geophysics, Geosystems*, *6*(6).

Erbacher, J., Huber, B.T., Norris, R.D. and Markey, M., 2001. Increased thermohaline stratification as a possible cause for an ocean anoxic event in the Cretaceous period. *Nature*, *409*(6818), p.325.

Erbacher, J., Thurow, J. and Littke, R., 1996. Evolution patterns of radiolaria and organic matter variations: a new approach to identify sea-level changes in mid-Cretaceous pelagic environments. *Geology*, *24*(6), pp.499-502.

Erickson, B.E. and Helz, G.R., 2000. Molybdenum (VI) speciation in sulfidic waters: stability and lability of thiomolybdates. *Geochimica et Cosmochimica Acta*, *64*(7), pp.1149-1158.

Erlich, R.N., Palmer-Koleman, S.E. and Lorente, M.A., 1999. Geochemical characterization of oceanographic and climatic changes recorded in upper Albian to lower Maastrichtian strata, western Venezuela. *Cretaceous Research*, *20*(5), pp.547-581.

Erlich, R.N., Nederbragt, A.J. and Lorente, M.A., 2000. Birth and death of the Late Cretaceous "La Luna Sea", and origin of the Tres Esquinas phosphorites. Journal of South American Earth Sciences, 13(1), pp.21-45.

Erlich, R.N., Villamil, T. and Keens-Dumas, J., 2003. Controls on the deposition of Upper Cretaceous organic carbon–rich rocks from Costa Rica to Suriname.

ETAYO-SERNA, F., 1985. Paleontología estratigráfica del Sistema Cretácico en la Sierra Nevada del Cocuy. *Proyecto Cretácico. Contribuciones. Publicaciones Geológicas Especiales del Ingeominas*, 16 (XXIV):1-47. Bogotá

Etayo, F., Cediel, F. and Cáceres, C., 1997. Mapa de distribución de facies y ámbito| tectónico a través del Fanerozoico de Colombia. *Escala*, *1*(1), pp.500-000.

Evangelou, V. P., & Zhang, Y. L. (1995). A review: pyrite oxidation mechanisms and acid mine drainage prevention. *Critical Reviews in Environmental Science and Technology*, *25*(2), 141-

199.

Fabre, A., 1985. Dinámica de la sedimentación Cretácica en la región de la Sierra Nevada del Cocuy (Cordillera Oriental de Colombia). *Proyecto Cretácico, Publicación Geológica Especial INGEOMINAS*, (16).

Fabre, A., 1987. Tectonique et géneration d'hydrocarbures: Un modèle de l'evolution de la Cordillère Orientale de Colombie et du Bassin de Llanos pendant le Crétacé et le Tertiaire. *Archives des Sciences Genève*, *40*(2), pp.145-190.

Farrimond, P., Taylor, A. and TelnÆs, N., 1998. Biomarker maturity parameters: the role of generation and thermal degradation. *Organic Geochemistry*, *29*(5), pp.1181-1197.

Fedo, C.M., Eriksson, K.A. and Krogstad, E.J., 1996. Geochemistry of shales from the Archean (~ 3.0 Ga) Buhwa Greenstone Belt, Zimbabwe: implications for provenance and source-area weathering. *Geochimica et Cosmochimica Acta*, *60*(10), pp.1751-1763.

Fedo, C.M., Young, G.M., Nesbitt, H.W. and Hanchar, J.M., 1997. Potassic and sodic metasomatism in the southern province of the Canadian Shield: evidence from the Paleoproterozoic Serpent Formation, Huronian Supergroup, Canada. *Precambrian Research*, *84*(1-2), pp.17-36.

Fischer, C., Schmidt, C., Bauer, A., Gaupp, R., & Heide, K. (2009). Mineralogical and geochemical alteration of low-grade metamorphic black slates due to oxidative weathering. *Chemie Der Erde-Geochemistry*, *69*(2), 127-142.

Flögel, S., 2001. *On the influence of precessional Milankovitch cycles on the Late Cretaceous climate system: Comparison of GCM-results, geochemical, and sedimentary proxies for the Western Interior Seaway of North America* (Doctoral dissertation, Christian-Albrechts-Universität).

Flögel, S., Beckmann, B., Hofmann, P., Bornemann, A., Westerhold, T., Norris, R.D., Dullo, C. and Wagner, T., 2008. Evolution of tropical watersheds and continental hydrology during the Late Cretaceous greenhouse; impact on marine carbon burial and possible implications for the future. *Earth and Planetary Science Letters*, *274*(1), pp.1-13.

Föllmi, K.B., 1995. 160 my record of marine sedimentary phosphorus burial: Coupling of climate and continental weathering under greenhouse and icehouse

conditions. *Geology*, *23*(6), pp.503-506.

Föllmi, K.B., Garrison, R.E., Ramirez, P.C., Zambrano-Ortiz, F., Kennedy, W.J. and Lehner, B.L., 1992. Cyclic phosphate-rich successions in the Upper Cretaceous of Colombia. *Palaeogeography, Palaeoclimatology, Palaeoecology*, *93*(3-4), pp.151-182.

Föllmi, K.B., 2012. Early Cretaceous life, climate and anoxia. *Cretaceous Research*, *35*, pp.230-257.

Friedrich, O., Norris, R.D. and Erbacher, J., 2012. Evolution of middle to Late Cretaceous oceans—a 55 my record of Earth's temperature and carbon cycle. *Geology*, *40*(2), pp.107-110.

Froelich, P., Klinkhammer, G.P., Bender, M.L., Luedtke, N.A., Heath, G.R., Cullen, D., Dauphin, P., Hammond, D., Hartman, B. and Maynard, V., 1979. Early oxidation of organic matter in pelagic sediments of the eastern equatorial Atlantic: suboxic diagenesis. *Geochimica et cosmochimica acta*, *43*(7), pp.1075-1090.

Fuquen, J. and Osorno, J., 2005. Geología de la Plancha 190 Chiquinquirá. *Instituto Colombiano de Geología y Minería–INGEOMINAS, Bogotá*.

Gallego-Torres, D., Reolid, M., Nieto-Moreno, V. and Martínez-Casado, F.J., 2015. Pyrite framboid size distribution as a record for relative variations in sedimentation rate: An example on the Toarcian Oceanic Anoxic Event in Southiberian Palaeomargin. *Sedimentary Geology*, *330*, pp.59-73.

Ganeshram, R.S., Calvert, S.E., Pedersen, T.F. and Cowie, G.L., 1999. Factors controlling the burial of organic carbon in laminated and bioturbated sediments off NW Mexico: Implications for hydrocarbon preservation. *Geochimica et Cosmochimica Acta*, *63*(11), pp.1723-1734.

Gaona-Narvaez, T., Florentin, J.M.M. and Etayo-Serna, F., 2013. Geochemistry, palaeoenvironments and timing of Aptian organic-rich beds of the Paja Formation (Curití, Eastern Cordillera, Colombia). *Geological Society, London, Special Publications*, *382*(1), pp.31-48.

García, C.A., Ríos, C.A. and Castellanos, O.M., 2005. Medium-pressure metamorphism in the Central Santander Massif, Eastern Cordillera, Colombian Andes. *Boletín de Geología*, *27*(2).

García, D.F., 2008. *Estudo dos sistemas petrolíferos no setor central da bacía dos "Llanos*

Orientales," Colômbia. Um modelo para explicar as mudanças na qualidade do petróleo (Doctoral dissertation, Ph. D. thesis, Universidade Federal do Rio de Janeiro, Rio de Janeiro, Brazil).

Grabowski, J., Lakova, I., Petrova, S., Stoykova, K., Ivanova, D., Wójcik-Tabol, P., Sobień, K. and Schnabl, P., 2016. Paleomagnetism and integrated stratigraphy of the Upper Berriasian hemipelagic succession in the Barlya section Western Balkan, Bulgaria: Implications for lithogenic input and paleoredox variations. *Palaeogeography, Palaeoclimatology, Palaeoecology*, *461*, pp.156-177.

Gregory, D. D., Large, R. R., Halpin, J. A., Baturina, E. L., Lyons, T. W., Wu, S., ... & Bull, S. W. (2015). Trace element content of sedimentary pyrite in black shales. *Economic Geology*, *110*(6), 1389-1410.

Guerrero, J. and Sarmiento, G., 1996. Estratigrafía física, palinológica, sedimentológica y secuencial del Cretácico Superior y Paleoceno del Piedemonte Llanero: Implicaciones en exploración petrolera. *Geología Colombiana*, *20*, pp.3-66.

Hallam, A., 1984. Continental humid and arid zones during the Jurassic and Cretaceous. *Palaeogeography, Palaeoclimatology, Palaeoecology*, *47*(3-4), pp.195-223.

Handoh, I.C. and Lenton, T.M., 2003. Periodic mid-Cretaceous oceanic anoxic events linked by oscillations of the phosphorus and oxygen biogeochemical cycles. *Global Biogeochemical Cycles*, *17*(4).

Haq, B.U., 2014. Cretaceous eustasy revisited. *Global and Planetary Change*, *113*, pp.44-58.

Hay, W. W., and Wold, C. N,, 1992. The fit of North America, Africa and South America about the site of the future Gulf of Mexico and Caribbean: VIII Congreso Espanol de Geologia y XII Congreso Latinoamericano de Geologia, Actas, no. 4, p. 122-126.

Hay, W.W., DeConto, R.M., Wold, C.N., Wilson, K.M., Voigt, S., Schulz, M., Wold, A.R., Dullo, W.C., Ronov, A.B., Balukhovsky, A.N. and Soding, E., 1999. Alternative global Cretaceous paleogeography. *Evolution of the Cretaceous ocean-climate system*, p.1.

Hay, W.W., 2008. Evolving ideas about the Cretaceous climate and ocean circulation. *Cretaceous Research*, *29*(5), pp.725-753.

Hay, W.W. and Floegel, S., 2012. New thoughts about the Cretaceous climate and

oceans. *Earth-Science Reviews*, *115*(4), pp.262-272.

Hay, W.W., 2016. Toward understanding Cretaceous climate—An updated review. *Science China Earth Sciences*, pp.1-15.

Heimhofer, U., Adatte, T., Hochuli, P.A., Burla, S. and Weissert, H., 2008. Coastal sediments from the Algarve: low-latitude climate archive for the Aptian-Albian. *International Journal of Earth Sciences*, *97*(4), pp.785-797.

Helz, G.R., Miller, C.V., Charnock, J.M., Mosselmans, J.F.W., Pattrick, R.A.D., Garner, C.D. and Vaughan, D.J., 1996. Mechanism of molybdenum removal from the sea and its concentration in black shales: EXAFS evidence. *Geochimica et Cosmochimica Acta*, *60*(19), pp.3631-3642.

Henkel, S., Mogollon, J.M., Nöthen, K., Franke, C., Bogus, K., Robin, E., Bahr, A., Blumenberg, M., Pape, T., Seifert, R. and März, C., 2012. Diagenetic barium cycling in Black Sea sediments–A case study for anoxic marine environments. *Geochimica et Cosmochimica Acta*, *88*, pp.88-105.

Herrle, J.O., Pross, J., Friedrich, O., Kößler, P. and Hemleben, C., 2003. Forcing mechanisms for mid-Cretaceous black shale formation: evidence from the Upper Aptian and Lower Albian of the Vocontian Basin (SE France). *Palaeogeography, Palaeoclimatology, Palaeoecology*, *190*, pp.399-426.

Hetzel, A., Böttcher, M.E., Wortmann, U.G. and Brumsack, H.J., 2009. Paleo-redox conditions during OAE 2 reflected in Demerara Rise sediment geochemistry (ODP Leg 207). *Palaeogeography, Palaeoclimatology, Palaeoecology*, *273*(3), pp.302-328.

Hetzel, A., März, C., Vogt, C. and Brumsack, H.J., 2011. Geochemical environment of Cenomanian-Turonian black shale deposition at Wunstorf (northern Germany). *Cretaceous Research*, *32*(4), pp.480-494.

Hild, E. and Brumsack, H.J., 1998. Major and minor element geochemistry of Lower Aptian sediments from the NW German Basin (core Hohenegglesen KB 40). *Cretaceous Research*, *19*(5), pp.615-633.

Hilton, R. G., Gaillardet, J., Calmels, D., & Birck, J. L. (2014). Geological respiration of a mountain belt revealed by the trace element rhenium. *Earth and Planetary Science Letters*, *403*, 27-36.

Hofmann, P., Stüsser, I., Wagner, T., Schouten, S. and Damsté, J.S.S., 2008. Climate–ocean coupling off North-West Africa during the Lower Albian: the oceanic anoxic event 1b. *Palaeogeography, Palaeoclimatology, Palaeoecology*, *262*(3), pp.157-165.

Hofmann, P. and Wagner, T., 2011. ITCZ controls on Late Cretaceous black shale sedimentation in the tropical Atlantic Ocean. *Paleoceanography*, *26*(4).

Hofmann, P., Stüsser, I., Wagner, T., Schouten, S. and Damsté, J.S.S., 2008. Climate–ocean coupling off North-West Africa during the Lower Albian: the oceanic anoxic event 1b. *Palaeogeography, Palaeoclimatology, Palaeoecology*, *262*(3), pp.157-165.

Holmden, C., Jacobson, A.D., Sageman, B.B. and Hurtgen, M.T., 2016. Response of the Cr isotope proxy to Cretaceous Ocean Anoxic Event 2 in a pelagic carbonate succession from the Western Interior Seaway. *Geochimica et Cosmochimica Acta*, *186*, pp.277-295.

Hsieh, M. L., & Knuepfer, P. L. (2001). Middle–late Holocene river terraces in the Erhjen River Basin, southwestern Taiwan—Implications of river response to climate change and active tectonic uplift. *Geomorphology*, *38*(3), 337-372.

Huber, B.T., Norris, R.D. and MacLeod, K.G., 2002. Deep-sea paleotemperature record of extreme warmth during the Cretaceous. *Geology*, *30*(2), pp.123-126.

Huerta-Diaz, M. A., & Morse, J. W. (1992). Pyritization of trace metals in anoxic marine sediments. *Geochimica et Cosmochimica Acta*, *56*(7), 2681-2702.

Huminicki, D. M., & Rimstidt, J. D. (2009). Iron oxyhydroxide coating of pyrite for acid mine drainage control. *Applied Geochemistry*, *24*(9), 1626-1634.

Hurst, A., 1985. Diagenetic chlorite formation in some Mesozoic shales from the Sleipner area of the North Sea. *Clay Minerals*, *20*(1), pp.69-79.

Ingall, E.D., Bustin, R.M. and Van Cappellen, P., 1993. Influence of water column anoxia on the burial and preservation of carbon and phosphorus in marine shales. *Geochimica et Cosmochimica Acta*, *57*(2), pp.303-316.

Jeng, A. S. (1992). Weathering of some Norwegian alum shales, II. Laboratory simulations to study the influence of aging, acidification and liming on heavy metal release. *Acta Agriculturae Scandinavica B-Plant Soil Sciences*, *42*(2), 76-87.

Jenkyns, H.C., Gale, A.S. and Corfield, R.M., 1994. Carbon-and oxygen-isotope stratigraphy of the English Chalk and Italian Scaglia and its palaeoclimatic significance. *Geological Magazine*, *131*(1), pp.1-34.

Jenkyns, H.C., Jones, C.E., Gröcke, D.R., Hesselbo, S.P. and Parkinson, D.N., 2002. Chemostratigraphy of the Jurassic System: applications, limitations and implications for palaeoceanography. *Journal of the Geological Society*, *159*(4), pp.351-378.

Jenkyns, H.C., 2010. Geochemistry of oceanic anoxic events. *Geochemistry, Geophysics, Geosystems*, *11*(3).

Jenkyns, H.C., Dickson, A.J., Ruhl, M. and Boorn, S.H., 2017. Basalt-seawater interaction, the Plenus Cold Event, enhanced weathering and geochemical change: deconstructing Oceanic Anoxic Event 2 (Cenomanian–Turonian, Late Cretaceous). *Sedimentology*, *64*(1), pp.16-43

Jin, L., Mathur, R., Rother, G., Cole, D., Bazilevskaya, E., Williams, J., & Brantley, S. (2013). Evolution of porosity and geochemistry in Marcellus Formation black shale during weathering. *Chemical Geology*, *356*, 50-63.

Joeckel, R. M., Clement, B. A., & Bates, L. V. (2005). Sulfate-mineral crusts from pyrite weathering and acid rock drainage in the Dakota Formation and Graneros Shale, Jefferson County, Nebraska. *Chemical Geology*, *215*(1), 433-452.

Jones, B. and Manning, D.A., 1994. Comparison of geochemical indices used for the interpretation of palaeoredox conditions in ancient mudstones. *Chemical Geology*, *111*(1-4), pp.111-129.

Jones, C.E., Jenkyns, H.C., Coe, A.L. and Stephen, H.P., 1994. Strontium isotopic variations in Jurassic and Cretaceous seawater. *Geochimica et Cosmochimica Acta*, *58*(14), pp.3061-3074.

Jones, C.E. and Jenkyns, H.C., 2001. Seawater strontium isotopes, oceanic anoxic events, and seafloor hydrothermal activity in the Jurassic and Cretaceous. *American Journal of Science*, *301*(2), pp.112-149.

Julivert, M., 1968. Lexique stratigraphique, Amérique Latine. *Colombie (première partie), Précambrien, Paléozoïque, Mésozoïque, et intrusions d'âge mésozoïque-tertiaire. Centre National de la Recherche Scientifique, Paris*.

Keil, R.G., Tsamakis, E., Giddings, J.C. and Hedges, J.I., 1998. Biochemical distributions (amino

acids, neutral sugars, and lignin phenols) among size-classes of modern marine sediments from the Washington coast. *Geochimica et Cosmochimica Acta*, *62*(8), pp.1347-1364.

Klinkhammer, G.P. and Palmer, M.R., 1991. Uranium in the oceans: where it goes and why. *Geochimica et Cosmochimica Acta*, *55*(7), pp.1799-1806.

Kolonic, S., Wagner, T., Forster, A., Sinninghe Damsté, J.S., Walsworth-Bell, B., Erba, E., Turgeon, S., Brumsack, H.J., Chellai, E.H., Tsikos, H. and Kuhnt, W., 2005. Black shale deposition on the northwest African Shelf during the Cenomanian/Turonian oceanic anoxic event: Climate coupling and global organic carbon burial. *Paleoceanography*, *20*(1).

Kraal, P., Slomp, C. P., Forster, A., Kuypers, M. M., & Sluijs, A. (2009). Pyrite oxidation during sample storage determines phosphorus fractionation in carbonate-poor anoxic sediments. *Geochimica et Cosmochimica Acta*, *73*(11), 3277-3290.

Kronberg, B.I., Nesbitt, H.W. and Lam, W.W., 1986. Upper Pleistocene Amazon deep-sea fan muds reflect intense chemical weathering of their mountainous source lands. *Chemical Geology*, *54*(3-4), pp.283-294.

Kujau, A., Heimhofer, U., Ostertag-Henning, C., Gréselle, B. and Mutterlose, J., 2012. No evidence for anoxia during the Valanginian carbon isotope event—an organic-geochemical study from the Vocontian Basin, SE France. *Global and Planetary Change*, *92*, pp.92-104.

Kuypers, M.M., Pancost, R.D. and Damste, J.S.S., 1999. A large and abrupt fall in atmospheric CO2 concentration during Cretaceous times. *Nature*, *399*(6734), p.342.

Lara, R. H., Monroy, M. G., Mallet, M., Dossot, M., González, M. A., & Cruz, R. (2015). An experimental study of iron sulfides weathering under simulated calcareous soil conditions. *Environmental Earth Sciences*, *73*(4), 1849-1869.

Larson, R.L., 1991. Latest pulse of Earth: Evidence for a mid-Cretaceous superplume. *Geology*, *19*(6), pp.547-550.

Leckie, R.M., Bralower, T.J. and Cashman, R., 2002. Oceanic anoxic events and plankton evolution: Biotic response to tectonic forcing during the mid-Cretaceous. *Paleoceanography*, *17*(3).

Lemiere, B., Laperche, V., Haouche, L. and Auger, P., 2014. Portable XRF and wet materials: application to dredged contaminated sediments from waterways. *Geochemistry: Exploration,*

Environment, Analysis, *14*(3), pp.257-264.

Lenniger, M., Nøhr-Hansen, H., Hills, L.V. and Bjerrum, C.J., 2014. Arctic black shale formation during Cretaceous Oceanic Anoxic Event 2. *Geology*, *42*(9), pp.799-802.

Leventhal, J.S., 1995. Carbon-sulfur plots to show diagenetic and epigenetic sulfidation in sediments. *Geochimica et Cosmochimica Acta*, *59*(6), pp.1207-1211.

Leythaeuser, D. (1973). Effects of weathering on organic matter in shales. *Geochimica et Cosmochimica Acta*, *37*(1), 113-120.

Liao, X., Chigira, M., Matsushi, Y., & Wu, X. (2014). Investigation of water–rock interactions in Cambrian black organic-rich mudrock via a flow-through experiment. Applied Geochemistry, 51, 65-78.

Lipinski, M., Warning, B. and Brumsack, H.J., 2003. Trace metal signatures of Jurassic/Cretaceous black shales from the Norwegian Shelf and the Barents Sea. *Palaeogeography, Palaeoclimatology, Palaeoecology*, *190*, pp.459-475.

Littke, R., Klussmann, U., Krooss, B., & Leythaeuser, D. (1991). Quantification of loss of calcite, pyrite, and organic matter due to weathering of Toarcian black shales and effects on kerogen and bitumen characteristics. *Geochimica et Cosmochimica Acta*, *55*(11), 3369-3378.

Littler, K., Robinson, S.A., Bown, P.R., Nederbragt, A.J. and Pancost, R.D., 2011. High sea-surface temperatures during the Early Cretaceous Epoch. *Nature Geoscience*, *4*(3), p.169.

López, L. and Mónaco, S.L., 2004. Geochemical implications of trace elements and sulfur in the saturate, aromatic and resin fractions of crude oil from the Mara and Mara Oeste fields, Venezuela. *Fuel*, *83*(3), pp.365-374.

Lundgren, D. G., & Silver, M. (1980). Ore leaching by bacteria. *Annual Reviews in Microbiology*, *34*(1), 263-283.

Luning, S., Kolonic, S., Loydell, D. K., & Craig, J. (2003). Reconstruction of the original organic richness in weathered Silurian shale outcrops (Murzuq and Kufra basins, southern Libya). *GEOARABIA-MANAMA-*, *8*, 299-308.

Lyons, T. W., & Severmann, S. (2006). A critical look at iron paleoredox proxies: new insights from modern euxinic marine basins. *Geochimica et Cosmochimica Acta*, *70*(23), 5698-5722.

Macellari, C.E. and De Vries, T.J., 1987. Late Cretaceous upwelling and anoxic sedimentation in northwestern South America. *Palaeogeography, Palaeoclimatology, Palaeoecology*, *59*, pp.279-292.

Macellari, C.E., 1988. Cretaceous paleogeography and depositional cycles of western South America. *Journal of South American Earth Sciences*, *1*(4), pp.373-418.

Mackenzie, F.T. and Lerman, A., 2006. *Carbon in the Geobiosphere:-Earth's Outer Shell* (Vol. 25). Springer Science & Business Media, pp1-21

Mann, U. and Stein, R., 1997. Organic facies variations, source rock potential, and sea level changes in Cretaceous black shales of the Quebrada Ocal, Upper Magdalena Valley, Colombia. *AAPG bulletin*, *81*(4), pp.556-576.

Mann, U. and Zweigel, J., 2008. Modelling Source-Rock Distribution and Quality Variations: The Organic Facies Modelling Approach. *Analogue and Numerical Modelling of Sedimentary Systems: From Understandintig to Prediction*, pp.239-274.

Martínez, J.I. and Vergara, L.E., 1999. La sucesión paleoambiental del Cretácico de la región de Tequendama y oeste de la Sabana de Bogotá, Cordillera Oriental Colombiana. *Geología Colombiana*, *24*, pp.107-147.

Martinez, J.I., 2003. The paleoecology of Late cretaceous upwelling events from the upper magdalena basin, Colombia. *Palaios*, *18*(4), pp.305-320.

März, C., Beckmann, B., Franke, C., Vogt, C., Wagner, T. and Kasten, S., 2009. Geochemical environment of the Coniacian–Santonian western tropical Atlantic at Demerara Rise. *Palaeogeography, Palaeoclimatology, Palaeoecology*, *273*(3), pp.286-301.

März, C., Poulton, S.W., Beckmann, B., Küster, K., Wagner, T. and Kasten, S., 2008. Redox sensitivity of P cycling during marine black shale formation: dynamics of sulfidic and anoxic, non-sulfidic bottom waters. *Geochimica et Cosmochimica Acta*, *72*(15), pp.3703-3717.

Maze, W.B., 1984. Jurassic La Quinta Formation in the Sierra de Perijá, northwestern Venezuela: Geology and tectonic environment of red beds and volcanic rocks. *Geological*

Society of America Memoirs, *162*, pp.263-282.

McAnena, A., Flögel, S., Hofmann, P., Herrle, J.O., Griesand, A., Pross, J., Talbot, H.M., Rethemeyer, J., Wallmann, K. and Wagner, T., 2013. Atlantic cooling associated with a marine biotic crisis during the mid-Cretaceous period. *Nature Geoscience*, *6*(7), p.558.

McArthur, J.M., Janssen, N.M.M., Reboulet, S., Leng, M.J., Thirlwall, M.F. and Van de Schootbrugge, B., 2007. Palaeotemperatures, polar ice-volume, and isotope stratigraphy (Mg/Ca, δ 18 O, δ 13 C, 87 Sr/86 Sr): the early cretaceous (Berriasian, Valanginian, Hauterivian). *Palaeogeography, Palaeoclimatology, Palaeoecology*, *248*(3), pp.391-430.

McManus, J., Berelson, W.M., Klinkhammer, G.P., Hammond, D.E. and Holm, C., 2005. Authigenic uranium: relationship to oxygen penetration depth and organic carbon rain. *Geochimica et Cosmochimica Acta, 69(1),* pp.95-108.

Mermut, A.R. and Cano, A.F., 2001. Baseline studies of the clay minerals society source clays: chemical analyses of major elements. *Clays and Clay Minerals*, *49*(5), pp.381-386.

Meyers, S.R., 2007. Production and preservation of organic matter: The significance of iron. *Paleoceanography*, *22*(4).

Meyers, S.R., Sageman, B.B. and Arthur, M.A., 2012. Obliquity forcing of organic matter accumulation during Oceanic Anoxic Event 2. *Paleoceanography*, *27*(3).

Mojica, J. and Scheidegger, A.E., 1984. Fósiles deformados y otras estructuras microtectónicas en la formación Hiló (Albiano) alrededores de Sasaima, Cundinamarca (Colombia). *Geología Colombiana*, *13*, pp.41-54.

Monaco, S.L., López, L., Rojas, H., Garcia, D., Premovic, P. and Briceno, H., 2002. Distribution of major and trace elements in La Luna Formation, southwestern Venezuelan basin. *Organic geochemistry*, *33*(12), pp.1593-1608.

Mongenot, T., Tribovillard, N.P., Desprairies, A., Lallier-Vergès, E. and Laggoun-Defarge, F., 1996. Trace elements as palaeoenvironmental markers in strongly mature hydrocarbon source rocks: the Cretaceous La Luna Formation of Venezuela. *Sedimentary Geology*, *103*(1-2), pp.23-37.

Mora, A., Casallas, W., Ketcham, R.A., Gomez, D., Parra, M., Namson, J., Stockli, D., Almendral, A., Robles, W. and Ghorbal, B., 2015. Kinematic restoration of contractional

basement structures using thermokinematic models: A key tool for petroleum system modeling. *AAPG Bulletin*, *99*(8), pp.1575-1598.

Mora, A., Parra, M., Strecker, M.R., Kammer, A., Dimaté, C. and Rodríguez, F., 2006. Cenozoic contractional reactivation of Mesozoic extensional structures in the Eastern Cordillera of Colombia. *Tectonics*, *25*(2).

Morales, C., Kujau, A., Heimhofer, U., Mutterlose, J., Spangenberg, J.E., Adatte, T., Ploch, I. and Föllmi, K.B., 2015. Palaeoclimate and palaeoenvironmental changes through the onset of the Valanginian carbon–isotope excursion: Evidence from the Polish Basin. *Palaeogeography, Palaeoclimatology, Palaeoecology*, *426*, pp.183-198.

Mort, H.P., Adatte, T., Keller, G., Bartels, D., Föllmi, K.B., Steinmann, P., Berner, Z. and Chellai, E.H., 2008. Organic carbon deposition and phosphorus accumulation during Oceanic Anoxic Event 2 in Tarfaya, Morocco. *Cretaceous Research*, *29*(5), pp.1008-1023.

Mutterlose, J., Brumsack, H., Flögel, S., Hay, W., Klein, C., Langrock, U., Lipinski, M., Ricken, W., Söding, E., Stein, R. and Swientek, O., 2003. The Greenland-Norwegian Seaway: A key area for understanding Late Jurassic to Early Cretaceous paleoenvironments. *Paleoceanography*, *18*(1).

Nadeau, P.H. and Bain, D.C., 1986. Composition of some smectites and diagenetic illitic clays and implications for their origin. *Clays and Clay Minerals*, *34*(4), pp.455-464.

Nameroff, T.J., Balistrieri, L.S. and Murray, J.W., 2002. Suboxic trace metal geochemistry in the eastern tropical North Pacific. *Geochimica et Cosmochimica Acta*, *66*(7), pp.1139-1158.

Negri, A., Wagner, T. and Meyers, P.A., 2006. Introduction to “Causes and consequences of organic carbon burial through time”.

Negri, A., Ferretti, A., Wagner, T. and Meyers, P.A., 2009. Organic-carbon-rich sediments through the Phanerozoic: Processes, progress, and perspectives.

Nesbitt, H. and Young, G.M., 1982. Early Proterozoic climates and plate motions inferred from major element chemistry of lutites. *Nature*, *299*(5885), pp.715-717.

Nicholson, R. V., Gillham, R. W., & Reardon, E. J. (1988). Pyrite oxidation in carbonate-buffered solution: 1. Experimental kinetics. *Geochimica et Cosmochimica Acta*, *52*(5), 1077-

1085.

Nicholson, R. V., Gillham, R. W., & Reardon, E. J. (1990). Pyrite oxidation in carbonate-buffered solution: 2. Rate control by oxide coatings. Geochimica et Cosmochimica Acta, 54(2), 395-402.

Nie, J. and Peng, W., 2014. Automated SEM–EDS heavy mineral analysis reveals no provenance shift between glacial loess and interglacial paleosol on the Chinese Loess Plateau. *Aeolian Research*, *13*, pp.71-75.

Nordstrom, D. K. (1982). Aqueous pyrite oxidation and the consequent formation of secondary iron minerals. *Acid sulfate weathering*, 37-56.

Núñez-Useche, F., Canet, C., Barragán, R. and Alfonso, P., 2016. Bioevents and redox conditions around the Cenomanian–Turonian anoxic event in Central Mexico. *Palaeogeography, Palaeoclimatology, Palaeoecology*, *449*, pp.205-226.

Ocean Drilling Stratigraphic Network (2011) Plate tectonic reconstruction. Retrieved frohttp://www.odsn.de/

Odin, G. P., Cabaret, T., Mertz, J. D., Menendez, B., Etienne, L., Wattiaux, A., & Rouchon, V. (2015, June). Alteration of fossil-bearing shale (Autun Basin, France; Permian), part I: Characterizing iron speciation and its vulnerability to weathering by combined use of Mössbauer spectroscopy, X-ray diffraction, porosimetry and permeability measurements. In *Annales de Paléontologie* (Vol. 101, No. 2, pp. 75-85). Elsevier Masson.

Odin, G. P., Vanmeert, F., Farges, F., Gand, G., Janssens, K., Romero-Sarmiento, M. F., ... & Rouchon, V. (2015, September). Alteration of fossil-bearing shale (Autun, France; Permian), part II: Monitoring artificial and natural ageing by combined use of S and Ca K-edge XANES analysis, Rock-Eval pyrolysis and FTIR analysis. In *Annales de Paléontologie* (Vol. 101, No. 3, pp. 225-239). Elsevier Masson.

Oelkers, E. H., & Schott, J. (2009). Thermodynamics and kinetics of water-rock interaction. P.p. 435-484

Olgun, N., Duggen, S., Croot, P.L., Delmelle, P., Dietze, H., Schacht, U., Óskarsson, N., Siebe, C., Auer, A. and Garbe-Schönberg, D., 2011. Surface ocean iron fertilization: the role of airborne volcanic ash from subduction zone and hot spot volcanoes and related iron fluxes

into the Pacific Ocean. *Global Biogeochemical Cycles*, *25*(4).

Orth, C.J., Attrep, M., Quintana, L.R., Elder, W.P., Kauffman, E.G., Diner, R. and Villamil, T., 1993. Elemental abundance anomalies in the late Cenomanian extinction interval: A search for the source (s). *Earth and Planetary Science Letters*, *117*(1-2), pp.189-204.

Owens, J.D., Gill, B.C., Jenkyns, H.C., Bates, S.M., Severmann, S., Kuypers, M.M., Woodfine, R.G. and Lyons, T.W., 2013. Sulfur isotopes track the global extent and dynamics of euxinia during Cretaceous Oceanic Anoxic Event 2. *Proceedings of the National Academy of Sciences*, *110*(46), pp.18407-18412.

Owens, J.D., Lyons, T.W., Hardisty, D.S., Lowery, C.M., Lu, Z., Lee, B. and Jenkyns, H.C., 2017. Patterns of local and global redox variability during the Cenomanian–Turonian Boundary Event (Oceanic Anoxic Event 2) recorded in carbonates and shales from central Italy. *Sedimentology*, *64*(1), pp.168-185.

Parra, M., Mora, A., Sobel, E.R., Strecker, M.R. and González, R., 2009. Episodic orogenic front migration in the northern Andes: Constraints from low-temperature thermochronology in the Eastern Cordillera, Colombia. *Tectonics*, *28*(4).

Pedersen, T.F. and Calvert, S.E., 1990. Anoxia vs. productivity: what controls the formation of organic-carbon-rich sediments and sedimentary Rocks?(1). *Aapg Bulletin*, *74*(4), pp.454-466.

Pedro, G. (1961). An experimental study on the geochemical weathering of crystalline rocks by water. Clay Miner. Bull, 4(26), 266-281.

Peng, B., Song, Z., Tu, X., Xiao, M., Wu, F., & Lv, H. (2004). Release of heavy metals during weathering of the Lower Cambrian black shales in western Hunan, China. *Environmental Geology*, *45*(8), 1137-1147.

Perez-Infante, J., Farrimond, P. and Furrer, M., 1996. Global and local controls influencing the deposition of the La Luna Formation (Cenomanian-Campanian), western Venezuela. *Chemical Geology*, *130*(3), pp.271-288.

Perkins, R. B., & Mason, C. E. (2015). The relative mobility of trace elements from short-term

weathering of a black organic-rich mudrock. Applied Geochemistry, 56, 67

Perkins, R.B., Piper, D.Z. and Mason, C.E., 2008. Trace-element budgets in the Ohio/Sunbury shales of Kentucky: constraints on ocean circulation and primary productivity in the Devonian–Mississippian Appalachian Basin. *Palaeogeography, Palaeoclimatology, Palaeoecology*, *265*(1), pp.14-29.

Petsch, S. T., Berner, R. A., & Eglinton, T. I. (2000). A field study of the chemical weathering of ancient sedimentary organic matter. *Organic Geochemistry*, *31*(5), 475-487.

Petsch, S.T. and Berner, R.A., 1998. Coupling the geochemical cycles of C, P, Fe, and S; the effect on atmospheric O 2 and the isotopic records of carbon and sulfur. *American Journal of Science*, *298*(3), pp.246-262.

Pogge von Strandmann, P.A., Jenkyns, H.C. and Woodfine, R.G., 2013. Lithium isotope evidence for enhanced weathering during Oceanic Anoxic Event 2. *Nature Geoscience*, *6*(8), pp.668-672.

Poulton, S. W., & Canfield, D. E. (2005). Development of a sequential extraction procedure for iron: implications for iron partitioning in continentally derived particulates. Chemical Geology, 214(3), 209-221.

Poulton, S. W., & Canfield, D. E. (2011). Ferruginous conditions: a dominant feature of the ocean through Earth's history. *Elements*, *7*(2), 107-112.

Poulton, S.W., Henkel, S., März, C., Urquhart, H., Flögel, S., Kasten, S., Damsté, J.S.S. and Wagner, T., 2015. A continental-weathering control on orbitally driven redox-nutrient cycling during Cretaceous Oceanic Anoxic Event 2. *Geology*, *43*(11), pp.963-966.

Pszczółkowski, A. and Myczyński, R., 2010. Tithonian–Early Valanginian evolution of deposition along the proto-Caribbean margin of North America recorded in Guaniguanico successions (western Cuba). *Journal of South American Earth Sciences*, *29*(2), pp.225-253.

Puchelt, H., 1969. Barium: abundance in rock-forming minerals. *Handbook of Geochemistry. Springer, Berlin*, pp.D1-D18.

Pye, K., & Miller, J. A. (1990). Chemical and biochemical weathering of pyritic mudrocks in a shale embankment. *Quarterly Journal of Engineering Geology and Hydrogeology*, *23*(4), 365-

382.

Raiswell, R. and Berner, R.A., 1986. Pyrite and organic matter in Phanerozoic normal marine shales. *Geochimica et Cosmochimica Acta*, *50*(9), pp.1967-1976.

Raiswell, R. and Canfield, D.E., 1998. Sources of iron for pyrite formation in marine sediments. *American Journal of Science*, *298*(3), pp.219-245.

Raiswell, R., Buckley, F., Berner, R.A. and Anderson, T.F., 1988. Degree of pyritization of iron as a paleoenvironmental indicator of bottom-water oxygenation. *Journal of Sedimentary Research*, *58*(5).

Raiswell, R., Newton, R., & Wignall, P. B. (2001). An indicator of water-column anoxia: resolution of biofacies variations in the Kimmeridge Clay (Upper Jurassic, UK). *Journal of Sedimentary Research*, *71*(2), 286-294.

Reinhard, C.T., 2012. Exploring the texture of ocean-atmosphere redox evolution on the early Earth.

Rey, O., Simo, J.A. and Lorente, M.A., 2004. A record of long-and short-term environmental and climatic change during OAE3: La Luna Formation, Late Cretaceous (Santonian–early Campanian), Venezuela. *Sedimentary Geology*, *170*(1), pp.85-105.

Richiano, S., 2014. Lower Cretaceous anoxic conditions in the Austral basin, south-western Gondwana, Patagonia Argentina. *Journal of South American Earth Sciences*, *54*, pp.37-46.

Ritsema, C. J., & Groenenberg, J. E. (1993). Pyrite oxidation, carbonate weathering, and gypsum formation in a drained potential acid sulfate soil. *Soil Science Society of America Journal*, *57*(4), 968-976.

Robinson, S.A., Williams, T. and Bown, P.R., 2004. Fluctuations in biosiliceous production and the generation of Early Cretaceous oceanic anoxic events in the Pacific Ocean (Shatsky Rise, Ocean Drilling Program Leg 198). *Paleoceanography*, *19*(4).

Rosser, N. J., Petley, D. N., Lim, M., Dunning, S. A., & Allison, R. J. (2005). Terrestrial laser scanning for monitoring the process of hard rock coastal cliff erosion. *Quarterly Journal of Engineering Geology and Hydrogeology*, *38*(4), 363-375.

Ruttenberg, K.C. and Berner, R.A., 1993. Authigenic apatite formation and burial in sediments

from non-upwelling, continental margin environments. *Geochimica et cosmochimica acta, 57(5),* pp.991-1007.

Ruvalcaba Baroni, I., Topper, R.P.M., van Helmond, N.A.G.M., Brinkhuis, H. and Slomp, C.P., 2014. Biogeochemistry of the North Atlantic during oceanic anoxic event 2: role of changes in ocean circulation and phosphorus input. *Biogeosciences*, *11*(4), pp.977-993.

Sageman, B.B., Meyers, S.R. and Arthur, M.A., 2006. Orbital time scale and new C-isotope record for Cenomanian-Turonian boundary stratotype. *Geology*, *34*(2), pp.125-128.

Sageman, B.B., Murphy, A.E., Werne, J.P., Ver Straeten, C.A., Hollander, D.J. and Lyons, T.W., 2003. A tale of shales: the relative roles of production, decomposition, and dilution in the accumulation of organic-rich strata, Middle–Upper Devonian, Appalachian basin. *Chemical Geology*, *195*(1), pp.229-273.

Saikia, B.J. and Parthasarathy, G., 2010. Fourier transform infrared spectroscopic characterization of kaolinite from Assam and Meghalaya, Northeastern India. *Journal of Modern Physics*, *1*(04), p.206.

Sánchez, N., Mora, A., Parra, M., Garcia, D., Cortes, M., Shanahan, T.M., Ramirez, R., Llamosa, O. and Guzman, M., 2015. Petroleum system modeling in the Eastern Cordillera of Colombia using geochemistry and timing of thrusting and deformation. *AAPG Bulletin*, *99*(8), pp.1537-1556.

Sarmiento, L.F., 2001. Mesozoic rifting and Cenozoic basin inversion history of the Eastern Cordillera, Colombian Andes. Inferences from tectonic models. *Ecopetrol. 295p.*

Sarmiento-Rojas, L.F., Van Wess, J.D. and Cloetingh, S., 2006. Mesozoic transtensional basin history of the Eastern Cordillera, Colombian Andes: Inferences from tectonic models. *Journal of South American Earth Sciences*, *21*(4), pp.383-411.

Schillawski, S., & Petsch, S. (2008). Release of biodegradable dissolved organic matter from ancient sedimentary rocks. *Global Biogeochemical Cycles*, *22*(3).

Schlanger, S.O. and Jenkyns, H.C., 1976. Cretaceous oceanic anoxic events: causes and consequences. *Geologie en mijnbouw*, *55*(3-4), pp.179-184.

Schmitz, B., 1987. The TiO2/Al2O3 ratio in the Cenozoic Bengal Abyssal Fan sediments and its

use as a paleostream energy indicator. *Marine Geology*, *76*, pp.195-206.

Schneider, R.R., Price, B., Müller, P.J., Kroon, D. and Alexander, I., 1997. Monsoon related variations in Zaire (Congo) sediment load and influence of fluvial silicate supply on marine productivity in the east equatorial Atlantic during the last 200,000 years. *Paleoceanography*, *12*(3), pp.463-481.

Schwarzacher, W., 1993. Cyclostratigraphy and the Milankovitch theory (Vol. 52), Elsevier, 1-4.

Schwertmann, U., & Taylor, R. M. (1989). Iron oxides. *Minerals in soil environments*, (mineralsinsoile), 379-438.

Scott, C. and Lyons, T.W., 2012. Contrasting molybdenum cycling and isotopic properties in euxinic versus non-euxinic sediments and sedimentary rocks: Refining the paleoproxies. *Chemical Geology*, *324*, pp.19-27.

Seidel, D.J., Fu, Q., Randel, W.J. and Reichler, T.J., 2008. Widening of the tropical belt in a changing climate. *Nature geoscience*, *1*(1), pp.21-24.

Senkayi, A. L., Dixon, J. B., & Hossner, L. R. (1981). Simulated weathering of lignite overburden shales from Northeast Texas. *Soil Science Society of America Journal*, *45*(5), 982-986.

Snow, L.J., Duncan, R.A. and Bralower, T.J., 2005. Trace element abundances in the Rock Canyon Anticline, Pueblo, Colorado, marine sedimentary section and their relationship to Caribbean plateau construction and oxygen anoxic event 2. *Paleoceanography*, *20*(3).

Stein, M., Föllmi, K.B., Westermann, S., Godet, A., Adatte, T., Matera, V., Fleitmann, D. and Berner, Z., 2011. Progressive palaeoenvironmental change during the late Barremian–early Aptian as prelude to Oceanic Anoxic Event 1a: Evidence from the Gorgo a Cerbara section (Umbria-Marche basin, central Italy). *Palaeogeography, Palaeoclimatology, Palaeoecology*, *302*(3), pp.396-406.

Stein, M., Westermann, S., Adatte, T., Matera, V., Fleitmann, D., Spangenberg, J.E. and Föllmi, K.B., 2012. Late Barremian–Early Aptian palaeoenvironmental change: The Cassis-La Bédoule section, southeast France. *Cretaceous Research*, *37*, pp.209-222.

Stumm, W. and Morgan, J.J., 1981. Aquatic Chemistry, 780 pp. *J. Wiley & Sons*.

Taylor, S.R. and McLennan, S.M., 1985. The continental crust: its composition and evolution.

Team, C.W., Pachauri, R.K. and Meyer, L.A., 2014. IPCC, 2014: Climate Change 2014: Synthesis Report. Contribution of Working Groups I. *II and III to the Fifth Assessment Report of the intergovernmental panel on Climate Change. IPCC, Geneva, Switzerland*, *151*.

Tebo, B. M., Bargar, J. R., Clement, B. G., Dick, G. J., Murray, K. J., Parker, D., ... & Webb, S. M. (2004). Biogenic manganese oxides: properties and mechanisms of formation. *Annu. Rev. Earth Planet. Sci.*, *32*, 287-328.

Terraza, R., 2003. Origen diagenético de cherts y porcelanitas en las formaciones lidita inferior y lidita superior (grupo oliní), al sur de san luis (tolima), valle superior del magdalena, colombia. *Geología Colombiana*, *28*.

Thurow, J., Moullade, M., Brumsack, H.J., Masure, E., Taugourdeau-Lantz, J. and Dunham, K., 1988. The Cenomanian/Turonian boundary event (CTBE) at Hole 641A, ODP Leg 103 (compared with the CTBE interval at Site 398). In *Proceedings of the Ocean Drilling Program, Scientific Results* (Vol. 103, pp. 587-634).

Tiratsoo, E.N., 1986. Oi lfields of the World. *Houston: Gulf Publishing*.

Tissot, B.W. and Welte, D.H., It (1984~ Petroleum Formation and Occurrence. *New York, Springler, Dpto. RR. PP. 451p*.

Trabucho Alexandre, J., Tuenter, E., Henstra, G.A., van der Zwan, K.J., van de Wal, R.S., Dijkstra, H.A. and de Boer, P.L., 2010. The mid-Cretaceous North Atlantic nutrient trap: Black shales and OAEs. *Paleoceanography*, *25*(4).

Tremolada, F., Erba, E., De Bernardi, B. and Cecca, F., 2009. Calcareous nannofossil fluctuations during the late Hauterivian in the Cismon core (Venetian Alps, northeastern Italy) and in selected sections of the Umbria-Marche Basin (central Italy): paleoceanographic implications of the Faraoni Level. *Cretaceous Research*, *30*(3), pp.505-514.

Tribovillard, N., Algeo, T. J., Lyons, T., & Riboulleau, A. (2006). Trace metals as paleoredox and paleoproductivity proxies: an update. *Chemical geology*, *232*(1), 12-32.

Tribovillard, N., Riboulleau, A., Lyons, T., & Baudin, F. (2004). Enhanced trapping of

molybdenum by sulfurized marine organic matter of marine origin in Mesozoic limestones and shales. *Chemical Geology*, *213*(4), 385-401.

Tribovillard, N.P., Stephan, J.F., Manivit, H., Reyre, Y., Cotillon, P. and Jautée, E., 1991. Cretaceous black shales of Venezuelan Andes: preliminary results on stratigraphy and paleoenvironmental interpretations. *Palaeogeography, Palaeoclimatology, Palaeoecology*, *81*(3-4), pp.313-321.

Tsikos, H., Karakitsios, V., VAN BREUGEL, Y.V.O.N.N.E., Walsworth-Bell, B.E.N., Bombardiere, L., Petrizzo, M.R., Damsté, J.S.S., Schouten, S., Erba, E., Silva, I.P. and Farrimond, P., 2004. Organic-carbon deposition in the Cretaceous of the Ionian Basin, NW Greece: the Paquier Event (OAE 1b) revisited. *Geological Magazine*, *141*(4), pp.401-416.

Tuttle, M. L., & Breit, G. N. (2009). Weathering of the New Albany Shale, Kentucky, USA: I. Weathering zones defined by mineralogy and major-element composition. *Applied Geochemistry*, *24*(8), 1549-1564.

Tuttle, M. L., Breit, G. N., & Goldhaber, M. B. (2009). Weathering of the New Albany Shale, Kentucky: II. Redistribution of minor and trace elements. *Applied Geochemistry*, *24*(8), 1565-1578.

Tyson, R.V. and Pearson, T.H., 1991. Modern and ancient continental shelf anoxia: an overview. *Geological Society, London, Special Publications*, *58*(1), pp.1-24.

Tyson, R.V., 2005. The" productivity versus preservation" controversy: cause, flaws, and resolution. *Special Publication-SEPM*, *82*, p.17.

Ulloa, C. & Rodriguez, E., 1979. Geología del cuadrángulo K-12, Guateque. *Boletín Geológico, Ingeominas, XXII (1976), No. 1:* 3-55. Bogotá

Van Cappellen, P. and Ingall, E.D., 1994. Benthic phosphorus regeneration, net primary production, and ocean anoxia: a model of the coupled marine biogeochemical cycles of carbon and phosphorus. *Paleoceanography*, *9*(5), pp.677-692.

van de Kamp, P.C., 2016. Potassium Distribution and Metasomatism In Pelites and Schists: How and When, Relation To Postdepositional Events. *Journal of Sedimentary Research*, *86*(6), pp.683-711.

Van de Schootbrugge, B., Kuhn, O., Adatte, T., Steinmann, P. and Föllmi, K., 2003. Decoupling

of P-and C org-burial following Early Cretaceous (Valanginian–Hauterivian) platform drowning along the NW Tethyan margin. *Palaeogeography, Palaeoclimatology, Palaeoecology*, *199*(3), pp.315-331.

van Helmond, N.A., Sluijs, A., Reichart, G.J., Damsté, J.S.S., Slomp, C.P. and Brinkhuis, H., 2014. A perturbed hydrological cycle during Oceanic Anoxic Event 2. *Geology*, *42*(2), pp.123-126.

Vásquez, M., Altenberger, U., Romer, R.L., Sudo, M. and Moreno-Murillo, J.M., 2010. Magmatic evolution of the Andean Eastern Cordillera of Colombia during the Cretaceous: Influence of previous tectonic processes. *Journal of South American Earth Sciences*, *29*(2), pp.171-186.

Vergara, L., Rodriguez, G. and Martinez, I., 1997. Agglutinated Foraminifera and sequence stratigraphy from the Chipaque Formation (Upper Cretaceous) of El Crucero section, Colombia, South America. *Micropaleontology*, pp.185-201.

Vergara, L.E. and Ch, G.R., 1997. The upper Cretaceous and Lower Paleocene of the Eastern Bogotá plateau and Llanos thrustbelt, Colombia: Alternative Appraisal to the nomenclature and sequence stratigraphy. *Geología Colombiana*, *22*, pp.51-79.

Villamil, T. and Arango, C., 1998. Chronology, relative sea-level history and a new stratigraphic model for basinal Cretaceous facies of Colombia. *Society for Sedimentary Geology Special Publication, 58.*

Villamil, T., 1996. Depositional and geochemical cyclicity in the Cretaceous fine-grained strata of Colombia. A model for organic matter content. *CT&F-Ciencia, Tecnología y Futuro*, *1*(2), pp.05-23.

Villamil, T., 1999. Campanian–Miocene tectonostratigraphy, depocenter evolution and basin development of Colombia and western Venezuela. *Palaeogeography, Palaeoclimatology, Palaeoecology*, *153*(1), pp.239-275.

Voigt, S., Gale, A.S. and Voigt, T., 2006. Sea-level change, carbon cycling and palaeoclimate during the Late Cenomanian of northwest Europe; an integrated palaeoenvironmental analysis. *Cretaceous Research*, *27*(6), pp.836-858.

Wagner, T., Herrle, J.O., Damsté, J.S.S., Schouten, S., Stüsser, I. and Hofmann, P., 2008. Rapid

warming and salinity changes of Cretaceous surface waters in the subtropical North Atlantic. *Geology*, *36*(3), pp.203-206.

Wagner, T., Hofmann, P. and Flögel, S., 2013. Marine black shale deposition and Hadley Cell dynamics: A conceptual framework for the Cretaceous Atlantic Ocean. *Marine and Petroleum Geology*, *43*, pp.222-238.

Wagner, T., Wallmann, K., Herrle, J.O., Hofmann, P. and Stuesser, I., 2007. Consequences of moderate∼ 25,000 yr lasting emission of light CO 2 into the mid-Cretaceous ocean. *Earth and Planetary Science Letters*, *259*(1), pp.200-211.

Wagreich, M., 2012. " OAE 3"-regional Atlantic organic carbon burial during the Coniacian-Santonian. *Climate of the Past*, *8*(5), p.1447.

Wanty, R.B. and Goldhaber, M.B., 1992. Thermodynamics and kinetics of reactions involving vanadium in natural systems: Accumulation of vanadium in sedimentary rocks. *Geochimica et Cosmochimica Acta*, *56*(4), pp.1471-1483.

Washburn, K. E., & Birdwell, J. E. (2013). Multivariate analysis of ATR-FTIR spectra for assessment of oil organic-rich mudrock organic geochemical properties. *Organic geochemistry*, *63*, 1-7.

Camp, W.K., Diaz, E. and Wawak, B., 2013. Frontmatter, Glossary and Image Catalog: Electron Microscopy of Shale Hydrocarbon Reservoirs.

Wedepohl, K. H. (1971). Environmental influences on the chemical composition of shales and clays. *Physics and Chemistry of the Earth*, *8*, 307-333.

Wedepohl, K. H. (1991). The composition of the upper earth's crust and the natural cycles of selected metals. Metals in natural raw materials. *Natural Resources. In: Merian, E.(Ed.), Metals and Their Compounds in the Environment. VCH, Weinheim*, 3-17.

Weedon, G.P., 2003. *Time-series analysis and cyclostratigraphy: examining stratigraphic records of environmental cycles*. Cambridge University Press. pp 1-23

Weissert, H. and Erba, E., 2004. Volcanism, CO2 and palaeoclimate: a Late Jurassic–Early Cretaceous carbon and oxygen isotope record. Journal of the Geological Society, 161(4), pp.695-702.

Westermann, S., Duchamp-Alphonse, S., Fiet, N., Fleitmann, D., Matera, V., Adatte, T. and Föllmi, K.B., 2013. Paleoenvironmental changes during the Valanginian: new insights from variations in phosphorus contents and bulk-and clay mineralogies in the western Tethys. *Palaeogeography, Palaeoclimatology, Palaeoecology*, *392*, pp.196-208.

Westermann, S., Föllmi, K.B., Adatte, T., Matera, V., Schnyder, J., Fleitmann, D., Fiet, N., Ploch, I. and Duchamp-Alphonse, S., 2010. The Valanginian δ 13 C excursion may not be an expression of a global oceanic anoxic event. *Earth and Planetary Science Letters*, *290*(1), pp.118-131.

White, A. F., Schulz, M. S., Lowenstern, J. B., Vivit, D. V., & Bullen, T. D. (2005). The ubiquitous nature of accessory calcite in granitoid rocks: implications for weathering, solute evolution, and petrogenesis. *Geochimica et Cosmochimica Acta*, *69*(6), 1455-1471.

Whitfield, M., 2001. Interactions between phytoplankton and trace metals in the ocean. *Advances in marine biology*, *41*, pp.1-128.

Wiggering, H. (1993). Sulfide oxidation—an environmental problem within colliery spoil dumps. *Environmental Geology*, *22*(2), 99-105.

Wignall, P. B., Newton, R., & Brookfield, M. E. (2005). Pyrite framboid evidence for oxygen-poor deposition during the Permian–Triassic crisis in Kashmir. *Palaeogeography, Palaeoclimatology, Palaeoecology*, *216*(3), 183-188.

Wignall, P.B. and Newton, R., 1998. Pyrite framboid diameter as a measure of oxygen deficiency in ancient mudrocks. *American Journal of Science*, *298*(7), pp.537-552.

Wijsman, J.W., Middelburg, J.J. and Heip, C.H., 2001. Reactive iron in Black Sea sediments: implications for iron cycling. *Marine Geology*, *172*(3), pp.167-180.

Wildman, R. A., Berner, R. A., Petsch, S. T., Bolton, E. W., Eckert, J. O., Mok, U., & Evans, J. B. (2004). The weathering of sedimentary organic matter as a control on atmospheric O2: I. Analysis of a black shale. *American Journal of Science*, *304*(3), 234-249.

Wilkin, R. T., Barnes, H. L., & Brantley, S. L. (1996). The size distribution of framboidal pyrite in modern sediments: an indicator of redox conditions. *Geochimica et Cosmochimica Acta*, *60*(20), 3897-3912.

Wilkin, R.T. and Barnes, H.L., 1997. Formation processes of framboidal pyrite. *Geochimica et*

Cosmochimica Acta, *61*(2), pp.323-339.

Wilson, P.A., Norris, R.D. and Cooper, M.J., 2002. Testing the Cretaceous greenhouse hypothesis using glassy foraminiferal calcite from the core of the Turonian tropics on Demerara Rise. *Geology*, *30*(7), pp.607-610.

Yang, Y. and Aplin, A.C., 1997. A method for the disaggregation of mudstones. *Sedimentology*, *44*(3), pp.559-562.

Yao, F. X., Arbestain, M. C., Virgel, S., Blanco, F., Arostegui, J., Maciá-Agulló, J. A., & Macìas, F. (2010). Simulated geochemical weathering of a mineral ash-rich biochar in a modified Soxhlet reactor. *Chemosphere*, *80*(7), 724-732.

Yu, J., Huang, Z., Chen, T., Qin, D., Zeng, X., & Huang, Y. (2012). Evaluation of ecological risk and source of heavy metals in vegetable-growing soils in Fujian province, China. *Environmental Earth Sciences*, *65*(1), 29-37.

Zabel, M., Schneider, R.R., Wagner, T., Adegbie, A.T., de Vries, U. and Kolonic, S., 2001. Late Quaternary climate changes in Central Africa as inferred from terrigenous input to the Niger Fan. *Quaternary Research*, *56*(2), pp.207-217.

Zell, P., Stinnesbeck, W., Beckmann, S., Adatte, T. and Hering, F., 2015. The Berriasian–Valanginian (Early Cretaceous) boundary transition at Santa Catarina Ticuá, Oaxaca state, southern Mexico: Ammonites, bivalves, calpionellids and their paleobiogeographic significance. *Journal of South American Earth Sciences*, *62*, pp.33-57.

Zhao, J., Jin, Z., Jin, Z., Hu, Q., Hu, Z., Du, W., Yan, C. and Geng, Y., 2017. Mineral types and organic matters of the Ordovician-Silurian Wufeng and Longmaxi Shale in the Sichuan Basin, China: Implications for pore systems, diagenetic pathways, and reservoir quality in fine-grained sedimentary rocks. *Marine and Petroleum Geology*, *86*, pp.655-674.

Zhu, B., & Wu, X. (2012). Weathering process of black strata and formation of corrosive environmental water. *Procedia Environmental Sciences*, *12*, 984-990.

Zhu, W., Young, L. Y., Yee, N., Serfes, M., Rhine, E. D., & Reinfelder, J. R. (2008). Sulfide-driven arsenic mobilization from arsenopyrite and black shale pyrite. *Geochimica et Cosmochimica Acta*, *72*(21), 5243-5250.